MOLECULAR SIMULATIONS

OF HYDROGEN STORAGE

AND GAS SEPARATION

IN METAL-ORGANIC FRAMEWORKS

Michael Fischer
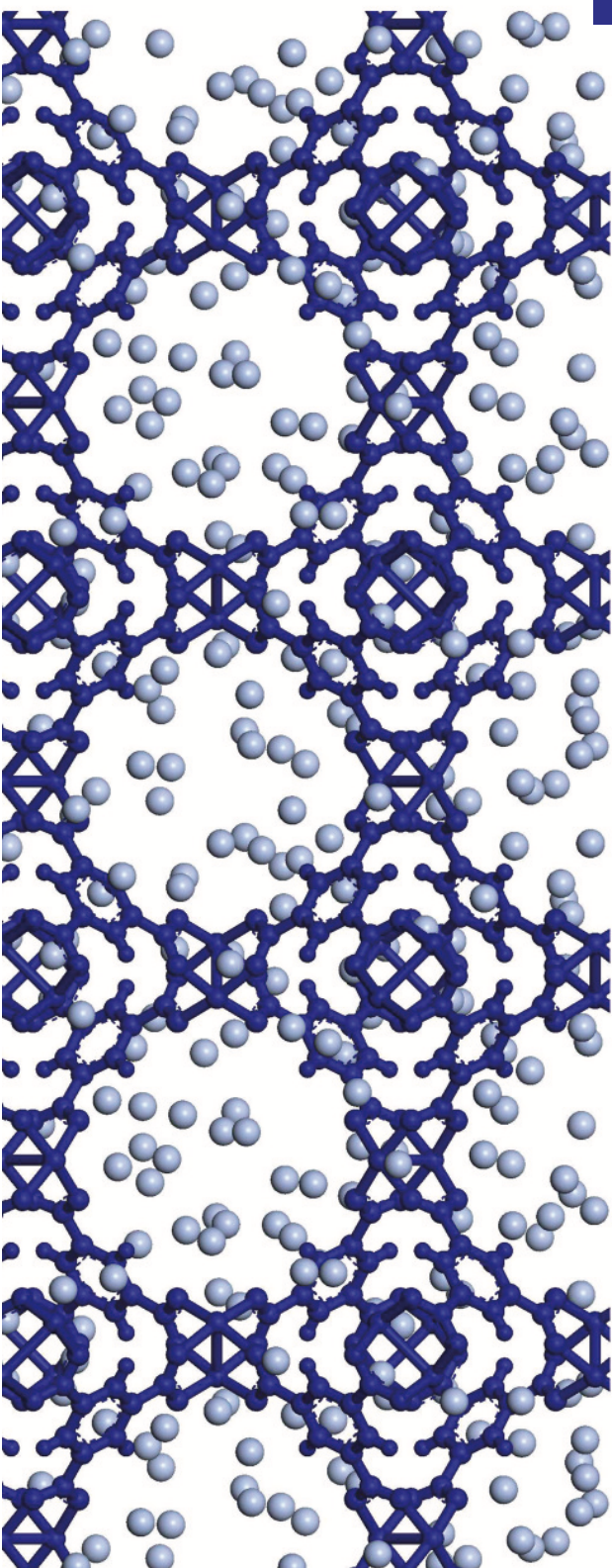
Dissertation

zur Erlangung des Grades

Doktor der Naturwissenschaften

(Dr. rer. nat.)

angefertigt im

Fachbereich Chemie

der Universität Hamburg

HAMBURG, JULI 2011

Die vorliegende Arbeit wurde im Zeitraum von Januar 2008 bis Juli 2011 in der Arbeitsgruppe von Prof. Dr. Michael Fröba am Institut für Anorganische und Angewandte Chemie im Fachbereich Chemie der Universität Hamburg angefertigt.

1. Gutachter: Prof. Dr. Michael Fröba
2. Gutachter: Prof. Dr. Jürgen Heck
Tag der Disputation: 16. September 2011

Erklärung über frühere Promotionsversuche

Hiermit erkläre ich, dass vorher keine weiteren Promotionsversuche unternommen worden sind. Die vorliegende Dissertationsschrift habe ich an keiner anderen Stelle in gleicher oder ähnlicher Form zur Promotion vorgelegt.

Hamburg, den 11. Juli 2011

Michael Fischer

Eidesstattliche Versicherung

Hiermit erkläre ich an Eides statt, dass ich die vorliegende Dissertationsschrift selbständig und allein angefertigt habe. Hierbei wurden keine anderen als die von mir angegebenen Quellen und Hilfsmittel verwendet.

Hamburg, den 11. Juli 2011

Michael Fischer

Contents

1. Introduction

1.1. Hydrogen - Energy carrier of the future?

1.1.1. Global carbon dioxide emissions and climate change

Since the advent of industrialization, the anthropogenic emission of carbon dioxide has led to a significant increase of the global carbon dioxide level. Figure 1.1 shows the atmospheric CO_2 concentration measured at the Mauna Loa laboratory, Hawaii. (*1*) The rise of the CO_2 concentration from 315 ppm in 1958 to 390 ppm in 2010 is evident. Carbon dioxide, like other gases (water vapour, methane, nitrous oxide), is a greenhouse gas: These gases absorb and re-emit heat radiation reflected by the earth's surface, and thus reduce the loss of heat from the planet into space. To a certain extent, the greenhouse effect is necessary to render the earth habitable. However, a considerable increase of the atmospheric concentration of greenhouse gases may have dramatic consequences, such as rapid global warming, rise of the sea level, and increasing frequency of extreme weather events. (*2*) While the first indications of global climate change are already observable, a more drastic evolution can be expected in the medium term. Even if a complete stop of anthropogenic carbon dioxide emissions was achieved within this century, the effects on global temperature and sea level are irreversible on a timescale of 1000 years. (*3*)

Some strategies to actively prevent the release of CO_2 into the atmosphere have been proposed, *e.g.* by sequestration in subterrestrial reservoirs, or by electrochemical or photochemical reduction of CO_2. (*4*) However, neither of these approaches is yet technologically mature. Therefore, the reduction of global carbon dioxide emissions is the most important challenge in order to prevent (or, at least, contain) climate change.

More than 80% of the anthropogenic CO_2 emissions stem from energy-related combustion of fossil fuels. Taking the U.S. as an example, 41% of the emissions produced in 2008 were due to the generation of electric power, and 33% were generated in transportation. (*5*) Thus, cutting down global CO_2 emissions involves two particularly important technological challenges:

Firstly, increasing amounts of electricity must be produced by "clean" technologies (wind power, solar thermal energy and photovoltaics, hydroelectric power), replacing the burning of fossil fuels (coal, oil, gas) in conventional power plants. While these technologies have seen a rapid development in the last years, it remains unclear how much of the global electricity demand can be covered by them. Therefore, it is also necessary to increase the energy efficiency of power-consuming processes.

Secondly, viable alternatives to automobiles powered by combustion engines must be developed. The two most promising technologies rely on electric motors to propel the vehicle: In the first approach, the electricity is stored onboard in a battery. The main drawback is the limited gravimetric energy density of available battery materials, which entails either a prohibitively high weight of the battery unit, or a relatively low range of the vehicle (< 100 km). Therefore, this technology may be applied in a useful way for vehicles that are mainly employed for short travel distances. (6) The second approach is the use of a fuel cell to generate electricity onboard. In principle, different compounds can serve as fuel in the fuel cell. Most research efforts, however, have been directed towards the use of hydrogen. It will be outlined in the following two subsections how hydrogen can be employed as energy carrier, and which obstacles need to be overcome before the large-scale application of hydrogen-powered vehicles can become a competitive option from a technological and economical point of view.
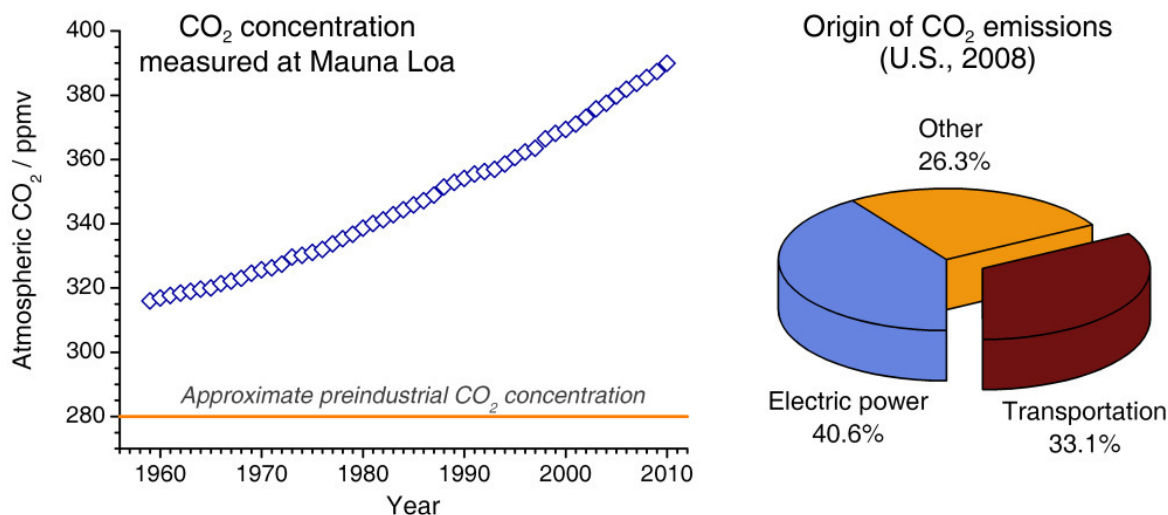
Figure 1.1. *Left:* Atmospheric CO_2 concentration (in parts per million in volume) measured at Mauna Loa laboratory, Hawaii. (*1*) The estimated preindustrial level is indicated by the orange line. (*3*) *Right:* Categorization of energy-related carbon dioxide emissions in the U.S. in 2008 by end-use sector. (*5*)

1.1.2. Hydrogen as a replacement for fossil fuels

In a hydrogen fuel cell, electricity is generated from an electrochemical reaction, which comprises the oxidation of hydrogen, H_2, at the anode, and the reduction of oxygen, O_2, at the cathode:

$$H_2 + \frac{1}{2} O_2 \rightarrow H_2O \qquad\qquad E^\circ = 1.23\,\text{V} \qquad\qquad (1.1)$$
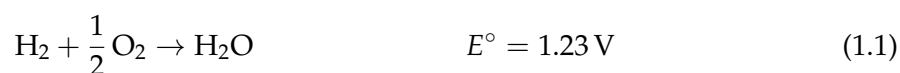
Here, E° is the standard cell potential. The different types of fuel cells that have been developed are classified according to the electrolyte, which seperates the cathode and the anode. The electrolyte is of crucial importance, because it is responsible for the transport of the charge-carrying species. Moreover, the type of electrolyte also determines the operating

temperature, which can vary between 40 °C and 1000 °C. While this issue is not discussed in depth in this context, it should be mentioned that the different fuel cell types have been reviewed exhaustively, for example, in the "Fuel Cell Handbook" published by the U.S. Department of Energy. (*7*)

The efficiency of a fuel cell is not limited by the Carnot cycle, because it does not involve the conversion of thermal energy into mechanical work. Therefore, fuel cells can reach high efficiencies, with a theoretical limit of 83%. (*8*) While the efficiency attained in real systems is considerably lower, it is still higher than the efficiency of typical combustion engines.

As it is apparent from equation 1.1, water is the only end product of the reaction in a hydrogen fuel cell. This makes the process highly attractive from an ecological point of view, because no emissions of CO_2 (or other undesirable by-products) are generated. Oxygen required for the fuel cell can be obtained from air, although the onboard purification can pose some difficulties. The supply of hydrogen, however, is more problematic: In contrast to fossil fuels, there are no natural resources of hydrogen that could be exploited. Instead, it is necessary to produce hydrogen beforehand, and then store it onboard until it is consumed in the fuel cell reaction. Because the H_2 production requires the input of energy, hydrogen must be considered as an energy carrier, rather than a fuel. (*8*) As it will be discussed below, the H_2 production process may generate considerable amounts of carbon dioxide. Therefore, a vehicle running on hydrogen is not necessarily a "zero-emission" vehicle.

As a final remark, it needs to be mentioned that hydrogen can also be used in combustion engines. Again, only water is generated as exhaust product. While some prototype applications have been designed, this technology appears to be less energy efficient than hydrogen fuel cells. (*8*)

1.1.3. Technological issues

There are several technological challenges that need to be tackled before a widespread use of hydrogen as an energy carrier for mobile applications is imaginable. The most important factors that are crucial for the establishment of a hydrogen-based economy are discussed in a recent essay by Armaroli and Balzani. (*8*) The following paragraphs are structured along the lines of this essay, summarizing the main technological requirements without being exhaustive.

As mentioned above, hydrogen must be produced from other chemical feedstocks. Current industrial processes mainly involve the steam reforming of methane, or the gasification of coal. While these processes are economically competitive, they generate considerable amounts of carbon dioxide, and are thus not particularly advantageous when aiming at a reduction of CO_2 emissions. Currently, fundamental research is carried out to produce hydrogen by photochemical or biochemical water splitting. An alternative route that is technically more mature is provided by water electrolysis. This process does not produce emissions, provided that the electricity consumed during electrolysis comes from "clean" sources. Therefore, the two technological challenges mentioned in the first subsection are

actually intertwined: Only the availability of electric power from emission-free electricity sources renders the use of fuel cell vehicles (or battery vehicles) ecologically beneficial.

Depending on the design of the end-use unit, hydrogen must fulfill certain purity requirements. For example, the catalysts used in low-temperature fuel cells can be poisoned even by trace amounts of carbon monoxide. The purification of H_2 on a large industrial scale is a well-established process. (*9*) However, new ways to produce hydrogen, *e.g.* in small decentralized units rather than in large chemical plants, may also necessitate the development of new technologies to obtain a product of the required purity.

Due to the low density of H_2 at ambient conditions, the efficient storage of hydrogen is another technological challenge, particularly with regard to mobile applications: Here, the tank unit can only have a limited weight, and occupy limited space. Because the hydrogen storage problem is a central motivation for this work, this issue is discussed in more detail in the following section.

In order to replace fossil fuels as an energy carrier for mobile applications, hydrogen must be distributed to the end user at regional filling stations. As pointed out by Armaroli and Balzani, there are two main strategies to do so: In a centralized infrastructure, hydrogen is produced in chemical plants, and then shipped to the filling stations. However, the transportation of hydrogen is technically challenging, and involves significant shipping costs. Alternatively, hydrogen could be produced on-site in decentralized units. While this decentralized approach may be advantageous in the long term, technologies to generate hydrogen on a smaller scale in a cost-efficient way are not yet well developed.

Finally, the end-use unit, *i.e.* the fuel cell or the hydrogen combustion engine, must be optimized to ensure maximal efficiency, high durability, and reliability under different conditions. Proton exchange membrane fuel cells, which operate at relatively low temperatures, are currently the most promising candidates. One main drawback is the high cost of the platinum catalyst and the sophisticated polymer membrane. Moreover, a stack of numerous fuel cells is necessary to reach a voltage that is sufficient to power a car, rendering the fuel cell unit heavy and cumbersome.

As an alternative to the approach outlined above, it has been proposed to generate hydrogen onboard by reforming of hydrocarbons or methanol, and then use it to power a fuel cell. (*10*) In particular, the storage of the energy carrier would be much less problematic than in the case of hydrogen. However, there are some important disadvantages: Firstly, the reforming generates carbon dioxide emissions, as mentioned previously. Secondly, the reforming unit is heavy, and requires a long start-up time, two features which are undesirable for mobile applications. However, it is expected that combinations of reforming units and fuel cells will find applications in auxiliary power units.

1.2. Hydrogen storage

1.2.1. Introduction

It is typically assumed that a hydrogen-powered vehicle should be able to cover the same range as a car powered by a conventional combustion engine. For an average consumption of 9 L $(100 \, \text{km})^{-1}$, this corresponds to 45 L of gasoline to travel a distance of 500 km. Hydrogen has a higher energy content than gasoline, with a lower heating value of 120 MJ kg^{-1}, compared to 45 MJ kg^{-1} for petrol (the lower heating value, LHV, corresponds to the amount of heat released during combustion after subtracting the latent heat of water evaporation). Moreover, fuel cells have a higher efficiency than combustion engines. Therefore, it can be estimated that 6 kg of hydrogen would be sufficient to reach comparable travel distances. (*11*) Other estimations arrive at different numerical values, such as 4 kg of hydrogen. (*12*) However, it is obvious that these differences in arithmetics do not affect the general aspects discussed below.

Due to the low density of gaseous hydrogen, 6 kg of hydrogen at room temperature and ambient pressure would occupy a volume of 67 m^3, corresponding to a cube with an edge length of approximately 4 m. Clearly, it is necessary to store hydrogen in a much more compact way for practical mobile applications. There are different approaches to solve this problem, which can be grouped as follows:

- storage of compressed, gaseous hydrogen at room temperature and pressures above 350 bar

- storage of liquid hydrogen at $T = 20 \, \text{K}$

- chemical storage in materials that have a high hydrogen content, such as metal hydrides and complex hydrides, or inorganic or organic molecules ("chemical hydrides")

- physisorption of hydrogen in porous adsorbents

In order to develop technological benchmark values, the U.S. Department of Energy (DOE) has proposed hydrogen storage targets for onboard storage in mobile applications. (*13*) The last version of the often-cited DOE targets values was published in 2009. The 2009 DOE targets are summarized in table 1.1, with intermediate goals for 2010 and 2015, as well as an ultimate target value. In addition to the hydrogen storage capacity, other issues, such as the refuelling time, are also addressed. It should be noted that the DOE targets refer to the system capacity, *i.e.* the hydrogen storage system as a whole, including tank, valves, and other components. In contrast to this, practically all values cited in the following correspond to material-based capacity values, which take into account only the weight (or volume) of the material itself. Thus, the realizable system capacity is necessarily lower. Moreover, the DOE targets refer to the useable capacity, *i.e.* the amount of hydrogen that can actually be delivered at the discharge pressure.

An overview of the different hydrogen storage technologies is given in the following, with a particular emphasis on hydrogen storage by physisorption. Exhaustive reviews covering the different materials have been published by Schüth and co-workers, (*10*) and by Siegel and co-workers, (*11*) among others. While the former article provides a thorough discussion from the point of view of fundamental research, with a particular focus on hydrides, the latter puts more emphasis on actual technological issues.

Table 1.1. Selected DOE targets for onboard H_2 storage systems in light-duty vehicles. (*13*)

		2010	*2015*	*Ultimate*
Gravimetric H_2 capacity	*MJ kg^{-1}*	5.4	6.5	9.0
	mg(H$_2$) g^{-1}	45	55	75
	wt% H$_2$	4.3	5.2	7.0
Volumetric H_2 capacity	*MJ L^{-1}*	3.2	4.7	8.3
	g(H$_2$) L^{-1}	28	40	70
Min./max. delivery temperature	*°C*	-40/85	-40/85	-40/85
Min./max. delivery pressure	*bar*	5/12	5/12	5/12
Filling time for 5 kg H_2	*min*	4.2	3.3	2.5

1.2.2. Conventional means of hydrogen storage

1.2.2.1. High-pressure storage of gaseous hydrogen

The critical temperature of hydrogen is $T_{crit} = 33\,\text{K}$. Therefore, hydrogen cannot be liquefied at room temperature. However, a compression of gaseous H_2 at pressures ranging from 350 to 700 bar permits storage densities that are sufficiently high to be technologically interesting. While pressures below 350 bar are too low to deliver an energy density that lies within the desired range, pressures above 700 bar are inefficient due to the non-ideal behaviour of gaseous H_2, which leads to a relatively small increase of the density on increasing pressure under these conditions. The maximal theoretical volumetric capacity, which can be derived from the bulk properties of hydrogen, corresponds to 23 g L^{-1} at $p = 350\,\text{bar}$, and 37 g L^{-1} at $p = 700\,\text{bar}$. In an actual H_2 benchmark system operating at $p = 700\,\text{bar}$, a gravimetric storage density of 48 mg g^{-1} and a volumetric storage density of 23 g L^{-1} can be reached. (*14*) This system consists of carbon fiber vessels, which are approximately four times lighter than a comparable steel system. (*10*) Compressed-gas hydrogen systems have very short refuelling times: The benchmark system can be completely refilled in three minutes.

The compression of hydrogen consumes an amount of energy that ranges between 12% and 15% of its lower heating value. While this is a considerable energy loss, it is much lower than the energy necessary to liquefy hydrogen. Due to the high degree of compression, safety concerns are particularly important for this storage technology: For mobile applications, it must be ensured that the tank system can withstand even severe crashes.

Although the values of the benchmark system mentioned above still fall short of the DOE targets, compressed-gas hydrogen storage is currently the most mature storage technology. It is used in prototype fuel cell vehicles by different manufacturers, such as Daimler-Benz and General Motors. (*6*) For example, the Mercedes-Benz B-Class F-CELL uses a system of three compressed-gas tanks with a pressure of 700 bar, which store approximately 4 kg of hydrogen (figure 1.2). The car can reach a travel distance of nearly 400 km. (*15*)

Figure 1.2. The Mercedes-Benz B-Class F-CELL as an example for a prototype fuel cell car. The sketch shows the most important technical features: 1 = stack of fuel cells; 2 = compressed-gas hydrogen storage system; 3 = auxiliary lithium-ion battery; 4 = electric motor. Figure reproduced with permission of Daimler-Benz AG. (*15*)

1.2.2.2. Low-temperature storage of liquid hydrogen

As early as 1971, liquid hydrogen was proposed as "fuel of the future" and "logical replacement for hydrocarbons in the 21st century" by Jones. (*16*) Indeed, the use of liquid hydrogen as a storage medium has some advantages: Firstly, the handling of liquids is easier than the handling of compressed gases. Secondly, liquid hydrogen permits higher storage densities: At $T = 20\,\text{K}$ and $p = 1\,\text{bar}$, liquid hydrogen has a density of 71 g L^{-1}, which is approxi-

mately twice the density of compressed hydrogen at room temperature and 700 bar. However, the liquefaction of hydrogen is very energy consuming, requiring approximately 30% of its lower heating value. (*10*)

Despite the use of a sophisticated insulation, the large temperature gradient between the tank and the environment leads to an unavoidable input of heat. Necessarily, some of the hydrogen boils off, and must be released through a valve to prevent an uncontrolled rise to pressures above 10 bar. (*14*) As a consequence, the system gradually loses hydrogen, even when the vehicle is not running, a behaviour that is certainly contrary to customers' expectations. In total, the low energy efficiency, together with boil-off problems, render the cryogenic storage of liquid hydrogen rather unattractive when compared to compressed-gas storage.

1.2.3. Chemical storage of hydrogen

1.2.3.1. Metal hydrides and complex hydrides

Many metals and alloys can absorb relatively large amounts of hydrogen when subjected to a hydrogen atmosphere. In the resulting metal hydride, hydrogen atoms occupy interstitial sites in a metallic matrix (figure 1.3a). This group comprises binary hydrides, such as MgH_2, as well as hydrides of multinary alloys, such as $LaNi_5H_6$. Of the two mentioned examples, MgH_2 is quite attractive due to its high gravimetric and volumetric capacity (7.7 wt% and 109 g L^{-1}, respectively). Although the volumetric storage efficiency of $LaNi_5H_6$ is comparable, it has a low gravimetric capacity of 1.4 wt%. (*17*) However, this system has thermodynamic advantages: Due to the low enthalpy of H_2 desorption of 31 kJ mol^{-1}, $LaNi_5H_6$ completely releases the hydrogen at room temperature and a pressure of 2 bar. (*12*) It is typically assumed that the desorption enthalpy should lie in a "thermodynamic window" between 20 and 50 kJ mol^{-1} for a viable storage system that operates at room temperature or slightly higher temperatures. (*11*) For MgH_2, the desorption enthalpy is considerably higher, ranging near 70 kJ mol^{-1}. Thus, a temperature of approximately 300 °C is necessary to fully desorb H_2. Similar drawbacks arise for several other metal hydrides with high storage densities. (*17*)

Different approaches to adjust the thermodynamics towards lower desorption enthalpies have been proposed. For example, the usage of a mixture of different hydrogen-containing compounds, *e.g.* MgH_2 and $LiBH_4$, can lead to a considerable decrease of the desorption enthalpy with respect to the pure systems due to destabilization. (*11*) Other approaches to change the thermodynamic properties are a reduction of the particle size (nanosizing), and the preparation of nanostructured metal hydrides (nanoconfinement). These techniques, which have been reviewed in (*18*), also accelerate the desorption kinetics. Moreover, the kinetics can be improved by adding suitable catalysts. (*19*)

In contrast to metal hydrides, complex hydrides contain anions in which hydrogen atoms are covalently bonded to a central atom (figure 1.3b). While complex hydrides of various transition metals have been reported, (*17*) the materials that are of particular interest for
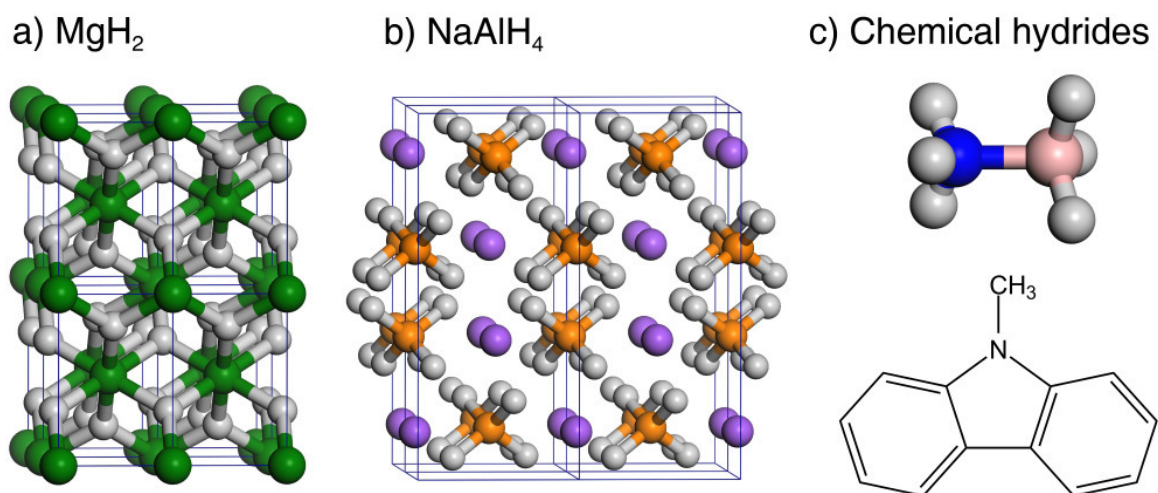
Figure 1.3. *a)* Structure of MgH_2. The compound has a rutile structure, with octahedrally coordinated Mg atoms, and trigonal-planar coordinated H atoms. Interatomic bonds are displayed to highlight the coordination geometry. *b)* Structure of $NaAlH_4$. Each Na cation is surrounded by eight tetrahedral $(AlH_4)^-$ ions in a distorted square antiprismatic geometry. *c)* Two examples for chemical hydrides: Ammonia borane (top), *N*-Methylcarbazole (bottom). The carbazole molecule shown corresponds to the dehydrogenated form.

hydrogen storage applications incorporate anions with main-group elements. The most important compounds incorporate either the alanate ion, $(AlH_4)^-$, the amide ion, $(NH_2)^-$, or the borohydride ion, $(BH_4)^-$, together with charge-balancing alkali or alkaline earth cations. [20] The hydrogen storage properties of sodium alanate ($NaAlH_4$) have been particularly well studied. While the total hydrogen content amounts to 7.5 wt%, only 5.6 wt% are useable for reversible storage applications. Hydrogen can be liberated at moderate temperatures ($< 150\,^\circ C$) in two subsequent decomposition steps with desorption enthalpies of 36 and 47 kJ mol^{-1}, respectively. [20] For pure $NaAlH_4$, the desorption kinetics are very slow, a problem that also exists for many other complex hydrides. However, it has been shown that the kinetics can be massively improved by doping with Ti-compounds and subsequent ball-milling to disperse the dopant in the hydride material. [10] Subsequent to the initial studies in the 1990s, much research has been directed towards an optimization of the storage system for practical applications. The Ti-doping also facilitates the rehydrogenation, which requires rather harsh conditions for the pure compound. Nanosizing is another approach to improve the rehydrogenation kinetics. In summary, $NaAlH_4$ can be considered as a hydride system that holds much promise for hydrogen storage. However, it has been pointed out by Orimo *et al.* that some problems remain with regard to mobile applications: In addition to the necessary improvement of the kinetics, the large amount of heat generated during the rehydrogenation renders an onboard recharging particularly difficult. [20] Amides like $LiNH_2$ have relatively high stoichiometric hydrogen contents up to 10%. The desorption enthalpies of these systems are typically higher than the desired range. In addition, the decomposition leads to the formation of corrosive ammonia in the gas phase. [20]

Lithium borohydride, LiBH$_4$, is a complex hydride with a very high overall hydrogen content of 18.5 wt%. The dehydrogenation occurs in a complex multi-step reaction that is not yet completely understood. The high desorption enthalpy, as well as slow kinetics, render LiBH$_4$ unattractive for practical applications. However, it may be an interesting component in destabilized hydride mixtures. (19) A general problem of borohydrides is the evolution of highly toxic diborane during the decomposition. (20)

In addition to experimental investigations, computational methods have delivered valuable insights into the hydrogen storage in metal hydrides and complex hydrides, particularly with regard to thermodynamics. Different possible applications of *ab-initio* calculations have been reviewed by Wolverton *et al.* (21) These authors focus on the computation of desorption thermodynamics, the prediction of new hydride structures, and the characterization of likely reaction pathways, with particular regard to destabilized hydride mixtures.

1.2.3.2. Chemical hydrides

The term "chemical hydrides" is used to designate hydrogen-rich molecular compounds that can deliver appreciable amounts of hydrogen, *e.g.* through thermal decomposition or hydrolysis (figure 1.3c). For example, ammonia borane, H$_3$N·BH$_3$ is a Lewis acid/base adduct with a total hydrogen content of 19.6 wt%. Approximately two thirds of the total hydrogen content are accessible for practical applications. (22) While the high gravimetric (and volumetric) storage density of this compound is very promising, there are several other obstacles: Firstly, it is required to carefully control the kinetics of a multi-step reaction for a controlled hydrogen release. Secondly, the formation of undesired side products like ammonia and borazine in the gas phase must be avoided. Finally, the decomposition is exothermic, leading to very stable end products. Therefore, onboard rehydrogenation is hardly possible, and it would be necessary to remove the tank from the vehicle and ship it to a chemical plant for regeneration. (10) Despite these limitations, the hydrogen storage properties of ammonia-borane and other amine-borane adducts are intensively studied.

Carbazoles are a group of organic molecules that can take up a significant amount of hydrogen by reaction to the perhydro-form. These compounds could potentially be used as reversible hydrogen storage materials, with gravimetric hydrogen contents between 4 and 6 wt%. However, the high hydrogen release temperature ($> 200\,°\mathrm{C}$ when using a catalyst) and the high boiling point of these compounds are important disadvantages with regard to use in mobile applications. (10)

Cyclic hydrocarbons could also be used as hydrogen carriers. For example, the conversion from cyclohexane to benzene can deliver 7.1 wt% of hydrogen. The high dehydrogenation temperature and the impracticality of onboard rehydrogenation rule out their use as vehicular hydrogen storage materials. It is thus more likely that these materials could come into use as large-scale storage media in a hydrogen-based economy. (10)

1.2.4. Hydrogen storage by physisorption

1.2.4.1. Carbon materials

Due to their high porosity, reflected by high specific surface areas, in combination with a ready availability, activated carbon materials have been used as adsorbents for a long time, *e.g.* in gas separation applications. (*23*) It is therefore not surprising that activated carbons were among the first materials that were investigated for hydrogen storage by physisorption. The body of experimental data on hydrogen adsorption in activated carbons and related materials, such as carbon nanotubes and nanohorns, has been reviewed by Thomas in 2007. (*24*) While excess capacities up to 5 wt% can be reached at $T = 77\,K$ and high pressure (the difference between excess and absolute amount adsorbed is discussed in section 4.5), the H_2 uptake at ambient temperature is much lower, typically not exceeding 0.5 wt%. For cryogenic conditions, a linear correlation between the saturation uptake and the micropore volume (or, alternatively, the specific surface area) can be established, which is sometimes referred to as "Chahine's rule".

The attainable storage capacity in pure carbon materials is limited due to the weak interaction of the hydrogen molecules with the adsorbent, with typical isosteric heats of adsorption ranging between 4 and 6 kJ mol^{-1}. Based on thermodynamic considerations, it has been shown by Bhatia and Myers that the optimal isosteric heat of adsorption for physisorptive hydrogen storage at room temperature amounts to 15.1 kJ mol^{-1}. (*25*) Therefore, much research effort has been directed towards an enhancement of the solid-fluid interaction by chemical modification of the adsorbent. For example, the influence of nitrogen-doping on the hydrogen adsorption properties of zeolite-templated carbons was investigated by Mokaya and co-workers. (*26*) For cryogenic conditions, it was found that N-doping slightly increases the uptake at low pressure, but diminishes the saturation uptake. A parallel study of similar materials by Wang and Yang showed an increase of the room-temperature H_2 uptake by 18% with respect to the unmodified material. (*27*) A solution-phase synthesis of carbon materials substituted with different heteroatoms (phosphorous, boron, nitrogen) was presented by Jin *et al.* (*28*) While the surface area was retained in most cases, an increase of the isosteric heat of adsorption to values ranging between 8 and 9 kJ mol^{-1} was observed for the phosphorous- and boron-substituted materials.

Much of the experimental research on hydrogen storage in activated carbons and related materials was complemented (or, in parts, even driven) by theoretical calculations. Broadly, these calculations can be subdivided in two categories: The prediction of macroscopic properties using force-field based simulations, and the detailed computation of interaction energies via *ab-initio* methods.

In the former category, the adsorption of hydrogen in a carbon slit pore model system was investigated using path-integral Monte Carlo simulations by Wang and Johnson as early as 1998. (*29*) In the same year, the adsorption of hydrogen in carbon nanotubes was studied by Darkrim and Levesque. (*30*) In 2001, Cracknell compared the suitability of different potential models to reproduce experimental adsorption isotherms published for different carbon

materials. (*31*) Interestingly, even a model that assumed a very strong binding massively underestimated the hydrogen uptake when compared to experiment. However, it is now commonly acknowledged that the early experimental measurements, upon which Cracknell had to rely, were actually erroneous, the measured uptakes being orders of magnitude too high. This modelling study can be seen as an early example of the usefulness of a cross-validation of experimental and simulation results. More recent studies of the adsorption of hydrogen in slit-like pores by Kowalczyk and co-workers were mainly directed at a fundamental understanding of the quantum behaviour of hydrogen confined in the pores. (*32, 33*) An exhaustive modelling investigation of the influence of different pore sizes and different potential models on the theoretically attainable H_2 storage capacity was reported by Kuchta and co-workers. (*34*) These authors found that a graphene-H_2 interaction strength of approximately -15 kJ mol^{-1} could allow for hydrogen uptakes of 5 wt% at ambient temperature. In a separate publication, the same authors investigated the effect of a partial substitution of carbon by boron, which led to a slight increase of the interaction energy on increasing boron content. (*35*)

As far as *ab-initio* studies of the interaction of hydrogen with carbon materials are concerned, the model systems that have been studied range from a molecular "complex" consisting of a hydrogen molecule over a benzene ring to periodic systems that contain extended graphene sheets or nanotubes. Due to the inadequacy of density-functional theory to accurately represent the dominant dispersive interactions, the majority of studies employed wave-function based methods. Because the results for molecular model systems will be discussed in more detail in other parts of this work, only some showcase examples for the study of periodic systems are mentioned here. In 2004, Heine *et al.* extrapolated their MP2 results for non-periodic model systems (benzene to coronene) to an extended graphene layer, arriving at an interaction energy of -7.2 kJ mol^{-1} for the most favourable orientation. (*36*) One year later, the same authors used further MP2 calculations to obtain an *ab-initio* benzene-H_2 potential, and then employed this potential to calculate the energy of adsorption for a hydrogen molecule between graphene layers of varying distance. (*37*) It was found that the interaction energy could reach -10 kJ mol^{-1} for interlayer distances of 7 to 8 Å. More recently, the DFT/CC correction scheme was employed by Rubes and Bludský to investigate the adsorption of H_2 at an extended graphene layer, and inside a single-walled carbon nanotube. (*38*) For graphene, the interaction energies ranged from -5.0 to -5.5 kJ mol^{-1} depending on the orientation, value that agreed well with experimental data. The interaction energy inside a nanotube reached up to -7.1 kJ mol^{-1}.

As a final remark on activated carbons, it should be highlighted that these materials are very cheap, and that they can be synthesized from ubiquitous feedstocks, *e.g.* by pyrolysis of corncobs. (*39*) Although their hydrogen storage properties are inferior to those of more sophisticated materials, this may render them economically competitive.

1.2.4.2. Metal-organic frameworks

Construction principle of metal-organic frameworks

As a relatively new class of hybrid materials, metal-organic frameworks (MOFs) have been extensively studied in the last decade, not only due to their versatile structural chemistry, but also with regard to various applications. While metal-organic coordination polymers had been known for a much longer period, the field started to thrive in the late 1990s, when the first MOFs with permanent porosity were presented. [40, 41] Today, the available literature on MOFs is so vast that even the compilation of a comprehensive list of review articles would be challenging. Therefore, only the review article by Férey [42] and the *Chemical Society Reviews* thematic issue on MOFs are mentioned at this point. [43] The diversity of the papers in this issue highlights the numerous applications for which MOFs have been proposed, with contributions on gas storage, gas separation, catalysis, magnetism, and luminescence, among others. Some MOFs exhibit an extraordinary degree of structural flexibility, with dramatic changes of the unit cell size ("breathing") induced by the adsorption of guest molecules or by temperature changes. While this unique behaviour will not be discussed in more detail in this work, it could be exploited for several applications. [44]

MOFs are crystalline frameworks that are generated by the connection of inorganic building units (connectors) by organic linker molecules. In this work, the term "secondary building unit", which is often used to designate the inorganic building units, is avoided, since it appears to be ill-defined. The connectors are often zero-dimensional, but can also be one-dimensional (chains) or two-dimensional (sheets). The topology of the network depends on the geometry of the connector and the linker, as well as the number of connection points. The construction principle of MOFs is visualized in figure 1.4 for two very well-known systems: In the case of IRMOF-1, each Zn_4O tetrahedron is coordinated by six ditopic benzene-dicarboxylate linkers in an octahedral fashion. In the resulting framework, eight $Zn_4O(OOC)_6$ octahedra are located at the corners of a cube, with the bdc linkers spanning the edges. In $Cu_3(btc)_2$, Cu_2 paddle wheels are coordinated in a square-planar fashion by four tritopic benzene-tricarboxylate linkers. As it will be discussed later, the resulting framework can be best described as a combination of octahedra and cuboctahedra.

The crystal structures of many MOFs contain pores whose diameters usually fall in the micropore range (< 20 Å), although some MOF structures with mesopores have also been reported. While these pores are filled with solvent molecules after the synthesis, desolvation leads to a permanent porosity that can be probed by the adsorption of guest molecules, *e.g.* by N_2 physisorption. The specific surface area and the micropore volume can be calculated from these data using well-known relationships that are reviewed, for example, in [45]. These quantities provide a means to compare the porosity of different MOFs, or, more generally speaking, different microporous materials. With ongoing synthetic efforts to prepare new MOF structures, ever-higher surface areas have been reported. In 2010, a new "record-holder" was presented by Yaghi and co-workers: MOF-210 has a BET surface area of 6240 m^2 g^{-1}, and a specific pore volume of 3.6 cm^3 g^{-1}. [46]

Inorganic building unit   Organic linker   Metal-organic framework

a)

Zn₄O tetrahedron   1,4-benzene-dicarboxylate   Zn₄O(bdc)₃ (IRMOF-1)

b)

Cu₂ paddle wheel   1,3,5-benzene-tricarboxylate   Cu₃(btc)₂ (HKUST-1)
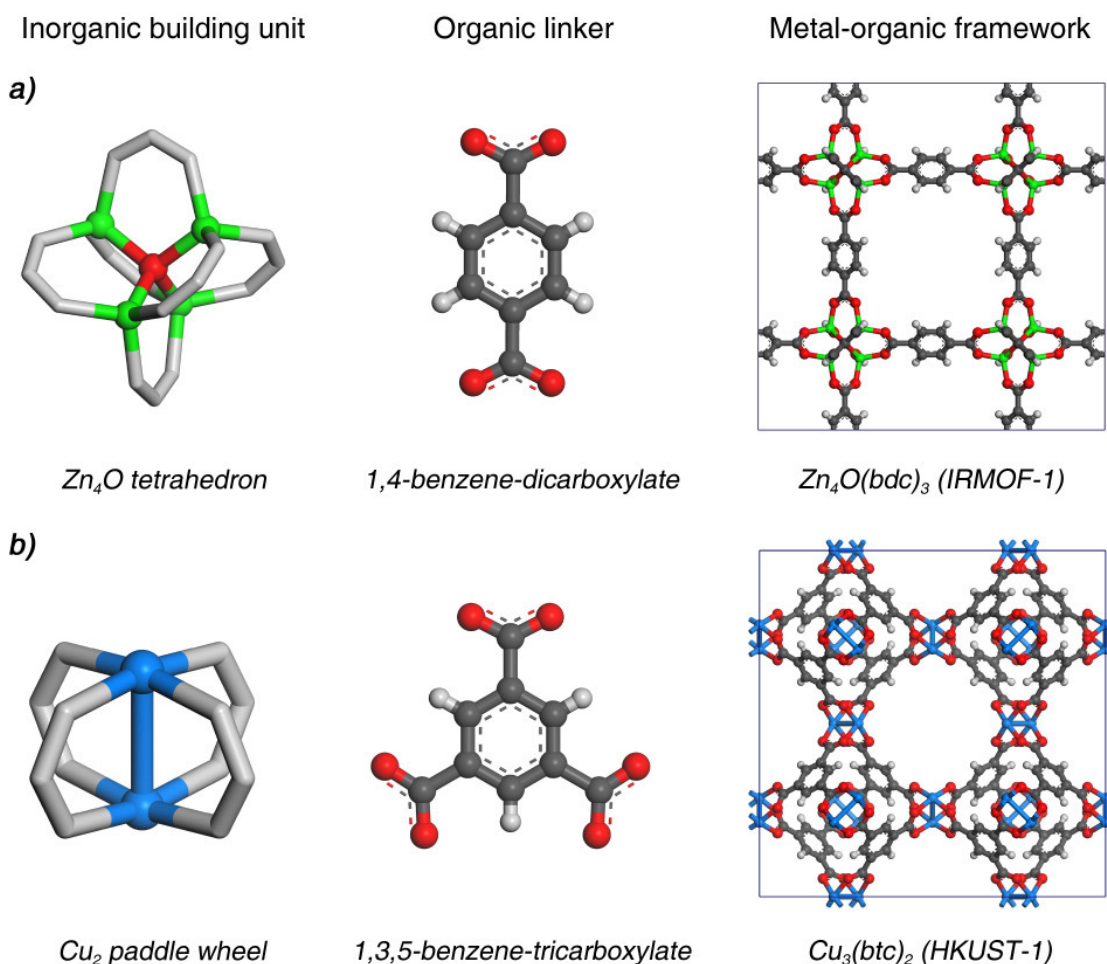
Figure 1.4. Construction principle of metal-organic frameworks, visualized for two show-case MOFs, IRMOF-1 (a) and $Cu_3(btc)_2$ (b). As it is discussed in more detail in 4.3, the "bond" between the two copper centers does not indicate actual metal-metal bonding, but is intended as a topological connection line to emphasize the rigidity of the building unit.

Due to the high porosity of these materials, it is not surprising that MOFs have been extensively investigated as adsorbent materials for the storage of hydrogen, methane, and carbon dioxide, as well as some more exotic guest molecules. In a similar fashion as for activated carbons, initial experimental studies delivered H_2 uptakes that were orders of magnitude too high due to measurement errors. (*47*) To date, the hydrogen adsorption properties of a large number of MOFs have been characterized experimentally, and review articles that compile much of the current literature are available. (*48*, *49*) In this introductory section, only some selected experimental studies will be presented, focussing on two topics of particular interest: Firstly, highly porous MOFs with promising high-pressure hydrogen uptakes will be addressed, which surpass the DOE targets on a gravimetric basis at $T = 77\,K$. Secondly, the enhancement of the solid-fluid interaction induced by the introduction of coordinatively unsaturated metal sites will be discussed. All uptake values reported in the following will refer to cryogenic conditions, *i.e.* $T = 77\,K$. It should be noted that the H_2 adsorption capacities of MOFs at room temperature hardly exceed 1 wt% at high pressures.

Hydrogen adsorption: Experimental studies

IRMOF-1 is not only one of the earliest MOFs for which a permanent porosity was established, but also one of the most well-characterized systems. Continued efforts to improve the synthesis led to an optimized preparation procedure, which was published by Kaye *et al.* in 2007. (*50*) It was found that a protection of the product from air and humidity during the synthesis afforded samples with very high porosity. An excess H_2 uptake of 7.1 wt% was obtained for this material at a pressure of 40 bar. While later studies on IRMOF-1 could not completely reproduce these values, (*51*) an uptake of nearly 6 wt% is still impressive. Also in 2007, a thorough characterization of the hydrogen adsorption properties of MOF-177 was published. (*52*) Independent measurements using different techniques delivered an excess uptake of slightly more than 7 wt% at pressures between 60 and 70 bar. In the original paper, MOF-177 was proposed as a "benchmark" material for characterizations of the H_2 uptake at high pressure and low temperature.

Indeed, the performance of this MOF remained unsurpassed until 2010, when a number of highly porous MOFs were reported (table 1.2). Zhou and co-workers presented a series of Cu-MOFs with hexacarboxylate linkers with identical topology (figure 1.5). (*53*) One of these MOFs, PCN-68, exhibited an exceptionally high porosity. While the excess hydrogen uptake was comparable to MOF-177, the larger pore volume led to a higher absolute uptake, reaching 11.6 wt% at $p = 100$ bar. In this publication, the structure of another MOF with an even higher theoretical pore volume was reported. However, the material collapsed upon desolvation. In a parallel effort, this MOF was synthesized by Farha *et al.*, who designated it as NU-100. (*54*) These authors were also able to completely desolvate the MOF, using an activation with supercritical carbon dioxide. Hydrogen uptake measurements revealed a very high saturation uptake of 9.0 wt%, which is currently the highest value that has been reported. However, MOF-210, a mixed-linker MOF recently synthesized by Yaghi and co-workers, exhibits a higher absolute uptake due to its larger pore volume. (*46*) Again, the desolvation was achieved by activation with supercritical CO_2. These very recent results highlight how the development of new synthesis and activation procedures has sparked the development of novel MOFs with "ultra-high" porosity, which can reach unprecedented gravimetric hydrogen uptakes. However, the performance of these materials on a volumetric basis is much less impressive due to their very low densities.

As discussed above in the context of hydrogen storage in porous carbons, an isosteric heat of H_2 adsorption (q_{st}) exceeding 15 kJ mol^{-1} is necessary to provide for significant uptakes at room temperature. The isosteric heats of MOFs like IRMOF-1 or MOF-177, which do not contain accessible metal centers, range between 4 and 6 kJ mol^{-1}. Thus, these values are similar to the q_{st} values obtained for activated carbon materials. One possibility to enhance the solid-fluid interaction is the development of MOF structures with coordinatively unsaturated ("open") metal sites. While this approach has been reviewed in detail in (*55*), some aspects are highlighted in this context.

Table 1.2. BET surface areas S_{BET}, free pore volumes V_p, and experimental high-pressure H_2 uptakes of highly porous MOFs. N_{sat} is the saturation (excess) uptake, and N_{abs} is the absolute uptake reported for the highest pressure considered. The chemical composition of the MOFs is as follows: IRMOF-1 = $Zn_4O(bdc)_3$; MOF-177 = $Zn_4O(btb)_2$; PCN-68 = $Cu_3(ptei)$; NU-100 = $Cu_3(ttei)$; MOF-210 = $Zn_4O(bte)_{4/3}(bpdc)$. The full names of the linker molecules are given in the Appendix, section A.1.

	S_{BET} / m^2 g^{-1}	V_p / cm^3 g^{-1}	N_{sat} / wt% (p)	N_{abs} / wt% (p)	Ref.
IRMOF-1	3800	n/a	7.1 (40 bar)	10.0 (100 bar)	*(50)*
	3100	1.20	5.8 (35 bar)	n/a	*(51)*
MOF-177	4750	1.69	7.1 (66 bar)	10.0 (72 bar)	*(52)*
PCN-68	5100	2.13	6.8 (50 bar)	11.6 (100 bar)	*(53)*
NU-100	6140	2.82	9.0 (56 bar)	14.1 (70 bar)	*(54)*
MOF-210	6240	3.60	7.9 (50 bar)	14.9 (80 bar)	*(46)*
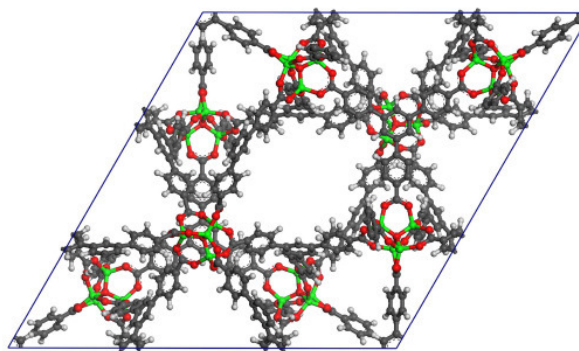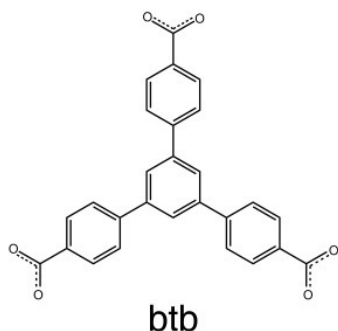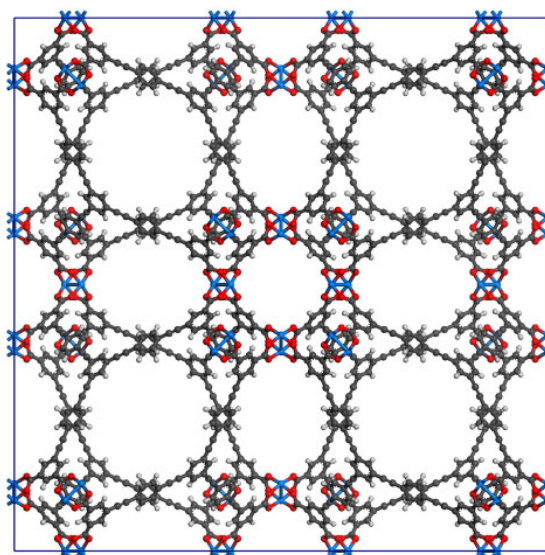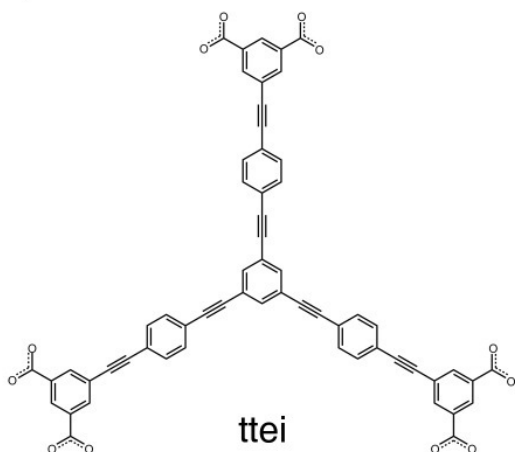
Figure 1.5. Linker molecules and unit cells of MOF-177 and NU-100, two MOFs that exhibit very large free pore volumes of 1.69 and 2.82 cm^3 g^{-1}, respectively.

$Cu_3(btc)_2$ is a showcase example of a MOF with unsaturated metal sites: As is visible from figure 1.4, each of the copper centers of the Cu_2 paddle wheel has one free axial coordination site. After the synthesis, solvent molecules are coordinated to these centers. However, the solvent molecules can be removed by a thermal activation in vacuum, rendering these sites accessible for other guest molecules in adsorption experiments. Because the interaction of the metal centers with hydrogen is stronger than the weak dispersive interaction with the rest of the framework, the adsorption at these sites is reflected by a relatively sharp rise in the adsorption isotherm at low pressures, and an isosteric heat of hydrogen adsorption that is somewhat higher than in MOFs without unsaturated metal sites, ranging between 6 and 7 kJ mol^{-1}. Apart from these phenomenological explanations, the first experimental evidence for hydrogen adsorption at the unsaturated copper centers of $Cu_3(btc)_2$ was obtained in IR-spectroscopic measurements: In their *in-situ* investigation of H_2-loaded samples published in 2006, Bordiga and co-workers observed an IR stretching band at 4100 cm^{-1} that was considered indicative for a specific metal-hydrogen interaction. [56] The same year, a direct observation of D_2 adsorption at the copper centers through low-temperature neutron diffraction experiments was reported by Peterson *et al.* [57] The Cu-D_2 distance of approximately 2.4 Å is significantly lower than the sum of the van der Waals radii of copper and D_2, an observation that provides further evidence for a relatively strong, localized interaction. Interestingly, no indications for a significant elongation of the H-H bond length have been observed in inelastic neutron scattering experiments, although it could be expected that such an elongation occurs upon coordination to the metal center. [58]

Following these initial investigations, much scientific effort has been directed towards the synthesis and characterization of new MOFs with unsaturated metal sites as potential hydrogen storage materials. The low-pressure adsorption isotherms of some characteristic examples are displayed in figure 1.6b. Shortly after the studies of $Cu_3(btc)_2$ had been published, two isostructural MOFs with a benzene-tris-tetrazolate linker and different metal species (Mn, Cu) were reported by Long and co-workers. [59, 60] Direct evidence for the adsorption of hydrogen at the metal centers was obtained in neutron diffraction experiments. The manganese compound exhibits a high isosteric heat of H_2 adsorption, exceeding 10 kJ mol^{-1} at low coverage. A value of q_{st} of nearly 12 kJ mol^{-1} was found more recently for an isostructural Fe-MOF. [61] In 2008, Chen *et al.* reported a mixed-metal MOF (M'MOF), which contains layers of trinuclear Zn_3 units bridged by bdc linkers. [62] These layers are pillared by a salen-type linker that incorporate a square-planar coordinated copper center (figure 1.6a). While the total hydrogen storage capacity of M'MOF is very limited due to the low pore volume, a high initial isosteric heat of H_2 adsorption of 12.3 kJ mol^{-1} was reported. Since the isosteric heats of other MOFs that contain layers with comparable zinc-containing building units are considerably lower, this observation was attributed to the strong interaction of hydrogen with the Cu centers, which are accessible from two sides.

In a combined theoretical and experimental study, Zhou and co-workers investigated the hydrogen adsorption in MOF-74 analogues with different metal centers (Mg, Mn, Co, Ni, Zn). [63] The sequence of the isosteric heats of H_2 adsorption observed for the different

metals was found to be in agreement with the Irving-Williams series. According to this sequence, which was derived from an extensive analysis of experimental data, the stability of high-spin complexes formed by divalent first-row transition-metal cations follows the order: Mn < Fe < Co < Ni < Cu > Zn. (*64*) In the original paper, the Irving-Williams series was rationalized with an increase of electrostatic interactions due to the decrease of the ionic radius (leading to an increase of the charge-to-radius ratio), as well as an increase of orbital interactions, which is correlated with the evolution of the second ionization potential. As no Cu-analogue of MOF-74 has been reported so far, the strongest interaction can be expected for the Ni-analogue. Indeed, the highest isosteric heat of hydrogen adsorption was observed for this material, with a value of 12.9 kJ mol^{-1}. This result is in excellent agreement with earlier spectroscopic investigations on the same material. (*65*)

Finally, it should be pointed out that the incorporation of unsaturated metal sites is not the only strategy to enhance the solid-fluid interaction. Another possibility is the postsynthetic introduction of metal cations, such as Li^+ or Mg^{2+}, into the MOF structure. In principle, each of the cations can coordinate several hydrogen molecules. An incorporation of these cations was achieved via alkoxide formation, and a moderate increase of the affinity towards H_2 was observed. (*66, 67*) Other researchers used a covalent postsynthetic modification of the linker molecules to tune the pore size, thereby increasing the solid-fluid interaction. (*68*) Finally, the doping of MOFs with small amounts of platinum can also enhance the amount of hydrogen adsorbed. This is attributed to a dissociation of the H_2 molecules at the Pt catalyst, a mechanism termed "spillover". (*69*)
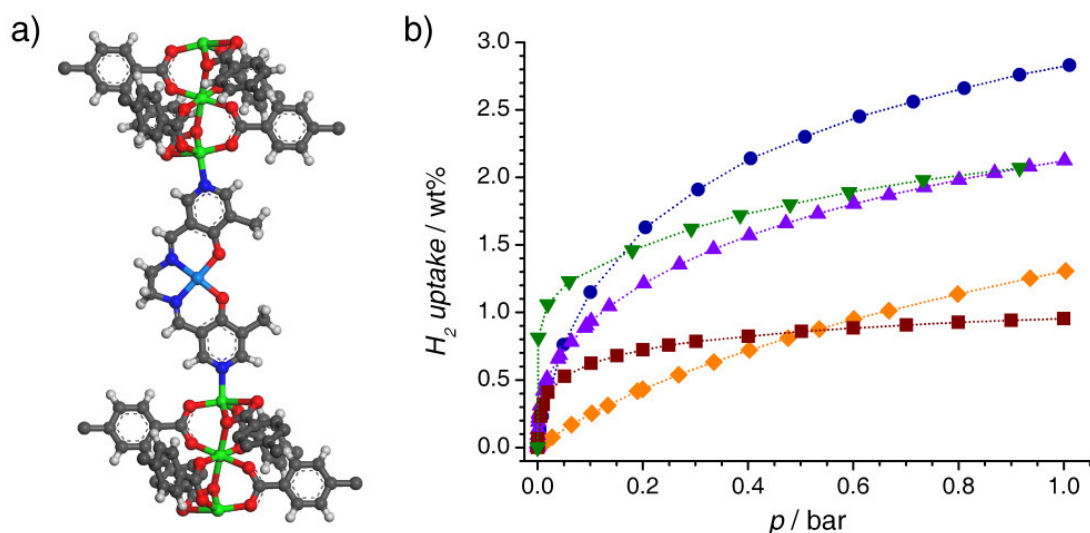
Figure 1.6. *a)* Salen-type linker of M'MOF, bridging two Zn_3 units. *b)* Hydrogen adsorption isotherms ($T = 77$ K) of MOFs with relatively high isosteric heats of adsorption: $Cu_3(btc)_2$ (blue circles), $(Mn_4Cl)_3(btt)_8$ (purple triangles), M'MOF (dark red squares), and $Ni_2(dhbdc)$ (green, inverse triangles). The adsorption isotherm of IRMOF-1 is displayed for comparison (orange diamonds). The plot shows the correlation between the isosteric heat of adsorption and the rise of the isotherm at very low pressures. Data are from (*70*) [IRMOF-1], (*71*) [$Cu_3(btc)_2$], (*59*) [$(Mn_4Cl)_3(btt)_8$], (*62*) [M'MOF], and (*63*) [$Ni_2(dhbdc)$].

Hydrogen adsorption: Molecular modelling

Molecular modelling methods have been widely employed to develop a better understanding of the mechanisms governing the adsorption of H_2 in MOFs, and to propose new materials with improved hydrogen storage properties. Computational studies of MOFs are facilitated by their crystallinity: A structural model of the adsorbent can be taken directly from published crystal structure data. In contrast to this, the construction of realistic models of amorphous materials is rather laborious. As the number of publications reporting results of theoretical calculations has grown rapidly over the last few years, several reviews have appeared quite recently: An exhaustive account of the literature on molecular modelling applied to MOFs published until early 2008 has been compiled by Keskin *et al.* (*72*) This paper gives a general survey of the application of computational methods, with the adsorption of hydrogen being only one field of interest. A review by Goddard and co-workers, published somewhat more recently, focusses specifically on H_2 adsorption, with a particular emphasis on strategies to enhance the solid-fluid interaction. (*73*) In 2010, Sastre provided an overview over the application of *ab-initio* methods in this field. (*74*) Due to the vast number of original research articles on this topic, only a few showcase examples will be presented in the following. They are ordered according to the applied methodology, rather than the specific system under study.

As it will be outlined in section 3.2, the macroscopic adsorption properties of a porous material can be predicted from grand-canonical Monte Carlo (GCMC) simulations. The application of this method requires an adequate representation of the interatomic interactions. The most straightforward way to obtain these interaction parameters is the use of generic force-field parameters from the literature. Early predictions of H_2 adsorption isotherms practically exclusively relied on literature force fields: In 2005, Garberoglio *et al.* studied the adsorption of hydrogen in different MOFs, such as IRMOF-1, IRMOF-8, and manganese formate, and compared the performance of different potential models. (*75*) Subsequently, a systematic investigation of the IRMOF series as a set of isoreticular systems (*i.e.* MOFs having the same network topology) was published by Snurr and co-workers. (*76*) Based on these computations, it was possible to establish some correlations between structural properties and the amount of H_2 adsorbed: While the uptake at 0.1 bar (and $T = 77\,\text{K}$) shows a correlation with the isosteric heat of adsorption, the uptake at 120 bar correlates with the free pore volume. In a subsequent study, the influence of framework catenation (*i.e.* the structural interpenetration of two frameworks) was studied. (*77*) It was found that the catenation tends to enhance the hydrogen uptake at low temperature and low pressure due to the decrease of the pore size, which results in a stronger interaction of the adsorbed molecules with the pore walls. On the other hand, catenation is not beneficial at higher temperatures and pressures due to the reduction of the free pore volume (figure 1.7).

While GCMC simulations with literature interaction parameters are quite routinely applicable for standard conditions, more recent studies have been directed at systems that cannot be realized experimentally: For example, Snurr and co-workers studied hypothetical IRMOFs assuming a strongly enhanced solid-fluid interaction in order to draw some con-

clusions on the interaction strength that would be necessary to fulfill the DOE targets at room temperature: In an early publication by Frost and Snurr, it was found that an isosteric heat of hydrogen adsorption of 10 to 15 kJ mol^{-1} in conjunction with a free pore volume of 1.6 to 2.4 cm^3 g^{-1} could be sufficient to achieve a storage capacity of 6 wt% at room temperature and 120 bar. (*78*) Later on, this approach was refined by Bae and Snurr, who focussed on the H$_2$ capacity that can be delivered between a maximal pressure of 120 bar and a discharge pressure of 1.5 bar. (*79*) For a MOF having a pore volume comparable to IRMOF-1, it was concluded that a q_{st} value of approximately 20 kJ mol^{-1} would be necessary to arrive at a deliverable capacity of 6 wt%. Another study by the same authors extended the pressure range beyond the pressures that are typically investigated experimentally and computationally. (*80*) The main findings were that a MOF with a very large pore volume (≈ 4 cm^3 g^{-1}) could meet the gravimetric DOE targets at pressures of 300 bar and room temperature. On the other hand, the volumetric DOE targets would require much higher pressures (> 1000 bar), or a massive increase of the isosteric heat of H$_2$ adsorption.
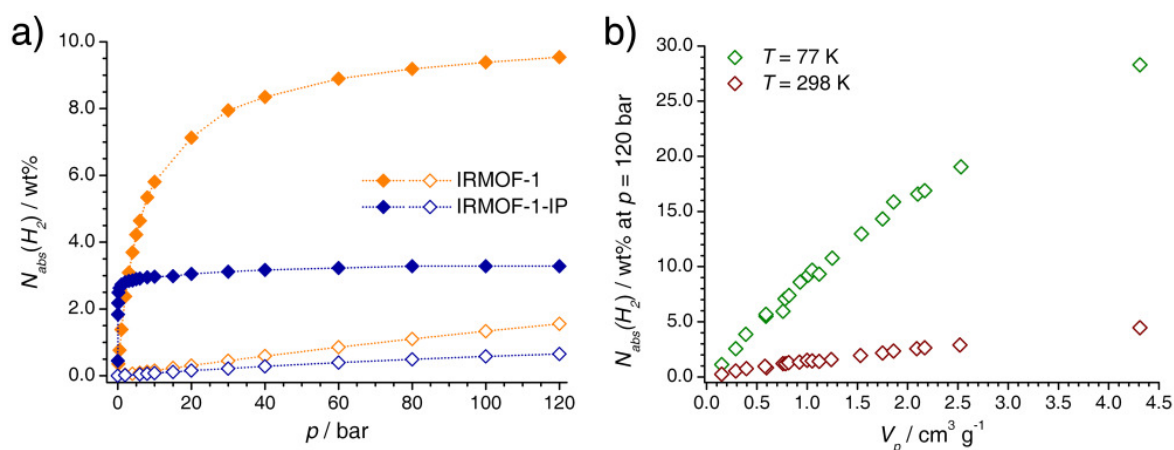
Figure 1.7. *a)* Calculated H$_2$ adsorption isotherms for IRMOF-1 and a hypothetical interpenetrated polymorph IRMOF-1-IP. (*77*) The hydrogen uptake is given in absolute values. Closed symbols correspond to a temperature of 77 K, open symbols to 298 K. *b)* Calculated absolute H$_2$ uptake at $p = 120$ bar for different MOFs, plotted as a function of the pore volume V_p. (*80*) The results clearly show the correlation between the high-pressure H$_2$ uptake and the pore volume. The data points for the largest pore volume of 4.3 cm^3 g^{-1} correspond to IRMOF-16, a MOF for which no successful activation has been reported so far.

Instead of using parameters from a literature force field, the interaction parameters can also be derived from *ab-initio* calculations. Because density-functional theory does not provide for an adequate description of dispersive interactions, most studies following this approach have used wave-function based methods. Pioneering work was carried out by Goddard and co-workers, who reported simulation results for IRMOF-1 and related compounds in 2007. (*81*) The parameters were obtained from MP2 calculations for molecular model systems that were designed to represent the interaction of a hydrogen molecule with the inorganic building unit and the linker molecule, respectively. In addition to IRMOF-1, isoreticular MOFs with longer linkers and other metal centers were studied. The same authors later

extended the approach to Li-functionalized MOFs, for which high H_2 uptakes at room temperature were predicted due to the strong electrostatic interaction of hydrogen molecules with the lithium atoms. (*81*) The authors assumed a direct binding of lithium atoms (rather than Li^+ ions) to the aromatic rings of the MOF linkers, a coordination that has not yet been reported experimentally. A similar route was followed by Klontzas *et al.*, who proposed a series of Li-alkoxide functionalized members of the IRMOF series. (*82*) GCMC simulations predicted a hydrogen uptake of up to 4 wt% at room temperature and a pressure of 100 bar. Interestingly, this simulation study preceded the first experimental reports of Li-alkoxide functionalized MOFs mentioned above. (*66*, *67*) Very recently, a detailed investigation by Snurr and co-workers showed that the interaction of H_2 with lithium alkoxide moieties is too weak to significantly enhance the storage capacity at room temperature. (*83*) Instead, these authors proposed a functionalization with magnesium or transition-metal alkoxides. In particular, binding energies of approximately 80 kJ mol^{-1} were obtained for copper and nickel alkoxides, which were due to strong orbital interactions between hydrogen and the metal center.

Typical modelling studies of hydrogen adsorption in MOFs either represent all interactions by a simple potential model (Lennard-Jones or Morse potential), or combine such a potential to account for dispersive interactions with a point-charge model for electrostatic interactions. A more sophisticated, but computationally very expensive approach has been proposed by Belof *et al.* (*84*) Here, polarization interactions were explicitly included in the Monte Carlo simulations using the Thole-Applequist model, which employs an iterative procedure to calculate the induced dipole contributions. A constant loading simulation for an In-MOF with a charged framework and charge-balancing nitrate anions showed a significant impact of the inclusion of polarization effects on the calculated radial distribution function. A subsequent study by the same authors showed that the effect of polarization interactions is negligible for IRMOF-1 due to the lower polarity of the pore walls. (*85*)

While the prediction of macroscopic properties, such as adsorption isotherms, requires the usage of simple analytical expressions to represent the interatomic interactions, thereby necessarily introducing an empirical element, electronic structure methods can provide detailed insights at a microscopic level. Numerous studies have addressed the interaction of hydrogen with specific regions of MOF frameworks, employing either wave-function based methods or density-functional theory (DFT). Most of the early papers, published between 2004 and 2008, used IRMOF-1 as a model system. As pointed out by Keskin *et al.*, there is considerable disagreement between the results obtained by different research groups. (*72*) On the one hand, this can be attributed to the frequent use of DFT in these works, which is not able to accurately represent dispersive interactions. On the other hand, the deviations among results obtained with the same method highlight the dependency of the results on other computational issues. In a study by Sauer and co-workers published in 2009, high-quality wave-function based methods were used to obtain accurate interaction energies for hydrogen adsorbed at four different adsorption sites of IRMOF-1, three of them being located at the inorganic connector, and the fourth one lying above the benzene ring of the

linker. (*86*) These authors also performed a detailed analysis of vibrational effects. The corrected interaction energies were then used to predict the adsorption isotherm at $T = 77\,\text{K}$ using a multi-site Langmuir model, which assumes a fractional filling of distinct adsorption sites. Good agreement with experimental data was observed.

Due to computational restrictions, it is (currently) not feasible to carry out calculations with highly accurate wave-function based methods for periodic MOF structures. While standard DFT calculations are not able to deliver quantitatively correct energies, a recent development by Langreth and co-workers permits an explicit treatment of these interactions. This method, termed vdW-DFT, has been applied to calculate an energy profile for hydrogen in $Zn_2(bdc)_2(ted)$, with (ted) = triethylendiamine. (*87*) Interaction energies up to -10 kJ mol^{-1} were obtained for the energetically most favourable regions of the pore. However, it was pointed out that the actual binding energy is reduced by 2 to 3 kJ mol^{-1} due to rotational and vibrational effects. An explicit prediction of rotational-translational transitions using the same method was applied in a subsequent study of MOF-74, the results being in good agreement with experimental inelastic neutron scattering data. (*88*)

While DFT is not adequate in cases where dispersive interaction are dominant, it can provide useful insights into the strongly localized interaction of hydrogen with unsaturated metal centers. For example, Head-Gordon and co-workers computed the binding energy for hydrogen interacting with bare metal centers and metal complexes with open coordination sites, using both DFT and MP2 calculations. (*89, 90*) The variations of the interaction strength induced by changes of the metal center and the ligand environment were analyzed in detail. Another study of metal complexes as model systems was reported by Kosa *et al.*, who focussed on a comparison of Mg^{2+} and Ni^{2+} centers. (*91*) It was observed that nickel binds hydrogen much more strongly than magnesium due to orbital interactions. Quite different conclusions were drawn by Zhou and Yildirim, who studied the interaction of H_2 with molecular $Mn_4Cl(N_4CH)_8$ units as a model system of the inorganic connector of $(Mn_4Cl)_3(btt)_8$. (*92*) Here, electrostatic interactions were found to be the dominant factor, whereas there were no indications of a significant charge transfer.

A few DFT studies of the interaction of hydrogen with unsaturated metal centers have used periodic MOF structures, rather than molecular model systems. For example, Zhou and co-workers studied the interaction of hydrogen with the metal sites in structural analogues of MOF-74 with different metal centers. (*63*) While there was no quantitative agreement between the DFT energies and the experimental isosteric heats of hydrogen adsorption due to the neglect of dispersive interactions in the computations, the DFT calculations reproduced the observed trend very well (figure 1.8). As mentioned above, the dependence of the interaction strength on the nature of the metal center was in accordance with the Irving-Williams sequence. In particular, the strongest interaction was observed for Ni^{2+}, the cation with the smallest ionic radius. Because electrostatic effects are a main basis of the Irving-Williams sequence, the authors concluded that the nature of the metal-hydrogen interaction is predominantly electrostatic. Another periodic DFT study was reported by Brown and co-workers, who predicted inelastic neutron scattering spectra of hydrogen in $Cu_3(btc)_2$. (*58*)
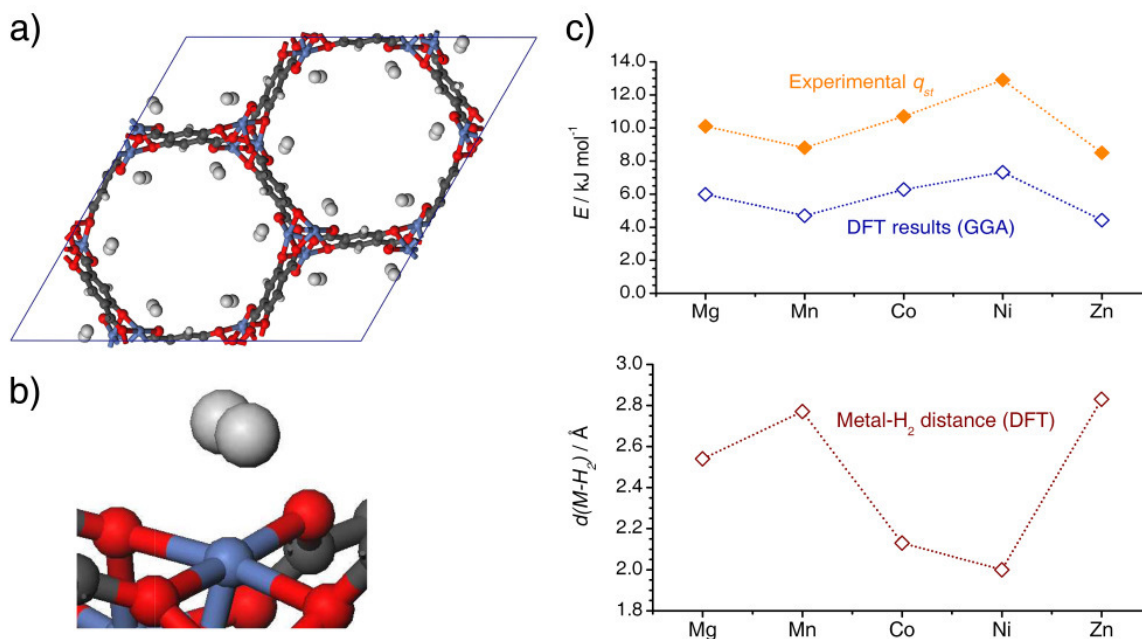
Figure 1.8. Results of DFT calculations for hydrogen adsorbed in MOF-74 analogues obtained by Zhou *et al.* (*63*) *a)* Unit cell of $Ni_2(dhbdc)$ with H_2 molecules adsorbed at the metal centers. *b)* Detailed view of a hydrogen molecule coordinated to the Ni^{2+} center, $d(Ni - H_2) = 2.0$ Å. *c)* Comparison of DFT interaction energies with experimental isosteric heats of H_2 adsorption obtained for five different metal centers (top), and plot of DFT metal-H_2 equilibrium distances (bottom).

It is well known from coordination chemistry that hydrogen can form stable ("Kubas-type") complexes with transition metals. (*93*) The metal-hydrogen bonding is based on an interaction of the filled (σ) orbital of the H_2 molecule with empty *d*-orbitals of the metal center, as well as a backdonation of electron density from the metal center to the empty σ^* orbital of the H_2 molecule. The interaction leads to an elongation of the H-H bond, and can even induce bond breaking and formation of a dihydride. Based on theoretical considerations, it has been proposed to exploit this effect in hydrogen storage materials. For example, Sun *et al.* predicted binding energies up to -47 kJ mol^{-1} for hypothetical Cr- and V-MOFs from DFT calculations. (*94*) A particular emphasis was put on the role of the electronic structure of the metal center. Experimentally, comparably strong interactions could not yet be observed in MOFs, with the metal-hydrogen interactions being orders of magnitude weaker than in actual Kubas-type metal-H_2 complexes. Alternatively, it has been proposed to graft silica surfaces with organometallic fragments, which can then form stable metal-hydrogen complexes. Indeed, initial experimental investigations revealed that metal-grafted mesoporous silicas exhibit a significantly higher heat of hydrogen adsorption than unmodified silica materials. (*95*) A DFT study of these systems confirmed the importance of Kubas-type interactions. (*96*) Of the three early transition metals studied (Ti, V, Cr), the strongest interaction was observed for titanium-containing fragments, with binding energies ranging from -16 to -48 kJ mol^{-1} depending on the auxiliary ligand.

1.2.4.3. Other microporous materials

Zeolites

Due to their continued importance as adsorbent materials, the hydrogen storage properties of zeolites were investigated relatively early. For example, H_2 adsorption measurements in Silicalite were reported as early as 1994. (*97*) In 2000, a combined experimental and computational study assessed the hydrogen adsorption properties of zeolite NaA. (*98*) A more exhaustive investigation of ion-exchanged zeolites with different topologies was published in 2005 by Langmi *et al.* (*99*) In this work, it was found that the uptake capacity of the best-performing system (zeolite CaX) does not exceed 2.2 wt% at a temperature of 77 K. Due to their relatively high densities, which translate into low specific pore volumes, zeolites cannot be considered as particularly promising materials for hydrogen storage.

Covalent-organic frameworks

Covalent-organic frameworks (COFs) are materials that are, in some sense, related to MOFs. Instead of containing metal clusters as inorganic building units, only non-metal molecular building blocks are connected via covalent bonds, forming periodic, highly porous structures, often with densities below $0.5\,g\,cm^{-3}$ (assuming a completely desolvated, uncollapsed framework). The first COFs were presented in 2005 by Yaghi and co-workers. (*100*) In the field of COFs, molecular simulation studies of hydrogen adsorption preceded the first successful experimental investigations. The earliest paper was published by Garberoglio, who predicted excess adsorption capacities of up to 10 wt% (at $T = 77\,K$) for COF-105 and COF-108 using generic force-field parameters (figure 1.9). (*101*) An investigation by Goddard and co-workers, who derived the force-field parameters from MP2 calculations, arrived at similar uptake values. (*102*) The corresponding experimental data, published by Furukawa and Yaghi in 2009, indeed revealed exceptionally high H_2 uptake values for COF-102, nearly reaching 7 wt%. (*103*) However, these capacities fell short of the most optimistic predictions based on molecular simulations. Since no adsorption measurements for the most highly porous COFs have been reported yet, it cannot be taken for granted that the very high uptake values obtained in simulations can be realized. In a similar fashion as for MOFs, the effect of Li-doping has been studied for COFs using molecular modelling methods. For Li-doped COF-108, high hydrogen storage capacities at room temperature were predicted by Cao *et al.*, nearly reaching 7 wt% at a pressure of 100 bar. (*104*) The experimental realization of these systems remains an unresolved issue.

Porous polymers

Polymers with intrinsic microporosity (PIMs) are another group of porous materials that have attracted much scientific attention during the last years. (*105*) Hydrogen adsorption measurements have been performed for some of these systems. For example, Cooper and co-workers measured a H_2 uptake of 1.7 wt% ($T = 77\,K$, $p = 1\,bar$) in a hypercrosslinked polymer obtained from *para*-dichloroxylene monomers. (*106*) These authors also constructed an atomistic model of the polymer and performed molecular simulations to develop

a better understanding of the microscopic structure. In particular, it was found that the model contained occluded voids which gave a significant contribution to the simulated hydrogen uptake. Due to this, a scaling of the simulation results was necessary to obtain good agreement with the experimental data. Quite recently, very high hydrogen uptakes were reported by Li *et al.* for Li-doped microporous polymers. (*107*) Doping of 0.5 wt% lithium resulted in a storage capacity of 6.1 wt% H_2 at $T = 77$ K and $p = 1$ bar, compared to 1.6 wt% for the undoped polymer. This value is among the highest reported for hydrogen storage in porous materials under these conditions. Interestingly, the isosteric heat of adsorption increased only slightly, from 7.7 to 8.1 kJ mol^{-1}. Moreover, doping with larger amounts of lithium led to a drastic reduction of the H_2 uptake. Therefore, it is apparent that these initial results require further validation to develop a better understanding of the underlying phenomena.
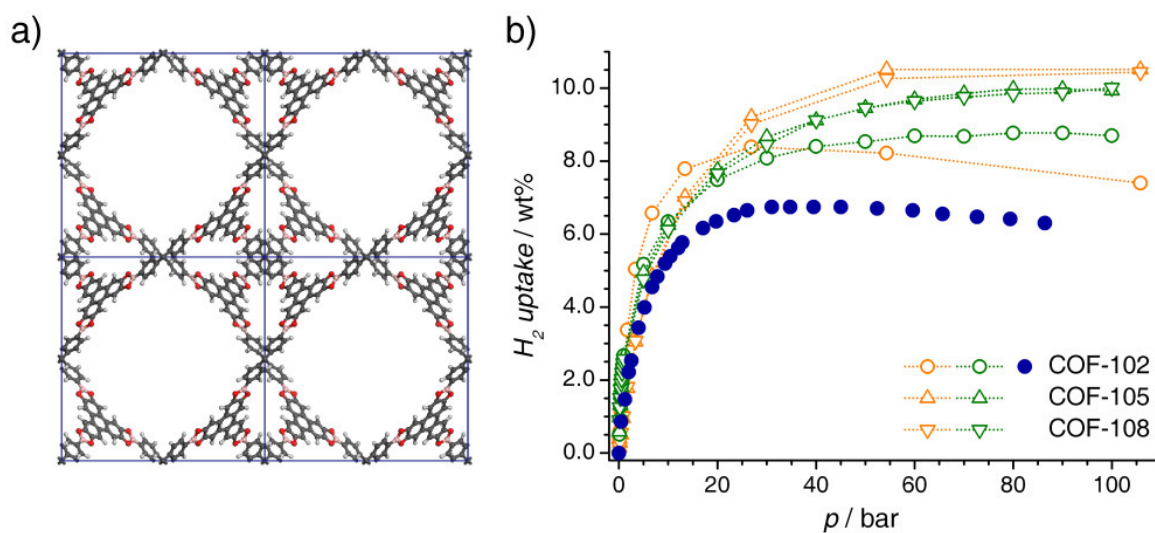
Figure 1.9. *a)* Structure of COF-108, a highly porous material with a theoretical density of 0.17 g cm^{-3} for a (hypothetical) completely activated form. (*108*) *b)* Calculated H_2 adsorption isotherms for COF-102, COF-105, and COF-108. Results from Garberoglio are shown as orange symbols, (*101*) results from Han *et al.* as green symbols. (*102*) The experimental isotherm obtained for COF-102 is shown for comparison (blue symbols). (*103*)

1.3. Gas separation

1.3.1. Introduction

Many chemical production processes involve the separation or purification of gases, either because the purified gas is the desired end product, or because the further processing requires a reactant gas of a certain purity. Therefore, the separation of gas mixtures is a topic of high economic relevance. Some particularly important examples are air separation, *i.e.* the production of pure N_2 and O_2 from air, purification of hydrogen or methane, removal of carbon dioxide or hydrogen sulfide from biogas, and separation of alkane/alkene mixtures. (*23*) The most important separation techniques are cryogenic distillation, absorption in solvents, adsorption-based separation, and membrane-based separation. While cryogenic distillation is able to deliver products of very high purity, it is also a very energy-consuming technology. Moreover, it is most efficient when operating on a large scale. The absorption in solvents, such as amine scrubbing to remove carbon dioxide, can also permit effective separations at reasonable cost, however, the regeneration of the solvent may require the input of a considerable amount of heat.

Adsorption-based separations exploit differences in the affinity of the adsorbent towards the components of the gas mixture: The component that is preferentially adsorbed is enriched in the adsorbed phase, and depleted in the gas phase. In the most extreme case, one component (or several components) are not adsorbed at all due to size or shape exclusion effects. Very high selectivities can be reached in these molecular sieve separations. (*109*)

The most important industrial adsorptive separation processes are pressure-swing adsorption (PSA) and temperature-swing adsorption (TSA). (*110*) During the second half of the 20th century, the increased availability of well-defined adsorbent materials (activated carbons, zeolites, silica gels) has led to the development of several PSA and TSA processes on an industrial scale. Activated carbons are the most widely used adsorbents due to their good availability, large surface areas, and easy regeneration. Applications in the field of gas separation include the removal of organic molecules (solvent vapours, volatile organic compounds) from air, the separation of steam-reforming off-gas, and gas desulfurization. (*111*) Molecular sieve carbons are employed in hydrogen and helium purification, and in the separation of nitrogen from air. The usage of zeolitic adsorbents in separation applications has been reviewed in detail by Dunne: (*112*) Here, industrial TSA separations comprise the dehydration and desulfurization of hydrocarbons, the removal of carbon dioxide from biogas, and the adsorption of volatile organic compounds. PSA separation is employed mainly in the fields of air separation and hydrogen purification. Silica gels and activated alumina are primarily used as desiccants. (*23*)

Membrane-based separations make use of differences in diffusivity between the components of a mixture. This technology has several advantages, such as high energy efficiency, low maintenance cost, and the possibility to operate in a continuous process. In comparison to adsorption-based processes, membrane-based separations can be employed on a smaller scale. Polymeric membranes, which are commercially available, are industrially used in

hydrogen recovery, air separation, and CO_2 removal, among others. (*113*) Non-polymeric adsorbents, such as zeolites or carbons, could permit higher selectivities than polymers. However, the synthesis of mechanically and chemically stable, defect-free membranes composed of these materials is more challenging. Despite continued research efforts in the synthesis and characterization of zeolite membranes, the only technological application so far is the dehydration of alcohols by pervaporation. (*109*) Mixed-matrix membranes constitute a promising approach to combine the properties of polymeric and inorganic membranes: They consist of inorganic micro- or nanoparticles (*e.g.* zeolite crystals or silica nanoparticles) embedded in a polymer matrix. Compared to the unmodified polymer, this can significantly enhance the selectivity, retaining the mechanical stability and easy processability. Several recent patents on mixed-matrix membranes have been filed, highlighting the increasing industrial relevance of these materials. (*113*)

In the course of the development of novel microporous materials, such as MOFs, porous polymers, and others, the investigation of their gas separation properties has become a highly active research field. As far as MOFs are concerned, it was highlighted in a recent review that the number of publications focussing on gas separation in MOFs approximately equals the number of papers dealing with gas storage. (*114*) The potential of MOFs has been investigated with regard to both adsorptive separation processes and membrane-based separation. In the following, selected examples from the literature will be presented, taking into account both experimental and computational studies. A more exhaustive account of the literature published until early 2009 was compiled by Zhou and co-workers. (*114*)

1.3.2. Metal-organic frameworks for adsorption-based separation

While the gas storage properties are experimentally accessible through the measurement of single-component adsorption isotherms, an accurate experimental determination of adsorption selectivities is considerably more difficult. (*110, 115*) Therefore, only relatively few experimental studies of mixture adsorption have been published so far. As early as 2002, pioneering work was carried out by scientists from BOC Process Plants Inc., who performed cyclic breakthrough experiments with $Cu_3(btc)_2$ as adsorbent. (*116*) The MOF exhibited a significantly higher adsorption capacity for the removal of hydrocarbons from a gas feed than commercially available activated alumina. Later, the performance of $Cu_3(btc)_2$ for the separation of isobutane and isobutene was tested by Hartmann and co-workers. (*117*) A preferred adsorption of isobutene led to a selectivity of 2.1, making the material promising for adsorptive separations in the petrochemical industry.

Binary and ternary mixtures containing carbon dioxide were studied by Rodrigues, Chen and co-workers, using a mixed-linker MOF designated as MOF-508b. (*118*) Moderate CO_2/N_2 and CO_2/CH_4 selectivities ranging from 3 to 6 were observed. Yaghi and co-workers used breakthrough experiments to assess the potential of six different MOFs for the removal of harmful gases (sulfur dioxide, ammonia, and benzene, among others) from air. (*119*) It was found that the presence of unsaturated metal sites, or amino groups in the

linker molecules, can significantly enhance the retention of the more strongly adsorbing contaminants. With few exceptions, however, the improvement in comparison to activated carbon materials remained mediocre. The same group investigated the separation of CO_2 from CH_4 in the Mg-analogue of MOF-74. (*120*) This MOF exhibited a high selectivity and could be regenerated under relatively mild conditions (figure 1.10). Therefore, Mg-MOF-74 was proposed as a promising material for energy-efficient CO_2/CH_4 separations. A very high ("almost infinite") selectivity for CO_2 over CH_4 was observed for the amino-functionalized analogue of the flexible MOF termed MIL-53(Al). (*121*) This effect was attributed to the enhanced affinity towards CO_2 caused by linker functionalization, as well as the influence of framework flexibility.
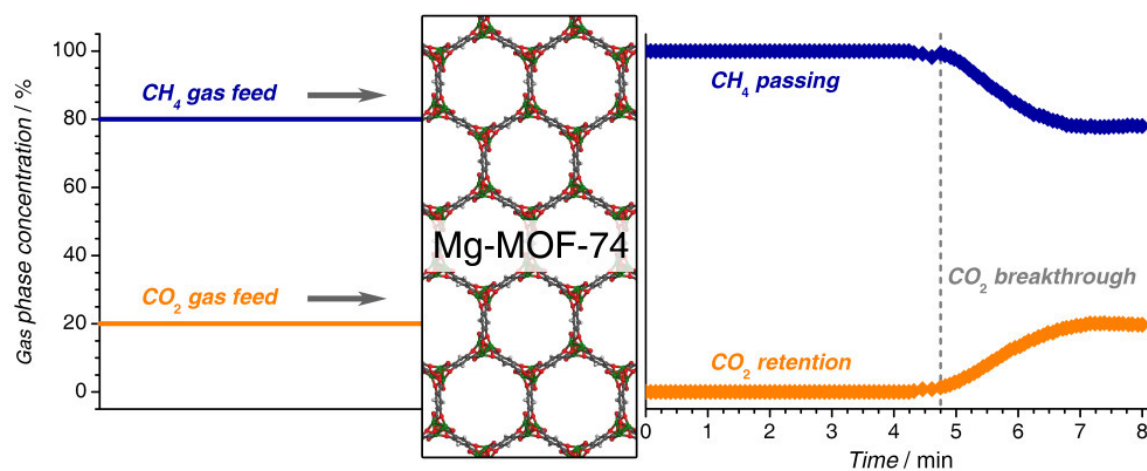
Figure 1.10. Visualization of CO_2 breakthrough measurements on a Mg-MOF-74 bed. (*120*) The feed gas has a CO_2/CH_4 ratio of 20:80. While the CH_4 breakthrough occurs practically immediately, a significant retention of CO_2 is observed. Figure designed in analogy to figure 2 of the original paper.

A direct measurement of mixture adsorption isotherms, in combination with breakthrough experiments, was performed by Kitagawa and co-workers for a flexible MOF termed CID-3. (*122*) A ternary gas mixture comparable to an exhaust gas with a low concentration of CO_2 was used as model system ($CO_2/O_2/N_2$: 1/21/78). The adsorption experiments revealed a preferential adsorption of CO_2 from the mixture, with a selectivity of 39, and the material showed good recyclability.

Because the direct determination of the separation properties requires an elaborate setup, most experimental studies have relied on predictions of mixture adsorption from single-component isotherms. In a simplistic manner, the selectivity can be taken as the ratio of the molar uptakes of the components for a given pressure. However, a variety of more sophisticated models has been proposed. (*110*) A particularly popular approach is provided by the framework of Ideal Adsorbed Solution Theory (IAST). (*123*) An attractive feature of IAST is the possibility to predict selectivities for varying mixture compositions and pressures from a relatively limited body of experimental data. Therefore, it has been widely used to assess the potential of MOFs as materials for gas separation applications.

The separation of carbon dioxide from other small molecules, such as methane, nitrogen, or hydrogen, is a potential application for which MOFs have been particularly well investigated. This is also reflected by two recent reviews that provide an exhaustive overview of the existing literature. (*124, 125*) The study of CO_2/CH_4 separation in a mixed-ligand MOF with Zn_2 paddle wheels by Bae *et al.* constitutes an example of the application of IAST in this context. (*126*) High selectivities were obtained for low pressures and low CO_2 concentrations, rendering the material particularly interesting for natural gas purification under vacuum-PSA conditions. The same group showed how the modification of the pore walls, *e.g.* by coordination of different pyridine derivatives to the metal centers, nearly doubled the CO_2/N_2 selectivity, whereas the CO_2/CH_4 selectivity remained practically unaffected. (*127*) In a recent study of CO_2/CH_4 separation in a newly synthesized Cu-MOF with unsaturated metal centers, it was observed that the selectivities obtained with the IAST model were significantly higher than the selectivities predicted from the ratio of the molar uptakes. (*128*) This finding implies that the preferential adsorption of carbon dioxide from the mixture decreases the affinity towards methane with respect to CH_4 single-component adsorption. Finally, it should be mentioned that zeolitic imidazolate frameworks (ZIFs) also hold much promise as materials for CO_2 capture. Moreover, their enhanced chemical and thermal stability could be advantageous with regard to practical applications. A review summarizing the experimental results obtained for different ZIFs has been published recently by Yaghi and co-workers. (*129*)

Due to its industrial importance, the potential of MOFs for the separation of hydrocarbon mixtures has also been investigated quite frequently. As early as 2006, Li and co-workers proposed a novel MOF with small pores as a material for the separation of butane from higher alkanes and alkenes. (*130*) Size and shape exclusion effects were responsible for the high separation efficiency. More recently, systematic studies of alkane/alkene pairs have been reported, such as the combined experimental and theoretical study of propane, propylene, and isobutane adsorption in $Cu_3(btc)_2$. (*131*)

Despite the relevance of air separation in industrial processes, the potential of MOFs in this field has been largely neglected so far. However, the recent finding that $Cr_3(btc)_2$ exhibits an unprecedented selectivity for oxygen over nitrogen may trigger further investigations. (*132*) The high affinity towards oxygen was rationalized with a strong binding of the O_2 molecules to the coordinatively unsaturated chromium sites.

In contrast to the difficulties encountered in experiment, the computational prediction of mixture adsorption isotherms is quite straightforward. The GCMC method described in section 3.2 can be directly extended to gas mixtures, specifying the desired composition of the gas phase. In other words, properties that are hard to access experimentally can be estimated at a relatively low computational cost from molecular simulations. It is therefore not surprising that the application of molecular modelling techniques for predictions of gas separation properties has become very popular.

Again, the separation of carbon dioxide from more weakly adsorbing gases (CH_4, CO, N_2, H_2) has been particularly well investigated. A very early GCMC study of CO_2/CH_4 mixture

adsorption in $Cu_3(btc)_2$ was reported by Yang and Zhong. (*133*) The predicted selectivities were moderate, ranging from 6 to 8. A subsequent computational study by Martín-Calvo *et al.* compared the performance of $Cu_3(btc)_2$ and IRMOF-1 for the separation of CO_2/N_2 and CO_2/CH_4 mixtures. (*134*) $Cu_3(btc)_2$ exhibited a considerably higher selectivity, because the smaller pores provide for a stronger solid-fluid interaction. A systematic investigation of several structurally different MOFs as potential materials for natural gas upgrading was carried out by Jiang and co-workers. (*135*) It was found that catenated MOFs provided for a higher selectivity than their non-catenated counterparts. However, the highest selectivity was obtained for a system with charge-balancing extra-framework nitrate ions. This was explained with the increased electrostatic interactions, which enhance the affinity towards carbon dioxide. Later, the same approach was employed for another MOF with a charged framework and extra-framework Na^+ ions. (*136*) Unprecented CO_2/H_2, CO_2/N_2, and CO_2/CH_4 selectivities were predicted, amounting to 1800, 500, and 80, respectively.

In addition to the selective adsorption of CO_2, computational studies of several other gas mixtures in MOFs have been reported. Examples include the separation of CH_4/H_2 mixtures, (*137*) the separation of carbon monoxide from other weakly interacting gases, (*138*) the separation of propane and propene, (*139*) and the removal of carbon tetrachloride from air. (*140*)

1.3.3. Metal-organic frameworks for membrane-based separation

As mentioned in the introduction to this section, the preparation of stable, defect-free membranes is a key challenge in the application of crystalline materials for membrane-based separations. As highlighted by Gascon and Kapteijn, significant advances in the field of MOF membranes have been achieved in the last three years. (*141*) The first gas permeation measurements were reported by Guo *et al.* for a $Cu_3(btc)_2$ membrane grown on a copper net in 2009. (*142*) Separation factors ranging from 5 to 7 were obtained for H_2/CO_2, H_2/CH_4, and H_2/N_2 mixtures.

Due to their high stability, zeolitic imidazolate frameworks are particularly interesting materials for the preparation of membranes. The successful synthesis of a ZIF-8 membrane on a porous titania support was reported by Caro and co-workers. (*143*) Because the pore windows of ZIF-8 are very narrow (with a diameter of approximately 3.4 Å), it was expected that the permeability of the membrane depends strongly on the molecular diameter of the guest molecule. Indeed, experimental measurements revealed a significant selectivity for hydrogen over larger molecules, *e.g.* a H_2/CH_4 selectivity of 11. The fact that methane could diffuse through the membrane in spite of its large kinetic diameter (3.76 Å) was explained with a certain flexibility of the ZIF-8 structure. In a parallel effort, a ZIF-8 membrane was prepared on a porous alumina support by Venna and Carreon. (*144*) This membrane exhibited a CO_2/CH_4 selectivity ranging from 6 to 10. In addition to pure MOF membranes, mixed-matrix membranes incorporating MOF nanocrystals in a polymer matrix have also been reported, *e.g.* a polyimide-$Cu_3(btc)_2$ mixed-matrix membrane. (*145*)

In contrast to the experimental difficulties in the synthesis of stable, defect-free MOF membranes, the computational prediction of membrane selectivities is relatively straightforward. The methodological approach has been outlined by Keskin and Sholl: (*146*) The membrane selectivity can be approximated as the product of the adsorption selectivity and the diffusion selectivity. While the former can be obtained from GCMC simulations of binary mixtures, the latter is computed from the self-diffusivities, which are accessible through molecular dynamics (MD) calculations. The modelling of diffusion in porous materials is a topic of its own, which will not be discussed in more detail. (*147*, *148*) However, some literature examples aimed at the prediction of membrane selectivities in MOFs are mentioned in this context.

While the first computational study of the diffusion of guest molecules in a MOF structure was published as early as 2004, (*149*) the first prediction of membrane selectivities was reported by Keskin and Sholl in 2007. (*150*) In this initial investigation, the theoretical membrane selectivity of IRMOF-1 towards a CO_2/CH_4 mixture was investigated. It was found that the membrane selectivity was lower than adsorption selectivity, because the more strongly adsorbed species (CO_2) diffuses more slowly, a behaviour that is quite frequently observed in similar computations. Therefore, the resulting selectivities were mediocre, not exceeding 3. In a subsequent publication, the same authors extended the approach to three different gas mixtures and eight different MOF structures. (*151*) Due to the aforementioned behaviour, the selectivities were at best moderate. A detailed study, combining MD simulations and DFT calculations, was carried out by Watanabe *et al.* to assess the CO_2/CH_4 selectivity of a MOF with channel-like pores and very narrow windows. (*152*) Because the energy barrier to a passage of the methane molecules through the narrow windows was very high, an exceptional CO_2/CH_4 membrane selectivity of the order of 10^4 to 10^5 was predicted.

In comparison to the prediction of adsorption isotherms, the calculation of diffusivities is computationally expensive, particularly in cases where different mixture compositions are considered. An efficient approach to estimate the diffusivity has been proposed by Sholl and co-workers. (*153*) Here, only a few key geometric properties of the structure, such as the limiting pore diameter, and relatively undemanding calculations are sufficient to predict the permeability for the desired combination of membrane material and guest molecule. This procedure could prove to be a valuable tool for screening purposes: Of a large group of materials, a subset that could warrant a more detailed investigation can be identified at a moderate computational expense.

2. Motivation and Aim of this Work

As it has become apparent from the overview provided in the introductory section, metal-organic frameworks and other newly developed porous materials hold much promise for applications in gas storage and gas separation. While a large body of experimental data has been published during the last few years, a complete understanding of the underlying phenomena at an atomic scale is often lacking. Therefore, theoretical methods can make valuable contributions in several respects: Firstly, they can be employed to predict the adsorption or separation properties of materials that are not yet fully characterized experimentally, or that have not even been synthesized. In other words, computational techniques can help to identify those materials which warrant further experimental characterization. Secondly, modelling methods can provide insights into properties that are difficult or impossible to access experimentally. For example, the determination of adsorption sites and adsorption energies requires sophisticated diffraction and spectroscopy experiments. In contrast to this, this information can be obtained relatively easily from molecular simulations. Finally, the usage of appropriate electronic structure methods can permit an understanding of the nature of the interactions that govern the adsorption behaviour, such as the preferential adsorption of molecules at specific sites.

In this work, computational methods are employed to study the adsorption of hydrogen, as well as the separation of gas mixtures, in metal-organic frameworks and related compounds at different levels of theory. On the one hand, empirical methods in conjunction with literature force-field parameters are used. In some instances, the force fields are augmented with additional interaction parameters derived from electronic structure calculations. On the other hand, model systems of particular interest are studied using density-functional theory and, in selected cases, dispersion-corrected density-functional theory.

In the first part, force-field based simulations are employed to predict the hydrogen adsorption properties of a set of structurally different MOFs. While several comparable studies have been reported in the literature, most of them have addressed only relatively few systems. Moreover, none of these investigations has exploited the full capabilities of modelling methods in the prediction of position-dependent quantities. The first aim of the computations reported here is to verify whether the usage of one transferable set of literature parameters can provide for a reasonably accurate calculation of hydrogen adsorption isotherms for MOFs with different structural features. More emphasis is put on the second objective, which comprises the derivation of approximate hydrogen adsorption positions from the simulation results, as well as their critical comparison to experimental adsorption sites

obtained from diffraction experiments. In an exemplary manner, it is shown how these predictions can be extended to systems for which no experimental information is available, and how the analysis of adsorption sites can provide insights into the structural features that are favourable to reach a high adsorption capacity.

The second part is dedicated towards the study of some selected MOFs with unsaturated metal sites. As it will become apparent in the course of this work, these systems are a particular challenge for force-field based simulations, because the interaction of hydrogen with the metal centers is not adequately represented when literature parameters are used. Therefore, improved potential parameters for this specific, localized interaction are derived from DFT calculations, taking MOFs with unsaturated copper sites as a model case. In order to validate the new potential model, its performance is assessed in simulations of hydrogen adsorption in different MOFs under different conditions. Due to the increased strength of the solid-fluid interaction, MOFs with unsaturated metal sites are often proposed as materials with improved hydrogen storage characteristics under ambient conditions. The actual contribution that can be expected from the interaction with the metal sites at room temperature is predicted from further calculations, comparing three potential models that represent different strengths of the metal-hydrogen interaction.

As a result of the chemical versatility of MOFs, numerous systems with heteroaromatic linkers, or with linkers carrying non-coordinated substituents have been reported. It can be expected that changes in the electronic structure caused by modifications of the linker will influence the interaction between a nearby metal center and an adsorbed molecule. The first half of the third part addresses this effect, employing DFT calculations for molecular model systems with unsaturated copper sites and different carboxylate ligands. It is studied how changes of the ligand change the interaction strength, and how geometric properties and partial charges are correlated with the interaction energy. One particular aim is to develop a qualitative understanding of the nature of the interactions. The second half of the third part investigates the interaction of hydrogen with organic molecules as representatives of the MOF linkers. Because dispersive interactions play a key role here, DFT calculations with an empirical dispersion correction scheme are employed (DFT-D). As a first step, the method is validated by comparison of the DFT-D results obtained for a well-characterized model system with literature data from high-quality *ab-initio* calculations. Further calculations are carried out to study the interaction of hydrogen with nitrogen-containing six-membered rings, and with models of non-linear linker molecules. The DFT-D interaction energies are partitioned into different, intuitively interpretable contributions using energy decomposition analysis. In particular, it is tested whether the incorporation of atoms with increased polarizability, *e.g.* by replacing carbon with silicon as the central atom of a non-linear molecule, has a significant impact on the interaction with hydrogen.

While the first three parts are, at least loosely, connected to the topic of hydrogen storage, the last part evaluates the potential of MOFs and related porous materials for gas separation applications. Only very few molecular simulation results have been reported for the three gas mixtures considered, which comprise hydrogen/carbon monoxide, hydrogen/oxygen,

and acetylene/carbon dioxide. These mixtures are interesting from the point of view of application (hydrogen and acetylene purification, removal of trace amounts of acetylene), but also for fundamental reasons, mainly due to the different electrostatic properties of the gas molecules. With the exception of one system, where modified parameters are derived from DFT calculations to represent the interaction of the adsorbed molecules with coordinatively unsaturated metal centers, force-field based GCMC calculations using literature parameters are employed. In addition to computing mixture isotherms for binary mixtures, the evolution of the adsorption selectivity as a function of the total pressure and the gas phase composition is predicted. Moreover, an analysis of the potential energy distribution in the unit cell is carried out, aiming at a better understanding of the origins of the observed selectivity at an atomistic level. For each of the three gas mixtures considered, these results can provide guidelines which structural features of a microporous material are most important to reach a high separation efficiency.

3. Methods: Theoretical Background

3.1. Force-field methods

3.1.1. Introduction: Basic principles

Force-field based atomistic simulations provide a computational framework that treats a system on the level of single particles, *i.e.* atoms or small groups of atoms. In contrast to electronic structure methods, which perform a quantum-mechanical treatment on the level of electrons, empirical interaction potentials are employed to describe the interparticle interactions. To highlight this fundamental difference, force-field methods are often paraphrased as molecular mechanics methods. Because the usage of mathematically simple expressions is computationally much less expensive than any (even approximate) first-principles description, force-field based methods provide access to various problems which are practically intractable with *ab-initio* methods.

For a given system, each particle must be assigned an appropriate "atom type" prior to the calculation. The atom type is typically determined by the atomic number and the direct environment of the atom: For example, an sp^3 hybridized carbon is treated differently than an sp^2 hybridized carbon. In contrast to electronic structure methods, which use only the nuclear coordinates as initial information, assumptions concerning the presence of chemical bonds must be made *a priori* by the user (or by a well-designed algorithm). The force field itself is nothing more than a collection of analytical expressions that define the interactions between different atom types. Local interactions between atoms that are bonded to each other are referred to as "bonded" interactions, whereas interactions between atoms which have no direct bond connection are termed "non-bonded" interactions. A typical force-field energy expression for a molecule reads (equation 2.1 in (*154*)):

$$E_{FF} = E_{stretch} + E_{bend} + E_{tors} + E_{cross} + E_{es} + E_{vdW} \tag{3.1}$$

Here, $E_{stretch}$ is the energy contribution from the elongation or compression of bonds with respect to their equilibrium length as defined by the force field. Similarly, E_{bend} gives the contribution of angle bending (three-body term), E_{tors} the contribution of torsions about a bond (four-body term), and E_{cross} represents the cross terms between these three terms. Taken together, these are the contributions from bonded interactions. Of the remaining two non-bonded terms, E_{es} represents the electrostatic contribution, and E_{vdW} corresponds to the contribution from dispersive interactions. Moreover, this term absorbs other interactions that are not treated explicitly, such as induced polarization. The non-bonded terms are only

evaluated for atoms which have a certain number of bonds between them: 1,2-interactions (= neighbours) and 1,3-interactions are always excluded, 1,4-interactions are sometimes scaled down or excluded. A graphical representation of the different contributions of equation 3.1 is given in figure 3.1.
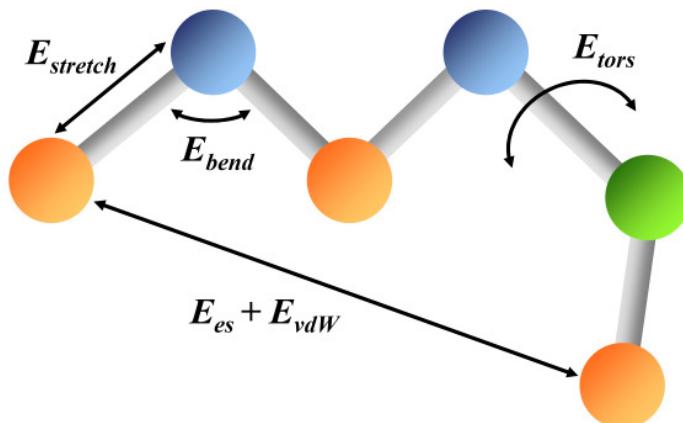
Figure 3.1. Schematic representation of the different energy terms of a force field. For each term, only one example is shown. The energy expression of the whole molecule contains five bond stretch, four angle bend, and three torsional terms. Figure modified after (*154*).

It should be pointed out that the wording in discussions of interaction energies (regardless how they have been obtained) can become confusing: Because an attractive interaction corresponds to a negative value of the energy, an energetically "more negative" configuration is more favourable than a "less negative" configuration. Therefore, a decrease of the numerical value, *e.g.* from -5 to -10 kJ mol^{-1}, corresponds to an actual increase of the interaction strength. Whenever such relationships are established in this work, an "increased" (or "higher") interaction corresponds to a more negative value of the interaction energy. This convention is used to avoid confusions between the actual energy and the interaction strength.

3.1.2. Force-field representation of interatomic interactions

3.1.2.1. Bonded interactions

The most typical choice to represent bond stretch terms is the Morse potential. It corresponds to an anharmonic potential which converges towards the dissociation energy D_0 when the bond is stretched to infinity. One typical expression for the Morse potential reads:

$$E_{Morse}(r_{AB}) = D_0(1 - \exp[-\alpha(r_{AB} - r_0)])^2 \tag{3.2}$$

Here, r_0 is the equilibrium distance of the pair A and B, and D_0 is the dissociation energy. α is often referred to as stiffness parameter. It is related to the force constant k as: $\alpha = \sqrt{\frac{k}{2D_0}}$. The evolution of the Morse potential on variation of r_0, D_0, and α is shown exemplarily in

figure 3.2. Because the evaluation of the exponential function in equation 3.2 is computationally relatively demanding, the Morse potential is often replaced by a simple polynomial expansion. A fourth-order polynomial is often sufficiently accurate in the range of all chemically relevant values of r. (*154*)
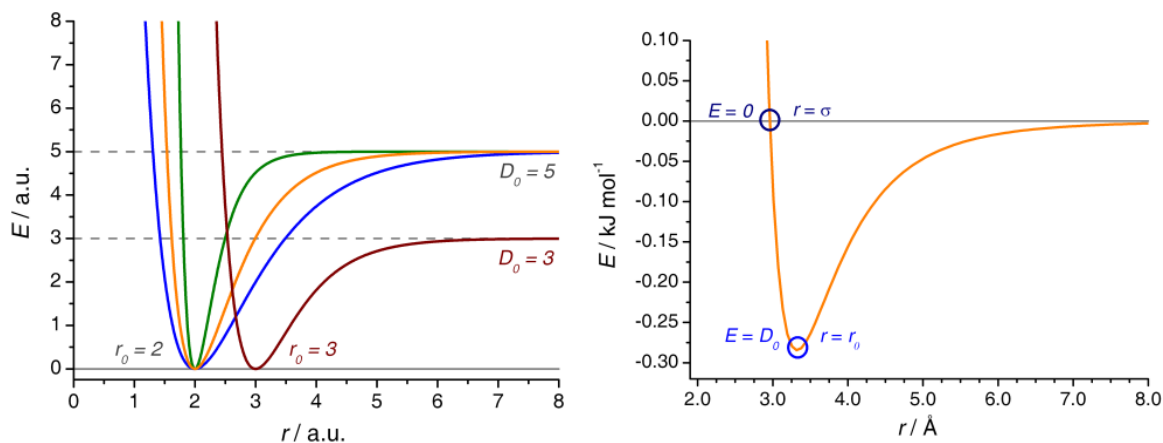
Figure 3.2. *Left:* Evolution of the Morse potential for different values of r_0, D_0, and α. For the curve displayed in dark red, r_0 is larger, and D_0 is smaller than for the other curves. For the three other curves, the stiffness parameter α is largest for the green curve. *Right:* Lennard-Jones potential describing the interaction between two H_2 molecules, parameters taken from the Buch potential. (*155*)

The angle bending energy is typically expressed as a Taylor series around an "equilibrium" bond angle θ_0. The most simple form is the harmonic expansion:

$$E_{bend}(\theta_{ABC}) = k(\theta_{ABC} - \theta_0)^2 \tag{3.3}$$

Higher-order expansions can be used to improve the accuracy. For planar geometries, *e.g.* the bonding environment of an sp^2 hybridized carbon atom, an additional "out-of-plane bending" term can be used to increase the energy penalty for a dislocation of the atom from the plane defined by its neighbouring atoms. An energy penalty for inversion of a non-planar system can be included in a similar manner.

The torsional energy is associated with a rotation about the *B-C* bond in an *A-B-C-D* arrangement of atoms. In contrast to the bond stretch and angle bending terms, the torsional energy is periodic, with local minima at certain torsional angles ω. It is commonly written as a Fourier series to represent the periodicity:

$$E_{tors}(\omega_{ABCD}) = \sum_{n=1} K_n \cos(n\omega_{ABCD}) \tag{3.4}$$

The value of n determines the periodicity ($n = 1$: periodicity of $360°$; $n = 2$: periodicity of $180°$...), and the constants K_n determine the size of the energy barrier. In addition to the torsional energy term itself, the non-bonded parameters also contribute to the change in energy upon rotation, because non-bonded terms are usually included for 1,4-interactions.

While the bonded terms discussed so far are included in all force fields in a similar manner, the treatment of cross terms is more specific. Cross terms describe the coupling between different bonded terms: For example, a cross term could describe how the change of an angle at a central atom B influences the bond lengths to the neighbouring atoms A and C. Cross terms are treated in a fundamentally different way in different force fields: The DREIDING force field (*156*) and the Universal Force Field (UFF) (*157*) completely dispense with cross terms. In contrast to this, the MM3 force field (*158*) explicitly treats bend-bend, bend-stretch, torsion-bend, and torsion-stretch cross interactions.

3.1.2.2. Electrostatic interactions

In the most simple treatment of electrostatic interactions, point charges are assigned to each atomic position. The electrostatic interaction between two atoms with charges q_A and q_B is then calculated from the Coulomb potential:

$$E_{es}(r_{AB}) = \frac{q_A q_B}{4\pi\varepsilon_0 r_{AB}} \tag{3.5}$$

There are different means to obtain the point charges: Some force fields have built-in point charges, (*159*) for others, it is recommended to use certain empirical charge derivation methods or ignore charges. (*156*, *157*) The commonly preferred method is the usage of point charges obtained from an electronic structure calculation. In particular, the ESP method delivers charges that reproduce the *ab-initio* electrostatic potential, and is therefore most suitable for the derivation of point charges used in force-field based calculations. (*154*, *160*, *161*) For periodic structures, it is necessary to use an appropriate scheme that accounts for the electrostatic contributions from neighbouring cells. The Ewald summation method and its refinements are a common choice. (*162*)

A more evolved treatment of electrostatic interactions may include the usage of point dipoles or higher multipoles at atom positions, or the definition of additional charge-carrying sites, such as the midpoints of bonds. An even more accurate description can be attained by explicit inclusion of polarization effects, for which several different approaches have been proposed. (*163*) However, these methods require an iterative procedure to determine the induced dipole contributions, and therefore become computationally quite expensive.

3.1.2.3. van der Waals interactions

The E_{vdW} term is used to account for the dispersion interaction between two atoms which are not bonded to each other. These attractive interactions between induced dipoles (and multipoles) originate from the correlated motion of the electrons. It can be derived from quantum mechanics that the interaction between two induced dipoles is proportional to r^{-6}, the interaction between an induced dipole and an induced quadrupole is proportional to r^{-8}, and so forth. (*164*) Typically, only the r^{-6} contribution is considered in force fields. It is obvious that the attractive r^{-6} relationship loses its validity at short interatomic distances,

where the exchange-repulsion term stemming from the overlap of the electron clouds will prevent the atoms from collapsing into each other. Therefore, the attractive term is always coupled to an empirical repulsive term. While other functional forms exist, the most typical choice is the Lennard-Jones 12-6 potential, where the repulsive term is proportional to r^{-12}:

$$E_{vdW}(r_{AB}) = D_0 \left[\left(\frac{r_0}{r_{AB}} \right)^{12} - 2 \left(\frac{r_0}{r_{AB}} \right)^6 \right] = 4D_0 \left[\left(\frac{\sigma}{r_{AB}} \right)^{12} - \left(\frac{\sigma}{r_{AB}} \right)^6 \right] \quad (3.6)$$

Again, D_0 is the depth of the potential well describing the interaction between atoms A and B. It is often denoted as ϵ rather than D_0 when given in Kelvin. r_0 is the equilibrium distance. In the last expression in equation 3.6, σ is used instead of r_0. It corresponds to the distance at which the potential energy is zero. For interactions between identical atoms, the parameter σ can be identified as the van der Waals diameter. It is related to r_0 as follows: $r_0 = 2^{1/6}\sigma$. The Lennard-Jones potential is visualized in figure 3.2.

In a force field, the parameters D_0 and r_0 are tabulated for each atom type. The off-diagonal parameters that are necessary to calculate the interaction between two different atom types can be derived explicitly. More often, however, these parameters are obtained from the atomic parameters using combination rules ("mixing rules"). The Lorentz-Berthelot mixing rules employ the geometric mean for D_0, and the arithmetic mean for r_0:

$$D_0(AB) = \sqrt{D_0(A) \cdot D_0(B)} \qquad r_0(AB) = \frac{1}{2}[r_0(A) + r_0(B)] \quad (3.7)$$

While it has been shown that more elaborate combination rules exhibit an improved performance in reproducing high-quality potential energy curves, (*165*) the Lorentz-Berthelot mixing rules remain extremely popular.

The Lennard-Jones 12-6 potential is computationally highly efficient, and therefore widely used. There are, however, numerous other potential models to represent long-range attraction and short-range repulsion. In particular, the repulsive r^{-12} term can be replaced by an exponential term, leading to the Buckingham potential, which has a physically more plausible evolution than the Lennard-Jones potential. (*164*) It is, however, less attractive from a computational point of view. Some force fields also use other, optimized potential forms which contain specific shape parameters. (*165*) The Morse potential, described above, is also employed quite frequently. It is then expressed in a different functional form than in equation 3.2, in a way that the minimum of the potential corresponds to $-D_0$, while the potential approaches zero for large values of r_{AB}:

$$E_{Morse}(r_{AB}) = D_0 \left(\exp \left[\alpha \left(1 - \frac{r_{AB}}{r_0} \right) \right] - 2 \exp \left[\frac{\alpha}{2} \left(1 - \frac{r_{AB}}{r_0} \right) \right] \right) \quad (3.8)$$

As for electrostatic interactions, the calculation of dispersive interactions for periodic systems requires special attention. A simple and effective way to treat the long-range evolution of the potential is the definition of a cutoff radius r_{ctof}: Equation 3.6 is evaluated only for atom pairs for which $r_{AB} < r_{ctof}$. A cutoff radius $r_{ctof} = 2.5\sigma$ is a typical (minimal) choice.

At the point where the potential is truncated, it can be smoothened or shifted to avoid unphysical kinks. (*162*)

3.1.3. Types of force fields

There is a wide variety of force fields available in the literature. While many of them have been specifically designed for certain applications, others are intended to have a rather broad applicability. These "generic" force fields rely on the approximate calculation of parameters for molecules for which no explicit parameters are available. An overview over the most important force fields is given in computational chemistry textbooks. (*154*, *166*)

From a general point of view, classical molecular-mechanics force fields can be divided into two classes: (*163*) Class I force fields are derived to reproduce condensed state properties, *e.g.* in the simulation of liquids or crystals. They contain only relatively simple diagonal (two-body) terms. The OPLS (*159*, *167*) and the TraPPE (*168*) force field are examples of class I force fields. Class II force fields aim at a more accurate description of molecular geometries, vibrational properties and related quantities. These force fields include more evolved higher-order terms. However, they usually perform poorly in condensed phase simulations, *e.g.* in the prediction of vapour-liquid equilibria and liquid densities. (*169*) The Universal Force Field (UFF) (*157*) and the MM3 force field (*158*) are class II force fields.

Furthermore, all-atom descriptions can be distinguished from united-atom models. In the latter, groups of atoms are treated as a single site. The most important example is the implicit treatment of hydrogens in hydrocarbons, where, for example, a CH_2 group is treated as a single site, ignoring the actual positions of the hydrogen atoms. Furthermore, a single-site model located at the center of mass can be used to represent small molecules like H_2 or CH_4 in simulations of fluid properties.

3.1.4. Applications of force-field based methods

The applications of force-field based methods can be subdivided in three classes: Geometry optimization, molecular dynamics, and Monte Carlo methods. For a (molecular or periodic) system where experimental structure information is lacking, an optimization of the nuclear coordinates with respect to the energy can be performed in order to generate a reasonable structural model. This model can be employed in a more detailed analysis, or as a starting geometry for further computations. A central problem in geometry optimization procedures is the occurrence of local energy minima. Different techniques to avoid these minima have been developed, which are discussed in more detail in (*166*). For the particular case of complex crystalline systems, such as MOFs, experimentally determined structures often exhibit structural disorder. After removing disordered atoms, a force-field based optimization is an efficient way to obtain an "idealized" structure that can be used in subsequent molecular simulations.

Molecular dynamics (MD) methods assess the evolution of a system of particles with time. The initial positions and momenta are given, and the evolution from one time step to the next is then calculated according to the classical equations of motion, making use of the parameters from the force field. Integration of the equations of motion yields a trajectory, from which time-dependent quantities can be derived. MD methods have found a wide range of applications in chemistry and physics. To mention one example, they are often used to calculate the diffusion coefficients of gases adsorbed in porous solids. (*148*)

Monte Carlo (MC) methods provide an efficient means to obtain ensemble averages for a collection of particles under specified thermodynamic conditions. They are described in detail in the following section. In contrast to MD methods, which evaluate the forces on the atoms, MC simulations only make use of the potential energy U of a given configuration, which determines its probability. Because a large number of simulation steps is necessary until convergence is reached, MC methods must rely on relatively simple analytical expressions to calculate U. Such expressions can be provided by an appropriately chosen force field.

Finally, some limitations of force-field based methods should be considered: Clearly, the quality of a force field depends on the quality of the (experimental or *ab-initio*) data used for the parameterization. Moreover, it is important to emphasize that every force field constitutes a compromise between accuracy and transferability. A force field which has been specifically derived for a small class of molecules should perform very well for these systems, but the parameters are hardly transferable to chemically different molecules. On the other hand, a fully generic force field, which is theoretically able to describe any imaginable system, will fail in many specific cases. Finally, it is clear from the discussion above that the presence of bonds must be defined *a priori*. Processes which involve the breaking and formation of bonds cannot be treated with standard force field methods, but require the use of specialized reactive force fields. (*154*)

3.2. Grand-canonical Monte Carlo simulations

3.2.1. Introduction: Theoretical background

3.2.1.1. Simulation boxes and thermodynamic ensembles

The purpose of the simulation approach described in this section is the derivation of macroscopically observable quantities from simulations for a limited, computationally tractable number of particles. In the context of atomistic simulations, a "particle" corresponds to an atom or a molecule with mass m. Interactions between atoms or small groups of atoms are treated explicitly. The connection between macroscopic quantities and the behaviour on an atomistic level is provided by the principles of statistical mechanics, which are not discussed in detail here. (*170*) For simplicity, all elaborations in the following will relate to systems containing only one particle type, but the extension to mixtures is quite straightforward. It is assumed that the particle is an atom or a rigid molecule. Molecules with conformational degrees of freedom require a more evolved treatment.

The simulations are carried out for a simulation box, a parallelepiped which accommodates the particles. The term "configuration" is used to describe a given number of particles with a defined set of coordinates located in the box. Periodic boundary conditions are employed, *i.e.* it is assumed the simulation box is surrounded by identical images containing the same configuration (figure 3.3). It is obvious that the simulation box must be large enough to avoid an artificial interaction of a particle with its image in a neighbouring box.
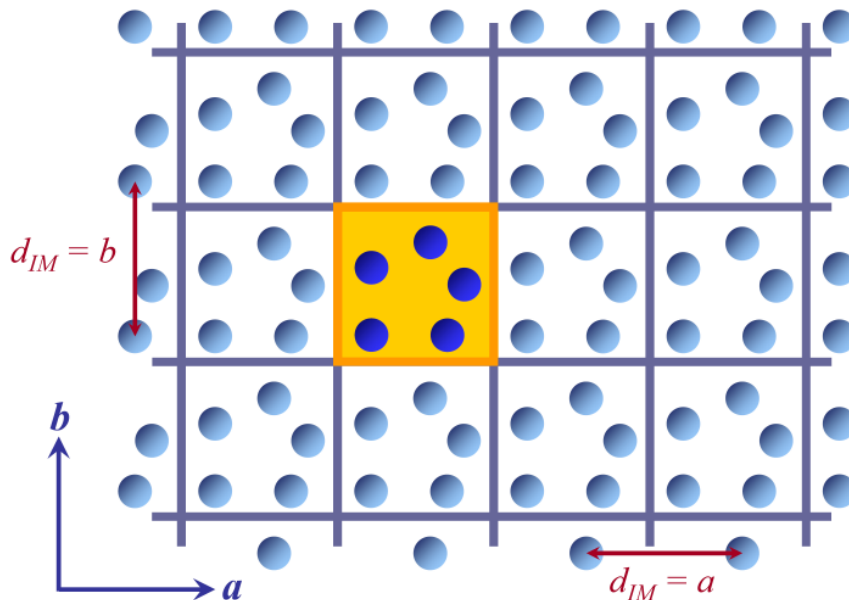
Figure 3.3. Visualization of a two-dimensional simulation box with periodic boundary conditions. The simulation box, highlighted in orange, is surrounded by identical images. The distance of one particle to its image d_{IM} is equal to the corresponding edge length of the box. The cutoff parameter r_{ctof} must be shorter than d_{IM}.

Some of the thermodynamic state functions of the simulation box are specified prior to the simulation. Depending on the quantities which are fixed, different ensembles can be defined, some of which are listed below:

- The microcanonical ensemble: The number of particles N, the volume V of the simulation box, and the total energy of the system E are fixed.

- The canonical ensemble: N, V, and the temperature T are fixed.

- The grand-canonical ensemble: V, T, and the chemical potential μ are fixed.

- The isothermal-isobaric ensemble: N, T, and the pressure p are fixed.

Of these ensembles, only the canonical ensemble and, most importantly, the grand-canonical ensemble are discussedd in the following sections.

3.2.1.2. The canonical ensemble

An ensemble of N particles with a set of coordinates $\vec{r}_N$ is assumed. In the canonical ensemble, the average value of an observable F which depends on the particle coordinates corresponds to: (*171*)

$$\langle F \rangle = \frac{\int F(\vec{r}_N) \exp\left[-\frac{U(\vec{r}_N)}{k_B T}\right] d\vec{r}_N}{\int \exp\left[-\frac{U(\vec{r}_N)}{k_B T}\right] d\vec{r}_N} \tag{3.9}$$

Here, U is the potential energy (the kinetic energy is not considered, because it is assumed that the observable depends on the coordinates, but not the momenta of the particles). The denominator is the partition function of the canonical ensemble. It is quite obvious that, for most cases, the numerical evaluation of these integrals is impossible due to the enormously large number of possible sets of particle coordinates (configurations) which must be considered. It is the general idea of the Monte Carlo method to carry out the integration by means of a statistical approach, taking into account a sufficiently large number of integration points (configurations $\vec{r}_N$ for the case of 3.9). The most simple implementation of this method to solve equation 3.9 would be the random generation of a configuration $\vec{r}_N$ with a subsequent calculation of its energy and a weighting according to $\exp\left[-\frac{U(\vec{r}_N)}{k_B T}\right]$. However, this direct implementation would generate a large number of extremely improbable configurations with a very low weight, and is therefore impractical.

The ingenious idea of Metropolis and co-workers is summarized in their pioneering work of 1953 as follows: "So the method we employ is actually a modified Monte Carlo scheme, where, instead of choosing configurations randomly, then weighting them by $\exp\left[-\frac{U(\vec{r}_N)}{k_B T}\right]$, we choose configurations with a probability $\exp\left[-\frac{U(\vec{r}_N)}{k_B T}\right]$ and weight them evenly."(*171*) In other words, the excessive evaluation of energetically unfavourable configurations, which are unlikely and contribute little to the observable F, is avoided by generating configurations according to their probability. This is reached through the employment of appropriate acceptance criteria (also termed "importance sampling"), which will be explained in detail

in the following. Metropolis and co-workers used this sampling technique to calculate the equation of state of a two-dimensional rigid sphere system.

After a sufficient number of configurations has been evaluated, the average value of the observable can be calculated by summation over the M configurations:

$$\langle F \rangle = \frac{1}{M} \sum_{j=1}^{M} F_j \tag{3.10}$$

Here, j is a running index running over the M configurations. Thus, the ratio of integrals expressed in equation 3.9 is replaced by a summation.

3.2.1.3. Simulations in the canonical ensemble: Metropolis sampling

A simulation in the canonical (N, V, T) ensemble corresponds to a "fixed loading" simulation, where the number of particles per volume is specified as initial information. If the particle consists of one interaction site, a simulation step comprises the generation of a new configuration by either particle translation or regrowth (removal and re-insertion at another point of the simulation box). For a particle consisting of more than one interaction site, the particle can also be rotated.

The acceptance or rejection of a new configuration generated by translation, rotation, or regrowth follows the Metropolis sampling scheme. In this context, it is described for the case of particle displacement, but identical acceptance criteria hold for particle rotation and regrowth. In a displacement step X, one particle in the simulation box is moved by an arbitrary step size (which can be variable or fixed, but should not exceed a reasonable limiting value) in an arbitrary direction. The energy of the new configuration U_X is calculated. If $U_X \leq U_{X-1}$, the new configuration is energetically favourable in comparison to the old configuration, and the displacement move is always accepted. If $U_X > U_{X-1}$, the displacement move is accepted with a probability which is proportional to $\exp\left[-\frac{U_X - U_{X-1}}{k_B T}\right]$: This expression implies that if the energy difference is small, *i.e.* the new configuration is only slightly less favourable in energy than the old configuration, it is still accepted with a relatively high probability. On the other hand, a new configuration that is energetically much less favourable will be rejected in (practically) all cases.

A more compact formulation of the acceptance criterion of the Metropolis sampling scheme is the following (equation 5.6.7 in (*172*)):

$$acc(X - 1 \rightarrow X) = \min\left\{1; \exp\left[-\frac{U_X - U_{X-1}}{k_B T}\right]\right\} \tag{3.11}$$

This useful, but rather unwieldy formulation can be summarized as follows: The probability of acceptance of a step equals the minimum of unity and the exponential term that depends on the energy difference. If the energy difference is negative, the exponential term is larger than unity, so the probability equals unity: The step is always accepted. If the energy difference is positive, the exponential term ranges between zero and unity. For a small

energy difference, it is close to unity, and the probability of acceptance is high. However, on increasing ΔU, the exponential term decreases, leading to an increasing probability of rejection. The technical problem of deciding whether a displacement step with an acceptance probability $acc < 1$ should be accepted or rejected is solved by comparison with a random number rnd ranging between 0 and 1. If $acc > rnd$, the step is accepted, if $acc < rnd$, it is rejected, and the old configuration is counted again.

After a sufficiently large number of simulation steps, the body of accepted configurations approaches a distribution where the probability of a configuration m is proportional to $\exp\left[-\frac{U_m}{k_B T}\right]$. The average value of a desired observable F can be calculated from equation 3.10.

3.2.1.4. Simulations in the grand-canonical ensemble

In the grand-canonical (μ, V, T) ensemble, the chemical potential μ is fixed, while the number of particles is variable. There is a direct relationship between the chemical potential and the fugacity f. In the case of an ideal gas, the chemical potential can be expressed as a function of the pressure p (equation 4.24 in (*170*)):

$$\mu_{ideal} = -k_B T \ln\left[\left(\frac{2\pi m k_B T}{h^2}\right)^{3/2} \frac{k_B T}{p}\right] \tag{3.12}$$

The equivalent to equation 3.9 for the grand-canonical ensemble is more involved and not given here ((*173*), p. 80). Translation, rotation, and regrowth are treated as described above. It is, however, obvious that the variable number of particles creates a necessity for additional types of simulation steps: Creation, *i.e.* insertion of a new particle into the box, and deletion, *i.e.* removal of a randomly chosen particle from the box. It is clear from intuition that the acceptance criteria for particle insertion and deletion must depend on pressure: Low pressure will favour a small number of particles per volume unit, while a high pressure will lead to a high particle density. The commonly used sampling scheme, which was first proposed by Norman and Filinov, employs the following criteria (equations 5.6.8 and 5.6.9 in (*172*)):

$$acc(N \rightarrow N+1) = \min\left\{1; \frac{Vp}{k_B T(N+1)} \exp\left[-\frac{U_{N+1} - U_N}{k_B T}\right]\right\} \tag{3.13}$$

$$acc(N \rightarrow N-1) = \min\left\{1; \frac{k_B T N}{Vp} \exp\left[-\frac{U_{N-1} - U_N}{k_B T}\right]\right\} \tag{3.14}$$

The employment of these acceptance criteria corresponds to the equilibration of the simulation box with an external reservoir containing an ideal gas under the specified conditions. A typical grand-canonical Monte Carlo (GCMC) run starts either from an empty simulation box or an arbitrary starting configuration. Therefore, the number of particles in the starting configuration may be quite different from equilibrium, and it will require a number of simulation steps until $\langle N \rangle$ in the box is equilibrated. Clearly, the configurations which are passed

through during this equilibration stage should not be counted when calculating quantities according to equation 3.10. Therefore, a GCMC run consists of an equilibration stage and a production stage. Only the configurations from the production stage are used to calculate the average of an observable, such as the average number of particles in the box:

$$\langle N \rangle = \frac{1}{M_{prod}} \sum_{j=1}^{M_{prod}} N_j \tag{3.15}$$

The ratio C/D of accepted creation and accepted deletion steps can be used to test whether equilibrium has been reached during the equilibration stage: If $C/D = 1$, the particle number in the box is fully equilibrated. If $C/D > 1$, creation steps are accepted with a higher probability than deletion steps because there are too few particles in the simulation box, *i.e.* the simulation is not yet in equilibrium. Similarly, if $C/D < 1$, equilibrium is not yet attained because there are too many particles in the simulation box. It is obvious that the ratio of attempts of creation and deletion steps should also be unity to avoid a bias. The ratio of attempted "exchange" steps (a term which comprises both insertion and deletion) to attempted translation (rotation, regrowth) steps is specified as an initial parameter. An exchange-translation ratio of two to one is often recommended. (*174*)

3.2.2. Quantities obtained from grand-canonical Monte Carlo simulations

3.2.2.1. Adsorption isotherms and adsorption selectivities

The average number of particles $\langle N \rangle$ in the simulation box can be calculated from the production stage according to equation 3.15. For a simulation box that contains no framework atoms (an "empty cell"), this number can be converted into the density of the bulk phase according to:

$$\rho = \langle N \rangle \frac{m_{m,gas}}{V_{box} \cdot N_A} \tag{3.16}$$

Here, $m_{m,gas}$ is the molar mass of the particle species, V_{box} is the volume of the simulation box, and N_A is the Avogadro constant. Calculations for empty cells can be used to evaluate whether a given potential model delivers the correct behaviour of the bulk phase under the specified conditions, *i.e.* the equation of state.

If the simulation box contains framework atoms representing a porous solid, the number of particles can be converted to the adsorbed amount in gravimetric units by using the molar mass of the adsorbent $m_{m,solid}$. The uptake in mmol g^{-1} is calculated as:

$$n_{ads}[\mathrm{mmol\,g^{-1}}] = \langle N \rangle \frac{1000}{m_{m,solid}} \tag{3.17}$$

The gravimetric uptake in mg g^{-1} can be obtained by multiplying this result with $m_{m,gas}$. The uptake in weight-% (wt%) is calculated as:

$$n_{ads}[\text{wt\%}] = \langle N \rangle \frac{100 \cdot m_{m,gas,}}{m_{m,solid} + \langle N \rangle m_{m,gas}} \tag{3.18}$$

Thus, the simulation result can be converted into a quantity which is directly comparable to macroscopic quantities that are experimentally accessible. The most important application is the prediction of adsorption isotherms by choosing a set of pressures of interest for a given temperature, thus being in complete analogy to the typical experimental setup. However, the simulation delivers the absolute amount adsorbed n_{abs}, whereas only the excess amount n_{exc} can be determined experimentally (see section 4.5).

In principle, it is also possible to convert the loading to volumetric units. This requires the density of the porous material. There is, however, a caveat: The simulation assumes an infinitely large, monolithic system. In contrast, an experimental measurement is usually carried out for a powder, and the packing density of the system is lower than the crystallographic density due to interparticular voids. Due to these differences, the volumetric uptake calculated from the simulations is an idealized value that is of limited relevance for practical use. Nonetheless, an "ideal" volumetric uptake can be useful to compare different materials. This quantity, which assumes a packing density of unity, can be calculated as:

$$n_{ads}[\text{g L}^{-1}] = \langle N \rangle \frac{1000 \cdot m_{m,gas} \cdot \rho_{cryst}}{m_{m,solid}} \tag{3.19}$$

Here, ρ_{cryst} is the crystallographic density (in g cm^{-3}). The ideal volumetric uptake can be understood as a theoretical upper boundary of the attainable volumetric storage density.

While the experimental determination of mixture isotherms is complicated, the simulation approach outlined above can be extended straightforwardly to mixtures containing several components. The loading of each species can then be expressed as a function of the total pressure. GCMC calculations for mixtures are particularly useful to determine the adsorption selectivity α, which determines the theoretical separation ability in an equilibrium-based process. For a binary mixture of components A and B, it can be calculated as: (*151*)

$$\alpha = \frac{n_{ads}(A)/n_{ads}(B)}{y(A)/y(B)} \tag{3.20}$$

The numerator corresponds to the ratio of the amounts adsorbed in the material (in molar units), and the denominator corresponds to the ratio of the concentrations in the gas phase. For an ideal gas mixture, this is the ratio of the partial pressures. The adsorption selectivity depends on temperature, pressure, and the ratio of the partial pressures.

It is also possible to estimate the adsorption selectivity from single-component isotherms, making use of the Ideal Adsorbed Solution Theory (IAST). (*123*) In the limit of very low coverage, the IAST becomes exact, and the selectivity corresponds to the ratio of the Henry constants (see below).

3.2.2.2. Isosteric heat of adsorption

The isosteric heat of adsorption q_{st} is defined as the change in energy (δU) induced by an (infinitesimally small) change of the adsorbate loading (δN) at constant pressure, temperature, and volume. (175, 176) It is defined with respect to a reference state of the bulk phase. Assuming an ideal gas reservoir as reference state, it can be expressed as:

$$q_{st} = k_B T - \left(\frac{\partial U}{\partial N} \right) \tag{3.21}$$

It can be shown that the derivative in this equation can be expressed in terms of the fluctuation of the number of adsorbed particles, and their correlations with the energy fluctuations. This permits the usage of the so-called "fluctuation formula": (170, 177)

$$q_{st} = k_B T - \frac{\langle NU \rangle - \langle N \rangle \langle U \rangle}{\langle N^2 \rangle - \langle N \rangle^2} \tag{3.22}$$

Thus, if the potential energy U of each configuration is stored during the production stage of the simulation, it permits the calculation of the isosteric heat. In a more approximate approach, fluctuations can be ignored by directly taking the average energy per particle, $\langle U/N \rangle$ to calculate the isosteric heat:

$$q_{st} = k_B T - \langle U/N \rangle \tag{3.23}$$

Finally, the isosteric heat can be determined in analogy to experiment, using a set of (at least two, preferably three or more) isotherms obtained at different temperatures. Because the isosteric heat itself depends on temperature, the isotherms should be obtained at reasonably closely spaced temperatures. (175) In a typical approach, a numerical fit to each isotherm is applied, *e.g.* by using a Langmuir or Langmuir-Freundlich model or a virial equation. The performance of three different fitting procedures was compared by Chen *et al.* for experimental hydrogen adsorption data. (62) In this study, the method proposed by Cole *et al.* showed the lowest statistical error. (178) In this approach, a virial expansion of $\ln(n_{ads}/p)$ as a function of n_{ads} is used:

$$\ln(n_{ads}/p) = A_0 + A_1 n_{ads} + A_2 n_{ads}{}^2 ... \tag{3.24}$$

Here, n_{ads} is the amount adsorbed. The first virial coefficient A_0 is related to the Henry constant K_H as: $K_H = \exp(A_0)$. At zero coverage, the isosteric heat of adsorption can be determined from the evolution of K_H with temperature according to:

$$q_{st} = \frac{R \partial \ln K_H}{\partial T^{-1}} \tag{3.25}$$

The isosteric heat of adsorption at zero coverage is a quantity that is often used to compare the affinities of different systems towards an adsorbed species.

More generally, q_{st} can be calculated for any loading n_{ads} from:

$$q_{st} = \frac{R \partial \ln(n_{ads}/p)}{\partial T^{-1}} \tag{3.26}$$

Naturally, it is sensible to calculate the isosteric heat only for loadings which are actually attained in the adsorption measurement (or simulation). Furthermore, it must be noted that the above equations, in addition to assuming ideal gas behaviour, ignore the molar volume of the adsorbed phase. It has been shown that this approximation influences the resulting isosteric heat at higher loadings. (*176*)

3.2.2.3. Henry constants

According to Henry's law, the amount adsorbed is directly proportional to the pressure at very low coverages. The relationship between the amount adsorbed and pressure is given by the Henry constant K_H:

$$n_{ads} = K_H \cdot p \tag{3.27}$$

The Henry constant can be used to derive some useful properties in the limit of zero coverage. As discussed above, there is a direct connection to the isosteric heat of adsorption (equation 3.25). Furthermore, the adsorption selectivity for a two-component mixture at very low coverages can be calculated directly from the ratio of the Henry constants (Henry's law selectivity). This is a special case where it is possible to determine the behaviour upon mixture adsorption from single-component data in a rigorous manner. (*123*)

In principle, the Henry constant can be calculated by determining the linear regime of an adsorption isotherm from a set of normal GCMC runs. However, there is a more efficient approach, permitting the direct calculation of K_H from the solid-fluid interaction energy as a function of the position in the simulation box. In the case of a particle species that has no conformational degrees of freedom, the following relationship is valid: (*179*)

$$K_H = \frac{V}{k_B T} \int \exp\left[-\frac{U(\vec{r})}{k_B T}\right] d\vec{r} \tag{3.28}$$

Here, $\vec{r}$ corresponds to the coordinates of a single particle. The integration is carried out as follows: One single particle is placed in the simulation box at an arbitrary position, and the energy is evaluated. This procedure is repeated for a very large number of steps (typically $> 10^7$). The integral is then replaced by the average over the energies:

$$K_H = \frac{V}{k_B T} \left\langle \exp\left[-\frac{U}{k_B T}\right] \right\rangle \tag{3.29}$$

Because all possible positions and orientations are equally likely, configurations having a significant overlap are also taken into account in the calculation of the average. Such configurations contribute a value of zero, so the Henry constant of a completely non-porous material becomes zero.

3.2.2.4. Position-dependent quantities: Density maps and potential energy maps

Up to this point, the quantities discussed that can be obtained from GCMC simulations have a direct connection to macroscopically measurable values. However, microscopic simulations also enable the calculation of quantities which are not directly accessible to experiment, or which can be obtained only with a sophisticated experimental setup. In particular, it is possible to derive position-dependent quantities, such as the particle "density" as a function of the position in the simulation box. Because the term density is not very useful on a microscopic level in the case of strong local variations, it is more correct to describe the property in question as a probability distribution of the adsorbed particles. The probability distribution can be determined from the particle positions of each configuration (or from a subset of the whole body of configurations). The simulation box is subdivided to generate a regularly spaced grid of smaller boxes. For every particle stored in a configuration, a counting value of the corresponding grid point is increased by one. After the end of the simulation, the values assigned to each grid point are normalized, taking into account the number of simulation steps and the volume of the box belonging to each grid point. The probability distribution is typically stored in units of particles/Å^3. It can be visualized as a function of position in one, two, or three dimensions (figure 3.4). While a quantitative interpretation is not very sensible, as the numerical values will strongly depend on the grid resolution, the graphical representations give important qualitative information concerning the preferential adsorption sites or regions in a structure. A semi-quantitative interpretation can be made by comparing the local density values with the bulk density.
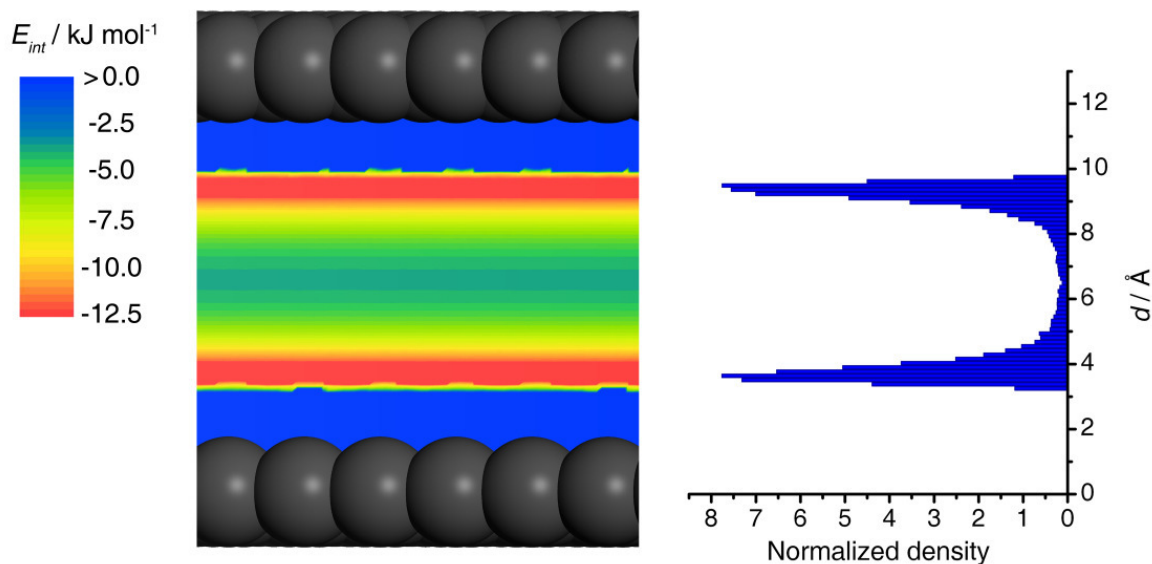
Figure 3.4. Results from GCMC simulation of methane adsorbed in a graphitic slit pore. The left side of the figure shows the potential energy distribution in a two-dimensional representation, while the histogram on the right-hand side gives the density as a function of the *z*-coordinate.

In a very similar manner, the potential energy of the adsorbed particles as a function of their position can be calculated if the energy of each particle, together with its position, is stored during the GCMC run. The potential energy distribution is then obtained on a grid, as described above for the density. It should be noted that, for particles consisting of more than one interaction site, the properties are stored for the grid point closest to the center of mass of the particle. The potential energy distribution is therefore a quantity which is averaged over different orientations, with energetically favourable orientations having a higher weight due to their higher probability during the GCMC run.

As an example, the potential energy of methane adsorbed in graphitic slit pore with an interplanar distance of 13 Å was calculated from a GCMC run at $T = 298$ K. A two-dimensional section through the resulting potential energy distribution is shown in figure 3.4. The plot clearly shows that the interaction strength is highest at a certain distance above the graphene layers, and becomes weaker towards the pore center. From this result, it can be expected that the methane molecules will be almost exclusively adsorbed at the pore walls. This is corroborated by the one-dimensional density profile, which is included in the same figure.

3.3. Electronic structure methods

3.3.1. Introduction

An accurate description of a chemical system on the level of electrons requires a quantum-mechanical treatment. There is a wide range of approaches to attack this problem, which are commonly summarized under the term electronic structure methods. Only a brief introduction to some of these methods can be given in this context. The whole treatment will proceed in the framework of the Born-Oppenheimer approximation, which simplifies the system by neglecting nuclear motion.

Assuming that a set of (fixed) nuclear coordinates is given, all information about a molecular electronic system in a stationary state is contained in the electronic wave function. The electronic wave function Ψ is the solution of the Schrödinger equation for an associated energy eigenvalue E:

$$\hat{H}\Psi = E\Psi \tag{3.30}$$

$\hat{H}$ is the electronic Hamiltonian operator, which is defined as (equation 4.3 in (*166*)):

$$\hat{H} = -\sum_i \frac{\hbar}{2m_e}\nabla_i^2 - \sum_i\sum_k \frac{e^2 Z_k}{4\pi\varepsilon_0 r_{ik}} + \sum_{i<j} \frac{e^2}{4\pi\varepsilon_0 r_{ij}} + \sum_{k<l} \frac{e^2 Z_k Z_l}{4\pi\varepsilon_0 r_{kl}} \tag{3.31}$$

Here, i and j are indexes running over the electrons, while k and l are indexes running over nuclei. $\hbar$ is Planck's constant divided by 2π, m_e is the mass of the electron, e is the elementary charge, Z is an atomic number, and ε_0 is the vacuum permittivity. ∇^2 is the Laplacian operator, the sum of the second partial derivatives with respect to the spatial coordinates, and each r_{xy} corresponds to the distance between the particles with the respective indices. The electronic Hamiltonian can be broken down into the following terms: The first term is the kinetic energy of the electrons. The remaining terms represent the potential energy arising from attraction between electrons and nuclei (second term), repulsion between electrons (third term), and repulsion between nuclei (fourth term). Due to the complexity of the Hamiltonian operator, any wave function that is a solution to the Schrödinger equation must be a function of the spatial coordinates of the N electrons. If spin is also represented as a fourth coordinate of each electron, the general expression for the wave function reads:

$$\Psi = \Psi(\vec{r}_1, s_1, \vec{r}_2, s_2 ... \vec{r}_N, s_N) \tag{3.32}$$

There is a set of orthonormal wave functions Ψ which constitute solutions to equation 3.30. Knowledge of the wave function permits the calculation of various physical observables. In particular, the energy eigenvalue associated with each wave function can be calculated from the secular equation. The wave function delivering the lowest energy is the ground-state wave function. An exact, analytical determination of the wave function is not possible for all cases of chemical interest due to the complex treatment of electron-electron interactions. Therefore, the solution of this problem requires the introduction of further approximations.

While no calculations using wave-function based methods are carried in this work, results from these methods are used as reference values at several points. A concise overview of the most important aspects of these methods is given in the following section. Density-functional theory (DFT) constitutes a different approach, permitting highly efficient electronic structure calculations for relatively large systems. DFT calculations are presented at various points of this work, which is why the theoretical framework of DFT is discussed in some more depth.

3.3.2. Wave-function based methods

3.3.2.1. The Hartree-Fock method

In the Hartree-Fock (HF) method, the wave function is expressed as a Slater determinant of one-electron wave functions ϕ (orbitals). (*166*) The Slater determinant is used to fulfill the antisymmetry requirement resulting from the Pauli principle. The orbitals are constructed as a linear combination of functions from the basis set, a set consisting of M appropriate functions χ:

$$\phi_i = \sum_j^M a_{ij} \chi_j \tag{3.33}$$

Therefore, the Slater determinant is fully determined by the matrix of coefficients a_{ij}. The variational principle states that, when different trial wave functions (constructed from the same basis set) are compared, the wave function that delivers the lowest energy eigenvalue is closest to the "true" wave function. Thus, the problem of finding the optimal wave function can be recast into the problem of minimizing the energy as a function of the coefficients a_{ij}. Starting from a trial Slater determinant, an iterative procedure, the self-consistent field (SCF) method, is used to determine the coefficients which minimize the energy. When the energy change from one iteration to the next falls below a pre-defined threshold, the calculation is converged, and the resulting wave function and energy correspond to the best HF solution which is attainable for the given basis set.

The Hartree-Fock method uses a Hamiltonian which is simplified when compared to equation 3.31. An average potential, the HF potential, is used to represent electron-electron interactions. Apart from errors arising from the finite size of the basis set, this approach exactly accounts for Coulomb interactions and exchange, a quantum-mechanical effect that rules out the occupancy of one spatial orbital by two electrons with equal spin (Pauli principle). Thus, by increasing the size of the basis set, the HF method will converge to a well-defined solution, the so-called Hartree-Fock limit. However, the HF method completely neglects electron correlation, *i.e.* effects arising from the correlated motion of electrons. This neglect affects different molecular properties to a different extent. (*180*) In particular, dispersive interactions, which are due to electron correlation effects, are completely absent in HF calculations. Thus, the HF potential energy surface for a rare-gas dimer is purely repulsive, whereas it is well-known from experimental observations that an energy minimum exists:

For example, the (weak) interatomic attraction between the fluctuating electron clouds is responsible for the formation of rare-gas crystals at low temperatures. (*181*)

3.3.2.2. Electron correlation methods

By construction, the HF method ignores the correlation of the motion of each electron with the other electrons. Typically, a conceptual distinction is made between dynamic and static correlation: Dynamic correlation refers to short-range effects, *e.g.* between electrons occupying the same orbital, whereas static correlation is a long-range contribution that is important in cases where several electron configurations have similar energies (near-degeneracy effects). (*154*) The inclusion of electron correlation requires the use of multi-determinant wave functions, which are a linear combination of several Slater determinants. The additional determinants correspond to singly, double, triply *etc.* excited states with respect to the HF ground state. The full configuration interaction (CI) method accounts for all possible excited states, and thus completely includes electron correlation. The full CI method becomes computationally very expensive with increasing size of the system. Truncated versions exist, which take into account only some excited states. (*180*)

A more approximate, yet more efficient way to account for electron correlation is provided by many-body perturbation theory. Assuming that the inclusion of correlation effects corresponds to a relatively small perturbation of the (uncorrelated) HF calculation, the correlation operator is applied as a perturbation to the HF Hamiltonian. The HF Slater determinant is expanded in a power series to give excited-state determinants. The accuracy of the calculation depends on the order of the highest-order correction term included. This approach, which was first proposed by Møller and Plesset, is commonly referred to as the MPx method, with x being the order of the highest correction term. The MP2 method, which is computationally tractable for relatively large systems, is frequently used in electronic-structure calculations. It is the most efficient possibility to improve the result with respect to a HF calculation, and typically recovers 80 to 90% of the correlation energy. (*154*) Higher-order perturbation methods (MP3, MP4 and beyond) improve the accuracy, but are used less frequently.

The coupled cluster (CC) method uses excitation operators to generate excited-state Slater determinants from the HF wave function. If excitation operators up to the highest order were included, the CC method would become equivalent to the full CI method. (*180*) However, for practical applications, only excitation operators up to a certain number of electrons are taken into account, *e.g.* only single and double excitations (CCSD - coupled cluster with singles and doubles). The important advantage of the CC formalism with respect to truncated CI methods is the fact that combinations of "disconnected" excitations are also included. For example, two separate, independent double excitations are included in a CCSD calculation, while they would require an inclusion of quadruply excited determinants in the CI method. While the CCSD method is already computationally very demanding, the explicit inclusion of triply excited determinants (CCSDT) is impractical for all but the small-

est systems. It is, however, possible to include the contribution of triply excited states by making use of a perturbative treatment, leading to the CCSD(T) method. This method is often referred to as the "gold standard" in quantum chemistry, permitting calculations of very high accuracy.

To summarize the brief outline of wave-function based methods, it should be emphasized that there are two main factors which determine the quality of a calculation: The first point, obviously, is the choice of method. The second crucial point is the size of the basis set, with increasing accuracy on increasing size of the basis set. (*182*) Naturally, it is impossible to carry out a calculation with a basis set of infinite size. When results obtained with two or more differently-sized basis sets are available, the possibility to extrapolate to the complete basis set limit is a frequently used option. (*180*) Alternatively, the result obtained with the best available basis set can be taken as is.

3.3.3. Density-functional theory

3.3.3.1. Fundamentals of density-functional theory

Density-functional theory (DFT) is a method that has become ubiquitous in electronic structure calculations for molecules and solids, both in quantum chemistry and solid-state physics. The following introduction outlines the conceptual framework behind DFT, with no emphasis on theoretical details. More theoretical information, as well as numerous examples of applications, can be found in computational chemistry textbooks (*154*, *166*) and comprehensive review articles on the topic. (*183*, *184*)

The foundations of DFT were laid in 1964 by Hohenberg and Kohn, who showed that the ground-state electronic energy of a system of N electrons is a functional of the electron density. (*185*) Knowledge of the electron density $\rho(\vec{r})$, which depends on the three spatial variables and spin, can deliver the same information as the evaluation of the wave function, which depends on $4N$ variables (three spatial variables plus spin for each electron, equation 3.32). The variational principle already mentioned in the context of the HF method is also valid in DFT: The electron density which delivers the lowest energy corresponds to the ground-state electron density, and it can be obtained in an iterative (SCF) procedure.

The practical application of DFT was made possible by a second seminal paper by Kohn and Sham in 1965. (*186*) Here, the electron density is expressed in terms of a set of auxiliary one-electron functions (orbitals):

$$\rho = \sum_{i=1}^{N} |\phi_i|^2 \tag{3.34}$$

In contrast to wave-function based methods, these orbitals do not lend themselves to a direct physical interpretation. Instead, they represent a hypothetical system of non-interacting electrons which has the same density as the real system.

In the Kohn-Sham approach, the DFT energy expression is written as:

$$E_{KS}[\rho] = T_s[\rho] + E_{ne}[\rho] + E_{ee}[\rho] + E_{xc}[\rho] \tag{3.35}$$

Here, T_s is the kinetic energy of a system of non-interacting electrons, E_{ne} is the electrostatic interaction between nuclei and electrons, and E_{ee} is the electrostatic interaction between electrons. In addition to a correction term to T_s arising from electron-electron interactions, the last term, E_{xc}, contains the inherently quantum-mechanical effects of exchange and correlation.

With the energy expression given above, the Kohn-Sham one-electron Hamiltonian $\hat{h}_{KS}$ can be derived accordingly. The optimal one-electron functions correspond to the N lowest-energy solutions of the Kohn-Sham equation:

$$\hat{h}_{KS}\phi_i = \epsilon_i\phi_i \tag{3.36}$$

While the sum of the values of ϵ_i gives the total energy E_{KS}, the single-particle energies ϵ_i do not correspond to real single-electron energies.

Taking the above information together, it is clear why a DFT calculation must proceed according to an iterative procedure: A starting density ρ_0 is guessed. Then, the elements of the Kohn-Sham Hamiltonian are calculated from the density, and the eigenvalue problem defined in equation 3.36 is solved via matrix diagonalization. The resulting orbitals $\phi_{i,1}$ are used to construct the new density ρ_1. The procedure is repeated until the changes of the density or energy fall below a defined threshold.

3.3.3.2. Exchange-correlation functionals

The local density approximation

As expressed in equation 3.35, the exchange-correlation energy E_{xc} is a functional of the electron density. If the "true" form of this exchange-correlation (XC) functional was known, DFT would be an exact method. However, such an exact expression of the XC functional is not available, and it is necessary to use an appropriate approximation. The XC functional itself is composed of different functionals that separately account for exchange and correlation. Thus, in addition to different means of approximating the exchange and correlation parts, there is also the possibility to use different combinations of X and C functionals, leading to an enormous number of XC functionals that have been proposed and tested. (*183*) The simplest approximation to the XC functional is the local density approximation (LDA). (*154*) It is based on the assumption that the electron density at each point in space can be treated as a uniform electron gas. The exchange energy of the uniform electron gas is known exactly. The correlation energy for different densities can be calculated numerically, and appropriate analytical interpolation schemes have been devised for use in DFT calculations. By definition, the LDA is formally exact for a homogeneous electron gas. For real systems, errors arise due to the variation of the electron density, and LDA is a showcase

example of a "local" functional: At a given point, it depends only on the electron density at this point. A "true" XC functional, however, depends on the electron density everywhere and is therefore completely nonlocal. Due to the lack of nonlocal contributions, LDA tends to underestimate exchange, and overestimate electron correlation. While it performs reasonably well for many solids, it is not suitable for molecules: LDA usually predicts bonds that are "too short" and "too strong", and massively overestimates the interaction energies in dispersion-bound systems. (*187*)

The generalized gradient approximation

The generalized gradient approximation (GGA) improves upon LDA by taking into account local variations of the electron density, *i.e.* the density gradient. An early attempt to improve the LDA exchange energy was made by Becke with the B88 functional, reducing the error in the exchange energy with respect to LDA by two orders of magnitude. (*154, 188*) At the same time, an improved correlation functional was proposed by Lee, Yang, and Parr (LYP). (*189*) A combination of the two, the BLYP functional, is widely used in computational chemistry. Both functionals use empirical parameters in the expansion of the energy, which are obtained from a fit to known data. A gradient correction that dispenses with empirical parameters was proposed by Perdew, Burke, and Ernzerhof (PBE). (*190*) The PBE functional, whose strengths and weaknesses are well documented and easily predictable, is among the most popular exchange-correlation functionals, particularly for solids.

Meta-GGA functionals further refine the GGA methodology by either taking into account higher order derivatives of the electron density, or by exploiting information on the kinetic energy density. Both parameterized and non-empirical versions exist.

Hybrid functionals

Hybrid functionals include a percentage of exact Hartree-Fock exchange, thereby introducing a nonlocal contribution. The B3LYP functional, which is by far the most widely used functional for molecules, (*183*) combines an exchange term consisting of three contributions (Hartree-Fock, B88, and LDA) with the LYP correlation energy. (*191*) The weight factors determining the different contributions are derived empirically. The B3LYP functional can be understood as the hybrid "counterpart" of the BLYP functional. Similarly, the PBE0 functional uses a combination of HF and PBE exchange. (*192*) Here, the weight factor is established in a non-empirical manner.

Several systematic studies assessing the performance of different XC functionals exist in the literature. (*193, 194*) However, general recommendations for the choice of functional are hardly possible. In order to find a suitable XC functional, the performance of different functionals should be assessed for a model system for which either experimental data or results from high-level theoretical methods are available. As it will be discussed below, systems in which dispersive interactions play an important role are particularly problematic.

3.3.3.3. Basis sets

Slater-type orbitals

In the electronic structure methods discussed above, the one-electron wave functions (orbitals) are expanded in a given basis set. In all cases discussed here, the functions of the basis set resemble atomic orbitals. There are other choices of functions, such as plane waves or muffin-tin orbitals, but they are not taken into account in this context. Generally, both accuracy and computational cost increase when the size of the basis set is increased. Therefore, the type of function should be chosen in a way that the highest possible accuracy is reached with the smallest possible number of basis functions.

In an atomic-orbital approach, the most straightforward choice are Slater-type orbitals (STOs), which are very similar to hydrogen-like orbitals. For the quantum numbers n, l, m, the expression of an STO in polar coordinates reads (equation 5.1 in (*154*)):

$$\chi_{\zeta,n,l,m}(r,\theta,\varphi) = NY_{l,m}(\theta,\varphi)r^{n-1}\exp(-\zeta r) \tag{3.37}$$

Here, N is a constant, and $Y_{l,m}$ are spherical harmonic functions. The number of values of ζ (zeta) determines the size of the basis set, and thus the quality of the calculation. A single-zeta (SZ) basis set contains just enough orbitals that all electrons of the system can be accommodated. Clearly, this choice represents the smallest number of basis functions possible, a minimal basis set. Correspondingly, double-zeta (DZ) and triple-zeta (TZ) basis sets use two and three functions per electron, respectively. Usually, the basis set is not restricted to the type of orbitals actually occupied, but orbitals with higher angular momentum are also included as polarization functions, resulting, for example, in a triple-zeta plus polarization (TZP) basis set. In order to limit the number of functions, inner orbitals are often treated on a lower level than valence orbitals, leading to split-valence basis sets.

An STO basis set has a number of favourable properties. In particular, the exponential dependence ensures a relatively rapid convergence with increasing size of the basis set. The main drawback of the STO basis set is the fact that the analytical calculation of two-electron integrals, as part of the SCF calculation, is computationally very demanding.

Gaussian-type orbitals

To overcome the aforementioned problem with analytical integration, Gaussian-type orbitals (GTOs) can be used, which have the following form (equation 5.2 in (*154*)):

$$\chi_{\zeta,n,l,m}(r,\theta,\varphi) = NY_{l,m}(\theta,\varphi)r^{2n-2-l}\exp(\zeta r^2) \tag{3.38}$$

In contrast to STOs, GTOs do not have a cusp at the nucleus, and they do not give a good description of the wave function at long distances. Therefore, approximately three times as many GTOs are needed to give the same accuracy when compared to STOs. However, the analytical integration is much easier, leading to a lower computational cost in spite of the larger number of basis functions needed, and GTOs are favoured over STOs in many

quantum chemistry programs. The size of the GTO basis set can be reduced by basis set contraction, which leads to a computationally more efficient description of the inner electrons. Several different flavours of GTO basis sets are availabe, depending on the contraction scheme and other parameterization issues. (*154*)

Numerical orbitals

Numerical orbitals constitute a fundamentally different approach when compared to STOs and GTOs. (*195, 196*) Instead of using analytical functions, the radial part of the basis functions is obtained from atomic DFT calculations, and then tabulated on a mesh. The angular part is calculated from the appropriate spherical harmonic $Y_{l,m}$. For a specific atom type, a minimal basis set is generated from calculation for a neutral atom. The extension to a double numerical basis set makes use of orbitals obtained from a calculation for a positively charged ion. Polarization functions and further extensions can be generated by including additional orbitals from calculations for cores with a different atomic number Z.

Numerical orbitals have a number of advantages in terms of computational cost: DFT studies on model systems have shown that a "Double Numerical plus Polarization" (DNP) basis set and (considerably larger) triple-zeta GTO basis sets deliver similarly accurate results, with the computations using numerical orbitals being at least a factor of 10 faster. (*197*) Moreover, there are indications that numerical basis sets minimize the basis set superposition error (see below), because molecules can be dissociated exactly into the constituent atoms. (*196*)

Effective core potentials and frozen cores

All elements except the lightest ones possess low lying orbitals which do not participate in the chemical bonding. In all-electron calculations, a large portion of the computational effort is used to accurately describe these "core electrons". Furthermore, the core electrons of heavier elements require a relativistic treatment, which makes the calculation even more demanding. A possible simplification to this problem is the usage of effective core potentials, which replace the explicit treatment of the core electrons by suitable functions. A similar approach is the frozen-core approximation, which includes the core electrons explicity, but fixes their orbitals to the atomic values.

Basis set superposition errors

The binding energy of a system AB consisting of two subsystems A and B is typically calculated from the differences of the computed energies: $E_{bind} = E(AB) - E(A) - E(B)$. There is, however, a complication when it is considered that the subsystems are treated with smaller basis sets than the combined system. The usage of a larger basis set for AB will lead to an artificial lowering of $E(AB)$, an effect which is termed basis set superposition error (BSSE). The BSSE is particularly important for weakly bonded systems, *e.g.* hydrogen bonds. It decreases with increasing size of the basis set. A possibility to approximately account for this error is the counterpoise correction (CP). (*198*) It requires additional cal-

culations for each subsystem using the full basis set of the system AB. However, it has been pointed out that the energy lowering in the combined system is only partly a mathematical artefact, whereas another part of it must be attributed to actual chemical reality, such as charge transfer processes. Therefore, the CP correction tends to over-correct the BSSE. (*166*) Particularly for HF and DFT calculations, where the BSSE is less pronounced when compared to correlated methods, it is sometimes recommended to dispense with a CP correction.

3.3.4. Dispersive interactions in DFT

3.3.4.1. Introduction

Dispersive interactions are caused by static electron correlation, the correlated motion of electrons at large separations. They are an inherently nonlocal effect, and require the inclusion of double (and, for accurate results, higher) excitations in wave-function based methods. (*181*) Due to the usage of local exchange-correlation functionals, these interactions are not well reproduced in standard DFT calculations. (*199, 200*) Moreover, both over- and underestimations of the interaction may occur, depending on the functional. (*187*) The inclusion of dispersive interactions in the DFT method is a current area of vivid research, and several different approaches have been proposed. (*201*) The empirical DFT-D method is particularly interesting due to its computational efficiency. Other approaches use more complicated formalisms, and have not yet been as widely tested.

3.3.4.2. The DFT-D method

The DFT-D method, proposed by Grimme, uses an empirical correction scheme to account for dispersion interactions. (*202, 203*) The total energy, E_{DFT-D}, is a simple sum of the contributions from the normal DFT calculation, and the dispersion energy:

$$E_{DFT-D} = E_{DFT} + E_{disp} \tag{3.39}$$

The dispersion energy is calculated in analogy to typical molecular mechanics approaches:

$$E_{disp} = -s_6 \sum_{i=1}^{N-1} \sum_{j=i+1}^{N} \frac{C_{6,ij}}{r_{ij}^6} f_{dmp}(r_{ij}) \tag{3.40}$$

In this equation, r_{ij} is the distance between two atoms labelled i and j out of the total number of atoms N. A damping function f_{dmp} is used to avoid singularities at small values of r_{ij}. s_6 is a global scaling factor which depends on the exchange-correlation functional, it has a value close to unity. $C_{6,ij}$ is the dispersion coefficient, which is calculated from the atomic coefficients for i and j by using the geometric mean. It is thus apparent that there is a close correspondence between the DFT-D approach and many force-field based methods. In the original version of DFT-D, the coefficients $C_{6,ij}$ are calculated from an interpolation formula

which is similar to the London approximation. Coefficients for all elements up to Xenon were reported in the original paper, making the DFT-D method applicable for the large majority of possible systems of interest. As a computationally efficient method to include dispersion interactions, the DFT-D method has been widely used in the literature. (*204*)

Very recently, an improved approach termed DFT-D3 has been proposed. It includes higher-order dispersion coefficients, uses an additional three-body term, and employs a non-empirical scheme to calculate the atomic dispersion coefficients. (*205*)

3.3.4.3. Other approaches to include dispersive interactions in DFT

A non-empirical approach developed by Becke and Johnson makes use of the dipole moment of an electron and its associated exchange hole to compute the dispersion coefficients. (*206*) The dispersion energy can then be calculated *a posteriori* from these coefficients using not only the r^{-6} expression, but also higher-order dispersion terms. Recent results show that the combination of the dispersion term resulting from these coefficients with standard GGA functionals provides for a good description of rare-gas dimers and other van der Waals complexes. (*207*, *208*)

Another efficient possibility to account for dispersion in an approximate manner is the usage of dispersion-corrected atom-centered potentials (DCACP), which are a special case of effective core potentials. (*209*) These potentials can be used in any DFT code which supports effective core potentials. However, DCACPs are so far available only for the rare gases and the most important elements in organic chemistry.

A very sophisticated approach has been presented by Langreth and co-workers. (*210*) Here, an additional term to evaluate the nonlocal correlation energy is added to the local part resulting from an adequately chosen, local exchange-correlation functional. The resulting functional, termed van der Waals density functional (vdW-DF), has the correct asymptotic behaviour at large intermolecular separations. It has been applied to a number of different systems, including small molecules, crystals, biological molecules, and interfaces. (*211*) In particular, a recent study used vdW-DF to calculate the potential energy surface for hydrogen adsorbed in MOF-74. (*88*)

3.3.5. Important applications of density-functional theory

3.3.5.1. Determination of interaction energies

In principle, the interaction energy between two or several subsystems (fragments) can be calculated straightforwardly by subtracting the DFT energy of the subsystems from the energy of the combined system. Obviously, the parameters that determine the quality of the calculation, such as the basis set size, must be identical in all calculations to permit a meaningful comparison. A distinction must be made between calculations for relaxed systems and calculations for systems consisting of rigid (unrelaxed) subsystems. In cases where important changes of the molecular geometry occur when the subsystems are combined, such as conformational changes or significant changes in bond lengths, the effect of the relaxation

should not be neglected. The usage of rigid subsystems is more convenient when this is not the case. If geometric changes are neglected, a potential energy surface (*e.g.* for a varying distance between the subsystems) can be calculated from a set of single-point calculations, without a necessity for a constrained geometry optimization.

It should be emphasized that the interaction energy as defined above is not identical to the bond dissociation energy. Taking a diatomic molecule as an example, the bond dissociation energy (often termed D_0 in spectroscopy) is somewhat smaller than the interaction energy calculated for the equilibrium distance (D_E). The difference is the zero-point vibrational energy (ZPVE), which is due to the zero-point motion of atoms. The ZPVE can be obtained from a calculation of the vibrational properties, which requires a set of DFT calculations for systems with displaced atoms. Therefore, it becomes computationally quite expensive for systems consisting of more than a few atoms.

3.3.5.2. Geometry optimization

Typically, it cannot be expected that the geometry specified at the beginning of a calculation corresponds to the equilibrium geometry. In this context, it should be emphasized that this energetically most favourable geometry may depend on the computational setup: For example, the equilibrium bond length of a diatomic molecule will slightly vary when different exchange-correlation functionals are used in a DFT calculation. In order to perform a geometry optimization, it is necessary to calculate the forces on the nuclei, *i.e.* the derivative of the energy with respect to a change in nuclear coordinates. It can be shown that this can be done in an efficient manner, making use of the basis function derivatives. (*166*) After the SCF calculation for the specified initial geometry is finished, the forces are calculated, the nuclei are moved according to the forces, and a new SCF cycle is started. This procedure is repeated until a convergence criterion is met, *e.g.* when the magnitude of the geometry change from one cycle to the next falls below a certain threshold.

3.3.5.3. Electron density, electrostatic potential, and partial charges

In addition to the interaction energy and the forces on the nuclei, different position-dependent quantities are accessible through DFT calculations. As it has become apparent from the description above, the electron density distribution is a direct result of a DFT calculation. An analysis of the electron density can provide interesting insights into the chemical bonding situation. While even simple qualitative approaches can provide useful information, the quantum theory of atoms in molecules (AIM) constitutes a rigorous approach. (*212*) AIM makes use of the electron density, as well as its derivatives, in order to define and classify chemical bonds.
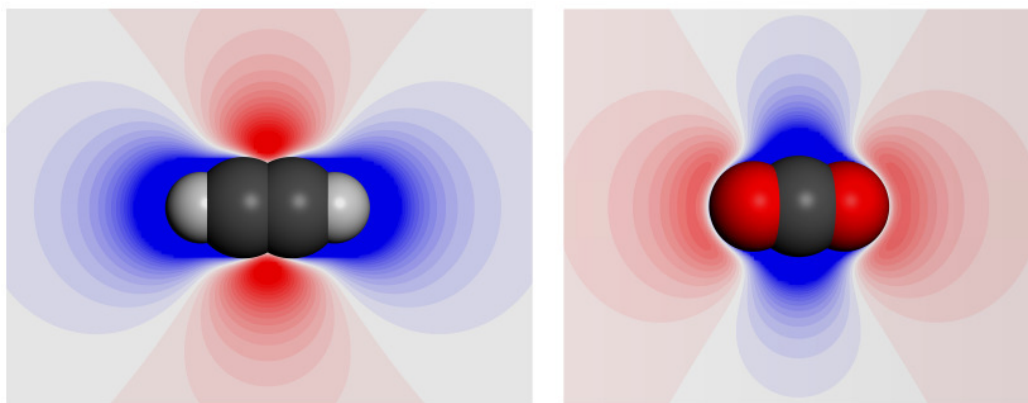
Figure 3.5. Two-dimensional visualization of the DFT electrostatic potential of acetylene (left) and carbon dioxide (right). Regions of positive potential are shown in blue, regions of negative potential in red.

Another interesting position-dependent quantity is the electrostatic potential, which corresponds to the attraction or repulsion that is exerted on a test charge by the electric field of a molecule (or crystal). The electrostatic potential V_{ESP} is given by (equation 9.11 in (*154*)):

$$V_{ESP}(\vec{r}) = \sum_A \frac{Z_A}{|\vec{r} - \vec{r}_A|} - \int \frac{\rho(\vec{r}_{el})}{|\vec{r} - \vec{r}_{el}|} d\vec{r}_{el} \tag{3.41}$$

The first part corresponds to the contribution of the nuclei, while the second part is due to the electron density. A common method to evaluate the electrostatic potential makes use of a multipole expansion of the electron density. (*166*, *213*) An alternative is the numerical solution of the Poisson equation. (*195*) Exemplarily, the electrostatic potential of two molecules discussed in this work is shown in figure 3.5.

The concept of partial charges is often used to facilitate the comparison of electronic structure calculations carried out for different systems. Several methods to derive partial charges have been devised, based either on a population analysis of the basis functions, an analysis of the electron density, or a fit to the electrostatic potential. The Mulliken population analysis employs the occupation of the orbitals to assign the electrons to the different atoms. Despite its popularity, this scheme has a number of deficiencies. (*154*) Hirshfeld charges are based on a partitioning of the molecular electron density with respect to the atomic densities. In contrast to Mulliken charges, which sometimes show an absurd evolution when large, diffuse basis sets are used, Hirshfeld charges show a more predictable behaviour with increasing basis set size. While both methods can be useful in a chemical interpretation of the results of DFT calculations, they are not able to reproduce the electrostatic potential in a point-charge (monopole) representation. (*161*) Therefore, both types of charges are not suitable to represent electrostatic interactions in force-field based calculations.

ESP charges are obtained from a least-squares fit of a set of charges positioned at the nuclei to the electrostatic potential obtained from the DFT calculation. The fit is carried out for a number of points in space around each atom. A number of schemes to derive ESP charges has been proposed, which differ mainly in the method of how to choose the points. For

example, the approach of Singh and Kollman uses points located at nested surfaces around each atom. (*214*) It has been found that this method delivers a superior representation of the electrostatic potential with respect to other ESP methods. (*215*)

Although ESP charges are not able to reproduce all features of the electrostatic potential due to the use of a point-charge representation, the long-distance interactions which are most important in molecular simulations are covered quite well by this approach. (*161*) Therefore, if the partial charges are intended for use in a force-field based calculation, ESP charges should be favoured over charges obtained with other derivation schemes. (*160*) Typical methods of calculating ESP charges are applicable for non-periodic systems, only. When treating periodic systems, it is necessary to calculate the ESP charges for a non-periodic cluster, and then transfer them to the periodic structure. Naturally, the charges must be normalized to obtain a neutral cell. In addition to a dependency on calculation parameters, this introduces a dependency on the size of the non-periodic cluster. Only recently, an extension of the ESP method to periodic systems has been developed, but this approach is not yet routinely applicable. (*216*)

3.3.5.4. Energy decomposition analysis

The energy decomposition analysis (EDA) aims at a partitioning of the total interaction energy, obtained from an electronic structure method, into "chemically intuitive" contributions. (*217*) As a first step, the total interaction energy E_{tot} is calculated by subtracting the energy of the (relaxed) fragments from the energy of the (relaxed) combined system. E_{tot} is then decomposed into two contributions: $E_{tot} = E_{prep} + E_{int}$. Here, E_{prep} is the energy associated with the distortion and change of electronic state of the fragments with respect to their equilibrium geometry and electronic ground state. E_{int} is the actual interaction energy between the two fragments in the combined system. It is divided into the following components:

$$E_{int} = E_{Pauli} + E_{elstat} + E_{orb} \tag{3.42}$$

E_{Pauli} corresponds to the repulsive interaction between the fragments arising from the Pauli exclusion principle. E_{elstat} is the electrostatic interaction energy between the frozen (unrelaxed) electron densities of the fragments. Finally, E_{orb} is the energy contribution originating from the relaxation of the orbitals. It can be further decomposed into the contributions from orbitals with different symmetry. In a first approximation, E_{orb} and E_{elstat} can be identified with the degree of covalent and ionic bonding, respectively. However, it must be pointed out that E_{orb} absorbs all effects of charge polarization, because E_{elstat} is calculated from the frozen electron densities. If dispersion corrections are applied in a simple *a posteriori* manner (equation 3.39), the dispersion energy E_{disp} simply becomes an additional term in equation 3.42.

The EDA has been used to develop an intuitive understanding of different chemical bonding situations, *e.g.* for transition-metal and main-group donor-acceptor complexes. (*217*)

4. Structural Models and Potential Parameters

4.1. Introduction

In this chapter, the models and parameters used in the simulations are described in detail. Section 4.2 assesses the adequacy of the chosen potential models for the different gases that are considered in this work. After a description of the potential models, the parameters are validated by simulating the bulk properties for relevant conditions. The corresponding force-field parameters (Lennard-Jones parameters and point charges) are summarized in the Appendix, tables A.1 to A.3. Because the discussion of relationships between adsorption properties and structure constitutes an important part of this work, section 4.3 provides a detailed discussion of the structural models of the microporous adsorbents. Section 4.4 discusses the choice of parameters used to represent the adsorbents in the simulations. The force-field parameters are given in the Appendix, tables A.4 to A.8, and the calculation of partial charges is reported in subsection A.2.3 of the Appendix. The calculation of the free pore volume is described in section 4.5. Finally, an overview over the software packages used is given in section 4.6.

4.2. Fluid molecules: Description and validation of potential models

4.2.1. Hydrogen

4.2.1.1. Potential models for dispersive interactions

Some key properties of hydrogen and all other fluid molecules discussed in this work are summarized in table 4.1. In the case of the H_2 molecule, the distance between the two hydrogen atoms amounts to 0.74 Å, a value that is significantly lower than the van der Waals diameter of the molecule. It can therefore be expected that the H_2 molecule can be quite well approximated by a single-site (united-atom) representation instead of a two-site model. Moreover, theoretical investigations indicate that the H_2 molecule retains its rotational degrees of freedom in the physisorbed state. (*218*) In the existing literature, both spherical (single-site) and dumbbell (two-site) models have been employed in simulations of hydrogen adsorption.

The most simple approach that delivers reasonably realistic results is a single-site Lennard-Jones potential. A widely used set of Lennard-Jones parameters for a spherical representation of the H_2 molecule was proposed by Buch, based on earlier compilations of reference

data. (*155*) The original values, which are slightly different, (*219*) have also been employed quite frequently. Another set of parameters, explicitly designed for use with Feynman-Hibbs quantum corrections (discussed below), was derived by Kumar *et al.* (*220*)

A straightforward extension is the usage of a dumbbell model, with the two LJ sites located at the atomic positions. Cracknell studied the performance of the Buch potential and a two-site potential derived from the Buch potential for predictions of hydrogen physisorption in graphitic nanofibers. (*31*) The difference between the two potential models was found to be negligible. A different set of parameters was obtained by Yang and Zhong, using a fit to the experimental equation of state of H_2 at two different temperatures. (*221*) A more exhaustive fitting procedure was carried out by Wang, who derived the potential from predictions of the second virial coefficient at various temperatures, explicitly taking into account quantum effects. (*222*)

There are numerous more sophisticated models employing different functional forms of the potential. For example, Han *et al.* used a two-site Morse potential derived from *ab-initio* calculations. (*81*) Detailed studies aimed at an accurate reproduction of the fluid properties showed that the more complex Silvera-Goldman potential is superior to the Lennard-Jones potential. (*223*) However, this potential uses eight adjustable parameters, and is therefore impractical for use with standard force fields.

Table 4.1. Molar mass, quadrupole moment θ, polarizability α, kinetic diameter d_{kin}, critical temperature, and critical pressure of all gases considered in this work. Unless stated otherwise in the text, the quadrupole moments and polarizabilities are taken from the *Computational Chemistry Comparison and Benchmark Database*. (*224*) All other data are from the compilation of Li *et al.* (*114*) Additionally, the isothermal properties of all fluids except acetylene are shown in the Appendix, section A.4.

	m_{molar} / g mol^{-1}	θ / eÅ^2	α / Å^3	d_{kin} / Å	T_{crit} / K	p_{crit} / bar
H_2	2.0158	0.1288	0.787	2.89	32.98	12.93
O_2	31.9988	-0.0975	1.562	3.47	154.58	50.43
CO	28.0104	-0.5911	1.953	3.69	132.85	34.94
CO_2	44.0098	-0.8908	2.507	3.3	304.12	73.74
C_2H_2	26.0378	1.3189	3.487	3.3	308.3	61.14

4.2.1.2. Inclusion of electrostatic interactions

Both experimental measurements and theoretical calculations deliver a quadrupole moment θ of the H_2 molecule of approximately 0.13 eÅ^2. (*224, 225*) A positive sign of the quadrupole moment corresponds to a negative polarization of the center of the molecule, while a negative sign of the quadrupole moment represents a positive polarization. In this work, the

value of 0.1288 eÅ^2 reported by Boehme and La Placa is used. (*225*) It is in very good agreement with high-quality theoretical values available in the *Computational Chemistry Comparison and Benchmark Database* (CCCBDB). (*224*) For a system of point charges, the quadrupole moment corresponds to: (*226*)

$$\theta = \frac{1}{2} \sum_i e_i \left(3z_i^2 - r_i^2\right) \tag{4.1}$$

Here, e_i is the charge located at the i-th point, and z_i is the projection of the distance $r_i = \sqrt{x_i^2 + y_i^2 + z_i^2}$ on the z-axis defining the orientation of the quadrupole. For a linear molecule, this equation simplifies to $\theta = \sum e_i z_i^2$. The quadrupole moment of the H_2 molecule is expressed as a three-site model, with a negative charge of $-2q$ located at the center of mass (Q_{com} = dummy atom at center of mass), and positive charges of $+q$ located at the atomic positions (figure 4.1). Taking the H-H distance to be 0.74 Å and the quadrupole moment of 0.1288 eÅ^2, equation 4.1 delivers $q = 0.4705$ e. This value is very similar to the point-charge model proposed by Darkrim *et al.*, which was used in several earlier modelling studies. (*98*)
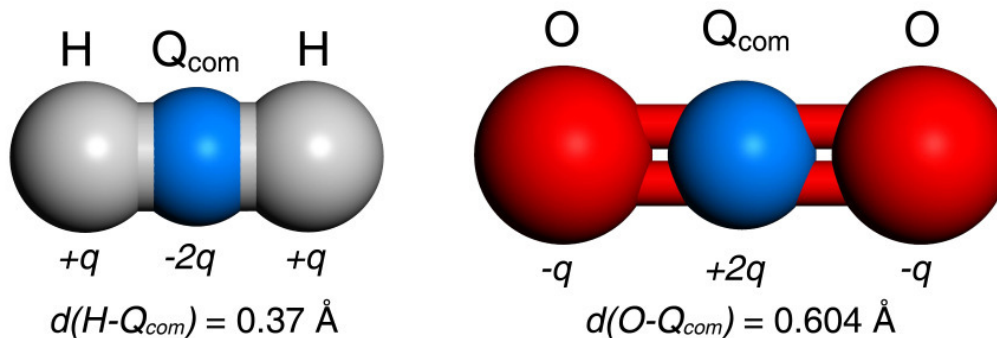
Figure 4.1. Models of the H_2 and the O_2 molecule. For hydrogen, the three-site model is used only when electrostatic interactions are included, otherwise, the molecule is represented as a single sphere. The corresponding LJ parameters are given in table A.1 and A.3, respectively.

4.2.1.3. Quantum effects and the Feynman-Hibbs correction

At low temperatures, the thermal wavelength $\lambda = h/\sqrt{2\pi k_B T m}$ of particles with low mass is non-negligible with respect to the average interparticle distance. (*33, 162*) Thus, the quantum delocalization of the particles must be accounted for. A sophisticated way to treat these quantum effects is the usage of path-integral Monte Carlo (PIMC) simulations: Here, a particle is modelled as a chain of classical beads (ring polymer), connected by springs. PIMC simulations have been used, for example, in a detailed study of the adsorption of hydrogen in carbon slit pores, a simple model system. (*33*) They are, however, computationally too demanding for simulations of adsorption in more complex adsorbents.

A more efficient, yet more approximate way to account for quantum effects is the use of effective interparticle potentials. The Feynman-Hibbs (FH) effective potential uses a temperature-dependent perturbation to the unperturbed potential U_0. In its simplest form, which uses only the second-order expansion, the Feynman-Hibbs effective potential reads (equation 3.115 in (*162*)):

$$U_{FH}(r) = U_0(r) + \frac{\hbar^2}{24\mu k_B T} \left(\frac{2U_0'(r)}{r} + U_0''(r) \right) \tag{4.2}$$

In this equation, μ is the reduced mass: $\mu = (m_i m_j)/(m_i + m_j)$. For interactions between identical particles, μ equals $m/2$, for interactions of a particle with an "infinitely heavy" particle (*e.g.* a periodic framework), it is $\mu = m$. For the Lennard-Jones potential, an evaluation of the derivatives delivers:

$$\frac{2U_{LJ}'(r)}{r} + U_{LJ}''(r) = D_0 \left(\frac{132 r_0^{12}}{r^{14}} - \frac{60 r_0^6}{r^8} \right) \tag{4.3}$$

As the Feynman-Hibbs correction is an approximation to the exact treatment, it is applicable only if the quantum delocalization is not too large. For the reduced thermal wavelength (the thermal wavelength divided by the van der Waals diameter σ), $\lambda^* \leq 0.5$ is suggested as a limiting value. (*227*) At 77 K, the reduced thermal wavelength of hydrogen is very close to this limiting value, with $\lambda^* = 0.497$. (*228*) It can thus be expected that the FH quantum correction will not work at significantly lower temperatures.

There are numerous examples employing the FH correction to the Lennard-Jones potential in the literature. Early studies were aimed at simple Lennard-Jones fluids like liquid Ne or gaseous He. (*227*, *229*) It has been used frequently in computational investigations of hydrogen storage in porous materials, *e.g.* in studies of porous carbon materials, (*33*, *230*, *231*) and MOFs and other ordered porous materials. (*71*, *101*) While it is commonly agreed that it is important to account for quantum effects under cryogenic conditions, there is some disagreement concerning their significance at room temperature. (*71*, *101*, *230*)

The FH correction is most often used with the LJ potential. In principle, however, it can be applied to any well-behaved potential expression U_0. For the Morse potential as expressed in equation 3.8, the corresponding derivatives read:

$$\begin{aligned}
U_{Morse}'(r) &= D_0 \frac{\alpha}{r_0} \left(-\exp\left[\alpha \left(1 - \frac{r}{r_0} \right) \right] + \exp\left[\frac{\alpha}{2} \left(1 - \frac{r}{r_0} \right) \right] \right) \\
U_{Morse}''(r) &= D_0 \frac{\alpha^2}{r_0^2} \left(\exp\left[\alpha \left(1 - \frac{r}{r_0} \right) \right] - \frac{1}{2} \exp\left[\frac{\alpha}{2} \left(1 - \frac{r}{r_0} \right) \right] \right)
\end{aligned} \tag{4.4}$$

Compared to the uncorrected potential (regardless of its precise functional form), the FH correction decreases the depth of the potential well, and shifts the position of the minimum to larger distances (figure 4.2). This can be understood intuitively when it is considered that the quantum delocalization leads to a smearing out with respect to the classical, spherical model.
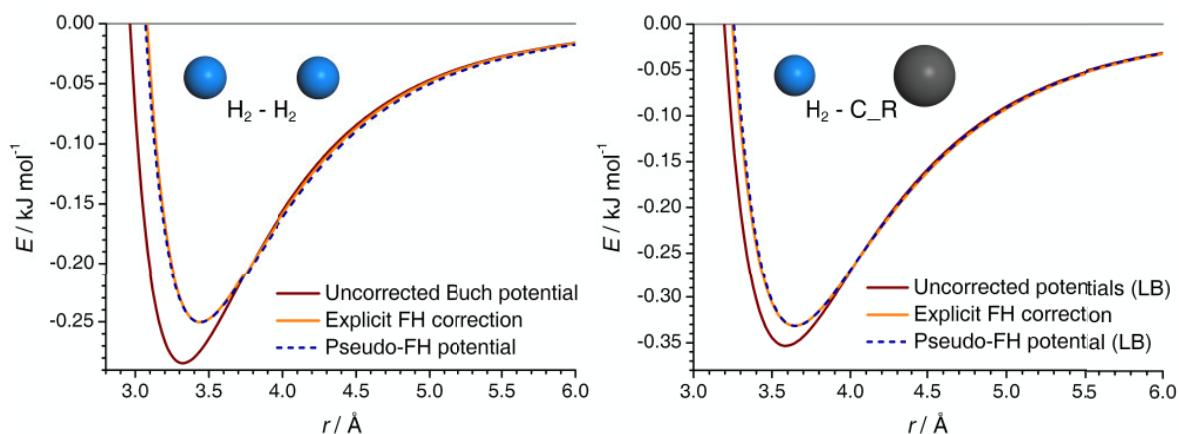
Figure 4.2. *Left:* Calculated H_2-H_2 interaction energy obtained with the Buch potential, the explicit FH correction to the Buch potential at $T = 77$ K, and the Pseudo-FH potential for this temperature. *Right:* Interaction energy obtained for the H_2-framework interaction. The Buch parameters are used for hydrogen, while aromatic carbon parameters (C_R) from the Universal Force Field (*157*) are employed to represent a typical framework atom. The inter-action energy resulting from Lorentz-Berthelot (LB) mixing of the uncorrected parameters is compared to the energy curves resulting from the explicit FH correction ($T = 77$ K), and from LB mixing of the Pseudo-FH parameters for H_2 with the C_R parameters.

4.2.1.4. The Pseudo-FH approach

The Feynman-Hibbs effective potential can be implemented straightforwardly in home-made codes, *e.g.* for Monte Carlo simulations. Commercially available software, how-ever, does not necessarily permit modifications to the potential model. As the necessity to include quantum effects in simulations of hydrogen adsorption at low temperatures has been demonstrated in numerous examples, an approach to mimic the FH correction in the framework of the conventional Lennard-Jones 12-6 potential is introduced here.

This simple approach, termed "Pseudo-FH" approximation, proceeds as follows: For a given temperature T, the FH corrected potential curve is calculated explicitly (equations 4.2 and 4.3). Then, a least-squares fit of the LJ 12-6 potential (equation 3.6) is carried out. The obtained parameters $r_{0,T}$ and $D_{0,T}$ are then used as temperature-specific (Pseudo-FH) pa-rameters in all calculations for the temperature T.

The Pseudo-FH approach for H_2 is visualized in figure 4.2: Both the uncorrected Buch po-tential and the FH corrected potential for $T = 77$ K are shown. As discussed above, the FH correction leads to an increase of the equilibrium distance r_0 and a decrease of the well depth D_0. Near the equilibrium distance, the Pseudo-FH potential is practically indistinguishable from the exact FH corrected potential. At larger distances, however, a slight overestimation of the interaction energy is observable.

The derivation of the Pseudo-FH potential uses the H_2-H_2 potential parameters, only. It is also important to ensure that the Pseudo-FH parameters derived for hydrogen give a correct representation of the H_2-framework interactions. Figure 4.2 shows the explicitly corrected potential curve ($T = 77$ K) for the interaction of H_2 with an aromatic carbon atom (param-

eters taken from the UFF), as well as the curve obtained from Lorentz-Berthelot mixing of the Pseudo-FH parameters derived above and the carbon parameters. Here, both potential curves are practically indistinguishable over the range of distances covered. From the difference between the uncorrected and the corrected potential, it is apparent that quantum effects have a significant impact on the strength of the interactions with the framework. In contrast to the contribution of fluid-fluid interactions, which will play a role at high densities only, this will influence the calculated adsorption properties even at low loadings.
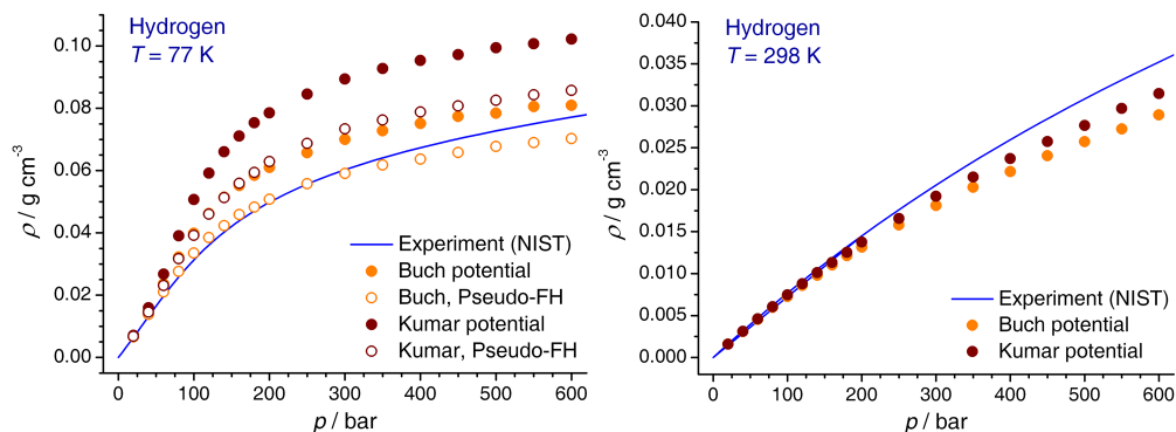
Figure 4.3. Bulk properties of hydrogen at $T = 77\,$K and room temperature obtained with different potential models. Experimental data from (*232*).

4.2.1.5. Performance of selected potential models: Bulk properties

For simulations of hydrogen, only united-atom models are considered in this work. The performance of the parameter sets by Buch (*155*) and Kumar *et al.* (*220*) was tested by simulating the equation of state at $T = 77\,$K and $T = 298\,$K (room temperature, RT). For $T = 77\,$K, both the unmodified and the Pseudo-FH parameters were considered. For room temperature, no quantum correction was applied. The inclusion of point charges was found to have no effect on the resulting pressure-density relationship, so only results for the uncharged model are reported. The different parameter sets considered are summarized in table A.1 of the Appendix.

GCMC simulations using the SORPTION module included in *Accelrys* "Materials Studio" package (*233*) were carried for an empty simulation box with an edge length of 20 Å. The predicted bulk properties at both temperatures are shown in figure 4.3, together with experimental reference data from the *NIST Chemistry Webbook*. (*232*) At 77 K, the uncorrected versions of both potentials significantly overestimate the density at pressures above 50 bar. This overestimation is much more pronounced for the Kumar potential than for the Buch potential. The Pseudo-FH version of the Buch potential performs very well up to pressures of 400 bar, but slightly underestimates the density at higher pressures. The Pseudo-FH version of the Kumar potential, however, overestimates the density in a similar manner as the

uncorrected Buch potential. These errors can be understood when it is considered that the Kumar potential was derived for use with a fourth-order FH correction, while the Pseudo-FH approach applied here accounts for the second-order term only.

At room temperature, both potential models show a similar performance, with the Kumar potential delivering a slightly better prediction of the density at high pressures. The agreement with experimental data is excellent up to 100 bar, which is the pressure range covered by the simulations of RT hydrogen adsorption reported in the following. However, both potential models underestimate the density at pressures above 200 bar. This may be an indication that the simple single-site LJ potential is no longer adequate to model the fluid behaviour of hydrogen at very high pressures. Moreover, the results highlight that it is most reasonable to dispense with the quantum correction under these conditions, as the underestimation would become even more pronounced if quantum effects were included.

In spite of the slightly superior performance of the Kumar potential at RT, the Buch potential is used to describe the H_2 molecule throughout this work for reasons of consistency. Quantum effects are taken into account at cryogenic temperatures, using either the Pseudo-FH model or an explicit second-order FH correction, depending on the type of GCMC code employed.

4.2.2. Oxygen

4.2.2.1. Potential model

In the O_2 molecule, the distance between the two oxygen atoms amounts to 1.208 Å (figure 4.1). Lennard-Jones parameters for a two-site model with the interaction sites located at the atomic positions were proposed by Zhang and Siepmann. (234) This model, referred to as TraPPE model due to its relationship to the corresponding force field, has been used in a previous modelling study of oxygen adsorption in $Cu_3(btc)_2$. (235) Concerning the quadrupole moment of the O_2 molecule, there seems to be a wide variation of experimentally determined values in the literature. (236) Therefore, the best available theoretical value from the CCCBDB was taken as reference value. (224) This value of $\theta = -0.09745 \, e\text{Å}^2$ was obtained in DFT-B3LYP calculations with a large basis set. To represent this quadrupole moment in a point-charge representation, a charge of $+2q$ is placed on the center of mass, and charges of $-q$ are placed on the atomic positions. With the given value of θ, $q = 0.1336 \, e$ is obtained.

4.2.2.2. Prediction of bulk properties

The bulk properties of oxygen at RT were calculated using a similar setup as described above. The results are displayed in figure 4.4. Up to 400 bar, the predicted density is in excellent agreement with the reference data from the literature. (232) Therefore, the TraPPE model will be used in all simulations of oxygen adsorption in this work.
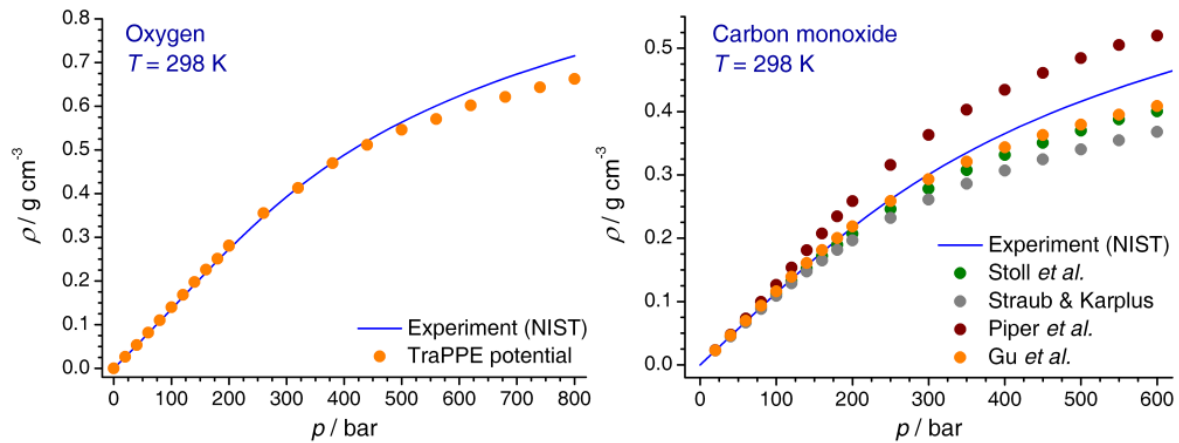
Figure 4.4. *Left:* Bulk properties of oxygen at room temperature obtained with the potential model taken from the TraPPE force field. *Right:* Bulk properties of carbon monoxide at room temperature obtained with different potential models. Experimental data from (*232*).

a) Stoll *et al.*

C   O

−q   +q

$d(C\text{-}O) = 1.14$ Å

b) Straub & Karplus

C Q_{com} O

$-q_C$ $+q_{com}$ $-q_O$

$d(C\text{-}Q_{com}) = 0.644$ Å
$d(Q_{com}\text{-}O) = 0.484$ Å

c) Piper *et al.*

Q_{ext1} C Q_{ext2} O

$-q_{ext1}$ $+q_C$ $-q_{ext2}$

$d(Q_{ext1}\text{-}C) = 0.437$ Å
$d(C\text{-}Q_{ext2}) = 0.970$ Å
$d(Q_{ext2}\text{-}O) = 0.158$ Å

$q_O = 0$
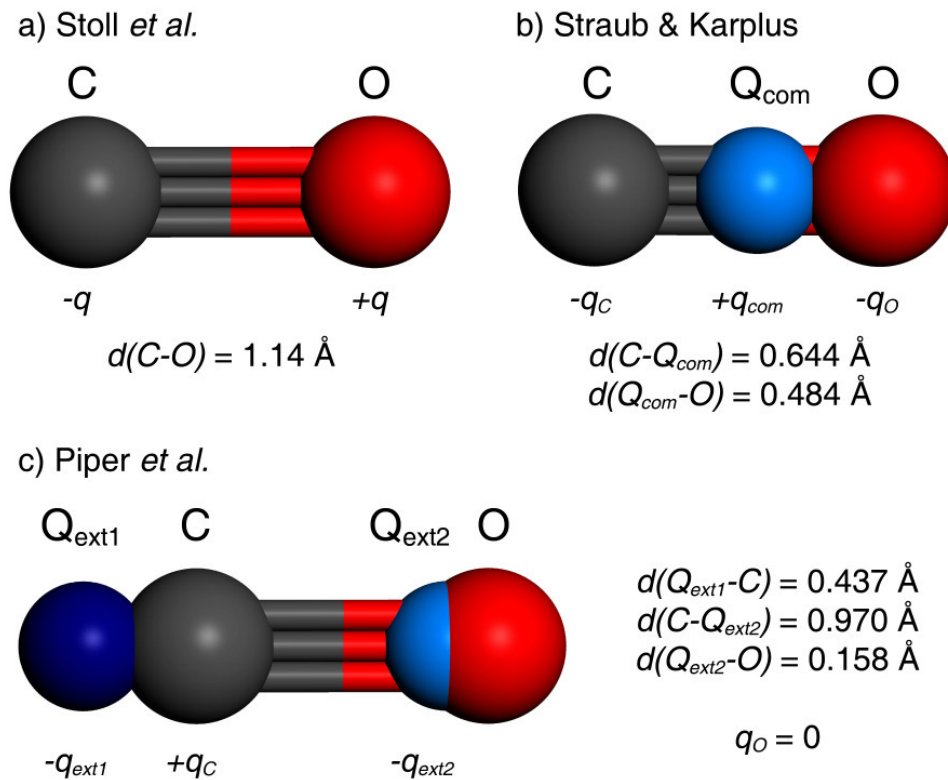
Figure 4.5. Different models for the CO molecule. The model of Gu *et al.*, which is not shown, uses the same charge distribution as the model of Straub and Karplus, but only one LJ site at the center of mass. The corresponding LJ parameters and charges are reported in table A.3.

4.2.3. Carbon monoxide

4.2.3.1. Potential models

The interatomic distance in the carbon monoxide molecule amounts to 1.14 Å. For dispersive interactions, the most simple representation uses a single LJ site located at the center of mass. Parameters for this model were proposed by Gu *et al.* (*237*) A two-site model with identical parameters for both sites was derived by Stoll *et al.* (*238*) Two-site models with different parameters for the carbon and oxygen atom were used by Piper *et al.*, (*239*) and by Straub and Karplus (figure 4.5). (*240*)

In addition to the various models for dispersive interactions, different representations of the electrostatic properties of carbon monoxide have been proposed. The CO molecule has a small dipole moment of 0.0233 eÅ, and a quadrupole moment of -0.591 eÅ^2. (*224*) The model of Stoll *et al.* approximates the electrostatic properties by using a point dipole, whose dipole moment is considerably larger than the experimental value to compensate for the missing quadrupole moment. (*238*) Straub and Karplus proposed a model consisting of three point charges located at the atom positions and the center of mass, (*240*) while Piper *et al.* placed charges on the carbon atom and on two additional positions, leading to a four-site model (together with the LJ parameters). For the computations reported here, the three-site model of Straub and Karplus was also combined with the LJ parameters of Gu *et al.* An overview over the different models is given in figure 4.5. In previous modelling studies of carbon monoxide adsorption in MOFs, the model of Straub and Karplus was used by some authors, (*241*) while others used the model of Piper *et al.* (*138*)

4.2.3.2. Performance of potential models: Bulk properties

The bulk properties of carbon monoxide at RT were simulated, using a similar setup as above, with the four models described in the previous paragraph. The results are shown in figure 4.4. Quite interestingly, the model of Straub and Karplus underestimates the density at pressures above 100 bar, while the model of Piper *et al.* significantly overestimates the density at pressures above 50 bar. The other two models show a similar performance, with a rather accurate prediction up to 200 bar, and a tendency to underestimate the density above this pressure. In total, the model of Gu *et al.* performs best, and is therefore used in all calculations of carbon monoxide adsorption in this work.

4.2.4. Carbon dioxide

4.2.4.1. Potential model

In contrast to the fluids discussed so far, which are supercritical at $T = 298\,\text{K}$ (and, in the case of hydrogen, also at 77 K), the critical temperature of carbon dioxide is somewhat higher than room temperature. Therefore, liquefaction occurs at a pressure of 64 bar (at $T = 298\,\text{K}$). A realistic model of the CO_2 molecule should give a reasonably accurate prediction of the phase transition pressure, as well as the associated change in density.

A single-site representation of the CO_2 molecule has been used in some studies. (*242*) However, due to the elongated shape of the carbon dioxide molecule, a three-site representation with the interaction sites at the atomic positions is usually preferred. Various different parameter sets exist in the literature, some of which have been compared in a recent modelling study of carbon dioxide adsorption in zeolites. (*243*) The Lennard-Jones parameters which were found to perform best correspond to a slightly modified version of the parameters derived earlier in the framework of the TraPPE force field. (*244*) In the context of this work, these LJ parameters are combined with ESP charges derived from a DFT calculation for the CO_2 molecule. These charges, given in table A.2, are somewhat smaller than typical values used in the literature. The resulting quadrupole moment of -0.804 e$Å^2$ is in reasonable agreement with the experimental value of -0.891 e$Å^2$. (*224*) Due to the high relevance of carbon dioxide sequestration and removal of CO_2 from flue gases, numerous modelling studies of carbon dioxide adsorption in MOFs have been published. (*235, 245, 246*) Typically, the parameters from the TraPPE force field or slightly modified version were used.
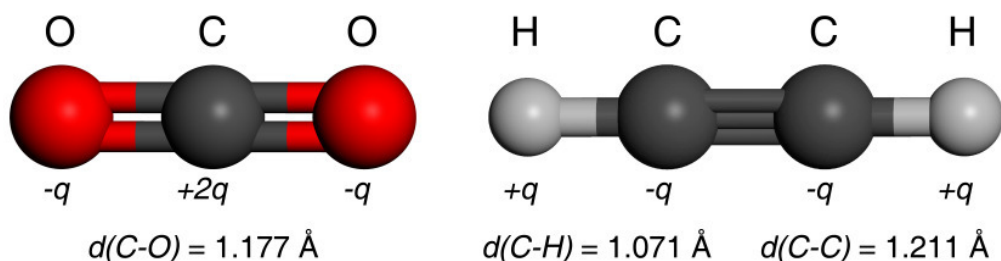
Figure 4.6. Models of the CO_2 and the C_2H_2 molecule. A visualization of the electrostatic potential which is approximated by the ESP point charges is given in figure 3.5. The corresponding LJ parameters are given in table A.2
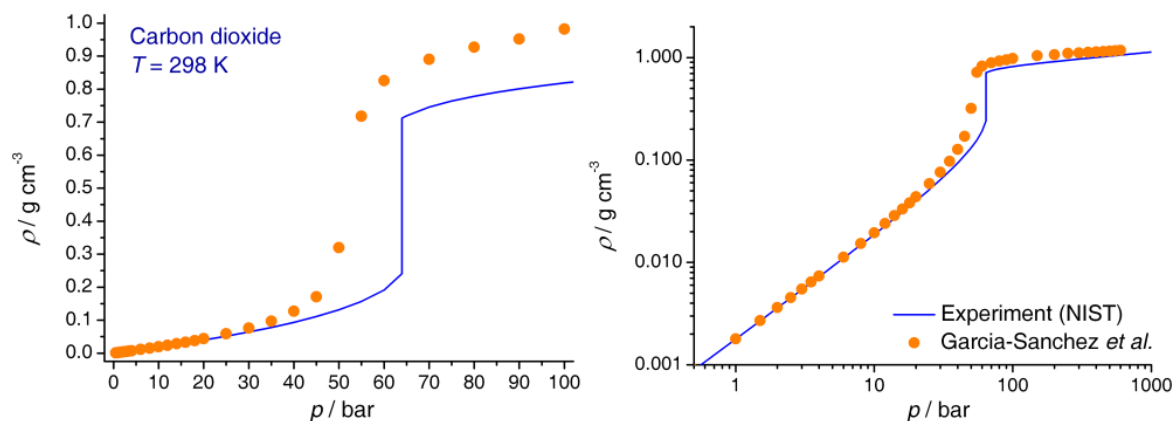
Figure 4.7. *Left:* Bulk properties of carbon dioxide at room temperature and pressures up to 100 bar obtained with the potential model of Garcia-Sanchez *et al.* Experimentally, the transition to a liquid phase occurs at a pressure of 64.1 bar. *Right:* Plot of the density extended to higher pressures. Both pressure and density are expressed on a logarithmic scale. Experimental data from (*232*).

4.2.4.2. Prediction of bulk properties

The bulk properties of carbon dioxide at RT were simulated, using a similar setup as above, with the LJ parameters of Garcia-Sanchez *et al.* (*243*) and the ESP charges described above. The results, together with experimental reference data, are shown in figure 4.7. (*232*) It is apparent that the model is not able to completely reproduce the sharp increase in density associated with the gas-liquid transition. Moreover, the density of the liquid phase is overestimated by approximately 15%. The origin of these deviations cannot be clarified in this context. However, previous work shows that an accurate modelling of the fluid properties is particularly difficult for conditions close to the critical point. A showcase example is provided by the original paper reporting the TraPPE parameters for carbon dioxide: (*244*) While the agreement between experimental and calculated vapour-liquid coexistence curve is excellent at lower temperatures, deviations arise for temperatures above 290 K. In particular, the density of the liquid phase is overestimated, similar to the observations made here. As is visible from figure 4.7, the agreement with experimental reference data is reasonably good up to a pressure of 30 bar. The simulations in this work will only deal with CO_2 adsorption at pressures up to 1 bar, where carbon dioxide behaves as an ideal gas. It can thus be expected that the chosen set of parameters provides a reasonable description of the properties of CO_2 for the conditions of interest, despite the observed deviations at higher pressures.

4.2.5. Acetylene

4.2.5.1. Potential model

Like carbon dioxide, acetylene (ethyne, C_2H_2) is subcritical at room temperature. Due to its low limit of compression and general high reactivity, the availability of experimental thermophysical data is very limited in comparison to all other fluids discussed so far. The NIST database does not include data for acetylene, (*232*) and even the entry "Acetylene" in *Ullmann's Encyclopedia of Industrial Chemistry* contains only a few data points that are not suitable for a parameter validation. (*247*) In addition, only few modelling studies involving an atomistic description of acetylene have been published. Two relatively recent works have employed MD calculations to understand the diffusion of acetylene in NaY zeolite. (*248, 249*) In both cases, a two-site model was used for the C_2H_2 molecule. The LJ parameters originally proposed for the sp^2-hybridized carbon atoms of butadiene in the OPLS-UA force field (*167*) were employed to represent the CH-groups of acetylene. As for carbon dioxide, a set of partial charges was derived from DFT calculations. These charges are reported in table A.2. The resulting quadrupole moment amounts to 1.359 eÅ^2, a value that agrees well with the experimental value of 1.319 eÅ^2. (*224*)

4.2.5.2. Parameter validation: Structure of solid acetylene

As mentioned above, the lack of available thermophysical data for acetylene makes it impossible to follow the same strategy of parameter validation as for the other four fluids. In order to ensure that the model gives a realistic description of the molecular properties of C_2H_2, the crystal structure of solid acetylene was used as a reference. The initial structural model was taken from experimental data, with the symmetry reduced to $P1$ (from $Pa\bar{3}$). (250) A geometry optimization, including an optimization of the lattice parameters, was carried out, using the LJ parameters described above as well as default parameters from the Universal Force Field (for comparison). (157) Both models were employed with and without charges.

To judge the quality of the optimized structure, the lattice parameter a and the nearest neighbour C-C distance (between different molecules) were evaluated. The results are summarized in table 4.2, together with experimental data measured at $T = 141$ K. It is obvious that the parameters from the OPLS-UA force field, together with the partial charges, give an accurate prediction of the structure, while all other tested parameter sets show significant deviations. It can be concluded that these parameters deliver a reasonable description of the molecular properties of acetylene. They are used in all calculation of C_2H_2 adsorption reported in this work.

Table 4.2. Predicted structural properties of solid acetylene using different parameter sets. Experimental data are given for comparison. Because no symmetry constraints were applied in the geometry optimization, the lattice parameters and distances show a certain variation in some cases.

	Experiment	OPLS-UA w/o charges	OPLS-UA with charges	UFF w/o charges	UFF with charges
a / Å	6.105	6.354	6.127	5.962 − 6.055	5.875
$d(C\text{-}C)$ / Å	3.867	4.02 − 4.10	3.87	3.78 − 3.87	3.69 − 3.76
ρ / g cm^{-3}	0.7601	0.6742	0.7519	0.7937	0.8529

4.3. Porous adsorbents: Structural models and pore topologies

4.3.1. Metal-organic frameworks

4.3.1.1. IRMOF-1

IRMOF-1 (also termed MOF-5) is a prototypical metal-organic framework, and arguably the most well-characterized MOF. It has the chemical composition $Zn_4O(bdc)_3$, with $H_2(bdc)$ being 1,4-benzene-dicarboxylic acid (terephthalic acid). Its crystal structure was first reported in 1999 by Yaghi and co-workers, together with adsorption measurements that confirmed its permanent porosity. (*40*) Subsequently, a series of isoreticular MOFs (IRMOFs) with other linear dicarboxylate linkers was reported. (*70*, *251*, *252*) It was demonstrated that a variation of the linker can be used to vary the pore size as well as the chemical composition of the pore wall, retaining the framework topology of IRMOF-1. As the archetype of the IRMOF series, IRMOF-1 has received considerable attention, and numerous experimental and theoretical studies have adressed various properties.

The structure IRMOF-1 consists of Zn_4O tetrahedra that are octahedrally coordinated by six bdc linkers, thereby forming a cubic network with *pcu* topology. This topological description ignores that the six neighbouring tetrahedra of one Zn_4O tetrahedron do not have the same orientation as the central tetrahedron, but are related to it by a mirror plane. More rigorously, the topology can be understood in analogy to the NaCl packing.

The IRMOF-1 structure contains two different types of spherical pores, which differ in size due to the different orientation of the surrounding linker molecules: For the larger pores, the phenyl rings are oriented tangentially, while they point into the smaller pores. The pore diameters correspond to approximately 15 Å and 12 Å, respectively (in this context, a pore diameter is defined as the atom-atom distance minus the approximate van der Waals radii). A unit cell of IRMOF-1 as well as one of the pore types are shown in figure 4.8.

The structural parameters used in all simulations in this work were taken from the work of Rowsell *et al.* (*253*) without further optimization.

4.3.1.2. MOF-74

MOF-74 has the chemical composition $Zn_2(dhbdc)$, where $H_4(dhbdc)$ is 2,5-dihydroxybenzene-1,4-dicarboxylic acid. By some authors, it is also referred to as $Zn_2(dhtp)$, or as CPO-27-Zn. MOF-74 was first reported in 2005 by Yaghi and co-workers. (*254*) Isostructural MOFs with the dhbdc linker and other metals were synthesized subsequently ((*63*) and references therein).

The inorganic building unit of MOF-74 is an infinite zig-zag chain of five-coordinated zinc atoms. One of the oxygen atoms of the carboxylate group coordinates to one zinc center, while the other oxygen bridges two neighbouring metals. The deprotonated hydroxyl group also bridges two neighbouring zinc atoms, thus each dhbdc molecule coordinates to eight different metal centers (figure 4.9). The coordination environment of the metal center is a distorted octahedron with one free coordination site. This coordination site is occupied

by a solvent molecule after the synthesis. Desolvation of the structure leads to the formation of coordinatively unsaturated zinc sites.

The complex connectivity described above leads to a hexagonal arrangement of the one-dimensional chains, bridged by the linkers, with *bnn* topology (*bnn* = boron nitride). The structure contains honeycomb-like channels with a diameter of approximately 12 Å, with the unsaturated zinc sites pointing into the channels. Compared to other MOFs with isolated inorganic building units, MOF-74 has a particularly high surface packing density of unsaturated metal sites. (*255*)

The structural parameters used in the simulations were taken from the work of Rosi *et al.* (*254*) After removal of the solvent molecules, the geometry was optimized using the UFF, (*157*) keeping the lattice parameters at their experimental values.
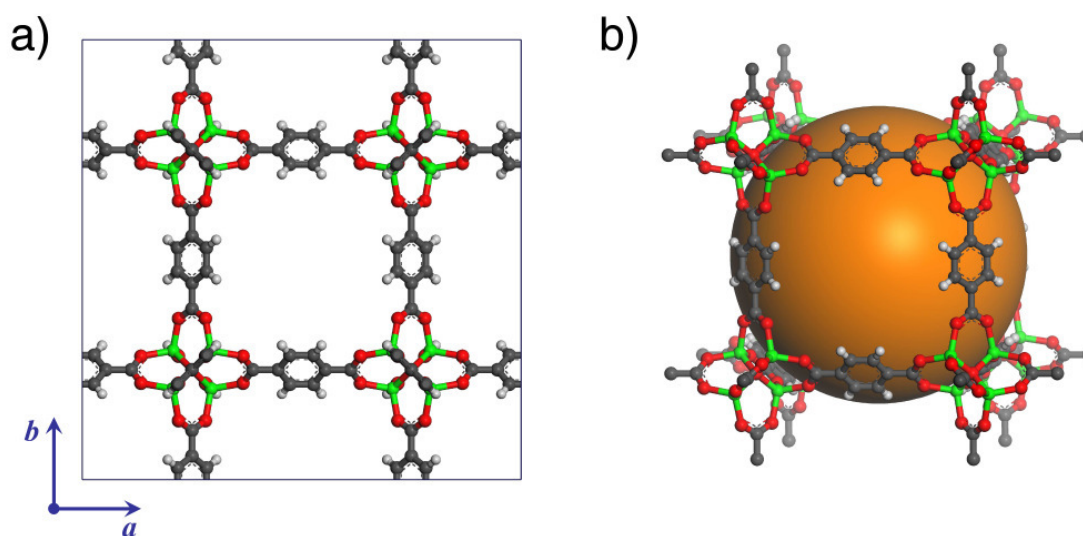
Figure 4.8. IRMOF-1: *a)* Unit cell, displayed along the *c*-axis. *b)* Pore located at the unit cell center. The phenyl rings are oriented tangentially. Colour scheme: Green = zinc, red = oxygen, grey = carbon, white = hydrogen.
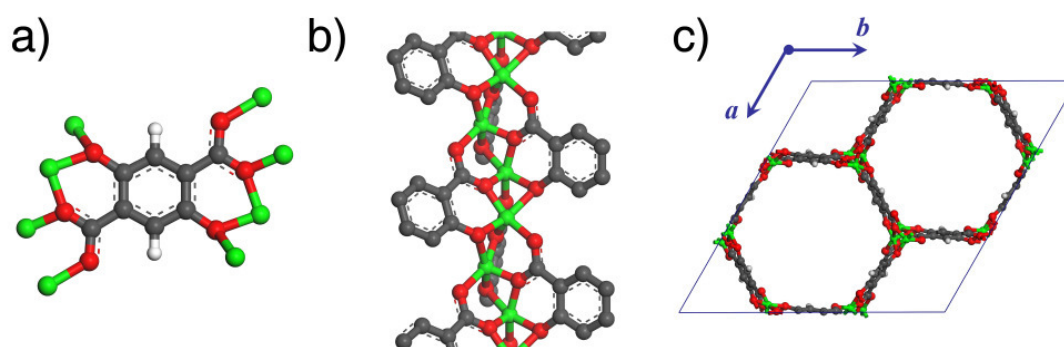
Figure 4.9. MOF-74: *a)* Coordination of one dhbdc linker to eight Zn centers. *b)* Chain of pentacoordinated Zn centers running along the *c*-axis. *c)* Unit cell, displayed along the *c*-axis. Colour scheme: Green = zinc, red = oxygen, grey = carbon, white = hydrogen.

4.3.1.3. ZIF-8

Zeolitic imidazolate frameworks (ZIFs), a sub-category of MOFs with imidazolate linkers and zeolite-like topologies, were first presented in 2006. (*256*) These materials are particularly interesting with regard to applications in adsorption, separation, and catalysis due to their enhanced thermal and chemical stability. (*129*) Of the numerous ZIFs reported so far, ZIF-8, $Zn(mim)_2$ with H(mim) being 2-methylimidazole, is probably the most well-characterized system.

In the structure of ZIF-8, tetrahedrally coordinated Zn^{II} atoms are connected by methylimidazolate linkers, forming a cubic network with *sod* topology (*sod* = sodalite). The structure contains relatively large pores, which have a diameter of approximately 12 Å, connected by narrow windows with a diameter of approximately 3 Å (figure 4.10). Due to these structural particularities, ZIF-8 is a very interesting system for kinetic separations of small molecules, as the diffusion velocity should strongly depend on the kinetic diameter of the molecule.

For the simulations reported, the structure of ZIF-8 was taken from the work of Park *et al.* (*256*) After removal of solvent molecules and structural disorder, the geometry was optimized using the UFF in space group $P1$, keeping the lattice parameters at their experimental values.
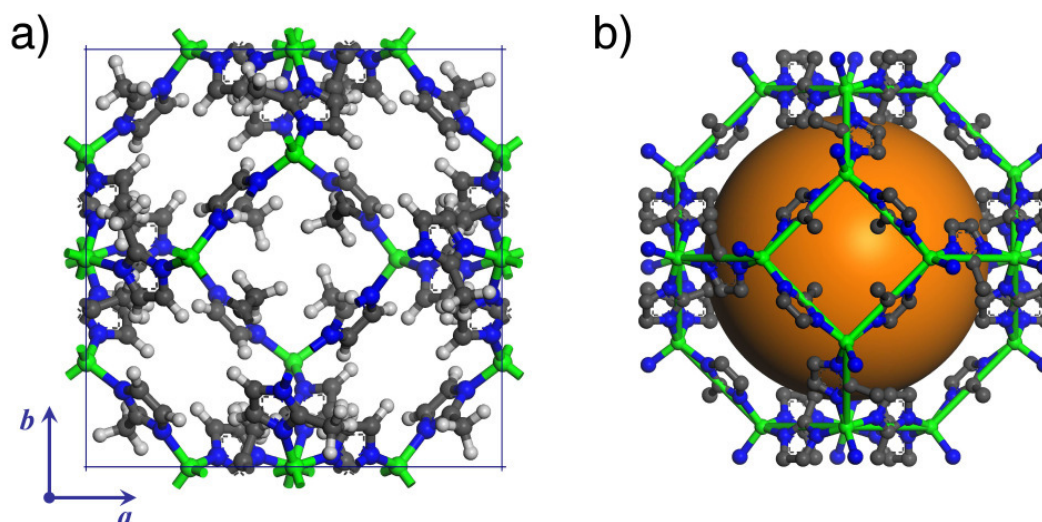
Figure 4.10. ZIF-8: *a)* Unit cell, displayed along the *c*-axis. *b)* Sodalite-like pore. The tetrahedral zinc centers surrounding the pore are connected by green lines to emphasize the topological analogy to sodalite. Colour scheme: Green = zinc, blue = nitrogen, grey = carbon, white = hydrogen.

4.3.1.4. Zn(dtp)

The metal-organic framework Zn(dtp), where H_2(dtp) is 2,3-di-1*H*-tetrazol-5-ylpyrazine, was reported by Bu, Kitagawa and co-workers in 2008. (*257*) Similar to the ZIFs mentioned above, the linker molecule coordinates to the zinc centers via nitrogen atoms of the aromatic rings. These metal-nitrogen bonds appear to be thermally more stable than the metal-oxygen bonds in MOFs with carboxylate linkers.

The dtp linker binds to three different Zn^{II} atoms, to each of them in a bidentate fashion (figure 4.11). Each zinc atom is coordinated by four tetrazole nitrogen atoms, with relatively short Zn-N distances ranging from 2.02 Å to 2.11 Å, and by two pyrazole nitrogen atoms, with considerably longer Zn-N distances of 2.39 Å and 2.63 Å, respectively. This leads to a distorted octahedral coordination environment of the metal centers. While the linker is achiral, racemic crystallization leads to formation of two enantiomers in the hexagonal space groups $P6_1$ and $P6_5$. The overall structure of Zn(dtp) corresponds to a zeolite-type network with a rare *etd* topology. (*258*) It contains one-dimensional, helical channels with nitrogen-rich walls and a channel diameter of approximately 5.2 Å.

The structure of Zn(dtp) used in the simulations was taken from experimental data, without further modifications. (*257*)
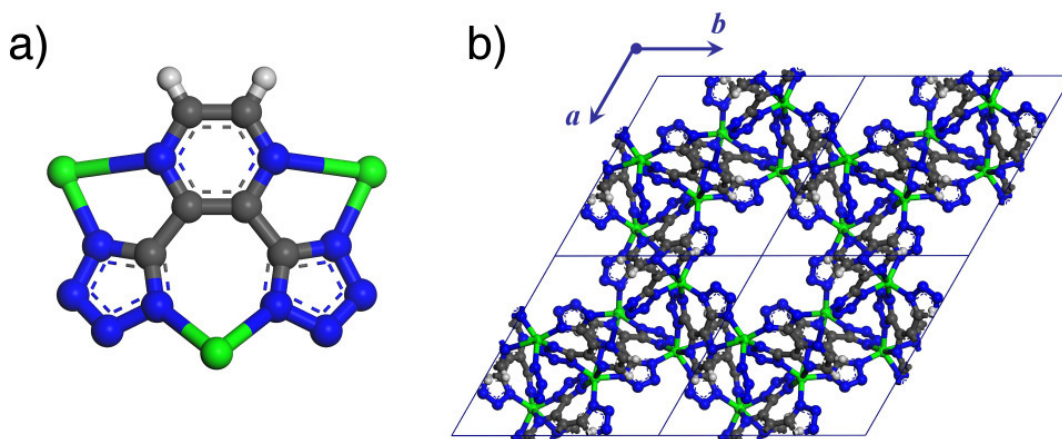
Figure 4.11. Zn(dtp): *a)* Coordination of one dtp linker to three Zn centers. *b)* 2 × 2 array of unit cells, displayed along the *c*-axis. More than one cell is shown to visualize the helical channels, which are centered around the cell edge. Colour scheme: Green = zinc, blue = nitrogen, grey = carbon, white = hydrogen.

4.3.1.5. Cu₃(btc)₂

$Cu_3(btc)_2$, where $H_3(btc)$ is 1,3,5-benzene-tricarboxylic acid, was reported by Williams and co-workers in 1999, shortly after the seminal publication of IRMOF-1. (*41*) Alternative names of this system are $Cu_3(tma)_2$ (tma = trimesate) and HKUST-1. It was the first MOF for which the specific surface area was determined from N_2 physisorption measurements using the BET equation (rather than the Langmuir equation). This has become an ubiquitous method to assess the porosity of MOFs in a (semi-)quantitative manner. Similarly to IRMOF-1, it is currently one of the most well-characterized MOFs, and it has been proposed for numerous applications.

The inorganic building unit of $Cu_3(btc)_2$ is the Cu_2 paddle wheel, a very common building unit in copper-based MOFs. After the synthesis, solvent molecules are coordinated to the metal centers, and desolvation of the MOF can generate unsaturated copper sites. An antiferromagnetic coupling of the two copper centers has been evidenced experimentally, (*259*)

indicating that there is a significant copper-copper interaction, but no metal-metal bonding. The Cu-Cu "bond" employed in all graphical representations of the Cu$_2$ paddle wheel throughout this work is intended as a topological connection line emphasizing the structural rigidity of the building unit, but should not be misinterpreted as a representative of actual metal-metal bonding.

In Cu$_3$(btc)$_2$, the paddle wheels are connected by the tritopic linkers, resulting in a face-centered cubic structure with a *pto* topology (*pto* = Pt$_3$O$_4$). Cu$_3$(btc)$_2$ has a bimodal pore size distribution, with smaller pores of a diameter of approximately 5 Å, and two different types of larger pores with a diameter of approximately 11 Å (figure 4.12). The smaller pores are octahedrally surrounded by paddle wheels and have triangular windows which connect them to the larger pores. Both types of larger pores are surrounded by a cuboctahedral arrangement of Cu$_2$ paddle wheels. The axes of the paddle wheel point into the pores of the first type, centered around the origin, and lie tangentially to the second type, which is centered around the center of the unit cell. The two types of pores are connected to each other via the windows corresponding to the square faces of the cuboctahedra.

The structure of Cu$_3$(btc)$_2$ used in the simulations was taken from the work of Chui *et al.* (*41*) Coordinated water molecules were removed.

4.3.1.6. MOF-505

MOF-505 is a copper-based MOF with a tetracarboxylate linker. It has the composition Cu$_2$(bptc), with H$_4$(bptc) being 3,3′,5,5′-biphenyl-tetracarboxylic acid. The synthesis and characterization of MOF-505 was published in 2005 by Yaghi's group. (*260*) Subsequently, several other Cu-MOFs with elongated or functionalized tetracarboxylate linkers were reported and designated as NOTT-100 (= MOF-505) to NOTT-109. (*261, 262*) With few exceptions, they have the same topology as MOF-505. In analogy to IRMOF-1, this system can be understood as a prototype MOF for a series of isoreticular compounds.

As in Cu$_3$(btc)$_2$, the inorganic building units of MOF-505 are Cu$_2$ paddle wheels. The connection of the paddle wheels by the tetratopic linkers leads to a trigonal structure with *nbo* topology (*nbo* = niobium^{II} oxide). Groups of three Cu$_2$ paddle wheels, which are connected to each other over two carboxylate groups belonging to the same phenyl ring, define triangular windows. The two different types of pores present in the MOF-505 structure are connected by these windows along the *c*-axis (figure 4.13). The first type of pore has a shape of a truncated rhombohedron, with twelve paddle wheels at the edges, and a pore diameter of nearly 10 Å. For the second pore type, the six surrounding paddle wheels are arranged at the corners of a trigonal antiprism (distorted octahedron). These pores are slightly smaller, having a diameter of approximately 7 Å. In addition to the triangular windows mentioned above, the pores are connected over windows which correspond to the faces of the truncated rhombohedra.

For the simulations, the structural parameters of MOF-505 were taken from the work of Chen *et al.* (*260*) Solvent molecules were removed.
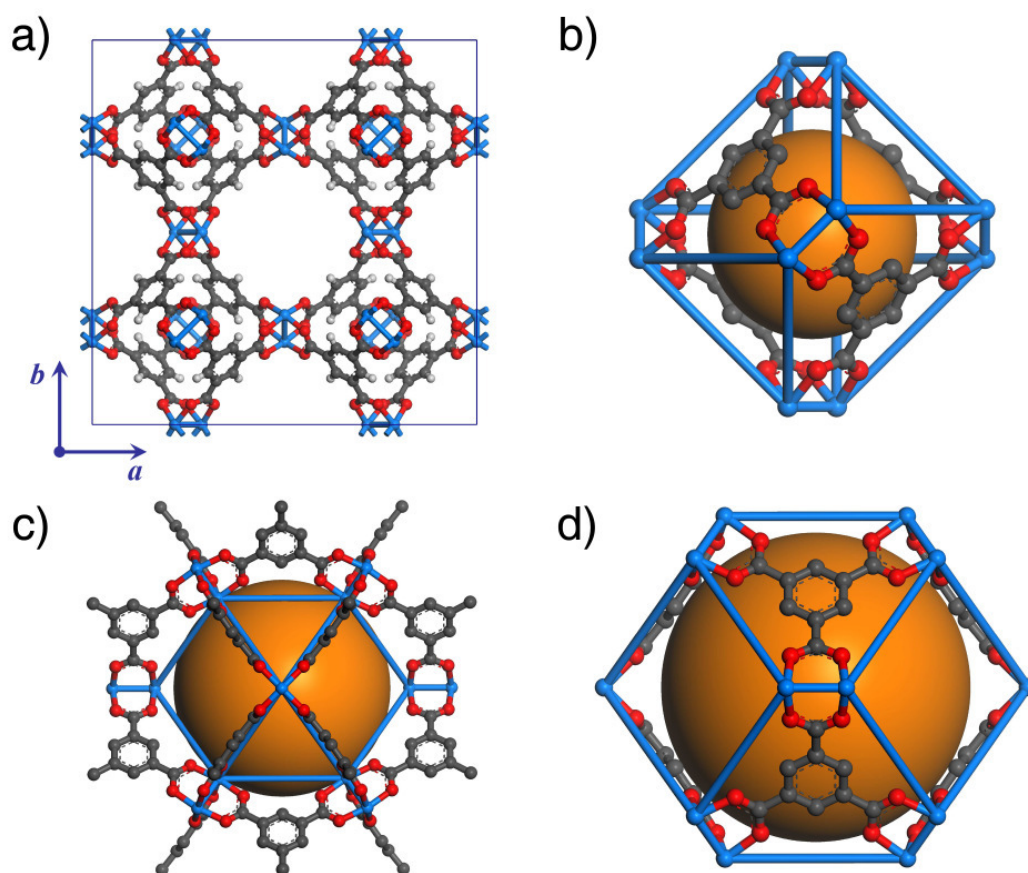
Figure 4.12. $Cu_3(btc)_2$: *a)* Unit cell, displayed along the *c*-axis. *b)* Small, octahedrally surrounded pore. Phenyl rings span four of the eight faces of the octahedron. *c)* Large, cuboctahedrally surrounded pore, centered around the origin, with Cu_2 paddle wheels pointing into the pore. *d)* Large, cuboctahedrally surrounded pore, centered around the unit cell center, with Cu_2 paddle wheels lying tangentially. The connecting square windows are visible in both *c)* and *d)*. The Cu_2 paddle wheels are connected to highlight the pore topology. Colour scheme: Light blue = copper, red = oxygen, grey = carbon, white = hydrogen.
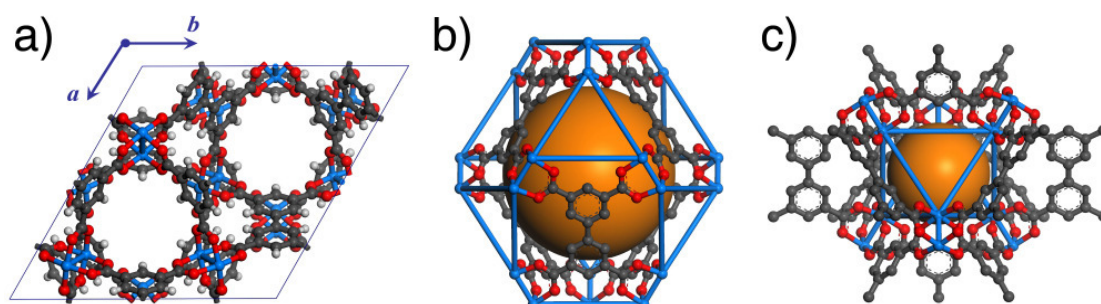
Figure 4.13. MOF-505: *a)* Unit cell, displayed along the *c*-axis. *b)* Truncated rhombohedral pore. *c)* Trigonal antiprismatic pore. The trigonal windows connecting these pores along the *c*-axis are visible at the top and the bottom of *b)* and *c)*. The Cu_2 paddle wheels are connected to highlight the pore topology. Colour scheme: Light blue = copper, red = oxygen, grey = carbon, white = hydrogen.

4.3.1.7. UMCM-150

The term UMCM-150 (UMCM = University of Michigan Crystalline Material) is used to describe $Cu_3(bhtc)_2$, with $H_3(bhtc)$ being 3,4',5-biphenyl-tricarboxylic acid. This highly porous MOF, which was presented by Matzger and co-workers in 2007, is rather unusual because it contains an unsymmetrically substituted linker molecule, as well as two different types of inorganic building units. (*263*)

The common Cu_2 paddle wheel is one of the inorganic building units. It is coordinated by the 3- and 5-carboxylate functions of the bhtc linker. The 4'-carboxylate function coordinates to unusual, trigonal Cu_3 units (figure 4.14). A hexagonal structure with a relatively large unit cell ($c > 40$ Å) and three different types of pores is formed. The first type of pore is similar to the truncated rhombohedral pores of MOF-505, the main difference being the small triangular faces, which are constituted by one trinuclear unit instead of three Cu_2 paddle wheels. Moreover, these pores are larger, having a dimension of approximately 11×16 Å. Similar to MOF-505, there are groups of three paddle wheels bordering triangular windows. The triangular windows constitute the axial positions of the other two pore types: These pores have shapes which cannot be represented as a single geometric body, but can be rationalized as the combination of a trigonal bipyramid and a trigonal prism. In both pore types, three Cu_3 units form the equatorial positions, and they have dimensions of approximately 12×15 Å. In the latter of these pore types, the copper centers of both inorganic building units point into the pore. In addition to the small trigonal windows, there are larger triangular and rhombic apertures connecting the pores.

The structure of UMCM-150 was taken from the work of Wong-Foy *et al.* (*263*) After removal of solvent molecules, the structure was optimized using the UFF. The positions of the copper atoms were held fixed to avoid unphysical distortions of the inorganic building units.

4.3.1.8. PCN-12

The MOFs of the PCN group (PCN = Porous Coordination Network) were developed by Zhou and co-workers. One particularly interesting member of this group is PCN-12, $Cu_2(mdip)$, where $H_4(mdip)$ is 5,5'-methylene-diisophthalic acid, which was first published in 2008. (*264*) It exhibits an exceptional hydrogen uptake at $T = 77\,K$ and low pressures, and is also very interesting due to its rather complex structural properties.

In contrast to most other linkers, the mdip linker is non-linear. Moreover, it can assume different conformations: The structure of PCN-12 contains two different conformers with symmetries C_s and C_{2v} in a ratio of 2:1 (figure 4.15). The linkers connect Cu_2 paddle wheels, leading to a tetragonal structure with a variety of symmetrically non-equivalent pores. A systematic analysis of all pore types has been attempted in a publication presenting the synthesis of an isostructural compound with an organosilicon linker, PCN-12-Si. (*265*) However, the irregular shape of some of the larger pores renders an intuitive classification difficult. Therefore, only the most prominent pores are described here.

There are two types of pores which are cuboctahedrally surrounded by Cu_2 paddle wheels. In both cases, the axes of the paddle wheels point into the pore, leading to a highly symmetrical arrangement of unsaturated copper sites. These pores have a diameter of approximately 12.5 Å. Furthermore, there are smaller pores which are bordered by two of the square faces of the cuboctahedra, with linkers with C_{2v} symmetry spanning the edges. These pores have a diameter of approximately 10 Å.

The structure of PCN-12 was taken from the original publication of Wang *et al.* (264) Coordinated water molecules were removed.
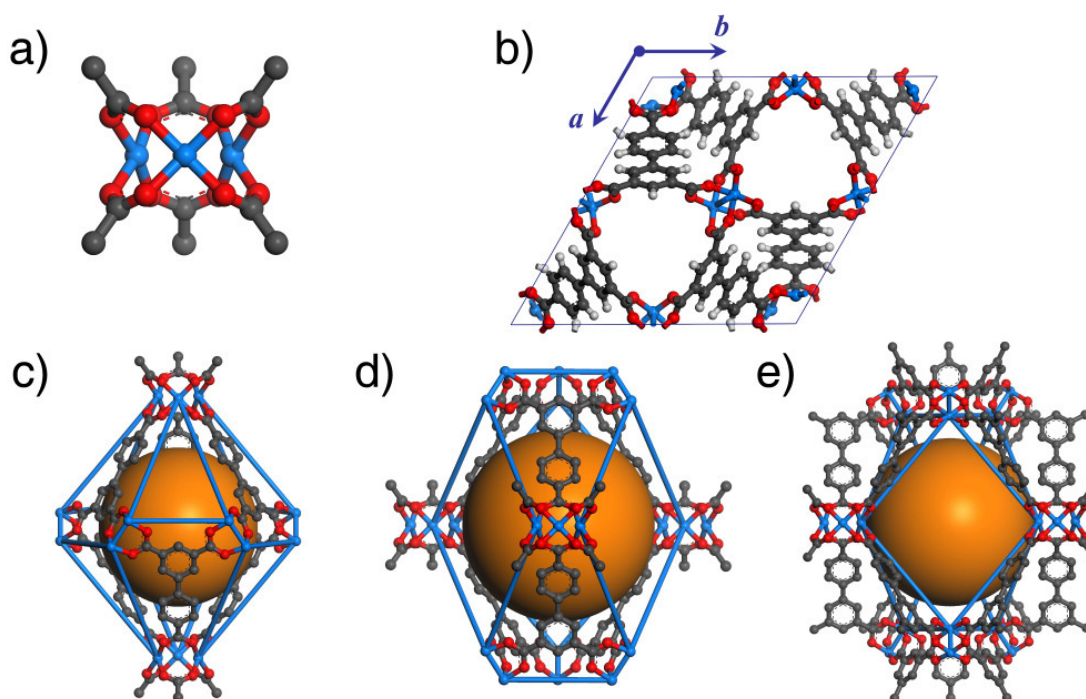
Figure 4.14. UMCM-150: *a)* Trigonal Cu_3 unit. *b)* Unit cell, displayed along the *c*-axis. *c)* Rhombohedral pore. *d)* First type of trigonal-bipyramidal pore. *e)* Second type of trigonal-bipyramidal pore, with copper centers pointing into the pore. The trigonal windows connecting the latter two pores along the *c*-axis are visible at the top and the bottom of *d)* and *e)*. The Cu centers bordering the pores are connected to highlight the pore topology. Colour scheme: Light blue = copper, red = oxygen, grey = carbon, white = hydrogen.
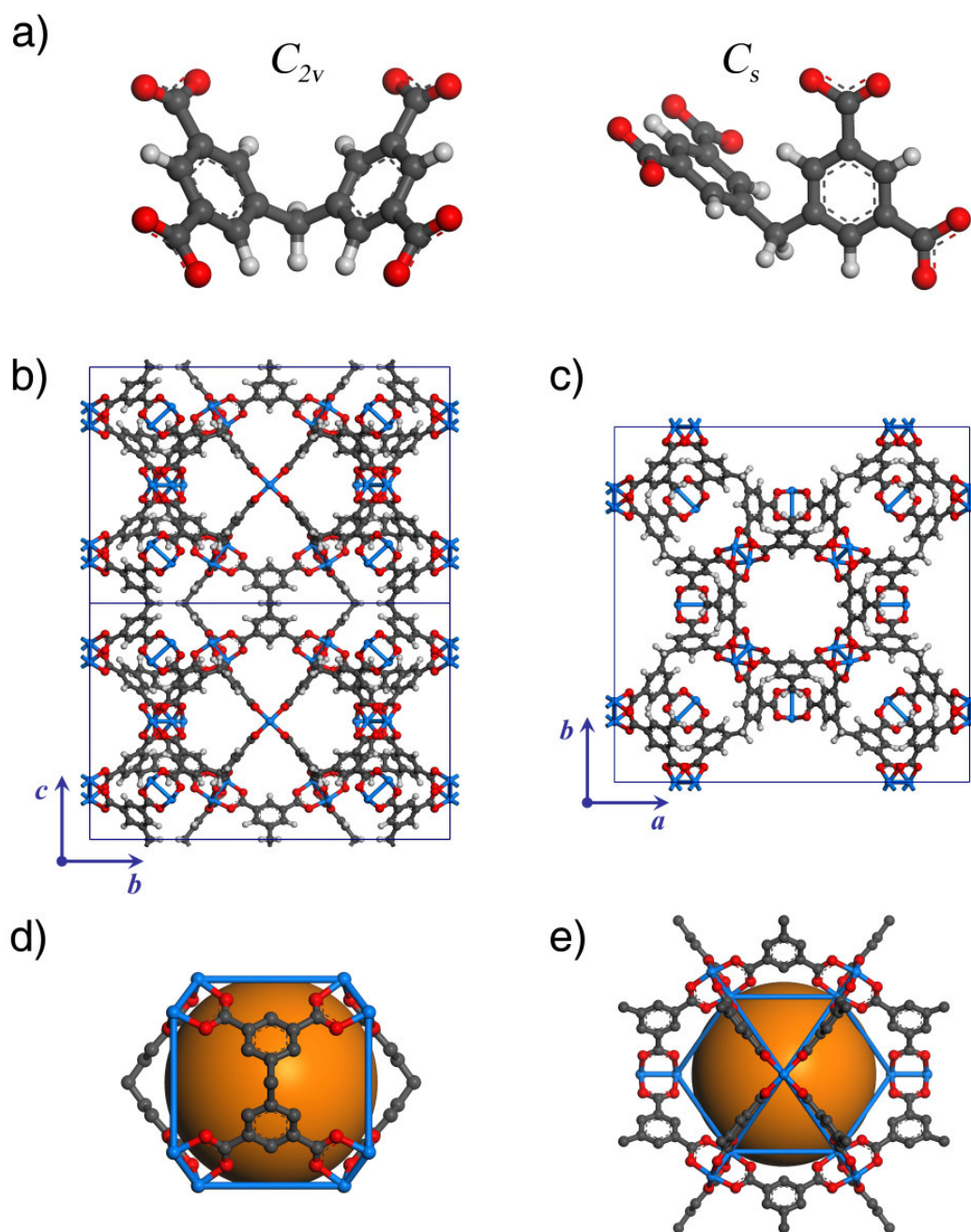
Figure 4.15. PCN-12: *a)* Different conformations of the mdip linker. *b)* 2 × 1 array of unit cells, displayed along the *a*-axis. *c)* Unit cell, displayed along the *c*-axis. *d)* Smaller pore surrounded by eight paddle wheels and four linkers in C_{2v} symmetry. *e)* Cuboctahedral pore, with Cu_2 paddle wheels pointing into the center of the pore. Both pore types are clearly visible in the plot along *a*: The center of the smaller pore is located at (1/2, 1/2, 0), the center of the large cuboctahedral pore at (1/2, 1/2, 1/2). The Cu_2 paddle wheels are connected to highlight the pore topology. Colour scheme: Light blue = copper, red = oxygen, grey = carbon, white = hydrogen.

4.3.1.9. $(M_4Cl)_3(btt)_8$ with M = Cu, Mn

The first MOF of this structure type, $(Mn_4Cl)_3(btt)_8$, with $H_3(btt)$ = 1,3,5-tris(tetrazol-5-yl)benzene, was reported by Long and co-workers in 2006. (*59*) In this Mn-MOF, charge-balancing extra-framework cations and residual methanol molecules are present in the framework even after evacuation at high temperature, thus giving the complete stoichiometry $Mn_3[(Mn_4Cl)_3(btt)_8(CH_3OH)_{10}]_2$. An isostructural compound with copper can be fully desolvated, but charge-balancing Cu^{2+} cations remain. (*60*)

The inorganic building unit of this MOF is a square-planar M_4Cl unit. Perpendicular to the M-Cl bond, each metal atom is coordinated by four nitrogen atoms of different btt linkers in a square-planar fashion, leading to a cubic network with *sod* topology. In total, the metal atoms have an octahedral coordination with one free cordination site. Groups of six M_4Cl units connected by eight btt linkers form truncated octahedral cages, which have a diameter of approximately 11 Å (figure 4.16). Between these cages, there are cylindrical channels with a similar diameter, with the metal sites pointing towards the interior of the channels. For the simulations, the structures of $(Mn_4Cl)_3(btt)_8$ and $(Cu_4Cl)_3(btt)_8$ were taken from experimental data. (*59*, *60*) Because the inclusion of extra-framework Mn^{2+} or Cu^{2+} cations in the simulations is difficult due to their high degree of structural disorder, the structures were idealized by removing them. Although these cations are important to ensure charge neutrality, it can be expected that their effect on the dispersive interaction potential is small. It is thus reasonable to ignore them in a first approximation, although it cannot be excluded that the adsorption at extra-framework cations may be of some significance, particularly at low pressures.
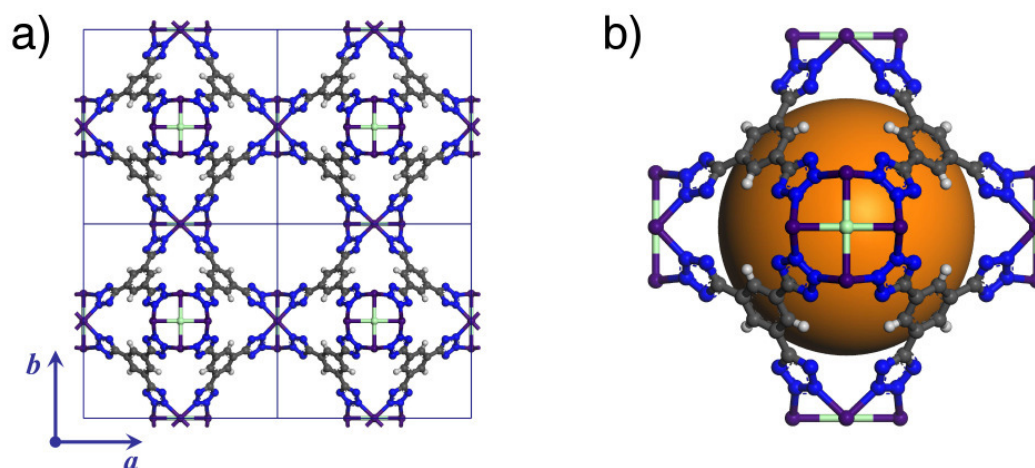
Figure 4.16. $(Mn_4Cl)_3(btt)_8$: *a)* 2 × 2 array of unit cells, displayed along the *c*-axis. More than one cell is shown to visualize the cylindrical channels, which are centered around the cell edge. *b)* Truncated octahedral cage. The square-planar inorganic building unit is clearly visible. Colour scheme: Puple = manganese, light green = chlorine, blue = nitrogen, grey = carbon, white = hydrogen.

4.3.1.10. Mg-formate

Porous metal formates with the stoichiometry $M(OOCH)_2$ have been reported for various metals, with M = Mg, Mn, Fe, Co, Ni, Zn. (*266*) For some of the metals, different polymorphs exist, which are distinguished by Greek letters. In this nomenclature, the structure type discussed in the following, which is also the most important, is designated as α-$M(OOCH)_2$. Permanent porosity was first evidenced for manganese formate in 2004, (*267*) and subsequently for magnesium formate in 2006. (*268*)

The structure of α-magnesium formate is monoclinic. One oxygen atom of each formate linker coordinates to one metal atom, whereas the other oxygen atom coordinates to two metal atoms (*syn-syn/anti*-bridging mode). All magnesium atoms are hexacoordinated, with a distorted octahedral coordination environment. One-dimensional zigzag chains of edge-sharing MgO_6 octahedra are connected by corner-sharing MgO_6 octahedra (figure 4.17). Between the zigzag chains, there are narrow channels with a cross-section of approximately 3×4.5 Å that run parallel to the *b*-axis.

The structure used in the simulations was taken from the experimental data published by Kim's group. (*269*)
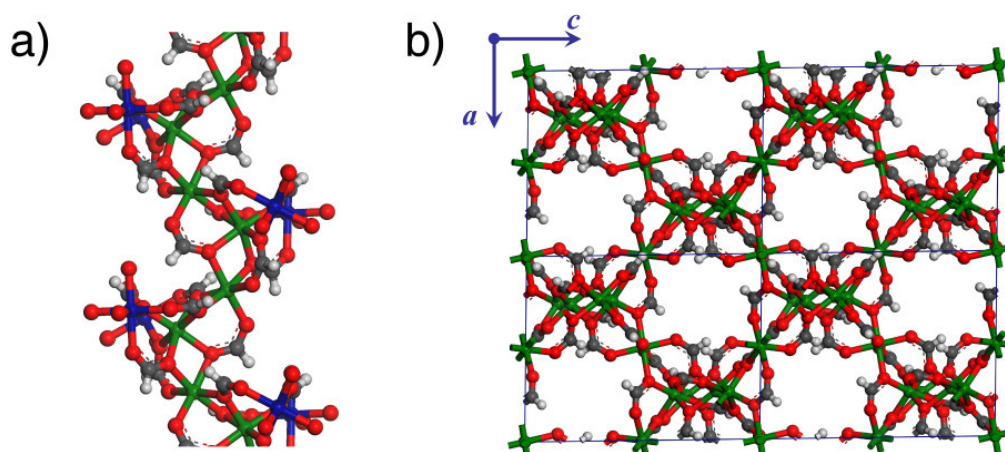
Figure 4.17. Mg-formate: *a)* Chain of octahedrally coordinated Mg atoms running in the direction of the *b*-axis. The *syn-syn/anti*-bridging mode of the formate linkers is apparent. MgO_6 octahedra connecting these chains are also displayed, with the Mg atoms shown in dark blue to distinguish them from those atoms constituting the chains, which are shown in green. *b)* 2×2 array of unit cells, displayed along the *b*-axis. Colour scheme: Dark green = magnesium, red = oxygen, grey = carbon, white = hydrogen.

4.3.2. Other microporous materials

4.3.2.1. Silicalite

The synthetic all-silica zeolite Silicalite was presented by Flanigen and co-workers in 1978. (*270*) In contrast to hydrophilic aluminosilicate zeolites, Silicalite is hydrophobic, and shows a high affinity for organic molecules. While an accurate theoretical description of

aluminosilicate zeolites is complicated due to the presence of extra-framework cations and the possibility of heterogeneities in the Si-Al distribution, the structure of Silicalite can be modelled straightforwardly, making it a particularly suitable zeolite for molecular simulation studies.

The structure of Silicalite belongs to the *MFI* framework type (MFI = mordenite framework inverted). (*271*) It can be understood as being composed of pentasil units consisting of eight five-membered rings, which are joined together to form infinte chains running along the *c*-axis (figure 4.18). These chains are connected by bridging oxygens in the other two crystallographic directions. The structure of silicalite has two types of intersecting channels, which are both surrounded by ten-membered rings. There are straight, elliptical channels running in the direction of the *b*-axis with a cross-section of approximately 5.2×5.8 Å, and sinusoidal channels running along the *a*-axis with a diameter of approximately 5.4 Å.

The structure of Silicalite was taken from the work of van Koningsveld *et al.* (*272*)
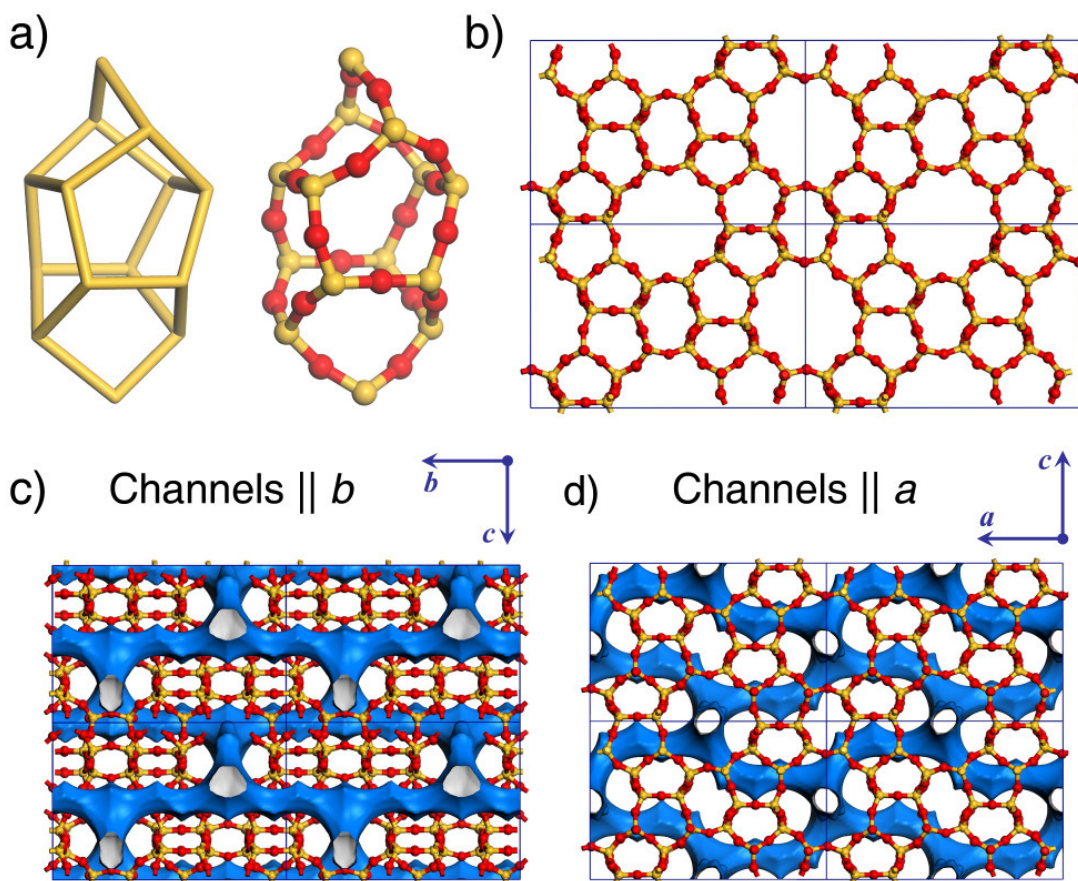
Figure 4.18. Silicalite: *a)* Schematic and atomistic representation of one pentasil unit, consisting of eight five-membered rings. *b)* 2×2 array of unit cells, displayed along the *b*-axis. *c, d)* Visualization of the two types of channels present in the structure, using the accessible surface area calculated from crystal structure data (light blue). Colour scheme: Yellow = silicon, red = oxygen.

4.3.2.2. Cucurbit[6]uril

The cucurbit[n]uril family is a group of macrocyclic organic molecules which are obtained by condensation of glycoluril and formaldehyde. One molecule consists of n glycoluril units, with $n = 5 - 11$. The name cucurbit[n]uril was coined due to the close resemblance of the macrocycles to pumpkins (*cucurbita* = pumpkin (Lat.)). Cucurbit[n]urils have been investigated for various applications due to their interesting host-guest chemistry. (*273, 274*)

A crystalline, microporous polymorph of cucurbit[6]uril (commonly abbreviated as CB[6]) was reported by Kim and co-workers in 2008. (*275*) In the structure of this porous polymorph, each CB[6] macrocycle interacts with four neighbouring molecules through hydrogen bonds: Two adjacent molecules are situated above the carbonyl-laced portals of the macrocycle, the central molecule acting as hydrogen-bond acceptor. Two other neighbours are located at the sides of the macrocycle, which behaves as hydrogen-bond donor due to the presence of CH and CH$_2$ groups. The closest C-H$\cdots$O distances between two neighbouring rings range below 2.3 Å. This local arrangement leads to a hexagonal structure with *nbo* topology. While the intramolecular cavities inside the macrocycles are blocked due to the presence of the neighbouring rings above the portals, there are intermolecular channels which run parallel to the *c*-axis (figure 4.19). After desolvation, these channels are accessible, generating a permanent porosity.

The structure of microporous CB[6] was taken from the work of Lim *et al.* (*275*) Solvent molecules were removed, and the intramolecular cavities were blocked for the simulation in order to avoid an artificial adsorption in these inaccessible voids.
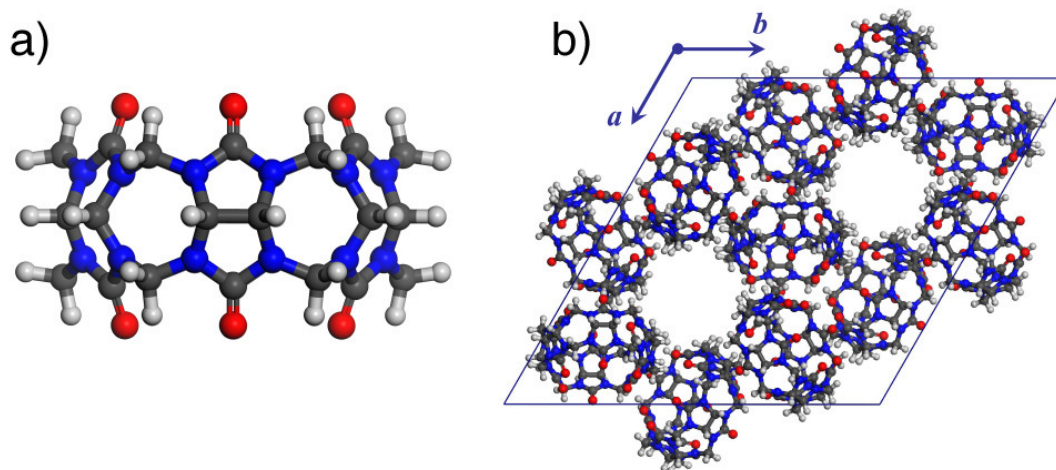
Figure 4.19. Cucurbit[6]uril: *a)* CB[6] macrocycle. *b)* Unit cell of crystalline, microporous cucurbit[6]uril, displayed along the *c*-axis. The complete coordination by four adjacent rings is visible for the central CB[6] ring. Colour scheme: Red = oxygen, blue = nitrogen, grey = carbon, white = hydrogen.

4.4. Porous adsorbents: Force-field parameters

4.4.1. Derivation of parameters from experimental data

As it has been shown in section 4.2, the force-field parameters used for the fluid molecules can be derived quite straightforwardly, provided that sufficient thermophysical data are available. For the framework compounds used as adsorbents, it is theoretically possible to employ a similar method, replacing pressure-density relationships with experimental adsorption isotherms. However, this procedure is very problematic for two reasons: Firstly, the experimental isotherms are determined much less accurately than the bulk properties of fluids, which are precisely known. Secondly, and even more severely, there is no unequivocal means of correlating deviations in the predicted isotherm with parameter changes.

To illustrate this with an example, it is assumed that the adsorption of molecule X in a system consisting of two different elements, A and B, is calculated using force-field based GCMC simulations, employing the typical mixing of atomic LJ parameters. If the predicted amount adsorbed is lower than the experimental value, it is obvious that the LJ parameters in the simulation underestimate the actual interaction strength. However, there are different possibilities to adjust the parameters in order to resolve this shortcoming: For both A and B, either r_0, or D_0, or both can be modified. It can be expected that different modifications can lead to a similar improvement of the predicted adsorption isotherm due to error compensations. Such errors are hard to detect and require an extensive scanning of a wide range of pT conditions, for which experimental data are rarely available.

From these considerations, it is apparent that the strategy of deriving parameters from experimental data is hardly applicable for MOFs, which usually contain at least four different elements. However, a selective modification of some parameters of a generic force field (see below) in order to improve the agreement with experimental data has been used occasionally. (221, 276) In contrast to MOFs, the derivation of parameters from experimental data has been regularly employed for systems which contain only few elements, and for which a large body of reliable experimental data is available. For example, a reparameterized H_2-C potential has been proposed very recently by Bhatia and co-workers, using a fit to high-quality experimental measurements of hydrogen adsorption in microporous carbons. (277) Similar strategies have been commonly applied for zeolites, which are reviewed in (278).

4.4.2. Generic force fields and tailor-made force fields

It has been discussed that generic force fields are intended to provide a set of transferable parameters that can be employed for a wide range of different compounds. Due to their broad applicability, only modest accuracy can be expected from these parameters. However, their transferability renders them suitable for calculations dealing with systems for which no specifically designed parameters are available. In GCMC simulations of adsorption, the non-bonded parameters are the only relevant part of the force field. It is usually assumed that these parameters are not very sensitive to the specific environment. For example, many

force fields use identical LJ parameters for carbon in all possible hybridizations. Therefore, it can be expected that a mixing of the fluid molecule parameters described above with generic parameters for the framework atoms should, on average, provide a reasonable description of the solid-fluid interaction. Of the different generic force fields that have been published, only three are commonly used in molecular simulation studies of adsorption in MOFs: The DREIDING force field (DrFF), the Universal Force Field (UFF), and the OPLS-AA force field (Optimized Potentials for Liquid Simulations - All Atoms).

All three force fields were published during the 1990s, indicating that less effort has been directed towards the improvement of generic, broadly applicable force fields more recently. This can be explained with the development of computational resources. Because *ab-initio* calculations are now routinely possible for relatively large systems, it is possible to directly derive a tailor-made set of parameters from these computations, eliminating the need for generic parameters. For modelling studies of gas adsorption in MOFs, this approach has been pioneered by Goddard and co-workers. (*73, 279*) Although it certainly warrants further development, the results published so far do not show a general superiority of tailor-made parameters when compared to generic parameters, at least for systems where the dispersive interaction is predominant. Therefore, generic parameters will be used throughout this work, but supplemented with *ab-initio* derived parameters in specific cases.

4.4.3. Generic force fields: An overview

The DREIDING force field was presented in 1990 by Goddard and co-workers as a general force field for predictions of structure and dynamics of organic, biological, and main-group inorganic molecules. (*156*) In addition to non-metals, it contains parameters for a few metals, among them Zn and Fe. Empirical relationships are used to obtain bond distances and angles as well as force constants. For the Lennard-Jones parameters, the DrFF uses parameters from previous work by Williams *et al.*, who derived non-bonding parameters from a careful analysis of experimental structural data ((*280*) and references therein). In the initial publication, the performance of the DrFF was evaluated mainly for the structure prediction of organic crystals.

The Universal Force Field, a force field that covers the whole periodic system, was published by Rappé *et al.* in 1992. (*157*) Similarly to the DrFF, the bonded UFF parameters are calculated from simple general rules, which employ the element type, the hybridization, and the connectivity. For the LJ parameters, the ionization potential and results from numerical Hartree-Fock calculations are used to develop an empirical estimation scheme that permits a definition for all elements. In subsequent publications to the paper that presents the parameters, the UFF was validated for structure predictions of organic molecules, main-group compounds, and metal complexes. (*281–283*)

The first version of the OPLS force field was presented by Jorgensen and co-workers in 1984. (*167*) It is intended mainly for simulations of organic liquids, rather than the prediction of crystal structures. While the first parameterization uses an implicit-hydrogen model

for CH_x groups, an all-atom version was presented in 1996. (*159*) Both LJ parameters and partial charges are derived from a fitting procedure in order to reproduce fluid properties of organic liquids, notably vaporization enthalpies and densities. In a more recent, comparative study of several force fields, it was found that the OPLS-AA force field provides a reasonable description of vapour-liquid equilibria and liquid densities, but performs worse than the TraPPE force field. (*169*)

Of these force fields, only the UFF contains a consistent set of parameters for all elements. This limits the applicability of the other two force fields for systematic studies of MOFs: The DrFF lacks parameters for most transition metals, whereas the OPLS-AA force field does not include any metal parameters. Therefore, some authors have combined the parameters of these force fields for non-metal atoms with the parameters from the UFF for the metal centers. (*276, 284*) However, there is a risk that a mixing of elements from different force fields may lead to an inconsistent description of the framework as a whole.

As a final remark, it should be emphasized that none of the force fields described here was originally developed for the task which is central to this work, namely the representation of framework atoms in molecular simulations of adsorption. Therefore, a good or even reasonable performance cannot be expected *a priori*. Whenever possible, a careful analysis of the predicted quantities, in particular with regard to available experimental data, is thus mandatory.

4.4.4. Partial modification of existing force fields

4.4.4.1. Interaction of hydrogen with aromatic systems

Due to the possible shortcomings of generic force fields discussed above, it can be worthwhile to use additional information on interatomic interaction energies, and modify the corresponding parameters accordingly, retaining all other parameters from the force field. This additional information can be obtained from experimental data, *e.g.* from spectroscopy, or from *ab-initio* calculations. In order to assess whether these changes actually improve the performance, results obtained with the unmodified force field should be compared to the "derivative". In the following, it will be described how a new set of parameters for the interaction of H_2 with aromatic carbon atoms (C_{aryl}) is derived from literature *ab-initio* data.

The interaction of hydrogen with aromatic hydrocarbons has been investigated with *ab-initio* methods by several authors. Due to the dominance of dispersive interactions, conventional DFT does not provide reasonable predictions of the interaction energy. (*36*). Therefore, most studies have used MP2 theory (*36, 285, 286*) or coupled cluster methods. (*38, 287*) Quantum Monte Carlo methods have also been employed. (*288*) A detailed discussion of the results published in the literature, which would need to account for numerous further publications not cited here, is clearly beyond the scope of this work. However, some aspects will be highlighted in section 5.3, where DFT-D calculations are compared to the CCSD(T) results of Rubeš and Bludský. (*38*)
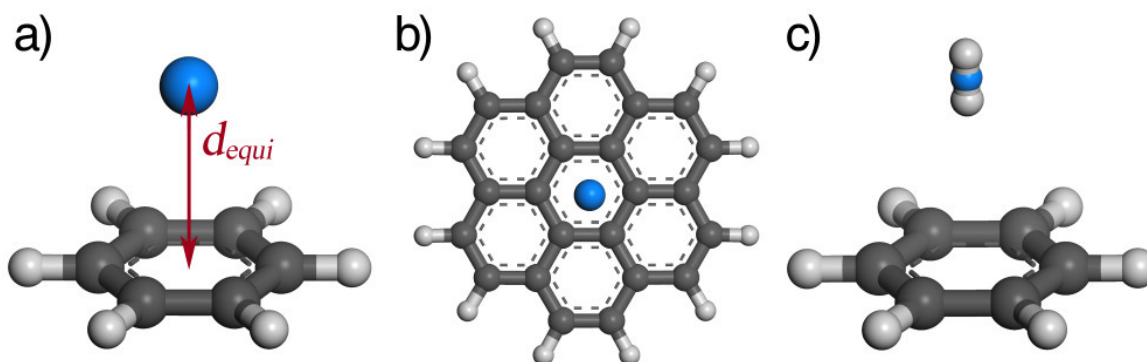
Figure 4.20. *a)* Hydrogen molecule (UA model) located above a benzene ring. *b)* Hydrogen molecule (UA model) located above the center of a coronene molecule. *c)* Three-site model of hydrogen, located above the center of a benzene ring in perpendicular orientation. In the benzene ring, the charge of the carbon atoms amounts to $-0.125\,e$, and the charge of the hydrogen atoms is $+0.125\,e$.

As reference *ab-initio* data, the MP2 results of Heine *et al.* are used here, (*36*) as the CCSD(T) study of Rubes and Bludský was published too late to be taken into account for the parameter modification. (*38*) In the article by Heine *et al.*, interaction energies for hydrogen over the center of a benzene molecule were calculated for two different orientations of the H_2 dumbbell, perpendicular and parallel to the ring plane. Additional results were reported for some polycyclic aromatics, and extrapolated to a graphene layer. Large basis sets were used, and a BSSE correction was applied. To account for the rotational degrees of freedom of the H_2 molecule, an orientation penalty of 1.3 kJ mol^{-1} was estimated from the results for benzene, an approximation which is debatable in the light of more recent results.

For the force-field modification, the Lennard-Jones parameters representing an aromatic carbon atom, C_{aryl}, were adjusted in a way that the results of Heine *et al.* for benzene, coronene, and an extended graphene layer were reproduced in the best possible way. The parameters representing the hydrogen molecule and H atoms attached to the rings were held fixed, using the Buch potential and UFF parameters, respectively. The usage of a united-atom model corresponds to an averaging over all possible orientations of the H_2 molecule. Therefore, the proposed orientation penalty is subtracted from the MP2 results for the perpendicular orientation to obtain the target values (table 4.3).

In comparison to the original UFF parameters, the best agreement is obtained for a parameter combination corresponding to a smaller equilibrium distance and a deeper potential well: The distance r_0 was reduced from 3.851 Å to 3.713 Å, and the well depth was increased from 0.439 kJ mol^{-1} to 0.575 kJ mol^{-1}. The resulting interaction energies with these parameters, as well as those obtained with the unmodified UFF, are given in table 4.3. For the adjusted C_{aryl} parameters, an excellent agreement with the MP2 values is observed for coronene and the extended graphene layer. For benzene, however, the agreement is less good, with a tendency to overestimate the equilibrium distance, and to underestimate the interaction energy. Tentatively, this can be related to the more inhomogeneous charge distribution in benzene as compared to the larger aromatic systems, which leads to a more significant contribution of electrostatic interactions.

In order to test this hypothesis, an additional calculation was carried out for one model system including charges: The H_2 molecule was represented as the three-site model described in section 4.2, whereas ESP charges were used for the benzene ring. The hydrogen molecule is placed over the center of the ring in perpendicular orientation. Using the modified parameters, the calculated equilibrium distance of 3.10 Å is in excellent agreement with the MP2 value of 3.08 Å. The interaction energy of -4.5 kJ mol^{-1} also corresponds well with the -4.8 kJ mol^{-1} obtained in the *ab-initio* calculations. These results indicate that the deviations observed above for benzene are, at least in part, indeed related to the neglect of electrostatic interactions.

For practical use, the parameters derived for aromatic carbon atoms are combined with the parameters from the UFF for all other framework atoms. This partially modified force field is referred to as UFF+C$_{aryl}$.

Table 4.3. H_2-ring equilibrium distance d_{equi} and interaction energy E_{int} calculated with the original UFF parameters, and the parameters adjusted to reproduce the results from MP2 calculations of Heine *et al.* (*36*)

		Benzene+H_2	Coronene+H_2	Graphene+H_2
MP2 results	d_{equi} / Å	3.08	3.08	3.08
	E_{int} / kJ mol^{-1}	-3.5	-5.1	-5.9
Force field, UFF	d_{equi} / Å	3.26	3.16	3.14
	E_{int} / kJ mol^{-1}	-2.6	-4.6	-5.3
Force field, UFF+C$_{aryl}$	d_{equi} / Å	3.19	3.09	3.08
	E_{int} / kJ mol^{-1}	-2.9	-5.1	-5.9

4.4.4.2. Adsorption at coordinatively unsaturated metal sites

From the overview of MOFs given in section 4.3, it is apparent that a number of the systems discussed in this work contain coordinatively unsaturated metal sites. A preferential adsorption of fluid molecules at these sites has been evidenced experimentally with different techniques, such as neutron diffraction or spectroscopic methods.

Throughout this work, it is frequently observed that experimental results obtained for systems with unsaturated metal sites cannot be reproduced in simulations with standard parameters. The specific interaction of the fluid molecules with these sites is not adequately represented in the simulations, which account for dispersive interactions (and, in some cases, electrostatic interactions) only. In order to resolve this issue, improved parameters are derived from DFT calculations for simple model systems. In analogy to the partial force-field modification described above, these parameters are then integrated into the UFF.

Because the adequate modelling of adsorption at metal centers is one of the central topics of this work, the DFT calculations and force-field modification strategies are not discussed at this point, but are described in the sections that deal with the corresponding molecular simulations of adsorption.

4.4.5. ESP charges

From the set of adsorbents presented in section 4.3, ESP charges were calculated for IRMOF-1, Zn(dtp), $Cu_3(btc)_2$, Mg-formate, Silicalite, and cucurbit[6]uril using DFT calculations. In principle, the recently presented REPEAT method, which is applicable for periodic solids, would be ideally suited for these calculations. [216] However, since this method is not yet available with most DFT codes, the calculations were carried out for non-periodic model systems. In these calculations, the DMOL^3 code [195, 289] as implemented in the *Accelrys* "Materials Studio" package [233] was employed. It uses the ESP method as proposed by Singh and Kollman. [214] The computational details of these calculations, as well as the resulting charges, are described in more detail in the Appendix, subsection A.2.3. Only some general aspects are discussed here.

The first problem concerns the choice of the non-periodic model system. For the molecular crystal cucurbit[6]uril, this choice is straightforward. It can be expected that the electrostatic potential of the crystal can be generated by superposition of the electrostatic potentials of the individual molecules. Therefore, one CB[6] macrocycle was used as model system. For IRMOF-1, Zn(dtp), and $Cu_3(btc)_2$, representative fragments were extracted from the periodic structure. These fragments were saturated by small coordinating molecules, such as benzoate, to obtain a system which is chemically similar to the MOF. For IRMOF-1 and $Cu_3(btc)_2$, these model systems are shown in figure 4.21. Only the ESP charges of the inner atoms of these systems are transferred to the periodic system. This leads to a necessity of scaling the charges in order to obtain charge neutrality of the framework. In this work, this is done by adjusting the charge of one selected atom, *e.g.* the central oxygen atom in the case of IRMOF-1, and the copper atom in $Cu_3(btc)_2$. Both the original and the adjusted charge are given in the Appendix. For Mg-formate, the complex connectivity of the framework does not lend itself to the extraction of a representative fragment. For simplicity, a $Mg_2(OOCH)_4$ cluster was used to calculate the ESP charges. Finally, the charges for Silicalite were derived for a cluster consisting of twelve Si atoms, sixteen bridging oxygens, and sixteen terminal hydroxyl groups.

In previous studies, it has been found that the resulting ESP charges show a non-negligible variation, which may depend on several factors. For $Cu_3(btc)_2$, a dependency of the results on the size of the model system has been observed by Johnson and co-workers (it should be noted, however, that both clusters used by these authors are smaller than the model system used here). [290] For some of the atoms of $Cu_3(btc)_2$, there are noteworthy discrepancies between the results obtained in this work, and the results of Yang and Zhong, who used a very similar model system. [133] In this case, the deviations are most probably re-

lated to differences in the computational setup (exchange-correlation functional, basis set, charge derivation scheme). Similarly, it has been pointed out by Keskin *et al.* that there are non-negligible differences between the partial charges reported by different authors for IRMOF-1. (*72*) A better understanding of the origin of these differences could facilitate recommendations concerning the most suitable setup for partial charge calculations.
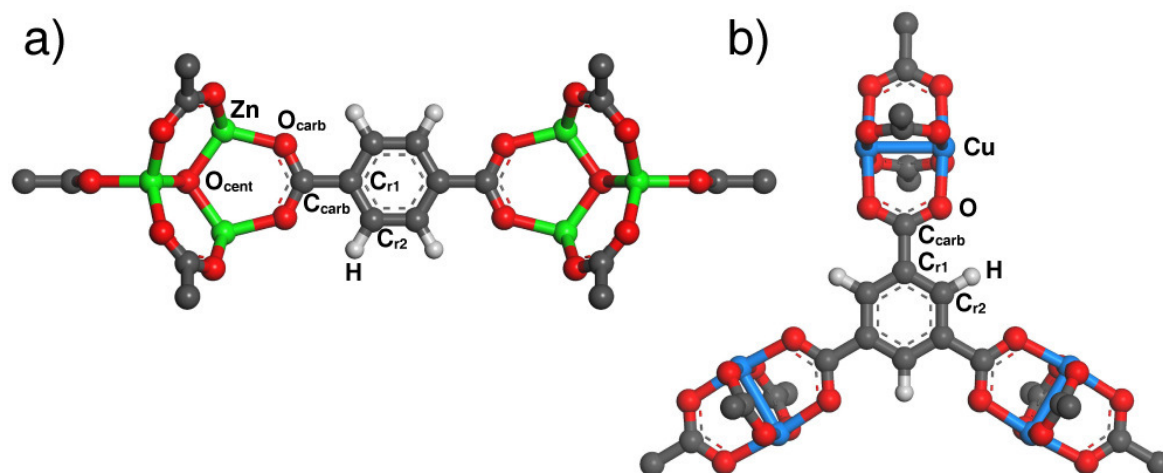
Figure 4.21. *a)* $(Zn_4O)_2(bdc)(bmc)_{11}$ cluster used for the ESP charge calculation of IRMOF-1. *b)* $(Cu_2)_3(btc)(bmc)_9$ cluster used for the ESP charge calculation of $Cu_3(btc)_2$. In both cases, phenyl rings of the benzoate (bmc) moieties are omitted for clarity.

4.5. Determination of the pore volume

4.5.1. Introduction

Experimental adsorption measurements deliver the excess amount adsorbed n_{exc}, *i.e.* take into account only the molecules adsorbed at the pore wall (figure 4.22). In contrast to this, molecular simulations deliver the total number of molecules per volume unit n_{abs}. While the precise relationship between these quantities is complicated because there is no way to determine the thickness of the adsorbed layer directly, (291, 292) the constant volume approximation permits a simple estimation according to:

$$n_{exc} = n_{abs} - \rho_{bulk} \cdot V_p \tag{4.5}$$

Here, ρ_{bulk} is the density of the bulk gas phase, which can be taken from tabulated data, and V_p is the free pore volume.
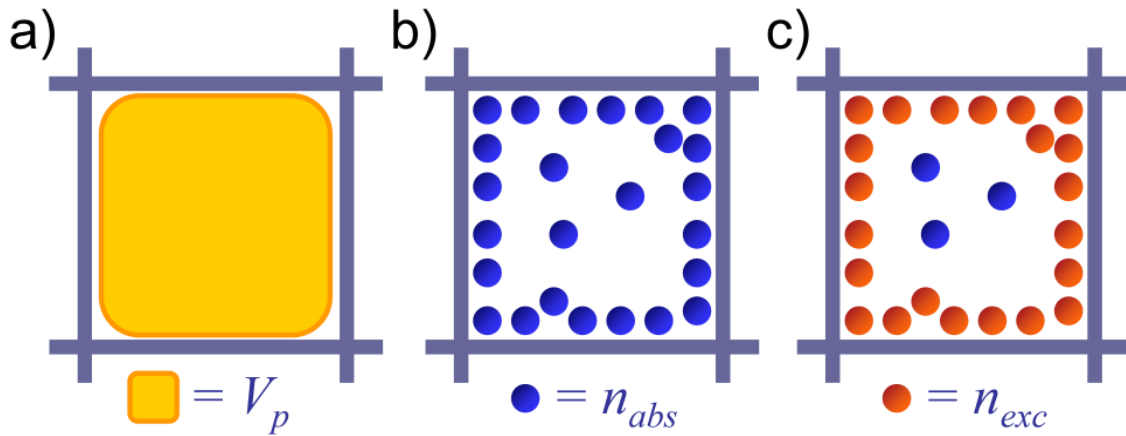
Figure 4.22. Schematic representation of absolute and excess amount adsorbed. *a)* Free pore volume. *b)* The total number of guest molecules in the pore constitutes the absolute amount adsorbed. *c)* The fraction of guest molecules that are adsorbed at the pore walls, shown in red, constitutes the excess amount adsorbed.

The pore volume can be determined experimentally using nitrogen or helium adsorption. In analogy to experiment, it has been proposed to determine the pore volume from molecular simulations of helium adsorption at room temperature or higher temperatures. (242, 293, 294) If the helium molecules only fill the free pore volume without forming an adsorbed layer of increased density, V_p can be determined from the ideal gas law:

$$V_p = \frac{R \cdot N_m \cdot T}{p \cdot m_{m,solid}} \tag{4.6}$$

In this equation, R is the ideal gas constant, and N_m is the number of helium molecules per molar mass $m_{m,solid}$ of the adsorbent.

When the free pore volume is known, the skeletal density of the framework can be calculated as:

$$\rho_{sk} = \frac{\rho_{cryst}}{1 - V_p \cdot \rho_{cryst}} \tag{4.7}$$

The crystallographic density ρ_{cryst} can be determined from crystal structure data.

4.5.2. Parameter modification

Grand-canonical Monte Carlo simulations of helium in an empty cell showed that the parameters from the UFF reproduce the equation of state at $T = 298\,K$ very well (figure 4.23). However, preliminary simulations of helium adsorption in a number of typical MOFs led to a massive overestimation of the pore volume when the UFF parameters were used to describe the framework atoms. Apparently, usage of the standard parameters leads to an artifical interaction of helium with the pore walls: The amount of helium in the framework is overestimated, and therefore, the pore volume which is calculated from equation 4.6 is too large. To ensure reliable predictions of the pore volume, the following strategy of parameter modification was used:

The parameters $r_0(He\text{-}X)$ representing the equilibrium distance between a helium atom and a framework atom X were obtained from Lorentz-Berthelot mixing of the atomic parameters $r_0(He)$ and $r_0(X)$ tabulated in the Universal Force Field. The parameters $D_0(He\text{-}X)$ representing the interaction strength obtained from Lorentz-Berthelot mixing of the UFF atomic parameters were scaled by a scaling factor s_X chosen within the limits: $0 \leq s_X \leq 1$. It is thus:

$$D_0(He\text{-}X)_{mod} = s_X \cdot \sqrt{D_0(He) \cdot D_0(X)} \tag{4.8}$$

Two different model systems were used for the derivation of the scaling factors s_X: A graphitic slit pore was used to obtain a scaling for the helium-carbon interaction, and Silicalite was used to obtain a "universal" scaling factor for the interaction of helium with other framework atoms, particularly the metal and oxygen atoms of the inorganic building units in MOFs. In order to calibrate the scaling factor, a target pore volume was defined, which is accessible either from geometric considerations or from experimental data. For the slit pore, two different distances $d_{C\text{-}C}$ between the graphitic planes were considered, amounting to 7 Å and 13 Å. The geometric pore volume for one unit cell was then obtained from geometric considerations, taking $d_{acc} = d_{C\text{-}C} - r_0(He\text{-}C)$ as the diameter of the accessible part of the pore. (295) For Silicalite, the experimental value obtained from the adsorption of different vapours at room temperature (methanol, n-butane) was taken as the target pore volume. (270) For this particular structure, this is a reasonable choice, because the channel-like pores in the structure of Silicalite have a diameter of more than 5 Å, and there are no small pores that could be accessible to helium only. Therefore, the observed pore volumes should be identical for helium and the organic vapours.

Figure 4.23 shows the pore volumes obtained from GCMC simulations of helium adsorption at $T = 298\,K$. Calculations at four different pressures ranging from 0.4 bar to 10 bar do

not indicate a significant dependency of the results on pressure, so the average value over all pressures is used. The target values are also displayed for comparison. A scaling factor of 0.33 accurately reproduces the geometrical pore volume for both interplanar distances of the slit pore. In the case of Silicalite, the ideal scaling factor is somewhat higher, amounting to 0.39. However, the two values are very close to each other, indicating that the resulting pore volumes are not very sensitive to small changes of s_X. In all calculations reported in the following, $s_X = 0.33$ is used for carbon, and $s_X = 0.39$ is used for all other elements.
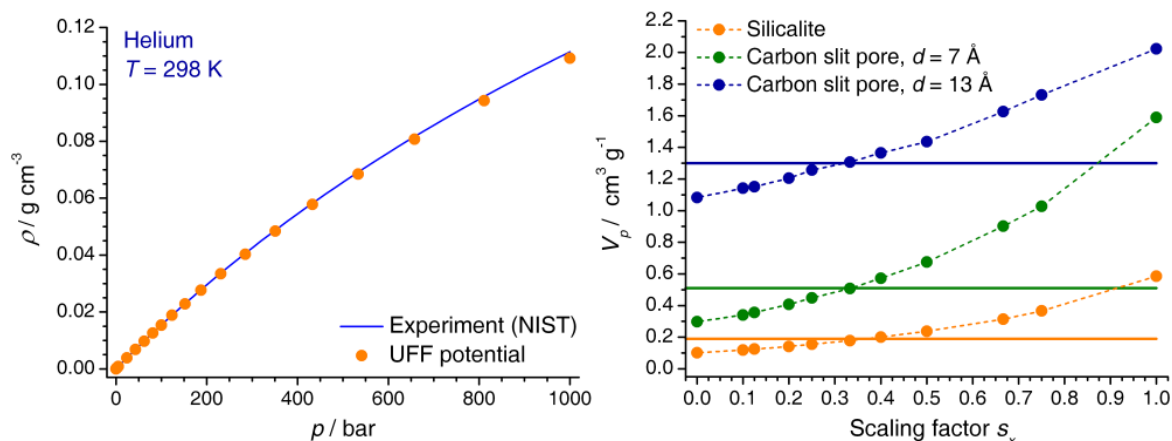
Figure 4.23. *Left:* Bulk properties of Helium at room temperature, calculated with the potential parameters taken from the UFF. Experimental data from (*232*). *Right:* Pore volumes obtained for three different model systems with values of the scaling factor s_X ranging from 0 to 1. The target pore volumes are shown as horizontal lines.

4.5.3. Results: Pore volumes of porous adsorbents

The free pore volumes calculated for all microporous adsorbents discussed in this work are reported in table 4.4, together with experimental data. While only one reference value is reported here for each system, it should be noted that there is considerable scatter between different experimental measurements. For $Cu_3(btc)_2$, a particularly well investigated system, experimental values range from 0.33 cm^3 g^{-1} to 0.83 cm^3 g^{-1}. (*71*) Clearly, the majority of these differences can be attributed to sample quality issues. However, some errors may also be introduced during the data analysis (see below).

Looking at table 4.4, the overall agreement between calculation and experiment is reasonably good, with the absolute deviations exceeding 0.1 cm^3 g^{-1} only in one case. Notably, there seems to be no systematic deviation towards higher or lower volumes. While it cannot be ruled out that an "ideal" choice of parameters would deliver somewhat different results, these observations indicate that the parameters derived above are, on average, well suited to calculate the free pore volume.

Table 4.4. Calculated pore volumes obtained for the MOFs discussed in this work. Selected experimental values are given for comparison. In addition to the data compiled here, results for a number of other MOFs have been reported in an earlier publication. (*296*) The crystallographic density ρ_{cryst} of the structures as described in section 4.3 is also given.

	$V_{p,calc}$ / cm^3 g^{-1}	$V_{p,exp}$ / cm^3 g^{-1} (Ref.)	ρ_{cryst} / g cm^{-3}
IRMOF-1	1.22	1.20 (*51*)	0.589
MOF-74	0.48	0.39 (*252*)	1.219
ZIF-8	0.47	0.37 (*297*)	0.924
Zn(dtp)	0.25	0.16 (*257*)	1.386
Cu$_3$(btc)$_2$	0.70	0.75 (*252*)	0.879
MOF-505	0.63	0.68 (*261*)	0.927
UMCM-150	1.07	1.00 (*263*)	0.636
PCN-12	0.81	0.94 (*264*)	0.762
(Mn$_4$Cl)$_3$(btt)$_8$	0.89	0.80 (*59*)	0.725
(Cu$_4$Cl)$_3$(btt)$_8$	0.79	0.72 (*60*)	0.801
Mg-formate	0.18	0.14 (*269*)	1.420
Silicalite	0.19	0.19 (*270*)	1.796
Cucurbit[6]uril	0.12	0.13 (*275*)	1.337

Apart from possible shortcomings of the parameter set, deviations between calculation and experiment can be rationalized as follows: In cases where the calculated pore volume is too large, the most probable reason is the non-ideality of the experimental samples. Incomplete activation and structural defects will inevitably lead to a decrease of V_p with respect to the ideal system, which is used in the calculations. Particularly for the (M$_4$Cl)$_3$(btt)$_8$ systems, these differences can be expected because the idealized structures used in the calculations do not contain extra-framework cations. Furthermore, it is also imaginable that pores are not accessible for nitrogen, which is usually used in experiments, but accessible for helium. In the case that the calculation delivers a lower pore volume than the experiment (a situation observed less frequently than the opposite), there are several possible explanations. On the one hand, the experimental determination from an N$_2$ adsorption isotherms can be carried out at different relative pressures. If the chosen relative pressure is too large, some "pore space" which is actually due to interparticular voids may be included in the resulting V_p. On the other hand, specific interactions of the quadrupolar nitrogen molecules with the framework may lead to local density variations that are not accounted for in the standard analysis of experimental data. In this context, it is interesting to note that significant deviations towards lower pore volumes occur only for MOFs with unsaturated copper sites.

Therefore, it can be speculated that an interaction of these sites with nitrogen may influence the determined pore volumes. Further evidence for the importance of these interactions was provided by Johnson and co-workers in a combined experimental and simulation study of nitrogen adsorption in $Cu_3(btc)_2$. (*71*) Ideally, a systematic investigation should compare experimental nitrogen and argon adsorption isotherms, because interactions with the metal sites can be ruled out for argon, which does not have a quadrupole moment. If the pore volumes obtained from argon data are systematically lower than those calculated from a nitrogen adsorption isotherm, it can be concluded that a localized adsorption of N_2 leads to density increases, and subsequently causes errors in the pore volume determination.

4.6. Description of software packages

4.6.1. Programs used for GCMC simulations

4.6.1.1. The Sorption module

The Sorption module, distributed by *Accelrys* in the "Materials Studio" package, (233) is a Monte Carlo code for simulations of adsorption in porous solids. It permits simulations in the canonical (NVT) ensemble ("Fixed loading" job) and in the grand-canonical (μVT) ensemble ("Fixed pressure" job), the theoretical background of which has been discussed in more detail in section 3.2. A series of fixed pressure calculations at a given temperature can be combined in an "Adsorption isotherm" job. Furthermore, the Sorption module permits Henry constant calculations according to equation 3.29, and the determination of the most favourable adsorption regions in a structure ("Adsorption locator" module, not used in this work). In addition to classical Metropolis sampling, molecules with conformational degrees of freedom can be treated using a configurational-bias sampling scheme.

The solid-fluid and fluid-fluid interactions are treated as a combination of dispersive and electrostatic interactions. Different force fields can be used with the Sorption module, such as the UFF and the DREIDING force field. While parameter modifications are possible, only a few types of potential functions to represent dispersive interactions are implemented (Lennard-Jones potential, Morse potential). The interactions are truncated at a user-specified cutoff radius, and a spline interpolation can be employed to provide for a smooth decrease to zero in the range of the cutoff radius. For electrostatic interactions, Ewald summation is used to account for long-range contributions.

After the completion of a GCMC run, the Sorption module delivers the amount adsorbed, as well as the isosteric heat of adsorption. Moreover, simulation snapshots can be stored in specified intervals, or for the energetically most favourable configurations. The calculation and analysis of position-dependent quantities (density and potential energy maps) is also possible.

4.6.1.2. Fortran GCMC code

As mentioned above, the possibilities to modify the functional form of the potential employed in the Sorption module are limited. For example, the explicit Feynman-Hibbs correction cannot be applied in this program. Therefore, a Fortran program provided by B. Kuchta and L. Firlej was used in some calculations. This Monte Carlo code is based on the routines described by Frenkel and Smit. (172) It permits simulations in the canonical and in the grand-canonical ensemble. To calculate an adsorption isotherm, a series of jobs can be run by using an appropriately designed script. In the current version of the code, only particles consisting of a single interaction site can be treated, *i.e.* rotational degrees of freedom are not implemented.

Different user-specified potential models can be employed to represent interatomic interactions. Prior to the Monte Carlo simulation, the values of the solid-fluid interaction energy

are calculated for points located on a grid covering the simulation box. For a guest molecule inserted in the simulation box, the interaction energy is then calculated from the surrounding grid points using a bilinear interpolation scheme. Fluid-fluid interactions are calculated using a simple atom-based summation. All interactions are truncated at a user-specified cutoff. In contrast to the SORPTION module, electrostatic interactions are not included in this program.

In addition to the amount adsorbed, this code also calculates the isosteric heat of adsorption using the fluctuation formula (equation 3.22). However, due to difficulties with the equilibration of the q_{st} values, it is more practical to use the derivation of the isosteric heat from three adsorption isotherms calculated at different temperatures (equation 3.26). Simulation snapshots and position-dependent quantities can also be extracted using auxiliary Fortran programs.

4.6.2. Programs used for DFT calculations

4.6.2.1. The DMOL^3 code

DMOL^3 is a DFT code included in the "Materials Studio" package distributed by *Accelrys*.(*195*, *289*) It can handle both molecules and periodic solids. A specific feature of this program is the use of numerical orbitals as basis sets, leading to a high degree of computational efficiency compared to codes that use other types of orbitals (GTOs, STOs) as basis sets. Both all-electron calculations and calculations using effective core potentials are possible, and relativistic effects can also be included. The exchange-correlation functional can be chosen from a set of LDA and GGA functionals. However, no hybrid functionals are available. Moreover, none of the approaches to account for dispersive interactions presented in section 3.3 has been implemented.

In addition to single-point calculations to compute the total energy (and, possibly, other properties of interest) of a given system, a geometry optimization can be performed to find a (local) minimum of the energy as a function of the nuclear coordinates. Other tasks that are possible with the DMOL^3 code are molecular dynamics calculations and transition state searches. These features are not exploited in the context of this work.

DMOL^3 permits the calculation and analysis of various properties. For example, the electron density and the electrostatic potential can be computed on a grid and displayed graphically. A population analysis using Mulliken or Hirshfeld charges can be carried out, and ESP charges can be calculated (for non-periodic systems). Other features include the calculation of vibrational properties and of the electronic density of states. For molecules, the orbitals can be analyzed, whereas a computation of the band structure is possible for periodic systems.

4.6.2.2. The ADF code

The Amsterdam Density Functional (ADF) program is a DFT code for molecules. (*298*) An extension to periodic systems termed BAND has also been published. ADF uses Slater-type orbitals (STOs) as basis sets. To avoid the difficulties arising from the analytical evaluation of the integrals, a sophisticated numerical integration scheme is employed. The use of STO basis sets permits calculations of high accuracy with a relatively small number of basis functions. All electrons can be treated explicitly in the computations. Alternatively, frozen cores of different size can be used, depending on the desired accuracy. The inclusion of relativistic effects is also possible. A variety of exchange-correlation functionals is available, ranging from standard LDA and GGA functionals to hybrid and meta-hybrid functionals. The empirical DFT-D scheme can be employed to include dispersive interactions.

ADF uses a fragment-based approach: The molecule of interest is built up of user-defined fragments, which can be single atoms or larger moieties that have been addressed in previous calculations. The fragment orbitals are then used as basis functions in the DFT calculation for the molecule. This approach is advantageous for an intuitive interpretation of the chemical bonding situation. In addition to single-point calculations and geometry optimizations, ADF permits several other tasks, which are not exploited in this work (*e.g.* transition state searches, calculations of the intrinsic reaction coordinate).

A variety of properties can be evaluated using ADF. In addition to the calculation of partial charges, different schemes to analyze the chemical bonding situation are implemented, such as natural bond order analysis and energy decomposition analysis. Vibrational properties can be computed for the prediction of IR and Raman spectra. Moreover, it is possible to calculate several other spectroscopic properties, such as UV/Vis and X-ray absorption spectra (using time-dependent DFT), NMR chemical shifts, and electron spin resonance spectra, among others. However, these features are not used in the context of this work.

5. Results and Discussion

5.1. Prediction of hydrogen adsorption sites

5.1.1. Introduction

In order to facilitate the synthesis of new metal-organic frameworks with improved hydrogen storage properties, it is highly desirable to develop a better understanding of the structural features which are most favourable for hydrogen adsorption. Therefore, it is important to obtain information on the areas of the MOF structure where H_2 is preferentially adsorbed. Experimentally, such information is accessible from neutron diffraction experiments, using samples that have adsorbed a defined amount of gas. For these experiments, H_2 is replaced by D_2 in order to avoid the strong incoherent scattering of hydrogen. [299] Due to the limited availability of neutron radiation, this very useful technique cannot be used for routine characterization. Nevertheless, deuterium adsorption sites in MOFs have been reported for a number of systems, *e.g.* IRMOF-1, [300, 301] MOF-74, [255] ZIF-8, [302] $Cu_3(btc)_2$, [57] NOTT-101 as a member of the NOTT series, [262] and both $(Mn_4Cl)_3(btt)_8$ and $(Cu_4Cl)_3(btt)_8$. [59, 60]

In principle, similar information is available from the calculated hydrogen density distributions obtained in GCMC simulations. However, this method has not yet been widely exploited to predict hydrogen adsorption sites, and comparisons with experimentally determined positions are mostly lacking. In a review published in early 2009, [72] only one publication focussing on the computational prediction of the preferential adsorption regions is mentioned. [303]

In this section, the preferential hydrogen adsorption sites are predicted from GCMC simulations using generic force fields. For a subset of experimentally well-characterized MOFs, the performance of different parameter sets in reproducing experimental adsorption isotherms at $T = 77\,\mathrm{K}$ is compared. Having identified the most suitable parameter set, additional calculations are carried out for a number of other MOFs, leading to a total of eight systems considered in this section. From the calculated density distributions, the visible density maxima are identified at sufficiently high pressure, where it can be expected that all preferential adsorption sites are occupied. Approximate x, y, z-coordinates are then assigned to these maxima, and interpreted as adsorption sites. For six of the MOFs considered, experimental data from neutron diffraction is available, and the simulation results are directly compared to these adsorption sites. For the other two systems, the method is used in a predictive manner. The overall agreement of the simulation results with experimental data is critically discussed.

5.1.2. Computational details

GCMC simulations of hydrogen adsorption at $T = 77\,\text{K}$ were carried out for pressures ranging from 0 to 60 bar using the SORPTION module included in the *Accelrys* "Materials Studio" package. (233) One million equilibration steps were followed by one million production steps. The hydrogen molecule was modelled using the Pseudo-FH parameters derived in section 4.2 for a temperature of 77 K. For the framework, different sets of force-field parameters were compared. A cutoff radius of 12.5 Å was employed for dispersive interactions, using a cubic spline interpolation to ensure a smooth evolution to zero in the range of the cutoff radius ("Medium quality" setting in SORPTION).

In addition, the performance of a model that accounts solely for dispersive interactions was compared with a model that includes electrostatics. In these calculations, the model consisting of three point charges was used for hydrogen, while ESP charges were used for the framework atoms. Ewald summation was used to account for the periodicity of the lattice. For comparison with experiment, the number of molecules per cell obtained was converted to wt% using equation 3.18. Because only excess values are measured experimentally, the correction according to equation 4.5 was applied, using the pore volumes listed in table 4.4, and the density of hydrogen at each pressure from experimental reference data. (232) The isosteric heat of adsorption, which is calculated by SORPTION using equation 3.23, was also evaluated. For the determination of adsorption positions, three-dimensional plots of the calculated hydrogen density distribution obtained at a pressure slightly below the saturation pressure were analyzed, because it can be expected that virtually all adsorption positions are occupied under these conditions. For MOFs with a relatively low free pore volume, saturation is attained between 10 and 20 bar. In these cases, the density distribution calculated for a pressure of 6 bar (or 4 bar) was used in the analysis. MOFs with a larger pore volume reach saturation at higher pressures. Here, the density distribution obtained for a pressure of 10 bar was analyzed. A resolution of 0.25 Å was used in these plots. This resolution is relatively coarse, but it provides for relatively smooth maxima (a finer resolution would require many more production steps). For visualization purposes, two-dimensional sections of the hydrogen density distribution are shown. In these plots, blue regions correspond to density values close to the bulk density, white regions represent intermediate density increases, and red regions are density maxima.

5.1.3. Comparison of different parameter sets

5.1.3.1. Comparison of generic force fields

To justify the choice of generic force field parameters used in the following, different sets of LJ parameters for the framework atoms were compared: For IRMOF-1, MOF-74, and ZIF-8, the performance of the UFF, the UFF+C_{aryl}, and the DREIDING force field (DrFF) was assessed. For $Cu_3(btc)_2$, only the UFF and the UFF+C_{aryl} were considered due to a lack of copper parameters in the DREIDING force field.

The calculated adsorption isotherms are shown in figure 5.1, together with experimental data. For IRMOF-1, all three parameter sets deliver relatively similar isotherms. While the differences between the UFF and the DrFF are almost negligible, adjustment of the C_{aryl} parameters leads to slightly better agreement with experimental data at low pressures. There is, however, a slight tendency to overestimate the uptake at high pressures when compared to the experimental results of Poirier and Dailly. (51) It is noteworthy that none of the force fields can reproduce the high-pressure data of Kaye *et al.*, who measured a saturation uptake that is nearly 1.0 wt% higher. (50) More significant differences are observable for the case of MOF-74: Here, the DrFF predicts a considerably higher hydrogen uptake in the low-pressure range than the UFF. The UFF+C_{aryl} performs nearly as well as the DrFF at low pressures. All three force fields tend to overestimate the saturation uptake. For ZIF-8, only the DrFF delivers a good agreement with experimental data at low pressures. However, it tends to underestimate the saturation uptake, while both versions of the UFF perform very well in this pressure range.
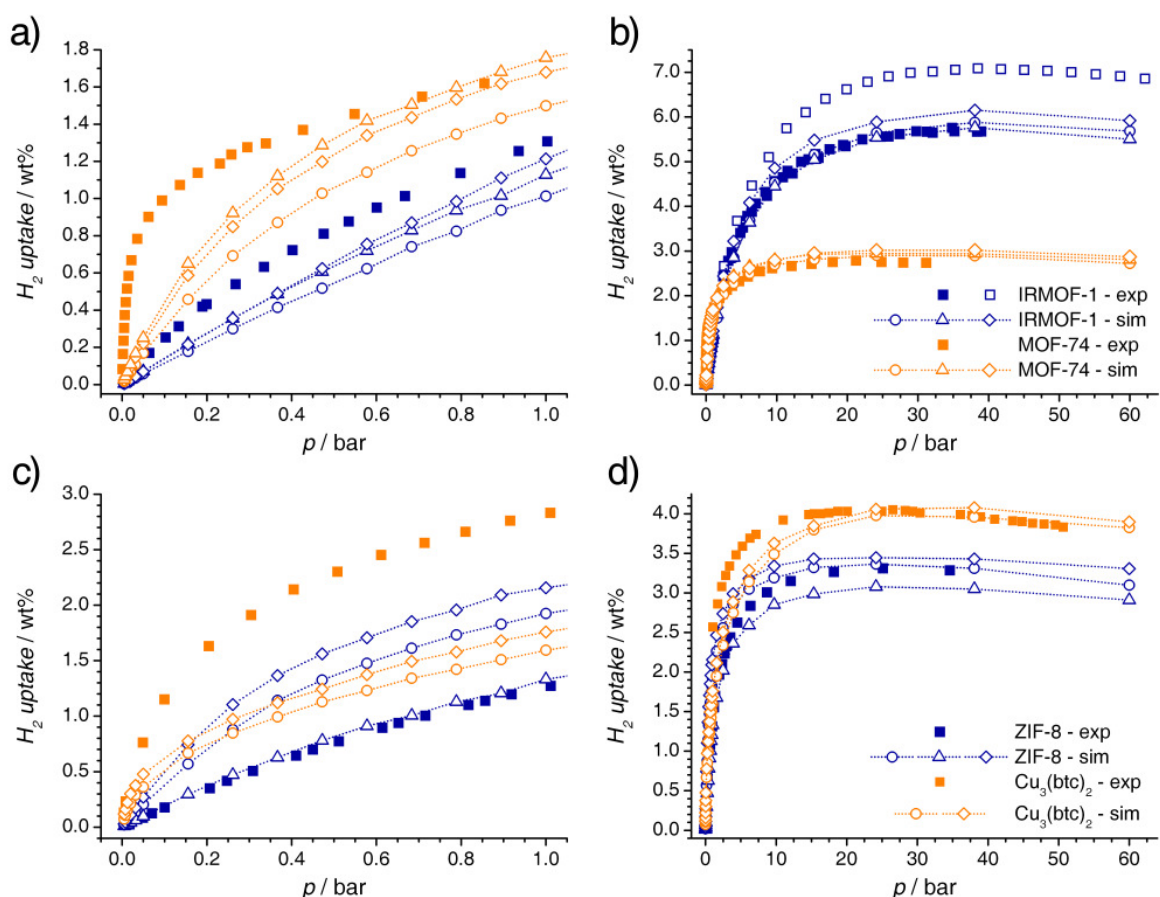
Figure 5.1. Predicted hydrogen adsorption isotherms for different MOFs. Open symbols represent simulation results, with circles = UFF, triangles = DrFF, diamonds = UFF+C_{aryl}. Experimental data are given as squares. *a)* and *b)* show results for IRMOF-1 and MOF-74, with experimental data from the following references: (70) [IRMOF-1, low pressure], (51) [IRMOF-1, high pressure, closed squares], (50) [IRMOF-1, high pressure, open squares], and (255) [MOF-74]. *c)* and *d)* show results for ZIF-8 and $Cu_3(btc)_2$, with experimental data from (256) [ZIF-8, low pressure], (297) [ZIF-8, high pressure], and (71) [$Cu_3(btc)_2$].

Because the LJ parameters for the non-metal atoms are relatively similar in the UFF and the DrFF, the observed differences for ZIF-8 and, to a lesser extent, MOF-74, are most probably related to the different zinc parameters: The Zn parameters of the UFF correspond to a relatively narrow, deep potential well (small r_0, large D_0), whereas the potential well employed in the DrFF is rather shallow (large r_0, intermediate D_0). The observed sensitivity of the calculated low-pressure isotherms to changes in the metal parameters might provide a model test case for future parameter development.

In the case of $Cu_3(btc)_2$, the UFF+C_{aryl} provides for a slightly better agreement with experimental data. However, none of the force fields can properly reproduce the adsorption characteristics at low pressures, with a pronounced tendency to underestimate the loading. This observation will be discussed and tentatively explained below.

From the simulation results presented, there is no indication that any of the force field performs generally better than the others. Although the DrFF often performs similarly well as the UFF, and even better in some instances, it is not suitable due to the lack of consistent parameters for different metals. Comparing the UFF and the UFF+C_{aryl}, the overall results seem to indicate that the modification of the C_{aryl} parameters improves the agreement with experimental data, particularly at low pressures. Tentatively, this can be explained with a more realistic description of the interaction of H_2 molecules with the carbon atoms of the aromatic linkers. From these findings, the partial modification of existing force fields using available *ab-initio* data appears to be a promising strategy to improve upon the performance of literature parameters. The central problem that remains is the unknown intrinsic error of the generic force-field parameters, which makes it very difficult to distinguish actual improvements from error cancellations. The UFF+C_{aryl} parameters will be used in all calculations reported in this section.

5.1.3.2. Inclusion of electrostatic interactions

For IRMOF-1 and $Cu_3(btc)_2$, additional calculations were carried out that accounted for electrostatic interactions by means of a point-charge model. For dispersive interactions, the UFF+C_{aryl} parameters as described above were used. The resulting isotherms are shown in figure 5.2, together with the results from calculations without partial charges. In both cases, the changes of the adsorption isotherms caused by the inclusion of electrostatic interactions are relatively small. For IRMOF-1, an increase of the calculated loading by up to 0.3 wt% is observed, which is reached at a pressure of approximately 4 bar. While the agreement with experiment is slightly improved at low pressures, the inclusion of electrostatic interactions leads to a somewhat more pronounced overestimation of the loading at high pressures. Similarly, an increase of the calculated hydrogen uptake is observed for $Cu_3(btc)_2$, which amounts to 0.4 wt% at pressures above 3 bar. In particular, the severe underestimation of the loading at low pressures cannot be overcome by including electrostatic contributions, as the increase at pressures below 1 bar does not exceed 0.25 wt%. In addition to the adsorption isotherms, the isosteric heats of adsorption and the hydrogen density

fields derived from these simulations were also compared to the results of calculations without electrostatic interactions. The observed changes were insignificant, and these results are not discussed separately.

As a general observation, it is apparent that the inclusion of electrostatic contributions in the framework of a point-charge model does not lead to significant changes of the simulation results. This is in contrast to an earlier simulation study of IRMOF-1, were the usage of a similar point-charge model led to a massive overestimation of the hydrogen loading. (75) However, a direct comparison is not possible, because the calculated framework charges were not provided in that work. For $Cu_3(btc)_2$, Johnson and co-workers also studied the effect of the inclusion of partial charges on adsorption isotherms and transport properties. (290) Although the results are similar, these authors concluded that the electrostatic interactions have a significant impact on the adsorption properties. While this interpretation is probably debatable, the effect on the diffusion coefficients is more obvious: For the model including charges, an increase of the self-diffusivity by a factor of 2 was observed at low coverages. It was concluded that the inclusion of electrostatic effects led to a reduction of the energy barrier for a diffusion out of the small pores of the $Cu_3(btc)_2$ structure, thereby increasing the diffusivity.

The calculations presented in the following neglect electrostatic interactions. It has been shown that their impact on the adsorption isotherms is relatively minor, and it can be firmly expected that the preferential adsorption sites are even less affected.
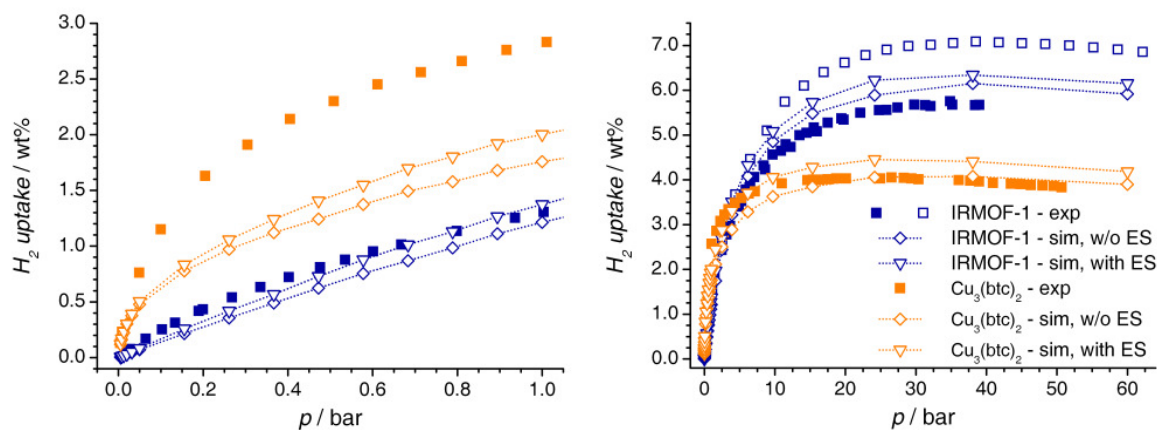
Figure 5.2. Predicted hydrogen adsorption isotherms for IRMOF-1 and $Cu_3(btc)_2$. Diamonds represent simulation results obtained with the UFF+C_{aryl} parameters, inverted triangles correspond to results obtained with the UFF+C_{aryl} parameters and point charges to account for electrostatic interactions. Experimental data (closed and open squares) are from the same references as in figure 5.1.

5.1.4. Results: Comparison with experimental adsorption sites

5.1.4.1. IRMOF-1

The hydrogen storage properties of IRMOF-1 have been investigated in numerous experimental and theoretical studies. The most recent experimental high-pressure data were reported by Kaye *et al.* (*50*) and by Poirier and Dailly. (*51*) These two isotherms, which are both included in figure 5.1, show remarkable differences, emphasizing the dependency of experimental results on sample preparation and activation, measurement procedure and other factors. It has already been discussed above that the agreement of the calculated isotherms with experiment at low pressure is reasonably good. In the high-pressure range, the simulated isotherm ranges between the two different experimental measurements, indicating the need for further experimental validation, even for a well-characterized system like IRMOF-1. A saturation uptake of 6.1 wt% is attained at a pressure of approximately 30 bar. This corresponds to an ideal volumetric uptake of 38 g L^{-1}. The isosteric heat of hydrogen adsorption is shown in figure 5.3. At zero coverage, q_{st} amounts to 3.7 kJ mol^{-1}, as compared to an experimental value of 4.8 kJ mol^{-1}.
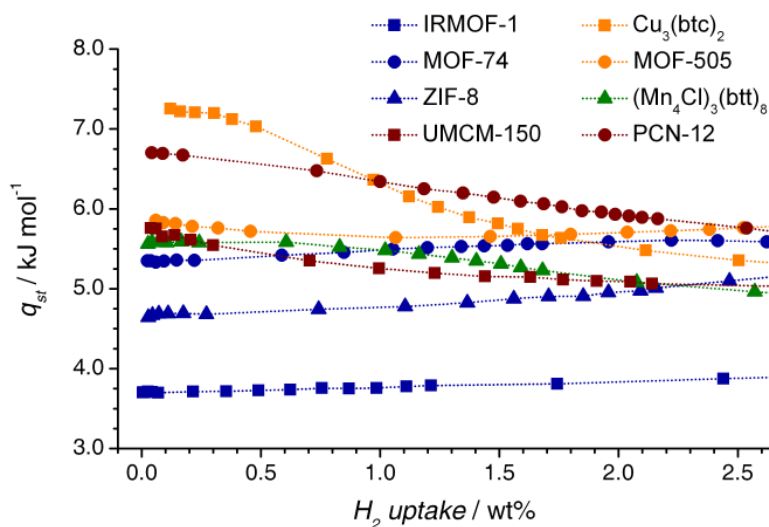
Figure 5.3. Calculated isosteric heat of hydrogen adsorption q_{st} as a function of coverage for all MOFs discussed in this section.

Various molecular simulation studies of hydrogen adsorption in IRMOF-1 have been reported in the literature. In many instances, other members of the IRMOF series were also included. For example, Snurr and co-workers also used generic force-field parameters to predict the hydrogen adsorption isotherms. (*76*, *77*) Due to the neglect of quantum effects, these simulations predicted slightly higher uptakes at low pressures, thus being in better agreement with experiment, but tended to overestimate the loading at higher pressures. A slightly improved prediction of the high-pressure adsorption isotherm was obtained with partially refitted parameters. (*221*) In a more recent study, it was shown that the usage of a sophisticated hydrogen potential model provides for excellent agreement of the low-

pressure isotherms with experimental data. (*85*) In contrast to this, the usage of a complete set of *ab-initio* derived parameters leads to a significant underestimation of the saturation uptake. (*279*) A completely different approach has been pursued by Sauer and co-workers, who used MP2 energies and a multi-site Langmuir model to predict hydrogen adsorption isotherms for IRMOF-1 at different temperatures. (*86*) The agreement of their results with experimental data was similarly good as in the present GCMC study.

In figure 5.4, a section through the hydrogen density distribution calculated at $p = 10\,\text{bar}$ is shown. There are four non-equivalent regions of increased hydrogen density, which can be identified as adsorption sites. The three most prominent adsorption regions are located at the inorganic building unit, and the fourth site is situated above the linker. Following the nomenclature employed in the neutron diffraction study by Yildirim and Hartman, the sites at the inorganic building units are identified as *cup site* (above the central oxygen atom of the inorganic cluster), *ZnO₃ site* (above a triangle formed by three Zn atoms), and *ZnO₂ site* (above the edge of a Zn₄O tetrahedron), whereas the position above the linker is termed *hex site*. (*300*) The crystallographic coordinates derived from the density distribution are given in the Appendix, table A.12, together with the data of Yildirim and Hartman. The agreement with experiment is excellent for all four sites. The first two adsorption sites were also obtained in another study which used single-crystal neutron diffraction. (*301*) If all sites predicted here were occupied simultaneously, the resulting loading of 208 molecules per unit cell would correspond to 6.37 wt%. This value is only slightly higher than the observed saturation uptake.
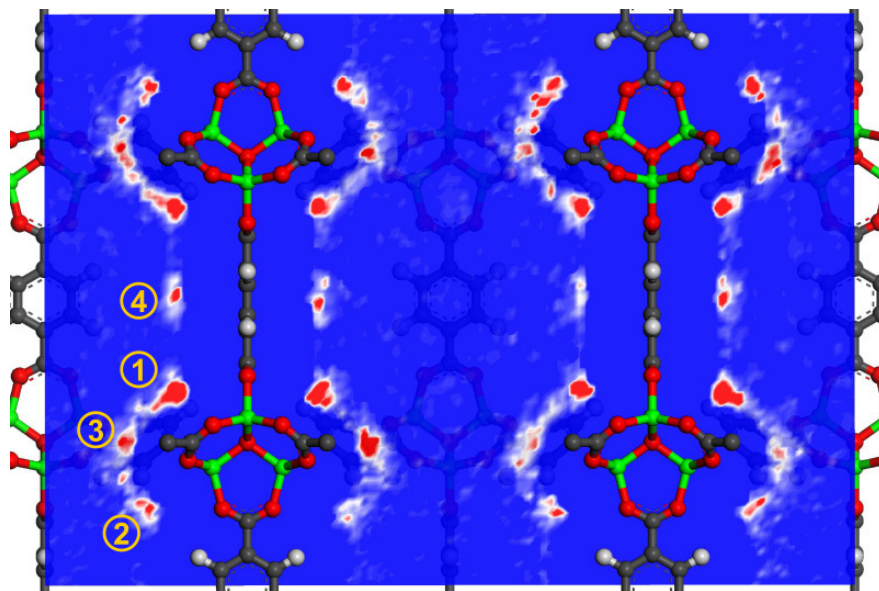
Figure 5.4. Calculated hydrogen density field for IRMOF-1, derived at $p = 10\,\text{bar}$. The viewing direction is the [110] direction. (1) = cup site, (2) = ZnO₃ site, (3) = ZnO₂ site, (4) = hex site.

5.1.4.2. MOF-74

Due to the relatively low pore volume of MOF-74, the maximal hydrogen uptake of this system is quite limited. Nevertheless, this MOF (and isostructural systems with different metal centers) have been studied extensively due to the presence of unsaturated metal sites. (*63, 252, 255*) The observed heat of hydrogen adsorption, which surpasses 8 kJ mol^{-1} at low coverages, was rationalized with the high surface packing density of unsaturated metal sites. (*255*)

With maximal deviations of 0.3 wt%, the calculated adsorption isotherm of MOF-74 is in good agreement with experimental data at pressures above 1 bar (figure 5.1). However, the remarkably sharp rise of the isotherm at low pressures is not reproduced by the simulation. At a pressure of approximately 20 bar, a saturation uptake of 3.0 wt% is reached. This is equivalent to an ideal volumetric uptake of 38 g L^{-1}. The calculated isosteric heat of adsorption at zero coverage amounts to 5.4 kJ mol^{-1}, which is distinctly lower than the experimental value of 8.8 kJ mol^{-1}. The agreement improves at higher loadings, with the experimental value falling below 5 kJ mol^{-1}. (*255*)
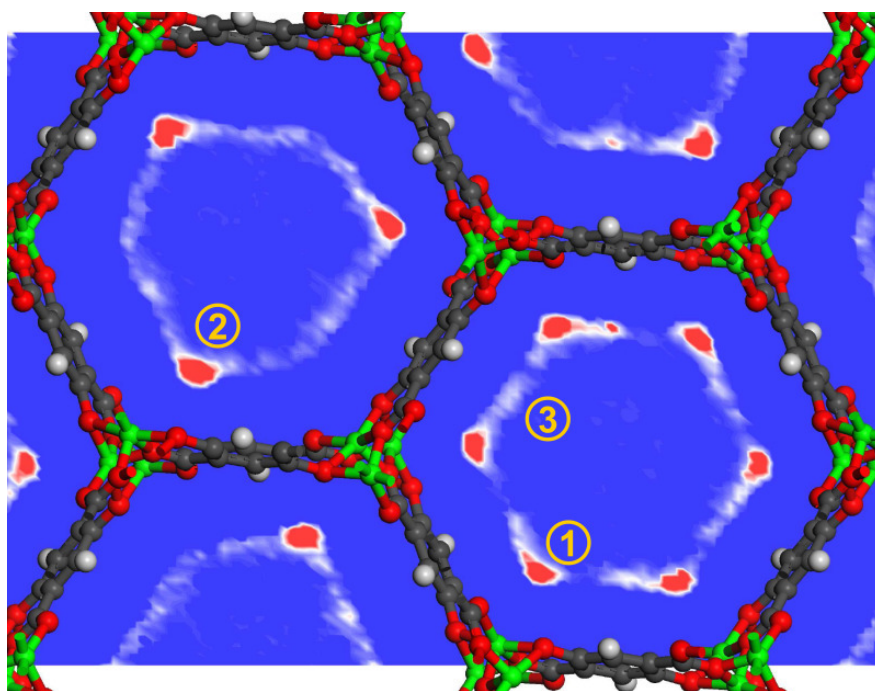
Figure 5.5. Calculated hydrogen density field for MOF-74, derived at $p = 6$ bar. The viewing direction is the *c*-axis. (1) = Zn site, (2) = pocket site, (3) = hex site.

A slice through the density distribution calculated at a pressure of 6 bar is shown in figure 5.5, and the predicted adsorption sites are given in the Appendix, table A.13, together with the neutron diffraction results of Liu *et al.* (*255*) The first site is located directly above the Zn atoms (*Zn site*), and the second site is located in a pocket surrounded by two carboxylate groups and one deprotonated hydroxyl group of the linker molecules (*pocket site*). These two positions are in excellent agreement with the adsorption sites determined by Liu

et al. The third site is located above the phenyl ring of the linker (*hex site*). This position is qualitatively similar to the third position determined experimentally. However, the crystallographic *z*-coordinate is different, because the experimental position is not situated above the center of the ring, but displaced towards one side. Experimentally, another adsorption site near the center of the channels was also observed. The calculated density distribution, however, does not show a significant density increase in this region. A complete occupation of all three adsorption sites observed here would correspond to an uptake of 3.6 wt% (56 molecules per unit cell), which is 0.6 wt% higher than the saturation value of the adsorption isotherm.

5.1.4.3. ZIF-8

While many studies of ZIFs have been directed at potential applications in carbon dioxide storage, (*129*) quite promising early results for hydrogen storage have not led to a more thorough investigation. (*256, 297*) As discussed above, the amount of hydrogen adsorbed in ZIF-8 is significantly overestimated by the simulation at low pressures, whereas good agreement with experiment is observed at higher pressures. A saturation loading of 3.4 wt%, corresponding to an ideal volumetric uptake of 33 g L^{-1}, is reached at a pressure of 15 bar. The calculated q_{st} at zero coverage of 4.6 kJ mol^{-1} is very close to the value of 4.5 kJ mol^{-1} estimated from experimental data. (*297*) It is interesting to note that the isosteric heat of adsorption of ZIF-8 slightly increases on increasing loading.
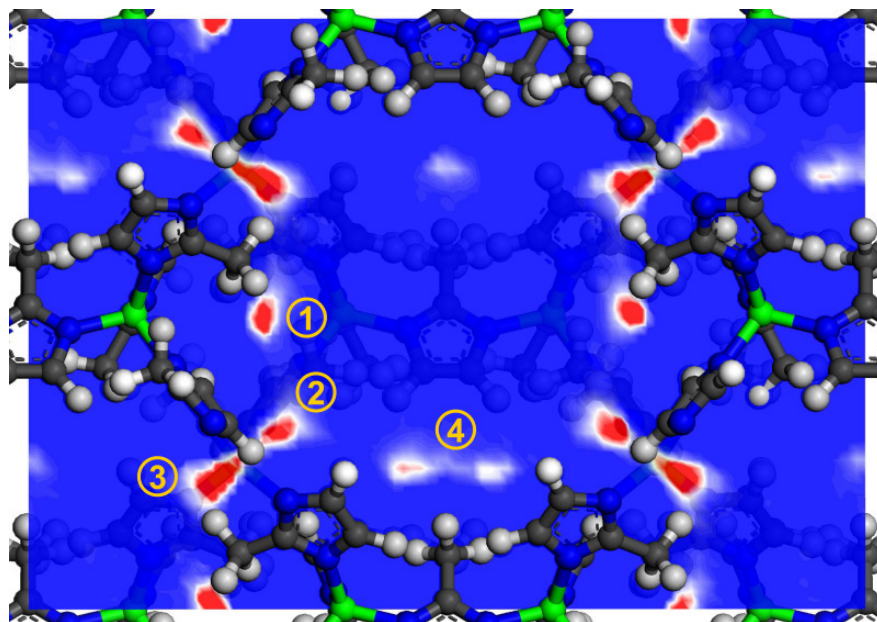
Figure 5.6. Calculated hydrogen density field for ZIF-8, derived at $p = 4$ bar. The viewing direction is the [110] direction. (1) = pentagon site, (2) = window site I, (3) = window site II, (4) = methyl site.

The hydrogen density distribution calculated at a pressure of 4 bar is shown in figure 5.6. It permits the identification of four adsorption sites: The first site is located above the imidazolate rings that point towards the center of the pore (*pentagon site*). Two non-equivalent sites are located at the two sides of the narrow triangular windows connecting the pores (*window site I, II*). Furthermore, there are regions of slightly increased hydrogen density above pairs of methyl moieties oriented towards the center of the pore (*methyl site*). These sites are located on the square faces of cuboctahedra formed by the pentagon sites. All four sites are in excellent agreement with the experimental positions determined by Yildirim and co-workers. (*302*) In this study, two other adsorption positions near the center of the pore were identified at high loadings. However, it must be considered that the experiments were carried out at $T = 3.5\,\text{K}$. It can be expected that the formation of a H_2 "nanocage" in the void space of the pore is possible only at very low temperatures, where bulk hydrogen is solid. A full occupation of the four sites observed in this work would correspond to a hydrogen loading of 3.7 wt% (52 molecules per cell), which is, again, somewhat higher than the saturation uptake.

5.1.4.4. Cu$_3$(btc)$_2$

The hydrogen storage properties of $Cu_3(btc)_2$ have been very well investigated. In 2007, Johnson and co-workers proposed an optimized activation procedure, which led to a further increase of the hydrogen uptake at low pressures. (*71*) The uptake of 2.8 wt% at 1 bar and 77 K is still among the highest values reported for MOFs under these conditions. From the simulated isotherm, it is quite evident that there is a remarkable underestimation of the hydrogen uptake at low pressures, whereas the agreement at high pressures is excellent. The same tendency has been observed in an earlier modelling study. (*71*) Saturation is reached at a pressure of approximately 25 bar, the saturation uptake amounting to 4.1 wt%, which translates into an ideal volumetric uptake of 37 g L^{-1}. The calculated isosteric heat of adsorption at zero coverage amounts to 7.3 kJ mol^{-1}, thus being somewhat higher than typical experimental values, which range between 6 and 7 kJ mol^{-1}. (*48*)

Figure 5.7 shows two different sections through the hydrogen density distribution, calculated at $p = 6\,\text{bar}$. While no density increase is visible at the unsaturated metal centers, there are crescent-like regions of increased hydrogen density perpendicular to the Cu-Cu axis of the paddle wheel (*paddle wheel site*). A relatively soft density peak is visible above the phenyl rings (*hex site*). Furthermore, there are extended density maxima above the triangular windows that connect the smaller pores and the larger pores (*window site*), and at the center of the smaller pores (*central site*).

The deuterium adsorption sites in $Cu_3(btc)_2$ were determined experimentally by Peterson *et al.* (*57*) The adsorption site that is occupied initially is located at the unsaturated copper centers, with a Cu-D$_2$ distance of 2.4 Å. This distance is considerably lower than the sum of van der Waals radii, indicating that the interaction is not dominantly dispersive. In the region perpendicular to the paddle wheels, two distinct positions were refined, which are

slightly too close together to be occupied simultaneously. In the small pores, a total of three positions was postulated for the pore center and the triangular windows. The distances between these positions are also very short, so that a simultaneous occupation must be considered unrealistic. This shows that it is difficult to determine localized adsorption sites in systems that contain relatively extended areas of increased interaction with the pore walls. Thus, it is probably more appropriate to designate them as adsorption regions.

An occupation of all sites derived from the simulations would correspond to a loading of 3.6 wt% (178 molecules per unit cell). This loading is lower than the observed saturation uptake, a behaviour which can be explained with the existence of additional adsorption sites at the copper centers. If one hydrogen molecule per Cu atom is added, the hypothetical uptake reaches 4.5 wt%.
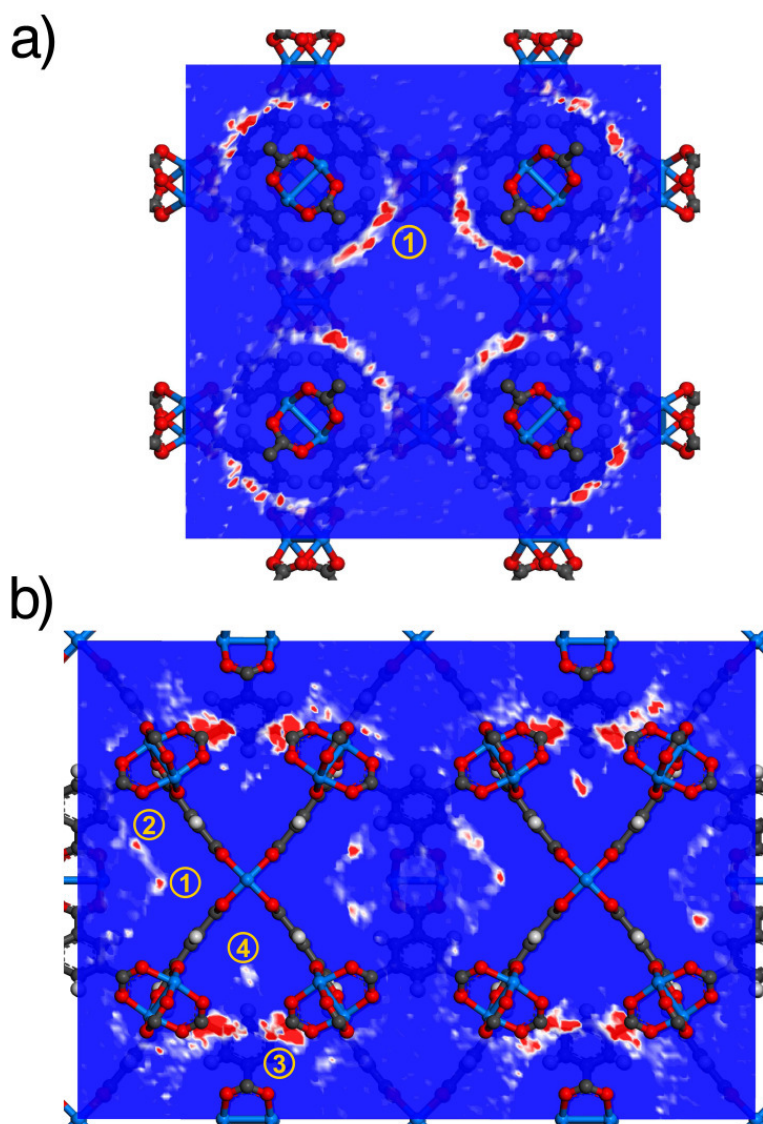
Figure 5.7. Calculated hydrogen density field for $Cu_3(btc)_2$, derived at $p = 6$ bar. *a)* View along the *a*-axis. (1) = paddle wheel site. It is apparent that there is no increase of the density at the unsaturated copper sites. *b)* View along the [110] direction. (1) = paddle wheel site, (2) = hex site, (3) = window site, (4) = central site.

5.1.4.5. MOF-505

In addition to the adsorption data reported in the initial publication on MOF-505, (*260*) a more thorough characterization of the hydrogen storage properties of this system, as well as the structurally related MOFs of the NOTT series, was carried out in subsequent studies. (*261, 262, 304*) The simulation results, which are shown in figure 5.8, are in relatively good agreement with the experimental measurements over the whole pressure range. A slight underestimation of the hydrogen uptake is observable at very low pressures below 0.2 bar, which is probably due to additional adsorption at the unsaturated copper sites in the real sample. Above this pressure, the hydrogen loading is slightly overestimated. A saturation uptake of 4.4 wt%, corresponding to an ideal volumetric uptake of 42 g L^{-1}, is reached at a pressure of 20 bar. The isosteric heat of adsorption predicted from the simulations amounts to 5.9 kJ mol^{-1}, which is close to the experimental value of 6.3 kJ mol^{-1}. (*262*)
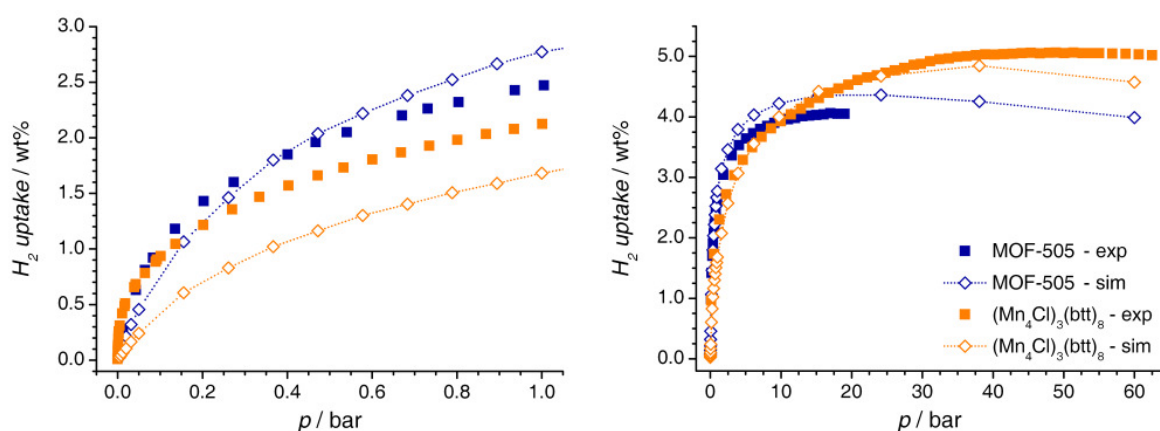
Figure 5.8. Predicted hydrogen adsorption isotherms for MOF-505 and $(Mn_4Cl)_3(btt)_8$. Experimental data (closed squares) are from (*260*) [MOF-505, low pressure], (*262*) [MOF-505, high pressure], and (*59*) [$(Mn_4Cl)_3(btt)_8$].

A section through the hydrogen density distribution calculated at a pressure of 4 bar is shown in figure 5.9. The most pronounced density maxima are located at the center of the triangular windows connecting the two types of pores (*triangle site*), and in the rhombohedral pores, close to to the larger windows which connect the pores perpendicular to the *c*-axis (*window site*). Less pronounced density maxima are visible inside the rhombohedral pores, above the linker molecules (*central site*), as well as perpendicular to the Cu_2 paddle wheels (*paddle wheel site*). No pronounced density maxima are observable in the trigonal antiprismatic pores.

In the case of MOF-505, the comparison with experimental data is hampered by different factors. Firstly, the experimental measurement was carried out for NOTT-101, an isostructural system with a different (terphenyl) linker. (*262*) Secondly, only relatively low deuterium loadings were reached in this study, and it is thus likely that not all adsorption sites were occupied. Finally, no crystallographic coordinates of the adsorption positions were reported. In analogy to $Cu_3(btc)_2$, the first experimental adsorption position in NOTT-101 is located at the unsaturated copper sites. The other two sites are in better agreement with the

simulation results. The second position coincides with the triangle site, and the third experimental position can be understood as a unification of three symmetry-equivalent window sites.

Assuming that all sites observed in the calculated density distribution are occupied, the resulting loading would correspond to 3.7 wt% (78 molecules per unit cell). After adding 18 molecules per cell to account for the metal sites, the hypothetical loading increases to 4.5 wt%. This value is in excellent agreement with the saturation loading that was obtained from the calculated hydrogen adsorption isotherm.
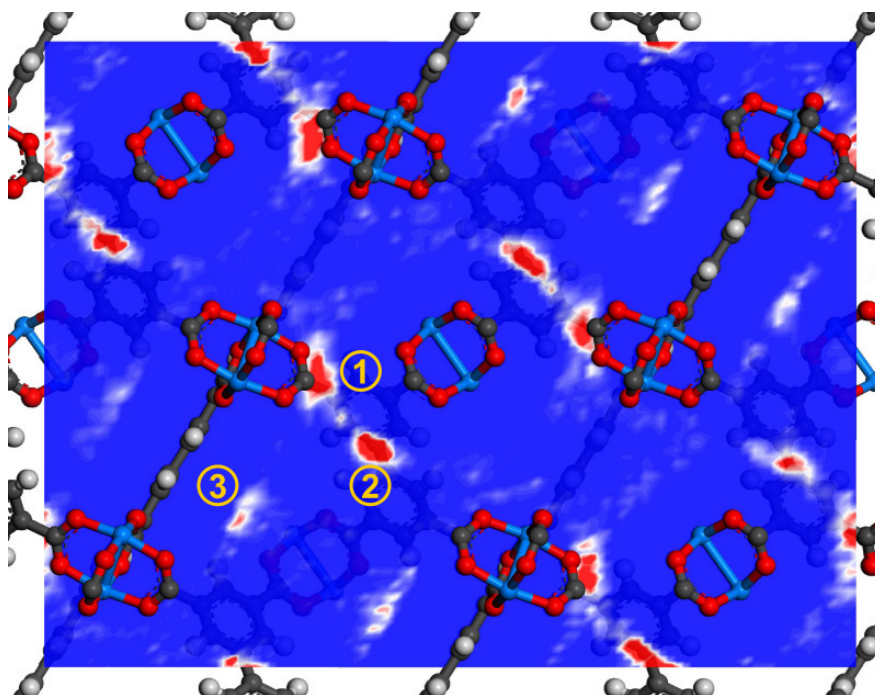
Figure 5.9. Calculated hydrogen density field for MOF-505, derived at $p = 4\,\text{bar}$. The viewing direction is the [110] direction. (1) = triangle site, (2) = window site, (3) = central site. The paddle wheel site does not lie in the plane of the section.

5.1.4.6. $(Mn_4Cl)_3(btt)_8$

Results of experimental hydrogen adsorption measurements have been reported for both $(Mn_4Cl)_3(btt)_8$ and $(Cu_4Cl)_3(btt)_8$. (*59*, *60*) While only simulation results for the manganese compound are reported at this point, the analogous copper compound will be discussed in more detail in section 5.2. The simulated adsorption isotherm is shown in figure 5.8. At low pressure, the amount adsorbed is underestimated by approximately 0.5 wt% when compared to experimental data, a behaviour which is most probably related to the presence of unsaturated metal sites in this MOF. At higher pressures, the agreement is excellent. Saturation is attained at a pressure of nearly 40 bar. The saturation loading amounts to 4.8 wt%, which is equivalent to an ideal volumetric uptake of 37 g L^{-1}. The experimental q_{st} at low coverage reaches 10.1 kJ mol^{-1}, a value that is drastically higher than the 5.7 kJ mol^{-1} ob-

tained in the simulations. However, the agreement becomes better at higher coverages due to the sharp decrease of the experimental isosteric heat of adsorption. (*59*)

The calculated density distribution at $p = 10\,\text{bar}$ is displayed in figure 5.10. The first adsorption position is observed perpendicular to the Mn_4Cl building unit. Six of these sites form a smaller octahedron within the octahedral cage (*vertex site*). A second adsorption site is observed in plane with the inorganic unit, above the edges of the Mn_4Cl squares. This site is located between two tetrazolate rings (*pentagon site*). Furthermore, there are regions of increased density at the two sides of the windows which connect the octahedral cages and the channels (*window site I and II*).
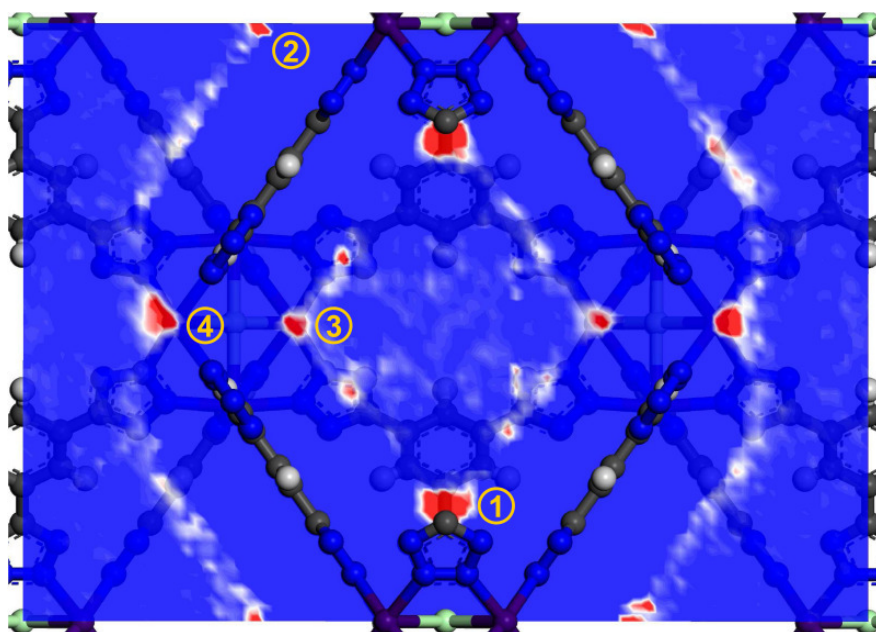
Figure 5.10. Calculated hydrogen density field for $(Mn_4Cl)_3(btt)_8$, derived at $p = 10\,\text{bar}$. The viewing direction is the [110] direction. (1) = vertex site, (2) = pentagon site, (3) = window site I, (4) = window site II.

Again, the first experimental adsorption site determined for $(Mn_4Cl)_3(btt)_8$ is located close to the unsaturated metal centers. (*59*) The second and third position correspond to the vertex site. With a site-site distance of 2.1 Å, these positions are too close together to be occupied by one H_2 molecule per site at the same time. Furthermore, the pentagon site was also refined from experimental data. However, no density maxima were observed at either side of the pore windows. A subsequent neutron diffraction study of deuterium adsorption in the analogous Cu-MOF delivered the following adsorption sites: Firstly, one site at the unsaturated metal centers, secondly, the vertex site, thirdly, the pentagon site, and finally one position near the windows, which is in good correspondence with window site I derived from the simulations.

A complete occupation of the four adsorption sites observed in the simulations would correspond to 42 molecules per cell, which equals 2.7 wt% for $(Mn_4Cl)_3(btt)_8$. Taking the metal sites into account, the hypothetical uptake reaches 3.5 wt%, a value that is still distinctly

lower than the saturation uptake. Therefore, it can be concluded that the adsorption in other regions, particularly in the channels, also contributes significantly to the total loading, although no pronounced maxima are observed in the calculated density distribution.

5.1.5. Results: Predictive calculations

5.1.5.1. UMCM-150

As it is evident from the description of the pore topology of UMCM-150 in section 4.3, this system is structurally more complex than the MOFs discussed so far. The determination of adsorption sites from experimental powder data becomes more difficult for larger unit cells (due to the increasing peak overlap) and for systems with many non-equivalent adsorption sites. Therefore, molecular simulations could predict adsorption sites that can be used as initial positions for further refinement.

The calculated hydrogen adsorption isotherm of UMCM-150 is shown in figure 5.11, together with experimental data. (263) The agreement between simulation and experiment is excellent throughout the whole pressure range. At a pressure of approximately 30 bar, the adsorption isotherm reaches saturation. The saturation loading of 5.7 wt% corresponds to an ideal volumetric uptake of 38 g L^{-1}. The isosteric heat of adsorption in the limit of zero coverage is underestimated, with 5.8 kJ mol^{-1} as compared to an experimental value of 7.3 kJ mol^{-1}, but the agreement improves at higher loadings.
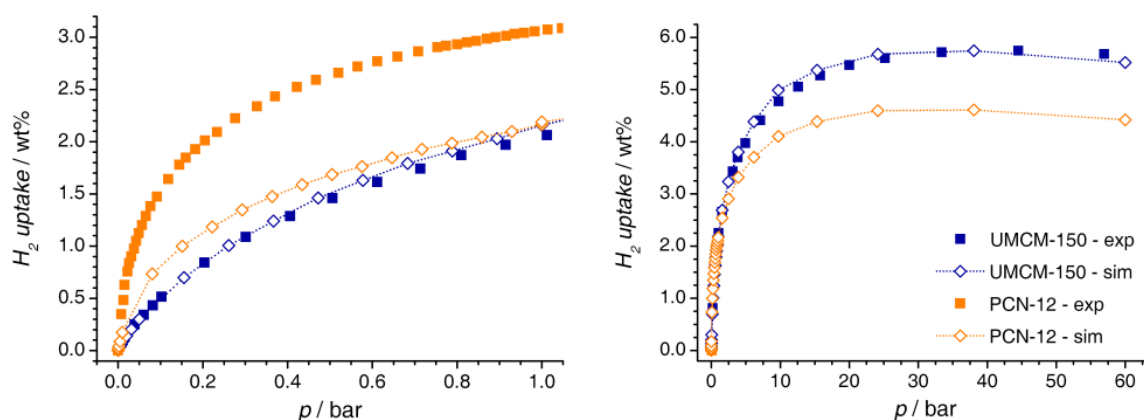
Figure 5.11. Predicted hydrogen adsorption isotherms for UMCM-150 and PCN-12. Experimental data (closed squares) are from (263) [UMCM-150] and (264) [PCN-12].

A section through the density distribution calculated at $p = 10$ bar is shown in figure 5.12. Three of the observed density maxima are similar to those observed in MOF-505: The first one is located at the center of the windows surrounded by three Cu_2 paddle wheels in a triangular fashion (*triangle site*), the second one lies near these windows, at the large openings of the trigonal-bipyramidal pores (*window site*), and the third site lies perpendicular to the paddle wheels (*paddle wheel site*). Furthermore, there are crescent-like regions of increased density in plane with the Cu_3 units (*Cu₃ site*). In the rhombohedral pores, there are density peaks situated at equal distance between three and two phenyl moieties, respectively (*tri-*

hex site, di-hex site). Finally, a density increase is observed above the central area of the linker molecule (*linker site*).

So far, no experimental results concerning the preferential hydrogen adsorption sites of UMCM-150 have been reported. In contrast to the MOFs discussed so far, the order in which the adsorption sites are occupied on increasing pressure is not clear. However, it can be expected that the positions corresponding to sharp, strong maxima are occupied at lower loadings than the weaker, more diffuse regions of increased density. A computational study that analyzes the density distribution at different pressures could also provide more insights.

If all sites which could be identified in this study were occupied by one H_2 molecule, a loading of 3.4 wt% would result. This is far lower than the observed saturation uptake. Taking the metal centers as additional adsorption sites, the uptake increases to 4.2 wt%, a value which still is significantly too low.
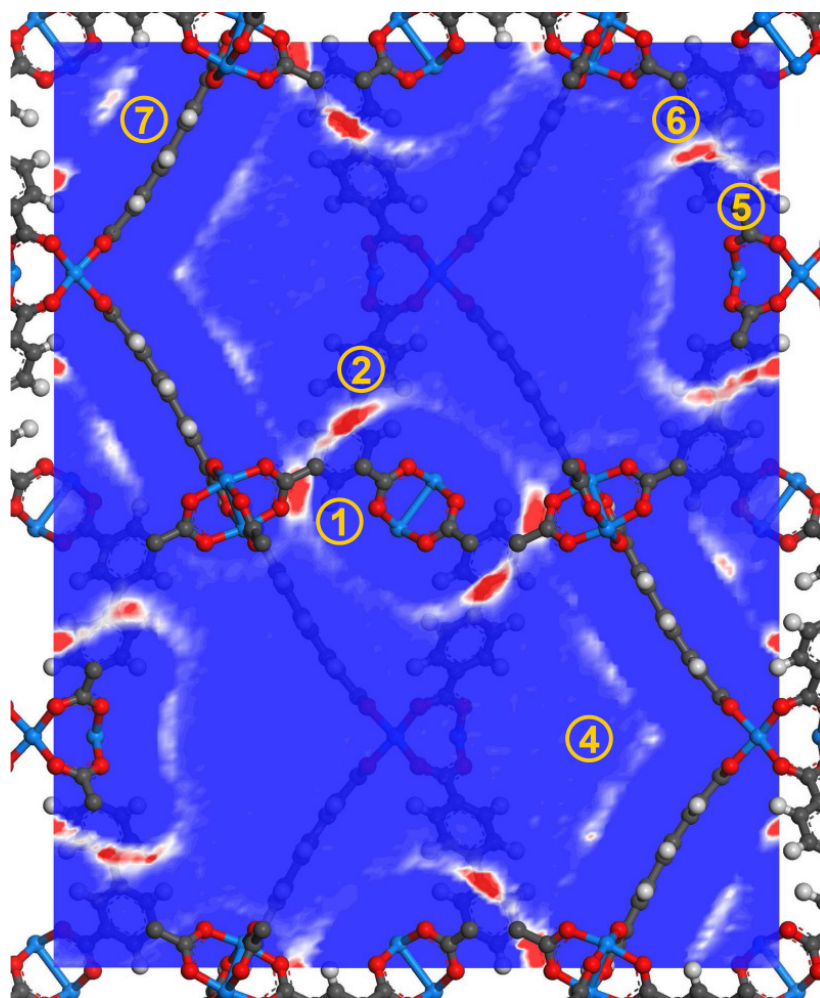
Figure 5.12. Calculated hydrogen density field for UMCM-150, derived at $p = 10$ bar. The viewing direction is the [110] direction. (1) = triangle site, (2) = window site, (4) = Cu$_3$ site, (5) = tri-hex site, (6) = di-hex site, (7) = linker site. The paddle wheel site does not lie in plane with the section.

5.1.5.2. PCN-12

In spite of the very promising results presented in the original publication dealing with PCN-12, (*264*) no further studies of the hydrogen adsorption properties have been reported so far. Thus, only a low-pressure adsorption isotherm for $T = 77$ K is available. The simulated adsorption isotherm is shown in figure 5.11. It is evident that the amount adsorbed at low pressures is drastically underestimated. In the high-pressure regime, a saturation uptake of 4.6 wt%, reached at a pressure of approximately 25 bar, is predicted. This value is equivalent to an ideal volumetric uptake of 37 g L^{-1}. The calculated q_{st} in the limit of zero coverage amounts to 6.7 kJ mol^{-1}.

Compared to UMCM-150, the situation is even more complex for PCN-12. While the unit cell is relatively large, the structure does not possess a very high symmetry. The multiplicity of a general position in $P4/mmm$, the space group of PCN-12, is 16 (for comparison: The multiplicity of a general position in $Fm\bar{3}m$, the space group of Cu$_3$(btc)$_2$, is 192). A total of 13 non-equivalent density maxima was identified from the density field, which was calculated for a pressure of 6 bar. The analysis was not even completely exhaustive, because weak and diffuse maxima were not considered. Since it is not possible to define a single section through the unit cell that contains the majority of the adsorption positions, two different sections are displayed in figure 5.13. Furthermore, all adsorption sites derived from the density distribution are listed in the Appendix, table A.19, together with a brief description of their location in the structure.

Because a comprehensive discussion of all sites is not very useful, only some general observations are described: The most pronounced maxima are located in the small pores surrounded by the linkers in C_{2v} conformation. The first of these maxima (sites 1 and 4) are located in the central plane, at equal distance of two phenyl rings. The other sites are located closer to the paddle wheel (sites 2 and 5) and at the center of the pore windows (sites 3 and 6). It is noteworthy that the distances between these positions range between 3.4 and 3.8 Å, and are thus very close to the equilibrium distance between two H$_2$ molecules. In addition to these sites, there are three non-equivalent sites above the triangular faces of the central cuboctahedral pore (sites 7 to 9), and two sites above the triangular faces of the cuboctahedral pore centered at the cell edge (sites 10 and 11). Again, the site-site distances range between 3.4 and 3.8 Å. Finally, density maxima were identified perpendicular to the Cu-Cu axis of the Cu$_2$ paddle wheels (sites 12 and 13).

An occupation of all adsorption sites listed in table A.19 would correspond to a hydrogen uptake of 1.8 wt%, or 2.7 wt% if one H$_2$ molecule per copper site was added. In spite of the large number of adsorption sites identified, their occupation does not even account for half of the observed hydrogen loading.
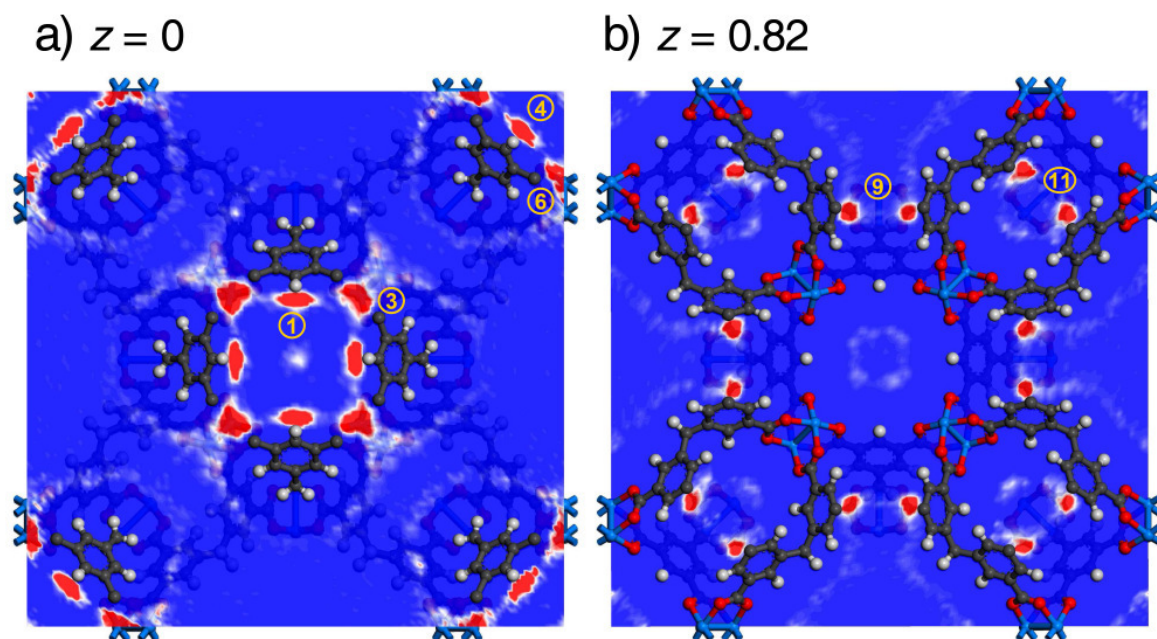
Figure 5.13. Calculated hydrogen density field for PCN-12, derived at $p = 6$ bar. The viewing direction is the c-axis. Two sections obtained for different z-coordinates are shown. *a)* The section at $z = 0$ contains four of the six density maxima located inside the small pores that are surrounded by C_{2v} linkers. *b)* The section at $z = 0.82$ contains two of the density maxima located at the triangular faces of the cuboctahedral pores.

5.1.6. Discussion

5.1.6.1. Adsorption isotherms and isosteric heats of adsorption

In the first part of this section, it has been demonstrated that a simple approach which uses generic force-field parameters is sufficiently accurate for a reasonable prediction of hydrogen adsorption isotherms for the majority of systems considered. A systematic comparison of three different parameter sets delivered a partially modified version of the UFF as the best choice. There are, however, some exceptions, which might be useful starting points for further investigations. For example, the DrFF performs much better than the UFF for ZIF-8, and it could be worth testing if this behaviour is also observed for other ZIFs. Furthermore, it has been found that the inclusion of electrostatic interactions leads to a relatively minor increase of the predicted hydrogen uptake. For the systems under consideration, this indicates that the neglect of electrostatic effects does not lead to significant errors. However, it should be pointed out that these interactions may play a more important role in MOFs with a charged framework, as it has been shown in a detailed study by Space and co-workers. (*84*) In particular, a good agreement of the predicted high-pressure adsorption isotherms with experimental data is observed. The tendency to overestimate the saturation uptake by up to 0.5 wt% can be explained with the fact that the MOF structures used in the simulations are ideal, while the capacity of real samples may be reduced due to impurities or incom-

plete activation. As established in earlier experimental and simulation studies, there is a clear correlation of the attained saturation uptake with the free pore volume. (*49*, *76*) At low pressures, the deviations with respect to experiment are much more significant. The most prominent errors are observed for $Cu_3(btc)_2$ and PCN-12, where the amount adsorbed is underestimated by up to 1.0 wt%. A similar, but less pronounced tendency is found for other MOFs with unsaturated metal sites, such as MOF-74 and $(Mn_4Cl)_3(btt)_8$. A possible explanation will be given at the end of this discussion section.

While the calculated isosteric heats of hydrogen adsorption at higher loadings usually agree relatively well with experimental data, the values at low coverage sometimes show significant deviations. The largest deviation is found for $(Mn_4Cl)_3(btt)_8$, where the experimental q_{st} is approximately 4 kJ mol^{-1} higher than the calculated value in the limit of zero coverage. In this particular case, it can be expected that the high interaction strength at low loadings observed in the real sample is caused by the adsorption at extra-framework cations. These Mn^{2+} cations, which remain in the structure even after evacuation at elevated temperature, (*59*) were not included in the simulations due to their high degree of disorder. More generally, deviations between the calculated isosteric heats and experimental values at low coverage may be related to adsorption at specific interaction sites, such as unsaturated metal centers, or at structural defects. It is interesting to note that the isosteric heat of adsorption of ZIF-8 (and, though less pronounced, of IRMOF-1) increases with increasing hydrogen loading. In some instances, similar observations have been made in other experimental and theoretical studies of hydrogen adsorption in MOFs. (*51*, *77*, *252*) However, the origins of this counterintuitive behaviour have not yet been fully elucidated. Since an important contribution of lateral hydrogen-hydrogen interactions can be considered quite unlikely for a weakly interacting molecule, it is more probable that this increase is caused by the approximations made during the calculation of q_{st}. The effects of these approximations have been analyzed in detail by Balbuena and co-workers for the case of alkane adsorption in activated carbons. (*176*) It was shown that the assumption of ideal gas behaviour, as well as the neglect of the volume of the adsorbed phase, leads to artificial increases of q_{st} at high coverages.

5.1.6.2. Adsorption sites

While the results discussed up to this point are quite similar to previous findings reported by other authors, a comparably detailed prediction of adsorption sites from GCMC simulations has not been carried out so far. The set of MOFs for which experimental data are available shows good to excellent agreement of the predicted adsorption positions with adsorption sites determined in neutron diffraction experiments. There is, however, the notable exception of MOFs with unsaturated metal sites, which will be analyzed in more detail below. Apart from this shortcoming, practically all other experimental adsorption sites are also visible as pronounced density maxima in the simulations. This confirms that GCMC simulations could be a very useful tool to obtain initial adsorption positions, *e.g.* for a Riet-

veld refinement using diffraction data. Exemplarily, the adsorption sites for two MOFs with a complex structure and various non-equivalent adsorption sites have been predicted. In itself, the knowledge of the adsorption sites might appear to be an issue that is mainly of academic interest. However, it must be emphasized that a better understanding of the preferential adsorption of hydrogen in certain regions of a MOF structure can aid the development of new materials with improved storage properties, *e.g.* by providing some insights concerning the most favourable pore size and, possibly, pore shape.

The fact that the density maxima calculated for $T = 77\,\mathrm{K}$ are in excellent agreement with experimental adsorption sites observed at very low temperatures (typically 4 K or lower) should not evoke the misleading interpretation of the adsorption of H_2 molecules at "fixed" positions. For these very light molecules, the thermal motion is rapid even at 77 K. Therefore, it can be expected that the density maxima become more and more diffuse on increasing temperature, so that the concept of adsorption sites gradually loses its usefulness.

For structurally simple MOFs, the saturation uptake can be estimated by summation over the observed adsorption sites. In a simplified manner, this can be interpreted as follows: The saturation uptake corresponds to a full occupation of a fixed set of adsorption sites, whereas the hydrogen density in the rest of the unit cell equals the bulk density (and, thus, does not contribute to the excess uptake). However, this simple approach fails for other systems, such as $(Mn_4Cl)_3(btt)_8$, UMCM-150, and, most severely, PCN-12. There are two possible explanations: Firstly, it can be imagined that those adsorption regions which are relatively extended can accommodate more than one molecule at a time. Secondly, the hydrogen density in other regions of the unit cell may also be increased considerably when compared to the bulk density, without exhibiting pronounced local density maxima that are visible in the hydrogen density fields.

In total, the results show that preferred adsorption sites exist in those regions of the structure that are characterized by a strong overlap of the potentials from the pore walls: Such a strong overlap typically occurs in the environment of complex inorganic building units, *e.g.* around the $Zn_4O(OOC)_6$ octahedron of IRMOF-1, in narrow pores or cavities with diameters below 10 Å, *e.g.* in the small pores of $Cu_3(btc)_2$, and at pore windows, *e.g.* at both sides of the windows of ZIF-8. In order to achieve a high hydrogen storage density in the framework, the most desirable features of the MOF structure appear to be narrow, interconnected pores as well as complex inorganic building units that permit the adsorption of several H_2 molecules at their surface. It is very challenging from a synthetic point of view to obtain structures that combine these features with a large free pore volume, which is a prerequisite to achieve high gravimetric uptakes.

5.1.6.3. MOFs with unsaturated metal sites

Discrepancies between simulation and experiment have been observed for some of the MOFs with unsaturated metal sites: In particular, the amount adsorbed at low pressures is underestimated. For the most severe cases, $Cu_3(btc)_2$ and PCN-12, the underestimation

reaches almost 1.0 wt%. Assuming an adsorption of one molecule per metal site would give an additional contribution of 0.99 wt% ($Cu_3(btc)_2$) and 0.86 wt% (PCN-12), respectively. This observation already indicates that the observed differences may be connected to the presence of unsaturated metal sites. Further indications in this direction are given by the analysis of the density fields, which do not exhibit any density increases close to the metal centers. This is in contrast to experimental neutron diffraction studies, where the adsorption site at the metal center is typically occupied as the first position, with metal-D_2 distances ranging from 2.3 Å for $(Mn_4Cl)_3(btt)_8$ ([59]) to 2.6 Å for MOF-74. ([255])

These observations can be explained straightforwardly with the type of interaction considered in the simulations: The parameters used account exclusively for long-range dispersive interactions, with equilibrium distances of more than 3.0 Å. The strongly repulsive core of the Lennard-Jones potential prevents a closer contact. Because the experimental metal-D_2 distances are significantly lower, it can be concluded that the interactions are not dominantly dispersive, but that other contributions, such as electrostatics or polarization interactions, play a more important role. Even a weak Kubas-type orbital interaction could be responsible for the adsorption at the metal centers. ([93]) It has already been shown that the inclusion of electrostatic interactions by means of a simple point-charge model does not significantly change the predicted adsorption isotherms. Therefore, it is necessary to replace the standard Lennard-Jones parameters by a new metal-H_2 potential model, which is suitable to predict a localized, attractive interaction at realistic distances (approximately 2.5 Å). An efficient approach will be proposed and tested in the following section.

Finally, it must be noted that the deviations in the predicted isotherms are not equally pronounced for all MOFs with unsaturated metal sites: While the effect is very clear for $Cu_3(btc)_2$ and PCN-12, a rather slight underestimation occurs for $(Mn_4Cl)_3(btt)_8$ and MOF-74, although the theoretical contribution of the metal sites would be similar. For MOF-505 and UMCM-150, MOFs that also contain Cu_2 paddle wheels and, thus, potentially accessible metal sites, the agreement with experiment is unexpectedly good. There are different possible explanations: In some cases, the MOFs used in the experimental studies may have been incompletely activated. In this case, the number of available metal sites is reduced with respect to the ideal system. Moreover, it is imaginable that other adsorption sites in the structures have similar binding energies as the unsaturated metal sites. This would lead to a simultaneous occupation of several sites, and a less pronounced effect of the adsorption at the metal sites on the isotherm at very low pressures. Experimentally, a simultaneous occupation of different adsorption sites, both at metal centers and in other parts of the structure, has been observed in D_2-loaded NOTT-101. ([262])

5.2. A new potential model for the interaction of hydrogen with unsaturated metal sites

5.2.1. Introduction

Several experimental techniques have provided evidence for a specific interaction of hydrogen with unsaturated metal sites in MOFs: (*55*) In addition to neutron diffraction techniques, which permit a direct identification of adsorption positions, evidence for the presence of specific interaction sites has been obtained in a more indirect manner via inelastic neutron scattering, (*58, 305*) thermal desorption spectroscopy, (*306*), and IR spectroscopy. (*65*)

The deficiencies of classical force-field parameters in GCMC simulations of hydrogen adsorption in these systems have been demonstrated in the previous section. Similar observations have been reported by other authors. (*71, 290*) It has been shown that DFT calculations are able to provide insights into the interactions between hydrogen and metal centers on a microscopic level, both for non-periodic model systems (*90, 91, 94*) and for periodic structures. (*58, 63, 92*) However, DFT calculations are computationally too demanding to permit a prediction of macroscopic properties using the principles described in section 3.2, which require the evaluation of the potential energy U for a large number of configurations.

In this section, a combined approach is used to bridge the gap between electronic structure methods and force-field based methods. As a first step, the potential energy curve of a hydrogen molecule interacting with an unsaturated metal center is calculated using DFT. Then, an appropriate potential function is fitted to this curve and integrated into the GCMC code. The interactions with all other framework atoms are treated with conventional force-field parameters (Lennard-Jones potential). The performance of the new potential model is then tested by running an extensive set of GCMC calculations, both for cryogenic conditions and room temperature.

As the most pronounced differences between simulation and experiment have been observed for $Cu_3(btc)_2$ and PCN-12, these two systems are used as reference for the calculations. Additionally, calculations are carried out for $(Cu_4Cl)_3(btt)_8$ in order to test the transferability of the potential model. For all MOFs, the results are compared to available experimental data and to simulation results obtained with standard force-field parameters. To assess the properties of a hypothetical system with a massively increased metal-hydrogen interaction with regard to hydrogen storage at room temperature, additional calculations using artificially enhanced parameters are reported.

5.2.2. Computational details

5.2.2.1. DFT calculations

A potential energy curve for H_2 adsorbed at the copper sites of a $Cu_2(bmc)_4$ paddle wheel (bmc = benzene-monocarboxylate) was obtained from all-electron DFT calculations. The calculations were carried out using the DMOL^3 code (*195, 289*) included in the *Accelrys* "Ma-

terials Studio" package. (*233*) A DNP basis set without BSSE correction was employed in all calculations, and the PBE exchange-correlation functional was used. (*190*) Preliminary tests showed that this functional delivers the best prediction of the Cu-H_2 equilibrium distance, which is known from neutron diffraction experiments, (*57*) of all functionals available in the $DMOL^3$ code.

5.2.2.2. GCMC simulations

GCMC simulations of hydrogen adsorption were carried out for cryogenic temperatures ($T = 77, 87, 100$ K) and pressures ranging from 0 to 60 bar, as well as higher temperatures ($T = 200, 298$ K) and pressures ranging from 0 to 100 bar. A Fortran GCMC code provided by B. Kuchta and L. Firlej was used for these calculations. It is based on the routines described by Frenkel and Smit. (*172*) As in the previous section, the Buch potential was used to represent the H_2 molecule. These parameters were combined with UFF+C_{aryl} parameters for the framework atoms using Lorentz-Berthelot mixing rules. Different potential models described below were used for the Cu-H_2 interaction. Electrostatic interactions were neglected. For cryogenic temperatures, quantum effects were accounted for explicitly, using the Feynman-Hibbs correction as described in 4.2.1.3.

For each pressure, 6.25 million equilibration steps and 12.5 million production steps were used for the calculation of the hydrogen uptake. To enhance the efficiency of the computations, the solid-fluid interaction energy was calculated on a grid prior to the actual GCMC run, using a grid resolution of 0.1 Å. For a H_2 molecule inserted at a random point of the unit cell, a bilinear interpolation between the closest grid points was employed to calculate the solid-fluid interaction energy. A cutoff of 15 Å was used for all interactions. Appropriately sized supercells were used to ensure a sufficient number of molecules in the simulation box for all conditions considered.

In analogy to the previous section, the calculated absolute hydrogen uptake was converted into excess values. The isotherms obtained for $T = 77, 87, 100$ K were used to calculate the isosteric heat of adsorption according to equation 3.26.

5.2.3. Derivation of Cu-H_2 potential parameters

Initially, the geometries of the $Cu_2(bmc)_4$ paddle wheel and the H_2 molecule were optimized separately. The symmetry of the paddle wheel was reduced to C_{2v} to allow for a correct reproduction of the antiferromagnetic coupling of the two Cu^{II} centers. (*259*) After the symmetry reduction, the calculation automatically converged to the expected singlet state. The equilibrium Cu-Cu distance amounts to 2.46 Å, a value that is only slightly lower than experimental values for fully desolvated samples. (*56, 57*)

As a next step, single-point calculations were carried out for a system with one H_2 molecule coordinated to the copper center, assuming fixed geometries of the subsystems. Three different orientations of the hydrogen molecule were considered: The first one is a side-on

orientation, with the H-H bond oriented along the Cu-O bonds (side-on orientation I). The second orientation is also side-on, with the H-H bond bisecting the Cu-O bonds (side-on orientation II). The third orientation is end-on. For varying Cu-H_2 distances, the binding energy was calculated by subtracting the energies of the isolated subsystems from the total energy of the combined system.
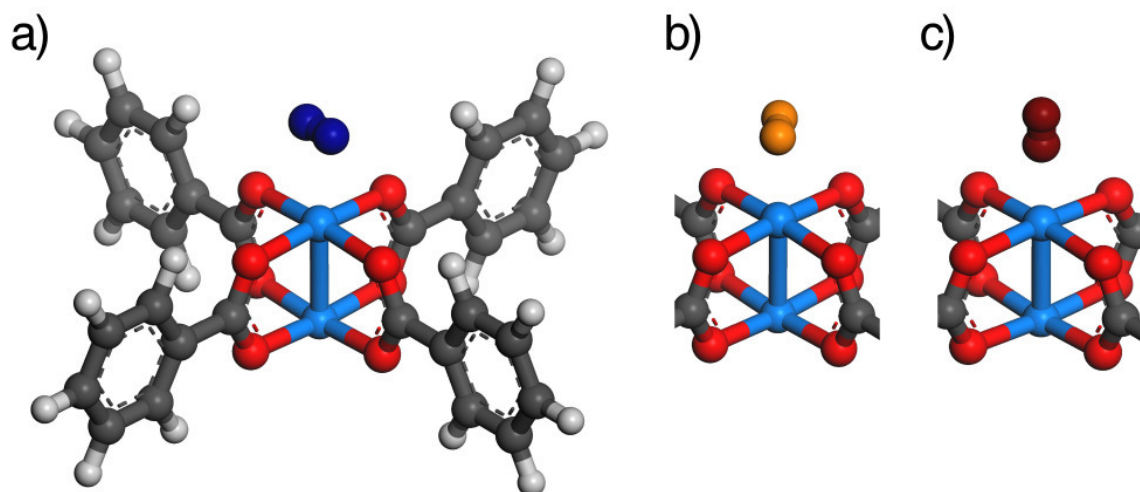
Figure 5.14. Visualization of the model system used in the DFT calculations. *a)* $Cu_2(bmc)_4$ paddle wheel with coordinated H_2 molecule, side-on orientation I. *b)* Side-on orientation II. *c)* End-on orientation.
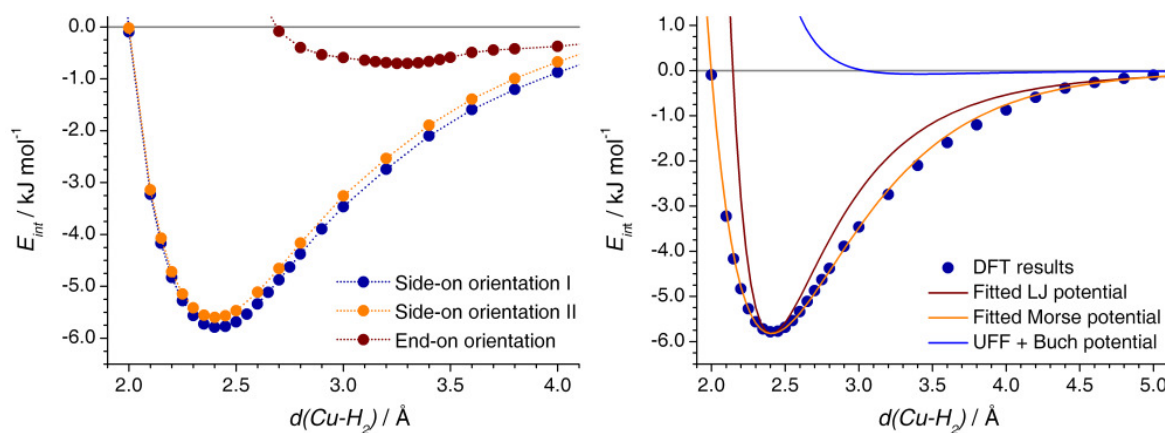
Figure 5.15. *Left:* Calculated DFT interaction energy for the three different orientations of the hydrogen molecule as explained in the text. *Right:* Fit of Lennard-Jones and Morse potential models to the DFT results for side-on orientation I. For comparison, the potential energy curve resulting from mixing of the literature parameters for copper and hydrogen is also shown (UFF + Buch).

The results of the DFT calculations are shown in figure 5.15. A very shallow energy minimum is predicted for the end-on orientation. It can be expected that even this weak binding is an artefact, and that the DFT potential energy curve for this orientation should be purely repulsive as long as dispersive interactions are not accounted for (spurious binding of dispersion-bound systems is well known for some XC functionals, among them PBE

(*187*)). The inadequacy of DFT for this case is further substantiated by the observation that the interaction energy does not show a smooth evolution on increasing distance. For both side-on orientations, a well-localized minimum is visible for a Cu-H_2 distance of 2.4 Å. This distance is in excellent agreement with the Cu-D_2 distance measured for a deuterium-loaded sample of $Cu_3(btc)_2$, which amounts to 2.39 Å. (*57*) The energy difference between the two side-on orientations usually ranges around 0.2 kJ mol^{-1}. It can thus be concluded that the energy barrier to a propeller-like rotation in a plane perpendicular to the Cu-Cu axis is very low. For the parameter derivation, the energy curve obtained for side-on orientation I is used.

The calculated binding energy amounts to approximately -5.8 kJ mol^{-1}. This value is considerably smaller than the binding energy of -10.1 kJ mol^{-1} determined for hydrogen adsorbed in $Cu_3(btc)_2$ using IR spectroscopy. (*65*) A comparison of the DFT energy with the spectroscopically determined value is not entirely legitimate, because the value obtained from IR spectroscopy includes the contributions of zero-point vibrations, which were neglected in the DFT calculations. Because the ZPVE reduces the interaction energy, the difference between the two energy values would become even larger if these effects were accounted for. Therefore, the discussion of other possible origins of this discrepancy is also important. In part, the underestimation can be explained with the neglect of long-range dispersive interactions in the DFT calculations. Using the UFF+C_{aryl} molecular mechanics parameters, the contribution of dispersive interactions between the hydrogen molecule and the non-metal atoms of the cluster can be estimated. It amounts to -2.5 kJ mol^{-1}, leading to a total estimated interaction energy of -8.3 kJ mol^{-1}, a value which is considerably closer to experiment. In addition, it must be taken into account that the cluster used in the DFT calculations is of finite size, while the experimental value was obtained for the periodic system.

In the following, the calculated DFT binding energy is understood as being constituted solely by the short-range interaction of hydrogen with the metal center. Due to this assumption, the DFT values can be directly used as starting point for the parameter derivation, without further corrections. In an attempt to fit a Lennard-Jones potential to the DFT energy curve, the parameters r_0 and D_0 are equated with the energy minimum obtained from the DFT calculations. The resulting curve, which is displayed in figure 5.15, clearly shows significant deviations with respect to the DFT values. In particular, the interaction energy at intermediate distances ($d(Cu\text{-}H_2) \approx 3.2$Å) is underestimated by up to 0.8 kJ mol^{-1}. On the other hand, a fit of a Morse potential to the calculated DFT energy curve leads to excellent agreement over the whole range of distances.

The resulting potential parameters r_0, D_0, and α, which are given in table A.6 of the Appendix, can be directly transferred to the GCMC code to model the interaction of hydrogen with the unsaturated copper centers. Such a one-to-one adoption corresponds to the assumption that the H_2 molecule is always coordinated to the metal site in a side-on fashion, and that other orientations do not play a role. If it is assumed that the H_2 molecule retains its rotational degrees of freedom, a scaling of the well depth D_0 appears to be more appropriate: The inherent assumption underlying the united-atom model is the equal like-

lihood of all possible orientations of the H_2 molecule, which justifies the representation of the dummbell-like molecule as a single interaction site. According to this assumption, it must be expected that the H_2 molecule will not always approach the copper center in side-on coordination, but that other, energetically less favourable orientations also occur with a significant probability. Therefore, only an orientation-averaged potential model is strictly compatible with the united-atom approximation. The averaging over different possible orientations is carried out by scaling the well depth derived from the DFT calculations by a factor of 2/3. This choice of the scaling factor assumes that all side-on orientations correspond to the maximal Cu-H_2 interaction energy, whereas the interaction for an end-on coordination of the hydrogen molecule can be approximated to be zero. While the usage of this orientation-averaged (oa) Morse potential is thus physically more plausible, the performance of both the full and the oa-Morse potential are assessed in this work. These modified potential models are compared to the standard LJ parameters for copper from the UFF.

For the different Cu-H_2 potential models, two-dimensional maps of the calculated total solid-fluid interaction energy are displayed for both $Cu_3(btc)_2$ and PCN-12 in figure 5.16. The sections are positioned in a way that they are in plane with several Cu_2 paddle wheels. In both cases, the maps obtained using the standard parameters do not show a local energy minimum at the unsaturated copper centers. There is a considerable energy increase in the regions perpendicular to the Cu-Cu axis, which have two carboxylate groups in their direct environment. Here, the energy increases to approximately -5 kJ mol^{-1} in the case of $Cu_3(btc)_2$, where the paddle wheels are well-separated from each other, and reaches more than -7 kJ mol^{-1} in PCN-12, where two neighbouring paddle wheels contribute to the total interaction. The energy plots obtained with both versions of the modified Cu-H_2 potential exhibit well-defined local minima at the copper sites. Apparently, the Morse potential is suitable to represent the relatively short-ranged, sharply localized metal-hydrogen interaction. The depth of the minima reaches -9.0 kJ mol^{-1} for the full Morse potential and -7.0 kJ mol^{-1} for the oa-Morse potential. While the minima at the metal sites created by the Morse potential are very pronounced, the changes of the potential energy in other regions of the unit cell are relatively small. In particular, the energy at the center of the pores of both $Cu_3(btc)_2$ and PCN-12 remains practically unaffected. Apparently, the implementation of the modified Cu-H_2 potential models does not induce an artificial enhancement of the long-range interactions far from the copper centers, provided that an adequate stiffness parameter α is chosen. However, for PCN-12, a relatively pronounced increase of the interaction energy is visible in the side pockets neighboured by two paddle wheels. It amounts to nearly 1.0 kJ mol^{-1} for the full Morse potential, and approximately 0.5 kJ mol^{-1} for the oa-Morse potential. A similar, but less pronounced increase by up to 0.5 kJ mol^{-1} is observed in regions perpendicular to the Cu-Cu axis of the paddle wheels in $Cu_3(btc)_2$. This non-negligible enhancement at intermediate distances must be taken into account when the performance of the potential models is evaluated.
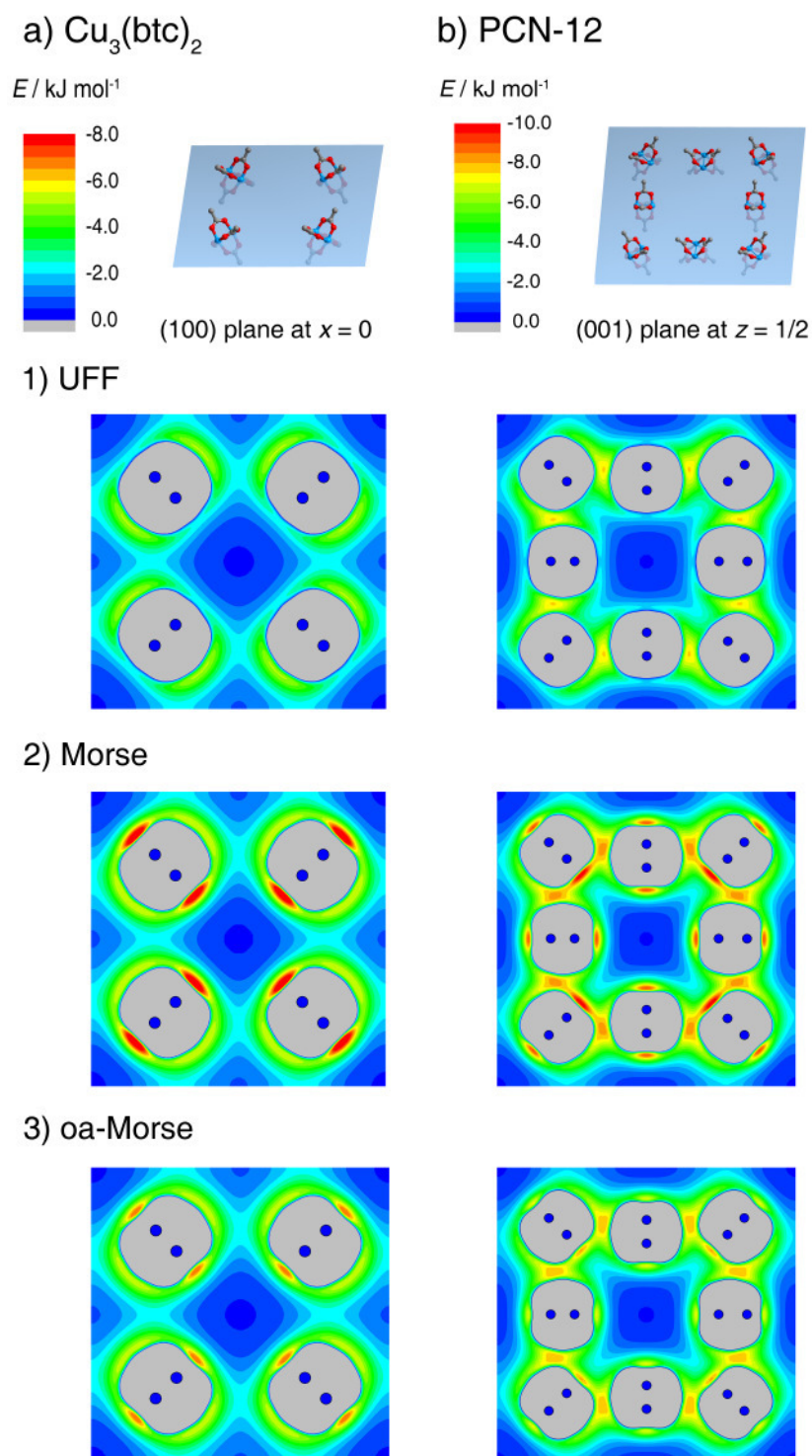
Figure 5.16. Two-dimensional sections through the unit cells of $Cu_3(btc)_2$ and PCN-12, showing the solid-fluid interaction energy for a hydrogen molecule as a function of its position. The energy was calculated with three different models for the Cu-H_2 interaction: (1) LJ potential with Cu parameters from the UFF and H_2 parameters from the Buch potential, (2) full Morse potential derived from DFT calculations, and (3) orientation-averaged Morse potential. The crystallographic orientation of the sections is indicated for each MOF, together with the position of the Cu_2 paddle wheels lying in plane with the section.

5.2.4. GCMC simulations: Hydrogen adsorption at cryogenic temperatures

The calculated hydrogen adsorption isotherms for $Cu_3(btc)_2$ and PCN-12 are shown in figures 5.17 and 5.18. Only those temperatures for which experimental data are availabe are included in the figures. Isotherms for the other temperatures are shown in the Appendix, section A.3.2. As discussed in the previous section, the conventional Cu-H_2 potential model leads to a pronounced underestimation of the hydrogen uptake at low pressures. The difference between simulation and experiment amounts to approximately 1.0 wt% for $Cu_3(btc)_2$ at 77 K, 0.7 wt% for $Cu_3(btc)_2$ at 87 K, and 1.0 wt% for PCN-12 at 77 K. There is a notable correspondence between these values and the hypothetical contribution of the copper sites if each site was occupied by one hydrogen molecule (0.99 wt% for $Cu_3(btc)_2$, 0.86 wt% for PCN-12). Of the two modified parameter sets, the full Morse potential overestimates the amount of hydrogen adsorbed in $Cu_3(btc)_2$, whereas the oa-Morse potential delivers an excellent prediction of the low-pressure isotherms at both temperatures. For PCN-12, the experimental isotherm at $T = 77$ K ranges between the isotherms obtained with the two modified parameter sets. While the full Morse potential performs better at very low pressures, the oa-Morse potential gives the best prediction at 1 bar.

High-pressure hydrogen adsorption data are available for $Cu_3(btc)_2$, only. Here, the results obtained using the conventional parameters range closest to the experimental isotherms. This observation is in line with the results from the previous section, where it was found that the UFF+C_{aryl} parameters deliver a reasonably accurate prediction of the saturation uptake, regardless of whether the MOF structure contains unsaturated metal sites or not. On the other hand, the modified potentials overestimate the saturation uptake by 0.4 to 0.8 wt%. The deviations between the uptakes predicted by the different potential models decrease at pressures above 5 bar, underlining that the adsorption capacity at high pressures is determined mostly by the available pore space, rather than the strength of the solid-fluid interaction.

The isosteric heat of hydrogen adsorption was calculated from the isotherms obtained for $T = 77, 87, 100$ K. The resulting q_{st} as a function of the loading is shown in figure 5.19 for both MOFs. For $Cu_3(btc)_2$, the predicted isosteric heat of adsorption at low coverage is very similar for all three potential models, ranging from 6.90 to 7.36 kJ mol^{-1} at a coverage of 0.5 mmol g^{-1} (which equals 5 molecules per unit cell). On increasing loading, the isosteric heat calculated using the conventional parameters decreases most rapidly and approaches a nearly constant value of approximately 4.3 kJ mol^{-1} at loadings above 8 mmol g^{-1} (approximately 80 molecules/cell). The q_{st} obtained using the full Morse potential remains at a nearly constant value up to a loading of 5 mmol g^{-1}, which corresponds to 48 molecules per unit cell. Since there are 48 Cu atoms in the cell, it can be concluded that each copper center is occupied by one H_2 molecule at this loading, which straightforwardly explains the decrease at higher loadings. The isosteric heat calculated with the oa-Morse potential exhibits a more pronounced decrease at low coverage, and there is no significant change in the slope at a loading of 5 mmol g^{-1}. At high hydrogen loadings, the isosteric heats calculated
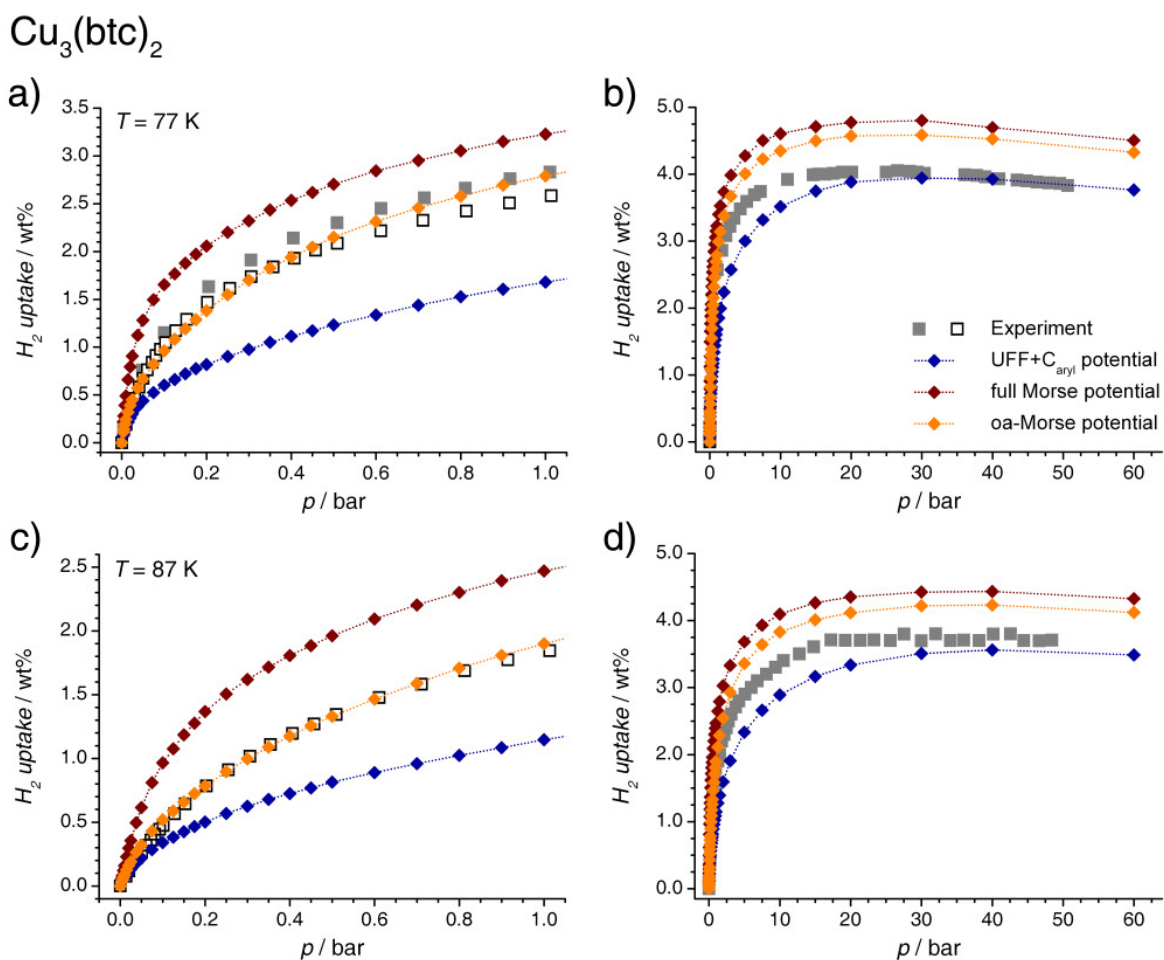
Cu$_3$(btc)$_2$

Figure 5.17. Calculated hydrogen adsorption isotherms for Cu$_3$(btc)$_2$ obtained with three different Cu-H$_2$ potential models ($T = 77, 87$ K). Experimental data are given for comparison: Closed grey squares are from (*71*), open black squares are from (*252*).
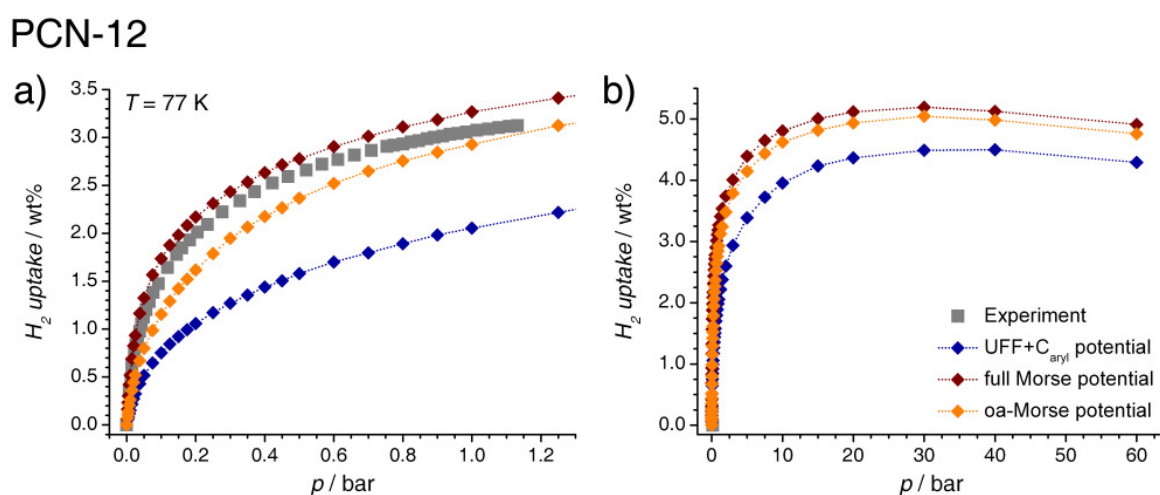
PCN-12

Figure 5.18. Calculated hydrogen adsorption isotherms for PCN-12 obtained with three different Cu-H$_2$ potential models ($T = 77$ K). Experimental data are from (*264*).

using the two versions of the Morse potential approach the same value. The evolution of the experimental q_{st} is somewhat different, with a lower initial value and a less pronounced decrease on increasing loading as compared to all three simulated curves. Quantitatively, it ranges between the two versions of the Morse potential. The calculated isosteric heats of hydrogen adsorption obtained for PCN-12 are also included in figure 5.19. Here, the initial value exhibits a stronger dependency on the potential model, ranging from 6.54 to 7.35 kJ mol^{-1}. The qualitative evolution on increasing loading is similar to the behaviour discussed above for $Cu_3(btc)_2$.
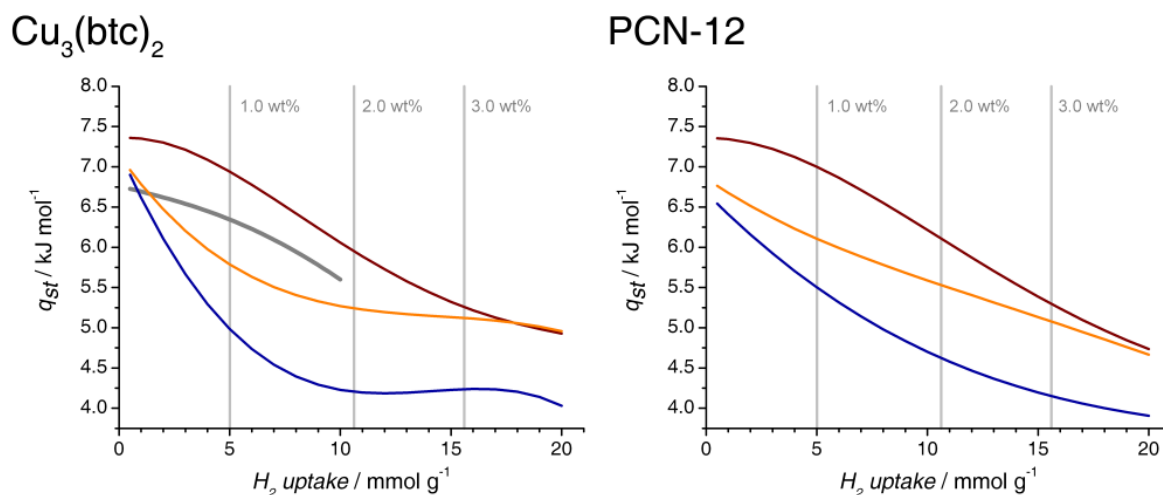
Figure 5.19. Calculated isosteric heat of hydrogen adsorption of $Cu_3(btc)_2$ and PCN-12 obtained with three different Cu-H_2 potential models. The same colour scheme as in figure 5.17 is used. For $Cu_3(btc)_2$, values derived from experimental data are shown as a thick grey line. (252)

5.2.5. GCMC simulations: Hydrogen adsorption at increased temperatures

The calculated adsorption isotherms for $Cu_3(btc)_2$ at $T = 200\,K$ and $T = 298\,K$ are shown in figure 5.20, together with experimental data. Compared to the results at cryogenic temperatures, the difference between the conventional parameters and the oa-Morse potential is significantly smaller, not exceeding 0.4 wt% at 200 K and 0.2 wt% at room temperature and a pressure of 100 bar. These observations already show that the interaction with the unsaturated metal sites is not strong enough to provide for a complete occupation of these sites at increased temperatures. More interesting insights can be gained from the comparison with the experimental isotherms. Here, it is notable that the isotherm calculated with the conventional parameters is in better agreement with the experimental data at both temperatures. Thus, the model that accounts solely for dispersive interactions delivers a better prediction of the hydrogen uptake at higher temperatures than the modified potential model including the localized Cu-H_2 interaction. The high-temperature isotherms calculated for PCN-12, which are also shown in figure 5.20, are very similar to those calculated for $Cu_3(btc)_2$. The hydrogen uptake predicted by the unmodified potential is slightly higher

at both temperatures, which can be attributed to the enhanced van der Waals interaction in the various small pores and pockets present in the PCN-12 structure. However, the increase of the uptake induced by replacing the conventional parameters by the oa-Morse potential is somewhat less pronounced due to the reduced number of unsaturated metal sites per unit weight with respect to $Cu_3(btc)_2$.

For higher temperatures, the full Morse potential has not been considered. The comparison of the unmodified potential and the oa-Morse potential shows that the influence on the resulting isotherm is relatively small, and an insignificant change can be expected when the oa-Morse parameters are replaced by the somewhat deeper potential well of the full Morse potential. Instead, the isotherms discussed so far are complemented by isotherms calculated with an additional parameterization of the Morse potential representing a strongly enhanced interaction.

The idea behind this potential is the following: It is obvious that a drastic increase of the framework-hydrogen interaction is necessary to attain technologically interesting hydrogen uptake capacities at room temperature, *e.g.* to reach the often-quoted q_{st} of 15 kJ mol^{-1} obtained by Bhatia and Myers from thermodynamic considerations. (*25*) Previous simulation studies have tested the performance of hypothetical materials with a strongly enhanced solid-fluid interaction, both for MOFs and carbon materials. (*34, 78*) In these publications, high hydrogen uptakes of more than 5 wt% at room temperature and moderate pressure were obtained when a strongly enhanced solid-fluid interaction was assumed for all framework atoms. From a synthetic chemistry viewpoint, such a homogeneous increase of the interaction energy is hard to imagine for MOFs. The typical strategy of incorporating unsaturated metal sites will enhance the interaction strength in some well-defined regions of the total available pore space only. Theoretical studies show that the interaction strength of these sites could be tuned, *e.g.* by replacing one metal center with another, more strongly interacting metal. The aim of the calculations using the artificially enhanced parameters is to determine the impact of the introduction of more strongly interacting metal sites, without modifying the interaction with the rest of the framework. Leaving the parameter r_0 of the Morse potential derived above unchanged, the well depth D_0 of the oa-Morse potential was multiplied by 4. This results in a metal-H_2 interaction energy of approximately -15 kJ mol^{-1}, a value which is in good correspondence with the "optimal" isosteric heat of adsorption proposed by Bhatia and Myers. (*25*) In order to retain the localized character of the potential, the stiffness parameter α was also increased. As is visible from figure 3.2, an increase of the stiffness parameter corresponds to a sharper potential well with steeper walls. In this case, α was adjusted in a way that the interaction at a metal-H_2 distance of 4 Å is equally strong as for the oa-Morse potential.

The isotherms calculated using this hypothetical metal-H_2 potential are shown in figure 5.20. It is obvious that the strong enhancement of the interaction leads to a significant rise of the hydrogen uptake. Compared to the conventional potential, the uptake is increased by 0.8 to 1.0 wt% at $T = 200$ K and 0.6 to 0.7 wt% at room temperature, indicating that the majority of the metal sites is occupied. As discussed above, the fact that the observed in-

creases are larger for $Cu_3(btc)_2$ is related to the higher total contribution of the unsaturated metal sites. The relatively sharp rise of the RT isotherm between 3 and 40 bar is within the desirable range of operating pressures with regard to the charge and delivery of a hydrogen storage system. (*11*) It is, however, obvious that the amount of hydrogen stored by these hypothetical systems is much too low to be technologically relevant.

$Cu_3(btc)_2$

PCN-12
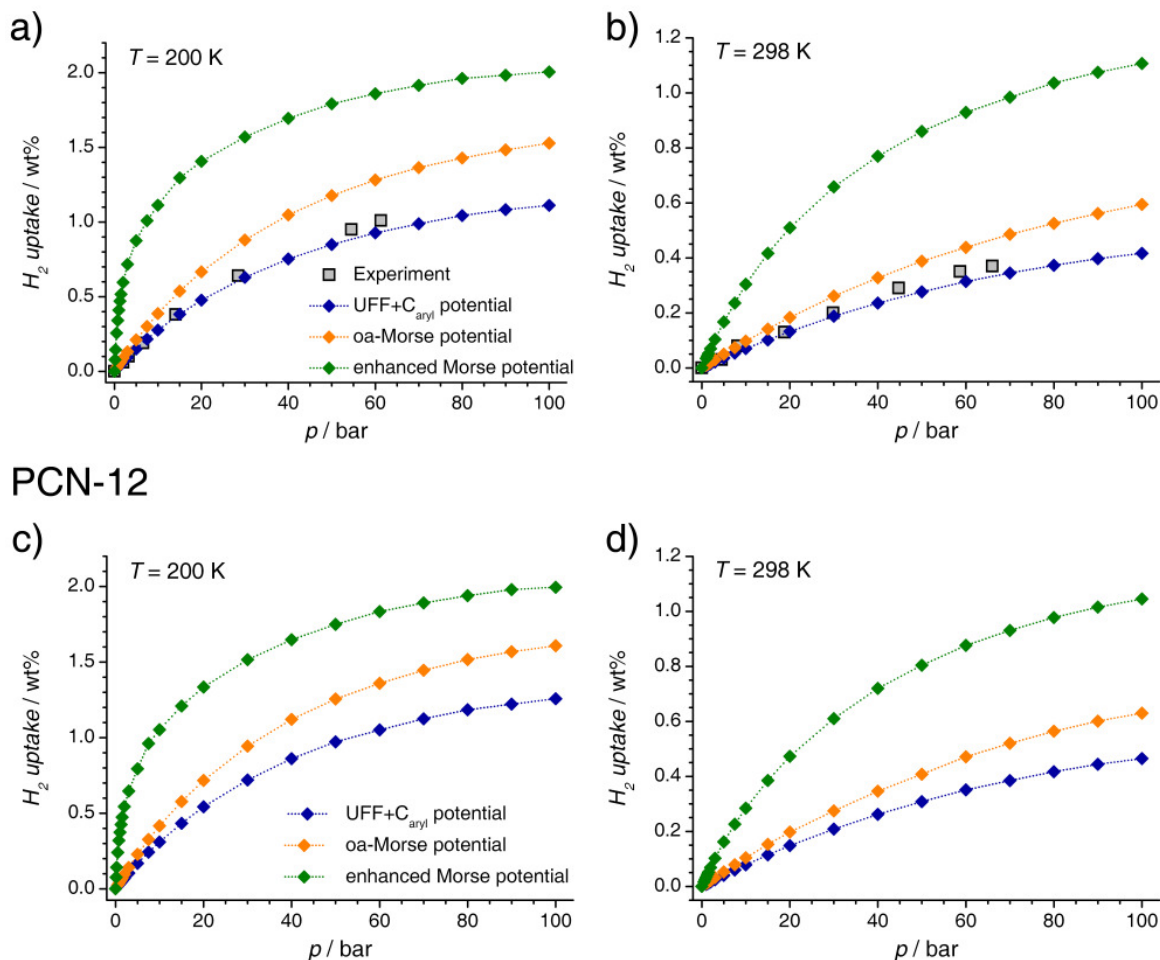
Figure 5.20. Calculated hydrogen adsorption isotherms obtained with three different Cu-H_2 potential models for increased temperatures ($T = 200, 298$ K). For $Cu_3(btc)_2$, experimental data from (*307*) are given for comparison.

5.2.6. Transferability of the potential model: Hydrogen adsorption in $(Cu_4Cl)_3(btt)_8$

In order to test the transferability of the potential model derived for a Cu_2 paddle wheel to a MOF with copper in a different coordination environment, additional calculations were carried out for $(Cu_4Cl)_3(btt)_8$. The calculated hydrogen adsorption isotherms at $T = 77, 87$ K are shown in figure 5.21, and the derived isosteric heat of hydrogen adsorption is given in figure 5.22. The conventional parameters lead to the expected underestimation of the hy-
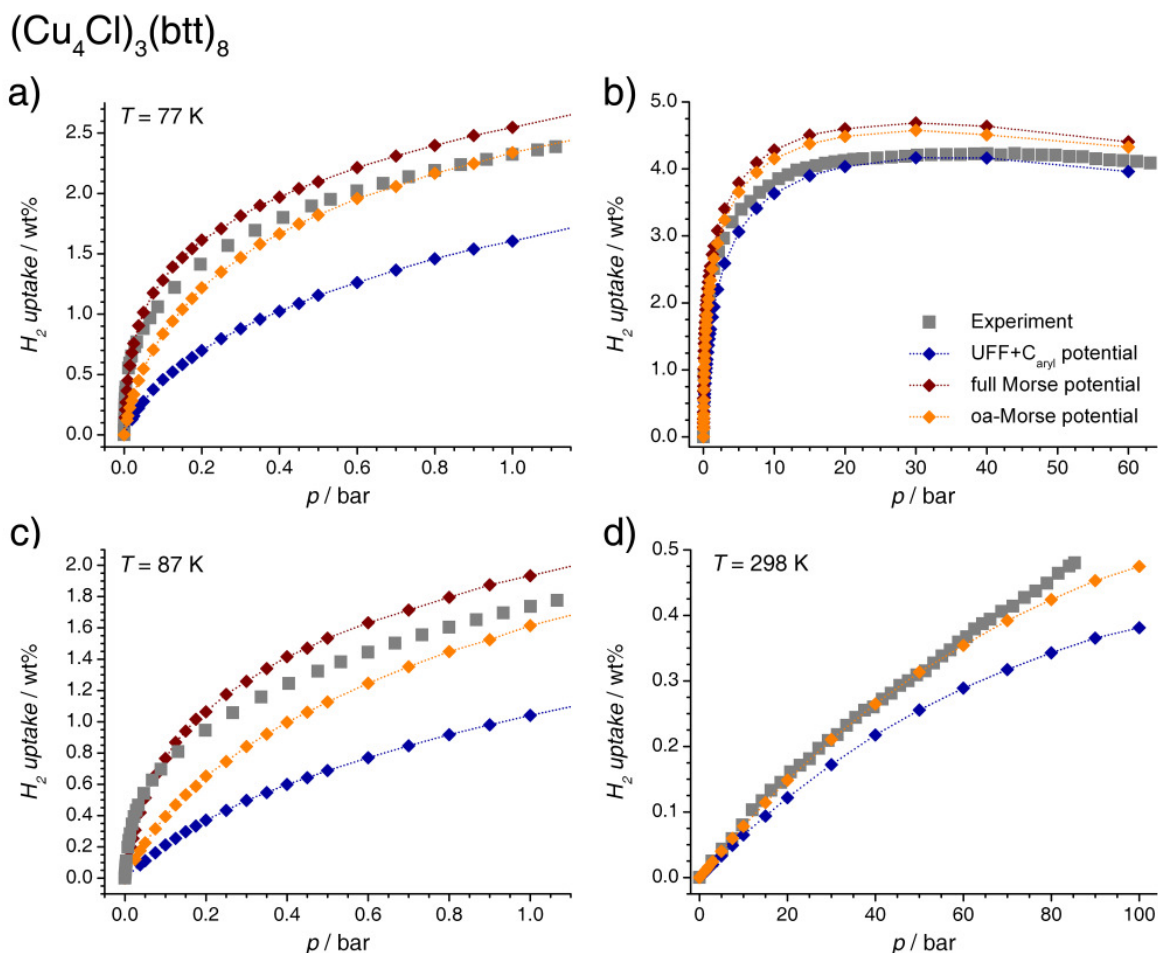
(Cu$_4$Cl)$_3$(btt)$_8$

Figure 5.21. Calculated hydrogen adsorption isotherms for (Cu$_4$Cl)$_3$(btt)$_8$ obtained with three different Cu-H$_2$ potential models ($T = 77, 87, 298$ K). Experimental data from (60) are given for comparison.
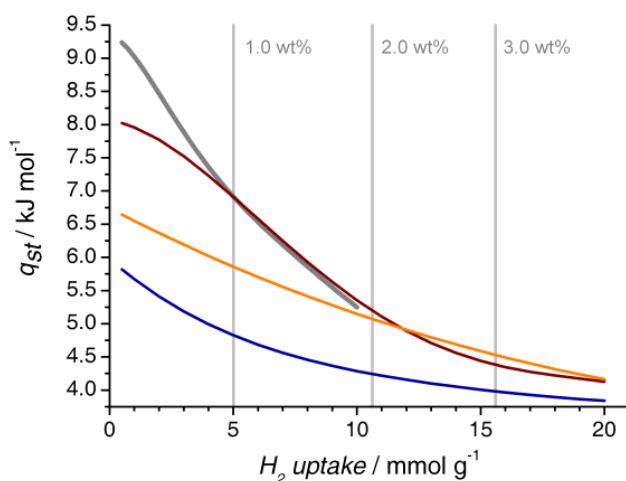
Figure 5.22. Calculated isosteric heat of hydrogen adsorption of (Cu$_4$Cl)$_3$(btt)$_8$ obtained with three different Cu-H$_2$ potential models. The same colour scheme as in figure 5.21 is used. Values derived from experimental data are shown as a thick grey line. (60)

drogen uptake, which amounts to approximately 0.7 wt% at both temperatures and 1 bar. These values are in good correspondence with the theoretical contribution of the unsaturated metal sites as defined above, which adds up to 0.77 wt%. Similar to PCN-12, the full Morse potential leads to a better prediction of the sharp rise of the isotherm at low pressures, whereas the best agreement at 1 bar is obtained with the oa-Morse potential. The hydrogen uptake at high pressures is moderately overestimated when the modified potential models are used. On the other hand, the unmodified parameters give a good prediction of the saturation uptake. A high isosteric heat of hydrogen adsorption was calculated from experimental data, exceeding 9 kJ mol^{-1} in the limit of zero coverage. It is apparent that the calculations using the full Morse potential give the best prediction of q_{st}, while the oa-Morse potential tends to underestimate the affinity of $(Cu_4Cl)_3(btt)_8$ towards hydrogen.

Additional results for room temperature obtained with the conventional potential and the oa-Morse potential are shown in figure 5.21d, together with experimental data. Here, the agreement with the experimental values is excellent for the oa-Morse potential, except for the highest pressures considered, whereas the unmodified parameters lead to a moderate underestimation of the amount adsorbed. This is in notable contrast to the observations made for $Cu_3(btc)_2$ for this temperature, where the best agreement was obtained with the conventional force-field parameters.

5.2.7. Discussion

5.2.7.1. Possible improvements of the parameter derivation procedure

In this section, improved potential parameters for the interaction of hydrogen with unsaturated metal sites have been derived from DFT calculations for a simple model system. The approach is highly efficient, with the necessary DFT computations requiring only a few days on a conventional desktop computer, and can be straightforwardly extended to other inorganic building units, *e.g.* different metal species, oxidation states, or coordination environments. While a Lennard-Jones potential is not suitable to reproduce all features of the DFT potential energy curve, the Morse potential, which has one additional adjustable parameter, provides for excellent agreement. The newly developed potential parameters for the metal-hydrogen interaction can be combined with Lennard-Jones parameters from literature force fields for the dispersive interaction with all other framework atoms. This "best of both worlds" approach augments the transferable and efficient generic force-field parameters used for the non-metal atoms with accurate *ab-initio* derived parameters for the metal centers as specific interaction sites.

It should be pointed out that the parameter derivation is based on a number of important approximations. Firstly, only a limited quality can be reached in the DFT calculations due to restrictions of the basis set size. A more thorough treatment should include the comparison of different basis sets, and possibly other parameters influencing the accuracy of the computations. Secondly, the effect of zero-point vibrations on the interaction energy has remained unassessed. Finally, and most importantly, it was assumed that the DFT interaction

energy for the system consisting of a hydrogen molecule and the $Cu_2(bmc)_4$ cluster corresponds exactly to the $Cu-H_2$ interaction energy, and that the contributions of other atoms of the cluster are negligible. In order to assess this in more detail, it would be necessary to use a more sophisticated *ab-initio* method that recovers all interactions, including dispersion. However, such a procedure would also require a more evolved parameter derivation scheme, as it would be necessary to subtract the contributions of the dispersive interaction with the non-metal atoms from the total interaction energy.

As it will be shown in the following section, the $Cu-H_2$ interaction depends on the chemical environment of the copper center. Neither this point, nor possible differences between the non-periodic cluster and a periodic crystal have been regarded in the context of the parameter derivation. In the end, however, it should be emphasized that the usefulness of "extremely accurate" $Cu-H_2$ parameter remains limited, as long as they are used with generic force-field parameters, which constitute a possible source of error in themselves.

5.2.7.2. Calculation results at cryogenic temperatures

It has been shown that the usage of the modified $Cu-H_2$ potential provides for an excellent prediction of adsorption isotherms at low temperatures and low pressures. Under these conditions, the adsorption at the unsaturated metal sites has a significant impact on the isotherm, and this behaviour is now correctly reflected in the simulations. This is a massive improvement over the performance of the $UFF+C_{aryl}$ parameter set (and the other generic force fields), whose inadequacy for MOFs with accessible metal site has been discussed in detail in the previous section. However, the modified potential models perform worse than the conventional parameters at high pressures, where the $UFF+C_{aryl}$ parameters are the best choice for the prediction of the saturation uptake. These results indicate that the saturation uptake is mainly determined by the long-range dispersive interactions with the whole framework, rather than the contributions of unsaturated metal sites. The overestimation of the saturation loading by the modified potential models is probably related to the enhancement of the potential energy at intermediate distances, particularly in the regions perpendicular to the Cu-Cu axis of the paddle wheel. In figure 5.16, this tendency is particularly well visible for the side pockets of the large cuboctahedral pore of PCN-12, which lie between two Cu_2 paddle wheels. However, a similar, though less pronounced increase of the interaction energy in regions perpendicular to the Cu-Cu axis is also observed for $Cu_3(btc)_2$. This enhancement, which will to some degree affect the simulation results, could be avoided by using a damping function that depends on the position of the hydrogen molecule with respect to the metal cluster, such as the atom-linear molecule potential models described by Kaplan. (*164*) However, the integration of an anisotropic potential model into the code is computationally considerably more evolved than the usage of a Morse potential, which is isotropic in nature.

In spite of the good agreement of the predicted isotherms with experimental data, which is particularly striking for the oa-Morse potential in the case of $Cu_3(btc)_3$, there are more

signifcant deviations for the isosteric heat of adsorption, and its evolution on increasing loading. In this context, it must be taken into account that the type of equation used to fit the isotherms in the q_{st} calculation has a certain influence on the results. (*62*) Moreover, a recent experimental study shows that the number of isotherms used in the calculation also affects the resulting q_{st} values, particularly at low coverage. (*308*)

In the case of $(Cu_4Cl)_3(btt)_8$, the agreement of the calculated isotherms with experimental adsorption data is also considerably better when the modified potential models are used. This indicates that the newly derived parameters are indeed to some extent transferable to other systems with unsaturated copper sites in a different coordination environment. In contrast to the two MOFs with Cu_2 paddle wheels, the full Morse potential delivers a slightly more accurate prediction of the hydrogen adsorption isotherms at cryogenic temperatures than the oa-Morse potential. Because the potential model assuming a stronger interaction provides for a better agreement with experimental isotherms, it can be concluded that the Cu-H_2 interaction in $(Cu_4Cl)_3(btt)_8$ is somewhat stronger when compared to the other two systems. This assumption is supported by the results of an earlier theoretical study of the interaction of hydrogen with a Cu_4Cl building unit. (*92*) Here, a maximum binding energy of -6.4 kJ mol^{-1} was obtained in DFT-PBE calculations, as compared to -5.8 kJ mol^{-1} calculated for the Cu_2 paddle wheel system in this work. Taken together, the results indicate that the transferability of the potential model is good enough to allow for reasonable predictions of adsorption isotherms. However, a more detailed study should always involve a new set of DFT calculations, taking into account the specific environment of the metal center.

5.2.7.3. MOFs with unsaturated metal sites - Promising materials for room-temperature hydrogen storage?

In the case of $Cu_3(btc)_2$, it is apparent that the conventional parameters deliver the best prediction of the adsorption isotherms at $T = 200\,\text{K}$ and room temperature. This result could indicate that the localized copper-hydrogen interactions, which doubtlessly play a significant role at low temperatures, are massively decreased or even absent at higher temperatures. A possible explanation might be the increased thermal motion of the hydrogen molecules, which could prevent a stable coordination to the metal centers. Such a behaviour would be consistent with the well-known fact that many of the known Kubas-type metal-H_2 complexes are stable at low temperatures only. (*93*) These observations highlight the hazards encountered when extrapolating from measurements or simulations carried out at cryogenic temperatures to room temperature.

The comparison of $Cu_3(btc)_2$ and PCN-12 shows that the influence of the metal sites on the room-temperature uptake is exclusively determined by the number of metal sites per unit weight, and is therefore somewhat higher for $Cu_3(btc)_2$. The calculations do not provide any evidence for the hypothesis that the particular cuboctahedral arrangement of the Cu_2 paddle wheels in PCN-12 has a beneficial influence on the hydrogen storage properties. (*264*)

Because the interaction with the metal center is sharply localized, each of the centers acts as an independent adsorption site, and the magnitude of the interaction energy is practically unaffected by the presence of other sites in the near environment. Therefore, only the number of sites per unit weight (or unit volume), *i.e.* the density of the metal sites, is the key factor determining their impact on the adsorption properties.

The results for $(Cu_4Cl)_3(btt)_8$ seem to contradict some of the conclusions drawn in the previous paragraph. Here, the agreement is best for the oa-Morse potential model, which assumes a significant interaction of hydrogen with the copper centers. This result could imply that there is a non-negligible adsorption at the unsaturated metal sites even under these conditions. In this context, however, it must also be considered that $(Cu_4Cl)_3(btt)_8$ contains charge-balancing extra-framework cations. Therefore, the difference between the predictions of the conventional force field and experimental data might also be caused by adsorption at these cations, not at the metal sites of the Cu_4Cl units. The concentration of extra-framework cations is rather low: According to the stoichiometry given in the original paper, a full occupation of the cations by hydrogen molecules would contribute approximately 0.2 wt% to the total uptake. (*60*) Moreover, the cation-H_2 interaction can be expected to be relatively strong. An overview of interaction energies of hydrogen with cations, *e.g.* in zeolites, is given in (*55*). Relatively few accessible, strongly interacting extra-framework cations would be sufficient to explain the difference of approximately 0.1 wt% between the predictions of the conventional force field and the experimental data. The high initial isosteric heat of adsorption observed for $(Cu_4Cl)_3(btt)_8$ could also be caused by adsorption at these sites. However, without further experimental results, the interpretation proposed here remains speculative.

Finally, the results obtained with the artificially enhanced potential give some insights concerning the possible impact of a boost of the metal-hydrogen interaction strength. It is shown that an interaction energy of approximately -15 kJ mol^{-1} is high enough to allow for an occupation of the majority of the metal centers at room temperature and sufficiently high pressure. However, it has been pointed out above that the total impact of the metal sites on the hydrogen is limited by the number of accessible sites. In typical MOFs, the contribution of the metal sites to the total uptake hardly exceeds 1.0 wt%, reaching 1.6 wt% for the lightweight $Mg_2(dhbdc)$, a MOF that is isostructural to MOF-74. (*63*) Taken together, an increase of both the interaction strength and the surface density of the metal sites, without sacrificing the low bulk density of the material, is a major challenge for synthetic chemistry. In this context, it should be reiterated that it has been assumed so far that each metal site cannot be occupied by more than one hydrogen molecule. MOFs with metal centers that could be accessed from more than one direction after desolvation might be promising due to the possibility to coordinate two or more H_2 molecules to each site. Some successful synthetic approaches to obtain such structures have been reported: As mentioned in the introduction, the mixed-metal MOF (M'MOF) presented by Chen *et al.* incorporates accessible copper centers into the salen-type linker. (*62*) The high isosteric heat of hydrogen adsorption observed for this system implies that MOFs with metal-containing linkers could be an

interesting alternative to the materials considered here, where the coordinatively unsaturated metal sites are part of the inorganic connectors. Another MOF with highly accessible copper centers in an unusual T-shaped coordination was reported by Eddaoudi and co-workers. (*309*) From the relatively high isosteric heat of hydrogen adsorption measured for this compound (9.5 kJ mol^{-1} at low coverage), it can be postulated that these sites might provide for an increased interaction with the adsorbed hydrogen molecules. Clearly, these rather unusual systems warrant further investigation, using both experimental and theoretical methods.

5.3. Interaction of hydrogen with molecular model systems

5.3.1. Introduction

An accurate, non-empirical calculation of interaction energies requires electronic structure methods. In principle, these methods are able to quantify the interaction strength for a molecule, such as hydrogen, adsorbed in a porous framework (apart from the methodological limitations discussed in section 3.3). However, the size of typical MOF unit cells constitutes a serious limitation to the applicability of *ab-initio* methods, because the computations become very demanding for periodic systems containing many atoms. Nonetheless, periodic boundary conditions have been used in a few computational studies of hydrogen adsorbed in MOFs, *e.g.* in studies of MOFs with open metal sites, (*58, 63*) as well as in the sophisticated applications of the vdW-DFT method reported by Kong *et al.* (*87, 88*)

Due to the computational cost of calculations for periodic systems, the structural regions of interest are often represented by non-periodic fragments, for which the calculations are much less demanding. Inevitably, some accuracy in the description of the system is lost due to the absence of long-range interactions. Moreover, the electronic structure of the fragment may be quite different when compared to the periodic structure. On the other hand, trends depending on the local chemical environment can be evaluated much more easily for molecular systems. To address this issue, several *ab-initio* studies of the interaction of hydrogen with unsaturated metal sites have been published for different representative model systems. (*89–91, 94*)

Another issue that is very relevant to hydrogen storage is the interaction of hydrogen with aromatic systems. In addition to being frequent constituents of MOF linkers, polycyclic aromatic hydrocarbons are a model system for porous carbon materials, which also hold promise for hydrogen storage applications. Due to the dominance of dispersive interactions, most studies have used wave-function based methods (MP2 and beyond). For simple aromatic hydrocarbons, a number of references have already been mentioned in subsection 4.4.4. Further computational investigations have been directed at the interaction with corannulenes and phtalocyanine-like molecules, (*310*) boron-nitrogen and sulfur-containing systems, (*311*) and functionalized (hetero)aromatics. (*312*)

In this section, two different types of model systems are studied using density-functional theory: The first part addresses the interaction of hydrogen with unsaturated copper sites, using a model system that is analogous to the Cu_2 paddle wheel complex used in the previous section. In particular, it is evaluated how chemical modifications of the carboxylate ligand L influence the interaction of hydrogen with the metal center. While a detailed analysis of the bonding is beyond the scope of this study, some conclusions concerning the nature of the interaction are drawn. The second part applies the DFT-D method to evaluate the interaction energy of hydrogen with simple aromatic systems. A comparison with high-quality CCSD(T) data is used for benzene and naphthalene in order to estimate the accuracy of the DFT-D scheme with the chosen exchange-correlation functional. Further calculations assess the interaction with nitrogen-containing six-membered aromatics, and with non-linear

organic molecules that correspond to the organic moiety of the recently synthesized UHM-2, -3, and -4, MOFs that are isostructural to PCN-12. (*313*) Because a variety of systems is studied, the main results are briefly summarized at the end of the section.

5.3.2. Computational details

5.3.2.1. DFT calculations for Cu_2 paddle wheel systems

All-electron DFT calculations were carried out using the DMOL^3 code (*195, 289*) included in the *Accelrys* "Materials Studio" package. (*233*) A DNP basis set was employed in all calculations, and the PBE exchange-correlation functional was used. (*190*) For each of the different $Cu_2(L)_4$ model systems, the geometry of the isolated system was optimized. Where necessary, the symmetry was reduced to obtain two non-equivalent copper centers in order to correctly reproduce the antiferromagnetic coupling. Afterwards, two H_2 molecules were placed above the metal sites in side-on coordination, and a second geometry optimization was carried out for the combined system. In addition to the interaction energy obtained from the difference $E_{int} = E(PDW + H_2) - E(PDW) - 2E(H_2)$, changes in the Cu-Cu distance and the H-H distance with respect to the isolated systems were evaluated. Moreover, a population analysis using Hirshfeld charges was employed to assess how changes of the ligand L affect the charge density at the metal center.

5.3.2.2. DFT-D calculations for organic molecules

All-electron DFT calculations including an empirical dispersion correction were carried out with the ADF code. (*298*) The geometries of the subsystems (hydrogen, organic molecule) were optimized using the BLYP-D functional (*188, 189, 203*) and a triple-zeta basis set with polarization functions (TZ2P). To obtain highly accurate energies, single-point calculations were carried out for the optimized subsystems using the B3LYP-D functional (*191, 203*) and a quadruple-zeta basis set (QZ4P). After combining the two fragments in the desired configuration, a potential energy curve was obtained from single-point calculations for varying distances. The ADF package directly uses the results of the two isolated fragments to calculate the binding energy E_{int} for the combined system. To estimate the accuracy, initial calculations were carried out for benzene and naphthalene, where high-quality CCSD(T) data are available. Here, the performance of three different basis sets was compared (TZP, TZ2P, QZ4P), and the magnitude of the basis set superposition error was calculated employing the counterpoise correction (CP). (*198*) In addition to evaluating the potential energy curves, an energy decomposition analysis was carried out.

5.3.3. Results and discussion: Interaction of hydrogen with Cu_2 paddle wheel complexes

5.3.3.1. Monocyclic and polycyclic aromatic ligands

The first model system considered is the unmodified $Cu_2(bmc)_4$ paddle wheel (figure 5.23). The geometry optimization of the combined system delivers a Cu-H_2 equilibrium distance of 2.40 Å and an interaction energy of -5.88 kJ mol^{-1}. These values are in excellent agreement with the energy minimum of the potential energy curve obtained in the previous section (figure 5.15), showing that the relaxation of the geometry does not significantly change the results. A slight elongation of the Cu-Cu distance is observed, which changes from 2.46 Å for the isolated paddle wheel to 2.48 Å for the combined system. A similar change of the Cu-Cu distance upon hydrogen coordination has been detected experimentally. (*57*) A much more pronounced elongation occurs when more strongly interacting molecules such as water are adsorbed. (*56*) In the optimized DFT geometry, a very slight increase of the H-H bond length with respect to the free H_2 molecule is also observed. However, with 0.003 Å, this value is orders of magnitude lower than typical changes in bond length in Kubas-type metal-H_2 complexes. (*93*) In the following, not only interaction energies E_{int} and Cu-H_2 equilibrium distances $d(Cu$-$H_2)$, but also changes in Cu-Cu and H-H distances upon coordination ($\Delta d(Cu$-$Cu)$, $\Delta d(H$-$H)$) are reported. Moreover, the difference between the Cu-Cu distance of the isolated $Cu_2(L)_4$ system and the Cu-Cu distance of the $Cu_2(bmc)_4$ reference system ($d(Cu$-$Cu)_L - d(Cu$-$Cu)_{bmc}$) is evaluated.

DFT calculations were carried out for $Cu_2(L)_4$ systems with L = monocarboxylate ligands containing two, three, or four isolated aromatic rings (biphenyl, terphenyl, quaterphenyl), and up to four annulated aromatic rings (naphthalene, anthracene, phenantrene, pyrene). The resulting energies and Cu-H_2 distances are reported in figure 5.24a and in table A.20 of the Appendix. For the systems with isolated rings, the interaction energy is nearly equal for all systems, regardless of the number of rings. The structural changes upon hydrogen coordination are also practically identical to those observed for bmc. Figure 5.25 shows that there are no remarkable correlations of the different geometric properties with the interaction energy. For the ligands with annulated rings, the interaction energy decreases with increasing size of the aromatic system, indicating a connection to the degree of electron delocalization. There is, however, no complete correlation with the aromaticity. In particular, the interaction energy for $Cu_2(anthracene$-$mc)_4$ is lower than for $Cu_2(phenantrene$-$mc)_4$, whereas it is known that phenantrene has a higher degree of electron delocalization, both from Clar's empirical rule and from more evolved approaches to define the aromaticity. (*314*)

From the observed energy changes, it could be expected that the size of the aromatic system has a significant impact on the electronic structure of the copper site, thereby influencing the strength of the Cu-H_2 interaction. While a detailed analysis of the electronic structure is beyond the scope of this study, a calculation of the Hirshfeld charge at the copper center for the isolated $Cu_2(L)_4$ system permits an evaluation of changes in the charge density induced

by changes of the ligand (the concept of Hirshfeld charges is briefly explained in subsection 3.3.5). As is visible from figure 5.26a (orange symbols), there is no correlation between the energy and the Hirshfeld charge: The charge density at the Cu atom appears to remain practically unchanged with increasing size of the aromatic system, whereas the interaction energy decreases significantly. This behaviour does not permit a straightforward explanation of the observed trend in the interaction energy. From the results, it can be expected that the introduction of extended aromatic systems in the linker molecule will lead to a decrease of the Cu-H_2 interaction strength. However, further computational studies will be required to elucidate the electronic effects that lie at the origin of this evolution.
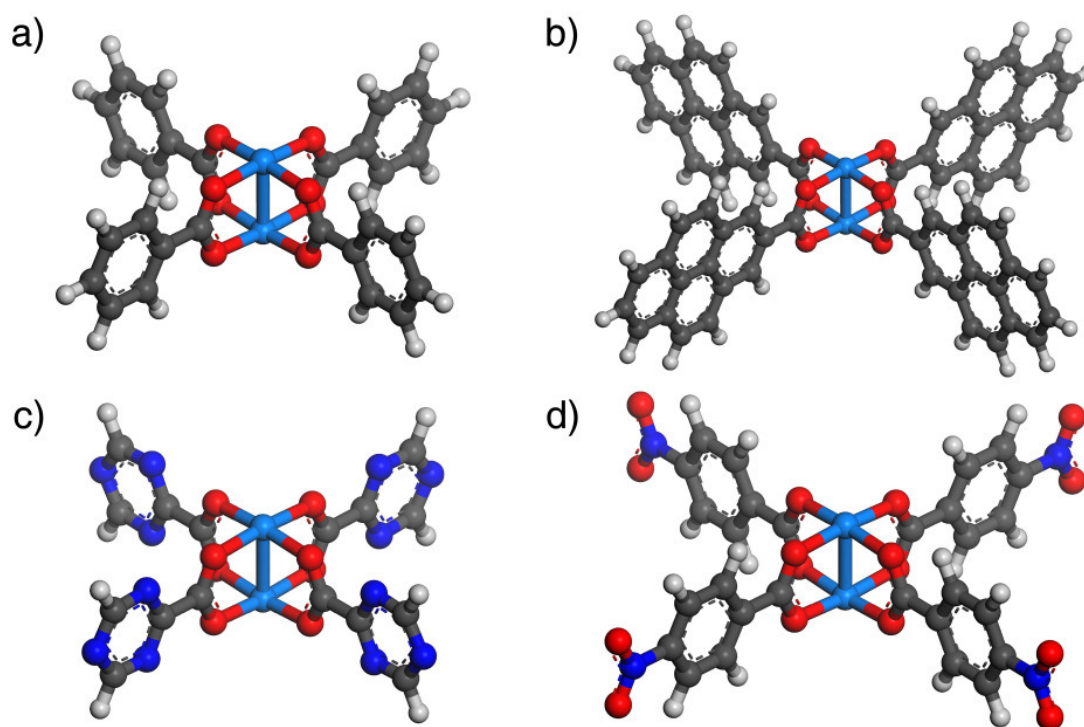
Figure 5.23. Examples of Cu_2 paddle wheels used in DFT calculations. *a)* Unmodified $Cu_2(bmc)_4$ paddle wheel. *b)* Ligand with extended aromatic system: Pyrene-2-carboxylate. *c)* Heteroaromatic ligand: 1,3,5-triazine-2-carboxylate. *d)* Substituted ligand: 4-nitrobenzoate.

5.3.3.2. Heteroaromatic ligands

In order to evaluate the influence of a replacement of carbon by heteroatoms in the ligands, calculations were carried out for $Cu_2(L)_4$ systems with L = monocarboxylate ligands with N-containing six-membered rings (pyridine, pyrazine, 1,3,5-triazine, 1,2,4,5-tetrazine) and five-membered rings (pyrrole, imidazole, 1,2,4-triazole, tetrazole), as well as oxygen- and sulfur-containing five-membered rings (furan, thiophene). The resulting energies and Cu-H_2 distances are given in figure 5.24b/c and in table A.21 of the Appendix. Moreover, the interaction energy is plotted versus different geometric properties in figure 5.25.
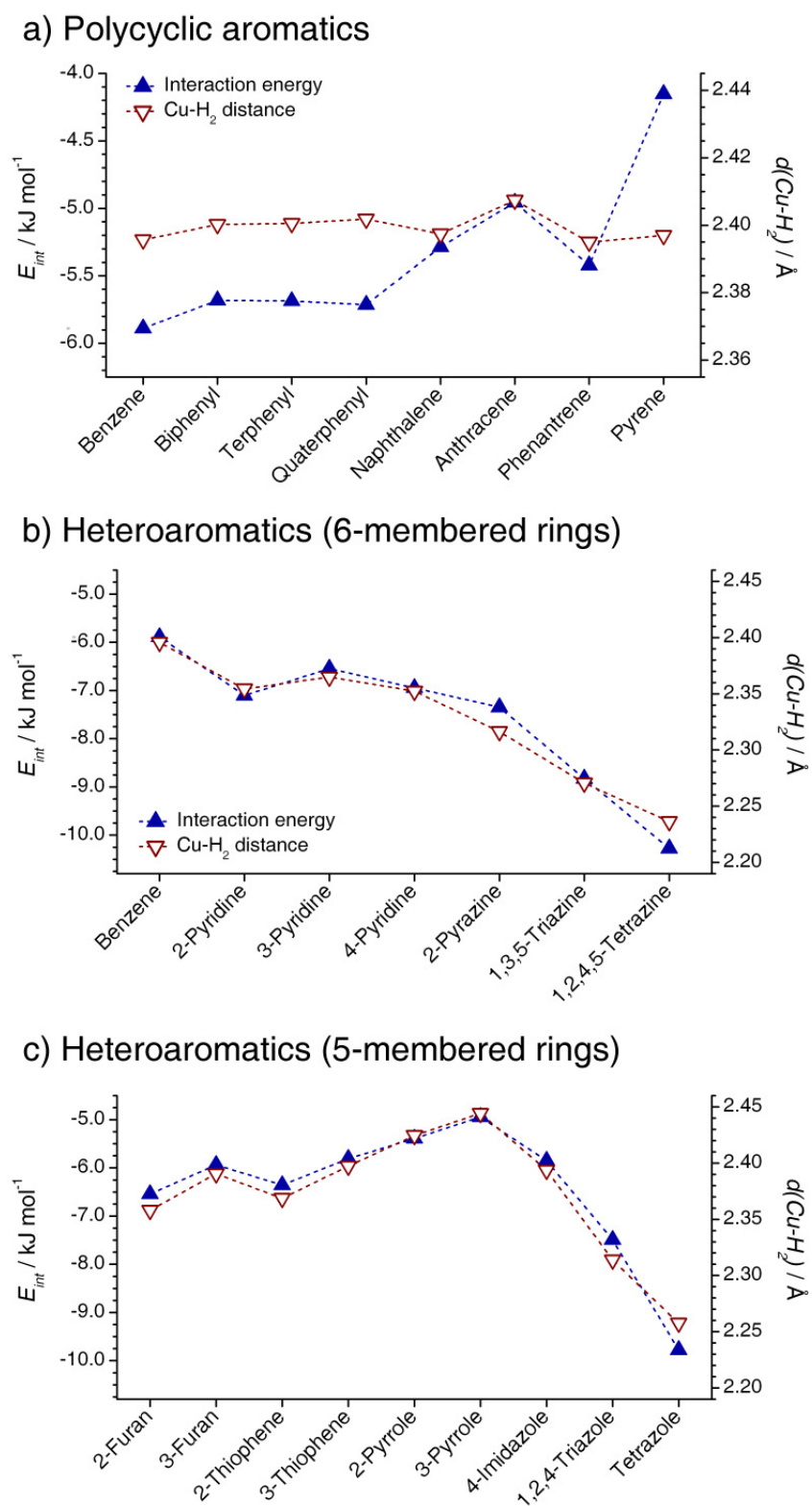
Figure 5.24. Interaction energies E_{int} and Cu-H_2 equilibrium distances $d(Cu\text{-}H_2)$ obtained from DFT calculations for $Cu_2(L)_4$ systems with different monocarboxylate ligands L. *a)* Polycyclic ligands. *b, c)* Heteroaromatic ligands. In each case, the aromatic moiety is given on the horizontal axis. The correlation between the interaction energy and the Cu-H_2 distance is evident.

For the nitrogen-containing systems, there is an apparent trend of increasing interaction energy with increasing number of nitrogen atoms: For the six-membered rings, it ranges from -5.9 kJ mol^{-1} for the bmc ligand to -10.3 kJ mol^{-1} for the tetrazolecarboxylate ligand. In the case of five-membered rings, E_{int} calculated for the pyrrole system is lower than the interaction energy obtained for the bmc reference system, comparable to bmc for imidazole, and higher for triazole and tetrazole. For isomers with the N atom located in different positions, the interaction energy is always highest when the heteroatom neighbours the carbon atom to which the carboxylate group is attached (2-pyridinecarboxylate, 2-pyrrolecarboxylate). In addition to possible changes in the electronic structure, which will be discussed in the following, this effect is probably caused by an increased electrostatic attraction between the negatively polarized heteroatom and the positively polarized ends of the hydrogen molecule: For example, the distance between the nitrogen atom and the H$_2$ molecule is approximately 1.5 Å shorter in 2-pyrrolecarboxylate than in 3-pyrrolecarboxylate, a difference that will have a significant impact on the strength of the electrostatic interactions.

Considering furan- and thiophenecarboxylate, the interaction energies for these systems are approximately 1.0 kJ mol^{-1} higher than for the analogous pyrrolecarboxylates. Comparing the 2- and 3-furan-/thiophenecarboxylates, the same trend as for the pyrrole systems is observed. When systems with different heteroatoms in the same position are compared, it is noteworthy that there is no correlation of E_{int} with the electronegativity of the heteroatom: While oxygen has a higher electronegativity than nitrogen, sulfur has a lower electronegativity. If the electronegativity was the key factor determining the interaction strength, a different evolution of the energies would be expected. Instead, the observed behaviour can be explained with the different magnitude of electrostatic interactions. In the case of pyrrole, part of the electrostatic attraction between the hydrogen molecule and the negatively polarized heteroatom is compensated by the repulsive interaction stemming from the hydrogen atom that is bonded to nitrogen. In contrast to this, the oxygen/sulfur atom in furan/thiophene is accessible, and can directly interact with the hydrogen molecule.

While these explanations based on simple electrostatic considerations can be useful to rationalize the differences between structurally similar systems, the drastic energy increase with increasing number of nitrogen atoms necessitates a more detailed study. In this context, the correlations between structural changes and interaction energy as shown in figure 5.25 are quite enlightening. It can be straightforwardly understood that the Cu-H$_2$ equilibrium distance is shorter for the more strongly interacting systems. The elongations of the H-H bond and the Cu-Cu distance are also correlated with the interaction energy. As mentioned above, these observations are in line with well-known relationships. It is, however, very interesting to note the correlation between E_{int} and the change in Cu-Cu distance with respect to the reference system, Cu$_2$(bmc)$_4$: Those cases where the copper-copper distance is most strongly elongated exhibit the strongest interaction, whereas $d(Cu\text{-}Cu)_L - d(Cu\text{-}Cu)_{bmc}$ is negative for the most weakly interacting systems. Apparently, a weaker interaction between the copper centers, reflected by the elongation of the Cu-Cu distance, enhances the affinity towards coordinated molecules.
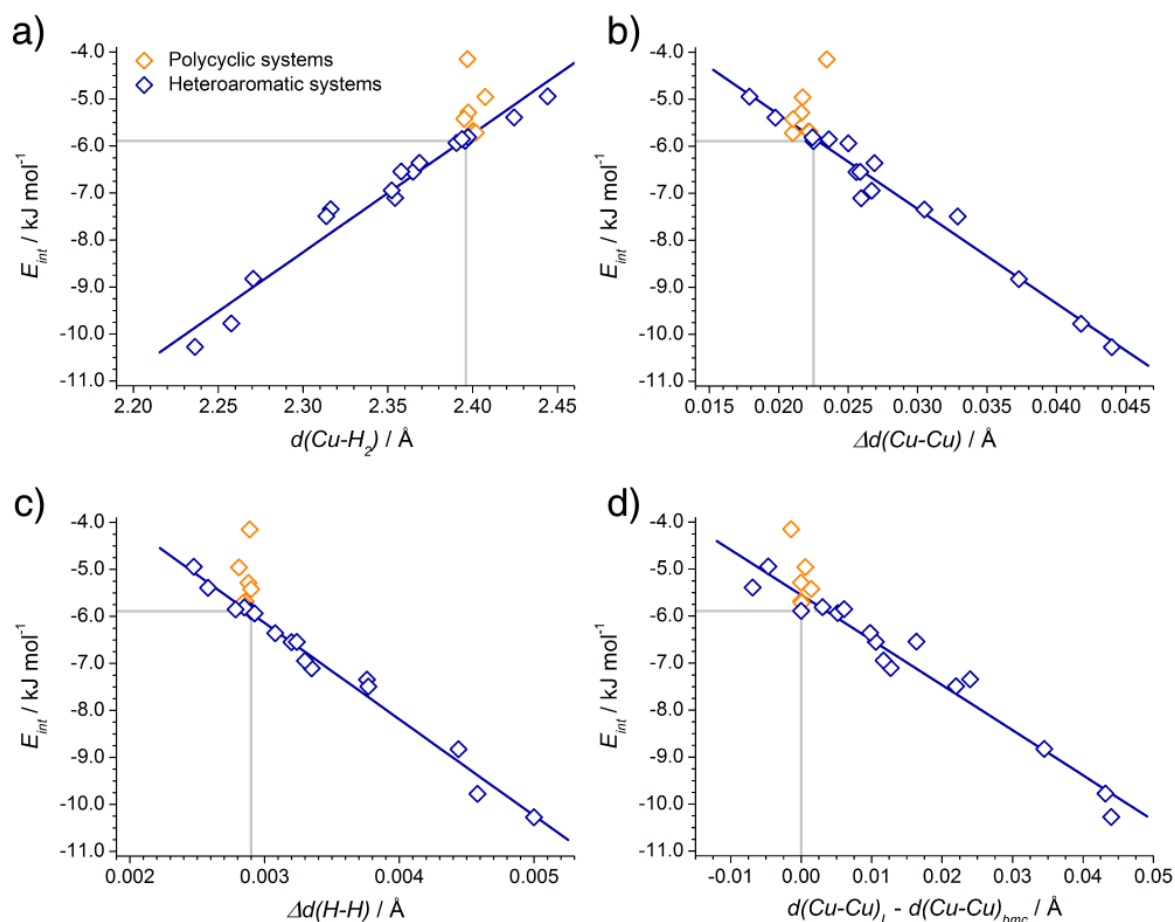
Figure 5.25. Calculated interaction energies for ligands with extended aromatic systems and heteroaromatic ligands, plotted as a function of different geometric properties. For the heteroaromatic ligands, a linear regression was carried out (dark blue line). The grey lines highlight the results obtained for the unmodified $Cu_2(bmc)_4$ system.
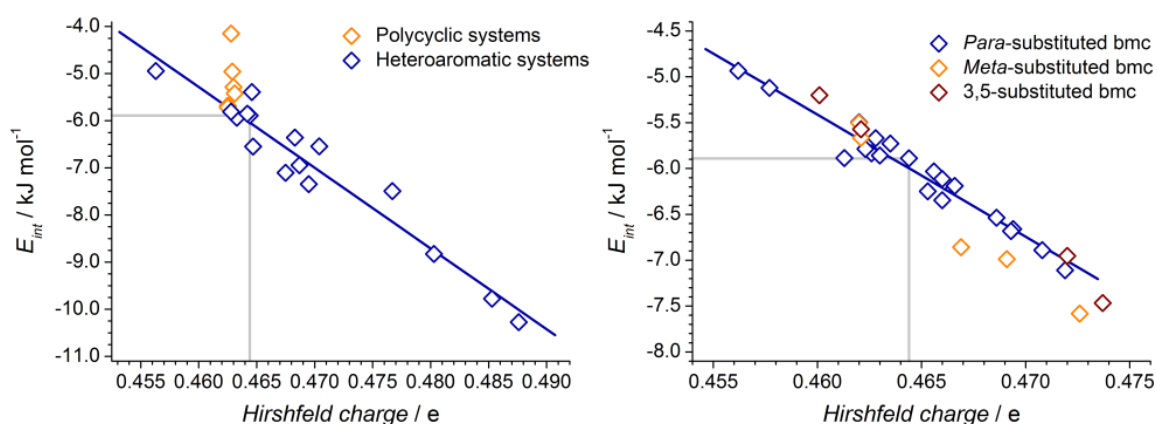
Figure 5.26. Calculated interaction energies, plotted as a function of the Hirshfeld charge at the Cu center. The dark blue lines correspond to a linear regression carried out for the heteroaromatic ligands and for the *para*-substituted ligands, respectively. The grey lines highlight the results obtained for the unmodified $Cu_2(bmc)_4$ system.

To gain more insights into this behaviour, the partial charges on the Cu atom were evaluated. While Mulliken and ESP charges do not show any particular trend, the Hirshfeld charges correlate very nicely with the interaction energy, as shown in figure 5.26. An increased Hirshfeld charge at the Cu atom corresponds to a decreased electron density. Ligands with a larger number of heteroatoms increase the polarity of the Cu-O bond, thereby withdrawing electron density from the copper atom. It can be straightforwardly understood that an increased positive polarization of the copper center tends to weaken the interaction between the copper centers, which is reflected by the observed increase of the Cu-Cu distance for systems with nitrogen-rich ligands.

As far as the Cu-H_2 interaction energy is concerned, the correlation of E_{int} with the Hirshfeld charge is evident: The interaction energy increases in cases where charge is withdrawn from the copper center. This behaviour can be rationalized with an augmentation of electrostatic interactions, because the increased positive charge at the copper center enhances the charge-quadrupole interaction and, moreover, polarizes the charge cloud of the H_2 molecule. On the other hand, the results do not provide any evidence for the presence of significant orbital interactions, *i.e.* Kubas-type metal-hydrogen bonding. Firstly, the observed H-H bond lengths always range well below 0.8 Å, a limiting value that is given by Kubas to distinguish between actual metal-hydrogen bonding and weaker non-covalent interactions classified as "physisorbed H_2". (93) Secondly, if orbital interactions were predominant, a decrease of the electron density at the metal center would lead to a weakening of the metal-hydrogen interaction due to reduced backdonation. As discussed above, the opposite evolution is observed here. Therefore, these results indicate that the main contributions to the copper-hydrogen interaction are Coulomb and polarization interactions, whereas there is no evidence for significant orbital interactions.

5.3.3.3. Substituted ligands

It can be expected that the introduction of different substituents at the ligand will also influence the interaction of hydrogen with the metal center. To assess these changes, DFT calculations were carried out for derivatives of the bmc ligand with 20 different substituents. In the first set of calculations, the substituents were located in the para-position with respect to the carboxylate group. For a subset of five substituents, additional calculations were carried out with one substituent in the meta-position, and with two substituents in both the 3- and the 5-position. The results are given in figure 5.27 and in table A.22 of the Appendix. The correlations with different geometric properties are summarized graphically in figure 5.28. The interaction energies for the systems with the substituent in the para-position range from -4.9 kJ mol^{-1} for 4-dimethylamino-bmc to -7.1 kJ mol^{-1} for 4-nitro-bmc. With respect to the unfunctionalized system, this corresponds to an absolute change of up to 1.2 kJ mol^{-1}, or a relative change of 20%. Because the substituent is located in the para-position, at a distance of approximately 8 Å from the H_2 molecule, it can be expected that the influence of a direct electrostatic attraction is negligible.
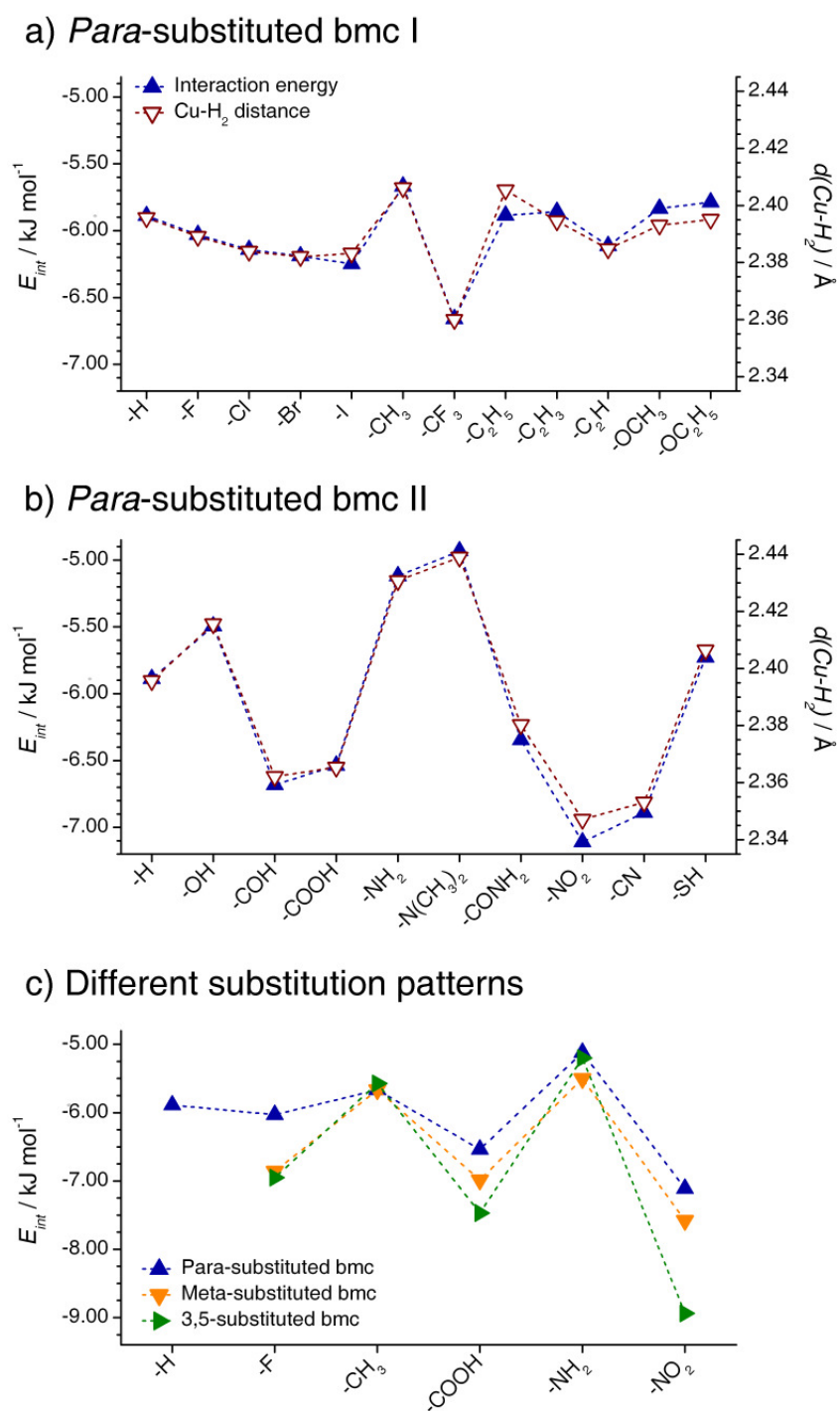
Figure 5.27. *a, b)* Interaction energies E_{int} and Cu-H$_2$ equilibrium distances $d(Cu\text{-}H_2)$ obtained from DFT calculations for Cu$_2$(L)$_4$ systems with different *para*-substituted benzoate ligands L. In each case, the substituent is given on the horizontal axis. For comparison, results for the unsubstituted system are included in both plots. *c)* Comparison of interaction energies for *para*-, *meta*-, and 3,5-disubstituted systems.

Therefore, the changes in energy can be attributed to changes in the electronic structure of the $Cu_2(L)_4$ cluster. This is substantiated by the correlation between E_{int} and the Hirshfeld charge at the copper center, which is shown in figure 5.26. The presence of electron-withdrawing substituents, such as nitro groups, cyano groups, or aldehyde groups leads to a decrease of the electron density at the copper center. As observed above for nitrogen-rich heteroaromatics, this effect increases the interaction energy. On the other hand, electron-donating substituents like dimethylamino or amino groups lead to a higher electron density at the copper atom, and result in a weaker binding. It has been mentioned previously that the opposite is typically observed in Kubas-type metal-H_2 complexes: In these systems, donor ligands tend to increase the interaction strength due to a higher degree of backdonation of electrons from the metal center to the empty σ^* orbital of the hydrogen molecule. (93) Therefore, the results for the substituted ligands provide further evidence for the assertion that the weak interaction between hydrogen and the copper center is dominantly electrostatic, whereas there are no indications for Kubas-type bonding.
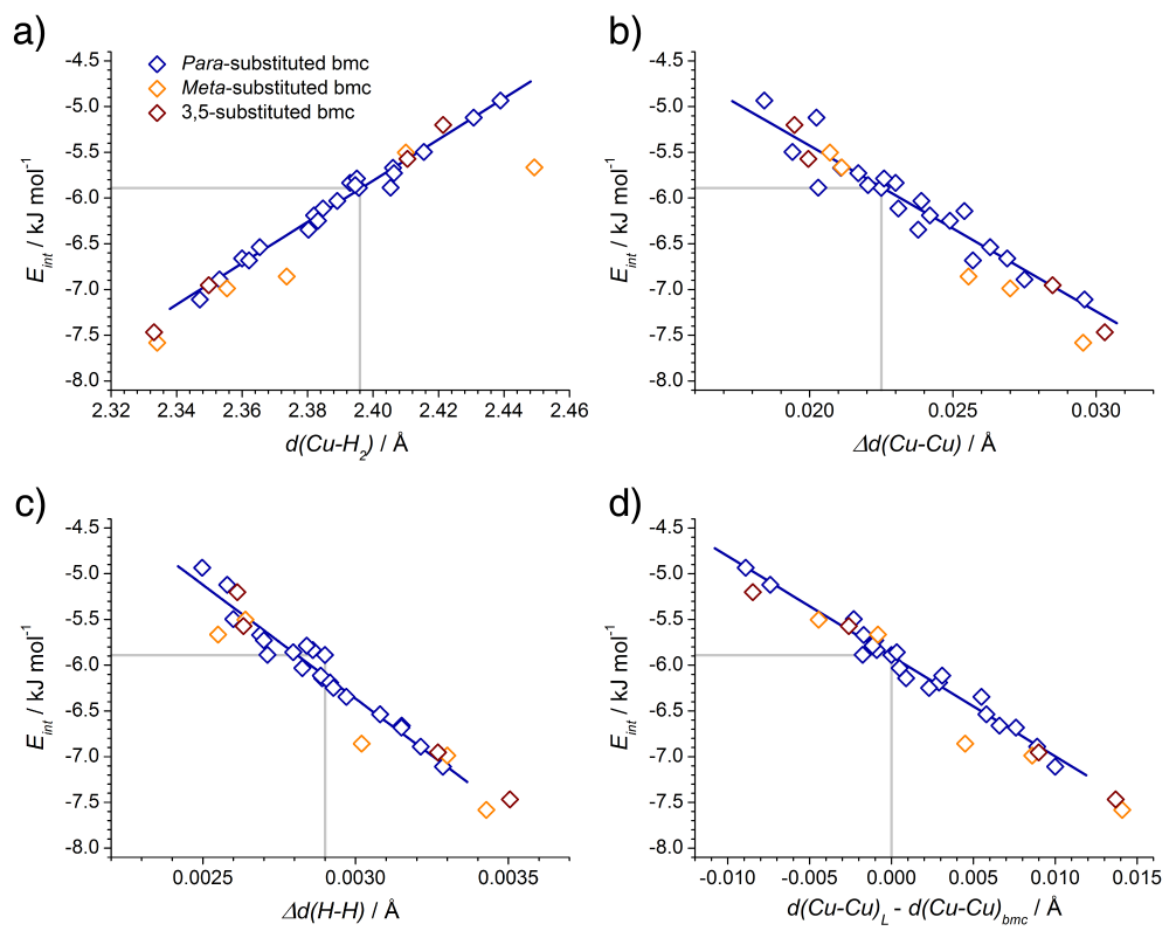
Figure 5.28. Calculated interaction energies for systems with substituted bmc-ligands, plotted as a function of different geometric properties. For the *para*-substituted ligands, a linear regression was carried out (dark blue line). The grey lines highlight the results obtained for the unmodified $Cu_2(bmc)_4$ system. Results for 3,5-dinitro-bmc are outside the plotted energy range.

For the ligands with the substituent in the meta-position, identical trends are observed. For the three electron-withdrawing subtituents that tend to enhance the copper-hydrogen interaction (nitro group, carboxylic acid group, fluorine atom), E_{int} is further increased by 0.5 to 0.8 kJ mol^{-1} with respect to the *para*-substituted system. While the energy change is quite pronounced, the Hirshfeld charges increase only slightly, indicating that the charge density at the copper atom is hardly affected by the position of the substituent. Therefore, the observed changes in the interaction strength are probably mainly due to direct electrostatic interactions of the hydrogen molecule with the substituent. Because the distance between the negatively polarized substituents and the hydrogen molecule is considerably lower than for the *para*-substituted systems, it is reasonable to expect a non-negligible electrostatic attraction. For the other two substituents, the interaction energy does not change in the case of the methyl group, and increases slightly for the amino group.

For the disubstituted systems, the effect of the additional substituent is most pronounced for 3,5-dinitro-bmc. Here, the interaction energy reaches -8.9 kJ mol^{-1}, and thus increases by 1.3 kJ mol^{-1} when compared to the *meta*-substituted system. A similar, although less pronounced evolution is observed for benzene-tricarboxylic acid. The Hirshfeld charges increase accordingly. It is not unexpected that the introduction of a second electron-withdrawing substituent enhances the positive polarization of the copper center. The second substituent has only a very limited impact for the difluoro- and the dimethyl-substituted system, where the values of E_{int} are practically identical to those calculated for the *meta*-substituted ligands. Apparently, the mesomeric (-*M*) effect of the nitro and the carboxylic acid group is dominant, whereas the inductive effect has little influence: Since a fluoro substituent is an electron-withdrawing (-*I*) substituent, whereas a methyl group is an electron-donating (+*I*) substituent, an important contribution of the inductive effect should lead to a qualitatively different behaviour for these two systems. For 3,5-diamino-bmc, the second substituent leads to a decrease of the energy with respect to the *meta*-substituted system, but the interaction is still stronger than for the monosubstituted system with the amino group in para-position.

Taken together, the results show that the functionalization of the ligand permits a tuning of the metal-hydrogen interaction. Electron-accepting substituents increase the interaction energy due to the enhanced positive polarization of the copper center. Although the overall effect on E_{int} is limited, the results from the previous section show that even a modest increase of 1.0 kJ mol^{-1} would have a detectable impact on the hydrogen storage properties, at least at low temperatures. On the other hand, it should not be neglected that the decreased electron density at the aromatic system may lead to a weakening of the interactions of hydrogen with the ring. This effect was quantified by Lochan and Head-Gordon, who carried out MP2 calculations to assess the influence of different substituents on the interaction of a H$_2$ molecule with an aromatic system. (*89*) In this study, it was found that the interaction, which is dominantly dispersive, changes only very slightly (up to 0.3 kJ mol^{-1}) with regard to the unsubstituted reference system. Here, electron-withdrawing substituents tend to reduce E_{int}, whereas electron-donating substituents lead to a slight increase. Because these

changes are relatively minor, it can be expected that the overall effect of electron-accepting substituents, such as nitro or cyano groups, is beneficial: Firstly, they lead to an increase of the metal-hydrogen interaction, as it has been discussed in detail in this section. Secondly, in cases where the substituents are located in a way that they point into the pore of a MOF structure, they will tend to enhance the solid-fluid interaction energy by providing additional dispersive and electrostatic contributions that are due to the direct interaction between the substituent and the adsorbed molecules. Naturally, this effect is not restricted to MOFs with coordinatively unsaturated metal sites, but can occur in all MOFs with substituted linkers. In particular, it may be quite significant with regard to hydrogen storage at ambient conditions, where the long-range interaction potential in the pore is more important than localized interactions.

Comparing the different possible positions of the substituents, *meta*-substituted ligands have a stronger influence on the Cu-H$_2$ interaction than *para*-substituted ligands (*ortho*-substituted systems were not considered, because it can be expected that steric effects will prevent a stable coordination of hydrogen to the metal center), and disubstituted systems provide for higher interaction energies than monosubstituted systems. It would be desirable to derive some implications for the synthesis of novel materials from these results. However, the observations made for non-periodic model systems cannot be directly transferred to real periodic MOFs. In particular, all substituents in the model systems (except the carboxylate group) are non-coordinated. To form a periodic structure, at least one additional substituent must be coordinated to a metal center, and the influence of the substituent on the electronic structure (and, thus, the metal-hydrogen interaction strength) may drastically change upon coordination. To mention one example, it cannot be taken for granted that the presence of a fully coordinated, deprotonated btc linker in Cu$_3$(btc)$_2$ will exhibit the same energy enhancement as the Cu$_2$(btc)$_4$ system with non-coordinated carboxylic acid groups investigated here. Therefore, subsequent computational studies of substituent effects should focus on periodic structures.

While the treatment of coordinated substituents constitutes a special complication, it can be expected that the trends observed here will hold for periodic systems with non-coordinated substituents, such as nitro groups. Unfortunately, there is hardly any experimental data for systems that contain both coordinatively unsaturated metal sites and linker molecules with non-coordinated substituents. For example, both Cu(mip) (mip = 5-methylisophthalate) and Cu(nip) (nip = 5-nitroisophthalate) have been synthesized, but no hydrogen adsorption data have been published. (*315, 316*) Moreover, the two systems are not isostructural. Therefore, the experimental verification of the substituent effects predicted by the DFT computations remains a challenge. In contrast to the scarcity of data on MOFs with both accessible metal sites and substituted linkers, a number of studies that compare isostructural MOFs with different substituents, but without unsaturated metal sites have been reported. For example, it has been shown by Cohen and co-workers that the postsynthetic introduction of aromatic side groups can enhance the affinity towards hydrogen when compared to the parent structure. (*68*) Yaghi and co-workers synthesized IRMOF-type materials with

bdc linkers with various substituents, and with mixtures of different linkers. (*317*) While the influence of small substituents (halogens, amino groups, nitro groups) on the low-pressure H_2 uptake was rather insignificant, bulky substituents led to a considerable increase due to the enhanced solid-fluid interaction in the narrower pores. These observations highlight that the impact of a substituent on the adsorption properties can rarely be explained as being caused by a single phenomenon, but that the total effect is due to a complex interplay of different contributions, such as direct electrostatic and dispersive interactions with the substituent, changes in the pore size, and changes in the electronic structure.

5.3.4. Results and discussion: Interaction of hydrogen with organic molecules

5.3.4.1. Benzene and naphthalene

It has been discussed in section 4.4.4 that the interaction of hydrogen with benzene and polycyclic aromatic hydrocarbons has been particularly well investigated with theoretical methods. For example, high-quality *ab-initio* data have been published by Rubes and Bludský. (*38*, *318*) Because these authors used the CCSD(T) method and an extrapolation to the complete basis set limit, their results can be considered highly reliable. In this section, these data are used as benchmark values to validate the DFT-D calculations.

Initial computations were carried out for the most thoroughly studied model system, which consists of a hydrogen molecule above the center of a benzene ring, with the H-H axis perpendicular to the ring plane. In preliminary calculations, it was found that the B3LYP-D functional provides for the best agreement of the DFT-D equilibrium distance and interaction energy with the CCSD(T) results. With this functional, calculations were carried out using three different basis sets of triple-zeta and quadruple-zeta quality (TZP, TZ2P, QZ4P). The basis set superposition error was estimated from further calculations using "ghost" fragments. (*198*) For all three basis sets, both the uncorrected and the BSSE-corrected potential energy curves are shown in figure 5.30. The calculated equilibrium distance is practically identical for all basis sets, amounting to approximately 2.95 Å. It is not significantly affected by the BSSE correction. For the TZP basis set, the BSSE correction leads to a reduction of the interaction energy by 0.8 kJ mol^{-1} at the equilibrium distance, and thus nearly reaches 20% of the total interaction energy. The use of additional polarization functions in the TZ2P basis set has little influence on the magnitude of the BSSE correction. However, the increased size of the QZ4P basis set leads to a massive reduction of the basis set superposition error: At the equilibrium distance, the BSSE correction reduces the interaction energy by only 0.25 kJ mol^{-1}. These results show that only a relatively negligible effect can be expected from the BSSE correction when a quadruple-zeta basis set is used. Therefore, the QZ4P basis set was used in all DFT calculations reported in the following, but no BSSE correction was applied to avoid tedious additional computations.

In order to assess the accuracy of the DFT-D calculations in comparison to the high-quality CCSD(T) results, three model systems were studied, with the H_2 molecule located in the following positions (figure 5.29): Above the center of a benzene ring (*B1*), above the cen-

ter of one of the rings of a naphthalene molecule (*N1*), and above the central C-C bond of a naphthalene molecule (*N2*). Different orientations of the H_2 molecule were considered, with $H_2 \parallel z$ corresponding to an end-on orientation, and $H_2 \parallel x, y$ corresponding to two different orientations with the molecular axis lying parallel to the ring plane. The resulting potential energy curves are shown in figure 5.30.

It is obvious that the orientation along the z-axis is always the most favourable, with interaction energies ranging from 4.0 to 4.6 kJ mol^{-1}. For the H_2 molecule lying in the xy-plane, the energies are 1.5 to 2.0 kJ mol^{-1} lower. In the case of benzene, the energy barrier for a rotation in a plane parallel to the ring is very low. It is, however, somewhat higher for the *N2* position, an evolution that can be explained with an increase of the repulsion when the H-H axis is oriented parallel to the C-C bond.

A full CCSD(T) energy curve is available only for the system consisting of benzene and H_2 oriented along the z-axis, (*318*) whereas only the equilbrium distance and the energy at this distance have been reported for the other systems. (*38*) Moreover, only the orientations along z and along x were considered in these calculations. In order to enable a direct comparison with the CCSD(T) values, DFT-D equilibrium distances and interaction energies were obtained by fitting a Morse potential to the energy curves displayed in figure 5.30. The comparison is visualized in figure 5.31. It is apparent that the DFT-D method always underestimates the equilibrium distance by 0.15 to 0.2 Å. The interaction energies are underestimated in cases where the H_2 molecule is oriented parallel to the x-axis, and slightly overestimated for orientations parallel to the z-axis. It should be pointed out, however, that the observed deviations in the interaction energies are considerably smaller than the differences between the CCSD(T) values from (*38*) and MP2 interaction energies reported in the same work, with the MP2 energies being usually more than 0.5 kJ mol^{-1} too high. Therefore, the calculations reported here show that the DFT-D method delivers reasonable interaction energies for hydrogen over aromatic systems. Although some quantitative deviations remain, particularly with regard to the equilibrium distance, it can be expected that qualitative trends will be reflected quite well.
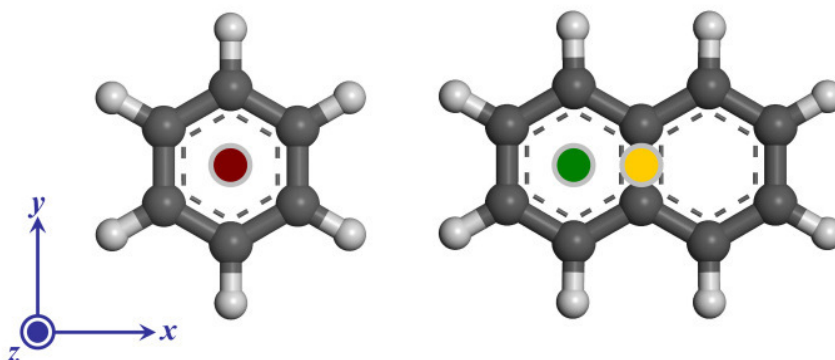
Figure 5.29. Model systems used for comparison of DFT-D results with CCSD(T) results of Rubeš and Bludský. The different positions of the hydrogen molecule are indicated as follows: *B1* = red, *N1* = green, *N2* = yellow.
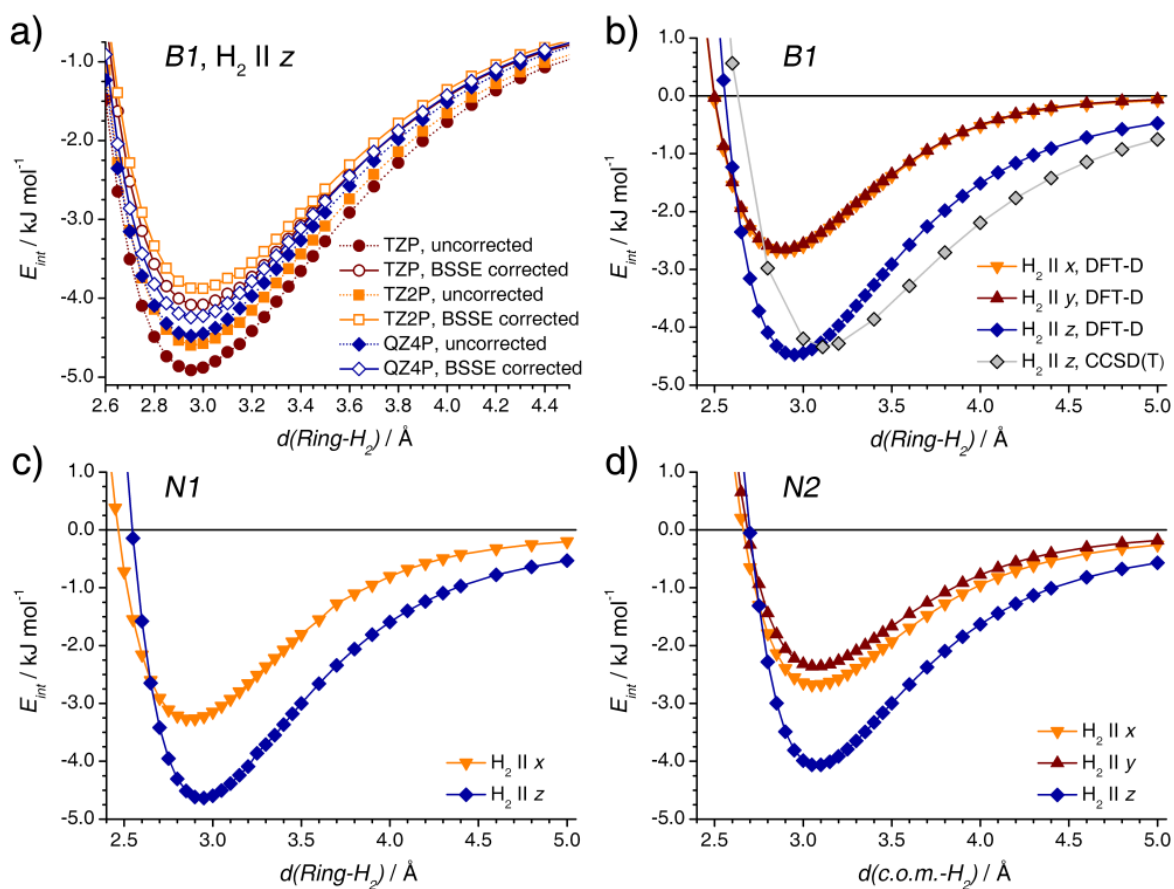
Figure 5.30. Potential energy curves for H_2 interacting with benzene and naphthalene obtained from DFT-D calculations. *a)* Comparison of uncorrected and BSSE-corrected results for benzene with $H_2 \parallel z$, using three different basis sets. *b)* Benzene, CCSD(T) results from Rubes and Bludský shown for comparison. (*38, 318*) *c, d)* Results for naphthalene.
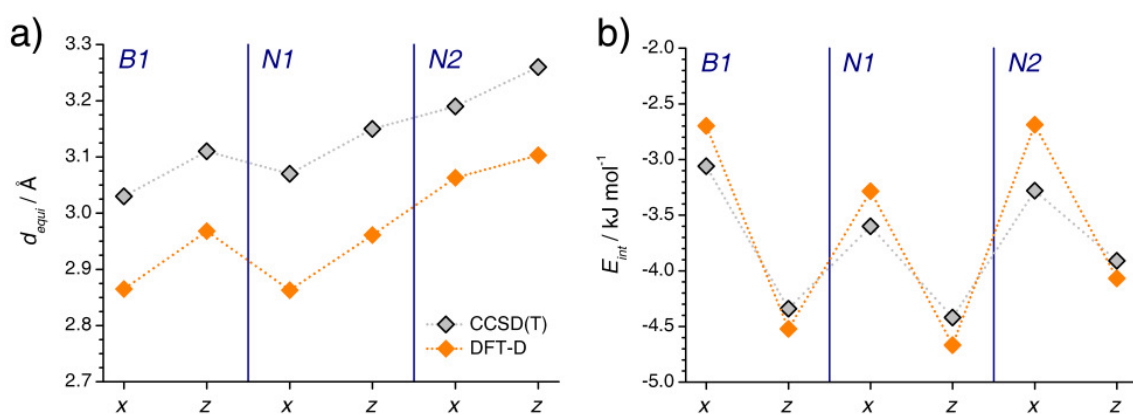
Figure 5.31. Comparison of DFT-D equilibrium distances d_{equi} (left) and interaction energies E_{int} (right) with CCSD(T) results from Rubes and Bludský. (*38, 318*) For each case, the orientation of the H_2 molecule is displayed on the horizontal axis.

Finally, it is worth noting that the energy difference between the orientations perpendicular to the ring and parallel to the ring decreases with increasing size of the aromatic system according to the CCSD(T) results published by Rubeš and Bludský: (*38*) While the energy difference between the two orientations amounts to 1.3 kJ mol^{-1} for benzene, it reduces to approximately 0.8 kJ mol^{-1} for naphthalene, and less than 0.1 kJ mol^{-1} for coronene and an extended graphene sheet. These results are in contrast to the earlier MP2 study of Heine *et al.*: Here, the interaction energies for different orientations of the H_2 molecule were calculated explicitly for benzene, only. (*36*) The authors then used this value as a constant orientation penalty to estimate the orientation-averaged interaction energy for larger polycyclic systems. The more recent results of Rubeš and Bludský, which were, moreover, obtained with a more sophisticated computational method, show that this approximation loses its validity for extended systems. (*38*) The MP2 data of Heine *et al.*, including the assumption of a constant orientation penalty, were employed as reference data in the modification of the C_{aryl} parameters reported in subsection 4.4.4. In the light of the more recent findings discussed above, it could be useful to repeat this procedure, using the CCSD(T) results of Rubeš and Bludský as reference data.

5.3.4.2. Heteroaromatic systems

MOFs with nitrogen-containing linker molecules are ubiquitous. The replacement of carbon by nitrogen in aromatic rings could be a strategy to increase the strength of the interaction with hydrogen, *e.g.* due to the more heterogeneous charge distribution, or by means of a stronger dispersive interaction. While this effect has not yet been studied in detail for MOFs, some experimental studies have investigated the hydrogen storage properties of N-doped microporous carbons. (*26, 27*) The results, however, were somewhat inconclusive.

In order to assess the effect of a replacement of a CH moiety by nitrogen in six-membered aromatic rings, DFT-D calculations were carried out to determine the interaction of hydrogen with the following monocyclic heteroaromatics: Pyridine, pyrazine (1,4-diazine), 1,3,5-triazine, and 1,2,4,5-tetrazine. These systems are visualized in figure 5.32. It is obvious that the reduced symmetry of these molecules leads to complications when detailed information on the potential energy surface is desired: Firstly, the position above the ring center is not necessarily a local energy minimum. Secondly, several orientations of the H_2 molecule in the *xy*-plane could be of interest. Since an exhaustive analysis is beyond the scope of this study, only the orientations along the three coordinate axes were considered to obtain some information on the qualitative trends.

The resulting potential curves are shown in figure 5.33. Moreover, the equilibrium distances and energy minima obtained from a Morse potential fit are summarized in table A.26 of the Appendix. For the orientations in the *xy*-plane, the equilibrium distance slightly decreases with an increasing number of nitrogen atoms in the ring. The most favourable interaction energies are reached in cases where the axis of H_2 molecule points towards the center of an N-N bond (H_2 over tetrazine, oriented along *x*), or towards two N atoms (H_2 over pyrazine,

oriented along y). For all heteroaromatics, the interaction energies for orientations in the xy-plane are higher than for benzene, but the energy changes remain moderate. However, a remarkable evolution is observed for the orientation along the z-axis. While the equilibrium distance remains nearly constant, the interaction energy shows a continuous decrease on increasing number of N atoms, falling from -4.5 kJ mol^{-1} for benzene to -1.8 kJ mol^{-1} for tetrazine.
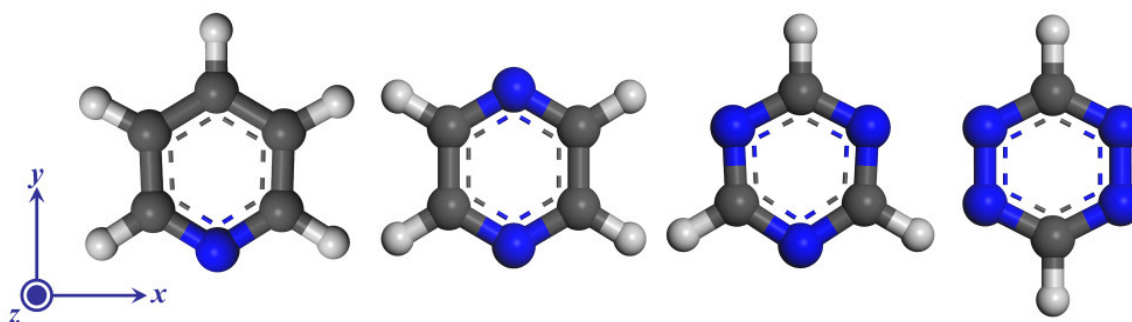
Figure 5.32. N-containing heteroaromatics used in DFT-D calculations: Pyridine, pyrazine, triazine, and tetrazine. Geometries were optimized using the BLYP functional.

To shed some light on this evolution, an exemplary energy decomposition analysis (EDA) was carried out for the DFT-D results obtained for benzene and triazine, with H$_2$ ∥ z, *i.e.* an end-on orientation of the hydrogen molecule. The results are shown in figure 5.34. An important general observation is the fact that the binding between the hydrogen molecule and the aromatic system is (practically) exclusively due to dispersive interactions: If the E_{disp} term is subtracted, the B3LYP energy curve is completely repulsive in the case of H$_2$ over triazine, and exhibits a very shallow minimum for H$_2$ over benzene. This is in line with the observation that the B3LYP functional, unlike many other XC functionals, does not give spurious binding for dispersion-bound systems. (*201*) The E_{disp} terms obtained for the two systems show a very similar evolution, with the dispersion energy being approximately 0.4 kJ mol^{-1} higher for benzene. The repulsive E_{Pauli} term is reduced for triazine, but this is partly compensated by a weaker attractive orbital (and polarization) interaction (E_{orb}). The most significant differences, however, are observed in the electrostatic interaction energy E_{elstat}. At the equilibrium distance, the electrostatic interaction is approximately 2.5 kJ mol^{-1} stronger for benzene than for triazine. This result indicates that the reduction of electrostatic effects is the main cause for the observed decrease of the total DFT-D energy for the nitrogen-containing systems. From a qualitative point of view, this electrostatic contribution can be understood as the interaction between the positively polarized end of the H$_2$ dumbbell, which approaches the ring in end-on orientation, and the negatively charged π-electron cloud above the ring. Because triazine has a different charge distribution, with a negative charge accumulation at the nitrogen atoms, rather than above the ring plane, the attractive electrostatic interaction for a hydrogen molecule located above the ring center in end-on orientation decreases. Although the EDA has been carried out for triazine only, this
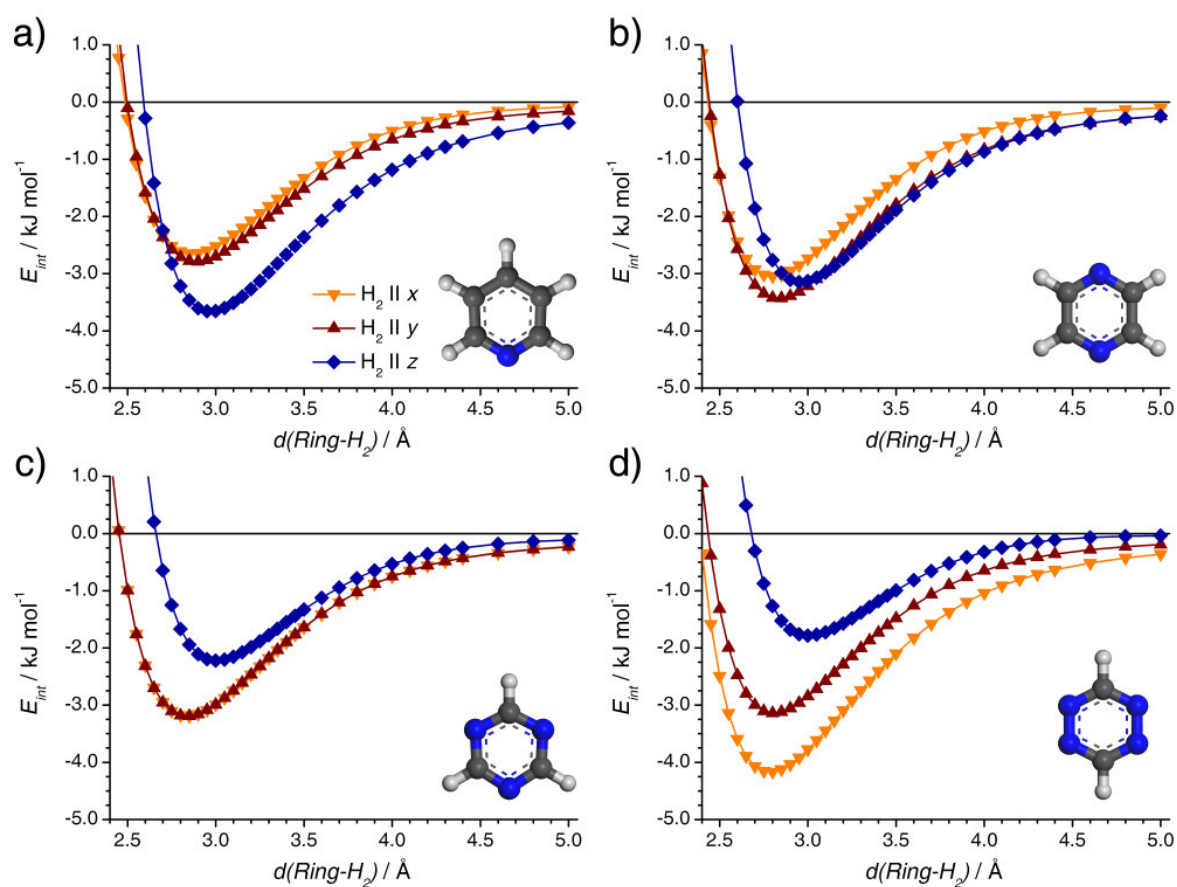
Figure 5.33. Potential energy curves for H_2 interacting with N-containing heteroaromatics obtained from DFT-D calculations, given in the order of increasing number of heteroatoms.
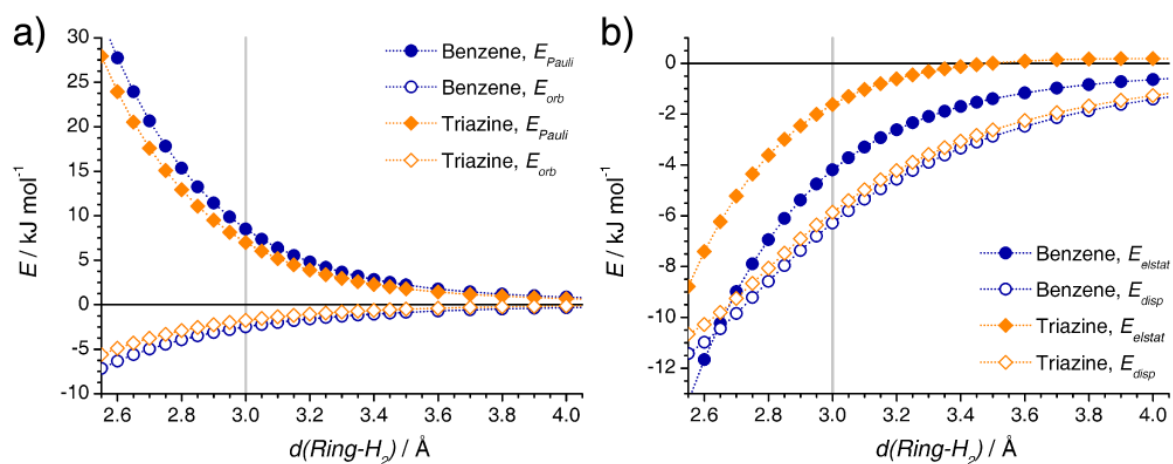
Figure 5.34. Results of energy decomposition analysis for H_2 over benzene and triazine, with $H_2 \parallel z$. *a)* Contributions of Pauli repulsion and orbital interactions. *b)* Contributions of electrostatic and dispersion interactions. The vertical grey lines correspond to the approximate equilibrium distance of 3.0 Å.

interpretation can be transferred to the other N-containing heteroaromatics. While the two side-on orientations are not studied in comparable detail here, similar electrostatic considerations can also serve to explain the increase of the interaction energy from benzene to tetrazine for $H_2 \parallel x$: Taking tetrazine as an example, the positively polarized ends of the H_2 point towards the bonds connecting the negatively polarized nitrogen atoms, thereby maximizing the electrostatic attraction. There is no comparable contribution for benzene, where the negative charge is delocalized above the ring.

It has been discussed previously that the hydrogen molecule retains its rotational degrees of freedom under physically relevant storage conditions. (*218*) Therefore, the interaction energies obtained above for the different orientations should be averaged in order to estimate the mean interaction of hydrogen with the aromatic molecule. Somewhat disappointingly, these averaged interaction energies are very similar, ranging from -2.9 kJ mol^{-1} for triazine to -3.3 kJ mol^{-1} for benzene. Thus, the DFT-D computations do not provide any evidence that the replacement of phenyl moieties by N-containing heteroaromatic linkers would have a favourable energetic effect as far as the interaction of the H_2 molecules with the aromatic system is considered.

As a final remark, it must be pointed out that this result cannot be generalized to other positions of the hydrogen molecule with respect to the ring. For example, it can be expected that a H_2 molecule which approaches the aromatic system from the side will interact more strongly with a nitrogen atom when compared to a CH moiety, firstly due to increased electrostatic interactions with the negative charge accumulated at the heteroatom, secondly because there is no proton attached to the ring that causes additional steric repulsion. To mention one example from previous computational studies, MP2 computations performed by Negri and Saendig revealed a particular stabilization of hydrogen at the "edge" site of pyridine (*i.e.* lying in plane with the ring, pointing towards the N atom), whereas the interaction for a position above the ring, $H_2 \parallel z$, was weaker than for benzene. (*312*)

Experimentally, it is quite difficult to show unequivocally whether the incorporation of nitrogen atoms into the aromatic systems of MOF linkers has a beneficial effect on the hydrogen storage properties. As mentioned previously, the synthesis of isostructural MOFs with different aromatic moieties can be challenging, as even small changes of the linker molecule may lead to different framework topologies. In the case of nitrogen-containing aromatics, the capability of nitrogen atoms to coordinate to the metal centers (which is observable, for example, in ZIF-8 and Zn(dtp)) adds further complexity to the problem.

5.3.4.3. Model systems of non-linear linkers

It has been discussed in section 4.3 that the non-linearity of the mdip linker, which assumes two different conformations, is responsible for the complex topology of the resulting framework PCN-12. (*264*) Subsequently to the publication reporting PCN-12, three isostructural MOFs termed UHM-2, -3, and -4 were synthesized. (*265*, *313*) Compared to the 5,5'-methylene-diisophthalate linker of PCN-12, the linker molecules of these MOFs differ in two respects: Firstly, the two hydrogen atoms attached to the central atom are replaced by methyl groups. Secondly, linker molecules with the following central atoms X were synthesized: Carbon (the corresponding MOF being UHM-2), silicon (UHM-3), and germanium (UHM-4). The idea of the synthesis of these different MOFs was the assessment of the central atom's influence on the hydrogen uptake. In particular, it was expected that the increased polarizability of the heavier central atoms leads to a stronger dispersive interaction with adsorbed molecules. However, the differences observed in the experimental hydrogen adsorption isotherms were related mainly to sample quality issues, which is why definitive conclusions concerning the influence of the central atom are yet lacking. (*313*)

To complement the experimental work, DFT-D calculations were carried out to evaluate the interaction of hydrogen with the C_{2v} conformers of three model systems as representatives of the MOF linkers: Dimethyldiphenylmethane (abbreviated as dmdpm, more correctly termed 2,2-diphenylpropane), dimethyldiphenylsilane (dmdps), and dimethyldiphenylgermane (dmdpg). Exemplarily, dmdps is shown in figure 5.35, together with some key geometric properties of the three molecules. Because a complete screening of the potential energy surface is beyond the scope of this study, only an approach of the hydrogen molecule along z (axis of rotation) from either side of the C_{2v} conformer was considered. Sets of calculations were carried out for orientations of the H_2 molecule parallel to the three coordinate axes (figure 5.36), varying the distance to the central atom X (X = C, Si, Ge) from 3 to 6 Å.

X = C
$d(C_c\text{-}C_{ph}) = 1.559$ Å $\alpha(C_{ph}\text{-}C_c\text{-}C_{ph}) = 108.5°$
$d(C_c\text{-}C_{me}) = 1.556$ Å $\alpha(C_{me}\text{-}C_c\text{-}C_{me}) = 105.3°$

X = Si
$d(Si\text{-}C_{ph}) = 1.902$ Å $\alpha(C_{ph}\text{-}Si\text{-}C_{ph}) = 111.0°$
$d(Si\text{-}C_{me}) = 1.899$ Å $\alpha(C_{me}\text{-}Si\text{-}C_{me}) = 109.9°$

X = Ge
$d(Ge\text{-}C_{ph}) = 1.995$ Å $\alpha(C_{ph}\text{-}Ge\text{-}C_{ph}) = 110.5°$
$d(Ge\text{-}C_{me}) = 1.998$ Å $\alpha(C_{me}\text{-}Ge\text{-}C_{me}) = 110.6°$
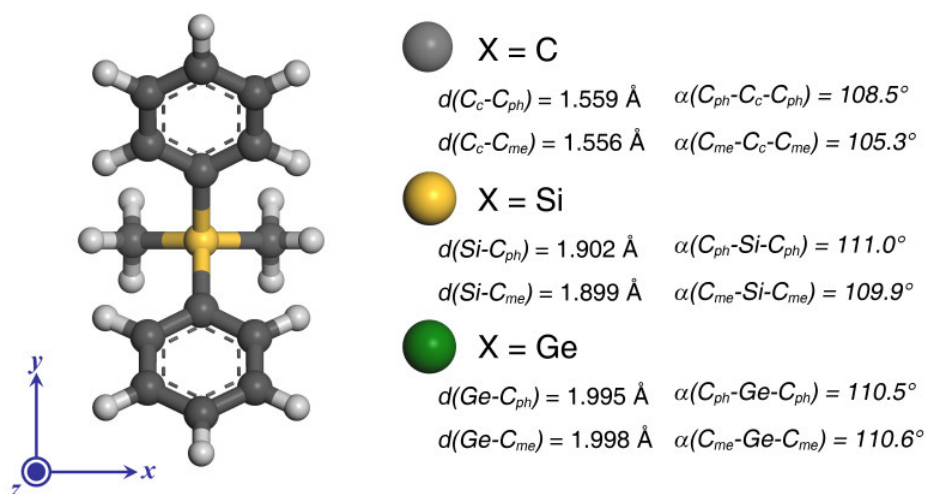
Figure 5.35. C_{2v} conformer of dimethyldiphenylsilane, together with the reference coordinate system. Some key geometric properties (bond lengths d and angles α around the central atom) are given. C_c = central carbon, C_{ph} = phenyl carbon, C_{me} = methyl carbon.
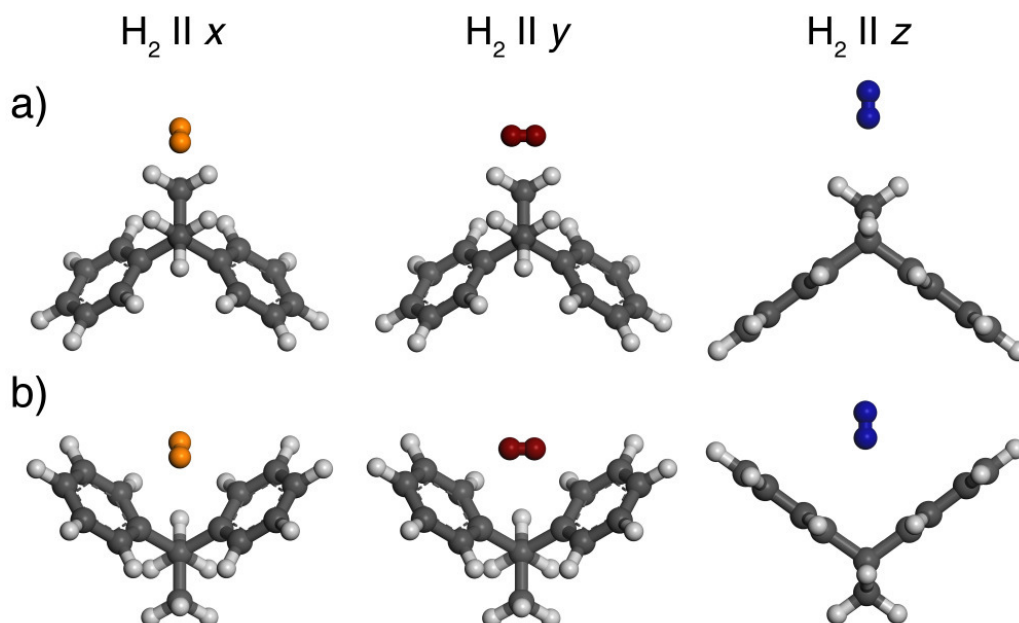
Figure 5.36. Different orientations of the hydrogen molecule with respect to dimethyldiphenylmethane considered in the DFT-D calculations. *a)* Approach from the side of the methyl groups. *b)* Approach from the side of the phenyl rings.

The resulting potential energy curves for an approach of the hydrogen molecule from the side of the methyl groups are shown in figure 5.37. For all three orientations, there is a clear tendency of increasing interaction energy and decreasing equilibrium distance on increasing atomic number of X. In all cases, the calculated interaction energies are low, ranging between -0.75 and -2.2 kJ mol^{-1}. The orientation parallel to the *z*-axis is the energetically favoured orientation, because the steric repulsion caused by the methyl hydrogens is minimized in this case.

To gain some insights into this behaviour, an energy decomposition analysis was carried out for H$_2$ ∥ *z* (figure 5.37). It could be expected that the increase of E_{int} is related to the stronger dispersive interaction with the central atom. However, the EDA reveals that the values of E_{disp} are practically identical for all three systems, and that orbital and electrostatic interaction are even slightly stronger for X = C in comparison to the other two systems. The determining factor, however, is the Pauli repulsion. Due to the increase of the bond length $d(X\text{-}C_{me})$ and the angle $\alpha(C_{me}\text{-}X\text{-}C_{me})$ with increasing atomic number of X, the distance between the H$_2$ molecule and the methyl groups increases in the order *C < Si < Ge*. The magnitude of these geometric changes can be quantified by considering the distance between the two methyl carbons: As it is shown in figure 5.38, the $C_{me}\text{-}C_{me}$ distance increases significantly with increasing atomic number of the central atom. Due to this increase, the Pauli repulsion between the methyl groups and a hydrogen molecule approaching the central atom decreases due to a reduced overlap of the electron clouds. The reduction of the repulsive term leads to a better accessibility of the central atom, which is reflected by a shift of the equilibrium distance to lower values, as well as a concurrent increase of the total

interaction energy. For the particular case considered, changes in the molecular geometry of the non-linear molecule have a much more important influence on the interaction with hydrogen than the dispersive contribution of the central atom.
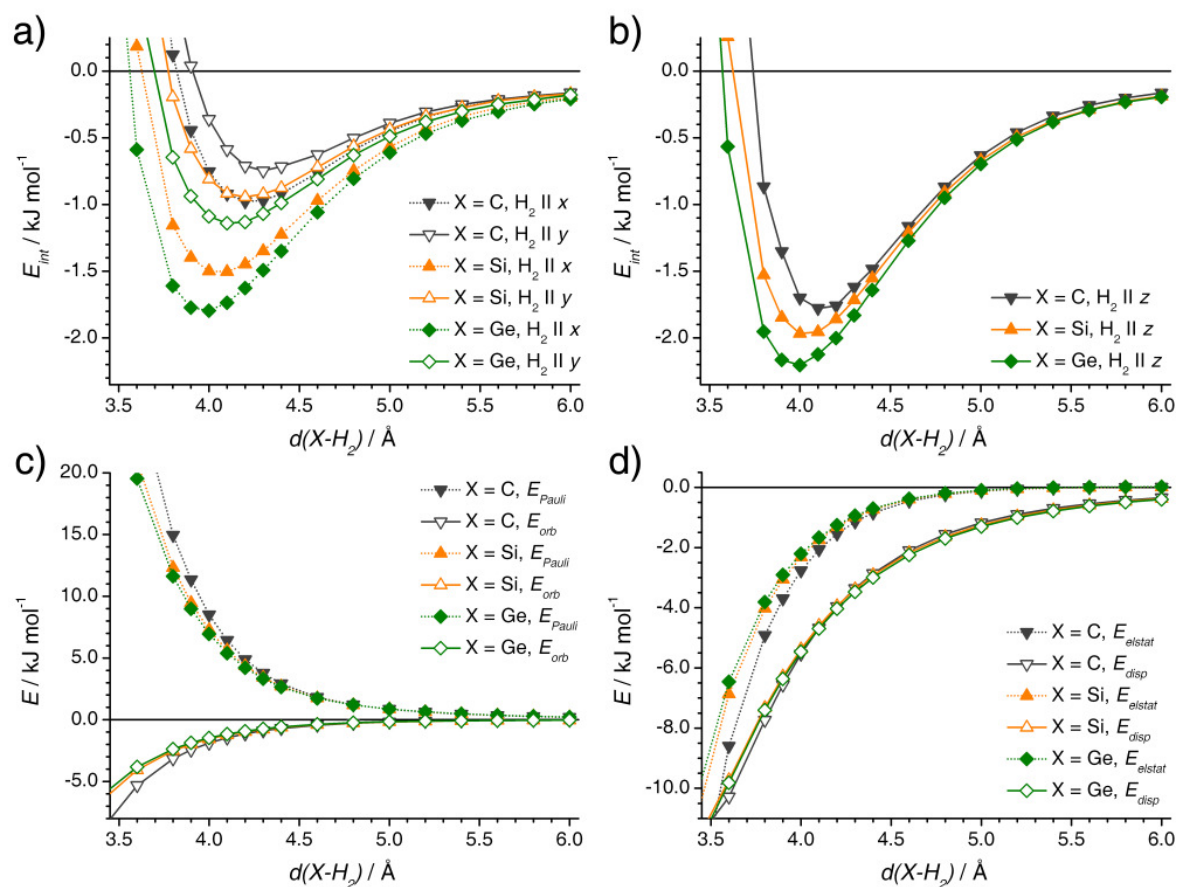
Figure 5.37. *a, b)* DFT-D interaction energy curves for H_2 interacting with C_{2v} conformers of dimethyldiphenylmethane/silane/germane, assuming an approach of the hydrogen molecule along the z-axis from the side of the methyl groups. *c, d)* Results of energy decomposition analysis for $H_2 \parallel z$.
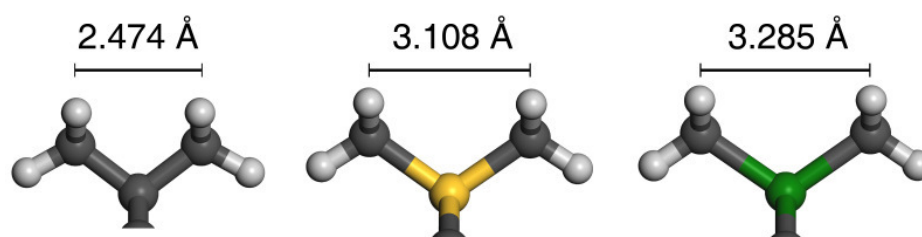
Figure 5.38. Visualization of the interatomic distance between the two methyl carbon atoms for dimethyldiphenylmethane/silane/germane.

The DFT-D results for the approach from the side of the phenyl rings are shown in figure 5.39. Here, the orientations parallel to the y- and z-axis show very similar interaction energies, ranging near -5.6 kJ mol^{-1} for the dmdpm, and between -4.1 and -4.4 kJ mol^{-1} for the silicon and germanium analogues. The interaction energy for the orientation parallel to the x-axis is considerably weaker. For the case of simple aromatic systems, it has been discussed above that the orientation of the H$_2$ molecular axis perpendicular to the benzene ring is most favourable due to electrostatic interactions. Similarly, the orientation parallel to the y-axis is favoured over H$_2 \parallel x$ in this case, because the electrostatic contribution is maximized when the positively polarized ends of the hydrogen dumbbell protrude into the negative charge clouds above the rings. It is interesting to note that the resulting energy curves for the silicon and germanium system are virtually identical. For X = C, the interaction is considerably stronger, and the equilibrium distance is somewhat shorter.
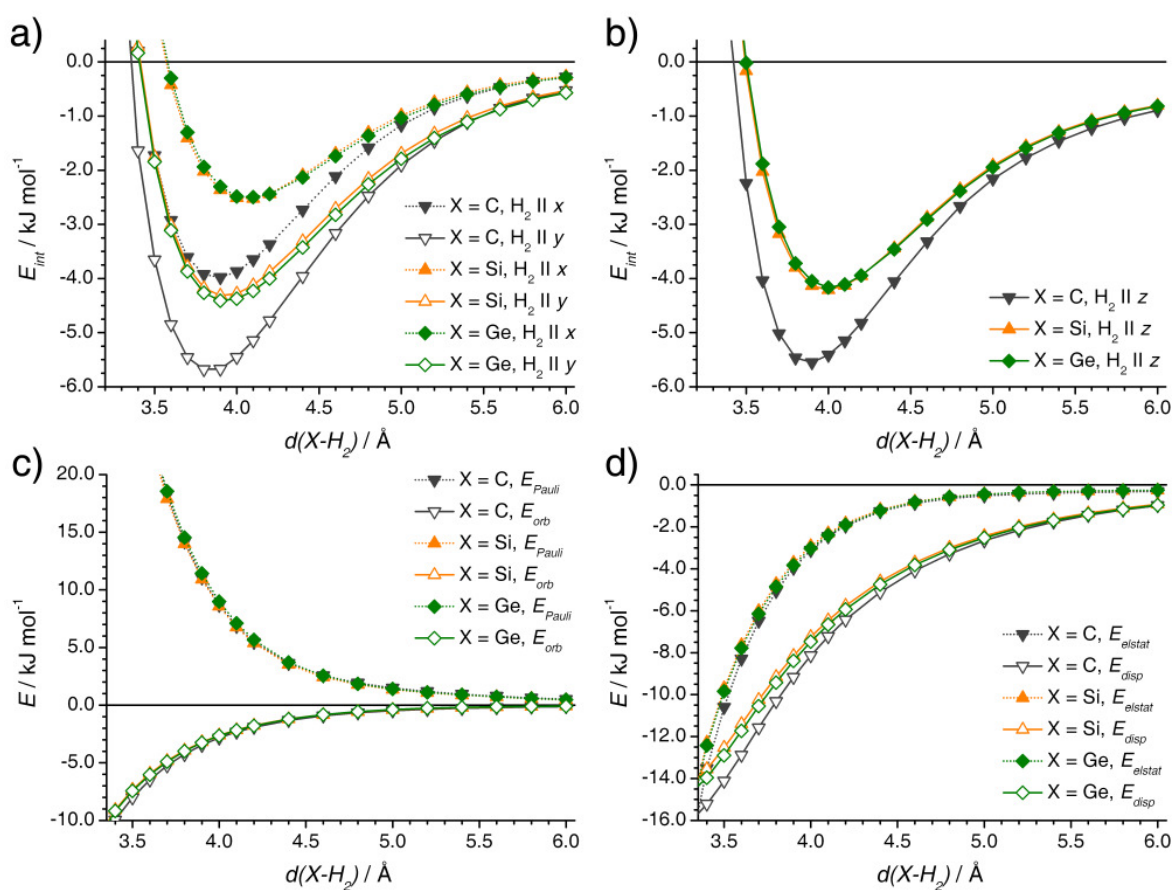
Figure 5.39. *a, b)* DFT-D interaction energy curves for H$_2$ interacting with C_{2v} conformers of dimethyldiphenylmethane/silane/germane, assuming an approach of the hydrogen molecule along the z-axis from the side of the phenyl groups. *c, d)* Results of energy decomposition analysis for $H_2 \parallel z$.

Again, an EDA was carried out for $H_2 \parallel z$ (figure 5.39). The contributions of E_{Pauli}, E_{orb}, and E_{elstat} are very similar, regardless of the central atom. In the light of the results obtained above for an approach of the H_2 molecule from the side of the methyl groups, it is quite surprising that the Pauli repulsion is practically identical for all three systems. From a geometric point of view, the distance between the phenyl carbons bonded to the central atom increases in a similar fashion as the distance between the methyl carbons displayed in figure 5.38, ranging from 2.53 Å for dmdpm to 3.28 Å for dmdpg. Clearly, the observed reduction of the Pauli repulsion arises from the differences in the electron distribution of the moieties attached to the central atom, *i.e.* the reduced bulkiness of the planar phenyl rings when compared to the more spherically shaped methyl groups. In the EDA results, the only pronounced difference is observed in the dispersion interaction, with E_{disp} for dmdpm being considerably larger than for the other systems. Given that the contribution of the central atom increases with atomic number as a consequence of the increased polarizability, this evolution is against the expectations mentioned at the beginning of this section. However, the observation can be rationalized when the geometric differences among the three systems are taken into account: Due to the shorter $d(C_c\text{-}C_{ph})$ bonds and smaller $\alpha(C_{ph}\text{-}C_c\text{-}C_{ph})$ angle in dmdpm, the distances from the hydrogen atoms of the H_2 molecule to the carbon atoms of the phenyl rings are shorter, and lie within a narrower range. This leads to a stronger dispersion interaction, because the atom-atom terms building up the E_{disp} term increase with decreasing distance (for the range of distances considered), and because their cumulative contribution is maximized when the individual distances are as close as possible to the equilibrium distance.

To substantiate this qualitative explanation by quantitative data, the distances from the two H atoms of the hydrogen molecule to the phenyl carbons for a given X-H_2 distance of 4.0 Å are tabulated in table A.29 of the Appendix. The average value of the twelve individual H-C distances is approximately 0.15 Å lower for dmdpm than for the other two systems, and the scatter around this mean value, reflected by the standard deviation, is also considerably smaller ($\sigma = 0.31$ Å for dmdpm, as compared to $\sigma \approx 0.38$ Å for dmdps and dmdpg). The fact that the H-C distances are very similar for the silicon and the germanium analogue are in line with the nearly identical evolution of the interaction energy. In total, the results of the EDA, together with an analysis of the interatomic distances, lead to the conclusion that dispersive contributions stemming from the central atom have only a minor influence on the total interaction energy. Instead, the differences in molecular geometry, particularly the bond length and angles around the central atom, play a crucial role in determining the interaction strength due to the important contribution of dispersive interactions of the hydrogen molecule with the two phenyl rings.

Although it needs to be emphasized that the results presented here are only showcase examples that cannot replace a full screening of the potential energy surface, the two cases considered permit some conclusions on the impact of the central atom of the non-linear linker molecule. Firstly, it is observed that the interaction energy is not necessarily enhanced when the central carbon atom is replaced by heavier elements: E_{int} increases slightly in the order

C < Si < Ge for one position of the H$_2$ molecule, but decreases in the order *C > Si ≈ Ge* for the other position considered. Secondly, a careful analysis of the DFT-D results reveals that the changes in interaction energy are not primarily related to dispersive interactions between the hydrogen molecule and the central atom, but are dominantly caused by changes in the geometry of the non-linear molecule, particularly by differences in the bond lengths and bond angles around the central atom.

In summary, the calculations do not provide any evidence for the assumption that the introduction of a few atoms with high polarizability in a MOF structure will lead to a significant enhancement of the interactions of adsorbed hydrogen molecules with the framework. Therefore, MOFs with organosilicon or organogermanium linkers cannot be considered as particularly promising hydrogen storage materials on the grounds of the computational results obtained in this work. On the other hand, the presence of relatively heavy elements with a high polarizability in the MOF linkers could be of greater use for some other applications: As the strength of the dispersive interactions depends on the polarizability of both the framework atoms and the guest molecules, a beneficial influence can be expected for the storage of more polarizable gases, such as methane (the polarizability of CH$_4$ is approximately three times higher than the polarizability of H$_2$). The separation of gas mixtures could be another potentially interesting field of application for these MOFs. Due to the increased polarizability of the central atom, a stronger variation of the affinity towards the different components of a mixture can be expected, leading to a higher selectivity. A tuning of the selectivity by introduction of highly polarizable elements has been recently demonstrated for aerogels: Here, the presence of "soft" cations such as Sb^{3+} leads to a selective adsorption of polarizable gases, and enhances the CO$_2$/H$_2$ separation efficiency. (*319*)

5.3.5. Section summary

In the first part of this section, standard DFT calculations were employed to assess how a modification of the ligand L influences the interaction of a hydrogen molecule with the copper center of a Cu$_2$(L)$_4$ paddle wheel. While the results could not be interpreted in a quantitative manner due to the inadequate representation of dispersive interactions in the DFT calculations, qualitative trends concerning the influence of the ligand on the Cu-H$_2$ interaction could be established. For ligands containing heteroaromatic rings, as well as substituted aryl ligands, a correlation of the interaction energy with the charge density at the Cu atom was evident. This observation was rationalized as follows: Ligands with a larger number of heteroatoms, or with electron-withdrawing substituents, tend to polarize the Cu-O bond, and the decrease of the electron density at the copper center is reflected by an increase of the Hirshfeld charge. The increased positive charge at the metal center leads to a stronger charge-quadrupole interaction, as well as an increased polarization of the charge cloud of the H$_2$ molecule. On the other hand, the DFT calculations did not deliver any indications for a significant contribution of (Kubas-type) orbital interactions. From these results, the use of linker molecules containing heteroatoms or electron-withdrawing substituents appears

to be a promising strategy to enhance the interaction of adsorbed hydrogen molecules with the metal center, thereby leading to improved H_2 adsorption properties. Moreover, the heteroatoms or substituents could also increase the interaction potential in other regions of the pore by providing additional electrostatic and/or dispersive contributions. In order to verify whether the energetic effects predicted by the calculations are actually observable in experiment, further efforts should be directed at the synthesis of MOFs with heteroaromatic or substituted linker molecules that contain accessible metal sites.

In the second part of this section, it was demonstrated that the DFT-D scheme, which adds an empirical dispersion term, is capable of predicting reasonably accurate interaction energies for hydrogen interacting with simple aromatic hydrocarbons (benzene, naphthalene). However, some systematic deviations with respect to high-quality CCSD(T) results remain. Having shown the applicability of the method, it was investigated how a replacement of CH moieties in the aromatic ring by nitrogen atoms alters the interaction energy. Different trends were observed for different orientations of the H_2 molecule. An EDA for benzene and triazine revealed that this behaviour is mainly due to changes in the charge distribution of the aromatic rings. It was found that the N-containing systems do not provide for an increase of the orientationally averaged interaction energy when compared to benzene.

Finally, the interaction of hydrogen with model systems of non-linear MOF linker molecules incorporating different central atoms (X = C, Si, Ge) were considered. Contrary to initial expectations, it was observed that the interaction energy is not dominantly influenced by the dispersive interaction with the central atom, which should increase with increasing atomic weight of X. The most significant differences in the interaction energy can be rationally explained with changes of the molecular geometry, *i.e.* the bond lengths and angles around the central atom. However, since only two possible configurations were considered, it cannot be ruled out that a different behaviour would be observed for other positions of the H_2 molecule with respect to the non-linear organic molecule. In this context, it is useful to explicitly calculate the dispersive interaction between the hydrogen molecule and X in order to estimate the magnitude of the contribution stemming from the central atom. Due to the simplicity of Grimme's DFT-D approach, this can be done straightforwardly, using equation 3.40 in conjunction with the parameters published in the original paper. (*203*) At a typical X-H_2 distance of approximately 4.0 Å, this contribution amounts to -0.2 kJ mol^{-1} for X = C, -0.6 kJ mol^{-1} for X = Si, and -0.8 kJ mol^{-1} for X = Ge. In some instances, this energy increase may be more pronounced in extended structures, *e.g.* in pores that are surrounded by several organosilicon/organogermanium linkers. Nonetheless, these values show that the impact of dispersive interactions with the central atom on the total interaction energy is only marginal, and that the intricate changes induced by replacing a single carbon atom in the linker molecule by silicon or germanium will not be sufficient to achieve a significant rise of the isosteric heat of hydrogen adsorption. On the other hand, the incorporation of elements with an increased polarizability in the MOF linker could be promising with regard to other applications in gas storage and separation, which involve the adsorption of more polarizable gases, such as methane or carbon dioxide.

5.4. Adsorption-based gas separation in novel microporous materials

5.4.1. Introduction

As it has been discussed in the introduction, the gas separation properties of MOFs and other microporous materials have been intensively investigated, using both experimental and computational methods. However, the majority of these studies have concentrated on relatively few gas mixtures, with a particular emphasis on CO_2/CH_4 separation. In this work, molecular simulations are employed to predict the adsorption selectivity of five different microporous materials (one zeolite, three MOFs, and one porous organic crystal) for mixtures of technological relevance which have been less well studied so far. In addition to the prediction of adsorption selectivities, a detailed analysis of the potential energy distribution in the unit cell is carried out to develop an understanding of the structural features that are most beneficial to reach high selectivities.

The first part of this section addresses the separation of carbon monoxide and oxygen from hydrogen. The removal of CO impurities from the H_2 gas feed is particularly important with regard to the use of proton exchange membrane fuel cells, because even trace amounts of carbon monoxide can poison the platinum catalyst. (*320*) Moreover, CO is a by-product of hydrogen production processes, such as steam reforming, where it is typically removed by pressure swing adsorption. (*9*) While the separation of oxygen from hydrogen is of lesser importance for industrial processes (although its importance may increase when hydrogen generation from water electrolysis becomes more widely used), it is of some interest from a fundamental point of view: O_2 is a weakly interacting molecule with a very small quadrupole moment. Thus, O_2/H_2 constitutes a model system for the separation of a mixture of hydrogen and another weakly adsorbed, non-polar species.

The second part of this section addresses the storage of acetylene, C_2H_2, and its separation from carbon dioxide. Due to its low compression limit, the safe storage of acetylene is technologically important. Typically, C_2H_2 is dissolved in acetone, and stored in a steel cylinder together with a porous filler material. (*247*) Although this technology is well developed, novel porous materials with high C_2H_2 uptake capacities could become an interesting alternative. In addition to storage applications, the separation of acetylene from other gases is also quite important: During acetylene production, it is necessary to remove several by-products. Moreover, an enrichment of acetylene in low-temperature processing plants, particularly air separators, is very hazardous due to the risk of violent explosions. (*247*) As a model system, the separation of C_2H_2/CO_2 mixtures is investigated in this context. This combination of gases is particularly interesting due to the similar fluid properties of acetylene and carbon dioxide, which render an efficient separation difficult. Moreover, the kinetic diameter of the two molecules is practically identical, ruling out size-selective separation. The materials studied were chosen for the following reasons: Mg-formate, Zn(dtp), and cucurbit[6]uril possess relatively narrow channels with similar diameters, but different pore

wall composition. A comparison of these systems might provide some insights concerning the influence of the pore wall chemistry on the separation properties. $Cu_3(btc)_2$ is interesting due to the presence of unsaturated metal sites, which may have a beneficial influence in separations of mixtures where one component interacts more strongly with the metal sites than the other component. Finally, Silicalite is included in order to compare the performance of novel microporous materials with a zeolitic model system. Partly, the choice of materials was also motivated by the availability of experimental data: In the case of Silicalite, Mg-formate, and $Cu_3(btc)_2$, experimental measurements have been reported for four of the five gases [Silicalite: (*97, 321*); Mg-formate: (*269, 322*); $Cu_3(btc)_2$: (*246, 284, 307, 323*)], with the exception of acetylene in the case of silicalite, carbon monoxide in the case of Mg-formate, and oxygen in the case of $Cu_3(btc)_2$. Experimental data for CO, CO_2, and C_2H_2 adsorption are available for cucurbit[6]uril. (*275, 324*) Zn(dtp) is the least well-characterized sytem. Here, adsorption measurements have been reported for three of the gases [O_2, CO_2, and C_2H_2]. (*257*) However, as the measurements were performed under cryogenic conditions, these data are of little use for the validation of the simulation results.

5.4.2. Computational details

GCMC simulations of single-component and mixture adsorption at $T = 298\,K$ were carried out using the SORPTION module included in the *Accelrys* "Materials Studio" package. (*233*) For hydrogen, oxygen, and carbon monoxide (*i.e.* gases that are supercritical at RT), the simulations covered a pressure range from 0.1 bar to 20 bar. In addition to equimolar CO/H_2 and O_2/H_2 mixtures, a molar ratio of 1:9 was also considered. Furthermore, calculations were carried out for a pressure of 1 bar, the composition varying from 19:1 to 1:19. It should be pointed out that actual hydrogen purification, such as the removal of trace amounts of carbon monoxide, involves much more extreme molar ratios. However, these conditions are difficult to model due to the large number of required simulation steps. For acetylene and carbon dioxide, simulations at $T = 298\,K$ were carried out for pressures from 10^{-4} bar to 1 bar. Here, a mixture isotherm for the pressure range from 0.01 bar to 1 bar was computed for the equimolar mixture, only. The dependency of the selectivity on gas phase composition was assessed from additional calculations for a constant total pressure of 1 bar and a mixture composition varying from 19:1 to 1:19.

The simulations of adsorption isotherms involved at least 2.5 million equilibration steps and 5 million production steps. More steps were used for the calculation of mixture isotherms, or in cases when the calculated isotherms indicated insufficient equilibration. The reported uptake values correspond to absolute uptakes, since the contribution of the excess correction is relatively small under these conditions. For a given pressure, the adsorption selectivity α was calculated according to equation 3.20. In addition to the adsorption isotherms, the Henry constants were calculated for all five species for a temperature range from 273 K to 373 K, using at least 50 million insertion steps for each temperature. Finally, high-quality calculations were carried out for a constant loading of one molecule per cell in order to cal-

culate the isosteric heat of adsorption at low coverages. The contributions of dispersive and electrostatic interactions to the total interaction were also derived from the results of these calculations. In addition, three-dimensional plots of the potential energy were created, using a resolution of 0.25 Å.

For the fluid molecules, the force-field parameters and point charges described in section 4.2 were used. Of the various parameter sets proposed for siliceous zeolites, the parameters obtained by Dubbeldam *et al.* were used for Silicalite. This choice will be discussed in the following subsection. For the three MOFs and for cucurbit[6]uril, unmodified parameters from the UFF were employed for the framework atoms. (*157*) In the case of $Cu_3(btc)_2$, a partial modification of the force field was carried out for simulations of CO_2 and C_2H_2 adsorption, which will be described in the subsection dealing with this MOF. In the GCMC calculations, a cutoff radius of 12.5 Å was employed for dispersive interactions, using a cubic spline interpolation to ensure a smooth evolution to zero in the range of the cutoff radius ("Medium quality" setting in SORPTION). Electrostatic interactions were included in all calculations. ESP charges were employed for the framework atoms, and Ewald summation was used to account for the periodicity of the lattice.

The unit cell of $Cu_3(btc)_2$ is sufficiently large to dispense with a supercell. For the other systems, appropriately sized supercells were employed: $2 \times 2 \times 2$-supercells were constructed for Silicalite, Mg-formate, and Zn(dtp), whereas a $1 \times 1 \times 2$-supercell was used for CB[6]. The intramolecular cavity of CB[6], which is expected to be inaccessible for adsorbed molecules, was blocked by a non-interacting sphere to avoid an artificial adsorption inside these cavities.

5.4.3. Silicalite: Performance of different force fields

In contrast to MOFs and other relatively new classes of microporous materials, gas adsorption in zeolites has been studied with computational methods for several decades (see (*278*) for an overview). Numerous parameter sets to describe the zeolite framework atoms have been published. In order to test the suitability of these parameter sets in conjunction with ESP charges for the description of Silicalite, adsorption isotherms of carbon dioxide and oxygen were calculated and compared to the experimental data reported by Dunne *et al.* (*321*) In addition to the LJ parameters provided in the UFF, four parameter sets specifically derived for Silicalite were considered: Hirotani *et al.* (*HI*) employed a fit to experimental argon and carbon dioxide adsorption data in their parameter derivation. (*325*) Similarly, Talu and Myers (*TM*) modified the framework oxygen parameters in order to reproduce the experimental argon adsorption isotherm. (*326*) Pascual *et al.* (*PA*) made use of butane adsorption data in the optimization of their oxygen parameters. (*327*) Finally, Dubbeldam *et al.* (*DU*) determined the parameters by a careful fit to experimental adsorption isotherms of different hydrocarbons. (*328*) It should be noted that silicon is treated as completely noninteracting in three of these parameter sets (*TM, PA, DU*), and interacts only very weakly in the fourth one (*HI*). This approximation is very common.
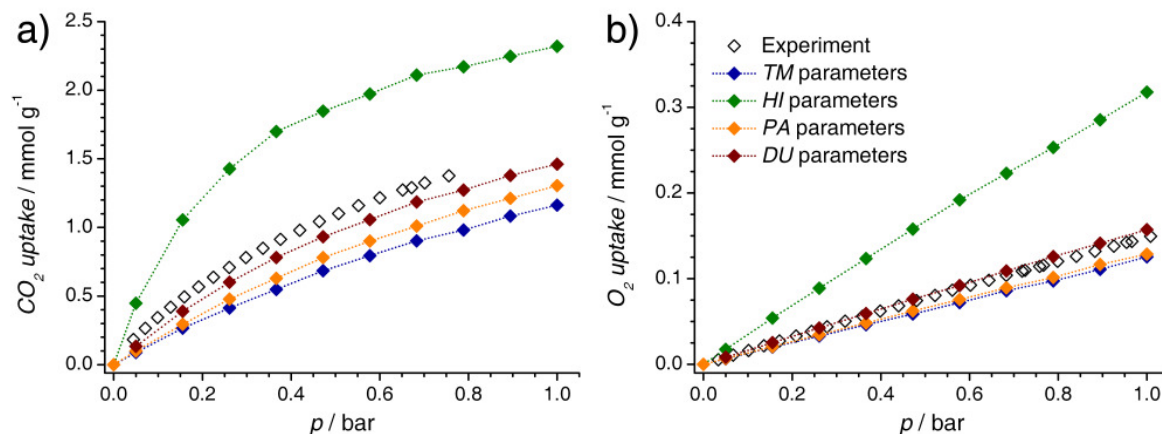
Figure 5.40. Calculated CO_2 (a) and O_2 (b) adsorption isotherms for Silicalite obtained with different parameter sets (see text). Experimental data are taken from (*321*).
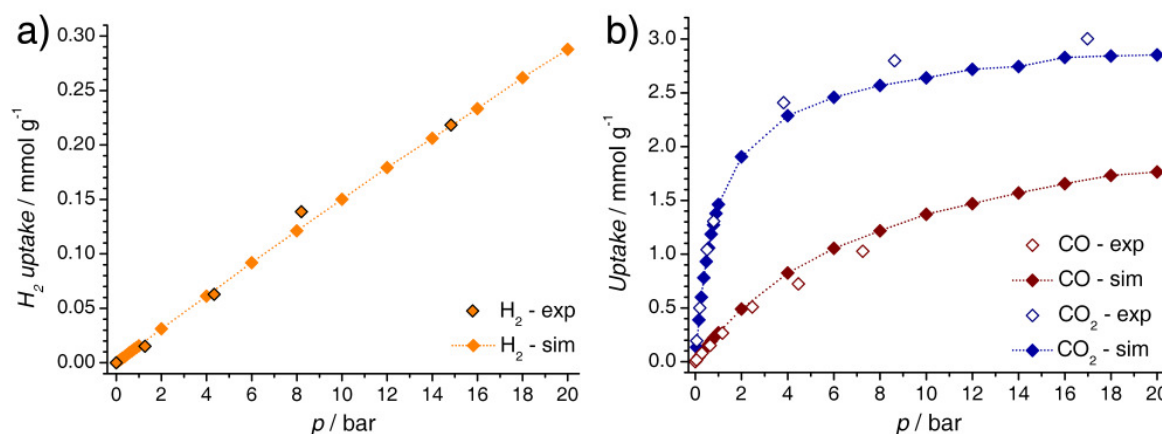
Figure 5.41. Calculated high-pressure H_2, CO, and CO_2 adsorption isotherms for Silicalite obtained with the *DU* parameter set. Experimental data are taken from (*97*).

GCMC simulations of carbon dioxide adsorption at $T = 304\,\mathrm{K}$ and oxygen adsorption at $T = 306\,\mathrm{K}$ were carried out for pressures ranging from 0.05 to 1 bar. The results are shown in figure 5.40. For both gases, the UFF parameters overpredict the amount adsorbed by up to two orders of magnitude, which is why the results are excluded from the figures. Of the four parameter sets designed for zeolites, the *HI* parameters also have a clear tendency to overestimate the adsorption capacity, whereas the *TM* and *PA* parameter sets deliver somewhat too low adsorption capacities. The *DU* parameters lead to the best agreement with experimental data. While a slight underestimation of the adsorption isotherm is observed for carbon dioxide, the predicted amount of oxygen adsorbed is somewhat too high, indicating that there is no systematic error concerning the strength of the solid-fluid interaction. For further validation, high-pressure H_2, CO, and CO_2 isotherms were calculated with the *DU* parameters, and compared to the data of Golden and Sircar, measured at $T \approx 304\,\mathrm{K}$. (*97*) The results are displayed in figure 5.41. For all three gases, good to excellent agreement with experimental data is observed. Therefore, the parameters of Dubbeldam *et al.* will be used in all simulations of gas adsorption in Silicalite reported in the following.

5.4.4. Results: Separation of CO/H$_2$ and O$_2$/H$_2$ mixtures

5.4.4.1. Silicalite

The calculated single-component isotherms show that the zeolite takes up very little H$_2$, whereas appreciable amounts of carbon monoxide and oxygen are adsorbed. The molar uptake of both gases is quite similar, with CO being only slightly favoured. This is also reflected by the calculated isosteric heats (table 5.1). The results correspond reasonably well with the experimental values, which amount to 6.0 kJ mol^{-1} for H$_2$, 16.7 kJ mol^{-1} for CO, and 16.3 kJ mol^{-1} for O$_2$. (*97*, *321*) The role of electrostatic interactions is negligible for all three molecules, contributing only 5% to the total potential energy for carbon monoxide, the most polar molecule. This is in accordance with the experimental observation that Silicalite acts as a non-polar adsorbent. (*97*)

From the results of the Henry constant and mixture isotherm calculations (table 5.2, figures 5.43 and 5.44), it is apparent that the predicted selectivities of Silicalite are modest for both gas mixtures, with $\alpha \approx 20$ for the CO/H$_2$ mixture, and $\alpha \approx 12$ for the O$_2$/H$_2$ mixture. The selectivities do not show any pronounced dependence on pressure or composition, although a slight decrease of the selectivity on increasing pressure is observable for an equimolar CO/H$_2$ mixture.

The calculated potential energy maps for H$_2$, CO, and O$_2$ are displayed in figure 5.45. Sections through the straight channels running along the *b*-axis and the sinusoidal channels running along the *a*-axis are shown. The highest value of the potential energy amounts to approximately -7 kJ mol^{-1} for hydrogen, -18 kJ mol^{-1} for carbon monoxide, and -15 kJ mol^{-1} for oxygen, numbers that are in good correspondence with the isosteric heats of adsorption. For all three species, the potential energy is most favourable in the narrow areas where the channels pass through the rings constituted by 10 silicon and 10 oxygen atoms, whereas it is considerably reduced in the channel intersections. The 10-rings have a minimal diameter of approximately 5 Å, (*271*) which is well above the kinetic diameter of all molecules.
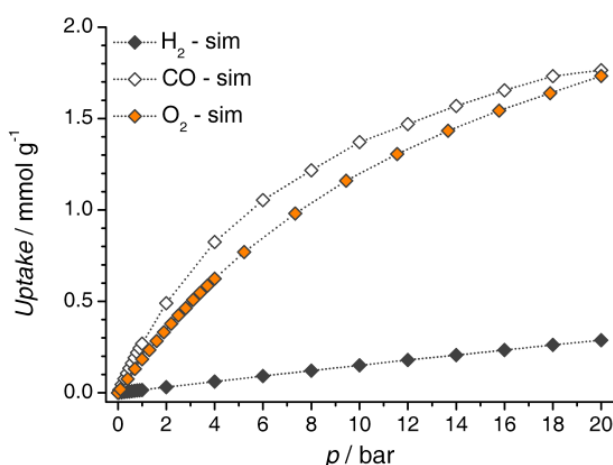
Figure 5.42. Calculated hydrogen, carbon monoxide, and oxygen adsorption isotherms for Silicalite.

Table 5.1. Results of simulations of H_2, CO, and O_2 single-component adsorption: Gas uptakes n (in mmol g^{-1}), isoteric heats of adsorption q_{st} derived at low loading (in kJ mol^{-1}), and relative contributions of dispersive and electrostatic interactions to the total interaction energy.

	Silicalite	Mg-formate	Zn(dtp)	Cu$_3$(btc)$_2$	CB[6]
$n(H_2)$, $p = 1\,\text{bar}$	0.016	0.018	0.025	0.062	0.018
$n(H_2)$, $p = 20\,\text{bar}$	0.29	0.34	0.46	1.16	0.32
$q_{st}(H_2)$	7.1	8.4	7.0	5.7	8.0
$E_{disp}/E_{es}(H_2)$	99% / 1%	92% / 8%	94% / 6%	98% / 2%	97% / 3%
$n(CO)$, $p = 1\,\text{bar}$	0.27	0.56	0.45	0.69	0.45
$n(CO)$, $p = 20\,\text{bar}$	1.76	2.51	2.58	6.85	1.77
$q_{st}(CO)$	17.5	21.8	17.8	18.1	19.2
$E_{disp}/E_{es}(CO)$	95% / 5%	84% / 16%	82% / 18%	61% / 39%	92% / 8%
$n(O_2)$, $p = 1\,\text{bar}$	0.18	0.24	0.21	0.42	0.28
$n(O_2)$, $p = 20\,\text{bar}$	1.73	2.07	2.24	4.68	1.81
$q_{st}(O_2)$	15.0	17.1	14.0	14.6	16.6
$E_{disp}/E_{es}(O_2)$	$E_{es} < 1\%$	$E_{es} < 1\%$	$E_{es} < 1\%$	$E_{es} < 1\%$	$E_{es} < 1\%$

Table 5.2. Comparison of adsorption selectivites α. The Henry's law selectivities and the selectivities derived from binary mixture isotherm calculations (equimolar composition) at two different pressures are given.

	Silicalite	Mg-formate	Zn(dtp)	Cu$_3$(btc)$_2$	CB[6]
$K_H(CO)/K_H(H_2)$	21.1	35.1	21.9	12.7	38.2
$\alpha(CO/H_2)$, $p = 1\,\text{bar}$	21.2	30.5	20.6	12.1	35.0
$\alpha(CO/H_2)$, $p = 20\,\text{bar}$	18.6	31.8	15.8	10.4	23.8
$K_H(O_2)/K_H(H_2)$	11.6	14.0	9.1	7.7	17.7
$\alpha(O_2/H_2)$, $p = 1\,\text{bar}$	11.6	12.2	8.9	7.2	17.6
$\alpha(O_2/H_2)$, $p = 20\,\text{bar}$	11.5	12.1	9.0	5.6	17.8
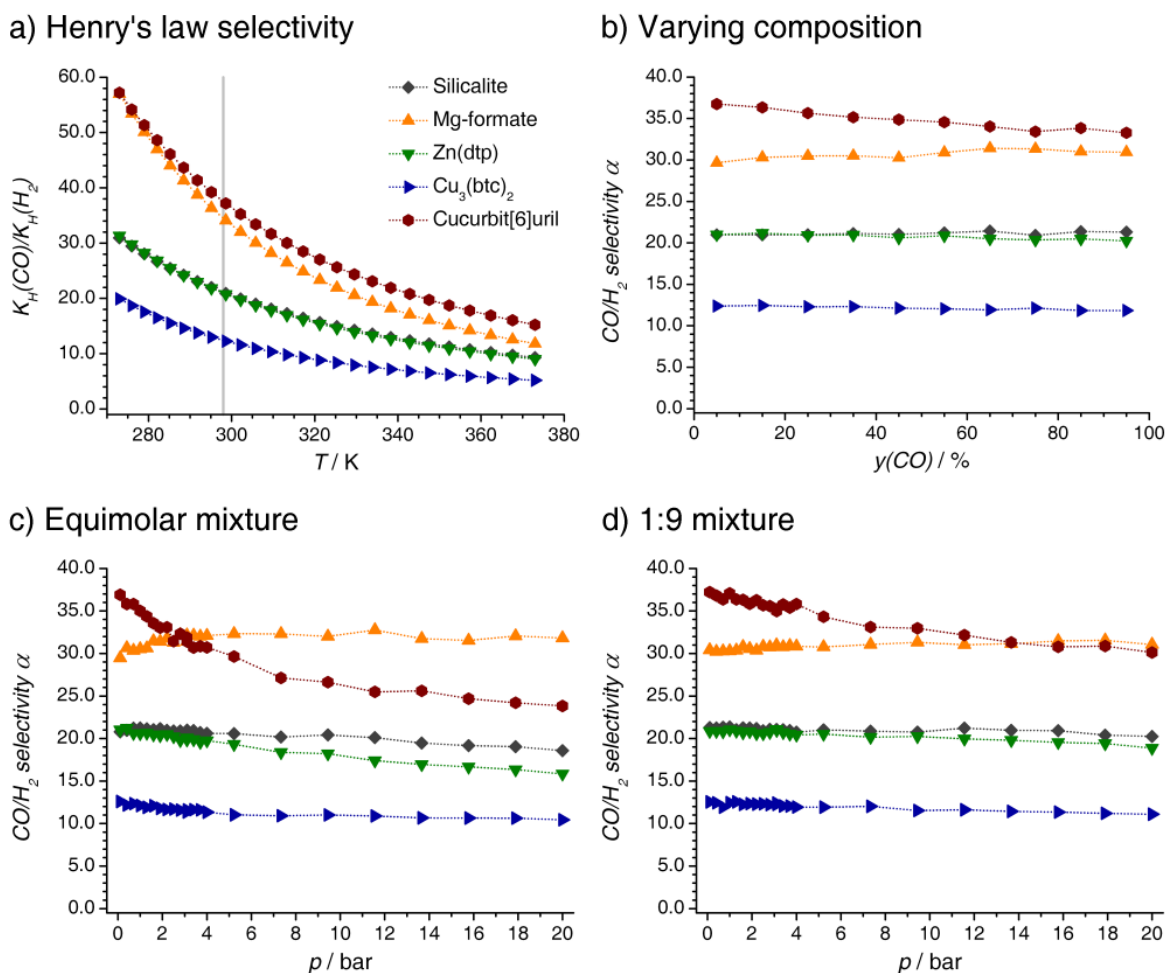
Figure 5.43. CO/H$_2$ selectivity: Summary of results. *a)* Henry's law selectivity. The vertical grey line marks $T = 298$ K. The CO/H$_2$ selectivities of Silicalite and Zn(dtp) are virtually identical over the whole temperature range. *b)* Adsorption selectivities derived from binary mixture isotherm calculations for varying compositions of the gas phase at $p = 1$ bar. The x-axis corresponds to the content of CO in relation to the total pressure. *c)* Adsorption selectivities derived from binary mixture isotherm calculations for an equimolar CO/H$_2$ mixture. *d)* Adsorption selectivities derived from binary mixture isotherm calculations for a 1:9 CO/H$_2$ mixture.

O$_2$/H$_2$ separation: Overview

a) Henry's law selectivity

b) Varying composition

c) Equimolar mixture

d) 1:9 mixture
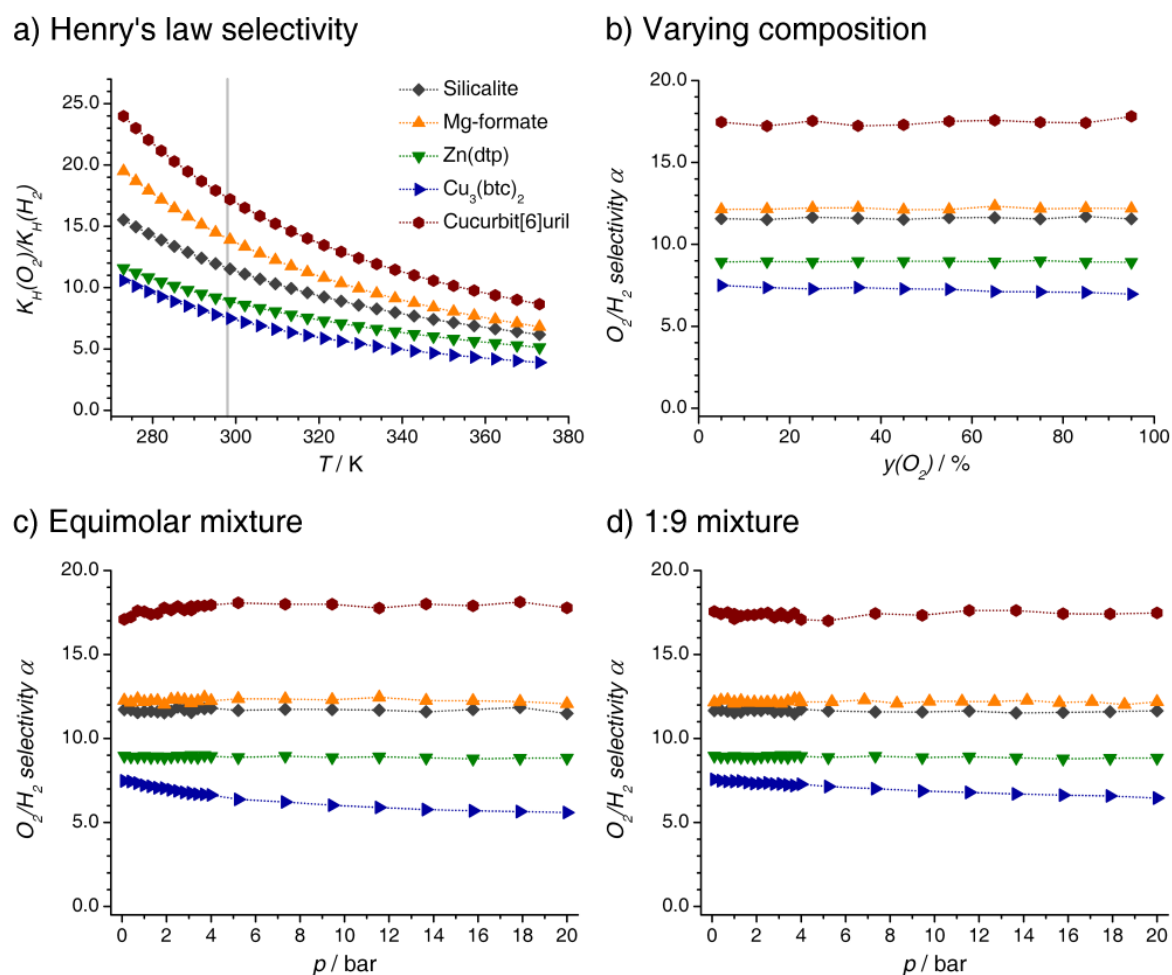
Figure 5.44. O$_2$/H$_2$ selectivity: Summary of results. *a)* Henry's law selectivity. The vertical grey line marks $T = 298$ K. *b)* Adsorption selectivities derived from binary mixture isotherm calculations for varying compositions of the gas phase at $p = 1$ bar. The *x*-axis corresponds to the content of O$_2$ in relation to the total pressure. *c)* Adsorption selectivities derived from binary mixture isotherm calculations for an equimolar O$_2$/H$_2$ mixture. *d)* Adsorption selectivities derived from binary mixture isotherm calculations for a 1:9 O$_2$/H$_2$ mixture.
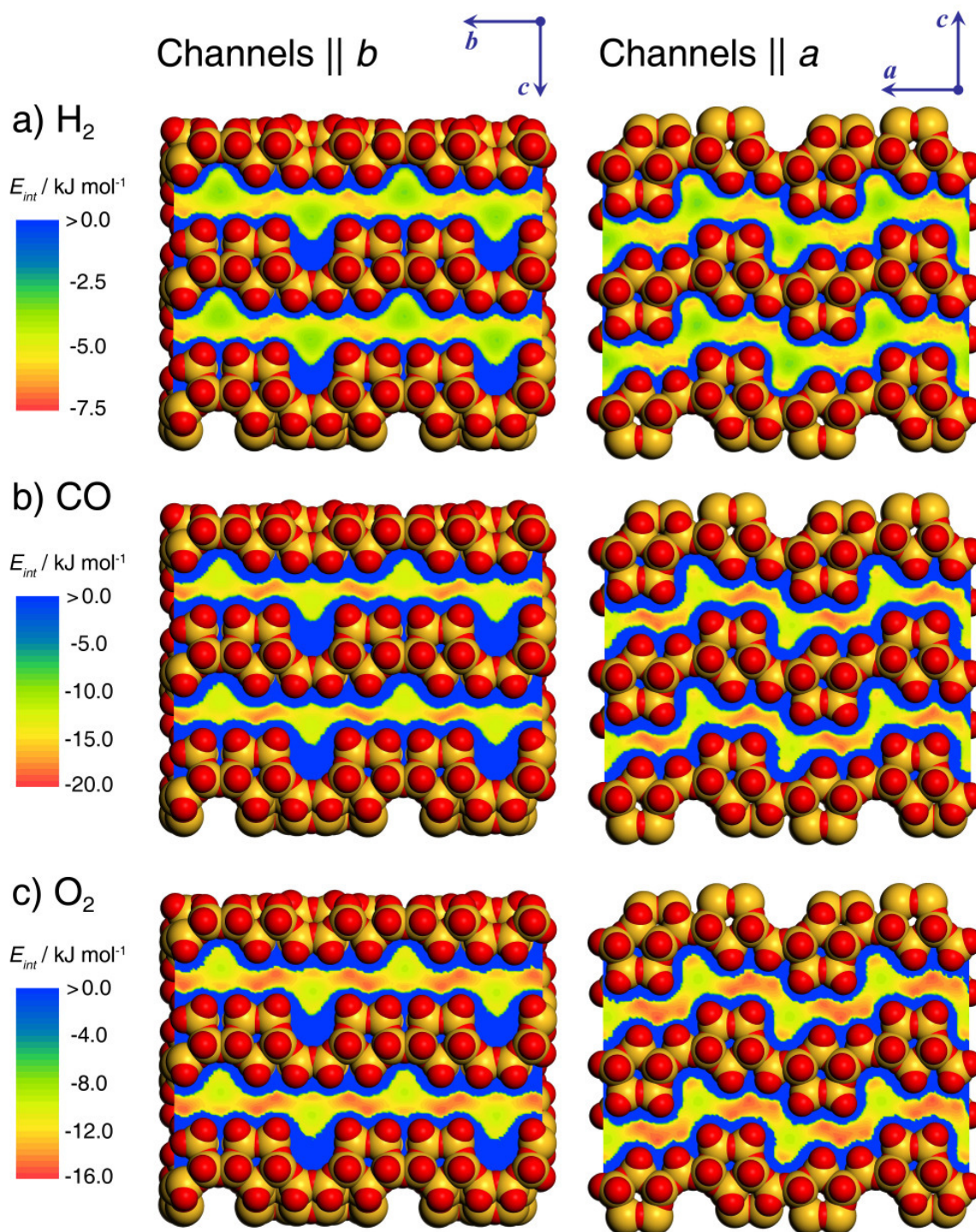
Figure 5.45. Potential energy maps derived from simulations of hydrogen, carbon monoxide, and oxygen adsorption in Silicalite. The straight channels running along the b-axis are shown on the left-hand side (section ‖ (100) plane), the sinusoidal channels running along the a-axis on the right-hand side (section ‖ (010) plane). The diameters of the framework atoms correspond to the van der Waals diameters. It should be noted that different energy ranges are displayed for the three different molecules to visualize all features of the interaction energy distribution.

5.4.4.2. Mg-formate

The calculated hydrogen adsorption isotherm of Mg-formate (figure 5.46) is in relatively good agreement with the experimental data of Schmitz *et al.* (*322*) At higher pressures, the simulation slightly overpredicts the H_2 uptake, an observation that can be explained with the difference between absolute adsorption and excess adsorption, since the simulated uptake values were not converted into excess quantities. Experimental O_2 measurements have been published only for pressures up to 1 bar. (*269*) The comparison of the simulation results with the available data (Appendix, figure A.31) indicates a tendency to overestimate the amount of oxygen adsorbed. It is noteworthy that the affinity towards carbon monoxide is remarkably higher than towards oxygen: At $p = 1\,bar$, the amount of CO adsorbed is more than twice as large than the amount of O_2. Comparing Mg-formate to the other four adsorbents considered, the isosteric heats of adsorption at low coverage (table 5.1) are the highest for all three gases. Experimental values have been reported for hydrogen, only. (*322*) Ranging between 6.5 and 7 kJ mol^{-1}, these values are lower than the q_{st} derived from the simulations. The contribution of electrostatic interactions to the total potential energy is insignificant for oxygen. For hydrogen and carbon monoxide, the electrostatic contribution amounts to 8% and 16%, respectively, showing that the charge-quadrupole and (for CO only) charge-dipole interactions in the narrow channels of Mg-formate are non-negligible. The evolution of α determined from the mixture isotherms (figures 5.43 and 5.44) reveals that the selectivity is nearly independent on total pressure for both mixtures for the range of pressures covered. Similarly, the variations of α as a function of the mixture composition do not show any pronounced trend. However, the Henry constant selectivity at $T = 298\,K$ is slightly higher than α derived from the mixture isotherms. Overall, the selectivity towards a CO/H_2 mixture ranges above 30, and is thus significantly higher than in Silicalite. In contrast, the O_2/H_2 selectivity is only modest, and very similar to the value of α obtained for the zeolitic system. These observations can be rationalized with the importance of electrostatic interactions, which lead to an increased affinity of Mg-formate for carbon monoxide, but do not affect the oxygen adsorption.

The calculated potential energy maps are shown in figure 5.47. As for Silicalite, the calculated energies in the regions of strongest interaction are in good correspondence with the isosteric heats of adsorption. For all three molecules, the maps show elongated minima of the potential energy, connected by window-like regions of weaker interaction. These apertures are bordered by three formate moieties that point into the channel, thereby narrowing the channel diameter to approximately 3 Å. While the potential energy at the windows is only slightly reduced for hydrogen, the smallest molecule, it is approximately halved for carbon monoxide. It is quite enlightening to note the differences between Mg-formate and Silicalite: In Silicalite, the preferential adsorption occurs in the narrowest areas of the channels, which have a diameter of approximately 5 Å, because the overlap of the interaction potentials from the surrounding framework atoms is maximized in these regions. In contrast to this, the highest interaction energies in Mg-formate are reached in the wider

parts of the channels, whereas the energy is reduced at the apertures. Apparently, the pore windows of Mg-formate are so narrow that a molecule that passes through the window comes so close to some of the surrounding atoms that the interatomic distance lies below the equilibrium distance of the Lennard-Jones potential ($r_{AB} < r_0$, see equation 3.6 and figure 3.2), thereby leading to a reduction of the interaction energy on decreasing distance. Thus, molecules that are considerably larger than the species considered here will not be able to pass through the pore apertures. Conversely, it can be expected that a further reduction of the channel diameter would render the material non-porous to the molecule with the largest kinetic diameter (CO in this case). Indeed, some researchers have found Mg-formate to be non-porous to nitrogen, whose kinetic diameter is almost the same as for carbon monoxide ($d_{kin} \approx 3.68\,\text{Å}$). (*322*) However, these observations are in disagreement with other studies on the same material, where measurements delivered a porosity that was accessible to both nitrogen and methane ($d_{kin} \approx 3.76\,\text{Å}$). (*268, 269*)
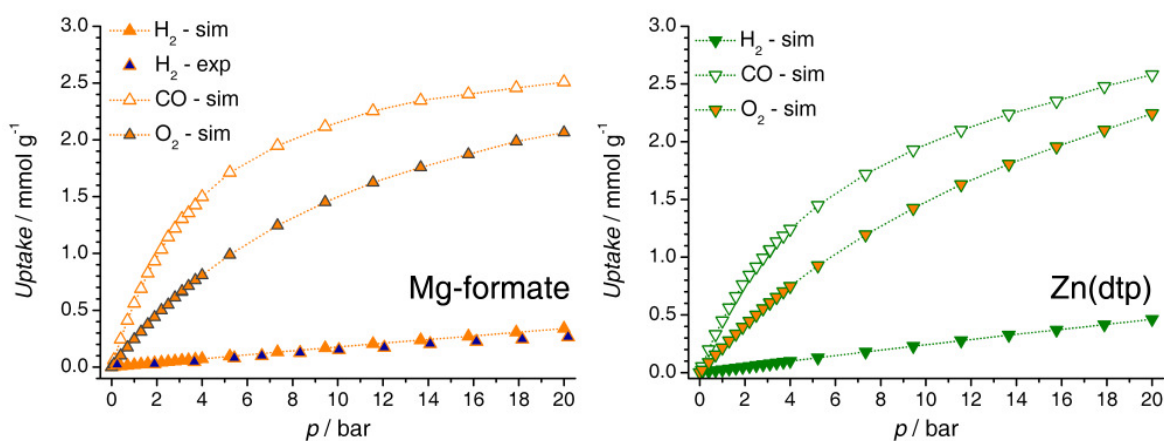
Figure 5.46. Calculated hydrogen, carbon monoxide, and oxygen adsorption isotherms for Mg-formate (left) and Zn(dtp) (right). For hydrogen adsorption in Mg-formate, experimental data from (*322*) are shown for comparison.

5.4.4.3. Zn(dtp)

The room-temperature adsorption isotherms calculated for Zn(dtp), displayed in figure 5.46, show a similar evolution to those obtained for Mg-formate. While a slightly lower uptake for CO and O_2 is observed at low pressures, the adsorption capacities at 20 bar are somewhat higher for all gases due to the slightly larger pore volume of Zn(dtp). The isosteric heats of adsorption are significantly lower than for Mg-formate, and relatively similar to the q_{st} values obtained for Silicalite. With an isosteric heat of 14.0 kJ mol^{-1}, the affinity towards oxygen is the lowest of all system considered. The relative contribution of electrostatic interactions to the total energy is similar to Mg-formate, indicating a comparable polarity of the framework.
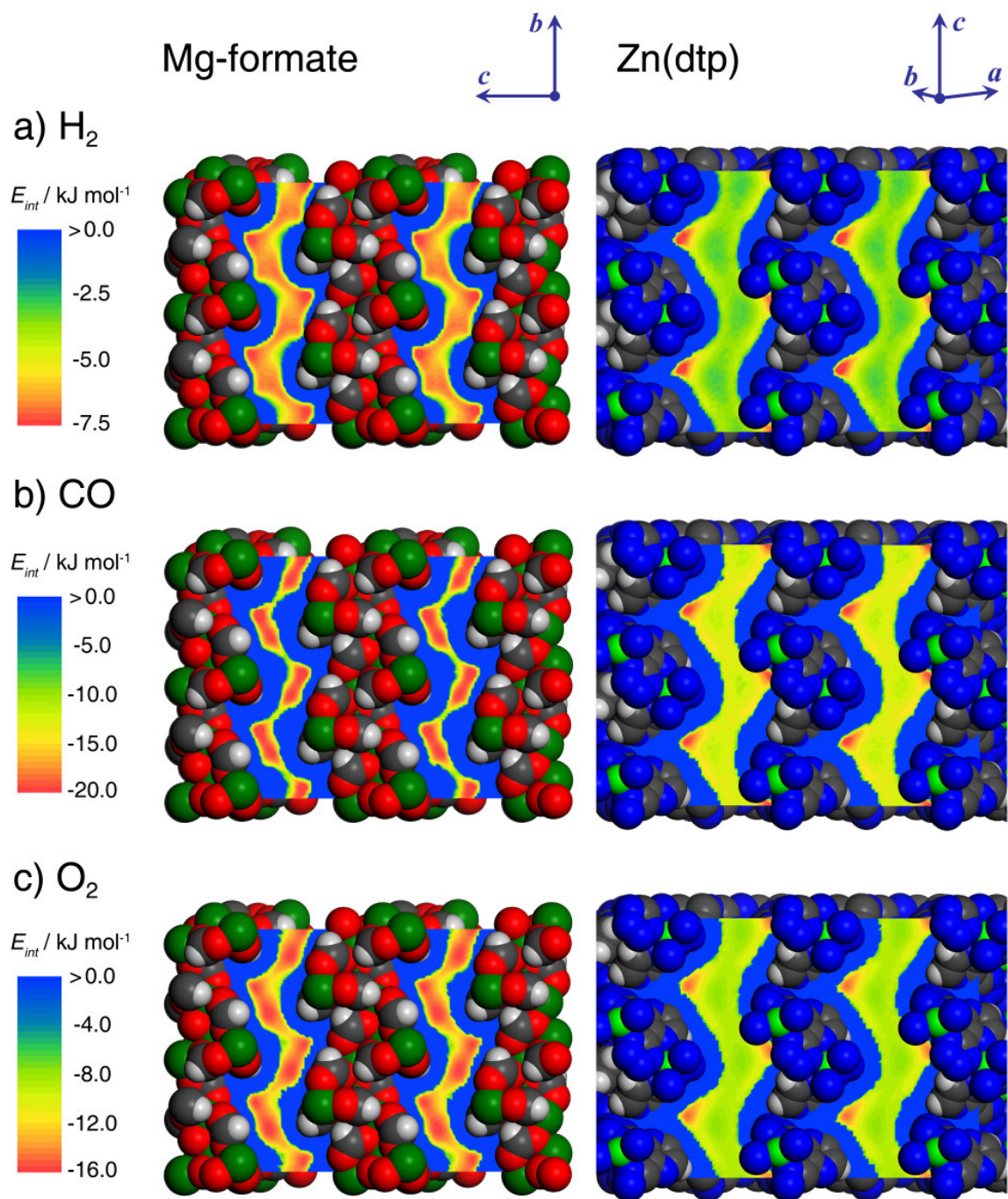
Figure 5.47. Potential energy maps derived from simulations of hydrogen, carbon monoxide, and oxygen adsorption in Mg-formate (left, section $\parallel$ (100) plane) and Zn(dtp) (right, section $\parallel$ (010) plane). The coordinate systems displayed at the top of the figure indicate the approximate orientation of the crystallographic axes with respect to the section.

The calculated adsorption selectivities of Zn(dtp) (figures 5.43 and 5.44) show a relatively modest separation performance, despite the presence of narrow channels in the structure. The CO/H_2 selectivity is comparable to Silicalite, with $\alpha \approx 20$ at low and intermediate coverages. In the case of an equimolar mixture, the selectivity decreases significantly at pressures above 5 bar, whereas only a slight decrease is observed for the 1:9 mixture. At a pressure of 1 bar, however, the selectivity shows no dependence on mixture composition. The O_2/H_2 selectivity is lower than for Silicalite, ranging near $\alpha \approx 9$, and exhibits no significant changes on varying pressure or composition.

The potential energy maps, shown in figure 5.47, reveal pronounced energy minima in lateral cavities of the helical channels. The highest potential energies amount to approximately -8 kJ mol^{-1} for H_2, -20 kJ mol^{-1} for CO, and -15 kJ mol^{-1} for O_2, and are thus higher than the isosteric heats of adsorption. This difference indicates that adsorption in other regions of the framework, where the interaction is weaker, also contributes to the total adsorption, even at low loadings. The lateral cavities are closely surrounded by three tetrazole and two pyrazine rings, which leads to maximization of the dispersive interaction in this region. It has been pointed out that the pore walls of Zn(dtp) are to a large extent constituted by negatively polarized nitrogen atoms. (257) The energy maps show that the interaction with the framework is strongest in the lateral cavities for all three molecules, regardless of the sign and magnitude of the molecular quadrupole moment. Because the cavities have a diameter of approximately 4.5 Å (similar to the diameter of the channels of Mg-formate), all molecules are small enough to assume an orientation inside the cavities that maximizes attractive electrostatic interactions. Due to the presence of energetically favoured adsorption regions, it could be expected that the drop in selectivity observed for a CO/H_2 mixture occurs at a loading that corresponds to a complete occupation of these regions. However, this is not the case: The selectivity decrease starts at a loading that equals approximately 12 molecules per supercell, whereas there is a total of 48 lateral cavities in the simulation box.

5.4.4.4. Cu$_3$(btc)$_2$

Due to its larger free pore volume, Cu$_3$(btc)$_2$ adsorbs much larger amounts of the three gases than the other adsorbents considered. Concerning the adsorption of hydrogen in this system, it has been discussed in section 5.2 that the agreement of the calculated RT hydrogen adsorption isotherm with experimental data is best for the model that neglects localized interactions with the metal centers. Therefore, unmodified UFF parameters were used to represent the framework atoms. The isosteric heat of hydrogen adsorption is significantly lower than the corresponding q_{st} calculated in section 5.1 for cryogenic temperatures, highlighting the dependency of q_{st} on temperature. The simulated CO isotherm (figure 5.48) is in relatively good agreement with experimental data, with a tendency to underestimate the loading. (284) As it will be discussed later, this might be related to the interaction of carbon monoxide with the unsaturated copper sites. Concerning the isosteric heats of adsorption, the q_{st} values for CO and O_2 are slightly higher when compared to Zn(dtp). Interestingly,

the contribution of electrostatic interactions is very high for carbon monoxide, amounting to 40% of the total potential energy. In contrast to this, electrostatic interactions are negligible for both hydrogen and oxygen.

As it is visible from figures 5.43 and 5.44, respectively, the selectivities towards both mixtures are the lowest of all systems considered: At 1 bar, the CO/H_2 selectivity amounts to $\alpha \approx 12$, and the O_2/H_2 selectivity ranges around $\alpha \approx 7$. A slight decrease of α on increasing pressure is observed. It is more pronounced for the equimolar mixture than for the 1:9 mixture. Moreover, a slight dependence of the selectivity on gas phase composition is detectable: α decreases with decreasing H_2 content. These observations are in line with the common expectation that the selectivity decreases with increasing pressure, and with increasing content of the more strongly adsorbed species. (*115*) In this context, it is interesting to note that similar GCMC simulations by Karra and Walton predicted a sharp rise of the CO/H_2 selectivity at $p > 20$ bar for a CO-rich and an equimolar mixture, while the selectivity for a H_2-rich mixture remained unaffected. (*138*) This was rationalized with the complete occupation of the cell by CO molecules, which prevented a significant co-adsorption of hydrogen. While the conditions under which this behaviour is most pronounced were not considered in the computations reported here, there are no indications that a comparable rise of the CO/H_2 selectivity at high pressures can be reproduced. Therefore, the interpretation given by Karra and Walton appears to be debatable, and it cannot be ruled out that the observed behaviour is related to an inadequate choice of framework parameters, which were specifically adjusted for each sorbate species. The significance of the differences in the parameter set is also reflected by a considerably higher CO/H_2 selectivity at low coverage obtained by these authors, with a Henry's law selectivity of $K_H(CO)/K_H(H_2) \approx 24$, as compared to a value of 13 calculated in this study.

The potential energy maps derived from the simulations are displayed in figure 5.49. There are notable differences between the results for hydrogen and oxygen on the one hand, and carbon monoxide on the other hand. For H_2 and O_2, the interaction strength is highest inside the small pores. For both molecules, the potential energies in these areas are 1 to 2 kJ mol^{-1} higher than the isosteric heats of adsorption. For carbon monoxide, the central areas of the small pores also correspond to regions of increased interaction. However, the interaction energies in these regions are only slightly higher than for oxygen. More pronounced, sharp energy minima are located at the unsaturated copper centers, at a distance of approximately 2.7 Å from the Cu atoms. The potential energy in these areas exceeds -25 kJ mol^{-1}, and is thus drastically higher than the isosteric heat of adsorption. It has been discussed before that the environment of the metal centers in $Cu_3(btc)_2$ is not particularly favourable as long as only dispersive interactions are considered, due to the small number of interaction partners at a similar distance. Thus, the preferential adsorption of CO at these sites must be attributed to electrostatic (charge-dipole and charge-quadrupole) interactions. This is in line with the large contribution of electrostatic effects to the total energy. As a final point, it must be emphasized that no specific adjustments were made in order to accurately represent the interaction of CO with the copper centers. Although the potential

energy distribution reveals that this interaction is qualitatively reproduced in the simulations, this does not automatically imply that the interaction strength predicted by the chosen parameters is also quantitatively correct. It is quite likely that the differences between the experimental and the calculated CO isotherm that are visible in figure 5.48 are due to an inaccurate representation of the Cu-CO interaction strength. Further computational work will be necessary to improve upon this issue.
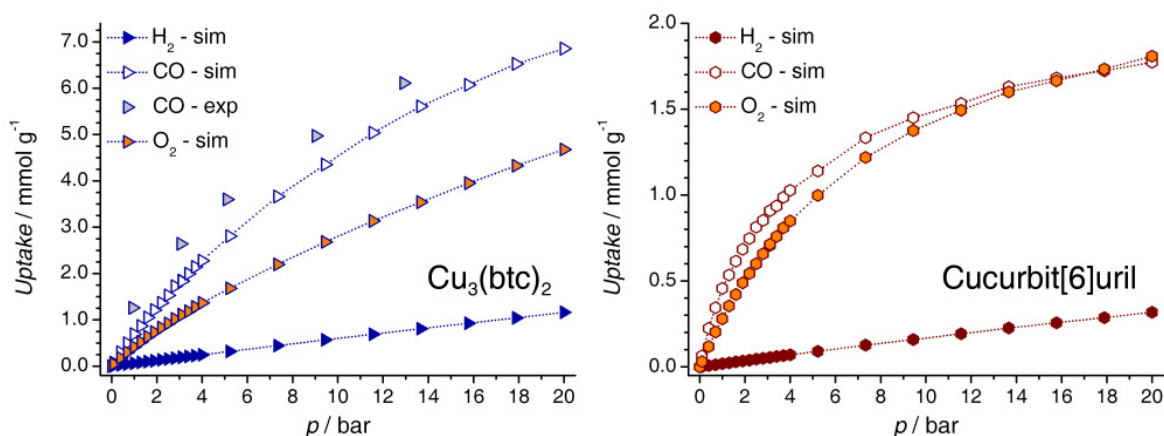
Figure 5.48. Calculated hydrogen, carbon monoxide, and oxygen adsorption isotherms for $Cu_3(btc)_2$ (left) and cucurbit[6]uril (right). For carbon monoxide adsorption in $Cu_3(btc)_2$, experimental data from (*284*) are shown for comparison.

5.4.4.5. Cucurbit[6]uril

Of the three gases considered in this section, experimental adsorption data are available for carbon monoxide only, for pressures up to 1 bar. (*324*) A comparison of the simulation results with this measurement is shown in the Appendix, figure A.31. It is noteworthy that the simulation overestimates the amount adsorbed by a factor of 2 to 3 in this pressure range. It cannot be elucidated whether this discrepancy is related to experimental issues, or to problems with an adequate description of the solid-fluid interactions in the simulation. The simulation results for CO_2 and C_2H_2 presented in the following subsection exhibit much better agreement with experiment, permitting the assumption that the force-field parameters should be generally quite well-suited to describe the system. Possibly, the diffusion of CO in the narrow channels is so limited that some areas of the structure remain inaccessible in real samples, thus leading to a reduced carbon monoxide uptake.

While the H_2 and CO amounts adsorbed at low pressures are quite similar to the uptakes obtained for Mg-formate and Zn(dtp), respectively, CB[6] exhibits the highest oxygen uptake of all systems with channel-like pores at 1 bar (table 5.1 and figure 5.48). At 20 bar, the storage capacities for all gases are very modest due to the limited pore volume. The isosteric heats of adsorption are relatively high for hydrogen and oxygen, ranging only 0.4 kJ mol^{-1} below the corresponding values calculated for Mg-formate. For carbon monoxide, however, the affinity is considerably lower, with q_{st} being 2.6 kJ mol^{-1} lower than for

Mg-formate. Compared to the three MOFs, the contribution of electrostatic interactions to the total potential energy is considerably reduced, but still slightly higher than for Silicalite. Interestingly, Cucurbit[6]uril exhibits the highest Henry's law selectivities of all five systems for both gas mixtures (figures 5.43a and 5.44a). Although the increases of the Henry's law selectivity in comparison to Mg-formate are relatively modest in absolute terms, a relative increase of the O_2/H_2 selectivity by 30% is quite remarkable. Similar to the observations made for some MOFs, the selectivity towards a CO/H_2 mixture decreases on increasing total pressure, and on increasing carbon monoxide content (figure 5.43b). For both compositions, the drop in selectivity is most pronounced at low pressures. The selectivity towards an O_2/H_2 mixture is practically unaffected by total pressure and mixture composition. Sections through the calculated potential energy are displayed in figure 5.49. The energy maps reveal elongated regions of high interaction strength in the lateral cavities of the channels. These energy minima have an arrow-like shape, which is why the values of highest energy are slightly displaced from the section. For each visible minimum, there are two other minima in the same channel at equal z-coordinate generated by the threefold rotation axis. Each of these lateral cavities is surrounded by four CB[6] moieties, two of which are approximately located in plane with the section (and thus well visible in figure 5.49), whereas the other two lie above and below the section. The cavities are mainly surrounded by CH and CH_2 groups, but there are also two carbonyl oxygens at relatively close distance. For hydrogen and carbon monoxide, the highest energy values reached are in good correspondence with the isosteric heat of adsorption. For oxygen, however, the highest energy values observed in the potential energy distribution exceed -19 kJ mol^{-1}, and are thus considerably higher than q_{st}.
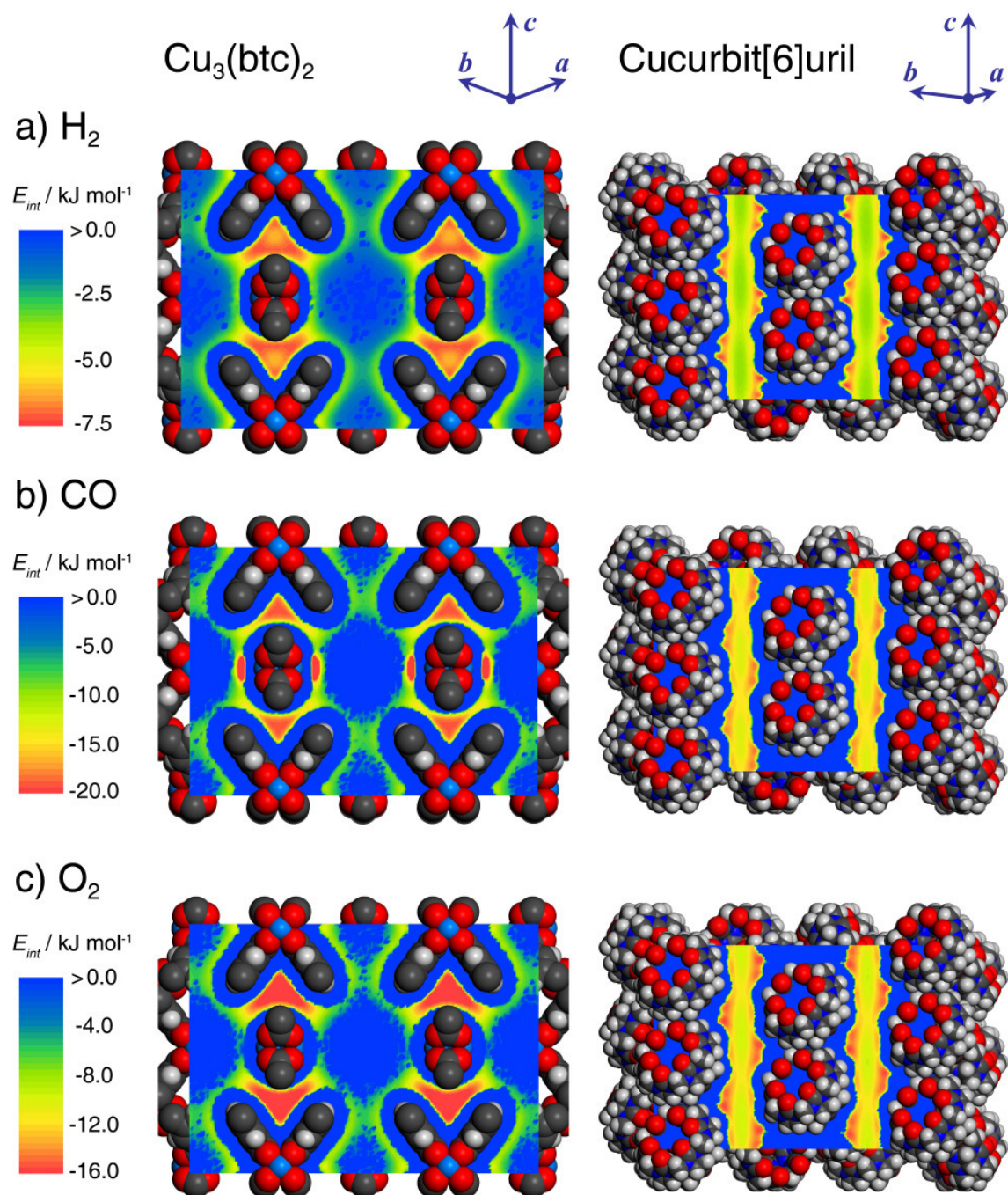
Figure 5.49. Potential energy maps derived from simulations of hydrogen, carbon monoxide, and oxygen adsorption in $Cu_3(btc)_2$ (left, section $\parallel$ (110) plane) and cucurbit[6]uril (right, section $\parallel$ (110) plane). The coordinate systems displayed at the top of the figure indicate the approximate orientation of the crystallographic axes with respect to the section.

5.4.5. Results: Acetylene storage and C_2H_2/CO_2 separation

5.4.5.1. Silicalite

The calculated single-component isotherms for Silicalite are shown in figure 5.50. While the agreement of the calculated CO_2 adsorption isotherm with experimental data has been discussed above, no C_2H_2 adsorption measurements have been reported. For both gases, the adsorption capacities are modest when compared to the other systems under consideration. The values of q_{st} are also relatively low. Two experimental isosteric heats of CO_2 adsorption in the limit of zero coverage have been reported. The calculated q_{st} (table 5.3) is in good agreement with these values, which amount to 24.1 kJ mol^{-1} (*97*) and 27.0 kJ mol^{-1} (*321*), respectively. While the influence of electrostatic effects is still relatively low, the contribution of electrostatic interactions to the total potential energy is higher for CO_2 and C_2H_2 than for the more weakly adsorbing gases discussed previously. Thus, for molecules with an increased quadrupole moment, electrostatic effects should be taken into account even when the adsorbent is relatively non-polar.
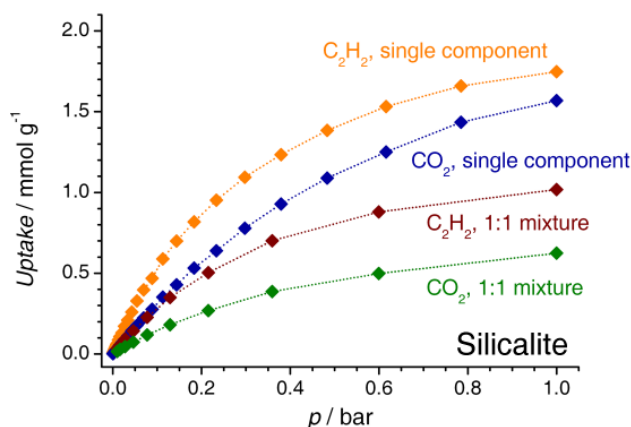
Figure 5.50. Calculated acetylene and carbon dioxide adsorption isotherms for Silicalite. Single-component isotherms are shown in orange and blue, whereas the amounts of C_2H_2 and CO_2 adsorbed from a binary mixture are displayed in dark red and green, respectively.

The selectivity of Silicalite towards a C_2H_2/CO_2 mixture, shown in figure 5.51, is very low, not exceeding $\alpha = 2.1$ at very low loadings, and slightly decreasing on increasing pressure. The potential energy maps, shown in figure 5.52 are qualitatively similar to the maps presented in the previous subsection. The highest interaction energies are observed at the windows where the channels pass through 10-rings. The energies reach -32 kJ mol^{-1} in the case of acetylene, and -27 kJ mol^{-1} in the case of carbon dioxide, and are thus somewhat higher than the corresponding isosteric heats. It is noteworthy that the regions of attractive interaction are considerably broader for CO_2 than for C_2H_2. This may explain the decrease of the selectivity on increasing pressure: A complete occupation of the energetically preferred window regions by one molecule per site would correspond to a loading of 1.4 mmol g^{-1}, a value which is reached at pressures below 1 bar for both gases. Although

acetylene is (slightly) favoured in these regions, a larger fraction of the unit cell is accessible to CO_2. As soon as the majority of preferential adsorption sites is occupied, this will favour the adsorption of additional CO_2 molecules, which can adopt a more efficient packing.

Table 5.3. Results of simulations of C_2H_2 and CO_2 single-component adsorption: Gas uptakes n (in mmol g^{-1}), isosteric heats of adsorption q_{st} derived at low loading (in kJ mol^{-1}), and relative contributions of dispersive and electrostatic interactions to the total interaction energy.

	Silicalite	*Mg-formate*	*Zn(dtp)*	*Cu$_3$(btc)$_2$*	*CB[6]*
$n(C_2H_2)$, $p = 0.01$ bar	0.065	0.662	0.242	0.249	0.255
$n(C_2H_2)$, $p = 1$ bar	1.75	2.84	2.73	8.35	1.76
$q_{st}(C_2H_2)$	29.5	40.4	31.1	30.1	33.2
$E_{disp}/E_{es}(C_2H_2)$	83% / 17%	60% / 40%	67% / 33%	73% / 27%	77% / 23%
$n(CO_2)$, $p = 0.01$ bar	0.035	0.060	0.059	0.102	0.091
$n(CO_2)$, $p = 1$ bar	1.57	2.21	2.87	4.04	2.17
$q_{st}(CO_2)$	25.1	29.6	25.7	27.0	31.1
$E_{disp}/E_{es}(CO_2)$	92% / 8%	86% / 14%	80% / 20%	97% / 3%	88% / 12%

Table 5.4. Comparison of adsorption selectivites α. The Henry's law selectivities and the selectivities derived from binary mixture isotherm calculations (equimolar composition) at two different pressures are given.

	Silicalite	*Mg-formate*	*Zn(dtp)*	*Cu$_3$(btc)$_2$*	*CB[6]*
$K_H(C_2H_2)/K_H(CO_2)$	2.1	12.7	4.5	2.2	4.0
$\alpha(C_2H_2/CO_2)$, $p = 0.01$ bar	2.1	12.4	4.2	2.3	3.6
$\alpha(C_2H_2/CO_2)$, $p = 1$ bar	1.6	13.0	2.1	2.4	1.1

C₂H₂ /CO₂ separation: Overview
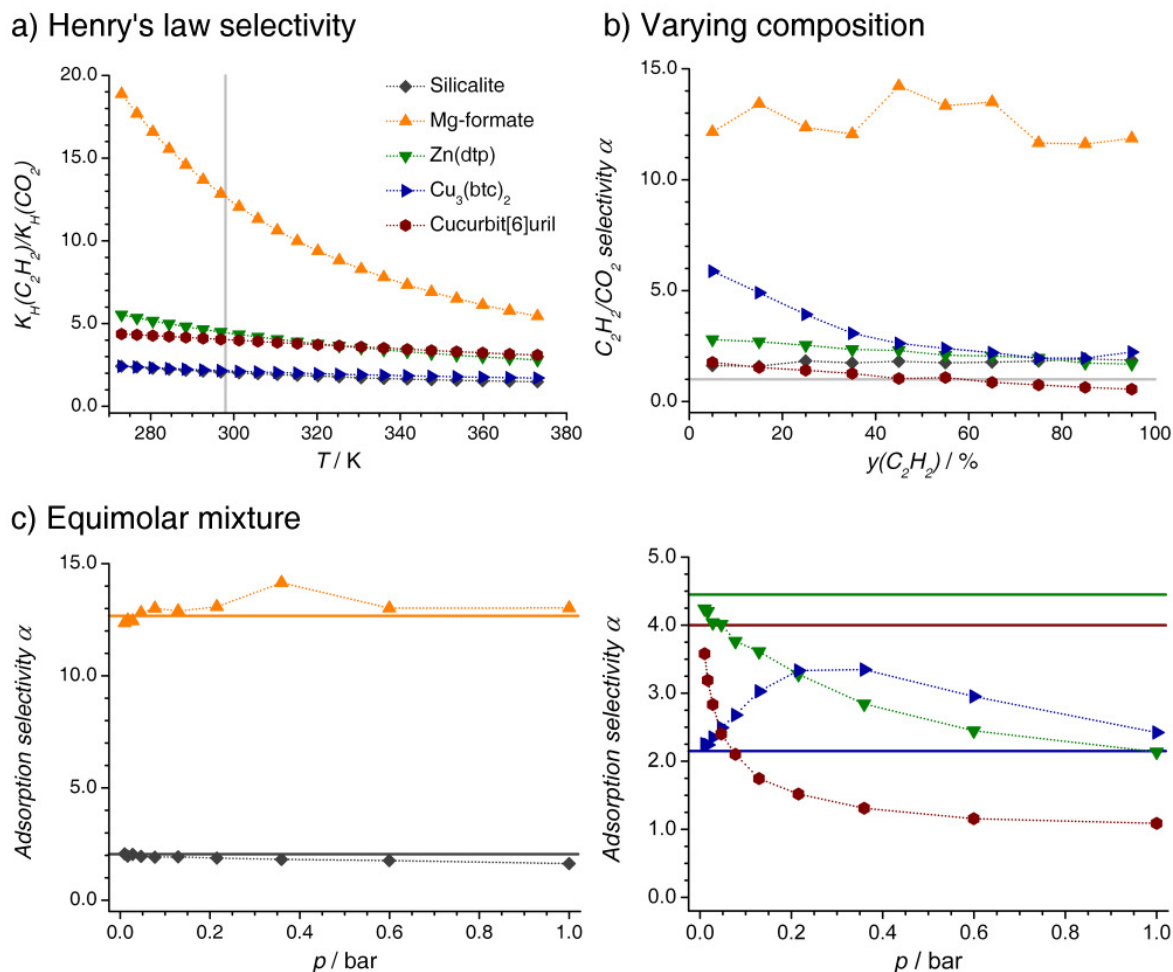
Figure 5.51. C_2H_2/CO_2 selectivity: Summary of results. *a)* Henry's law selectivity. The vertical grey line marks $T = 298\,\text{K}$. The C_2H_2/CO_2 selectivities of Silicalite and $Cu_3(btc)_2$ are virtually identical over the whole temperature range. *b)* Adsorption selectivities derived from binary mixture isotherm calculations for varying compositions of the gas phase at $p = 1\,\text{bar}$. The *x*-axis corresponds to the content of C_2H_2 in relation to the total pressure. The horizontal line marks a selectivity of unity. Particularly for Mg-formate, the selectivity shows some oscillations, as it is very hard to fully equilibrate the calculations with respect to the more weakly adsorbed species. *c)* Adsorption selectivities derived from binary mixture isotherm calculations for Silicalite and Mg-formate (left) and Zn(dtp), $Cu_3(btc)_2$, and cucurbit[6]uril (right). The horizontal lines indicate the Henry's law selectivities at $T = 298\,\text{K}$.
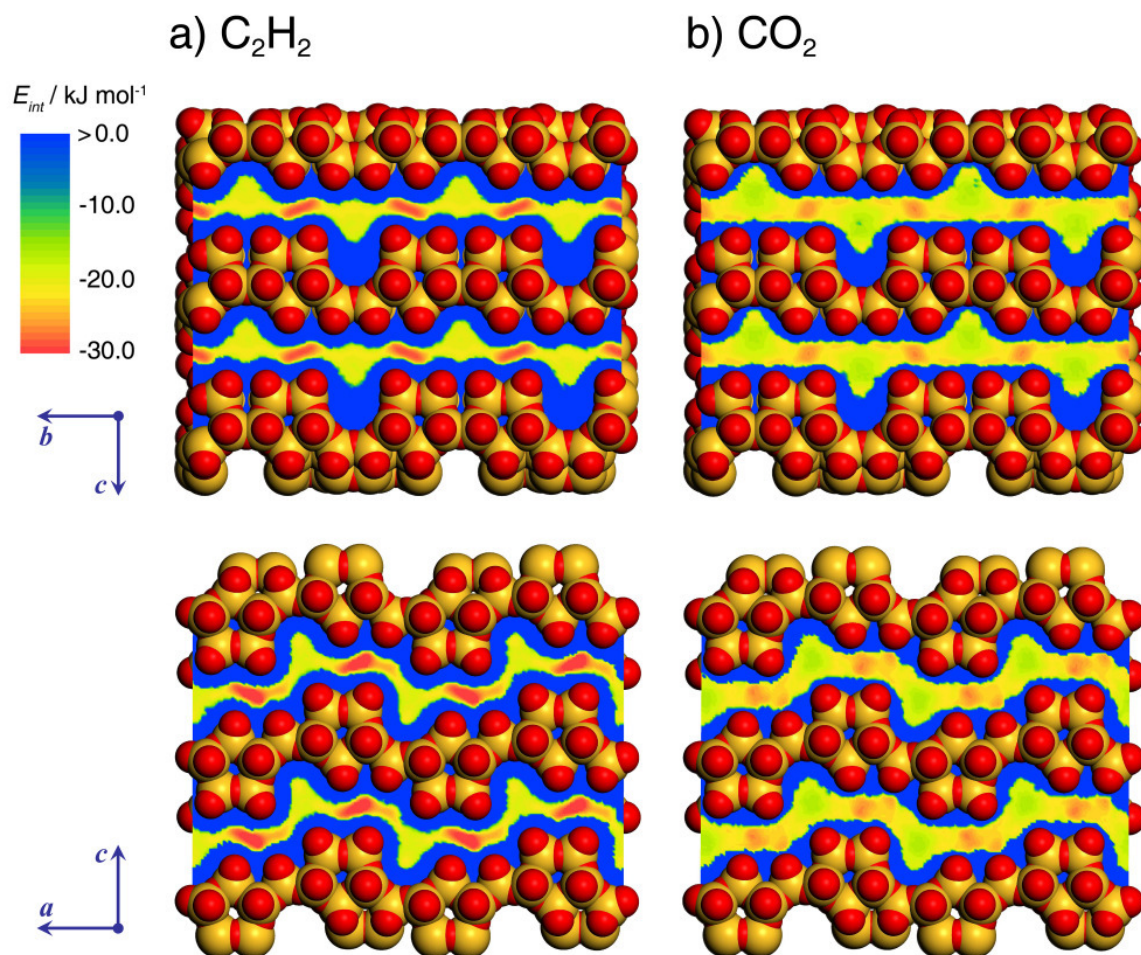
Figure 5.52. Potential energy maps derived from simulations of acetylene and carbon dioxide adsorption in Silicalite. The straight channels running along the *b*-axis are shown in the upper part of the figure, the sinusoidal channels running along the *a*-axis in the lower part. The diameters of the framework atoms correspond to the van der Waals diameters.

5.4.5.2. Mg-formate

Figure 5.53 shows the calculated C_2H_2 and CO_2 adsorption isotherms, together with experimental data. (*269*) The agreement between simulation and experiment is very good for both gases, with the quantitative deviations not exceeding 0.25 mmol g^{-1}. Moreover, the isosteric heat of acetylene adsorption is in good correspondence with the experimental value of q_{st} = 38.5 kJ mol^{-1} derived at a loading of 0.5 mmol g^{-1}. It should, however, be noted that higher isosteric heats of adsorption (> 40 kJ mol^{-1}) have been obtained at low coverages. The calculated q_{st} for carbon dioxide is more than 10 kJ mol^{-1} lower than for acetylene, indicating a distinctly weaker interaction with the framework. The contributions of electrostatic interactions to the total potential energy also exhibit remarkable differences: While electrostatic effects account for 40% of the total interaction for C_2H_2, they make up for a mere 14% in the case of CO_2.
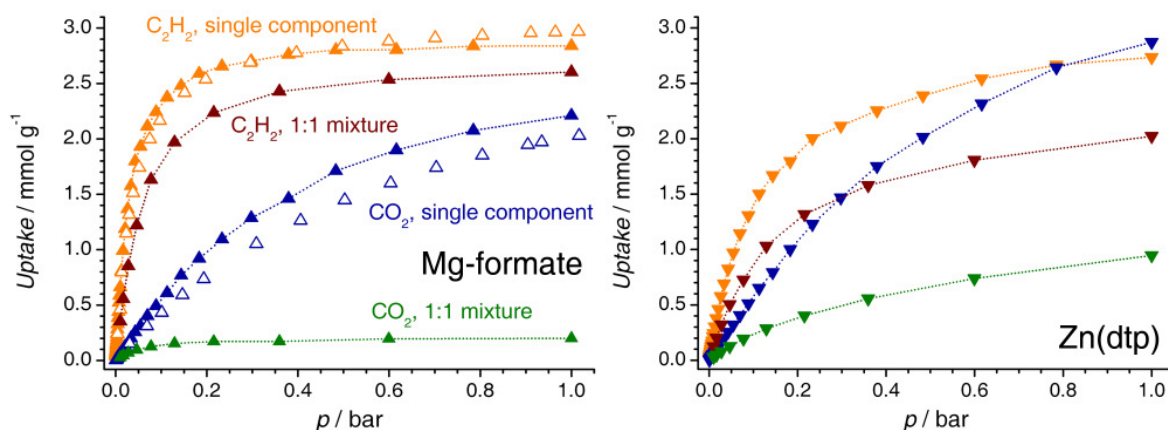
Figure 5.53. Calculated acetylene and carbon dioxide adsorption isotherms for Mg-formate (left) and Zn(dtp) (right). Single-component isotherms are shown in orange and blue, whereas the amounts of C_2H_2 and CO_2 adsorbed from a binary mixture are displayed in dark red and green, respectively. For Mg-formate, experimental adsorption data from (*269*) are given as open symbols.

As is visible from figure 5.53, which includes the binary mixture isotherm, hardly any CO_2 is adsorbed from an equimolar C_2H_2/CO_2 mixture. In contrast to this, the C_2H_2 uptake is only slightly reduced with respect to the single-component isotherm. This translates into the highest selectivity of all systems considered. While a value of $\alpha \approx 12$ appears to be modest in absolute terms, it constitutes indeed a significant selectivity due to the very similar fluid properties of the two gases. α seems to exhibit a slight increase on increasing pressure, a behaviour that may be related to a nearly complete occupation of the pores by acetylene molecules, which do not permit a co-adsorption of carbon dioxide. Moreover, there are some oscillations of the selectivity as a function of the gas phase composition. However, since there is no clear trend, it must be expected that these oscillations are related to incomplete equilibration.
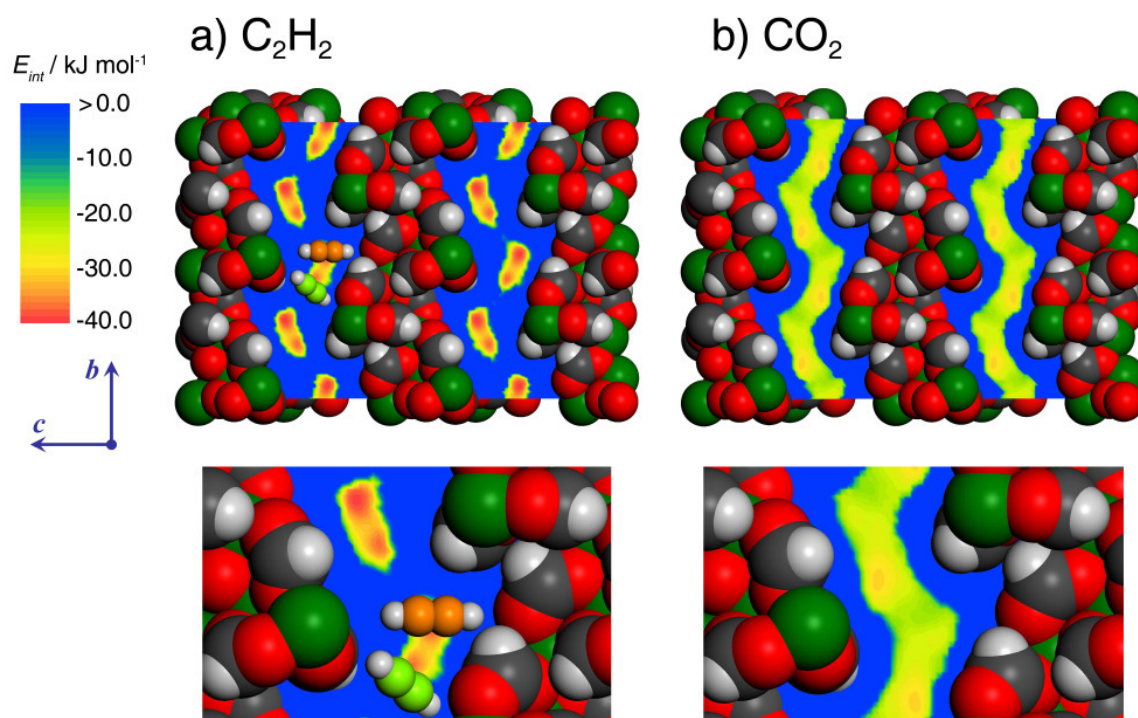
Figure 5.54. Potential energy maps derived from simulations of acetylene and carbon dioxide adsorption in Mg-formate. For selected points of the simulation box, experimental C_2H_2 positions from (*269*) are also shown, molecule A in orange, molecule B in light green. An expanded view of a single channel is given in the lower part of the figure.

Sections through the potential energy distribution are shown in figure 5.54. For acetylene, peanut-like shaped regions of high potential energy are visible at the center of the channels. The interaction strength exceeds -25 kJ mol^{-1} throughout the regions and reaches up to -40 kJ mol^{-1} at the two "peanut cores". Interestingly, the interaction in the apertures connecting these regions is repulsive, which may indicate a relatively high energy barrier to diffusion. From geometric considerations, it can be concluded that each of the peanut-like regions cannot be occupied by more than one C_2H_2 molecule. This occupation corresponds to a loading of 2.9 mmol g^{-1}, a value that is nearly reached at a pressure of 1 bar. Experimentally, positions of the adsorbed acetylene molecules were determined by using single-crystal X-ray diffraction at $T = 90$ K. (*269*) Two non-equivalent positions could be refined (molecules A and B), which were found to be occupied in a ratio of 0.75:0.25. The two positions are too close together to be occupied simultaneously. For comparison, these two sites are also displayed at selected points of the simulation box in figure 5.54. Molecule A is located nearly in plane with the section, the center of the molecule lying in an area of high interaction potential. For molecule B, one of the carbon atoms is slightly displaced from the section, but again, the center of the molecule is located in an area of strong attractive interaction. In both cases, the hydrogen atoms, which are positively polarized, are pointing towards oxygen atoms of the framework, which carry a negative partial charge, the interatomic distances ranging between 2.5 and 2.7 Å. Although these distances are somewhat too high to postulate hydrogen bonding, the fact that the acetylene molecules are prefer-

entially oriented perpendicular to the running direction of the channels can be understood from the charge distribution of the channel walls. These considerations are in line with the aforementioned observation that electrostatic interactions constitute an important contribution to the total potential energy.

The calculated potential energy distribution for CO_2 shows that the regions of strong interaction are more diffuse than in the case of acetylene. The interaction strength hardly exceeds -30 kJ mol^{-1}. The interaction remains attractive at the pore apertures, which could lead to a considerably faster diffusion for CO_2 when compared to C_2H_2. Because the walls of the channels are mainly decorated by oxygen atoms, it can be expected that the CO_2 molecules are mostly oriented with their molecular axis parallel to the running direction of the channels, thus minimizing the electrostatic repulsion.

5.4.5.3. Zn(dtp)

The calculated adsorption isotherms are displayed in figure 5.53. As mentioned previously, experimental data are available exclusively for low temperatures. (257) It is noteworthy that the single-component isotherms cross at $p \approx 0.8\,\mathrm{bar}$. There is an interesting correspondence with experimental observations: At $T = 195\,\mathrm{K}$ and $p = 1.0\,\mathrm{bar}$, conditions under which the saturation uptake is reached, Zn(dtp) adsorbs approximately 0.4 mmol g^{-1} more carbon dioxide than acetylene (4.5 mmol g^{-1} vs. 4.1 mmol g^{-1}). This indicates a more efficient packing of the CO_2 molecules in the pores. Apparently, these effects are already visible at room temperature at sufficiently high pressure, although the isotherms have not reached saturation. The calculated isosteric heats of adsorption reveal a moderate affinity towards both gases, being much lower than the q_{st} values obtained for Mg-formate. In contrast to this, the relative contribution of electrostatic interactions has a similar magnitude as for Mg-formate, which substantiates the assumption made above that both frameworks have a similar polarity.

The C_2H_2/CO_2 selectivity of Zn(dtp) is relatively modest (figure 5.51). The Henry's law selectivity amounts to $\alpha \approx 4.5$, and despite being the second-highest of the five systems, it is drastically lower than the selectivity observed for Mg-formate. The selectivity decreases considerably on increasing total pressure, and on increasing acetylene content in the mixture, a behaviour that is in line with the common expectations. There is also a direct correspondence of this observation with the results from the single-component isotherm calculations: At low pressures and low C_2H_2 concentrations, the selectivity is (relatively) high because acetylene is preferred due to the stronger interaction with the framework, reflected by the higher isosteric heat of adsorption (table 5.3). However, when the number of adsorbed C_2H_2 molecules increases, the adsorption of additional CO_2 molecules appears to become more favourable, leading to a reduction of the selectivity. This behaviour is completely in line with the aforementioned assumption that carbon dioxide can fill the pores more efficiently than acetylene, which was proposed on the grounds of the differences in saturation uptake observed in the single-component isotherms.
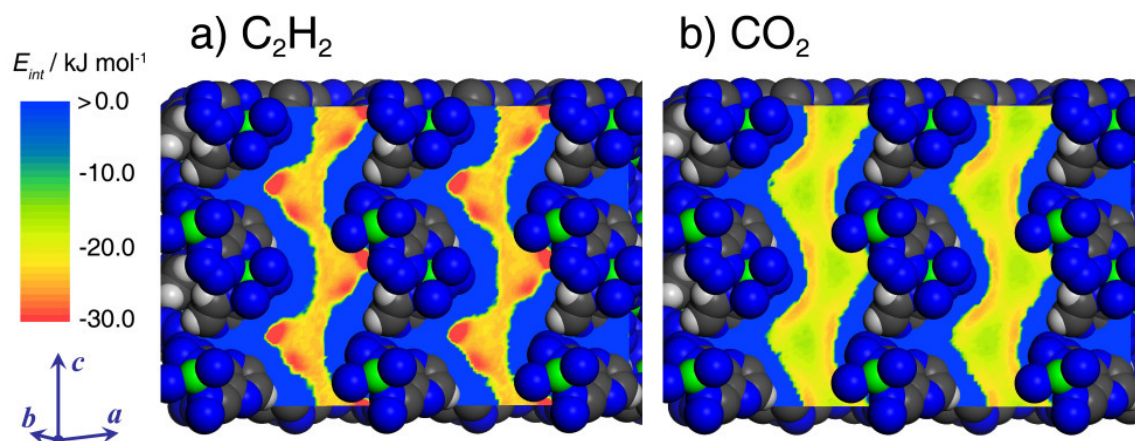
Figure 5.55. Potential energy maps derived from simulations of acetylene and carbon dioxide adsorption in Zn(dtp).

The potential energy maps shown in figure 5.55 reveal a strong preference for acetylene in the lateral cavities of the channels. In the center of these areas, the interaction energy exceeds -35 kJ mol^{-1}, and is considerably higher than the corresponding isosteric heat. A complete occupation of these areas would correspond to an uptake of 3.6 mmol g^{-1}, a value that is not reached at room temperature and 1 bar. The potential energy map derived for CO_2 is remarkably different: Minima of the interaction energy are not located in the lateral cavities, but at the opposite side of the channels at equal z-coordinate, where one tetrazolate moiety points into the pore. From the observations of the previous subsection, it was concluded that the lateral cavities are preferential adsorption sites for the small molecules H_2, CO, and O_2, regardless of the sign of the quadrupole moment. Apparently, carbon dioxide behaves differently. Since the molecular axis of CO_2 is approximately 5.8 Å long, it can enter the cavity of the Zn(dtp) structure (diameter 4.5 Å) only in a head-on configuration. However, this is energetically unfavourable due to electrostatic interactions, because an oxygen atom would point towards the negatively polarized pore wall. A different behaviour is observed for acetylene: Despite the similar length of the molecular axis (5.4 Å), C_2H_2 can maximize electrostatic interactions in the head-on configuration due to the different molecular charge distribution. While the cavities are always energetically favoured as long as only dispersive interactions are considered, these findings highlight the importance of the inclusion of electrostatic effects, which lead to a qualitatively different behaviour depending on the sign of the molecular quadrupole moment. Regarding the separation properties of Zn(dtp), the presence of distinct areas of strongest interaction for acetylene and carbon dioxide permits an efficient co-adsorption, and thus has a negative effect on the adsorption selectivity.

5.4.5.4. Cu$_3$(btc)$_2$

The single-component C$_2$H$_2$ and CO$_2$ adsorption isotherms obtained with the default UFF parameters for copper are shown in figure 5.56a, together with experimental data. (*246*, *323*) It is evident that the simulations fail to reproduce the experimental results, underestimating the acetylene uptake at 1 bar by 75%, and the carbon dioxide uptake by 45%. It has been discussed in detail in previous parts of this work that a similar underestimation occurs in the modelling of hydrogen adsorption in Cu$_3$(btc)$_2$ at low temperature, which is related to the presence of unsaturated metal sites. A similar behaviour can be expected for acetylene, where experimental evidence for a preferential adsorption at the copper centers has been obtained in neutron diffraction experiments using acetylene-loaded samples. (*323*) Moreover, significant deviations between simulated and experimental isotherms have also been reported for propylene (*131*) and carbon dioxide. (*246*) In the computational study of propylene adsorption, it was demonstrated that an adjustment of the well depth D_0 of the Lennard-Jones potential can be sufficient to reproduce experimental data. (*131*) However, it is clear that such a purely empirical approach is highly dependent on the quality of the experimental data. To adequately represent the interaction of the copper centers with acetylene and carbon dioxide molecules, improved parameters for the Cu-C(C$_2$H$_2$) and Cu-O(CO$_2$) interaction were derived from DFT computations for small model systems.
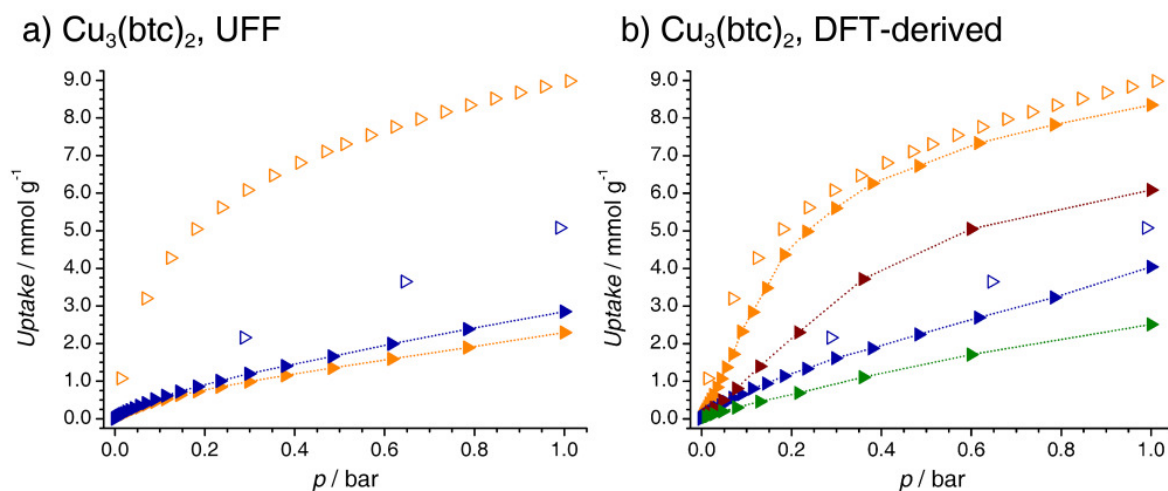
Figure 5.56. *a)* Calculated acetylene (orange) and carbon dioxide (blue) adsorption isotherms for Cu$_3$(btc)$_2$ obtained with unmodified UFF parameters to represent the framework atoms. Experimental data from (*323*) (acetylene) and (*246*) (carbon dioxide) are given as open symbols. *b)* Calculated acetylene and carbon dioxide adsorption isotherms for Cu$_3$(btc)$_2$ obtained with DFT-derived parameters to represent the interaction with unsaturated copper sites. Amounts of C$_2$H$_2$ and CO$_2$ adsorbed from a binary mixture are displayed in dark red and green, respectively.

The parameter derivation procedure was carried out in a similar manner as the development of the improved Cu-H$_2$ potential reported in section 5.2, with the additional requirement of accounting for electrostatic interactions. The calculations were carried out using

the DMOL^3 code, (*195, 289*) employing a DNP basis set and the PBE exchange-correlation functional. (*190*) Instead of a $Cu_2(bmc)_4$ paddle wheel, a $Cu_2(fa)_4$ (fa = formate) model system was used to minimize electrostatic long-range contributions. A side-on coordination was assumed for the C_2H_2 molecule, whereas an end-on coordination was used for CO_2 (figure 5.57). The opposite coordinations (end-on for C_2H_2, side-on for CO_2) do not result in significant binding, because the positively polarized regions of the adsorbed molecule point towards the copper center. The resulting potential energy curves are shown in figure 5.57.
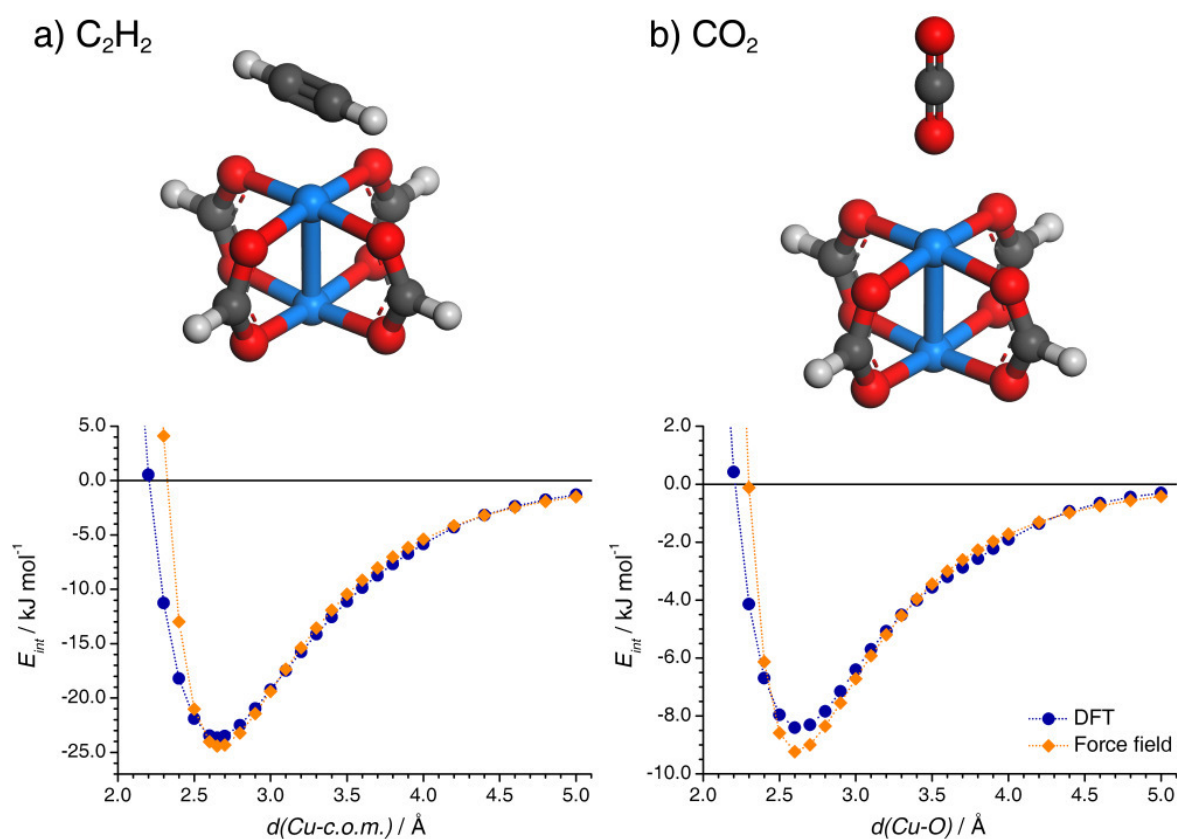
Figure 5.57. *Top:* Model systems used in DFT calculations for the Cu-C(C_2H_2) and Cu-O(CO_2) parameter derivation. *Bottom:* Resulting potential energy curves: DFT interaction energy (blue circles) and force-field energy (orange diamonds).

The DFT computations for acetylene predict a relatively strong binding of the C_2H_2 molecule to the unsaturated copper center, with an equilibrium distance of approximately 2.65 Å. This result is in line with experimental findings. (*323*) The Cu-C(C_2H_2) distance is significantly shorter than the sum of the van der Waals radii, straightforwardly implying that this short-range interaction cannot adequately be modelled with the default force-field parameters. In order to account for this metal-acetylene binding in the force-field based simulations, the parameters r_0 and D_0 representing the Cu-C(C_2H_2) interaction were adjusted to values that minimize the deviation between the DFT results and the force-field energy for

distances from 2.5 to 5 Å. While the electrostatic interactions with all atoms of the $Cu_2(fa)_4$ cluster were included in the calculation of the force-field term, the Lennard-Jones term was included only for the copper atom and the two nearest oxygen atoms that lie in plane with the molecular axis of the acetylene molecule. The optimized parameters are given in the Appendix, table A.8. As it is visible from figure 5.57, these adjusted LJ parameters provide for very good agreement of the two energy curves.

While the binding energy for CO_2 is much weaker than for acetylene, the DFT calculations still predict a significant interaction, and the $Cu-O(CO_2)$ equilibrium distance is much lower than the sum of the van der Waals radii. As for acetylene, the parameters r_0 and D_0 representing the $Cu-O(CO_2)$ interaction were adjusted to values that minimize the deviation between the DFT results and the force-field energy for distances ranging from 2.4 to 4 Å. Again, the electrostatic interaction with all atoms of the cluster was included in the force-field term, whereas the Lennard-Jones term was included only for the copper-oxygen interaction. The resulting force-field energy obtained with the optimized $Cu-O(CO_2)$ parameters is displayed in figure 5.57, and the parameters are given in table A.8.

All macroscopic quantities (isotherms, isosteric heats, selectivities) discussed in the following were obtained from simulations that employed the DFT-derived interaction parameters. The adsorption isotherms are shown in figure 5.56b. For acetylene, the agreement between simulation and experiment is almost perfect at pressures above 0.3 bar, whereas the uptake at lower pressures is significantly underestimated, indicating that the solid-fluid interaction predicted by the DFT-derived parameters is still somewhat too low. On the other hand, the calculated isosteric heat of adsorption at low coverage agrees well with the experimental value of approximately 32 kJ mol^{-1}. In the case of carbon dioxide, the results for the adjusted potential are not quite as satisfactory, as the uptake at a pressure of 1 bar is still underestimated by 20%. The isosteric heat of adsorption is approximately 3 kJ mol^{-1} lower than for acetylene. A considerably higher value has been obtained experimentally, reaching 35 kJ mol^{-1} in the limit of low coverage. [116] However, the fact that the experimental q_{st} decreases very quickly upon increasing loading might indicate a preferential adsorption at structural defects. The contribution of electrostatic interactions to the total potential energy is significant for acetylene, amounting to nearly 30%, but negligible for carbon dioxide.

The calculated C_2H_2/CO_2 adsorption selectivity of $Cu_3(btc)_2$ in the Henry's law regime is very low (figure 5.51a). On increasing pressure, the selectivity first increases until $\alpha = 3.3$ is reached at a pressure of 0.2 bar, and then decreases at pressures above 0.3 bar. Near this pressure, the number of C_2H_2 molecules per cell reaches the number of unsaturated metal sites (equivalent to 5.0 mmol g^{-1}). Accordingly, all sites where C_2H_2 is strongly favoured over CO_2 (as it will be discussed below) are occupied. The evolution of the C_2H_2/CO_2 selectivity on varying mixture composition is also quite interesting: Whereas the selectivity is low for acetylene-rich and equimolar mixtures, the selectivity increases considerably for CO_2-rich mixtures, reaching $\alpha = 5.9$ for a 1:19 C_2H_2/CO_2 mixture. This may indicate that $Cu_3(btc)_2$ could show interesting separation properties for even more extreme compositions, *e.g.* in the removal of trace amounts of acetylene.
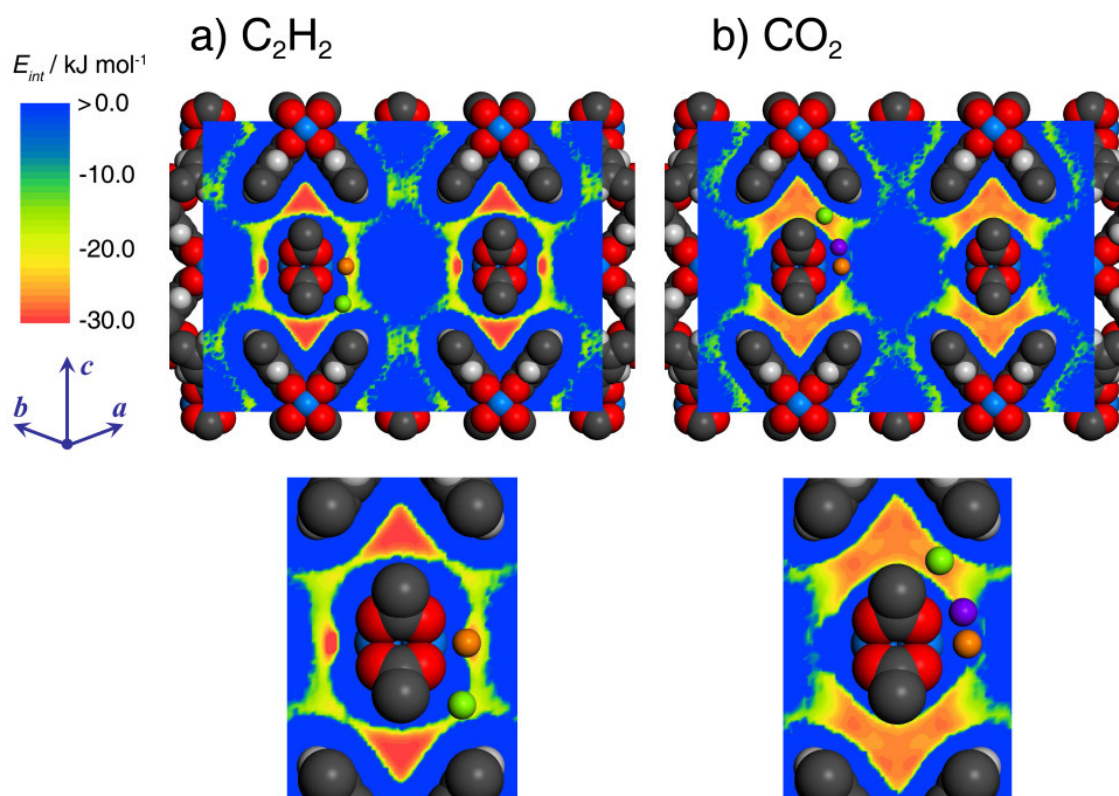
Figure 5.58. Potential energy maps derived from simulations of acetylene and carbon dioxide adsorption in $Cu_3(btc)_2$. Experimental adsorption sites are also shown at selected points of the simulation box. Due to the high degree of disorder of the adsorbed molecules, they are represented as spheres. For acetylene, the primary adsorption site at the unsaturated copper centers is displayed in orange, while the secondary adsorption site is shown in light green. (323) For carbon dioxide, two distinct position were refined for the adsorption site at the copper centers, which are given in orange and purple, respectively. (329) The secondary site is displayed in light green. An expanded view of the environment of one Cu_2 paddle wheel is given in the lower part of the figure.

Sections through the calculated potential energy distribution are displayed in figure 5.58. The interaction energy map for acetylene shows two preferential adsorption regions: The highest energy values are located at a distance of about 2.7 Å from the unsaturated metal centers, with an interaction strength of up to -33 kJ mol^{-1}. This is in line with the results from neutron diffraction experiments, where the adsorption site at the metal atoms (site A) was found to be occupied first. (323) Clearly, the correct prediction of this behaviour is related to the modification of the Cu-C(C_2H_2) parameters, which create a deep, narrow potential well in these regions. A second region of increased interaction energy is visible in the small pores. The second experimental position, site B, is located at a somewhat different position, at the entrance windows to these pores, rather than inside the pores. There are several possible explanations for this difference. Firstly, the accessibility of the pore under real conditions might be limited, owing to the rotational motion of the molecule. Secondly,

the adsorption of acetylene molecules at the copper sites could lead to an additional attractive contribution at the pore windows, because the distance between the two experimental positions is close to the equilibrium distance between two acetylene molecules. Finally, it must be considered that only one acetylene molecule could occupy the pore center, whereas all four windows can be occupied simultaneously. At sufficient pressure, geometric considerations should favour the window sites.

The potential energy map calculated for carbon dioxide exhibits only one region of significantly increased interaction, which is located inside the small pores, extending towards the pore windows. With approximately -27 kJ mol^{-1}, the interaction energy in these regions is in good correspondence with the isosteric heat of adsorption. It is approximately 3 kJ mol^{-1} lower than in the case of acetylene. In a very recent neutron diffraction study, these regions were found to be secondary adsorption sites. [329] The primary CO_2 adsorption positions, however, are located at the unsaturated metal sites. The sites were refined as two crystallographically non-equivalent positions, both of them being slightly displaced from the axial site directly above the metal center. The experimental adsorption sites are also included in figure 5.58. In the potential energy distribution, the increase at the unsaturated metal sites remains insignificant. Together with the observation that the simulation underestimates the carbon dioxide uptake, this indicates that the affinity of the copper centers towards CO_2 is still underestimated, despite the adjustment of the Cu-O(CO_2) parameters.

Similar to the behaviour observed above with regard to the separation of hydrogen-containing mixtures, the modest performance of $Cu_3(btc)_2$ for the separation of C_2H_2/CO_2 mixtures can be understood from the calculated potential energy distributions: Because the acetylene molecules are preferentially adsorbed at the copper centers, the small pores remain available for the co-adsorption of CO_2 molecules. The fact that the regions of increased interaction energy for CO_2 extend further towards the pore windows will also favour the preferential occupation of these regions by carbon dioxide molecules. However, the increased selectivity for CO_2-rich mixtures shows that the presence of preferential C_2H_2 adsorption sites could be beneficial for separation under special conditions: When the small pores are practically completely filled by carbon dioxide molecules, the affinity towards CO_2 decreases, while some of the metal sites are still accessible for acetylene. As a consequence, the C_2H_2/CO_2 selectivity increases.

5.4.5.5. Cucurbit[6]uril

The calculated C_2H_2 and CO_2 adsorption isotherms are displayed in figure 5.59, together with experimental data. [275, 324] It is noteworthy that the acetylene uptake is considerably underestimated by the simulation, with quantitative deviations up to 0.8 mmol g^{-1}. In addition, the isosteric heat of C_2H_2 adsorption derived from the simulations is much lower than the experimental values: q_{st} values up to 75 kJ mol^{-1} have been obtained for low coverages, with a sharp decrease to 35 kJ mol^{-1} at a loading of 2 mmol g^{-1}. [275] For carbon dioxide, a hysteresis of the adsorption and desorption branch has been reported from exper-

iment. (*324*) Both branches are included in figure 5.59. At a pressure of 1 bar, the agreement between simulation and experiment is excellent. However, the simulation tends to moderately overestimate the amount adsorbed at intermediate pressures, and ranges between the adsorption and desorption branch at $p < 0.1$ bar. The calculated isosteric heat of CO_2 adsorption is the highest of the five systems considered. It is in good correspondence with the experimental value, which amounts to 33 kJ mol^{-1} in the limit of zero coverage. Electrostatic interactions contribute less to the total potential energy in CB[6] than in most MOFs, but are somewhat more pronounced than in Silicalite.
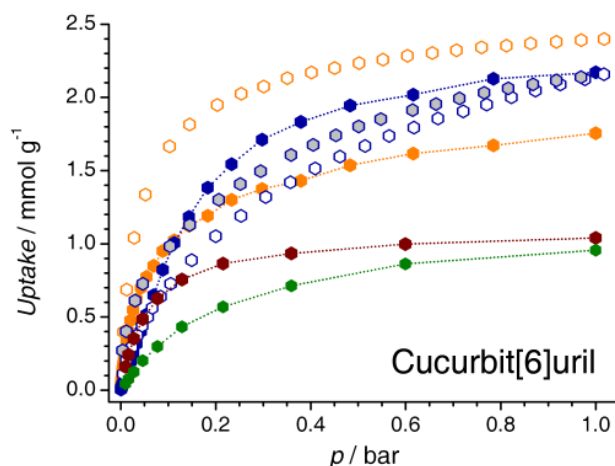
Figure 5.59. Calculated acetylene (orange) and carbon dioxide (blue) adsorption isotherms for cucurbit[6]uril. Experimental adsorption data from (*275*) (acetylene) and (*324*) (carbon dioxide) are given as open symbols. Symbols representing the experimental CO_2 adsorption branch are displayed with a white interior, whereas the desorption branch is represented with symbols having a grey interior. Amounts of C_2H_2 and CO_2 adsorbed from a binary mixture are displayed in dark red and green, respectively.

In a previous publication that reports some of the results presented here, it has been speculated that the differences between the experimental and the simulated acetylene isotherm may be due to the possibility of a partial occupation of the intramolecular cages of the CB[6] macrocycle by C_2H_2 molecules. (*330*) Experimentally, there is no evidence for an occupation of these cages: Thermogravimetric measurements indicate that water molecules remain in these cavities even after activation at elevated temperature under vacuum, and no acetylene adsorption at these positions was observed in X-ray diffraction experiments. On the other hand, the quantitative deviation of 0.8 mmol g^{-1} would correspond well with an occupation of the majority of cages by one C_2H_2 molecule (a complete occupation of the cages would equal 1.0 mmol g^{-1}). Moreover, this assumption could also serve to explain the high isosteric heat of adsorption, because calculations for a model system consisting of an isolated CB[6] molecule delivered a high potential energy of nearly -60 kJ mol^{-1} inside the cages (Appendix, figure A.32). However, the observations for carbon dioxide, for which experimental data were published only recently, are quite contradictory: Here, relatively good agreement between simulation and experiment is observed, although X-ray diffraction measurements

on CO_2-loaded samples have delivered an occupation of some of the intramolecular cages by carbon dioxide molecules. (*324*) Taking together these conflicting observations, the body of experimental and simulation results does not permit any definite conclusions concerning the accessibility of the intramolecular cavities for adsorbed molecules. For an ideal, static structure, the access to the cavities should be completely blocked. Therefore, it can be expected that structural defects and/or thermal motion may play a key role. A further elucidation would require additional experimental studies, possibly supplemented by molecular dynamics calculations. In the context of this work, however, it is assumed that the cavities are completely blocked.

The Henry's law selectivity of cucurbit[6]uril towards a C_2H_2/CO_2 mixture is modest, amounting to $\alpha = 4.0$. The selectivity decreases on increasing pressure, almost reaching unity at a pressure of 1 bar. Interestingly, the evaluation of the selectivity as a function of the mixture composition reveals that carbon dioxide is favoured over acetylene for C_2H_2-rich mixtures, leading to selectivity values $\alpha < 1$ (figure 5.51b). A qualitatively similar (though quantitatively different) behaviour has been observed above for the case of Zn(dtp). The decrease of the selectivity at high acetylene loadings was rationalized with the ability of CO_2 molecules to fill the channels more efficiently than C_2H_2 molecules, *e.g.* by orienting in a way that the average molecule-molecule distance is minimized. The peculiar evolution observed for CB[6] can be interpreted in a similar manner: At low pressures and low C_2H_2 concentrations, acetylene is preferentially adsorbed due to the higher affinity of the framework towards this species, which is reflected by the higher isosteric heat of adsorption. However, under conditions where the acetylene saturation uptake is nearly reached, the adsorption of additional carbon dioxide molecules is still possible, which is why CO_2 is favoured over C_2H_2. The underlying assumption that carbon dioxide can adopt a more efficient packing in the channels is also in line with the higher CO_2 adsorption capacity observed in the single-component isotherms.

Figure 5.60 shows sections through the calculated potential energy distributions. As for $Cu_3(btc)_2$, experimental adsorption sites have been reported for both acetylene and carbon dioxide. (*275, 324*) However, a direct comparison is hampered in the case of CO_2 due to differences of the cucurbit[6]uril parent structures that were determined in the two experimental studies. For example, a different choice of origin was used, and a higher degree of structural disorder of the parent structure was found in the study by Kim *et al.* (*324*) While the experimental C_2H_2 adsorption sites are included in figure 5.60, only a qualitative comparison is made for carbon dioxide.

The potential energy distribution obtained for C_2H_2 exhibits regions of strongly increased interaction energy of more than -35 kJ mol^{-1} in the lateral cavities of the channels, surrounded by four CB[6] macrocycles. In experimental X-ray diffraction measurements at low temperature, a disorder of the acetylene molecules over two possible positions was observed, molecule A having an occupancy of 0.66, molecule B an occupancy of 0.34. (*275*) The carbon atoms of molecule A lie in the region of highest interaction potential obtained in the simulation. One of the hydrogen atoms of the C_2H_2 molecule points towards the carbonyl

oxygen, with a C-H$\cdots$O distance of 2.47 Å. This indicates a contribution of hydrogen bonding. Concerning molecule B, one of the carbon atoms coincides with molecule A. However, the molecule as a whole has a completely different orientation, directly pointing towards the pocket formed by four CB[6] molecules. The distance to the carbonyl oxygen is slightly higher (2.51 Å). The larger part of this molecule lies outside the highly attractive region.
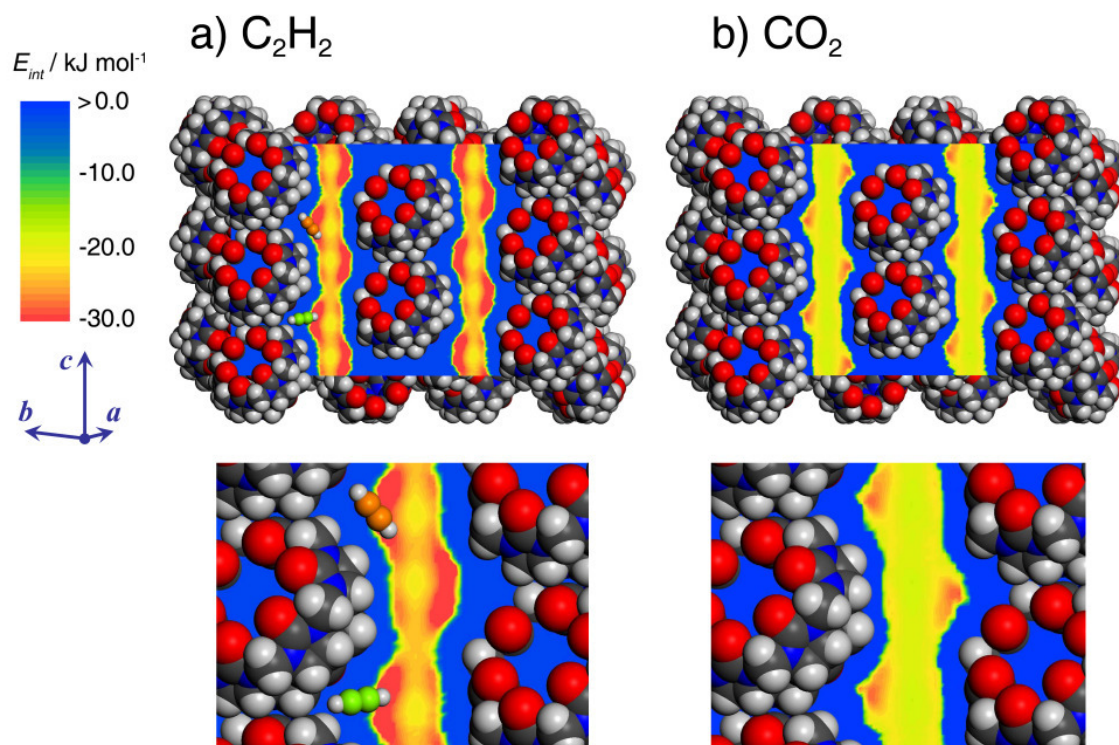
Figure 5.60. Potential energy maps derived from simulations of acetylene and carbon dioxide adsorption in cucurbit[6]uril. Experimental acetylene adsorption sites from (*275*) are shown at selected points of the simulation box, molecule A in orange, molecule B in light green. An expanded view of a single channel is given in the lower part of the figure.

The potential energy distribution for carbon dioxide also exhibits minima of the interaction energy in the lateral cavities. While the energy values visible in the section displayed in figure 5.60 do not exceed -30 kJ mol^{-1}, higher interaction energies up to -35 kJ mol^{-1} are reached slightly above and below the section. Experimentally, two distinct adsorption sites in the channels of CB[6] were determined (the position inside the macrocycle is not considered in this context). (*324*) Molecule A, which has an occupancy of 0.64, directly points into the lateral cavities, providing for a strong interaction with several of the CH$_2$ groups. The average C=O$\cdots$H-C distance amounts to 2.58 Å, a value that was considered indicative of hydrogen bonding by Kim and co-workers. (*324*) Molecule B, which has an occupancy of 0.33 (the occupancies do not add up to 1 because the channels are not completely filled) is located closer to the center of the channels. One of the oxygen atoms also points towards the CH$_2$ moieties of two macrocycles, but the C=O$\cdots$H-C distances are higher (> 2.8 Å).

As the lateral cavities of the channels are preferential adsorption regions for both molecules, it can be expected that a full occupation of these sites will lead to a change in the slope of the isotherm. A complete occupation would correspond to an uptake of 2.0 mmol g^{-1}. In the case of carbon dioxide, this amount is surpassed at pressures slightly below 1 bar. While the slope of the isotherm is quite shallow, it seems that the adsorption of additional molecules in the center of the channel is still possible. For acetylene, saturation seems to be nearly reached at a loading of 1.7 mmol g^{-1}, which may indicate that a complete occupation of the cavities is hampered by an intermolecular repulsion between neighbouring molecules.

5.4.6. Results: Henry's law selectivities for other gas mixtures

In the previous subsections, a very good correspondence between the Henry's law selectivity and adsorption selectivities derived from mixture isotherm calculations has been observed. While a rigorous relationship between the ratio of the Henry constants and the selectivity holds only in the limit of zero coverage, the agreement remains good even at considerably higher loadings in many cases. Because a calculation of the Henry constant is computationally much less demanding than the calculation of a complete mixture isotherm, an evaluation of the Henry constants for different gas mixtures is a useful first step to identify promising candidate materials for the separation of a particular mixture of interest. For example, routine calculations of the Henry constant of methane for a tremendous number (> 100) of MOF structures have been reported recently by Haldoupis *et al.* (*153*)

Since Henry constant calculations have been carried out for a total of five gases, there are ten different binary mixtures for which the adsorption selectivity in the limit of zero coverage can be calculated. Three of these mixtures have already been discussed. For the remaining seven mixtures, the ratios of the Henry constants at $T = 298\,\mathrm{K}$ are summarized in table 5.5.

Table 5.5. Ratio of calculated Henry constants at $T = 298\,\mathrm{K}$ for gas mixtures which were not discussed previously. Particularly high selectivities are highlighted with bold letters.

	Silicalite	Mg-formate	Zn(dtp)	Cu$_3$(btc)$_2$	CB[6]
$K_H(CO)/K_H(O_2)$	1.8	2.5	2.4	1.7	2.2
$K_H(CO_2)/K_H(H_2)$	206	330	240	171	**506**
$K_H(CO_2)/K_H(O_2)$	17.8	23.6	26.5	22.3	28.7
$K_H(CO_2)/K_H(CO)$	9.8	9.6	11.0	13.5	13.2
$K_H(C_2H_2)/K_H(H_2)$	425	**4187**	1073	369	2027
$K_H(C_2H_2)/K_H(O_2)$	36.6	**299**	118	48.0	115
$K_H(C_2H_2)/K_H(CO)$	20.1	**121**	49.1	29.0	53.0

None of the system shows a promising selectivity towards CO/O_2, CO_2/CO, or CO_2/O_2 mixtures. In all cases, it is noteworthy that the ratios of the Henry constants lie in a very similar range despite the different adsorption properties of the five materials. For both CO_2/CO and CO_2/O_2 mixtures, considerably higher selectivities can be expected for ZIFs with linkers that contain nitro groups, due to the strong electrostatic interaction of the carbon dioxide molecules with the nitro group. (*129*) Interestingly, a higher CO_2/CO selectivity has been derived for cucurbit[6]uril from experimental data, amounting to $\alpha = 46$ in the Henry's law region. (*324*) This may be related to a partial accessibility of the intramolecular cages in the real system.

In contrast to this, the selectivity of cucurbit[6]uril towards a CO_2/H_2 mixture is exceptionally high in comparison to the other systems. While an even higher selectivity has been predicted for a MOF with an anionic framework, (*136*) the values of α obtained from similar computations for other MOFs and ZIFs are typically much lower. (*331, 332*) Experimentally, a much higher Henry's law selectivity has been determined for a 5A zeolite. (*9*) To a large part, the high affinities of these materials towards carbon dioxide can be attributed to electrostatic interactions. Therefore, it is interesting to note that cucurbit[6]uril exhibits a high CO_2/H_2 selectivity in spite of the low polarity of the framework. Instead, the pore topology leads a maximization of dispersive interactions with adsorbed carbon dioxide molecules, thereby providing for a high selectivity.

Another interesting observation is made for the mixtures that contain acetylene. Here, Mg-formate exhibits a very high selectivity towards C_2H_2, the values of α typically being at least twice as high than the values calculated for the other four systems. These observations highlight the very high affinity of Mg-formate towards acetylene, which is caused by a favourable combination of strong dispersive interactions in the narrow pores and strong electrostatic interactions of the positively polarized ends of the C_2H_2 molecule with the negatively polarized pore walls. Therefore, Mg-formate could be a very useful material for the removal of acetylene impurities from the gas feed in processing plants, such as air separation units.

5.4.7. Discussion

5.4.7.1. Methodology: Advantages and possible improvements

In the sections 5.1 and 5.2, which addressed the hydrogen storage properties of MOFs at low temperatures, a strong emphasis was put on the agreement of simulation results with experimental data. Such a rigorous comparison with experimental data is not possible in this context, where adsorption data of gases like oxygen, carbon monoxide, or acetylene are often lacking. Moreover, even in those cases where experimental data are available, the results are sometimes ambiguous: For cucurbit[6]uril, a reasonable agreement with experiment is attained for carbon dioxide, whereas the gas uptake is underestimated for acetylene, but strongly overestimated for carbon monoxide. From these conflicting observations, it can only be concluded that a more detailed characterization using both experimental and computational methods is necessary to identify the origin of the deviations.

From a methodological point of view, the extension from single-component adsorption isotherms to binary mixture isotherms is straightforward. Provided that there are no systematic errors in the description of the solid-fluid interaction, it can be expected that the computed adsorption selectivities can be considered to be relatively accurate. Thus, a combined experimental-theoretical approach appears most promising, which uses experimental high-quality measurements of the single-component isotherms for parameter validation, but employs molecular simulations to predict the selectivities. Tedious experimental measurement of mixture isotherms could be avoided with this procedure. Moreover, such an approach could replace or complement methods that predict mixture data from single-component isotherms, such as the Ideal Adsorbed Solution Theory (IAST). In this context, it should be mentioned that the breakdown of IAST has been demonstrated for energetically very heterogeneous adsorbents. (*333*) For a given system, GCMC simulations may serve to test the applicability of IAST. A combination of experimental measurements and GCMC simulations has been reported, for example, by Lamia *et al.* for the separation of propane/propylene mixtures in $Cu_3(btc)_2$. (*131*)

In this section, it has been shown how the calculated potential energy distribution can be used to quantify the strength of the solid-fluid interactions in different regions of the structure. A comparison of the potential energy distributions obtained for different molecules can lead to a better understanding of the separation behaviour of the material. However, this information does not necessarily provide for a complete understanding of the nature of the interactions: For molecules consisting of more than one interaction site, the strength of the interactions may strongly depend on the orientation of the molecule. This is particularly important for electrostatic interactions. The potential energy distribution delivers only the interaction energy at the center of mass, and averages over different orientations according to their probability. Only a knowledge of the most favourable orientation delivers full insights into the importance of electrostatic interactions, *e.g.* by observing that a positively polarized area of the molecule points towards a negatively charged framework atom. Where available, such orientational information can be taken from experimental data, as it

has been done for the adsorption of C_2H_2 in some of the systems. Alternatively, additional simulations could be used to identify the most favourable location of an adsorbed molecule, as well as its orientation, from simulation snapshots which have a particularly low energy. A final remark should be made on the derivation of improved parameters for the interaction of acetylene and carbon dioxide with the copper centers in $Cu_3(btc)_2$. In principle, similar limitations as those discussed in 5.2.7.1 apply here. In addition to the limited accuracy of the DFT computations, it should be pointed out that the representation of the interactions with the metal center by a simple Lennard-Jones potential is purely artificial. The actual interactions, which may include orbital interactions with the π-system in the case of acetylene, or polarization interactions, will show a much more complex behaviour on variations of the distance and angle than the simple combination of electrostatic interactions and modified Lennard-Jones parameters can reflect. Possible improvements, however, will not only require a refined potential model, but also a more extensive screening of the potential energy surface using *ab-initio* methods.

Table 5.6. Summary of simulation results on gas separation. In a simplified manner, the importance of dispersive and electrostatic interactions is reported for each of the three mixtures under consideration.

Separation	Dispersive interactions	Electrostatic interactions	Most promising material(s)
CO/H_2	favour CO over H_2	important, strongly favour CO over H_2	Mg-formate, cucurbit[6]uril
O_2/H_2	favour O_2 over H_2	minor, slightly favour H_2 over O_2	cucurbit[6]uril
C_2H_2/CO_2	similar for both species	important, depend on pore wall polarity due to different sign of the quadrupole moment θ	Mg-formate

5.4.7.2. Towards an understanding of the structural origins of selectivity

An overview of the most important findings reported in this section is given in table 5.6, with a particular emphasis on the significance of dispersive and electrostatic interactions. Of the materials under consideration, Mg-formate shows the highest selectivity towards a CO/H_2 mixture. The narrow channels lead to a high affinity towards carbon monoxide over hydrogen due to the enhanced dispersive interactions. Moreover, the electrostatic interactions of the adsorbed molecules with the pore wall favour carbon monoxide, which has a weak dipole and a relatively strong quadrupole moment, over the weakly quadrupolar hy-

drogen molecule. Despite the much weaker electrostatic interactions in cucurbit[6]uril, the CO/H_2 selectivity of this system is similarly high at low loadings. However, it decreases rapidly on increasing loading. This decrease may be due to the fact that the interaction energy throughout the channels shows relatively pronounced variations: At higher loadings, it becomes more and more probable that some carbon monoxide molecules will occupy regions where the interaction strength is not maximal, thereby reducing the selectivity over hydrogen. In contrast to this, the interaction energy in the channels of Mg-formate exhibits extended minima of similar interaction strength. It can thus be expected that the potential energy of adsorption of additional molecules will remain nearly constant up to relatively high loadings.

Compared to Mg-formate and cucurbit[6]uril, the channels of Zn(dtp) and Silicalite are too wide to reach similarly high selectivities. Moreover, electrostatic interactions, which generally tend to increase the affinity towards CO over H_2, are practically absent in Silicalite. For $Cu_3(btc)_2$, the unsaturated metal sites act as strongly preferred CO adsorption sites due to the electrostatic interactions of the carbon monoxide molecules with the copper centers. However, the CO/H_2 selectivity remains low, because the large free volume of the structure permits a significant co-adsorption of hydrogen. In total, it can be expected that systems that combine narrow channels with sites that provide for a localized interaction with the CO molecules appear as most promising materials that could exhibit an enhanced selectivity. The very high Henry's law selectivity of zeolite 5A, which contains Ca^{2+} cations, should be mentioned in this context. It amounts to $\alpha = 125$ according to the experimental work of Sircar and Golden. (9) From the results presented here, it can be deduced that considerable optimization efforts are necessary to surpass this selectivity in a metal-organic framework. Due the importance of electrostatic interactions, the investigation of systems with extra-framework cations could be most rewarding.

In contrast to the observations made for a CO/H_2 mixture, the selectivity of a material towards an O_2/H_2 mixture is decreased with increasing magnitude of electrostatic interactions: Whereas dispersive interactions favour oxygen due to its higher polarizability, the contribution of electrostatic interactions is higher for hydrogen due to its larger quadrupole moment. Thus, the affinity for oxygen over hydrogen is decreased in systems where electrostatic effects play a significant role. This explains why Mg-formate exhibits a much higher CO/H_2 selectivity than Silicalite, while the O_2/H_2 selectivity of both systems is practically identical. A similar effect is observed for Zn(dtp). For $Cu_3(btc)_2$, the low selectivity is again related to the large pore volume, which permits a co-adsorption of the more weakly adsorbed species. Of the five materials considered, the porous molecular crystal cucurbit[6]uril emerges as the most promising material for O_2/H_2 separation. While dispersive interactions with the oxygen molecules are maximized in the lateral cavities, electrostatic interactions do not play a role due to the low polarity of the pore walls. Because the absence of significant electrostatic interactions is beneficial for the separation of oxygen and hydrogen, it can be concluded that the screening of new potential materials should concentrate on non-polar adsorbents with narrow pores.

From the single-component acetylene adsorption isotherms presented, it is obvious that $Cu_3(btc)_2$ is the material with the highest acetylene adsorption capacity. The important role of the unsaturated metal sites for the total C_2H_2 uptake has been demonstrated by comparing calculations with different parameters for the interaction of acetylene with the Cu sites. The importance of the metal centers is further highlighted by the fact that $Cu_3(btc)_2$ can adsorb much more acetylene at room temperature and $p = 1$ bar than other MOFs with a larger pore volume, *e.g.* IRMOF-1. (*323*) It is noteworthy that comparably high uptake capacities have been reported for other MOFs with unsaturated metal sites, such as MOF-74 analogues with different metal centers. (*334*)

Similarly to what has been observed for CO/H_2 separation, Mg-formate is the best material for C_2H_2/CO_2 separation. This can be explained with the particular role of electrostatic interactions: While the interaction strength in the central regions of the narrow channels is comparably favourable for both acetylene and carbon dioxide when dispersive interactions are considered, only the C_2H_2 molecules can maximize the electrostatic contribution by assuming an orientation perpendicular to the running direction of the channels. Thus, the separation of the two molecules in Mg-formate takes advantage of the different molecular charge distributions of acetylene and carbon dioxide, reflected by the opposite sign of the quadrupole moment. It would be interesting to extend this concept to other pairs of molecules with quadrupole moments of similar magnitude, but opposite sign. Because the channels of Mg-formate are very narrow, the preferential adsorption of C_2H_2 in the widest regions leaves practically no space for the adsorption of additional CO_2 molecules. This efficient blocking of the pores is responsible for the high C_2H_2/CO_2 selectivity. Moreover, the calculation of the Henry's law selectivities revealed that Mg-formate exhibits a very high preference for acetylene over all other gases considered. This indicates that the favourable combination of dispersive interactions and electrostatics in the narrow channels makes Mg-formate a nearly "ideal" material for the selective adsorption of acetylene. In contrast to this, both Zn(dtp) and $Cu_3(btc)_2$ permit a significant co-adsorption of carbon dioxide, because acetylene is only favoured in some regions of the available pore volume. Silicalite and cucurbit[6]uril lack a significant polarity of the pore wall, which is necessary to separate two molecules with similar polarizabilities, but different electrostatic properties.

6. Conclusions and Outlook

In this work, force-field based simulations, DFT calculations, as well as combinations of both force-field methods and electronic structure methods have been employed to study a range of topics related to the adsorption and separation of gases in metal-organic frameworks and other microporous materials. It must be emphasized that none of the computational approaches used can be considered completely "novel" from a methodological point of view. Instead, most emphasis has been put on the development of a better understanding of the relationships between macroscopically observable quantities, such as adsorption isotherms, and microscopic interatomic interactions. Therefore, this study provides a showcase example how molecular simulations can provide a molecular-scale explanation of materials properties observed experimentally.

The GCMC study of hydrogen adsorption in eight structurally different MOFs (IRMOF-1, MOF-74, ZIF-8, $Cu_3(btc)_2$, MOF-505, $(Mn_4Cl)_3(btt)_8$, UMCM-150, PCN-12) showed that the prediction of low-temperature hydrogen adsorption isotherms is practically routinely applicable. A set of transferable parameters was used, without any system-specific adjustments. In spite of this rather crude way of choosing the parameters, a reasonably good agreement of the adsorption isotherms with experimental data was observed, with the exception of those systems that contain unsaturated metal centers as strong interaction sites. In particular, the saturation uptake was correctly predicted for all systems, with a maximal error of 0.5 wt%. Therefore, it can be expected that analogous simulations are able to deliver a good estimate of the attainable hydrogen uptake for other structurally distinct systems. These predictions could be highly useful in combined experimental and theoretical studies, *e.g.* for a cross-validation with experimental isotherms.

In addition to the adsorption isotherms, the hydrogen density fields obtained from the simulations were analyzed in detail. Approximate Wyckoff coordinates were assigned to the visible density maxima and compared to experimental H_2 adsorption sites. A very good agreement was observed for the large majority of positions. This finding highlights that the relatively simple simulation approach is capable of reproducing both macroscopic and microscopic features that can be determined experimentally. Because the molecular simulations provide similar insights as neutron diffraction techniques, the method could be used to complement or replace these sophisticated experiments, which can only be carried out for selected systems of particular interest. Moreover, the observation of density maxima permits some conclusions which regions of the structure are most favourable for hydrogen adsorption, thus providing guidelines for the development of better H_2 storage materials.

In the systems studied, the most pronounced density maxima are located near the inorganic building units, whereas maxima above the linker molecules are typically rather weak and diffuse. Therefore, the creation of MOF topologies with a relatively high density of inorganic connectors could be a promising route to obtain materials with an increased affinity towards hydrogen.

Another important feature is the diameter and shape of the pores, as shown by the example of PCN-12: Here, the adsorption sites observed in the small cages have a site-site distance that is close to the equilibrium distance between two H_2 molecules ($\approx$ 3.4 Å). In other words, the specific features of the pore geometry provide for a high density of preferred adsorption positions, a property that is very desirable for materials with an optimized storage performance. Unfortunately, it is not straightforward to transfer this concept to the synthesis of new materials, because there is no general, reliable procedure to determine the resulting MOF structure prior to an experimental realization of the system. Instead, various experimental studies have shown that even intricate changes of the reactants (linker, metal salt) or synthesis conditions (solvent, temperature, additives) may lead to the formation of completely different structures. For a given topology, however, the simulations can make useful predictions on how possible modifications of the structure would affect the hydrogen storage properties. Such modifications could include the replacement of the linker by an analogous, longer molecule, the introduction of non-coordinated substituents, or postsynthetic modification. Linker functionalization strategies can be expected to have a beneficial influence for two reasons: In the first place, they permit a certain tuning of the pore size. Moreover, the hydrogen molecules may interact more strongly with the substituents due to enhanced dispersive and, possibly, electrostatic interactions.

While the methodological approach is quite mature, there is always space for improvement. It should be emphasized that there is no particular justification for the choice of the force-field parameters used, apart from their capability to reproduce experimental adsorption isotherms. Thus, the development of new parameter sets specifically designed for the modelling of adsorption in MOFs could help to improve the accuracy of the GCMC simulations. The physical consistency of the description of interatomic interactions is another issue: In this work, all interactions were modelled by a simple Lennard-Jones potential. In a real system, the total interaction corresponds to a superposition of several contributions that behave differently as a function of the interatomic distance. A more detailed representation, *e.g.* the explicit inclusion of polarization interactions, would be another desirable improvement that could lead to new physical insights. Finally, an automatted procedure to identify the hydrogen density maxima, rather than a user-based search, would be most useful for routine determinations of preferred hydrogen adsorption sites.

During the analysis of the simulation results obtained with literature parameters, it became apparent that MOFs with coordinatively unsaturated metal sites constitute a particular challenge to the application of modelling methods: Because the strongly localized interaction of an adsorbed H_2 molecule with the metal center is not adequately represented by the

standard force-field parameters, the simulations underestimate the hydrogen uptake at low pressures. Moreover, no density maxima are visible at the unsaturated metal sites, although experimental studies deliver these positions as primary adsorption sites. In order to correct for this shortcoming, improved parameters were derived from DFT calculations for a model system with accessible copper centers, which delivered an interaction energy of approximately -6 kJ mol^{-1} and an equilibrium distance of 2.4 Å. These parameters were integrated into the GCMC code and tested for two systems with unsaturated copper sites, $Cu_3(btc)_2$ and PCN-12. While the usage of the parameters in their unscaled form led to an overestimation of the H_2 uptake, a scaling that averages over all possible orientations provided for excellent agreement with experimental adsorption isotherms, particularly for low pressures. As it was expected, the additional amount of hydrogen adsorbed is equivalent to one H_2 molecule per copper center. On the other hand, the saturation uptake was slightly overestimated, possibly due to an artificial increase of the interaction at intermediate distances caused by the parameter modification. Further computations for copper in a different coordination environment (($Cu_4Cl)_3(btt)_8$) indicated a certain degree of transferability.

In addition to the simulations carried out for cryogenic conditions, hydrogen adsorption isotherms were calculated for $T = 200\,K$ and $T = 298\,K$. Here, the differences between the isotherms obtained with the unmodified parameters and the improved Cu-H_2 potential model were much less pronounced, indicating that the metal-hydrogen interaction is too weak to lead to a significant occupation of the metal sites by H_2 molecules under these conditions. It would therefore be necessary to enhance the metal-hydrogen interaction strength in order to permit a stable coordination of hydrogen to the metal sites at increased temperatures. Possible strategies could include chemical modifications of the environment of the metal center that lead to a stronger affinity towards adsorbed molecules, *e.g.* through substituent effects, or the introduction of metal sites in a completely different coordination environment, *e.g* in porphyrin or salen groups that could be incorporated into the linker molecule. In principle, an optimization of the pore topology could also be a promising option, if it was possible to arrive at a structure that permits an overlap of the contributions stemming from neighbouring metal centers. However, this is hardly imaginable due to the short-range character of the interaction: Even in PCN-12, where the copper atoms assume a very close packing, it was observed that the interaction energy at one metal center is practically unaffected by its neighbours. To assess the influence of a strongly enhanced interaction strength, additional simulations employing a hypothetical metal-H_2 potential with a well depth of -15 kJ mol^{-1} were carried out. These calculations showed that the assumed interaction strength would be sufficient to provide for a complete occupation of the metal centers at increased temperatures. However, the overall gravimetric uptake of the hypothetical systems remained very modest due to the limited number of metal sites. This last aspect highlights a central problem of the concept of introducing coordinatively unsaturated metal centers to enhance the solid-flud interaction strength: In typical MOF structures, a full occupation of the metal sites corresponds to a hydrogen uptake of only 1.0 to 1.5 wt%. While it would be desirable to increase the density of metal sites, this will inevitably lead to

an increase of the density of the MOF, because the metal atoms have a higher atomic weight than typical atoms constituting the linker molecules. In turn, this density increase will reduce the attainable gravimetric uptake.

The proposed parameter derivation constitutes a computationally very efficient approach that permits a significantly improved prediction of adsorption isotherms for MOFs with unsaturated metal sites. Because the potential parameters for the metal center are combined with literature force-field parameters for all other atoms of the framework, only a limited set of DFT computations is necessary. Therefore, the procedure could be easily extended to other MOFs with different metal centers. However, it must be emphasized that the derivation as presented here is based on a relatively crude approximation, since it was assumed that the DFT interaction energy equals the interaction of hydrogen with the metal center, and that all other contributions to the total DFT energy are negligible. A more sophisticated approach should use an electronic structure method that recovers all long-range interactions, particularly dispersive interactions, and then employ an adequate decomposition scheme to unequivocally determine the magnitude of the metal-H_2 interaction. Moreover, usage of an anisostropic potential model, rather than the isotropic Morse potential, would give a physically more sound description. As mentioned previously, the explicit inclusion of electrostatic and polarization interactions would be another option. Possibly, part of the interaction with the metal center could already be recovered by this approach, without the necessity of deriving specific metal-H_2 parameters.

An extended set of DFT calculations for model systems with coordinatively unsaturated copper centers with different ligand environments has shown that modifications of the ligand lead to significant changes of the electron density at the Cu atoms, which in turn influence the strength of the copper-hydrogen interaction. The most prominent indicator is the correlation between the DFT interaction energy and the Hirshfeld charge at the copper center: Electron-withdrawing ligands, such as nitro groups or nitrogen-rich heteroaromatics, polarize the Cu-O bonds, thereby leading to a decrease of the electron density at the Cu center reflected by an increased Hirshfeld charge. For these systems, the interaction with an adsorbed hydrogen molecule is stronger than for the reference system (containing unmodified benzoic acid ligands), whereas the interaction is weakened for systems with electron-donating substituents. The observed trends show that the copper-hydrogen interaction is dominated by electrostatic and polarization contributions. On the other hand, there are no indications for Kubas-type orbital interactions.

It must be emphasized that the DFT results cannot be interpreted in a quantitative manner due to the neglect of long-range interactions (dispersion) and vibrational effects. However, the qualitative evolution can provide some insights into the relative change of the interaction energy induced by a modification of the ligand. With a maximal increase of the interaction energy by 30% for a monosubstituted system, the computational results indicate that modifications of the MOF linker molecule could be employed to tune the strength of the metal-hydrogen interaction within a certain range. It would be very interesting to

attempt an experimental verification of these results by synthesizing a series of isostructural MOFs with different substituents (or different heteroaromatic linkers) and unsaturated metal sites. Additionally, similar calculations could be carried out for periodic systems to assess whether these effects are increased, decreased, or even absent in an extended structure. Another aspect that has not yet been widely studied is the change of the interaction strength in the direct environment of the substituents. Further computational work could be useful to identify those substituents which have the most favourable effect.

From the discussion of the GCMC simulations assuming different strengths of the metal-H_2 interaction, it is apparent that the interaction energies observed here, even for the functionalized systems, are too weak to lead to a significant adsorption at the metal sites at room temperature. A much more pronounced increase of the interaction strength would be necessary for the development of hydrogen storage materials with an improved performance under ambient conditions. In this context, it would be worthwhile to investigate analogous systems with different metal centers that might provide for a stronger electrostatic interaction, or even Kubas-type metal-hydrogen bonding. While a screening of a wide range of systems could be very rewarding from a theoretical point of view, the synthetic feasibility remains the most important limiting factor with regard to applications.

Initial DFT-D computations aiming at a validation of the method showed that the method gives nearly quantitative agreement with the results of high-quality wave-function based methods for the interaction of hydrogen with simple aromatic molecules. Further calculations were then employed to assess whether modifications of the organic molecule can enhance the interaction strength. It was found that the introduction of nitrogen heteroatoms into aromatic six-membered rings does not lead to a significant increase of the interaction with a hydrogen molecule located above the ring. An energy decomposition analysis performed for benzene and triazine revealed the importance of electrostatic interactions, which are determined by the charge distribution of the aromatic system. From the results, it can be expected that the introduction of nitrogen-containing linkers in MOFs will not lead to a stronger direct interaction of adsorbed hydrogen molecules with the linkers (however, there may be an indirect influence on the interaction with adjacent metal sites, as discussed above). Having demonstrated the applicability of the method, it could be interesting to extend the investigation to aromatic molecules with other heteroatoms, such as sulfur. Moreover, periodic, graphene-like systems with a certain concentration of heteroatoms as "defects" could be worth studying. Here, the heteroatoms, which constitute local inhomogeneities in the electrostatic potential, could act as preferential adsorption sites.

DFT-D computations addressing the interaction of hydrogen with non-linear organic molecules with different central atoms (carbon, silicon, germanium) revealed that the incorporation of single atoms with an increased polarizability has relatively little impact on the total interaction energy. Instead, geometric properties, particularly the bond distances and angles around the central atom, were found to be more important. In the specific case investigated, the highest interaction energies were reached when the interaction of the H_2

molecule with two phenyl moieties was maximized. As a consequence, the introduction of atoms with a higher polarizability in the linker molecules does not seem to be a very promising strategy to obtain MOFs with improved hydrogen storage properties. However, the influence of the central atoms could become more important when gases with a higher polarizability are adsorbed, *e.g.* for methane storage applications, or in the separation of Kr/Xe mixtures. These topics could be addressed in further DFT-D studies, possibly in combination with force-field based simulations or, ultimately, adsorption experiments.

Taken together, the computations reported in this work have provided valuable insights into the adsorption of hydrogen in MOFs at an atomistic level. In particular, the results permitted some conclusions concerning the possibilities to enhance the affinity of a MOF towards hydrogen, *e.g.* by optimizing the pore topology, or by tuning the interaction of H_2 molecules with unsaturated metal sites through the introduction of non-coordinated substituents. It can be firmly expected that these issues warrant further exploration, both from the theoretical and experimental side. However, even if significant progress in this direction can aid the development of better-performing hydrogen storage materials, it cannot be expected that these advances will be sufficient to reach the technological targets described in the introductory chapter: Because these target values are approximately one order of magnitude higher than the hydrogen uptake capacities of typical MOFs at room temperature and moderate pressure, a massive improvement, rather than a fine-tuning of materials properties, will be necessary to meet these targets. Therefore, the development of technologically viable hydrogen storage materials remains a formidable task, and it is impossible to predict whether MOFs will ever play a role in practical applications in this field. Even if this is not the case, however, some members of this novel group of highly porous, versatile compounds will certainly find technological use in the future. Possible applications that are currently intensively investigated include, among others, the storage of other gases, such as methane or nitric oxide, gas separation, and heterogeneous catalysis.

In the last part of this work, one particular application that goes beyond the storage of gases was investigated, namely the adsorption-based separation of gas mixtures. The adsorption selectivity towards three gas mixtures (CO/H_2, O_2/H_2, C_2H_2/CO_2) was predicted for five microporous materials with different structural properties (one zeolite, three MOFs, one microporous molecular crystal) from GCMC calculations. In addition to the computation of adsorption isotherms and selectivities, the potential energy in the unit cell was studied to understand the structural origins of the observed separation properties.

Silicalite was studied as a well-characterized zeolitic reference system. It behaves essentially as a non-polar adsorbent, although electrostatic effects are not completely negligible for molecules with a large quadrupole moment. Because the pore wall is very homogeneous, and even the narrowest regions of the pore are wide enough to accommodate all of the molecules studied, neither a strongly preferred adsorption of one species, nor size-exclusion effects occur, and the resulting selectivities remain modest. In Mg-formate, all

molecules are relatively strongly adsorbed in the narrow pores due to the strong dispersive interactions. Additionally, a relatively large electrostatic contribution is observed for molecules with a significant dipole or quadrupole moment. This leads to a strong preference for CO over H_2. On the other hand, the selectivity for O_2 over H_2 is relatively low, because dispersive interactions favour one species (oxygen), whereas electrostatic interactions favour the other. The most interesting behaviour, however, was observed for the mixture of acetylene and carbon dioxide: Here, Mg-formate exhibits by far the highest selectivity of all systems. While the dispersive interaction is similar for both molecules, the high selectivity can be explained with the differences in the molecular charge distribution of C_2H_2 and CO_2: Because the pore walls are mainly decorated by negatively polarized oxygen atoms, C_2H_2 molecules can maximize the electrostatic attraction by orienting perpendicular to the channel, whereas electrostatic interactions are much weaker for carbon dioxide. An evaluation of the Henry's law selectivities revealed that Mg-formate exhibits an exceptionally high preference for acetylene over all other gases studied, highlighting that this material could be employed for selective acetylene adsorption in different applications.

Similar to the observations made in studies of hydrogen adsorption at low temperature, the adsorption at the coordinatively unsaturated metal sites of $Cu_3(btc)_2$ plays an important role at room temperature for carbon monoxide, acetylene, and carbon dioxide. In the case of acetylene and carbon dioxide, a derivation of modified potential parameters from DFT calculations was employed to account for this interaction, and it was found that these parameters provide for a much better agreement between the calculated adsorption isotherms and experimental data than the literature parameters. In spite of the preferential adsorption of some molecular species at the metal sites, the selectivity of $Cu_3(btc)_2$ is low for all gas mixtures studied. This can be rationalized with the relatively large pore volume of the system, which permits a co-adsorption of the more weakly adsorbed species in each case, and is thus detrimental to reaching a significant adsorption selectivity. For similar reasons, the separation performance of Zn(dtp) remains very modest, despite the presence of lateral cavities where the interaction with the adsorbed molecules is strongly enhanced.

Finally, the porous molecular crystal cucurbit[6]uril shows very promising separation properties towards CO/H_2 and O_2/H_2 mixtures. While electrostatic effects are practically negligible in this case, the more strongly interacting molecules are preferentially adsorbed in the lateral cavities due to increased dispersion interactions. Because the occupation of these cavities leaves hardly any space for the co-adsorption of hydrogen, a high selectivity arises. While the C_2H_2/CO_2 selectivity of cucurbit[6]uril is low, the system exhibits the highest affinity towards carbon dioxide of all systems. An unresolved issue that would be worth studying in more detail is the role of the intramolecular cavity of the CB[6] macrocycle: In an idealized system, the access to this cavity is blocked by neighbouring molecules. In a real system, however, some of the cavities could be accessible at structural defects. It can be expected that this will lead to changes in the separation behaviour, since the intramolecular cavity could act as a strongly favoured adsorption site.

In summary, the analysis of the simulation results provides some guidelines for the development of new materials with improved separation properties. For the separation of CO/H_2 mixtures, the electrostatic interaction of the dipolar CO molecule with the pore walls should be maximized by using a highly polar adsorbent. However, the example of $Cu_3(btc)_2$ shows that the existence of specific interaction sites for carbon monoxide does not necessarily lead to a high CO/H_2 selectivity. Therefore, an ideal adsorbent should combine strongly preferred interaction sites with relatively narrow pores.

In contrast to this, non-polar adsorbents are most promising for the separation of O_2/H_2 mixtures. Therefore, further efforts to develop optimized adsorbents should focus mainly on the effect of pore size and pore topology. An alternative route that has not been discussed in this work would be the introduction of chemical species that interact strongly with molecular oxygen.

The study of C_2H_2/CO_2 separation has shown how electrostatic effects can be exploited to separate molecules with relatively similar fluid properties, but a different sign of the quadrupole moment. As pointed out above, Mg-formate appears to have very favourable properties for this particular separation. However, the investigation of other microporous materials with narrow channels and highly polar pore walls could deliver additional insights. Since acetylene exhibits a strong interaction with coordinatively unsaturated metal sites, it would also be interesting to exploit this interaction for separation applications, similar to what has been outlined above for carbon monoxide.

Clearly, the computational studies of mixture separation in MOFs and related porous materials reported in this work could be extended in various directions. For example, practical applications often require the removal of trace components. While being computationally very demanding, simulations considering more extreme compositions (*e.g.* in the range of some 10 to 100 ppm) would be necessary to make a direct prediction of the selectivity for practically relevant conditions. Furthermore, the methodology could be applied to other gas mixtures and adsorbents of interest. In particular, porous molecular crystals that combine intermolecular pores and accessible intramolecular cavities could be very promising materials, as a preferential adsorption in the intramolecular cavities might lead to very high adsorption selectivities. Finally, molecular dynamics simulations could be employed to elucidate the diffusion behaviour: If the diffusivity of the guest molecules is too low, this could rule out the practical applicability of the adsorbent due to excessively long equilibration times.

Summary

In this work, molecular simulation techniques are employed to study the potential of metal-organic frameworks (MOFs) and related compounds as materials for hydrogen storage, and for the separation of gas mixtures. Both force-field based computations and electronic structure calculations are carried out. A particular focus is put on the development of a better understanding of the microscopic origins of macroscopically observable quantities, using a detailed analysis of the interatomic interactions governing the adsorption behaviour.

In the first part of the work, force-field based grand-canonical Monte Carlo (GCMC) simulations are employed to predict hydrogen adsorption isotherms for eight structurally different MOFs. It is found that this method is practically routinely applicable to compute low-temperature hydrogen adsorption isotherms that are in good agreement with experimental data, an observation that is in accordance with previous studies. There is, however, the notable exception of MOFs with coordinatively unsaturated metal sites, which exhibit large deviations in the low-pressure regime. This is rationalized with the inadequacy of literature parameters to recover the localized interaction of hydrogen with the metal sites, an aspect that is dealt with in more detail in the second part. In the evaluation of the simulation results, a special emphasis is put on the prediction of hydrogen adsorption sites. For each MOF, the hydrogen density distribution obtained from the simulations is analyzed in detail, and approximate Wyckoff coordinates are assigned to the visible density maxima. In cases where adsorption sites from neutron diffraction experiments are available, a very good agreement with experimental data is observed for the majority of positions.

The problem of modelling the adsorption of hydrogen at coordinatively unsaturated metal sites is addressed in the second part, using MOFs with accessible copper sites as a showcase example. A modified potential to model the Cu-H_2 interaction is derived from density-functional theory (DFT) calculations for a small, non-periodic model system that represents a typical MOF building unit. It is found that GCMC simulations employing this new potential model deliver a drastically improved prediction of the low-temperature hydrogen adsorption isotherms. Further calculations show that the interaction with the metal centers is too weak to permit a significant adsorption at these sites at room temperature. When the metal-hydrogen interaction is artificially enhanced to -15 kJ mol^{-1}, the simulations predict the majority of the metal sites to be occupied under ambient conditions. However, the overall hydrogen uptake of this hypothetical system remains limited by the total number of available metal sites.

In the third part, DFT calculations are used to develop a more detailed understanding of the interaction of hydrogen with molecular model systems that represent fragments of typical MOF structures. The influence of the chemical environment of a coordinatively unsaturated copper center is assessed, using paddle-wheel type Cu$_2$(L)$_4$ complexes with different carboxylate ligands L as a model system. The computations reveal that the copper-hydrogen interaction is enhanced by electron-withdrawing ligands (nitrogen-rich heteroaromatics, ligands with electron-withdrawing substituents). This observation is explained with an in-

crease of electrostatic interactions induced by a decrease of the electron density at the metal center. Further computations using dispersion-corrected DFT (DFT-D) are carried out to elucidate the interaction of H_2 with organic molecules as representatives of MOF linkers. In two case studies, it is assessed whether modifications of an organic molecule can lead to an increase of the interaction strength: Firstly, aromatic six-membered rings with a different number of nitrogen atoms are compared. It is found that the orientation-averaged interaction energy is very similar for all systems considered. Secondly, non-linear molecules with different central atoms (C, Si, Ge) are studied. Here, it is observed that differences in the molecular geometry have a stronger impact on the interaction strength than the dispersive contribution of the central atom, which increases with atomic number. The DFT-D results are interpreted using energy decomposition analysis (EDA).

The last part of the work addresses the adsorption-based separation of gas mixtures in MOFs and other microporous compounds. GCMC simulations for three different mixtures are carried out for five model adsorbents (three MOFs, one zeolite, one porous molecular crystal): The separation of CO/H_2 and O_2/H_2 mixtures is investigated because the removal of weakly adsorbing impurities plays an important role in hydrogen purification. Furthermore, the separation of C_2H_2/CO_2 mixtures is studied, which is difficult due to the similar fluid properties of the two gases. In addition to the prediction of adsorption selectivities, the interaction energy in the pores is analyzed in detail to develop an atomic-level understanding of the observed separation properties. It is found that polar materials with narrow pores are the most suitable materials for CO/H_2 separation, while non-polar adsorbents are preferable for O_2/H_2 separation applications. In the case of acetylene and carbon dioxide, the opposite sign of the quadrupole moment of the two molecules leads to a strong dependency of the selectivity on the charge distribution of the pore walls.

In total, the computations reported in this work contribute to a better understanding of the relationships between structural properties and the adsorption behaviour of MOFs and other ordered microporous materials. It is demonstrated how a detailed analysis of the simulation results can be employed in order to identify adsorbents that hold most promise with regard to a particular application. Moreover, the observations provide some implications for the development of new materials with optimized properties.

Zusammenfassung

In dieser Arbeit werden molekulare Simulationsmethoden verwendet, um das Potential metallorganischer Gerüstverbindungen (*metal-organic frameworks* - MOFs) und verwandter Substanzen für die Wasserstoffspeicherung und für die Trennung von Gasgemischen zu untersuchen. Es werden sowohl Kraftfeld-Methoden als auch quantenchemische Rechnungen genutzt. Ein besonderes Augenmerk wird darauf gelegt, ein besseres Verständnis für die mikroskopischen Ursachen makroskopisch beobachtbarer Eigenschaften zu entwickeln. Hierzu wird eine detaillierte Analyse der interatomaren Wechselwirkungen durchgeführt, welche das Adsorptionsverhalten bestimmen.

Im ersten Teil der Arbeit werden kraftfeld-basierte großkanonische Monte-Carlo-Simulationen (GCMC) verwendet, um die Adsorption von Wasserstoff in acht strukturell unterschiedlichen MOFs vorherzusagen. Es wird beobachtet, dass die für tiefe Temperaturen berechneten Wasserstoff-Adsorptionsisothermen gut mit experimentellen Daten übereinstimmen. Dieses Ergebnis entspricht den Resultaten früherer Arbeiten. MOFs mit koordinativ ungesättigten Metallzentren stellen jedoch eine wichtige Ausnahme dar, da sich hier große Abweichungen im Bereich niedriger Drücke ergeben. Das beobachtete Verhalten wird damit erklärt, dass die verwendeten Kraftfeld-Parameter aus der Literatur nicht geeignet sind, um die lokalisierte Wechselwirkung von Wasserstoff mit den Metallzentren abzubilden, ein Aspekt, der im zweiten Teil der Arbeit genauer behandelt wird. In der Auswertung der Simulationsergebnisse stellt die Vorhersage von Wasserstoff-Adsorptionspositionen einen besonderen Schwerpunkt dar. Für jeden MOF wird die Aufenthaltswahrscheinlichkeit der Wasserstoffmoleküle in der Elementarzelle analysiert, wobei jedem Maximum der Aufenthaltswahrscheinlichkeit eine ungefähre Wyckoff-Lage zugeordnet wird. In den Fällen, in denen experimentelle Adsorptionspositionen aus Neutronenbeugungsexperimenten bekannt sind, wird für die meisten Positionen eine sehr gute Übereinstimmung mit den experimentellen Daten beobachtet.

Das Problem der Modellierung der Adsorption von Wasserstoff an koordinativ ungesättigten Metallzentren wird im zweiten Teil untersucht, wobei MOFs mit zugänglichen Kupferzentren als typisches Beispiel dienen. Ein modifiziertes Potentialmodell zur Abbildung der Cu-H_2-Wechselwirkung wird aus Dichtefunktionaltheorie-Rechnungen (DFT) für ein kleines, molekulares Modellsystem abgeleitet, welches einer typischen MOF-Baueinheit entspricht. GCMC-Simulationen, die dieses Potentialmodell verwenden, liefern eine deutlich verbesserte Vorhersage der Wasserstoff-Adsorptionsisothermen bei tiefen Temperaturen. Weitere Rechnungen zeigen, dass die Wechselwirkung mit den Metallzentren zu schwach ist, um bei Raumtemperatur zu einer nennenswerten Adsorption an diesen Positionen zu führen. Wenn die Metall-Wasserstoff-Wechselwirkung künstlich auf -15 kJ mol^{-1} erhöht wird, sagen die Simulationen voraus, dass die Mehrheit der Metallzentren auch bei Raumtemperatur besetzt wird. Insgesamt bleibt die Wasserstoff-Aufnahmekapazität dieses hypothetischen Systems jedoch durch die Anzahl der verfügbaren Metallzentren begrenzt.

Im dritten Teil werden DFT-Rechnungen genutzt, um ein besseres Verständnis der Wechselwirkung von Wasserstoff mit molekularen Modellsystemen zu entwickeln. Hierbei sind die

Modellsysteme typische MOF-Strukturfragmente. Zunächst wird der Einfluss der chemischen Umgebung eines koordinativ ungesättigten Metallzentrums untersucht, wobei $Cu_2(L)_4$-Komplexe mit unterschiedlichen Carboxylat-Liganden L als Modellsysteme dienen. Die Rechnungen zeigen, dass die Cu-H_2-Wechselwirkung durch elektronenziehende Liganden (Stickstoff-reiche Heteroaromaten, Liganden mit elektronenziehenden Substituenten) verstärkt wird. Diese Beobachtung wird damit erklärt, dass sich die elektrostatische Wechselwirkung durch die Abnahme der Elektronendichte am Metallzentrum verstärkt. Aus weiteren Rechnungen wird die Wechselwirkung von H_2 mit organischen Molekülen als typischen Bausteinen der MOF-Linker vorhergesagt, wobei hier die dispersionskorrigierte DFT (DFT-D) verwendet wird. In zwei Fallstudien wird untersucht, inwieweit Modifikationen des organischen Moleküls die Wechselwirkungsstärke erhöhen können: Zunächst werden aromatische Sechsringe mit einer unterschiedlichen Anzahl von Stickstoffatomen verglichen. Wenn über verschiedene Orientierungen des H_2-Moleküls gemittelt wird, ist die Wechselwirkungsenergie für alle Systeme sehr ähnlich. Weiterhin werden nicht-lineare Moleküle mit verschiedenen Zentralatomen (C, Si, Ge) untersucht. Hier wird beobachtet, dass Unterschiede in der Molekülgeometrie eine größere Rolle spielen als die dispersiven Beiträge des Zentralatoms, welche mit dem Atomgewicht zunehmen. Die DFT-D-Resultate werden mit Hilfe der Energiedekompositionsanalyse (EDA) interpretiert.

Der letzte Teil der Arbeit befasst sich mit der adsorptiven Trennung von Gasgemischen in MOFs und anderen mikroporösen Materialien. Für fünf Adsorbentien (drei MOFs, ein Zeolith, ein poröser Molekülkristall) werden GCMC-Simulationen durchgeführt, um die Adsorption dreier verschiedener Gemische zu untersuchen: Einerseits wird die Trennung von CO/H_2- und O_2/H_2-Mischungen berücksichtigt, da die Abtrennung schwach adsorbierender Gase eine wichtige Rolle in der Reinigung von Wasserstoff spielt. Weiterhin wird die Trennung von C_2H_2/CO_2-Gemischen untersucht, welche durch die ähnlichen Fluideigenschaften der beiden Gase erschwert wird. Zusätzlich zur Vorhersage der Adsorptionsselektivitäten wird eine detaillierte Analyse der Wechselwirkungsenergie in den Poren durchgeführt, um die beobachteten Trenneigenschaften auf atomarer Ebene zu verstehen. Polare Materialien mit engen Poren werden als am Besten geeignete Materialien für die CO/H_2-Trennung identifiziert. Im Gegensatz dazu sind unpolare Adsorbentien für Anwendungen in der O_2/H_2-Trennung zu bevorzugen. Bei der Trennung von Acetylen und Kohlenstoffdioxid führt das unterschiedliche Vorzeichen des Quadrupolmoments der beiden Moleküle zu einer starken Abhängigkeit der Selektivität von der Polarität der Porenwände.

Insgesamt tragen die in dieser Arbeit vorgestellten Rechnungen zu einem besseren Verständnis der Zusammenhänge zwischen den strukturellen Eigenschaften und dem Adsorptionsverhalten von MOFs und anderen geordneten mikroporösen Materialien bei. Es wird gezeigt, wie eine detaillierte Analyse der Simulationsergebnisse dazu genutzt werden kann, Adsorbentien zu identifizieren, die für eine bestimmte Anwendung besonders vielversprechend sind. Weiterhin lassen die Beobachtungen einige Schlussfolgerungen zu, die für die Entwicklung neuer Materialien mit optimierten Eigenschaften hilfreich sein können.

Curriculum vitae

NAME:	Michael Fischer
DATE OF BIRTH:	19/07/1981
PLACE OF BIRTH:	Henstedt-Ulzburg
MARITAL STATUS:	Married
ADDRESS:	Hasselbrookstrasse 48, 22089 Hamburg

08/1988 to 06/1992:   PRIMARY SCHOOL: Grundschule Glashütte, Norderstedt

08/1992 to 06/2001:   SECONDARY SCHOOL: Lise-Meitner-Gymnasium, Norderstedt

22/06/2001:   ABITUR (general qualification for university entrance)

07/2001 to 03/2002:   MILITARY SERVICE: Marinemusikkorps Ostsee, Kiel

04/2002 to 07/2002:   INTERNSHIP: Institute of Materials Research, GKSS Geesthacht

10/2002 to 12/2007:   UNIVERSITY STUDIES: Mineralogy, University of Hamburg

24/03/2005:   INTERMEDIATE EXAM (*Diplom-Vorprüfung*) in Mineralogy

10/2005 to 03/2006:   ERASMUS EXCHANGE SEMESTER: University of Geneva

10/2006 to 08/2007:   DIPLOMA THESIS IN MINERALOGY-CRYSTALLOGRAPHY
TITLE: Ab-initio Calculation of Low Temperature Phases of Cadmium Pyroniobate
SUPERVISION: Prof. Dr. Ulrich Bismayer, Dr. Thomas Malcherek

11/12/2007:   FINAL EXAM (*Diplom-Hauptprüfung*) in Mineralogy
DEGREE: *Diplom-Mineraloge (Dipl.-Min.)*

since 16/01/2008:   PHD STUDIES IN INORGANIC CHEMISTRY
Research group Prof. Dr. Michael Fröba
Institute of Inorganic and Applied Chemistry
Department of Chemistry
University of Hamburg

List of publications

S. E. Wenzel, M. Fischer, F. Hoffmann, M. Fröba
Highly Porous Metal-Organic Framework Containing a Novel Organosilicon Linker - A Promising Material for Hydrogen Storage
Inorg. Chem. **2009**, *48*, 6559-6565

M. Fischer, F. Hoffmann, M. Fröba
Preferred Hydrogen Adsorption Sites in Various MOFs - A Comparative Computational Study
ChemPhysChem **2009**, *10*, 2647-2657

M. Fischer, F. Hoffmann, M. Fröba
Molecular Simulation of Hydrogen Adsorption in Metal-Organic Frameworks
Colloids Surf. A **2010**, *357*, 35-42

M. Fischer, F. Hoffmann, M. Fröba
New Microporous Materials for Acetylene Storage and C_2H_2/CO_2 Separation: Insights from Molecular Simulations
ChemPhysChem **2010**, *11*, 2220-2229

M. Fischer, B. Kuchta, L. Firlej, F. Hoffmann, M. Fröba
Accurate Prediction of Hydrogen Adsorption in Metal-Organic Frameworks with Unsaturated Metal Sites via a Combined Density-Functional Theory and Molecular Mechanics Approach
J. Phys. Chem. C **2010**, *114*, 19116-19126

Acknowledgments

> WE ARE LIKE DWARFS ON THE SHOULDERS OF GIANTS, SO THAT WE CAN SEE MORE THAN THEY, AND THINGS AT A GREATER DISTANCE, NOT BY VIRTUE OF ANY SHARPNESS OF SIGHT ON OUR PART, OR ANY PHYSICAL DISTINCTION, BUT BECAUSE WE ARE CARRIED HIGH AND RAISED UP BY THEIR GIANT SIZE.
>
> *attributed to Bernard of Chartres*

As no dwarf can climb the giant's shoulders on his own, this thesis would have never been written without the intellectual guidance and moral support of numerous people. It is my pleasure and my duty to express my gratitude to them.

First of all, I would like to thank Prof. Dr. Michael Fröba for offering me to join his group in order to work on this (rather unusual) PhD project, for providing continuous support with all administrative issues, for giving me a lot of freedom in picking my research topics, and for many important discussions that helped to unblur the "big picture".

I am also very grateful to Prof. Dr. Jürgen Heck for his willingness to act as co-examiner.

I am deeply indebted to Dr. Frank Hoffmann for introducing me to the field of molecular simulations, for countless enlightening discussions on computational, chemistry, and computational chemistry issues, and for always giving a clear-cut and well-justified opinion on everything related to layout and design.

The vivid exchange with the experimental "hydrogen adsorption team" (Dr. Stephanie Wenzel, Daniela Frahm, Uta Sazama, and Sandra Maracke) has been very helpful to develop a better understanding of the challenges connected to the experimental characterization of MOFs. I thank them for answering numerous questions that only a theorist can ask.

The constant helpfulness of Dr. Boris Ufer in resolving various software problems is gratefully acknowledged.

From the very beginning, I felt very welcome in the Fröba research group, and I am thankful to all current and former members of the group who created such a friendly working atmosphere. It has always been a pleasure to stop by at somebody's office (or, more frequently, the coffee machine) for a brief chat before getting back to more serious issues.

In particular, I would like to thank Frank, Daniela, and all other frequent and occasional participants of the inevitable "Cube Time" at 15.45 h, as these daily events could brighten up even the dullest afternoons.

The implementation of the improved metal-hydrogen potential would not have been possible without the immense helpfulness of my French collaboration partners. Therefore, I would like to thank Prof. Dr. Bogdan Kuchta and Prof. Dr. Lucyna Firlej for their proposition to start a common project, for welcoming me in Marseille, for taking over practically all of the programming work, and for many discussions that helped me to understand the "action behind the scenes" in a Monte Carlo code. *Merci beaucoup!*

I am very grateful to my parents for their continuous moral support, which was an indispensable help to overcome all moments of self-doubt (and for spotting numerous typos that would otherwise have remained unnoticed).

Finally, I want to thank Anne for her endless love and near-endless patience.

Bibliography

[1] Keeling, R. F.; Piper, S. C.; Bollenbacher, A. F.; Walker, S. J. Scripps CO_2 program: Atmospheric CO_2 concentrations (ppm) derived from in situ air measurements at Mauna Loa Observatory, Hawai'i. 2011; available from: *http://scrippsco2.ucsd.edu*.

[2] Pachauri, R. K., Reisinger, A., Eds. *Climate Change 2007: Synthesis Report - Contribution of Working Groups I, II and III to the Fourth Assessment Report of the Intergovernmental Panel on Climate Change*; IPCC: Geneva, CH, 2007.

[3] Solomon, S.; Plattner, G.-K.; Knutti, R.; Friedlingstein, P. Irreversible climate change due to carbon dioxide emissions. *Proc. Natl. Acad. Sci. U. S. A.* **2009**, *106*, 1704–1709.

[4] Maginn, E. J. What to do with CO_2. *J. Phys. Chem. Lett.* **2010**, *1*, 3478–3479.

[5] Emissions of greenhouse gases in the United States 2008. 2009; available from: *http://eia.doe.gov/environment/data.cfm*.

[6] Eberle, U.; von Helmolt, R. Sustainable transportation based on electric vehicle concepts: A brief overview. *Energy Environ. Sci.* **2010**, *3*, 689–699.

[7] *Fuel Cell Handbook*, 7th ed.; U.S. Department of Energy: Morgantown, WV, USA, 2004.

[8] Armaroli, N.; Balzani, V. The hydrogen issue. *ChemSusChem* **2011**, *4*, 21–36.

[9] Sircar, S.; Golden, T. Purification of hydrogen by pressure swing adsorption. *Sep. Sci. Technol.* **2000**, *35*, 667–687.

[10] Eberle, U.; Felderhoff, M.; Schüth, F. Chemical and physical solutions for hydrogen storage. *Angew. Chem., Int. Ed.* **2009**, *48*, 6608–6630.

[11] Yang, J.; Sudik, A.; Wolverton, C.; Siegel, D. J. High capacity hydrogen storage materials: Attributes for automotive applications and techniques for materials discovery. *Chem. Soc. Rev.* **2010**, *39*, 656–675.

[12] Schlapbach, L.; Züttel, A. Hydrogen-storage materials for mobile applications. *Nature* **2001**, *414*, 353–358.

[13] DOE targets for onboard hydrogen storage systems for light-duty vehicles, version 4.0. 2009; available from: *http://www1.eere.energy.gov/hydrogenandfuelcells/storage/pdfs/targets_onboard_hydro_storage.pdf*.

[14] Felderhoff, M.; Weidenthaler, C.; von Helmolt, R.; Eberle, U. Hydrogen storage: The remaining scientific and technological challenges. *Phys. Chem. Chem. Phys.* **2007**, *9*, 2643–2653.

[15] Press release: The new Mercedes-Benz B-Class F-Cell. 2009; available from: *http://www.media.daimler.com*.

[16] Jones, L. W. Liquid hydrogen as a fuel for the future. *Science* **1971**, *174*, 367–370.

[17] Yvon, K.; Renaudin, G. HYDRIDES: SOLID STATE TRANSITION METAL COMPLEXES in *Encyclopedia of Inorganic Chemistry*; King, R. B.; Crabtree, R. H.; Lukehart, C. M.; Atwood, D. A.; Scott, R. A. (Eds.), John Wiley & Sons, Ltd: Chichester, UK. 2006.

[18] de Jongh, P. E.; Adelhelm, P. Nanosizing and nanoconfinement: New strategies towards meeting hydrogen storage goals. *ChemSusChem* **2010**, *3*, 1332–1348.

[19] Dornheim, M.; Doppiu, S.; Barkhordarian, G.; Boesenberg, U.; Klassen, T.; Gutfleisch, O.; Bormann, R. Hydrogen storage in magnesium-based hydrides and hydride composites. *Scr. Mater.* **2007**, *56*, 841–846.

[20] Orimo, S.-I.; Nakamori, Y.; Eliseo, J. R.; Züttel, A.; Jensen, C. M. Complex hydrides for hydrogen storage. *Chem. Rev.* **2007**, *107*, 4111–4132.

[21] Wolverton, C.; Siegel, D. J.; Akbarzadeh, A. R.; Ozolins, V. Discovery of novel hydrogen storage materials: An atomic scale computational approach. *J. Phys.: Condens. Matter* **2008**, *20*, 064228.

[22] Staubitz, A.; Robertson, A. P. M.; Manners, I. Ammonia-borane and related compounds as dihydrogen sources. *Chem. Rev.* **2010**, *110*, 4079–4124.

[23] Yang, R. T. *Adsorbents: Fundamentals and Applications*, 1st ed.; John Wiley & Sons, Inc: Hoboken, NJ, USA, 2003.

[24] Thomas, K. M. Hydrogen adsorption and storage on porous materials. *Catal. Today* **2007**, *120*, 389–398.

[25] Bhatia, S. K.; Myers, A. L. Optimum conditions for adsorptive storage. *Langmuir* **2006**, *22*, 1688–1700.

[26] Xia, Y.; Walker, G. S.; Grant, D. M.; Mokaya, R. Hydrogen storage in high surface area carbons: Experimental demonstration of the effects of nitrogen doping. *J. Am. Chem. Soc.* **2009**, *131*, 16493–16499.

[27] Wang, L.; Yang, R. T. Hydrogen storage properties of N-doped microporous carbon. *J. Phys. Chem. C* **2009**, *113*, 21883–21888.

[28] Jin, Z.; Sun, Z.; Simpson, L. J.; O'Neill, K. J.; Parilla, P. A.; Li, Y.; Stadie, N. P.; Ahn, C. C.; Kittrell, C.; Tour, J. M. Solution-phase synthesis of heteroatom-substituted carbon scaffolds for hydrogen storage. *J. Am. Chem. Soc.* **2010**, *132*, 15246–15251.

[29] Wang, Q.; Johnson, J. K. Hydrogen adsorption on graphite and in carbon slit pores from path integral simulations. *Mol. Phys.* **1998**, *95*, 299–309.

[30] Darkrim, F.; Levesque, D. Monte Carlo simulations of hydrogen adsorption in single-walled carbon nanotubes. *J. Chem. Phys.* **1998**, *109*, 4981–4984.

[31] Cracknell, R. F. Molecular simulation of hydrogen adsorption in graphitic nanofibres. *Phys. Chem. Chem. Phys.* **2001**, *3*, 2091–2097.

[32] Kowalczyk, P.; Tanaka, H.; Holyst, R.; Kaneko, K.; Ohmori, T.; Miyamoto, J. Storage of hydrogen at 303 K in graphite slitlike pores from grand canonical Monte Carlo simulation. *J. Phys. Chem. B* **2005**, *109*, 17174–17183.

[33] Kowalczyk, P.; Gauden, P. A.; Terzyk, A. P.; Bhatia, S. K. Thermodynamics of hydrogen adsorption in slit-like carbon nanopores at 77 K. Classical versus path-integral Monte Carlo simulations. *Langmuir* **2007**, *23*, 3666–3672.

[34] Kuchta, B.; Firlej, L.; Pfeifer, P.; Wexler, C. Numerical estimation of hydrogen storage limits in carbon-based nanospaces. *Carbon* **2010**, *48*, 223–231.

[35] Firlej, L.; Kuchta, B.; Wexler, C.; Pfeifer, P. Boron substituted graphene: Energy landscape for hydrogen adsorption. *Adsorption* **2009**, *15*, 312–317.

[36] Heine, T.; Zhechkov, L.; Seifert, G. Hydrogen storage by physisorption on nanostructured graphite platelets. *Phys. Chem. Chem. Phys.* **2004**, *6*, 980–984.

[37] Patchkovskii, S.; Tse, J. S.; Yurchenko, S. N.; Zhechkov, L.; Heine, T.; Seifert, G. Graphene nanostructures as tunable storage media for molecular hydrogen. *Proc. Natl. Acad. Sci. U. S. A.* **2005**, *102*, 10439–10444.

[38] Rubes, M.; Bludský, O. DFT/CCSD(T) investigation of the interaction of molecular hydrogen with carbon nanostructures. *ChemPhysChem* **2009**, *10*, 1868–1873.

[39] Burress, J.; Kraus, M.; Beckner, M.; Cepel, R.; Suppes, G.; Wexler, C.; Pfeifer, P. Hydrogen storage in engineered carbon nanospaces. *Nanotechnology* **2009**, *20*, 204026.

[40] Li, H.; Eddaoudi, M.; O'Keeffe, M.; Yaghi, O. M. Design and synthesis of an exceptionally stable and highly porous metal-organic framework. *Nature* **1999**, *402*, 276–279.

[41] Chui, S. S.-Y.; Lo, S. M.-F.; Charmant, J. P. H.; Orpen, A. G.; Williams, I. D. A chemically functionalizable nanoporous material $[Cu_3(TMA)_2(H_2O)_3]_n$. *Science* **1999**, *283*, 1148–1150.

[42] Férey, G. Hybrid porous solids: Past, present, future. *Chem. Soc. Rev.* **2008**, *37*, 191–214.

[43] Long, J. R.; Yaghi, O. M. Editorial: The pervasive chemistry of metal-organic frameworks. *Chem. Soc. Rev.* **2009**, *38*, 1213–1214.

[44] Férey, G.; Serre, C. Large breathing effects in three-dimensional porous hybrid matter: Facts, analyses, rules and consequences. *Chem. Soc. Rev.* **2009**, *38*, 1380–1399.

[45] Thommes, M. Physical adsorption characterization of nanoporous materials. *Chem. Ing. Tech.* **2010**, *82*, 1059–1073.

[46] Furukawa, H.; Ko, N.; Go, Y. B.; Aratani, N.; Choi, S. B.; Choi, E.; Yazaydin, A. O.; Snurr, R. Q.; O'Keeffe, M.; Kim, J.; Yaghi, O. M. Ultra-high porosity in metal-organic frameworks. *Science* **2010**, *329*, 424–428.

[47] Rosi, N. L.; Eckert, J.; Eddaoudi, M.; Vodak, D. T.; Kim, J.; O'Keeffe, M.; Yaghi, O. M. Hydrogen storage in microporous metal-organic frameworks. *Science* **2003**, *300*, 1127–1129.

[48] Murray, L. J.; Dinca, M.; Long, J. R. Hydrogen storage in metal-organic frameworks. *Chem. Soc. Rev.* **2009**, *38*, 1294–1314.

[49] Zhao, D.; Yuan, D.; Zhou, H.-C. The current status of hydrogen storage in metal-organic frameworks. *Energy Environ. Sci.* **2008**, *1*, 222–235.

[50] Kaye, S. S.; Dailly, A.; Yaghi, O. M.; Long, J. R. Impact of preparation and handling on the hydrogen storage properties of $Zn_4O(1,4$-benzenedicarboxylate$)_3$ (MOF-5). *J. Am. Chem. Soc.* **2007**, *129*, 14176–14177.

[51] Poirier, E.; Dailly, A. Investigation of the hydrogen state in IRMOF-1 from measurements and modeling of adsorption isotherms at high gas densities. *J. Phys. Chem. C* **2008**, *112*, 13047–13052.

[52] Furukawa, H.; Miller, M. A.; Yaghi, O. M. Independent verification of the saturation hydrogen uptake in MOF-177 and establishment of a benchmark for hydrogen adsorption in metal-organic frameworks. *J. Mater. Chem.* **2007**, *17*, 3197–3204.

[53] Yuan, D.; Zhao, D.; Sun, D.; Zhou, H.-C. An isoreticular series of metal-organic frameworks with dendritic hexacarboxylate ligands and exceptionally high gas-uptake capacity. *Angew. Chem., Int. Ed.* **2010**, *49*, 5357–5361.

[54] Farha, O. K.; Yazaydin, A. O.; Eryazici, I.; Malliakas, C. D.; Hauser, B. G.; Kanatzidis, M. G.; Nguyen, S. T.; Snurr, R. Q.; Hupp, J. T. De novo synthesis of a metal-organic framework material featuring ultrahigh surface area and gas storage capacities. *Nat. Chem.* **2010**, *2*, 944–948.

[55] Dinca, M.; Long, J. R. Hydrogen storage in microporous metal-organic frameworks with exposed metal sites. *Angew. Chem., Int. Ed.* **2008**, *47*, 6766–6779.

[56] Prestipino, C.; Regli, L.; Vitillo, J. G.; Bonino, F.; Damin, A.; Lamberti, C.; Zecchina, A.; Solari, P. L.; Kongshaug, K. O.; Bordiga, S. Local structure of framework Cu(II) in HKUST-1 metallorganic framework: Spectroscopic characterization upon activation and interaction with adsorbates. *Chem. Mater.* **2006**, *18*, 1337–1346.

[57] Peterson, V. K.; Liu, Y.; Brown, C. M.; Kepert, C. J. Neutron powder diffraction study of D_2 sorption in Cu_3(1,3,5-benzenetricarboxylate)$_2$. *J. Am. Chem. Soc.* **2006**, *128*, 15578–15579.

[58] Brown, C. M.; Liu, Y.; Yildirim, T.; Peterson, V. K.; Kepert, C. J. Hydrogen adsorption in HKUST-1: A combined inelastic neutron scattering and first-principles study. *Nanotechnology* **2009**, *20*, 204025.

[59] Dinca, M.; Dailly, A.; Liu, Y.; Brown, C. M.; Neumann, D. A.; Long, J. R. Hydrogen storage in a microporous metal-organic framework with exposed Mn^{2+} coordination sites. *J. Am. Chem. Soc.* **2006**, *128*, 16876–16883.

[60] Dinca, M.; Han, W. S.; Liu, Y.; Dailly, A.; Brown, C. M.; Long, J. R. Observation of Cu^{2+}-H_2 interactions in a fully desolvated sodalite-type metal-organic framework. *Angew. Chem., Int. Ed.* **2007**, *46*, 1419–1422.

[61] Sumida, K.; Horike, S.; Kaye, S. S.; Herm, Z. R.; Queen, W. L.; Brown, C. M.; Grandjean, F.; Long, G. J.; Dailly, A.; Long, J. R. Hydrogen storage and carbon dioxide capture in an iron-based sodalite-type metal-organic framework (Fe-BTT) discovered via high-throughput methods. *Chem. Sci.* **2010**, *1*, 184–191.

[62] Chen, B.; Zhao, X.; Putkham, A.; Hong, K.; Lobkovsky, E. B.; Hurtado, E. J.; Fletcher, A. J.; Thomas, K. M. Surface interactions and quantum kinetic molecular sieving for H_2 and D_2 adsorption on a mixed metal-organic framework material. *J. Am. Chem. Soc.* **2008**, *130*, 6411–6423.

[63] Zhou, W.; Wu, H.; Yildirim, T. Enhanced H_2 adsorption in isostructural metal-organic frameworks with open metal sites: Strong dependence of the binding strength on metal ions. *J. Am. Chem. Soc.* **2008**, *130*, 15268–15269.

[64] Irving, H.; Williams, R. J. P. The stability of transition-metal complexes. *J. Chem. Soc.* **1953**, 3192–3200.

[65] Vitillo, J. G.; Regli, L.; Chavan, S.; Ricchiardi, G.; Spoto, G.; Dietzel, P. D. C.; Bordiga, S.; Zecchina, A. Role of exposed metal sites in hydrogen storage in MOFs. *J. Am. Chem. Soc.* **2008**, *130*, 8386–8396.

[66] Himsl, D.; Wallacher, D.; Hartmann, M. Improving the hydrogen-adsorption properties of a hydroxy-modified MIL-53(Al) structural analogue by lithium doping. *Angew. Chem., Int. Ed.* **2009**, *48*, 4639–4642.

[67] Mulfort, K. L.; Farha, O. K.; Stern, C. L.; Sarjeant, A. A.; Hupp, J. T. Post-synthesis alkoxide formation within metal-organic framework materials: A strategy for incorporating highly coordinatively unsaturated metal ions. *J. Am. Chem. Soc.* **2009**, *131*, 3866–3868.

[68] Wang, Z.; Tanabe, K. K.; Cohen, S. M. Tuning hydrogen sorption properties of metal-organic frameworks by postsynthetic covalent modification. *Chem.–Eur. J.* **2010**, *16*, 212–217.

[69] Li, Y.; Yang, R. Hydrogen storage in metal-organic and covalent-organic frameworks by spillover. *AIChE J.* **2008**, *54*, 269–279.

[70] Rowsell, J. L. C.; Millward, A. R.; Park, K. S.; Yaghi, O. M. Hydrogen sorption in functionalized metal-organic frameworks. *J. Am. Chem. Soc.* **2004**, *126*, 5666–5667.

[71] Liu, J.; Culp, J. T.; Natesakhawat, S.; Bockrath, B. C.; Zande, B.; Sankar, S. G.; Garberoglio, G.; Johnson, J. K. Experimental and theoretical studies of gas adsorption in $Cu_3(BTC)_2$: An effective activation procedure. *J. Phys. Chem. C* **2007**, *111*, 9305–9313.

[72] Keskin, S.; Liu, J.; Rankin, R. B.; Johnson, J. K.; Sholl, D. S. Progress, opportunities, and challenges for applying atomically detailed modeling to molecular adsorption and transport in metal-organic framework materials. *Ind. Eng. Chem. Res.* **2009**, *48*, 2355–2371.

[73] Han, S. S.; Mendoza-Cortés, J. L.; Goddard, W. A. Recent advances on simulation and theory of hydrogen storage in metal-organic frameworks and covalent organic frameworks. *Chem. Soc. Rev.* **2009**, *38*, 1460–1476.

[74] Sastre, G. Hydrogen physisorption in metal-organic frameworks: Concepts and quantum chemical calculations. *Theor. Chem. Acc.* **2010**, *127*, 259–270.

[75] Garberoglio, G.; Skoulidas, A. I.; Johnson, J. K. Adsorption of gases in metal organic materials: Comparison of simulations and experiments. *J. Phys. Chem. B* **2005**, *109*, 13094–13103.

[76] Frost, H.; Düren, T.; Snurr, R. Q. Effects of surface area, free volume, and heat of adsorption on hydrogen uptake in metal-organic frameworks. *J. Phys. Chem. B* **2006**, *110*, 9565–9570.

[77] Ryan, P.; Broadbelt, L. J.; Snurr, R. Q. Is catenation beneficial for hydrogen storage in metal-organic frameworks? *Chem. Commun.* **2008**, 4132–4134.

[78] Frost, H.; Snurr, R. Design requirements for metal-organic frameworks as hydrogen storage materials. *J. Phys. Chem. C* **2007**, *111*, 18794–18803.

[79] Bae, Y.-S.; Snurr, R. Q. Optimal isosteric heat of adsorption for hydrogen storage and delivery using metal-organic frameworks. *Microporous Mesoporous Mater.* **2010**, *132*, 300–303.

[80] Bae, Y.-S.; Snurr, R. Q. Molecular simulations of very high pressure hydrogen storage using metal-organic frameworks. *Microporous Mesoporous Mater.* **2010**, *135*, 178–186.

[81] Han, S. S.; Goddard, W. A. Lithium-doped metal-organic frameworks for reversible H_2 storage at ambient temperature. *J. Am. Chem. Soc.* **2007**, *129*, 8422–8423.

[82] Klontzas, E.; Mavrandonakis, A.; Tylianakis, E.; Froudakis, G. E. Improving hydrogen storage capacity of MOF by functionalization of the organic linker with lithium atoms. *Nano Lett.* **2008**, *8*, 1572–1576.

[83] Getman, R. B.; Miller, J. H.; Wang, K.; Snurr, R. Q. Metal alkoxide functionalization in metal-organic frameworks for enhanced ambient-temperature hydrogen storage. *J. Phys. Chem. C* **2011**, *115*, 2066–2075.

[84] Belof, J. L.; Stern, A. C.; Eddaoudi, M.; Space, B. On the mechanism of hydrogen storage in a metal-organic framework material. *J. Am. Chem. Soc.* **2007**, *129*, 15202–15210.

[85] Belof, J. L.; Stern, A. C.; Space, B. A predictive model of hydrogen sorption for metal-organic materials. *J. Phys. Chem. C* **2009**, *113*, 9316–9320.

[86] Sillar, K.; Hofmann, A.; Sauer, J. Ab initio study of hydrogen adsorption in MOF-5. *J. Am. Chem. Soc.* **2009**, *131*, 4143–4150.

[87] Kong, L.; Cooper, V. R.; Nijem, N.; Li, K.; Li, J.; Chabal, Y. J.; Langreth, D. C. Theoretical and experimental analysis of H_2 binding in a prototypical metal-organic framework material. *Phys. Rev. B* **2009**, *79*, 081407(R).

[88] Kong, L.; Román-Pérez, G.; Soler, J. M.; Langreth, D. C. Energetics and dynamics of H_2 adsorbed in a nanoporous material at low temperature. *Phys. Rev. Lett.* **2009**, *103*, 096103.

[89] Lochan, R. C.; Head-Gordon, M. Computational studies of molecular hydrogen binding affinities: The role of dispersion forces, electrostatics, and orbital interactions. *Phys. Chem. Chem. Phys.* **2006**, *8*, 1357–1370.

[90] Lochan, R. C.; Khaliullin, R. Z.; Head-Gordon, M. Interaction of molecular hydrogen with open transition metal centers for enhanced binding in metal-organic frameworks: A computational study. *Inorg. Chem.* **2008**, *47*, 4032–4044.

[91] Kosa, M.; Krack, M.; Cheetham, A. K.; Parrinello, M. Modeling the hydrogen storage materials with exposed M^{2+} coordination sites. *J. Phys. Chem. C* **2008**, *112*, 16171–16173.

[92] Zhou, W.; Yildirim, T. Nature and tunability of enhanced hydrogen binding in metal-organic frameworks with exposed transition metal sites. *J. Phys. Chem. C* **2008**, *112*, 8132–8135.

[93] Kubas, G. J. Fundamentals of H_2 binding and reactivity on transition metals underlying hydrogenase function and H_2 production and storage. *Chem. Rev.* **2007**, *107*, 4152–4205.

[94] Sun, Y. Y.; Kim, Y.-H.; Zhang, S. B. Effect of spin state on the dihydrogen binding strength to transition metal centers in metal-organic frameworks. *J. Am. Chem. Soc.* **2007**, *129*, 12606–12607.

[95] Hamaed, A.; Mai, H. V.; Hoang, T. K. A.; Trudeau, M.; Antonelli, D. Functionalized porous silicas with unsaturated early transition metal moieties as hydrogen storage materials: Comparison of metal and oxidation state. *J. Phys. Chem. C* **2010**, *114*, 8651–8660.

[96] Skipper, C. V. J.; Hamaed, A.; Antonelli, D. M.; Kaltsoyannis, N. Computational study of silica-supported transition metal fragments for Kubas-type hydrogen storage. *J. Am. Chem. Soc.* **2010**, *132*, 17296–17305.

[97] Golden, T. C.; Sircar, S. Gas adsorption on Silicalite. *J. Colloid Interface Sci.* **1994**, *162*, 182–188.

[98] Darkrim, F.; Aoufi, A.; Malbrunot, P.; Levesque, D. Hydrogen adsorption in the NaA zeolite: A comparison between numerical simulations and experiments. *J. Chem. Phys.* **2000**, *112*, 5991–5600.

[99] Langmi, H.; Book, D.; Walton, A.; Johnson, S.; Al-Mamouri, M.; Speight, J.; Edwards, P.; Harris, I.; Anderson, P. Hydrogen storage in ion-exchanged zeolites. *J. Alloys Compd.* **2005**, *404-406*, 637–642.

[100] Côté, A. P.; Benin, A. I.; Ockwig, N. W.; O'Keeffe, M.; Matzger, A. J.; Yaghi, O. M. Porous, crystalline, covalent organic frameworks. *Science* **2005**, *310*, 1166–1170.

[101] Garberoglio, G. Computer simulation of the adsorption of light gases in covalent organic frameworks. *Langmuir* **2007**, *23*, 12154–12158.

[102] Han, S. S.; Furukawa, H.; Yaghi, O. M.; Goddard, W. A. Covalent organic frameworks as exceptional hydrogen storage materials. *J. Am. Chem. Soc.* **2008**, *130*, 11580–11581.

[103] Furukawa, H.; Yaghi, O. M. Storage of hydrogen, methane, and carbon dioxide in highly porous covalent organic frameworks for clean energy applications. *J. Am. Chem. Soc.* **2009**, *131*, 8875–8883.

[104] Cao, D.; Lan, J.; Wang, W.; Smit, B. Lithium-doped 3D covalent organic frameworks: High-capacity hydrogen storage materials. *Angew. Chem., Int. Ed.* **2009**, *48*, 4730–4733.

[105] McKeown, N. B.; Budd, P. M. Exploitation of intrinsic microporosity in polymer-based materials. *Macromolecules* **2010**, *43*, 5163–5176.

[106] Wood, C. D.; Tan, B.; Trewin, A.; Niu, H.; Bradshaw, D.; Rosseinsky, M. J.; Khimyak, Y. Z.; Campbell, N. L.; Kirk, R.; Stöckel, E.; Cooper, A. I. Hydrogen storage in microporous hypercrosslinked organic polymer networks. *Chem. Mater.* **2007**, *19*, 2034–2048.

[107] Li, A.; Lu, R.-F.; Wang, Y.; Wang, X.; Han, K.-L.; Deng, W.-Q. Lithium-doped conjugated microporous polymers for reversible hydrogen storage. *Angew. Chem., Int. Ed.* **2010**, *49*, 3330–3333.

[108] El-Kaderi, H. M.; Hunt, J. R.; Mendoza-Cortés, J. L.; Côté, A. P.; Taylor, R. E.; O'Keeffe, M.; Yaghi, O. M. Designed synthesis of 3D covalent organic frameworks. *Science* **2007**, *316*, 268–272.

[109] Ruthven, D. M. Molecular sieve separations. *Chem. Ing. Tech.* **2011**, *83*, 44–52.

[110] Yang, R. T. *Gas Separation by Adsorption Processes*; Imperial College Press: London, UK, 1997.

[111] Sircar, S. Basic research needs for design of adsorptive gas separation processes. *Ind. Eng. Chem. Res.* **2006**, *45*, 5435–5448.

[112] Dunne, S. R. INDUSTRIAL GAS PHASE ADSORPTIVE SEPARATIONS in *Zeolites in Industrial Separation and Catalysis*; Kulprathipanja, S. (Ed.), Wiley-VCH Verlag GmbH & Co. KGaA: Weinheim, D. 2010.

[113] Bernardo, P.; Drioli, E.; Golemme, G. Membrane gas separation: A review/state of the art. *Ind. Eng. Chem. Res.* **2009**, *48*, 4638–4663.

[114] Li, J.-R.; Kuppler, R. J.; Zhou, H.-C. Selective gas adsorption and separation in metal-organic frameworks. *Chem. Soc. Rev.* **2009**, *38*, 1477–1504.

[115] Talu, O. Measurement and analysis of mixture adsorption equilibrium in porous solids. *Chem. Ing. Tech.* **2011**, *83*, 67–82.

[116] Wang, Q. M.; Shen, D.; Bülow, M.; Lau, M. L.; Deng, S.; Fitch, F. R.; Lemcoff, N. O.; Semanscin, J. Metallo-organic molecular sieve for gas separation and purification. *Microporous Mesoporous Mater.* **2002**, *55*, 217–230.

[117] Hartmann, M.; Kunz, S.; Himsl, D.; Tangermann, O.; Ernst, S.; Wagener, A. Adsorptive separation of isobutene and isobutane on $Cu_3(BTC)_2$. *Langmuir* **2008**, *24*, 8634–8642.

[118] Bastin, L.; Barcia, P.; Hurtado, E.; Silva, J.; Rodrigues, A.; Chen, B. A microporous metal-organic framework for separation of CO_2/N_2 and CO_2/CH_4 by fixed-bed adsorption. *J. Phys. Chem. C* **2008**, *112*, 1575–1581.

[119] Britt, D.; Tranchemontagne, D.; Yaghi, O. M. Metal-organic frameworks with high capacity and selectivity for harmful gases. *Proc. Natl. Acad. Sci. U. S. A.* **2008**, *105*, 11623–11627.

[120] Britt, D.; Furukawa, H.; Wang, B.; Glover, T. G.; Yaghi, O. M. Highly efficient separation of carbon dioxide by a metal-organic framework replete with open metal sites. *Proc. Natl. Acad. Sci. U. S. A.* **2009**, *106*, 20637–20640.

[121] Couck, S.; Denayer, J. F. M.; Baron, G. V.; Rémy, T.; Gascon, J.; Kapteijn, F. An amine-functionalized MIL-53 metal-organic framework with large separation power for CO_2 and CH_4. *J. Am. Chem. Soc.* **2009**, *131*, 6326–6327.

[122] Nakagawa, K.; Tanaka, D.; Horike, S.; Shimomura, S.; Higuchi, M.; Kitagawa, S. Enhanced selectivity of CO_2 from a ternary gas mixture in an interdigitated porous framework. *Chem. Commun.* **2010**, *46*, 4258–4260.

[123] Myers, A. L.; Prausnitz, J. M. Thermodynamics of mixed-gas adsorption. *AIChE J.* **1965**, *11*, 121–127.

[124] D'Alessandro, D. M.; Smit, B.; Long, J. R. Carbon dioxide capture: Prospects for new materials. *Angew. Chem., Int. Ed.* **2010**, *49*, 6058–6082.

[125] Keskin, S.; van Heest, T. M.; Sholl, D. S. Can metal-organic framework materials play a useful role in large-scale carbon dioxide separations? *ChemSusChem* **2010**, *3*, 879–891.

[126] Bae, Y.-S.; Mulfort, K. L.; Frost, H.; Ryan, P.; Punnathanam, S.; Broadbelt, L. J.; Hupp, J. T.; Snurr, R. Q. Separation of CO_2 from CH_4 using mixed-ligand metal-organic frameworks. *Langmuir* **2008**, *24*, 8592–8598.

[127] Bae, Y.-S.; Farha, O. K.; Hupp, J. T.; Snurr, R. Q. Enhancement of CO_2/N_2 selectivity in a metal-organic framework by cavity modification. *J. Mater. Chem.* **2009**, *19*, 2131–2134.

[128] Mu, B.; Li, F.; Walton, K. S. A novel metal-organic coordination polymer for selective adsorption of CO_2 over CH_4. *Chem. Commun.* **2009**, 2493–2495.

[129] Phan, A.; Doonan, C. J.; Uribe-Romo, F. J.; Knobler, C. B.; O'Keeffe, M.; Yaghi, O. M. Synthesis, structure, and carbon dioxide capture properties of zeolitic imidazolate frameworks. *Acc. Chem. Res.* **2010**, *43*, 58–67.

[130] Pan, L.; Olson, D. H.; Ciemnolonski, L. R.; Heddy, R.; Li, J. Separation of hydrocarbons with a microporous metal-organic framework. *Angew. Chem., Int. Ed.* **2006**, *45*, 616–619.

[131] Lamia, N.; Jorge, M.; Granato, M. A.; Almeida Paz, F. A.; Chevreau, H.; Rodrigues, A. E. Adsorption of propane, propylene and isobutane on a metal-organic framework: Molecular simulation and experiment. *Chem. Eng. Sci.* **2009**, *64*, 3246–3259.

[132] Murray, L. J.; Dinca, M.; Yano, J.; Chavan, S.; Bordiga, S.; Brown, C. M.; Long, J. R. Highly-selective and reversible O_2 binding in $Cr_3(1,3,5$-benzenetricarboxylate$)_2$. *J. Am. Chem. Soc.* **2010**, *132*, 7856–7857.

[133] Yang, Q.; Zhong, C. Electrostatic-field-induced enhancement of gas mixture separation in metal-organic frameworks: A computational study. *ChemPhysChem* **2006**, *7*, 1417–1421.

[134] Martín-Calvo, A.; García-Pérez, E.; Castillo, J. M.; Calero, S. Molecular simulations for adsorption and separation of natural gas in IRMOF-1 and Cu-BTC metal-organic frameworks. *Phys. Chem. Chem. Phys.* **2008**, *10*, 7085–7091.

[135] Babarao, R.; Jiang, J.; Sandler, S. I. Molecular simulations for adsorptive separation of CO_2/CH_4 mixture in metal-exposed, catenated, and charged metal-organic frameworks. *Langmuir* **2009**, *25*, 5239–5247.

[136] Babarao, R.; Jiang, J. Unprecedentedly high selective adsorption of gas mixtures in *rho* zeolite-like metal-organic framework: A molecular simulation study. *J. Am. Chem. Soc.* **2009**, *131*, 11417–11425.

[137] Keskin, S. Molecular simulation study of CH_4/H_2 mixture separations using metal organic framework membranes and composites. *J. Phys. Chem. C* **2010**, *114*, 13047–13054.

[138] Karra, J. R.; Walton, K. S. Effect of open metal sites on adsorption of polar and nonpolar molecules in metal-organic framework Cu-BTC. *Langmuir* **2008**, *24*, 8620–8626.

[139] Jorge, M.; Lamia, N.; Rodrigues, A. E. Molecular simulation of propane/propylene separation on the metal-organic framework CuBTC. *Colloids Surf., A* **2010**, *357*, 27–34.

[140] Calero, S.; Martín-Calvo, A.; Hamad, S.; García-Pérez, E. On the performance of Cu-BTC metal organic framework for carbon tetrachloride gas removal. *Chem. Commun.* **2011**, *47*, 508–510.

[141] Gascon, J.; Kapteijn, F. Metal-organic framework membranes – high potential, bright future? *Angew. Chem., Int. Ed.* **2010**, *49*, 1530–1532.

[142] Guo, H.; Zhu, G.; Hewitt, I. J.; Qiu, S. "Twin copper source" growth of metal-organic framework membrane: $Cu_3(BTC)_2$ with high permeability and selectivity for recycling H_2. *J. Am. Chem. Soc.* **2009**, *131*, 1646–1647.

[143] Bux, H.; Liang, F.; Li, Y.; Cravillon, J.; Wiebcke, M.; Caro, J. Zeolitic imidazolate framework membrane with molecular sieving properties by microwave-assisted solvothermal synthesis. *J. Am. Chem. Soc.* **2009**, *131*, 16000–16001.

[144] Venna, S. R.; Carreon, M. A. Highly permeable zeolite imidazolate framework-8 membranes for CO_2/CH_4 separation. *J. Am. Chem. Soc.* **2010**, *132*, 76–78.

[145] Hu, J.; Cai, H.; Ren, H.; Wei, Y.; Xu, Z.; Liu, H.; Hu, Y. Mixed-matrix membrane hollow fibers of $Cu_3(BTC)_2$ MOF and polyimide for gas separation and adsorption. *Ind. Eng. Chem. Res.* **2010**, *49*, 12605–12612.

[146] Keskin, S.; Sholl, D. S. Assessment of a metal-organic framework membrane for gas separations using atomically detailed calculations: CO_2, CH_4, N_2, H_2 mixtures in MOF-5. *Ind. Eng. Chem. Res.* **2009**, *48*, 914–922.

[147] Dubbeldam, D.; Snurr, R. Q. Recent developments in the molecular modeling of diffusion in nanoporous materials. *Mol. Simul.* **2007**, *33*, 305–325.

[148] Krishna, R. Describing the diffusion of guest molecules inside porous structures. *J. Phys. Chem. C* **2009**, *113*, 19756–19781.

[149] Skoulidas, A. I. Molecular dynamics simulations of gas diffusion in metal-organic frameworks: Argon in CuBTC. *J. Am. Chem. Soc.* **2004**, *126*, 1356–1357.

[150] Keskin, S.; Sholl, D. S. Screening metal-organic framework materials for membrane-based methane/carbon dioxide separations. *J. Phys. Chem. C* **2007**, *111*, 14055–14059.

[151] Keskin, S.; Sholl, D. S. Efficient methods for screening of metal organic framework membranes for gas separations using atomically detailed models. *Langmuir* **2009**, *25*, 11786–11795.

[152] Watanabe, T.; Keskin, S.; Nair, S.; Sholl, D. S. Computational identification of a metal organic framework for high selectivity membrane-based CO_2/CH_4 separations: $Cu(hfipbb)(H_2hfipbb)_{0.5}$. *Phys. Chem. Chem. Phys.* **2009**, *11*, 11389–11394.

[153] Haldoupis, E.; Nair, S.; Sholl, D. S. Efficient calculation of diffusion limitations in metal organic framework materials: A tool for identifying materials for kinetic separations. *J. Am. Chem. Soc.* **2010**, *132*, 7528–7539.

[154] Jensen, F. *Introduction to Computational Chemistry*, 2nd ed.; John Wiley & Sons, Ltd: Chichester, UK, 2007.

[155] Buch, V. Path integral simulations of mixed *para*-D_2 and *ortho*-D_2 clusters: The orientational effects. *J. Chem. Phys.* **1994**, *100*, 7610–7629.

[156] Mayo, S. L.; Olafson, B. D.; Goddard, W. A. DREIDING: A generic force field for molecular simulations. *J. Phys. Chem.* **1990**, *94*, 8897–8909.

[157] Rappe, A. K.; Casewit, C. J.; Colwell, K. S.; Goddard III, W. A.; Skiff, W. M. UFF, a full periodic table force field for molecular mechanics and molecular dynamics simulations. *J. Am. Chem. Soc.* **1992**, *114*, 10024–10035.

[158] Allinger, N. L.; Yuh, Y. H.; Lii, J. H. Molecular mechanics. The MM3 force field for hydrocarbons. 1. *J. Am. Chem. Soc.* **1989**, *111*, 8551–8566.

[159] Jorgensen, W. L.; Maxwell, D. S.; Tirado-Rives, J. Development and testing of the OPLS All-Atom force field on conformational energetics and properties of organic liquids. *J. Am. Chem. Soc.* **1996**, *118*, 11225–11236.

[160] Tafipolsky, M.; Amirjalayer, S.; Schmid, R. Atomistic theoretical models for nanoporous hybrid materials. *Microporous Mesoporous Mater.* **2010**, *129*, 304–318.

[161] Wiberg, K. B.; Rablen, P. R. Comparison of atomic charges derived via different procedures. *J. Comput. Chem.* **1993**, *14*, 1504–1518.

[162] Berendsen, H. J. C. *Simulating the Physical World - Hierarchical Modeling from Quantum Mechanics to Fluid Dynamics*; Cambridge University Press: Cambridge, UK, 2007.

[163] Cieplak, P.; Dupradeau, F.-Y.; Duan, Y.; Wang, J. Polarization effects in molecular mechanical force fields. *J. Phys.: Condens. Matter* **2009**, *21*, 333102.

[164] Kaplan, I. G. *Intermolecular Interactions: Physical Picture, Computational Methods and Model Potentials*, 1st ed.; John Wiley & Sons, Ltd: Chichester, UK, 2006.

[165] Halgren, T. A. The representation of van der Waals (vdW) interactions in molecular mechanics force fields: Potential form, combination rules, and vdW parameters. *J. Am. Chem. Soc.* **1992**, *114*, 7827–7843.

[166] Cramer, C. J. *Essentials of Computational Chemistry*, 2nd ed.; John Wiley & Sons, Ltd: Chichester, UK, 2004.

[167] Jorgensen, W. L.; Madura, J. D.; Swenson, C. J. Optimized intermolecular potential functions for liquid hydrocarbons. *J. Am. Chem. Soc.* **1984**, *106*, 6638–6646.

[168] Martin, M. G.; Siepmann, J. I. Transferable Potentials for Phase Equilibria. 1. United-atom description of *n*-alkanes. *J. Phys. Chem. B* **1998**, *102*, 2569–2577.

[169] Martin, M. G. Comparison of the AMBER, CHARMM, COMPASS, GROMOS, OPLS, TraPPE and UFF force fields for prediction of vapor-liquid coexistence curves and liquid densities. *Fluid Phase Equilib.* **2006**, *248*, 50–55.

[170] Hill, T. L. *An Introduction to Statistical Thermodynamics*; Dover Publications: Mineola, NY, USA, 1987.

[171] Metropolis, N.; Rosenbluth, A. W.; Rosenbluth, M. N.; Teller, A. H.; Teller, E. Equation of state calculations by fast computing machines. *J. Chem. Phys.* **1953**, *21*, 1087–1092.

[172] Frenkel, D.; Smit, B. *Understanding Molecular Simulation: From Algorithms to Applications*, 2nd ed.; Academic Press: San Diego, USA, 2002.

[173] Vlugt, T. J. H.; van Der Eerden, J. P. J. M.; Dijkstra, M.; Smit, B.; Frenkel, D. *Introduction to Molecular Simulation and Statistical Thermodynamics*, 1st ed.; available from *http://www.phys.uu.nl/~vlugt/imsst*: Delft, NL, 2008.

[174] Allen, M. P.; Tildesley, D. J. *Computer Simulation of Liquids*, 1st ed.; Clarendon Press: Oxford, UK, 1987.

[175] Do, D. D.; Nicholson, D.; Do, H. D. On the Henry constant and isosteric heat at zero loading in gas phase adsorption. *J. Colloid Interface Sci.* **2008**, *324*, 15–24.

[176] Pan, H.; Ritter, J. A.; Balbuena, P. B. Examination of the approximations used in determining the isosteric heat of adsorption from the Clausius-Clapeyron equation. *Langmuir* **1998**, *14*, 6323–6327.

[177] Kuchta, B.; Firlej, L.; Maurin, G. Mechanism of adsorption in cylindrical nanopores: The roles of fluctuations and correlations in stabilizing the adsorbed phase. *J. Chem. Phys.* **2005**, *123*, 174711.

[178] Cole, J. H.; Everett, D. H.; Marshall, C. T.; Paniego, A. R.; Powl, J. C.; Rodriguez-Reinoso, F. Thermodynamics of the high temperature adsorption of some permanent gases by porous carbons. *J. Chem. Soc., Faraday Trans. 1* **1974**, *70*, 2154–2169.

[179] Broadbelt, L. J.; Snurr, R. Q. Applications of molecular modeling in heterogeneous catalysis research. *Applied Catal., A* **2000**, *200*, 23–46.

[180] Helgaker, T.; Ruden, T. A.; Jorgensen, P.; Olsen, J.; Klopper, W. A priori calculation of molecular properties to chemical accuracy. *J. Phys. Org. Chem.* **2004**, *17*, 913–933.

[181] van Mourik, T.; Gdanitz, R. J. A critical note on density functional theory studies on rare-gas dimers. *J. Chem. Phys.* **2002**, *116*, 9620–9623.

[182] Pople, J. A. Quantum chemical models (Nobel Lecture). *Angew. Chem., Int. Ed.* **1999**, *38*, 1894–1902.

[183] Cramer, C. J.; Truhlar, D. G. Density functional theory for transition metals and transition metal chemistry. *Phys. Chem. Chem. Phys.* **2009**, *11*, 10757–10816.

[184] Kohn, W. Nobel Lecture: Electronic structure of matter – Wave functions and density functionals. *Rev. Mod. Phys.* **1999**, *71*, 1253–1266.

[185] Hohenberg, P.; Kohn, W. Inhomogeneous electron gas. *Phys. Rev.* **1964**, *136*, B864–B871.

[186] Kohn, W.; Sham, L. Self-consistent equations including exchange and correlation effects. *Phys. Rev.* **1965**, *140*, A1133–A1138.

[187] Johnson, E. R.; Wolkow, R. A.; DiLabio, G. A. Application of 25 density functionals to dispersion-bound homomolecular dimers. *Chem. Phys. Lett.* **2004**, *394*, 334–338.

[188] Becke, A. D. Density-functional exchange-energy approximation with correct asymptotic behavior. *Phys. Rev. A* **1988**, *38*, 3098–3100.

[189] Lee, C.; Yang, W.; Parr, R. G. Development of the Colle-Salvetti correlation-energy formula into a functional of the electron density. *Phys. Rev. B* **1988**, *37*, 785–789.

[190] Perdew, J. P.; Burke, K.; Ernzerhof, M. Generalized Gradient Approximation made simple. *Phys. Rev. Lett.* **1996**, *77*, 3865–3868.

[191] Stephens, P. J.; Devlin, F. J.; Chabalowski, C. F.; Frisch, M. J. Ab initio calculation of vibrational absorption and circular dichroism spectra using density functional force fields. *J. Phys. Chem.* **1994**, *98*, 11623–11627.

[192] Adamo, C.; Barone, V. Toward reliable density functional methods without adjustable parameters: The PBE0 model. *J. Chem. Phys.* **1999**, *110*, 6158–6170.

[193] Cohen, A. J.; Handy, N. C. Assessment of exchange correlation functionals. *Chem. Phys. Lett.* **2000**, *316*, 160–166.

[194] Sousa, S. F.; Fernandes, P. A.; Ramos, M. J. General performance of density functionals. *J. Phys. Chem. A* **2007**, *111*, 10439–10452.

[195] Delley, B. An all-electron numerical method for solving the local density functional for polyatomic molecules. *J. Chem. Phys.* **1990**, *92*, 508–517.

[196] Inada, Y.; Orita, H. Efficiency of numerical basis sets for predicting the binding energies of hydrogen bonded complexes: Evidence of small basis set superposition error compared to Gaussian basis sets. *J. Comput. Chem.* **2008**, *29*, 225–232.

[197] Benedek, N. A.; Snook, I. K.; Latham, K.; Yarovsky, I. Application of numerical basis sets to hydrogen bonded systems: A density functional theory study. *J. Chem. Phys.* **2005**, *122*, 144102.

[198] Boys, S.; Bernardi, F. The calculation of small molecular interactions by the differences of separate total energies. Some procedures with reduced errors. *Mol. Phys.* **1970**, *19*, 553–566.

[199] Kohn, W.; Meir, Y.; Makarov, D. E. Van der Waals energies in density functional theory. *Phys. Rev. Lett.* **1998**, *80*, 4153–4156.

[200] Kristyán, S.; Pulay, P. Can (semi)local density functional theory account for the London dispersion forces? *Chem. Phys. Lett.* **1994**, *229*, 175–180.

[201] Johnson, E. R.; Mackie, I. D.; DiLabio, G. A. Dispersion interactions in density-functional theory. *J. Phys. Org. Chem.* **2009**, *22*, 1127–1135.

[202] Grimme, S. Accurate description of van der Waals complexes by density functional theory including empirical corrections. *J. Comput. Chem.* **2004**, *25*, 1463–1473.

[203] Grimme, S. Semiempirical GGA-type density functional constructed with a long-range dispersion correction. *J. Comput. Chem.* **2006**, *27*, 1787–1799.

[204] Foster, M. E.; Sohlberg, K. Empirically corrected DFT and semi-empirical methods for non-bonding interactions. *Phys. Chem. Chem. Phys.* **2010**, *12*, 307–322.

[205] Grimme, S.; Antony, J.; Ehrlich, S.; Krieg, H. A consistent and accurate ab initio parametrization of density functional dispersion correction (DFT-D) for the 94 elements H-Pu. *J. Chem. Phys.* **2010**, *132*, 154104.

[206] Becke, A. D.; Johnson, E. R. Exchange-hole dipole moment and the dispersion interaction revisited. *J. Chem. Phys.* **2007**, *127*, 154108.

[207] Kannemann, F. O.; Becke, A. D. Van der Waals interactions in density-functional theory: Rare-gas diatomics. *J. Chem. Theory Comput.* **2009**, *5*, 719–727.

[208] Kannemann, F. O.; Becke, A. D. Van der Waals interactions in density-functional theory: Intermolecular complexes. *J. Chem. Theory Comput.* **2010**, *6*, 1081–1088.

[209] von Lilienfeld, O. A.; Tavernelli, I.; Rothlisberger, U.; Sebastiani, D. Optimization of effective atom centered potentials for London dispersion forces in density functional theory. *Phys. Rev. Lett.* **2004**, *93*, 153004.

[210] Dion, M.; Rydberg, H.; Schröder, E.; Langreth, D. C.; Lundqvist, B. I. Van der Waals density functional for general geometries. *Phys. Rev. Lett.* **2004**, *92*, 246401.

[211] Langreth, D. C.; Lundqvist, B. I.; Chakarova-Käck, S. D.; Cooper, V. R.; Dion, M.; Hyldgaard, P.; Kelkkanen, A.; Kleis, J.; Kong, L.; Li, S.; Moses, P. G.; Murray, E.; Puzder, A.; Rydberg, H.; Schröder, E.; Thonhauser, T. A density functional for sparse matter. *J. Phys.: Condens. Matter* **2009**, *21*, 084203.

[212] Popelier, P. *Atoms in Molecules - An Introduction*, 1st ed.; Pearson Education: Harlow, UK, 2000.

[213] Stone, A. Distributed multipole analysis, or how to describe a molecular charge distribution. *Chem. Phys. Lett.* **1981**, *83*, 233–239.

[214] Singh, U. C.; Kollman, P. A. An approach to computing electrostatic charges for molecules. *J. Comput. Chem.* **1984**, *5*, 129–145.

[215] Sigfridsson, E.; Ryde, U. Comparison of methods for deriving atomic charges from the electrostatic potential and moments. *J. Comput. Chem.* **1998**, *19*, 377–395.

[216] Campaná, C.; Mussard, B.; Woo, T. K. Electrostatic potential derived atomic charges for periodic systems using a modified error functional. *J. Chem. Theory Comput.* **2009**, *5*, 2866–2878.

[217] Frenking, G.; Wichmann, K.; Fröhlich, N.; Loschen, C.; Lein, M.; Frunzke, J.; Rayòn, V. M. Towards a rigorously defined quantum chemical analysis of the chemical bond in donor-acceptor complexes. *Coord. Chem. Rev.* **2003**, *238-239*, 55–82.

[218] Kuc, A.; Heine, T.; Seifert, G.; Duarte, H. A. On the nature of the interaction between H_2 and metal-organic frameworks. *Theor. Chem. Acc.* **2008**, *120*, 543–550.

[219] Silvera, I. F. The solid molecular hydrogens in the condensed phase: Fundamentals and static properties. *Rev. Mod. Phys.* **1980**, *52*, 393–452.

[220] Kumar, A. V. A.; Jobic, H.; Bhatia, S. K. Quantum effects on adsorption and diffusion of hydrogen and deuterium in microporous materials. *J. Phys. Chem. B* **2006**, *110*, 16666–16671.

[221] Yang, Q.; Zhong, C. Molecular simulation of adsorption and diffusion of hydrogen in metal-organic frameworks. *J. Phys. Chem. B* **2005**, *109*, 11862–11864.

[222] Wang, W. Atomic-potential parameters for H_2 and D_2: Quantum corrections in the calculation of second-virial coefficients. *J. Quant. Spectrosc. Radiat. Transfer* **2003**, *76*, 23–30.

[223] Wang, Q.; Johnson, J. K.; Broughton, J. Q. Thermodynamic properties and phase equilibrium of fluid hydrogen from path integral simulations. *Mol. Phys.* **1996**, *89*, 1105–1119.

[224] Johnson, R. D. NIST Computational Chemistry Comparison and Benchmark Database, NIST Standard Reference Database Number 101. 2010; available from: *http://srdata.nist.gov/cccbdb*.

[225] Boehme, R. F.; La Placa, S. J. Empirical molecular hydrogen wave function modeled from theoretically derived X-ray diffraction data. *Phys. Rev. Lett.* **1987**, *59*, 985–987.

[226] Buckingham, A. D.; Disch, R. L.; Dunmur, D. A. Quadrupole moments of some simple molecules. *J. Am. Chem. Soc.* **1968**, *90*, 3104–3107.

[227] Sesé, L. M. Feynman-Hibbs potentials and path integrals for quantum Lennard-Jones systems: Theory and Monte Carlo simulations. *Mol. Phys.* **1995**, *85*, 931–947.

[228] Kowalczyk, P.; MacElroy, J. M. D. Equilibrium properties of dense hydrogen isotope gases based on the theory of simple fluids. *J. Phys. Chem. B* **2006**, *110*, 14971–14975.

[229] Sesé, L. M. Study of the Feynman-Hibbs effective potential against the path-integral formalism for Monte Carlo simulations of quantum many-body Lennard-Jones systems. *Mol. Phys.* **1994**, *81*, 1297–1312.

[230] Kuchta, B.; Firlej, L.; Cepel, R.; Pfeifer, P.; Wexler, C. Structural and energetic factors in designing a nanoporous sorbent for hydrogen storage. *Colloids Surf., A* **2010**, *357*, 61–66.

[231] Tanaka, H.; Kanoh, H.; Yudasaka, M.; Iijima, S.; Kaneko, K. Quantum effects on hydrogen isotope adsorption on single-wall carbon nanohorns. *J. Am. Chem. Soc.* **2005**, *127*, 7511–7516.

[232] Lemmon, E.; McLinden, M.; Friend, D. In *NIST Chemistry WebBook, NIST Standard Reference Database Number 69*; Linstrom, P., Mallard, W., Eds.; National Institute of Standards and Technology: Gaithersburg, MD, USA, 2010.

[233] *Materials Studio Version 4.4*; Accelrys Inc.: San Diego, 2009.

[234] Zhang, L.; Siepmann, J. I. Direct calculation of Henry's law constants from Gibbs ensemble Monte Carlo simulations: Nitrogen, oxygen, carbon dioxide and methane in ethanol. *Theor. Chem. Acc.* **2006**, *115*, 391–397.

[235] Yang, Q.; Xue, C.; Zhong, C.; Chen, J.-F. Molecular simulation of separation of CO_2 from flue gases in CU-BTC metal-organic framework. *AIChE J.* **2007**, *53*, 2832–2840.

[236] Vrabec, J.; Stoll, J.; Hasse, H. A set of molecular models for symmetric quadrupolar fluids. *J. Phys. Chem. B* **2001**, *105*, 12126–12133.

[237] Gu, C.; Gao, G.-H.; Yu, Y.-X.; Nitta, T. Simulation for separation of hydrogen and carbon monoxide by adsorption on single-walled carbon nanotubes. *Fluid Phase Equilib.* **2002**, *194-197*, 297–307.

[238] Stoll, J.; Vrabec, J.; Hasse, H. A set of molecular models for carbon monoxide and halogenated hydrocarbons. *J. Chem. Phys.* **2003**, *119*, 11396–11407.

[239] Piper, J.; Morrison, J.; Peters, C. The adsorption of carbon monoxide on graphite. *Mol. Phys.* **1984**, *53*, 1463–1480.

[240] Straub, J. E.; Karplus, M. Molecular dynamics study of the photodissociation of carbon monoxide from myoglobin: Ligand dynamics in the first 10 ps. *Chem. Phys.* **1991**, *158*, 221–248.

[241] Wang, S.; Yang, Q.; Zhong, C. Adsorption and separation of binary mixtures in a metal-organic framework Cu-BTC: A computational study. *Sep. Purif. Technol.* **2008**, *60*, 30–35.

[242] Talu, O.; Myers, A. L. Reference potentials for adsorption of helium, argon, methane, and krypton in high-silica zeolites. *Colloids Surf., A* **2001**, *187-188*, 83–93.

[243] García-Sánchez, A.; Ania, C. O.; Parra, J. B.; Dubbeldam, D.; Vlugt, T. J. H.; Krishna, R.; Calero, S. Transferable force field for carbon dioxide adsorption in zeolites. *J. Phys. Chem. C* **2009**, *113*, 8814–8820.

[244] Potoff, J.; Siepmann, J. Vapor-liquid equilibria of mixtures containing alkanes, carbon dioxide, and nitrogen. *AIChE J.* **2001**, *47*, 1676–1682.

[245] Babarao, R.; Jiang, J. Molecular screening of metal-organic frameworks for CO_2 storage. *Langmuir* **2008**, *24*, 6270–6278.

[246] Yazaydin, A. O.; Benin, A. I.; Faheem, S. A.; Jakubczak, P.; Low, J. J.; Willis, R. R.; Snurr, R. Q. Enhanced CO_2 adsorption in metal-organic frameworks via occupation of open-metal sites by coordinated water molecules. *Chem. Mater.* **2009**, *21*, 1425–1430.

[247] Pässler, P.; Hefner, W.; Buckl, L.; Meinass, H.; Meiswinkel, A.; Wernicke, H.-J.; Ebersberg, G.; Müller, R.; Bässler, J.; Behringer, H.; Mayer, D. ACETYLENE in *Ullmann's Encyclopedia of Industrial Chemistry*; Wiley-VCH Verlag GmbH & Co. KGaA: Weinheim, D. 2008.

[248] Gautam, S.; Mitra, S.; Mukhopadhyay, R.; Chaplot, S. L. Diffusion of acetylene inside Na-Y zeolite: Molecular dynamics simulation studies. *Phys. Rev. E* **2006**, *74*, 041202.

[249] Ghorai, P. K.; Yashonath, S.; Demontis, P.; Suffritti, G. B. Diffusion anomaly as a function of molecular length of linear molecules: Levitation effect. *J. Am. Chem. Soc.* **2003**, *125*, 7116–7123.

[250] McMullan, R. K.; Kvick, A.; Popelier, P. Structures of cubic and orthorhombic phases of acetylene by single-crystal neutron diffraction. *Acta Crystallogr., Sect. B: Struct. Sci.* **1992**, *48*, 726–731.

[251] Eddaoudi, M.; Kim, J.; Rosi, N.; Vodak, D.; Wachter, J.; O'Keeffe, M.; Yaghi, O. M. Systematic design of pore size and functionality in isoreticular MOFs and their application in methane storage. *Science* **2002**, *295*, 469–472.

[252] Rowsell, J. L. C.; Yaghi, O. M. Effects of functionalization, catenation, and variation of the metal oxide and organic linking units on the low-pressure hydrogen adsorption properties of metal-organic frameworks. *J. Am. Chem. Soc.* **2006**, *128*, 1304–1315.

[253] Rowsell, J. L. C.; Spencer, E. C.; Eckert, J.; Howard, J. A. K.; Yaghi, O. M. Gas adsorption sites in a large-pore metal-organic framework. *Science* **2005**, *309*, 1350–1354.

[254] Rosi, N. L.; Kim, J.; Eddaoudi, M.; Chen, B.; O'Keeffe, M.; Yaghi, O. M. Rod packings and metal-organic frameworks constructed from rod-shaped secondary building units. *J. Am. Chem. Soc.* **2005**, *127*, 1504–1518.

[255] Liu, Y.; Kabbour, H.; Brown, C. M.; Neumann, D. A.; Ahn, C. C. Increasing the density of adsorbed hydrogen with coordinatively unsaturated metal centers in metal-organic frameworks. *Langmuir* **2008**, *24*, 4772–4777.

[256] Park, K. S.; Ni, Z.; Côté, A. P.; Choi, J. Y.; Huang, R.; Uribe-Romo, F. J.; Chae, H. K.; O'Keeffe, M.; Yaghi, O. M. Exceptional chemical and thermal stability of zeolitic imidazolate frameworks. *Proc. Natl. Acad. Sci. U. S. A.* **2006**, *103*, 10186–10191.

[257] Li, J.-R.; Tao, Y.; Yu, Q.; Bu, X.-H.; Sakamoto, H.; Kitagawa, S. Selective gas adsorption and unique structural topology of a highly stable guest-free zeolite-type MOF material with N-rich chiral open channels. *Chem.–Eur. J.* **2008**, *14*, 2771–2776.

[258] O'Keeffe, M.; Peskov, M. A.; Ramsden, S. J.; Yaghi, O. M. The Reticular Chemistry Structure Resource (RCSR) database of, and symbols for, crystal nets. *Acc. Chem. Res.* **2008**, *41*, 1782–1789.

[259] Zhang, X. X.; Chui, S. S.-Y.; Williams, I. D. Cooperative magnetic behavior in the co-ordination polymers $Cu_3(TMA)_2(L)_3$ (L=H_2O, pyridine). *J. Appl. Phys.* **2000**, *87*, 6007–6009.

[260] Chen, B.; Ockwig, N. W.; Millward, A. R.; Contreras, D. S.; Yaghi, O. M. High H_2 adsorption in a microporous metal-organic framework with open metal sites. *Angew. Chem., Int. Ed.* **2005**, *44*, 4745–4749.

[261] Lin, X.; Jia, J.; Zhao, X.; Thomas, K. M.; Blake, A. J.; Walker, G. S.; Champness, N. R.; Hubberstey, P.; Schröder, M. High H_2 adsorption by coordination-framework materials. *Angew. Chem., Int. Ed.* **2006**, *45*, 7358–7364.

[262] Lin, X.; Telepeni, I.; Blake, A. J.; Dailly, A.; Brown, C. M.; Simmons, J. M.; Zoppi, M.; Walker, G. S.; Thomas, K. M.; Mays, T. J.; Hubberstey, P.; Champness, N. R.; Schröder, M. High capacity hydrogen adsorption in Cu(II) tetracarboxylate framework materials: The role of pore size, ligand functionalization, and exposed metal sites. *J. Am. Chem. Soc.* **2009**, *131*, 2159–2171.

[263] Wong-Foy, A. G.; Lebel, O.; Matzger, A. J. Porous crystal derived from a tricarboxylate linker with two distinct binding motifs. *J. Am. Chem. Soc.* **2007**, *129*, 15740–15741.

[264] Wang, X.-S.; Ma, S.; Forster, P. M.; Yuan, D.; Eckert, J.; López, J. J.; Murphy, B. J.; Parise, J. B.; Zhou, H.-C. Enhancing H_2 uptake by "close-packing" alignment of open copper sites in metal-organic frameworks. *Angew. Chem., Int. Ed.* **2008**, *47*, 7263–7266.

[265] Wenzel, S. E.; Fischer, M.; Hoffmann, F.; Fröba, M. Highly porous metal-organic framework containing a novel organosilicon linker - A promising material for hydrogen storage. *Inorg. Chem.* **2009**, *48*, 6559–6565.

[266] Wang, Z.; Hu, K.; Gao, S.; Kobayashi, H. Formate-based magnetic metal-organic frameworks templated by protonated amines. *Adv. Mater.* **2010**, *22*, 1526–1533.

[267] Dybtsev, D. N.; Chun, H.; Yoon, S. H.; Kim, D.; Kim, K. Microporous manganese formate: a simple metal-organic porous material with high framework stability and highly selective gas sorption properties. *J. Am. Chem. Soc.* **2004**, *126*, 32–33.

[268] Rood, J. A.; Noll, B. C.; Henderson, K. W. Synthesis, structural characterization, gas sorption and guest-exchange studies of the lightweight, porous metal-organic framework α-[$Mg_3(O_2CH)_6$]. *Inorg. Chem.* **2006**, *45*, 5521–5528.

[269] Samsonenko, D. G.; Kim, H.; Sun, Y.; Kim, G.-H.; Lee, H.-S.; Kim, K. Microporous magnesium and manganese formates for acetylene storage and separation. *Chem.– Asian J.* **2007**, *2*, 484–488.

[270] Flanigen, E. M.; Bennett, J. M.; Grose, R. W.; Cohen, J. P.; Patton, R. L.; Kirchner, R. M.; Smith, J. V. Silicalite, a new hydrophobic crystalline silica molecular sieve. *Nature* **1978**, *271*, 512–516.

[271] Baerlocher, C.; McCusker, L. B.; Olson, D. H. *Atlas of Zeolite Framework Types*, 6th ed.; Elsevier B.V.: Amsterdam, NL, 2007.

[272] van Koningsveld, H.; van Bekkum, H.; Jansen, J. C. On the location and disorder of the tetrapropylammonium (TPA) ion in zeolite ZSM-5 with improved framework accuracy. *Acta Crystallogr., Sect. B: Struct. Sci.* **1987**, *43*, 127–132.

[273] Lagona, J.; Mukhopadhyay, P.; Chakrabarti, S.; Isaacs, L. The cucurbit[n]uril family. *Angew. Chem., Int. Ed.* **2005**, *44*, 4844–4870.

[274] Kim, K.; Selvapalam, N.; Ko, Y. H.; Park, K. M.; Kim, D.; Kim, J. Functionalized cucurbiturils and their applications. *Chem. Soc. Rev.* **2007**, *36*, 267–279.

[275] Lim, S.; Kim, H.; Selvapalam, N.; Kim, K.-J.; Cho, S. J.; Seo, G.; Kim, K. Cucurbit[6]uril: Organic molecular porous material with permanent porosity, exceptional stability, and acetylene sorption properties. *Angew. Chem., Int. Ed.* **2008**, *47*, 3352–3355.

[276] Yang, Q.; Zhong, C. Understanding hydrogen adsorption in metal-organic frameworks with open metal sites: A computational study. *J. Phys. Chem. B* **2006**, *110*, 655–658.

[277] Nguyen, T. X.; Bae, J.-S.; Wang, Y.; Bhatia, S. K. On the strength of the hydrogen-carbon interaction as deduced from physisorption. *Langmuir* **2009**, *25*, 4314–4319.

[278] Smit, B.; Maesen, T. L. M. Molecular simulations of zeolites: Adsorption, diffusion, and shape selectivity. *Chem. Rev.* **2008**, *108*, 4125–4184.

[279] Han, S.-S.; Deng, W.-Q.; Goddard, W. A. Improved designs of metal-organic frameworks for hydrogen storage. *Angew. Chem., Int. Ed.* **2007**, *46*, 6289–6292.

[280] Williams, D. E.; Houpt, D. J. Fluorine nonbonded potential parameters derived from crystalline perfluorocarbons. *Acta Crystallogr., Sect. B: Struct. Sci.* **1986**, *42*, 286–295.

[281] Casewit, C. J.; Colwell, K. S.; Rappe, A. K. Application of a universal force field to organic molecules. *J. Am. Chem. Soc.* **1992**, *114*, 10035–10046.

[282] Casewit, C. J.; Colwell, K. S.; Rappe, A. K. Application of a universal force field to main group compounds. *J. Am. Chem. Soc.* **1992**, *114*, 10046–10053.

[283] Rappe, A. K.; Colwell, K. S.; Casewit, C. J. Application of a universal force field to metal complexes. *Inorg. Chem.* **1993**, *32*, 3438–3450.

[284] Karra, J. R.; Walton, K. S. Molecular simulations and experimental studies of CO_2, CO, and N_2 adsorption in metal-organic frameworks. *J. Phys. Chem. C* **2010**, *114*, 15735–15740.

[285] Donchev, A. G. *Ab initio* study of the effects of orientation and corrugation for H_2 adsorbed on polycyclic aromatic hydrocarbons. *J. Chem. Phys.* **2007**, *126*, 124706.

[286] Figueroa-Gerstenmaier, S.; Giudice, S.; Cavallo, L.; Milano, G. A molecular model for H_2 interactions in aliphatic and aromatic hydrocarbons. *Phys. Chem. Chem. Phys.* **2009**, *11*, 3935–3942.

[287] Ferre-Vilaplana, A. Numerical treatment discussion and *ab initio* computational reinvestigation of physisorption of molecular hydrogen on graphene. *J. Chem. Phys.* **2005**, *122*, 104709.

[288] Beaudet, T. D.; Casula, M.; Kim, J.; Sorella, S.; Martin, R. M. Molecular hydrogen adsorbed on benzene: Insights from a quantum Monte Carlo study. *J. Chem. Phys.* **2008**, *129*, 164711.

[289] Delley, B. From molecules to solids with the DMol^3 approach. *J. Chem. Phys.* **2000**, *113*, 7756–7764.

[290] Liu, J.; Rankin, R. B.; Johnson, J. K. The importance of charge-quadrupole interactions for H_2 adsorption and diffusion in CuBTC. *Mol. Simul.* **2009**, *35*, 60–69.

[291] Murata, K.; El-Merraoui, M.; Kaneko, K. A new determination method of absolute adsorption isotherm of supercritical gases under high pressure with a special relevance to density-functional theory study. *J. Chem. Phys.* **2001**, *114*, 4196–4205.

[292] Mertens, F. O. Determination of absolute adsorption in highly ordered porous media. *Surf. Sci.* **2009**, *603*, 1979–1984.

[293] Myers, A. L.; Calles, J. A.; Calleja, G. Comparison of molecular simulation of adsorption with experiment. *Adsorption* **1997**, *3*, 107–115.

[294] Myers, A. L.; Monson, P. A. Adsorption in porous materials at high pressure: Theory and experiment. *Langmuir* **2002**, *18*, 10261–10273.

[295] Neimark, A. V.; Ravikovitch, P. I. Calibration of pore volume in adsorption experiments and theoretical models. *Langmuir* **1997**, *13*, 5148–5160.

[296] Fischer, M.; Hoffmann, F.; Fröba, M. Preferred hydrogen adsorption sites in various MOFs - A comparative computational study. *ChemPhysChem* **2009**, *10*, 2647–2657.

[297] Zhou, W.; Wu, H.; Hartman, M.; Yildirim, T. Hydrogen and methane adsorption in metal-organic frameworks: A high-pressure volumetric study. *J. Phys. Chem. C* **2007**, *111*, 16131–16137.

[298] te Velde, G.; Bickelhaupt, F. M.; Baerends, E. J.; Fonseca Guerra, C.; van Gisbergen, S. J. A.; Snijders, J. G.; Ziegler, T. Chemistry with ADF. *J. Comput. Chem.* **2001**, *22*, 931–967.

[299] Weller, M. T.; Henry, P. F.; Ting, V. P.; Wilson, C. C. Crystallography of hydrogen-containing compounds: Realizing the potential of neutron powder diffraction. *Chem. Commun.* **2009**, 2973–2989.

[300] Yildirim, T.; Hartman, M. R. Direct observation of hydrogen adsorption sites and nanocage formation in metal-organic frameworks. *Phys. Rev. Lett.* **2005**, *95*, 215504.

[301] Spencer, E. C.; Howard, J. A. K.; McIntyre, G. J.; Rowsell, J. L. C.; Yaghi, O. M. Determination of the hydrogen absorption sites in $Zn_4O(1,4\text{-benzenedicarboxylate})$ by single crystal neutron diffraction. *Chem. Commun.* **2006**, 278–280.

[302] Wu, H.; Zhou, W.; Yildirim, T. Hydrogen storage in a prototypical zeolitic imidazolate framework-8. *J. Am. Chem. Soc.* **2007**, *129*, 5314–5315.

[303] Zhang, L.; Wang, Q.; Liu, Y.-C. Design for hydrogen storage materials via observation of adsorption sites by computer tomography. *J. Phys. Chem. B* **2007**, *111*, 4291–4295.

[304] Poirier, E.; Dailly, A. Thermodynamic study of the adsorbed hydrogen phase in Cu-based metal-organic frameworks at cryogenic temperatures. *Energy Environ. Sci.* **2009**, *2*, 420–425.

[305] Forster, P. M.; Eckert, J.; Heiken, B. D.; Parise, J. B.; Yoon, J. W.; Jhung, S. H.; Chang, J.-S.; Cheetham, A. K. Adsorption of molecular hydrogen on coordinatively unsaturated Ni(II) sites in a nanoporous hybrid material. *J. Am. Chem. Soc.* **2006**, *128*, 16846–16850.

[306] Panella, B.; Hönes, K.; Müller, U.; Trukhan, N.; Schubert, M.; Pütter, H.; Hirscher, M. Desorption studies of hydrogen in metal-organic frameworks. *Angew. Chem., Int. Ed.* **2008**, *47*, 2138–2142.

[307] Panella, B.; Hirscher, M.; Pütter, H.; Müller, U. Hydrogen adsorption in metal-organic frameworks: Cu-MOFs and Zn-MOFs compared. *Adv. Funct. Mater.* **2006**, *16*, 520–524.

[308] Moellmer, J.; Celer, E.; Luebke, R.; Cairns, A.; Staudt, R.; Eddaoudi, M.; Thommes, M. Insights on adsorption characterization of metal-organic frameworks: A benchmark study on the novel *soc*-MOF. *Microporous Mesoporous Mater.* **2010**, *129*, 345–353.

[309] Nouar, F.; Eubank, J. F.; Bousquet, T.; Wojtas, L.; Zaworotko, M. J.; Eddaoudi, M. Supermolecular building blocks (SBBs) for the design and synthesis of highly porous metal-organic frameworks. *J. Am. Chem. Soc.* **2008**, *130*, 1833–1835.

[310] Scanlon, L. G.; Feld, W. A.; Balbuena, P. B.; Sandi, G.; Duan, X.; Underwood, K. A.; Hunter, N.; Mack, J.; Rottmayer, M. A.; Tsao, M. Hydrogen storage based on physisorption. *J. Phys. Chem. B* **2009**, *113*, 4708–4717.

[311] Wong, M.; Van Kuiken, B. E.; Buda, C.; Dunietz, B. D. Multiadsorption and coadsorption of hydrogen on model conjugated systems. *J. Phys. Chem. C* **2009**, *113*, 12571–12579.

[312] Negri, F.; Saendig, N. Tuning the physisorption of molecular hydrogen: Binding to aromatic, hetero-aromatic and metal-organic framework materials. *Theor. Chem. Acc.* **2007**, *118*, 149–163.

[313] Wenzel, S. E. *Mikroporöse Anorganisch-Organische Hybridmaterialien: Synthese, Charakterisierung und Anwendung als Wasserstoffspeicher*. PhD thesis, University of Hamburg, 2010.

[314] Ciesielski, A.; Krygowski, T. M.; Cyranski, M. K.; Balaban, A. T. Defining rules of aromaticity: A unified approach to the Hückel, Clar and Randić concepts. *Phys. Chem. Chem. Phys.* **2011**, *13*, 3737–3747.

[315] Zou, R.-Q.; Sakurai, H.; Han, S.; Zhong, R.-Q.; Xu, Q. Probing the Lewis acid sites and CO catalytic oxidation activity of the porous metal-organic polymer [Cu(5-methylisophthalate)]. *J. Am. Chem. Soc.* **2007**, *129*, 8402–8403.

[316] Zhao, Y.; Padmanabhan, M.; Gong, Q.; Tsumori, N.; Xu, Q.; Li, J. CO catalytic oxidation by a metal organic framework containing high density of reactive copper sites. *Chem. Commun.* **2011**, *47*, 6377–6379.

[317] Deng, H.; Doonan, C. J.; Furukawa, H.; Ferreira, R. B.; Towne, J.; Knobler, C. B.; Wang, B.; Yaghi, O. M. Multiple functional groups of varying ratios in metal-organic frameworks. *Science* **2010**, *327*, 846–850.

[318] Rubes, M.; Bludský, O. Intermolecular π-π interactions in solids. *Phys. Chem. Chem. Phys.* **2008**, *10*, 2611–2615.

[319] Bag, S.; Kanatzidis, M. G. Chalcogels: Porous metal-chalcogenide networks from main-group metal ions. Effect of surface polarizability on selectivity in gas separation. *J. Am. Chem. Soc.* **2010**, *132*, 14951–14959.

[320] Bhatia, K. K.; Wang, C.-Y. Transient carbon monoxide poisoning of a polymer electrolyte fuel cell operating on diluted hydrogen feed. *Electrochim. Acta* **2004**, *49*, 2333–2341.

[321] Dunne, J. A.; Mariwala, R.; Rao, M.; Sircar, S.; Gorte, R. J.; Myers, A. L. Calorimetric heats of adsorption and adsorption isotherms. 1. O_2, N_2, Ar, CO_2, CH_4, C_2H_6, and SF_6 on Silicalite. *Langmuir* **1996**, *12*, 5888–5895.

[322] Schmitz, B.; Krkljus, I.; Leung, E.; Höffken, H. W.; Müller, U.; Hirscher, M. A high heat of adsorption for hydrogen in magnesium formate. *ChemSusChem* **2010**, *3*, 758–761.

[323] Xiang, S.; Zhou, W.; Gallegos, J. M.; Liu, Y.; Chen, B. Exceptionally high acetylene uptake in a microporous metal-organic framework with open metal sites. *J. Am. Chem. Soc.* **2009**, *131*, 12415–12419.

[324] Kim, H.; Kim, Y.; Yoon, M.; Lim, S.; Park, S. M.; Seo, G.; Kim, K. Highly selective carbon dioxide sorption in an organic molecular porous material. *J. Am. Chem. Soc.* **2010**, *132*, 12200–12202.

[325] Hirotani, A.; Mizukami, K.; Miura, R.; Takaba, H.; Miya, T.; Fahmi, A.; Stirling, A.; Kubo, M.; Miyamoto, A. Grand canonical Monte Carlo simulation of the adsorption of CO_2 on silicalite and NaZSM-5. *Appl. Surf. Sci.* **1997**, *120*, 81–84.

[326] Talu, O.; Myers, A. L. Molecular simulation of adsorption: Gibbs dividing surface and comparison with experiment. *AIChE J.* **2001**, *47*, 1160–1168.

[327] Pascual, P.; Ungerer, P.; Tavitian, B.; Pernot, P.; Boutin, A. Development of a transferable guest-host force field for adsorption of hydrocarbons in zeolites I. Reinvestigation of alkane adsorption in silicalite by grand canonical Monte Carlo simulation. *Phys. Chem. Chem. Phys.* **2003**, *5*, 3684–3693.

[328] Dubbeldam, D.; Calero, S.; Vlugt, T. J. H.; Krishna, R.; Maesen, T. L. M.; Beerdsen, E.; Smit, B. Force field parametrization through fitting on inflection points in isotherms. *Phys. Rev. Lett.* **2004**, *93*, 088302.

[329] Wu, H.; Simmons, J. M.; Srinivas, G.; Zhou, W.; Yildirim, T. Adsorption sites and binding nature of CO_2 in prototypical metal-organic frameworks: A combined neutron diffraction and first-principles study. *J. Phys. Chem. Lett.* **2010**, *1*, 1946–1951.

[330] Fischer, M.; Hoffmann, F.; Fröba, M. New microporous materials for acetylene storage and C_2H_2/CO_2 separation: Insights from molecular simulations. *ChemPhysChem* **2010**, *11*, 2220–2229.

[331] Chen, Y.; Jiang, J. A bio-metal-organic framework for highly selective CO_2 capture: A molecular simulation study. *ChemSusChem* **2010**, *3*, 982–988.

[332] Keskin, S. Atomistic simulations for adsorption, diffusion, and separation of gas mixtures in zeolite imidazolate frameworks. *J. Phys. Chem. C* **2011**, *115*, 800–807.

[333] Murthi, M.; Snurr, R. Q. Effects of molecular siting and adsorbent heterogeneity on the ideality of adsorption equilibria. *Langmuir* **2004**, *20*, 2489–2497.

[334] Xiang, S.; Zhou, W.; Zhang, Z.; Green, M. A.; Liu, Y.; Chen, B. Open metal sites within isostructural metal-organic frameworks for differential recognition of acetylene and extraordinarily high acetylene storage capacity at room temperature. *Angew. Chem., Int. Ed.* **2010**, *49*, 4615–4618.

A. Appendix

A.1. List of abbreviations

A.1.1. General abbreviations

AA	=	all-atom
ADF	=	Amsterdam Density Functional program
AIM	=	Atoms in Molecules
B3LYP	=	hybrid XC functional, based on BLYP
B88	=	exchange functional proposed by Becke
BLYP	=	GGA XC functional (B88 + LYP)
BSSE	=	basis set superposition error
CC	=	coupled cluster
CCCBDB	=	Computational Chemistry Comparison and Benchmark Database
CCSD	=	coupled cluster method with single and double excitations
CCSDT	=	CCSD with explicit treatment of triple excitations
CCSD(T)	=	CCSD with perturbative treatment of triple excitations
CI	=	configuration interaction
CID	=	coordination polymer with an interdigitated structure
COF	=	covalent-organic framework
CP	=	counterpoise
CPO	=	coordination polymer of Oslo
DCACP	=	dispersion-corrected atom-centered potential
DFT	=	density-functional theory
DFT-D	=	DFT with empirical dispersion correction
DNP	=	double numerical basis set with polarization functions
DOE	=	U.S. Department of Energy
DrFF	=	DREIDING force field
DU	=	parameter set for Silicalite proposed by Dubbeldam *et al.*
DZ	=	double-zeta basis set
EDA	=	energy decomposition analysis
ESP	=	electrostatic potential
FF	=	force field
FH	=	Feynman-Hibbs
GCMC	=	grand-canonical Monte Carlo
GGA	=	generalized gradient approximation

GTO	=	Gaussian-type orbital
HF	=	Hartree-Fock
HI	=	parameter set for Silicalite proposed by Hirotani *et al.*
HKUST	=	Hong Kong University of Science and Technology
IAST	=	ideal adsorbed solution theory
IR	=	infrared
IRMOF	=	isoreticular MOF
LB	=	Lorentz-Berthelot
LDA	=	local density approximation
LHV	=	lower heating value
LJ	=	Lennard-Jones
LYP	=	correlation functional proposed by Lee, Yang, and Parr
MC	=	Monte Carlo
MD	=	molecular dynamics
MIL	=	material (synthesized at) Institut Lavoisier
MM3	=	Molecular Mechanics 3 (force field)
M'MOF	=	mixed-metal MOF
MOF	=	metal-organic framework
MP2	=	second-order Møller-Plesset perturbation theory
NMR	=	nuclear magnetic resonance
NOTT	=	(MOF synthesized at) University of Nottingham
NU	=	(MOF synthesized at) Northwestern University
PA	=	parameter set for Silicalite proposed by Pascual *et al.*
PBE	=	GGA XC functional proposed by Perdew, Burke, and Ernzerhof
PBE0	=	hybrid XC functional, based on PBE
PCN	=	porous coordination network
PDW	=	paddle wheel
PIM	=	polymer with intrinsic microporosity
PIMC	=	path-integral Monte Carlo
PSA	=	pressure-swing adsorption
oa	=	orientation-averaged
OPLS	=	Optimized Potentials for Liquid Simulations (force field)
QZ4P	=	quadruple-zeta basis set with polarization functions
REPEAT	=	repeating electrostatic potential extracted atomic charges
RT	=	room temperature
SCF	=	self-consistent field
STO	=	Slater-type orbital
SZ	=	single-zeta basis set
TM	=	parameter set for Silicalite proposed by Talu and Myers
TraPPE	=	Transferable Potentials for Phase Equilibria (force field)
TSA	=	temperature-swing adsorption

TZ   =   triple-zeta basis set
TZP   =   triple-zeta basis set with polarization functions
TZ2P   =   triple-zeta basis set with polarization functions
UA   =   united-atom
UFF   =   Universal Force Field
UHM   =   University of Hamburg material
UMCM   =   University of Michigan crystalline material
UV   =   ultraviolet
vdW-DF   =   van der Waals density functional
XC   =   exchange-correlation
ZIF   =   zeolitic imidazolate framework
ZPVE   =   zero-point vibrational energy

A.1.2. Linker molecules and other chemical compounds

bdc	=	1,4-benzene-dicarboxylate
bhtc	=	3,4',5-biphenyl-tricarboxylate
bmc	=	benzene-monocarboxylate (benzoate)
bpdc	=	biphenyl-4,4'-dicarboxylate
bptc	=	3,3',5,5'-biphenyl-tetracarboxylate
btb	=	1,3,5-benzene-tribenzoate
btc	=	1,3,5-benzene-tricarboxylate
bte	=	4,4',4''-(benzene-1,3,5-triyltris(ethyne-2,1-diyl))tribenzoate
btt	=	1,3,5-tris(tetrazolate-5-yl)benzene
CB[6]	=	cucurbit[6]uril
dhbdc	=	2,5-dihydroxy-1,4-benzene-dicarboxylate
dhtp	=	2,5-dihydroxy-terephthalate
dmdpg	=	dimethyldiphenylgermane
dmdpm	=	dimethyldiphenylmethane (2,2-diphenylpropane)
dmdps	=	dimethyldiphenylsilane
dtp	=	2,3-ditetrazolate-5-ylpyrazine
fa	=	formate
mc	=	monocarboxylate
mdip	=	5,5'-methylene-diisophthalate
mim	=	2-methylimidazolate
mip	=	5-methylisophthalate
nip	=	5-nitroisophthalate
ptei	=	5,5'-((5'-(4-((3,5-dicarboxyphenyl)ethynyl)phenyl)-[1,1':3',1''-terphenyl]-4,4''-diyl)-bis(ethyne-2,1-diyl))diisophthalate
ted	=	triethylendiamine
tma	=	trimesate
ttei	=	5,5',5''-(((benzene-1,3,5-triyltris(ethyne-2,1-diyl))tris(benzene-4,1-diyl))tris-(ethyne-2,1-diyl))triisophthalate

A.2. Force-field parameters and partial charges

A.2.1. Fluid molecules: Force-field parameters

Table A.1. Lennard-Jones parameters used to represent the hydrogen molecule. In all cases, the parameters are assigned to the center of mass (site Q_{com} in figure 4.1). Buch potential parameters are from (*155*), Kumar potential parameters from (*220*).

	r_0 / Å	D_0 / kJ mol^{-1}
Buch potential	3.3225	0.2844
Buch potential, Pseudo-FH, T = 77 K	3.4394	0.2503
Kumar potential	3.1227	0.3218
Kumar potential, Pseudo-FH, T = 77 K	3.2439	0.2798

Table A.2. Lennard-Jones parameters and point charges used to represent the carbon dioxide molecule and the acetylene molecule. The LJ parameters for CO_2 are from (*243*), the LJ parameters for C_2H_2 from (*167*). ESP charges were obtained from DFT calculations.

	r_0 / Å	D_0 / kJ mol^{-1}	q / e
CO_2, Garcia-Sanchez et al.			
C site	3.0811	0.2444	0.5810
O site	3.3865	0.7121	-0.2905
C_2H_2, OPLS-UA model			
C site	4.2654	0.4812	-0.278
H site	-	-	0.278

Table A.3. Lennard-Jones parameters and point charges used to represent the oxygen molecule and the carbon monoxide molecule. Oxygen parameters are from (*234*). The carbon monoxide parameters are from (*238*) [Stoll *et al.*], (*240*) [Straub and Karplus], (*239*) [Piper *et al.*], and (*237*) [Gu *et al.*].

	r_0 / Å	D_0 / kJ mol^{-1}	q / e
Oxygen, TraPPE model			
O site	3.3898	0.4074	-0.1336
Q$_{com}$ site	-	-	0.2672
Carbon monoxide			
a) Model of Stoll et al.			
C site	3.7051	0.3068	-0.1347
O site	3.7051	0.3068	0.1347
b) Model of Straub & Karplus			
C site	4.2990	0.1096	-0.75
Q$_{com}$ site	-	-	1.60
O site	3.5021	0.6657	-0.85
c) Model of Piper et al.			
Q$_{ext1}$ site	-	-	-0.636
C site	3.7995	0.3316	0.831
Q$_{ext2}$ site	-	-	-0.195
O site	3.2383	0.5117	-
d) Model of Gu et al.			
C site	-	-	-0.75
Q$_{com}$ site	4.2238	0.8330	1.60
O site	-	-	-0.85

A.2.2. Adsorbents: Force-field parameters

Table A.4. Unmodified Lennard-Jones parameters from the Universal Force Field (UFF, (*157*)) employed for the porous adsorbents (except Silicalite) in sections 5.1, 5.2, and 5.4. In the UFF+C_{aryl} force field applied in sections 5.1 and 5.2, modified parameters were used for aromatic carbon atoms, which are also given. The modified parameters for the interaction of hydrogen, carbon dioxide, and acetylene with unsaturated copper sites (sections 5.2 and 5.4) are listed in separate tables.

Atom type	r_0 / Å	D_0 / kJ mol^{-1}	Description
H_	2.886	0.1841	hydrogen
C_R, C_2, C_3	3.851	0.4393	carbon (different hybridizations) - UFF
C_R	3.713	0.5753	aromatic carbon - UFF+C_{aryl}
N_R	3.660	0.2887	nitrogen
O_R, O_2	3.500	0.2510	oxygen (different hybridizations)
Cl	3.947	0.9498	chlorine
Mg3+2	3.021	0.4644	magnesium
Mn6+2	2.961	0.0544	manganese
Cu3+1	3.495	0.0209	copper
Zn3+2	2.763	0.5188	zinc
He4+4	2.362	0.2343	helium (probe particle for pore volume determination)

Table A.5. Lennard-Jones parameters from the DREIDING force field (DrFF, (*156*)) employed for some Zn-MOFs in section 5.1.

Atom type	r_0 / Å	D_0 / kJ mol^{-1}	Description
H_	3.195	0.0636	hydrogen
C_R, C_2, C_3	3.898	0.3979	carbon (different hybridizations)
N_R	3.662	0.3238	nitrogen
O_R, O_2	3.405	0.4004	oxygen (different hybridizations)
Zn	4.540	0.2301	zinc

Table A.6. Different potential models to represent the Cu-H_2 interaction employed in section 5.2. The UFF+Buch parameters correspond to the LJ parameters obtained from Lorentz-Berthelot mixing of the UFF parameters for copper, and the Buch potential for hydrogen. The full Morse potential parameters were directly obtained from DFT calculations. In the oa-Morse potential, D_0 is scaled by 2/3. In the enhanced Morse potential, D_0 is multiplied by 8/3, and α is increased.

Model	r_0 / Å	D_0 / kJ mol^{-1}	α
UFF + Buch	3.409	0.0771	-
full Morse	2.407	5.8228	8.163
oa-Morse	2.407	3.8819	8.163
enhanced Morse	2.407	15.528	12.43

Table A.7. Parameters used for simulations of gas adsorption in Silicalite in section 5.4. O_z = oxygen in zeolite, Si_z = silicon in zeolite. Silicon parameters are omitted in cases where Si is treated as non-interacting site. Lennard-Jones parameters are taken from (*325*) [Hirotani *et al.*], (*326*) [Talu and Myers], (*327*) [Pascual *et al.*], and (*328*) [Dubbeldam *et al.*; O_z parameters were calculated from the O_z-CH_4 interaction parameters given in the original work]. In all cases, ESP charges from DFT calculations for a cluster were assigned to the framework atoms, with $q(Si) = 1.206$ e, and $q(O) = -0.603$ e. It is worth noting that quite similar charges were obtained for sodalite using the (periodic) REPEAT method. (*216*)

	r_0 / Å	D_0 / kJ mol^{-1}
a) Hirotani et al.		
O_z	3.412	1.0669
Si_z	0.853	0.1548
b) Talu and Myers		
O_z	3.665	0.6004
c) Pascual et al.		
O_z	3.367	0.7778
d) Dubbeldam et al.		
O_z	3.614	0.6937

Table A.8. Modified Lennard-Jones parameters used to represent the interaction of acetylene and carbon dioxide with unsaturated copper sites. The parameter derivation is described in section 5.4.

Interaction	r_0 / Å	D_0 / kJ mol^{-1}
Cu-C(C_2H_2)	2.766	4.6831
Cu-O(CO_2)	2.937	1.4630

A.2.3. Calculation of ESP charges

A.2.3.1. Computational details

ESP charges were obtained from DFT calculations for two of the molecules considered (CO_2, C_2H_2), and for representative fragments of selected adsorbents. In each case, the geometry was optimized prior to the partial charge calculation.

The all-electron DFT calculations were carried out using the DMOL^3 code (*195, 289*) included in the *Accelrys* "Materials Studio" package. (*233*) A DNP basis set was employed in all calculations, and the PBE exchange-correlation functional was used. (*190*) The DMOL^3 code uses the ESP method as proposed by Singh and Kollman. (*214*) This method relies on a least-squares fit of the partial charges to the DFT electrostatic potential for a set of grid points located on shells around the nuclei. These shells are generated for a range of distances lying between the van der Waals radius and an upper limiting value. The quality of the calculation depends mainly on the distance between the grid points. In the DMOL^3 code, the default grid spacing corresponds to 0.5 Å. Default settings were used in all calculations.

A.2.3.2. ESP charges: Results
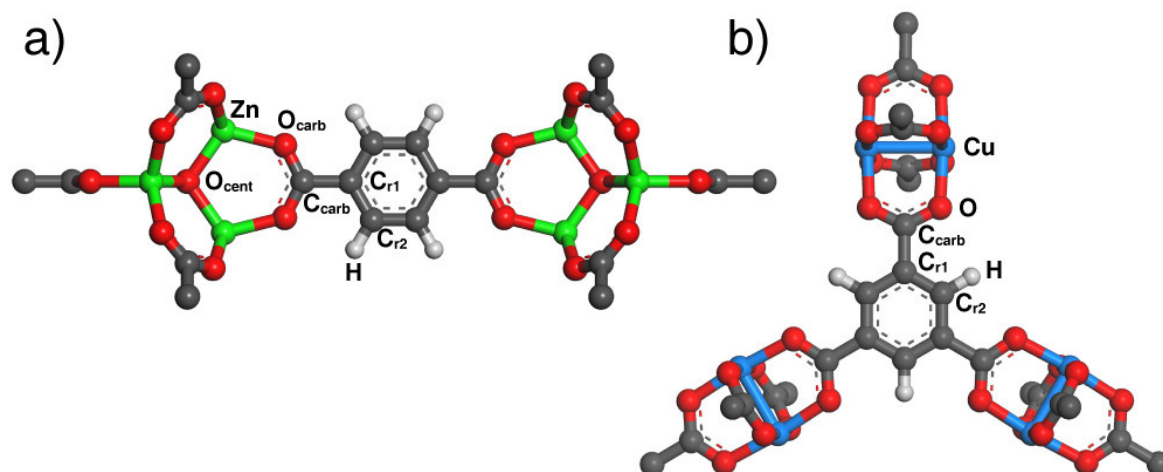
Figure A.1. *a)* $(Zn_4O)_2(bdc)(bmc)_{11}$ cluster used in the ESP charge calculation for IRMOF-1. *b)* $(Cu_2)_3(btc)(bmc)_9$ cluster used in the ESP charge calculation for $Cu_3(btc)_2$. In both cases, phenyl rings of the benzoate (bmc) moieties are omitted for clarity.

Table A.9. Resulting ESP charges for IRMOF-1 and $Cu_3(btc)_2$, atom labels assigned according to figure A.1. To ensure charge neutrality of the framework, some of the charges were slightly adjusted. For these atoms, the original charge from the DFT calculation is given in brackets, and the adjusted value is displayed without brackets.

a) IRMOF-1		*b) $Cu_3(btc)_2$*	
Atom label	*q / e*	*Atom label*	*q / e*
Zn	1.515	Cu	1.030 (1.015)
O_{cent}	-1.830 (-1.884)	O	-0.574
O_{carb}	-0.708	C_{carb}	0.573
C_{carb}	0.606	C_{r1}	0.215
C_{r1}	0.193	C_{r2}	-0.364
C_{r2}	-0.234	H	0.209
H	0.190		
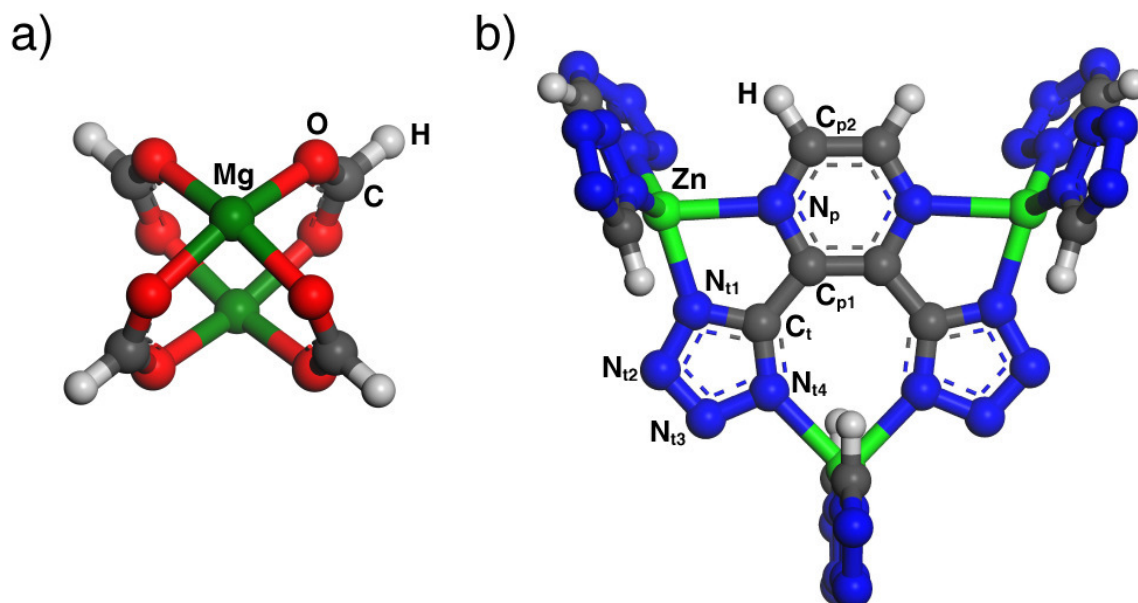
Figure A.2. *a)* Mg$_2$(fa)$_4$ paddle wheel used in the ESP charge calculation for Mg-formate. *b)* [Zn$_3$(dtp)(tetraz)$_6$]$^{2-}$ cluster used in the ESP charge calculation for Zn(dtp).

Table A.10. Resulting ESP charges for Mg-formate and Zn(dtp), atom labels assigned according to figure A.2. In the case of Zn(dtp), the charge assigned to the Zn atom is the weighted average of the ESP charges obtained for the two non-equivalent Zn atoms of the cluster. The charge of N$_{t4}$ was adjusted to ensure charge neutrality.

a) Mg-formate		*b) Zn(dtp)*	
Atom label	*q* / e	*Atom label*	*q* / e
Mg	1.636	Zn	0.6490
O	-0.766	N$_p$	-0.3840
C	0.671	C$_{p1}$	-0.0220
H	0.043	C$_{p2}$	0.2240
		H	0.0750
		C$_t$	0.6670
		N$_{t1}$	-0.1780
		N$_{t2}$	-0.2130
		N$_{t3}$	-0.0710
		N$_{t4}$	-0.4225 (-0.5150)
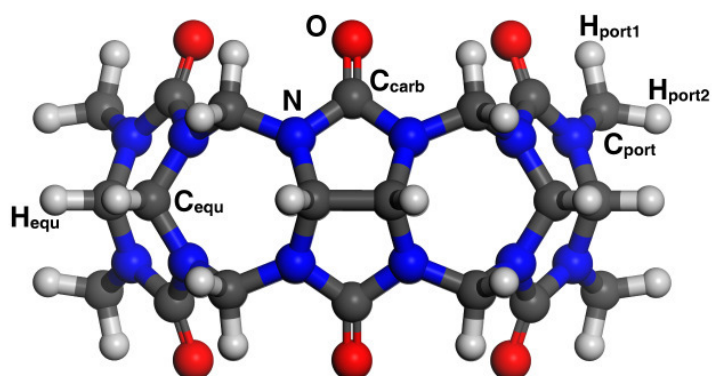
Figure A.3. Cucurbit[6]uril macrocycle used in the ESP charge calculation.

Table A.11. Resulting ESP charges for cucurbit[6]uril, atom labels assigned according to figure A.3.

Atom label	q / e
N	-0.0030
C_{carb}	0.4070
O	-0.4200
C_{port}	-0.2240
H_{port1}	0.1470
H_{port2}	0.1400
C_{equ}	-0.2035
H_{equ}	0.1595

A.3. Additional results

A.3.1. Section 5.1: Predicted and experimental hydrogen adsorption sites

Table A.12. Hydrogen adsorption sites in IRMOF-1 (space group $Fm\bar{3}m$): Positions derived from GCMC simulations are compared to experimental sites from (*300*).

	Sim			*Exp*			
	x	*y*	*z*	*x*	*y*	*z*	*Wyckoff*
Cup site	0.34	0.34	0.34	0.334	0.334	0.334	32f
ZnO₃ site	0.125	0.125	0.125	0.127	0.127	0.127	32f
ZnO₂ site	0.10	0.10	0.25	0.095	0.095	0.250	96k
Hex site	0.16	0.16	1/2	0.162	0.162	1/2	48i
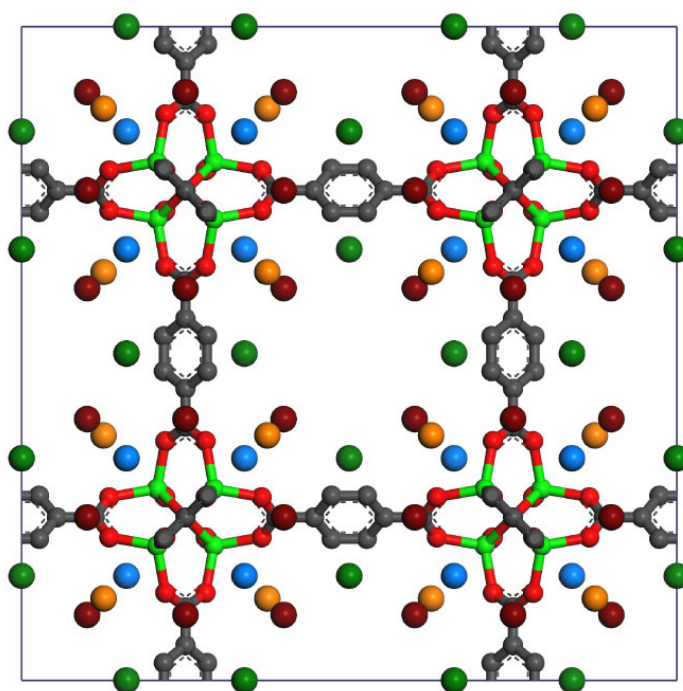
Figure A.4. IRMOF-1: Visualization of calculated hydrogen adsorption sites. Framework hydrogen atoms are omitted for clarity. Light blue = cup site, orange = ZnO_3 site, dark red = ZnO_2 site, dark green = hex site.

Table A.13. Hydrogen adsorption sites in MOF-74 (space group $R\bar{3}$): Positions derived from GCMC simulations are compared to experimental sites from (*255*).

	Sim			*Exp*			
	x	*y*	*z*	*x*	*y*	*z*	*Wyckoff*
Zn site	0.13	0.48	0.69	0.126	0.468	0.722	18f
Pocket site	0.16	0.46	0.32	0.165	0.465	0.297	18f
Hex site	0.48	0.24	0.28	0.493	0.252	0.129	18f
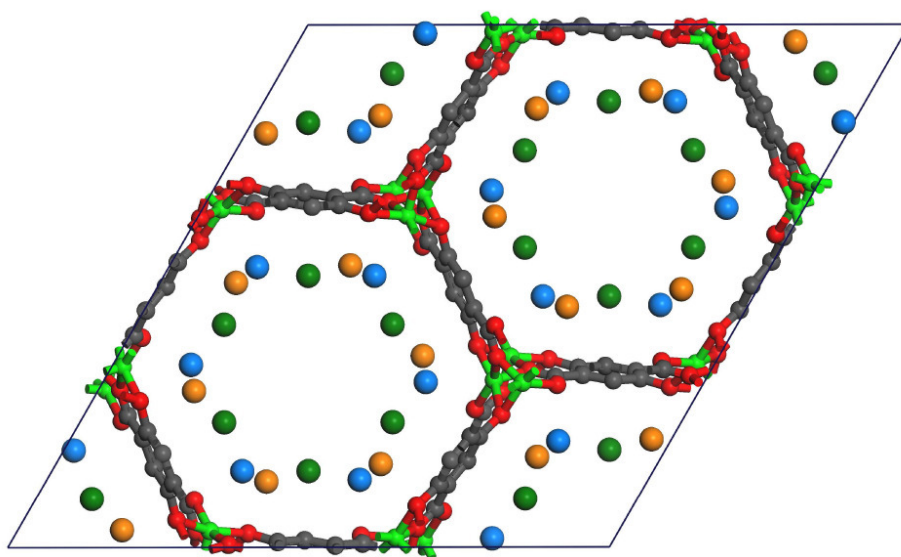
Figure A.5. MOF-74: Visualization of calculated hydrogen adsorption sites. Framework hydrogen atoms are omitted for clarity. Light blue = Zn site, orange = pocket site, dark green = hex site.

Table A.14. Hydrogen adsorption sites in ZIF-8 (space group $I\bar{4}3m$): Positions derived from GCMC simulations are compared to experimental sites from (*302*).

	Sim			Exp			
	x	*y*	*z*	*x*	*y*	*z*	*Wyckoff*
Pentagon site	0.21	0.21	0.00	0.230	0.230	0.009	24g
Window site I	0.20	0.20	0.20	0.201	0.201	0.201	8c
Window site II	0.30	0.30	0.30	0.309	0.309	0.309	8c
Methyl site	0.23	0	0	0.254	0	0	12e
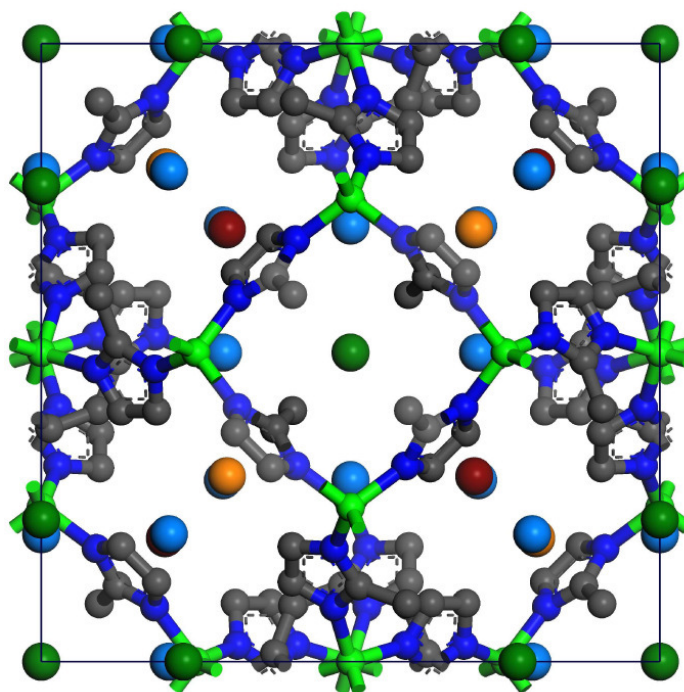
Figure A.6. ZIF-8: Visualization of calculated hydrogen adsorption sites. Framework hydrogen atoms are omitted for clarity. Light blue = pentagon site, orange = window site I, dark red = window site II, dark green = methyl site.

263

Table A.15. Hydrogen adsorption sites in $Cu_3(btc)_2$ (space group $Fm\bar{3}m$): Positions derived from GCMC simulations are compared to experimental sites from (57).

	Sim			
	x	*y*	*z*	*Wyckoff*
Pdw site	0.09	0.35	0	96j
Window site	0.18	0.18	0.18	32f
Central site	1/4	1/4	1/4	8c
Hex site	0.42	0.42	0.42	32f
	Exp			
	x	*y*	*z*	*Wyckoff*
Cu site	0.1515	0.1515	0	48h
Pdw site I	0.076	0.282	0	96j
Pdw site II	0.129	0.371	0	48i
Window site I	0.156	0.156	0.156	32f
Window site II	0.206	0.206	0.206	32f
Central site	0.188	1/4	1/4	48g
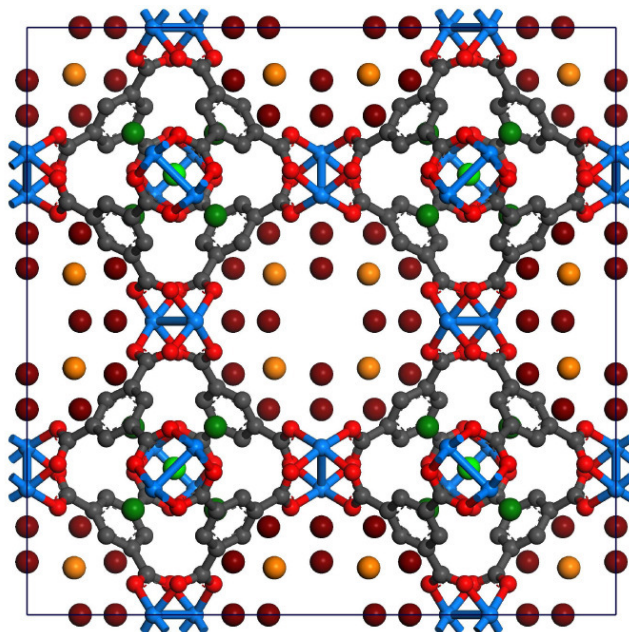
Figure A.7. $Cu_3(btc)_2$: Visualization of calculated hydrogen adsorption sites. Framework hydrogen atoms are omitted for clarity. Dark red = Pdw site, dark green = window site, light green = central site, orange = hex site.

Table A.16. Hydrogen adsorption sites in MOF-505 (space group $R\bar{3}m$). Only positions derived from GCMC simulations are given.

	x	y	z	Wyckoff
Triangle site	0	0	0.21	6c
Window site	0.75	0.25	0.02	18h
Central site	0.43	0.57	0.09	18h
Pdw site	0.40	0.43	0.23	36i
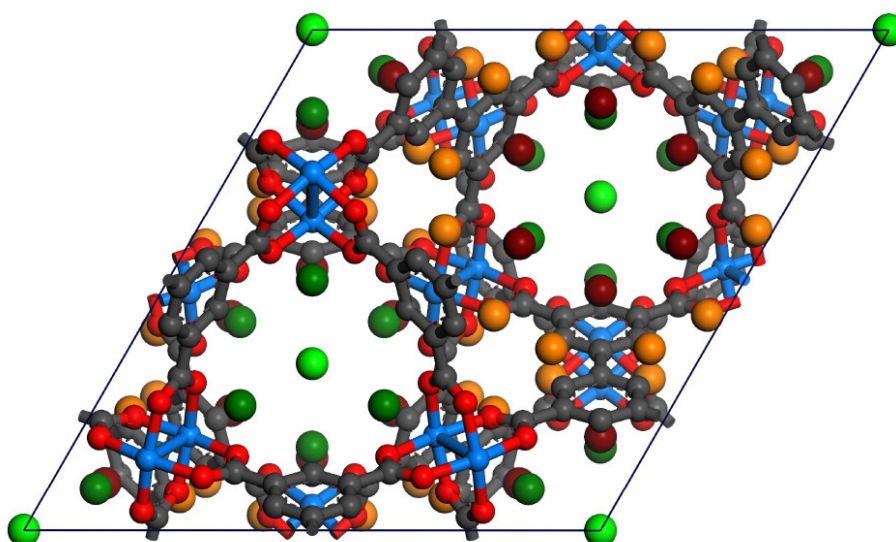
Figure A.8. MOF-505: Visualization of calculated hydrogen adsorption sites. Framework hydrogen atoms are omitted for clarity. Light green = triangle site, dark green = window site, dark red = central site, orange = Pdw site.

Table A.17. Hydrogen adsorption sites in $(Mn_4Cl)_3(btt)_8$ (space group $Pm\bar{3}m$): Positions derived from GCMC simulations are compared to experimental sites from (*59*).

	Sim			
	x	*y*	*z*	*Wyckoff*
Vertex site	0.19	1/2	1/2	6f
Pentagon site	0.28	0.28	0	12i
Window site I	0.32	0.32	1/2	12j
Window site II	0.16	0.16	1/2	12j
	Exp			
	x	*y*	*z*	*Wyckoff*
Mn site	0.236	1/2	0	12h
Vertex site I	0.182	1/2	1/2	6f
Vertex site II	0.293	1/2	1/2	6f
Pentagon site	0.285	0.285	0	12i
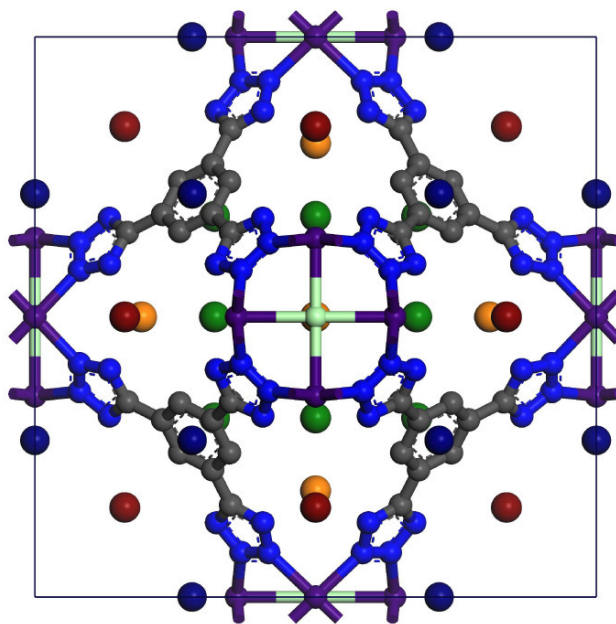
Figure A.9. $(Mn_4Cl)_3(btt)_8$: Visualization of calculated hydrogen adsorption sites. Framework hydrogen atoms are omitted for clarity. Orange = vertex site, dark blue = pentagon site, dark green = window site I, dark red = window site II.

Table A.18. Hydrogen adsorption sites in UMCM-150 (space group $P6_3/mmc$). Only positions derived from GCMC simulations are given.

	x	y	z	Wyckoff
Triangle site	1/3	2/3	0.52	4f
Window site	0.40	0.80	0.59	12k
Pdw site	0.06	0.29	0.03	24l
Cu_3 site	0.34	0.28	1/4	12j
Tri-hex site	0	0	0.15	4e
Di-hex site	0.11	0.22	0.11	12k
Linker site	0.08	0.16	0.94	12k
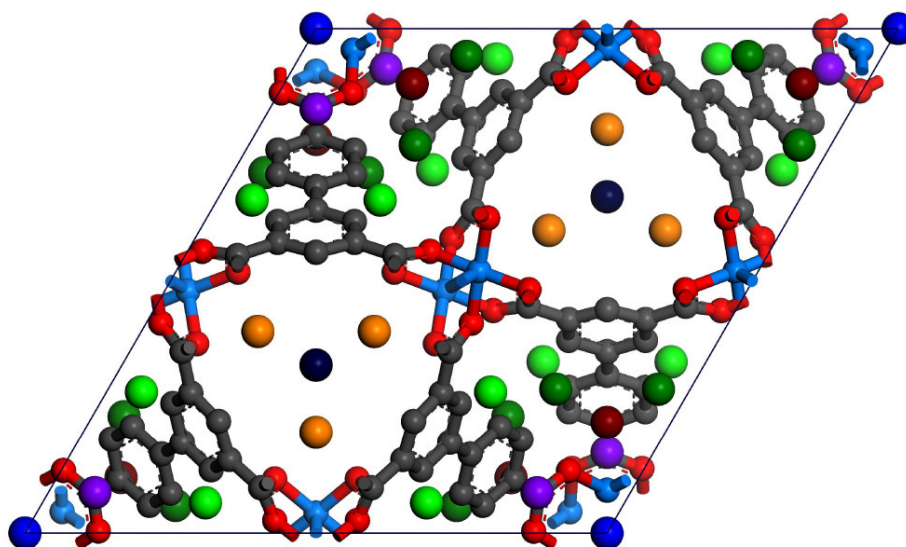
Figure A.10. UMCM-150: Visualization of calculated hydrogen adsorption sites. Framework hydrogen atoms are omitted for clarity. Dark blue = triangle site, orange = window site, dark green = Pdw site, light green = Cu_3 site, blue = tri-hex site, dark red = di-hex site, purple = linker site.

Table A.19. Hydrogen adsorption sites in PCN-12 (space group $P4/mmm$). Only positions derived from GCMC simulations are given. The sixth column gives the colour code employed in figure A.11. The locations within the structure are briefly described in the last column, employing the following abbreviations: SCF = small pore centered around the face center of the unit cell (figure 4.15d); SCO = small pore centered around the origin; TFC = triangular face of central cuboctahedral pore; TFE = triangular face of cuboctahedral pore centered around the cell edge; SqFC = square face of central cuboctahedral pore; SqFC = square face of cuboctahedral pore centered around the cell edge. PDW indicates sites located perpendicular to the Cu-Cu axis of a Cu_2 paddle wheel.

Site	x	y	z	Wyckoff	Colour	Description
1	0.388	1/2	0	4n	orange	SCF, above phenyl ring
2	0.445	0.445	0.100	8r	dark red	SCF, near PDW
3	0.385	0.385	0	4j	light brown	SCF, window
4	0.078	0.078	0	4j	violet	SCO, above phenyl ring
5	0.079	0	0.105	8s	blue	SCO, near PDW
6	0.160	0	0	4l	yellow	SCO, window
7	0.290	1/2	0.290	8t	dark green	TFC, window
8	0.180	1/2	0.290	8t	green	TFC, near PDW (I)
9	0.228	0.440	0.179	16u	light green	TFC, near PDW (II)
10	0.145	0.145	0.290	8r	dark blue	TFE, window
11	0.150	0.230	0.177	16u	cyan	TFE, near PDW
12	0.190	0.340	1/2	8q	purple	SqFC, near PDW
13	0.080	0.265	1/2	8q	pink	SqFE, near PDW
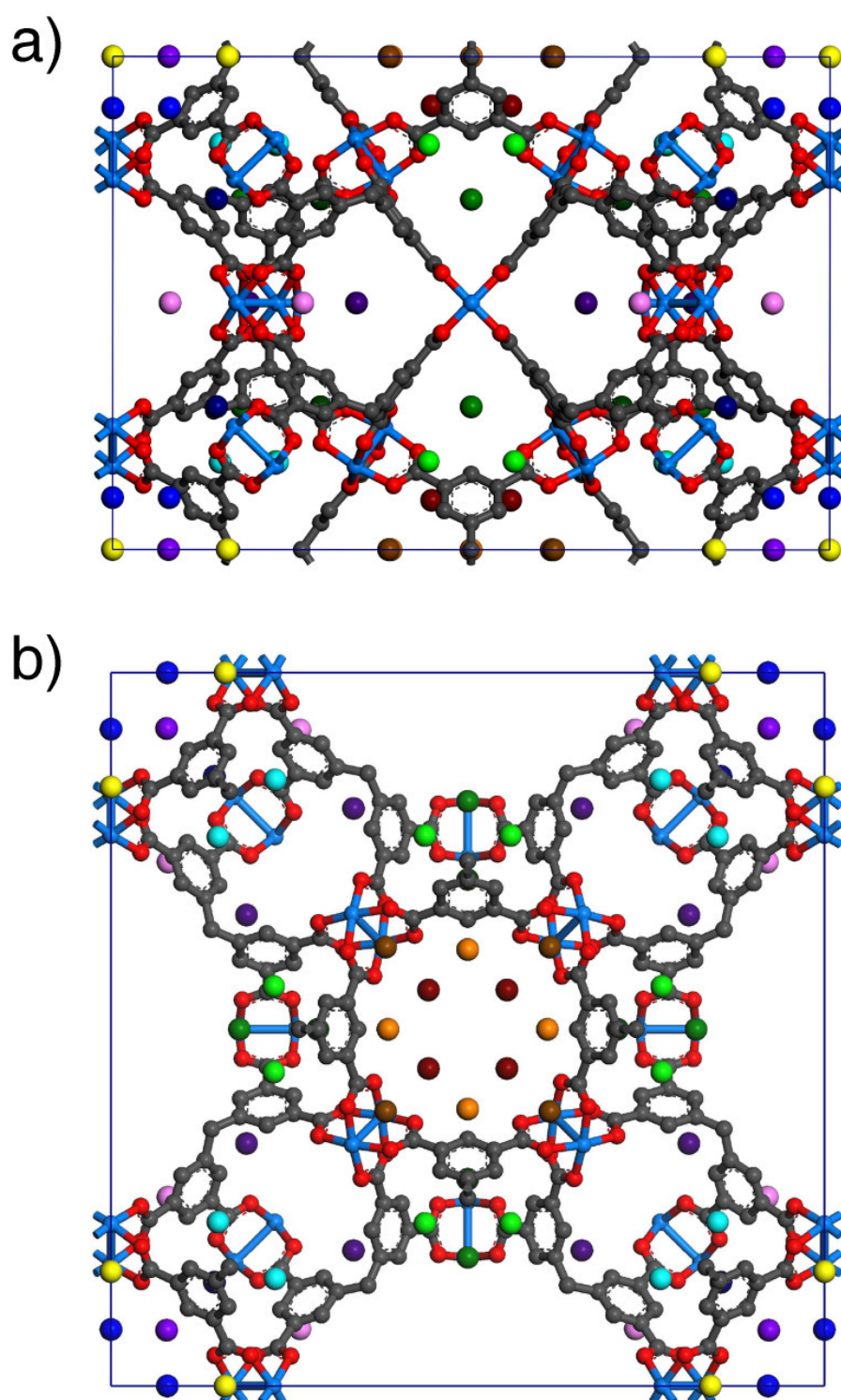
Figure A.11. PCN-12: Visualization of calculated hydrogen adsorption sites. Framework hydrogen atoms are omitted for clarity. The colour code of each site is given in table A.19. *a)* View along the *a*-axis. *b)* View along the *c*-axis.

A.3.2. Section 5.2: Adsorption isotherms

The following figures show additional hydrogen adsorption isotherms calculated for $T = 87\,\text{K}$ and $T = 100\,\text{K}$ for the systems discussed in section 5.2. Together with the simulation results obtained for $T = 77\,\text{K}$, these isotherms were used to calculate the isosteric heats of hydrogen adsorption for the three MOFs.

All figures use the same colour scheme: Blue = UFF+C_{aryl} potential; dark red = full Morse potential; orange = oa-Morse potential.
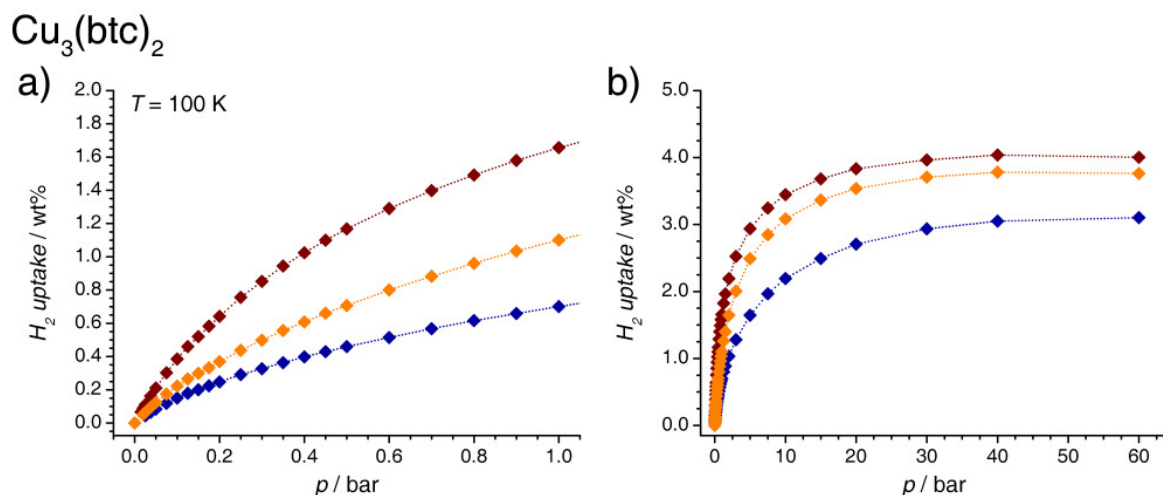
Figure A.12. Calculated hydrogen adsorption isotherms for $Cu_3(btc)_2$ obtained with three different Cu-H_2 potential models ($T = 100\,\text{K}$).
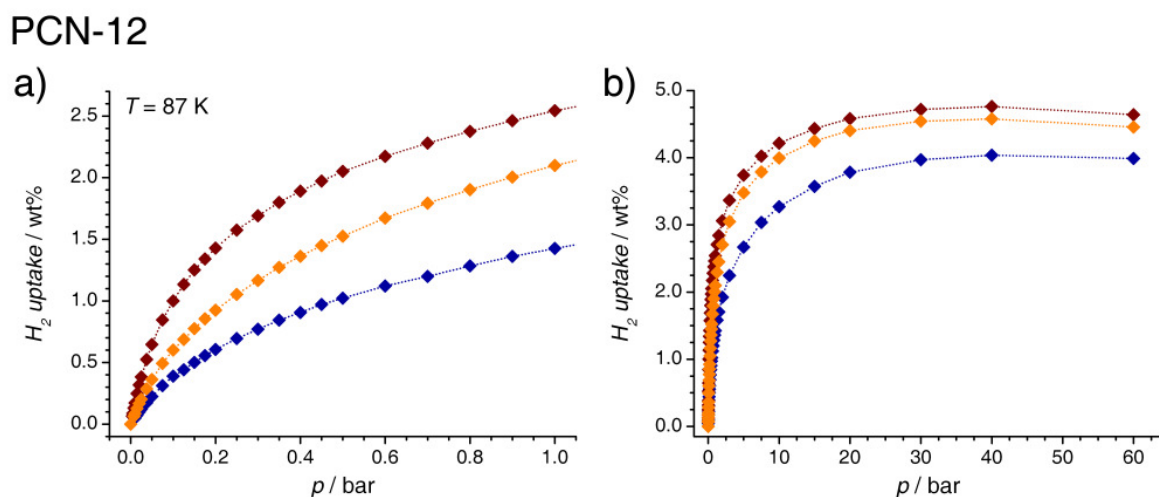
Figure A.13. Calculated hydrogen adsorption isotherms for PCN-12 obtained with three different Cu-H_2 potential models ($T = 87\,\text{K}$).
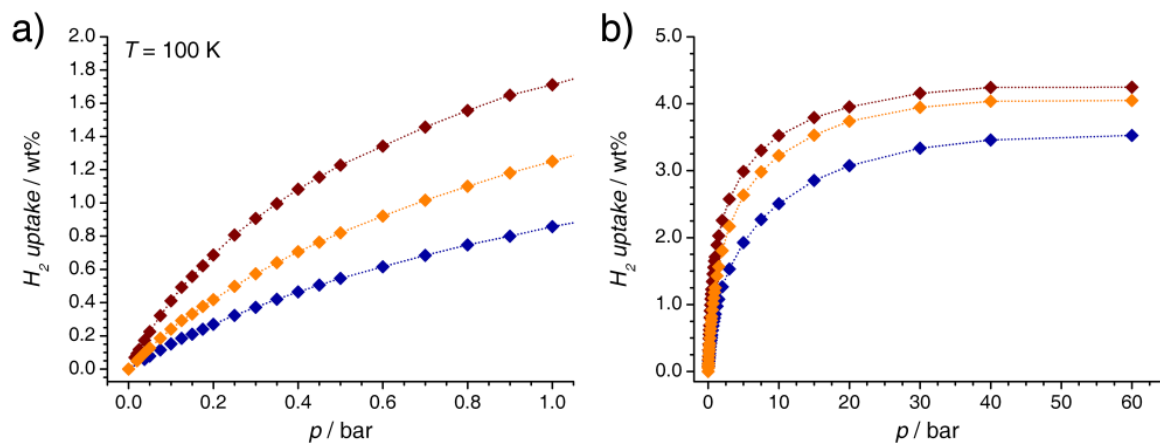
Figure A.14. Calculated hydrogen adsorption isotherms for PCN-12 obtained with three different Cu-H$_2$ potential models ($T = 100$ K).
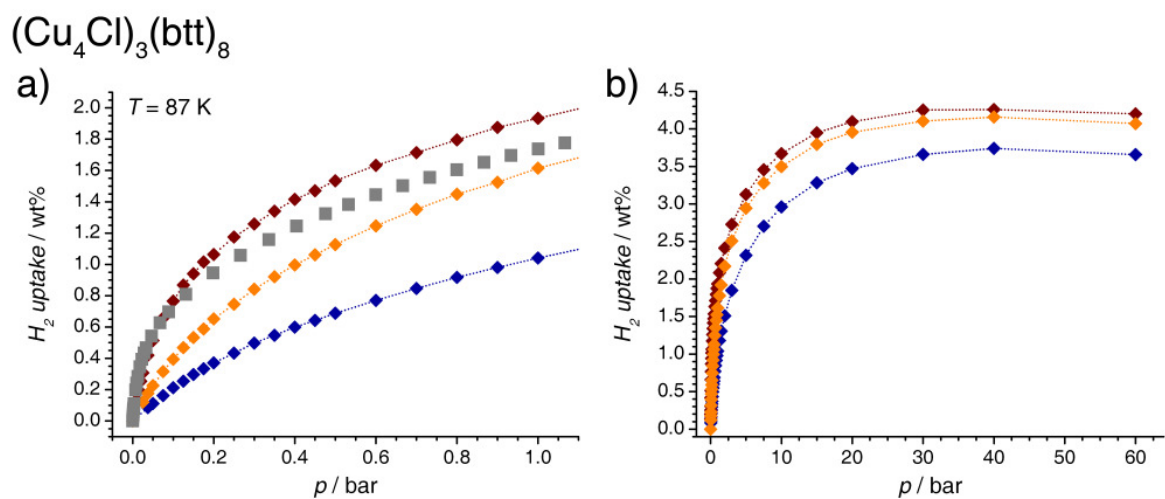
$(Cu_4Cl)_3(btt)_8$

Figure A.15. Calculated hydrogen adsorption isotherms for $(Cu_4Cl)_3(btt)_8$ obtained with three different Cu-H$_2$ potential models ($T = 87$ K).
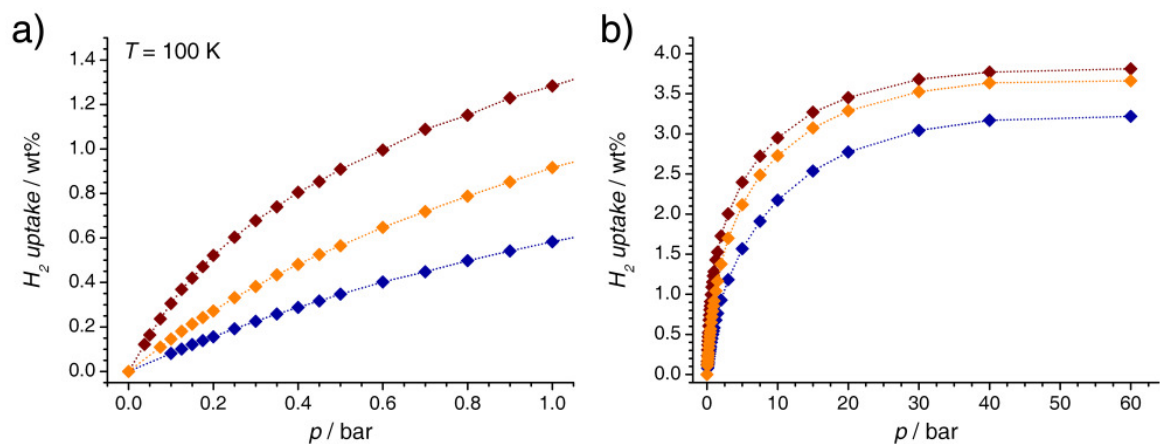
Figure A.16. Calculated hydrogen adsorption isotherms for $(Cu_4Cl)_3(btt)_8$ obtained with three different Cu-H$_2$ potential models ($T = 100$ K).

A.3.3. Subsection 5.3.3: DFT energies, geometric properties, partial charges

The following tables report the interaction energies, changes of interatomic distances, and partial charges obtained in the DFT calculations reported in subsection 5.3.3. The geometric properties are defined as follows:

- $d(Cu\text{-}H_2)$ = equilibrium distance between the copper center and the center of mass of the coordinated H_2 molecule

- $\Delta d(H\text{-}H)$ = elongation of the H-H bond length with respect to the free H_2 molecule; the equilibrium DFT-PBE value amounts to 0.7518 Å

- $\Delta d(Cu\text{-}Cu)$ = elongation of the Cu-Cu distance upon coordination of the H_2 molecule

- $d(Cu\text{-}Cu)_L - d(Cu\text{-}Cu)_{bmc}$ = difference between the Cu-Cu distance in the (isolated) $Cu_2(L)_4$ system and the Cu-Cu distance in the $Cu_2(bmc)_4$ reference system; the equilibrium DFT-PBE value of the Cu-Cu distance in $Cu_2(bmc)_4$ amounts to 2.4604 Å

Table A.20. Summary of DFT results for hydrogen interacting with $Cu_2(L)_4$ paddle wheel systems, the ligand L being a monocarboxylate with a polycyclic aromatic hydrocarbon. For compactness, the properties are abbreviated as follows: $d_{CuH2} = d(Cu\text{-}H_2)$; $\Delta_H = \Delta d(H\text{-}H)$; $\Delta_{Cu} = \Delta d(Cu\text{-}Cu)$; $\Delta_{PDW} = d(Cu\text{-}Cu)_L - d(Cu\text{-}Cu)_{bmc}$; q_{Cu} = Hirshfeld charge at the Cu atom; E_{int} = interaction energy.

Ligand L	d_{CuH2} / Å	Δ_H / Å	Δ_{Cu} / Å	Δ_{PDW} / Å	q_{Cu} / e	E_{int} / kJ mol^{-1}
Benzene-mc	2.396	0.00290	0.0225	-	0.4644	-5.89
Biphenyl-mc	2.400	0.00286	0.0221	0.00000	0.4625	-5.68
Terphenyl-mc	2.401	0.00286	0.0222	0.00004	0.4625	-5.69
Quaterphenyl-mc	2.402	0.00284	0.0210	0.00006	0.4625	-5.71
Naphthalene-mc	2.397	0.00288	0.0216	-0.00003	0.4630	-5.29
Anthracene-mc	2.407	0.00281	0.0217	0.00059	0.4629	-4.96
Phenantrene-mc	2.395	0.00290	0.0210	0.00145	0.4631	-5.42
Pyrene-mc	2.397	0.00289	0.0235	-0.00144	0.4628	-4.15

Table A.21. Summary of DFT results for hydrogen interacting with $Cu_2(L)_4$ paddle wheel systems, the ligand L being a heteroaromatic carboxylate. The same abbreviations as in table A.20 are employed.

Ligand L	d_{CuH2} / Å	Δ_H / Å	Δ_{Cu} / Å	Δ_{PDW} / Å	q_{Cu} / e	E_{int} / kJ mol^{-1}
Benzene-mc	2.396	0.00290	0.0225	-	0.4644	-5.89
2-pyridine-mc	2.354	0.00335	0.0259	0.0127	0.4675	-7.10
3-pyridine-mc	2.365	0.00320	0.0256	0.0106	0.4647	-6.55
4-pyridine-mc	2.352	0.00330	0.0267	0.0117	0.4687	-6.95
2-pyrazine-mc	2.316	0.00376	0.0305	0.0240	0.4695	-7.35
1,3,5-triazine-mc	2.271	0.00444	0.0373	0.0345	0.4803	-8.83
1,2,4,5-tetrazine-mc	2.236	0.00500	0.0440	0.0440	0.4876	-10.27
2-furan-mc	2.358	0.00324	0.0259	0.0164	0.4704	-6.54
3-furan-mc	2.391	0.00293	0.0250	0.0052	0.4633	-5.94
2-thiophene-mc	2.369	0.00308	0.0269	0.0098	0.4683	-6.36
3-thiophene-mc	2.397	0.00285	0.0224	0.0030	0.4628	-5.81
2-pyrrole-mc	2.424	0.00258	0.0198	-0.0069	0.4646	-5.39
3-pyrrole-mc	2.444	0.00248	0.0179	-0.0046	0.4563	-4.94
4-imidazole-mc	2.394	0.00278	0.0236	0.0061	0.4642	-5.85
1,2,4-triazole-mc	2.314	0.00377	0.0329	0.0220	0.4767	-7.49
tetrazole-mc	2.258	0.00458	0.0418	0.0432	0.4853	-9.77

Table A.22. Summary of DFT results for hydrogen interacting with $Cu_2(L)_4$ paddle wheel systems, with L being a *para*-substituted bmc ligand. The same abbreviations as in table A.20 are employed. **1** = trifluoromethyl-bmc; **2** = dimethylamino-bmc.

Substituent	d_{CuH2} / Å	Δ_H / Å	Δ_{Cu} / Å	Δ_{PDW} / Å	q_{Cu} / e	E_{int} / kJ mol^{-1}
-H (bmc)	2.396	0.00290	0.0225	-	0.4644	-5.89
-F (fluoro-bmc)	2.389	0.00283	0.0239	0.0005	0.4656	-6.03
-Cl (chloro-bmc)	2.384	0.00289	0.0254	0.0009	0.4661	-6.14
-Br (bromo-bmc)	2.382	0.00292	0.0242	0.0029	0.4666	-6.19
-I (iodo-bmc)	2.383	0.00293	0.0249	0.0023	0.4653	-6.25
-CH$_3$ (methyl-bmc)	2.406	0.00269	0.0211	-0.0017	0.4628	-5.67
-CF$_3$ (**1**)	2.360	0.00315	0.0269	0.0066	0.4694	-6.66
-C$_2$H$_5$ (ethyl-bmc)	2.405	0.00271	0.0203	-0.0018	0.4613	-5.89
-C$_2$H$_3$ (vinyl-bmc)	2.395	0.00280	0.0220	0.0003	0.4630	-5.86
-C$_2$H (ethynyl-bmc)	2.385	0.00289	0.0231	0.0031	0.4660	-6.11
-OCH$_3$ (methoxy-bmc)	2.393	0.00286	0.0230	-0.0009	0.4626	-5.83
-OC$_2$H$_5$ (ethoxy-bmc)	2.395	0.00284	0.0226	-0.0011	0.4623	-5.79
-OH (hydroxy-bdc)	2.416	0.00260	0.0194	-0.0023	0.4620	-5.50
-COH (aldehyde-bmc)	2.362	0.00315	0.0257	0.0076	0.4693	-6.68
-COOH (1,4-bdc)	2.365	0.00308	0.0263	0.0058	0.4686	-6.54
-NH$_2$ (amino-bmc)	2.431	0.00258	0.0202	-0.0074	0.4577	-5.12
-N(CH$_3$)$_2$ (**2**)	2.439	0.00250	0.0184	-0.0089	0.4562	-4.93
-CONH$_2$ (amido-bmc)	2.380	0.00297	0.0238	0.0055	0.4660	-6.35
-NO$_2$ (nitro-bmc)	2.347	0.00329	0.0296	0.0100	0.4719	-7.11
-CN (cyano-bmc)	2.353	0.00321	0.0275	0.0089	0.4708	-6.89
-SH (mercapto-bmc)	2.406	0.00270	0.0217	-0.0010	0.4635	-5.73

Table A.23. Summary of DFT results for hydrogen interacting with $Cu_2(L)_4$ paddle wheel systems, with L being a *meta*-substituted bmc ligand. The same abbreviations as in table A.20 are employed.

Substituent	d_{CuH2} /Å	Δ_H /Å	Δ_{Cu} /Å	Δ_{PDW} /Å	q_{Cu} /e	E_{int} / kJ mol^{-1}
-H (bmc)	2.396	0.00290	0.0225	-	0.4644	-5.89
-F (m-fluoro-bmc)	2.374	0.00302	0.0256	0.0045	0.4669	-6.86
-CH$_3$ (m-methyl-bmc)	2.449	0.00255	0.0211	-0.0008	0.4621	-5.67
-COOH (1,3-bdc)	2.355	0.00330	0.0270	0.0086	0.4691	-6.99
-NH$_2$ (m-amino-bmc)	2.410	0.00264	0.0207	-0.0044	0.4620	-5.50
-NO$_2$ (m-nitro-bmc)	2.334	0.00343	0.0296	0.0141	0.4726	-7.58

Table A.24. Summary of DFT results for hydrogen interacting with $Cu_2(L)_4$ paddle wheel systems, with L being a 3,5-disubstituted bmc ligand. The same abbreviations as in table A.20 are employed.

Substituent	d_{CuH2} /Å	Δ_H /Å	Δ_{Cu} /Å	Δ_{PDW} /Å	q_{Cu} /e	E_{int} / kJ mol^{-1}
-H (bmc)	2.396	0.00290	0.0225	-	0.4644	-5.89
-F (3,5-difluoro-bmc)	2.350	0.00327	0.0285	0.0090	0.4720	-6.95
-CH$_3$ (3,5-dimethyl-bmc)	2.411	0.00263	0.0200	-0.0026	0.4621	-5.57
-COOH (1,3,5-btc)	2.333	0.00350	0.0303	0.0137	0.4737	-7.47
-NH$_2$ (3,5-diamino-bmc)	2.421	0.00261	0.0195	-0.0085	0.4601	-5.20
-NO$_2$ (3,5-dinitro-bmc)	2.287	0.00404	0.0385	0.0248	0.4817	-8.94

A.3.4. Subsection 5.3.4: DFT-D energy minima

The equilibrium distances and interaction energies reported in the following tables were obtained from a fit of a Morse potential (equation 3.8) to the corresponding DFT-D potential energy curve.

Table A.25. Equilibrium distances d_{equi} and interaction energies E_{int} obtained for H_2 interacting with benzene and naphthalene, abbreviations defined as in figure 5.29. DFT-D values calculated in this work are compared to CCSD(T) values from the literature. (*38, 318*)

	d_{equi} /Å		E_{int} / kJ mol^{-1}	
	CCSD(T)	DFT-D	CCSD(T)	DFT-D
B1, $H_2 \parallel x$	3.03	2.87	-3.06	-2.70
B1, $H_2 \parallel z$	3.11	2.97	-4.34	-4.52
N1, $H_2 \parallel x$	3.07	2.86	-3.60	-3.29
N1, $H_2 \parallel z$	3.15	2.96	-4.42	-4.67
N2, $H_2 \parallel x$	3.19	3.06	-3.28	-2.69
N2, $H_2 \parallel z$	3.26	3.10	-3.91	-4.07

Table A.26. Equilibrium distances d_{equi} and interaction energies E_{int} obtained for H_2 interacting with different heteroaromatic systems. All distances are given in Å, all energies are given in kJ mol^{-1}. The last column corresponds to the orientation-averaged interaction energy.

	$H_2 \parallel x$		$H_2 \parallel y$		$H_2 \parallel z$		*Average*
	d_{equi}	E_{int}	d_{equi}	E_{int}	d_{equi}	E_{int}	E_{ave}
Benzene	2.87	-2.70	2.87	-2.65	2.97	-4.52	-3.29
Pyridine	2.85	-2.66	2.88	-2.79	2.98	-3.71	-3.05
Pyrazine	2.79	-3.06	2.83	-3.44	2.97	-3.18	-3.23
Triazine	2.84	-3.20	2.84	-3.21	3.00	-2.24	-2.88
Tetrazine	2.79	-4.17	2.81	-3.15	3.00	-1.78	-3.03

Table A.27. Equilibrium distances d_{equi} and interaction energies E_{int} obtained for H_2 interacting with model systems of non-linear linkers, the H_2 molecule approaching from the side of the methyl groups. All distances are given in Å, all energies are given in kJ mol^{-1}.

	$H_2 \parallel x$		$H_2 \parallel y$		$H_2 \parallel z$	
	d_{equi}	E_{int}	d_{equi}	E_{int}	d_{equi}	E_{int}
Dmdpm (X = C)	4.24	-0.975	4.34	-0.735	4.11	-1.77
Dmdps (X = Si)	4.05	-1.51	4.21	-0.935	4.03	-1.97
Dmdpg (X = Ge)	3.98	-1.79	4.12	-1.13	3.97	-2.21

Table A.28. Equilibrium distances d_{equi} and interaction energies E_{int} obtained for H_2 interacting with model systems of non-linear linkers, the H_2 molecule approaching from the side of the phenyl groups. All distances are given in Å, all energies are given in kJ mol^{-1}.

	$H_2 \parallel x$		$H_2 \parallel y$		$H_2 \parallel z$	
	d_{equi}	E_{int}	d_{equi}	E_{int}	d_{equi}	E_{int}
Dmdpm (X = C)	3.86	-3.97	3.83	-5.72	3.91	-5.56
Dmdps (X = Si)	4.03	-2.51	3.92	-4.32	4.01	-4.20
Dmdpg (X = Ge)	4.05	-2.46	3.92	-4.41	4.03	-4.16
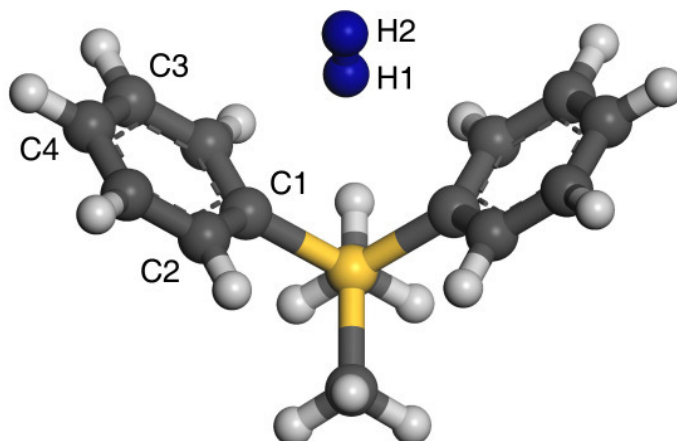
Figure A.17. Model system of DFT-D calculations: Dimethyldiphenylsilane with H_2 molecule approaching from the side of the phenyl rings, $H_2 \parallel z$. The atom labels used in table A.29 are included.

Table A.29. Distances between the hydrogen atoms of a H_2 molecule and the carbon atoms of the phenyl rings of non-linear molecules for a constant distance between the central atom X and the center of mass of the hydrogen molecule of 4.0 Å. The atom labels as given in figure A.17 are used. The weighted and averaged H-C distance, $d(H-C)_{mean}$, as well as the standard deviation, $\sigma(d(H-C))$, which represents the scatter around the mean value, are also included.

	Dmdpm (X = C)	Dmdps (X = Si)	Dmdpg (X = Ge)
$d(H1-C1)$ / Å	2.996	2.993	2.981
$d(H1-C2)$ / Å	3.167	3.267	3.272
$d(H1-C3)$ / Å	3.515	3.768	3.794
$d(H1-C4)$ / Å	3.688	3.998	4.033
$d(H2-C1)$ / Å	3.686	3.649	3.628
$d(H2-C2)$ / Å	3.739	3.795	3.788
$d(H2-C3)$ / Å	3.880	4.090	4.101
$d(H2-C4)$ / Å	3.958	4.232	4.252
$d(H-C)_{mean}$ / Å	3.578	3.726	3.734
$\sigma(d(H-C))$ / Å	0.314	0.378	0.387

A.3.5. Section 5.4: Calculated CO/H$_2$ and O$_2$/H$_2$ mixture isotherms
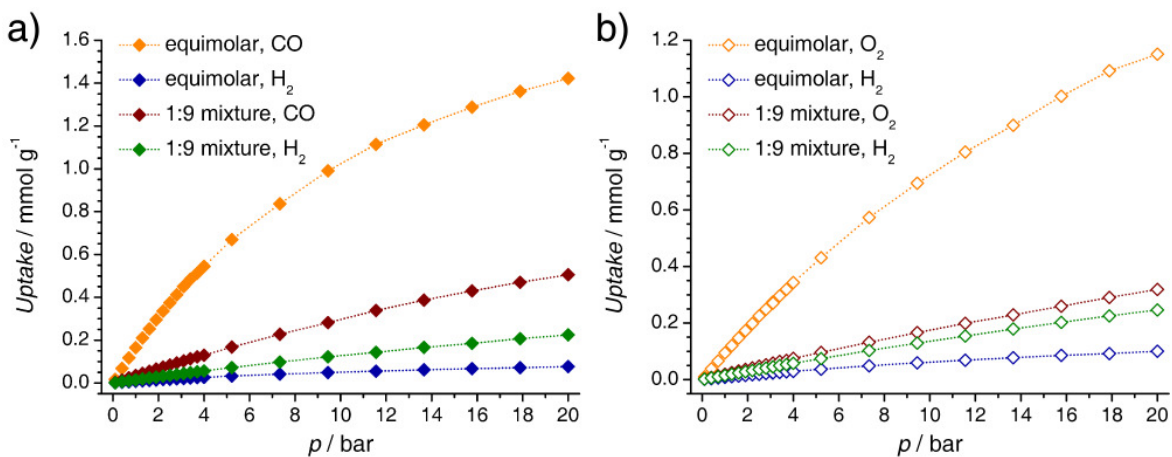
Figure A.18. Mixture isotherms obtained for Silicalite: *a)* CO/H$_2$ mixture. *b)* O$_2$/H$_2$ mixture.
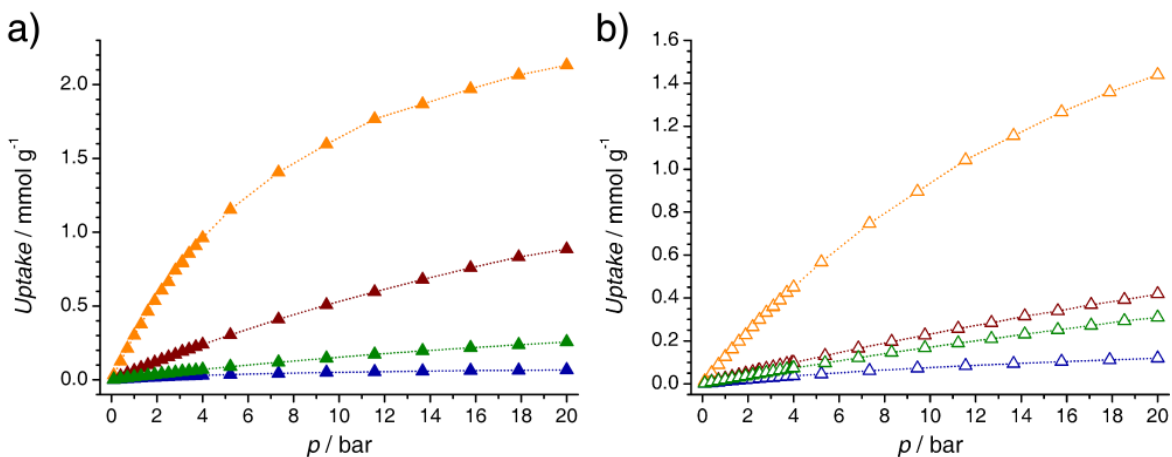
Figure A.19. Mixture isotherms obtained for Mg-formate: *a)* CO/H$_2$ mixture. *b)* O$_2$/H$_2$ mixture. The same colour scheme as in figure A.18 is used.
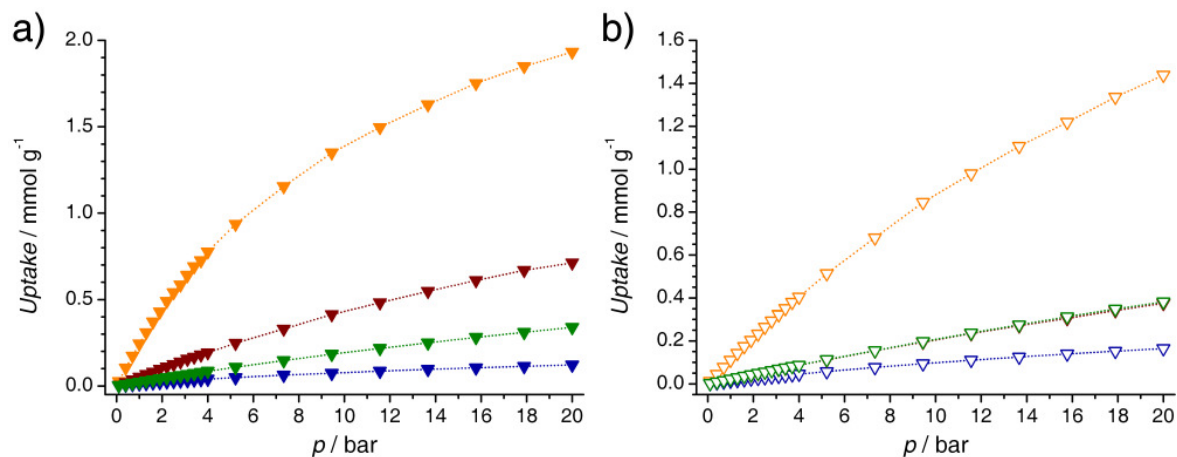
Figure A.20. Mixture isotherms obtained for Zn(dtp): *a)* CO/H_2 mixture. *b)* O_2/H_2 mixture. The same colour scheme as in figure A.18 is used. For the 1:9 mixture of oxygen and hydrogen, the molar uptakes of the two components are practically identical.
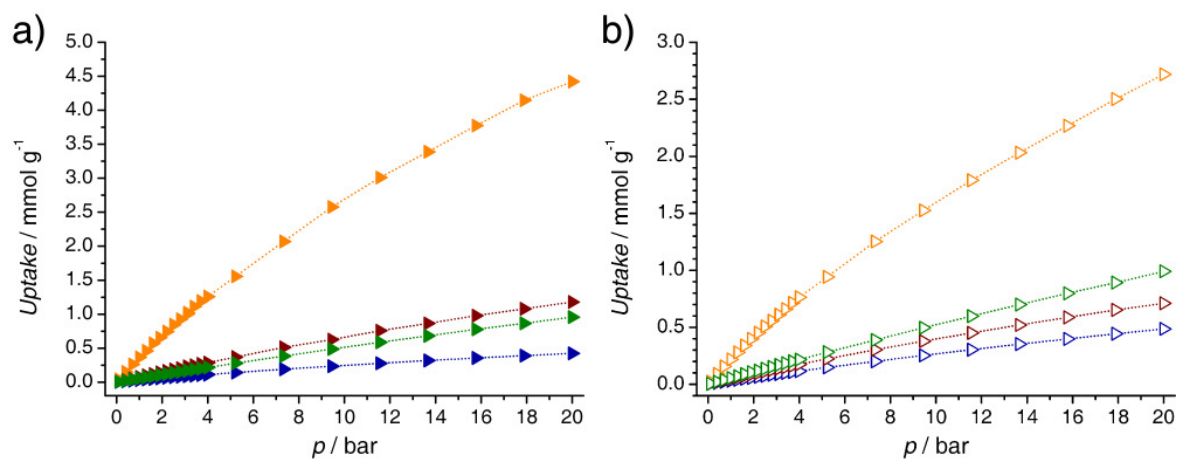
Figure A.21. Mixture isotherms obtained for $Cu_3(btc)_2$: *a)* CO/H_2 mixture. *b)* O_2/H_2 mixture. The same colour scheme as in figure A.18 is used.
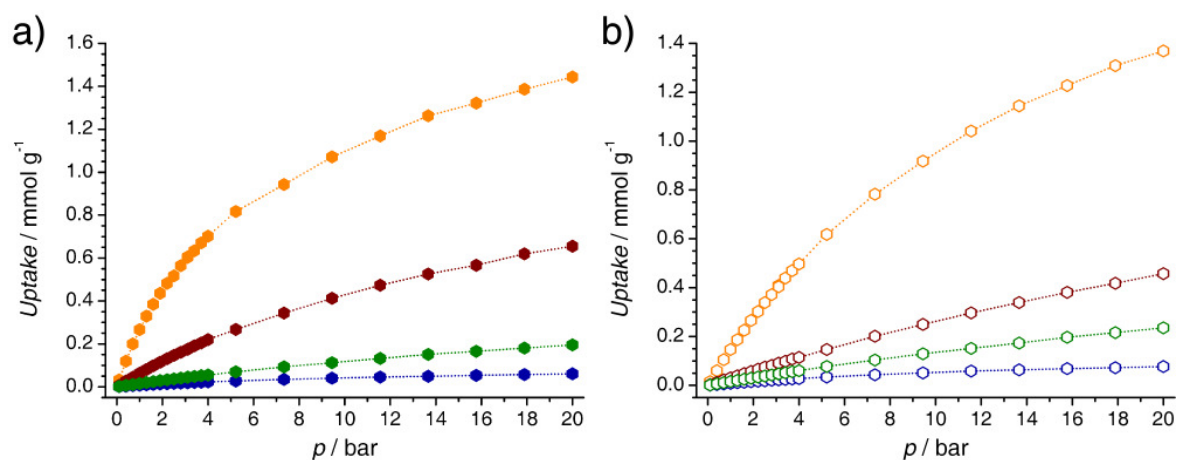
Figure A.22. Mixture isotherms obtained for cucurbit[6]uril: *a)* CO/H_2 mixture. *b)* O_2/H_2 mixture. The same colour scheme as in figure A.18 is used.

A.3.6. Section 5.4: Calculated Henry constants
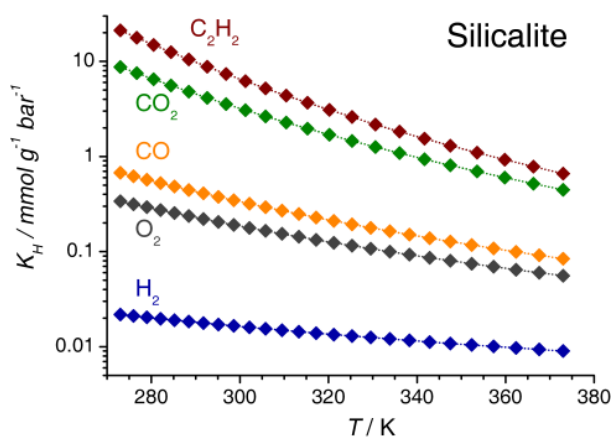
Figure A.23. Henry constants obtained for Silicalite. The values of K_H, which are displayed on a logarithmic scale, are given in molality vs. partial pressure.
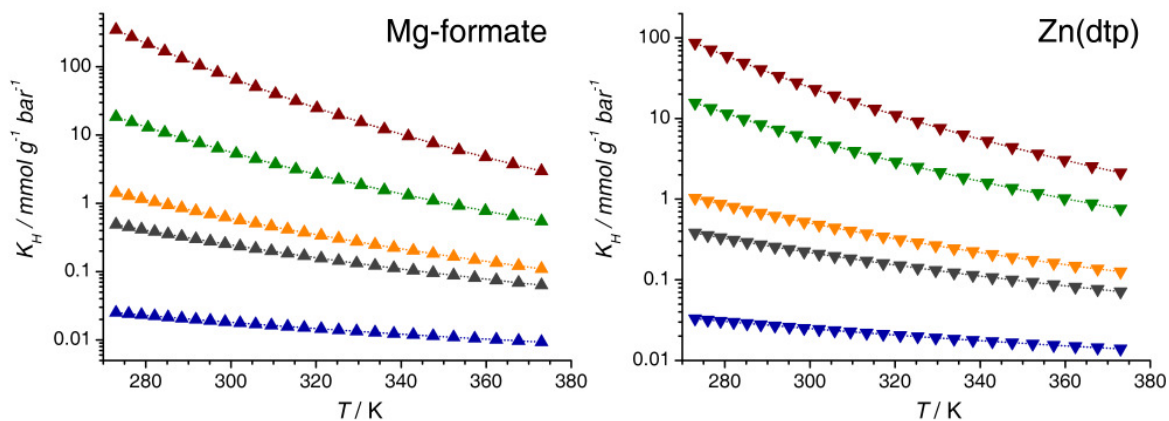
Figure A.24. Henry constants obtained for Mg-formate (left) and Zn(dtp) (right). The same colour scheme as in figure A.23 is used.
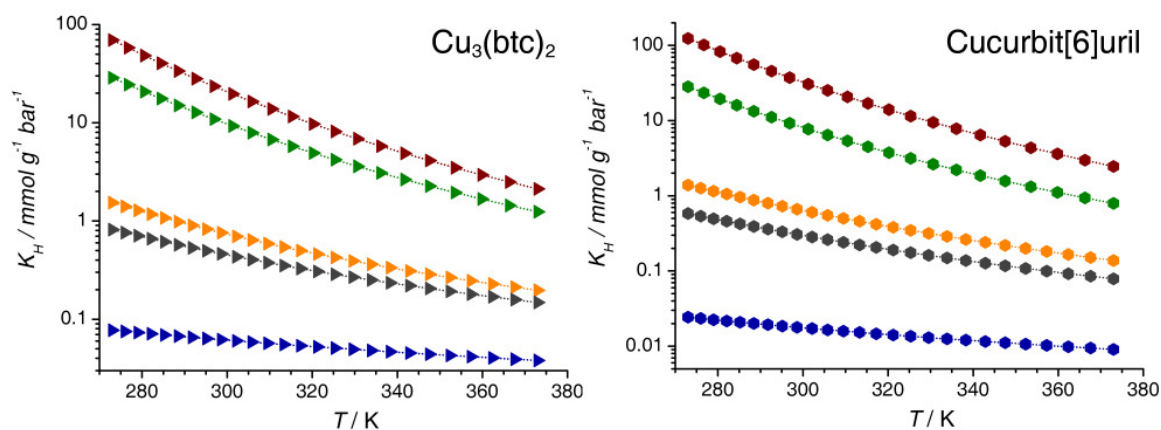
Figure A.25. Henry constants obtained for $Cu_3(btc)_2$ (left) and cucurbit[6]uril (right). The same colour scheme as in figure A.23 is used.

A.3.7. Section 5.4: Mixture isotherms with varying composition

The following figures show adsorption isotherms calculated for binary mixtures of varying composition at a total pressure of 1 bar. The x-axis corresponds to the content of the more strongly adsorbed component in relation to the total pressure. For the hydrogen-containing mixtures, the amount of hydrogen adsorbed from the CO/H_2 and O_2/H_2 mixture is virtually identical.
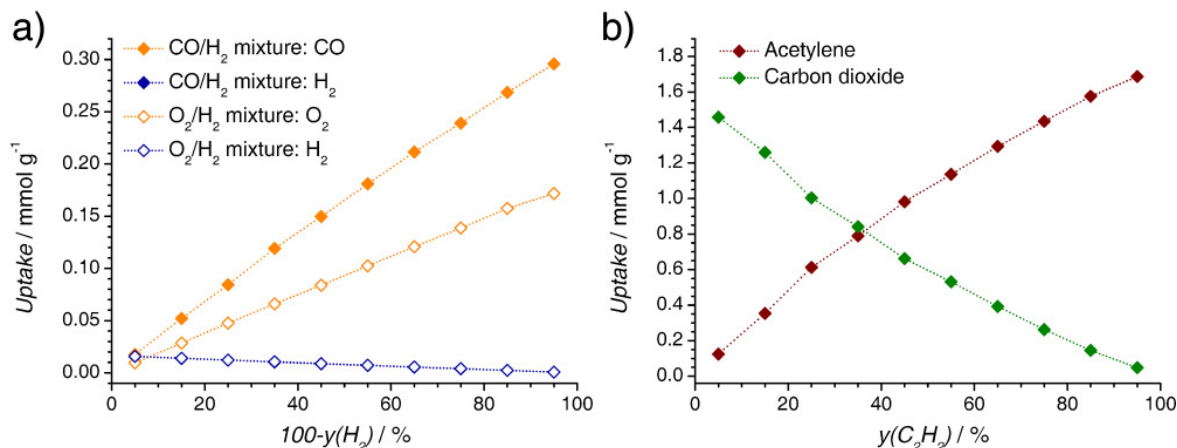
Figure A.26. Adsorption isotherms obtained for Silicalite for mixtures of varying composition, $p = 1$ bar. *a)* CO/H_2 and O_2/H_2 mixture. *b)* C_2H_2/CO_2 mixture.
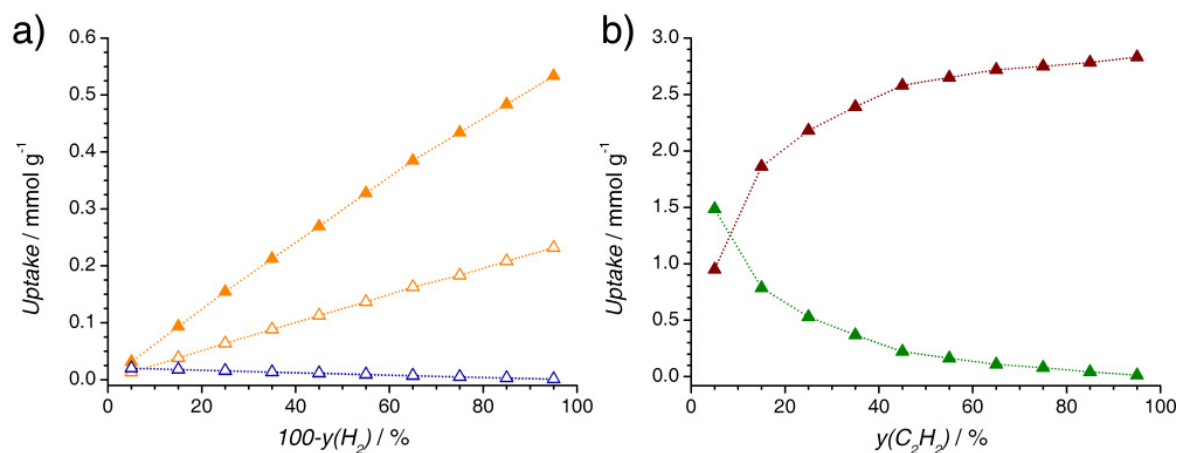
Figure A.27. Adsorption isotherms obtained for Mg-formate for mixtures of varying composition, $p = 1$ bar. *a)* CO/H_2 and O_2/H_2 mixture. *b)* C_2H_2/CO_2 mixture. The same colour schemes as in figure A.26 are used.
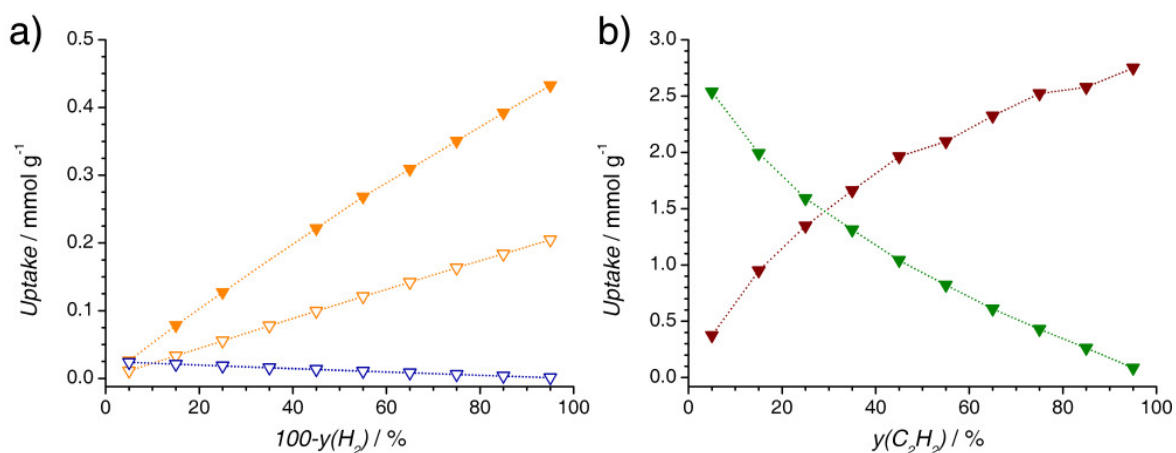
Figure A.28. Adsorption isotherms obtained for Zn(dtp) for mixtures of varying composition, $p = 1$ bar. *a)* CO/H_2 and O_2/H_2 mixture. *b)* C_2H_2/CO_2 mixture. The same colour schemes as in figure A.26 are used.
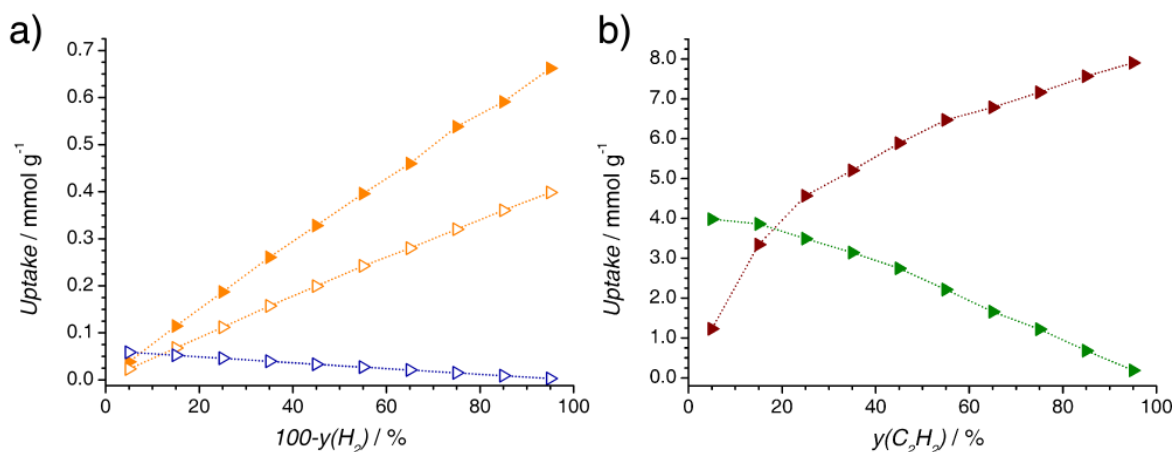
Figure A.29. Adsorption isotherms obtained for $Cu_3(btc)_2$ for mixtures of varying composition, $p = 1$ bar. *a)* CO/H_2 and O_2/H_2 mixture. *b)* C_2H_2/CO_2 mixture. The same colour schemes as in figure A.26 are used.
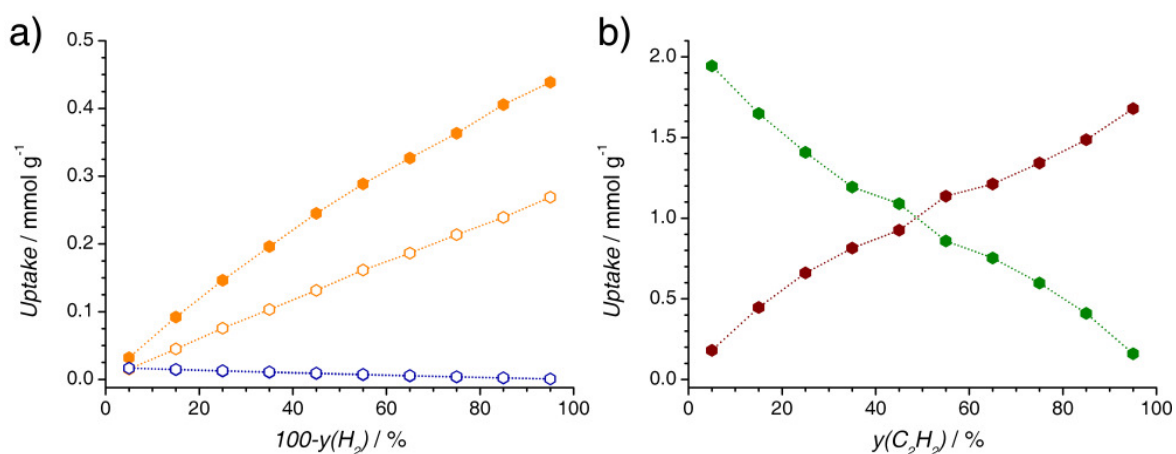
Figure A.30. Adsorption isotherms obtained for cucurbit[6]uril for mixtures of varying composition, $p = 1$ bar. *a)* CO/H_2 and O_2/H_2 mixture. *b)* C_2H_2/CO_2 mixture. The same colour schemes as in figure A.26 are used.

A.3.8. Section 5.4: Comparison of simulation results to experimental data
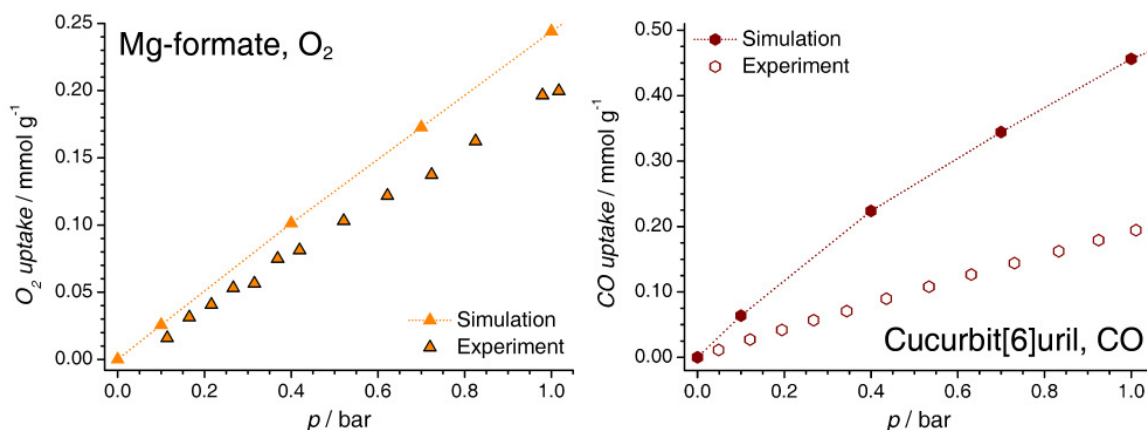
Figure A.31. Comparison of simulated low-pressure adsorption isotherms with available experimental data. *Left:* Oxygen adsorption in Mg-formate, experimental data from (*269*). *Right:* Carbon monoxide adsorption in cucurbit[6]uril, experimental data from (*324*).

A.3.9. Section 5.4: Computations for a single cucurbit[6]uril molecule

As it has been discussed in section 5.4, the accessibility of the intramolecular cavity of cucurbit[6]uril remains an unresolved issue. In an ideal structure, the cavity should be inaccessible, because the portals of each CB[6] macrocycle are blocked by adjacent molecules. However, X-ray diffraction experiments have revealed a partial occupation of the cavity by carbon dioxide molecules in CO_2-loaded samples. (*324*) In the case of acetylene, there is no such direct experimental evidence. However, some observations, such as the high heat of C_2H_2 adsorption at low coverage and the deviations between simulated and experimental isotherms, may indicate that some of the intramolecular cavities are accessible to acetylene molecules, possibly at structural defects.

To elucidate the strength of the interaction potential inside the intramolecular cavity, additional low-pressure GCMC simulations were carried out for a single CB[6] molecule placed in a supercell. The potential energy distribution for acetylene, displayed in figure A.32, shows a region of high interaction strength of nearly -60 kJ mol^{-1} at the center of the intramolecular cavity. This value is in much better correspondence with the initial experimental isosteric heat of adsorption (which ranges above 70 kJ mol^{-1}) than the highest interaction energies obtained for the periodic system with blocked cavities. For the case of carbon dioxide, the interaction potential inside the cavity amounts to approximately -40 kJ mol^{-1}, and there are additional regions of nearly equal interaction strength at the portals of the CB[6] molecule. Although the contribution of dispersive interactions is nearly identical for both species, the electrostatic contribution is almost three times higher for acetylene than for carbon dioxide, accounting for 40% of the total interaction. This can be rationalized when the different charge distributions of the molecules are taken into account. Assuming an orienta-

tion of the adsorbed species parallel to the hexagonal axis of the CB[6] molecule, there will be an attractive electrostatic interaction between the positively polarized hydrogen atoms of the acetylene molecule and the negatively polarized carbonyl groups surrounding the portals of the cavity. In contrast to this, the electrostatic interactions between the oxygen atoms of the CO_2 molecule and the portals are repulsive.

While the actual accessibility of the intramolecular cavities cannot be clarified in the context of this study, the results from the calculations for an isolated CB[6] molecule show that acetylene is strongly favoured over carbon dioxide inside these cavities. Therefore, a high C_2H_2/CO_2 selectivity can be expected for hypothetical systems with accessible intramolecular cavities. (*330*)
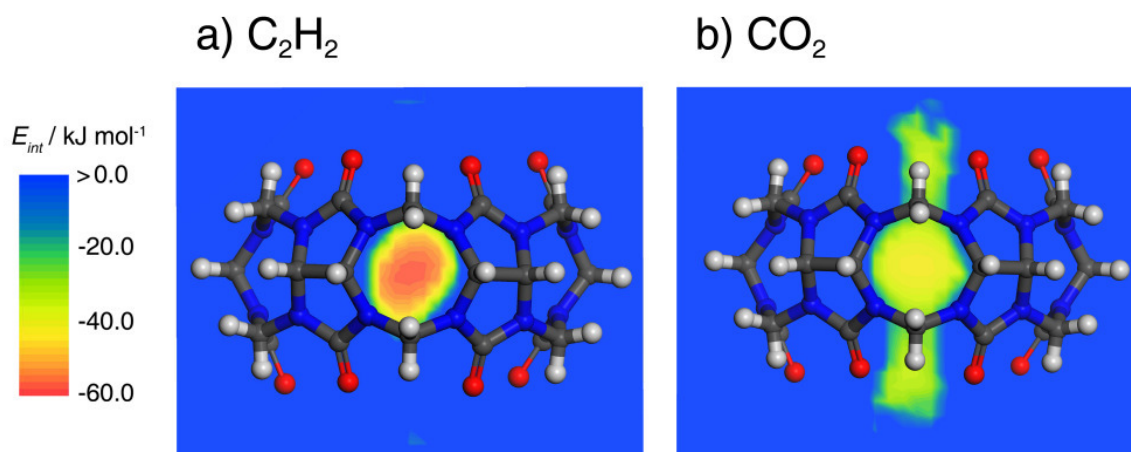
Figure A.32. Potential energy maps derived from simulations of acetylene and carbon dioxide adsorption for a system consisting of an isolated CB[6] molecule in a supercell.

A.4. Thermophysical properties of fluid systems
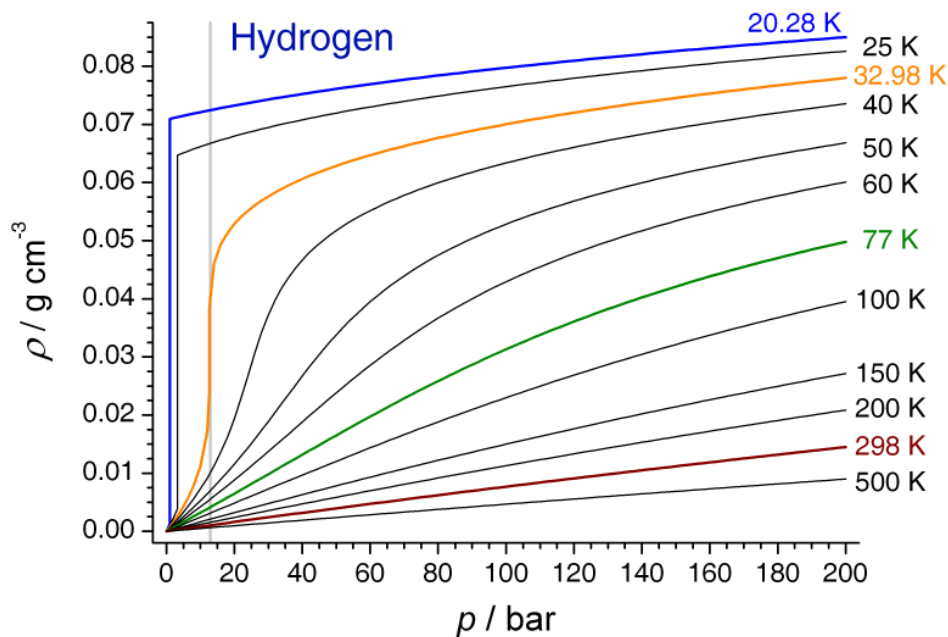
Figure A.33. Isothermal properties of hydrogen, taken from (*232*). The blue curve corresponds to the normal boiling temperature, the orange curve designates the critical temperature, and the green and dark red curves correspond to the temperatures for which the calculations reported in this work were performed. The critical pressure is shown as a thin grey line.
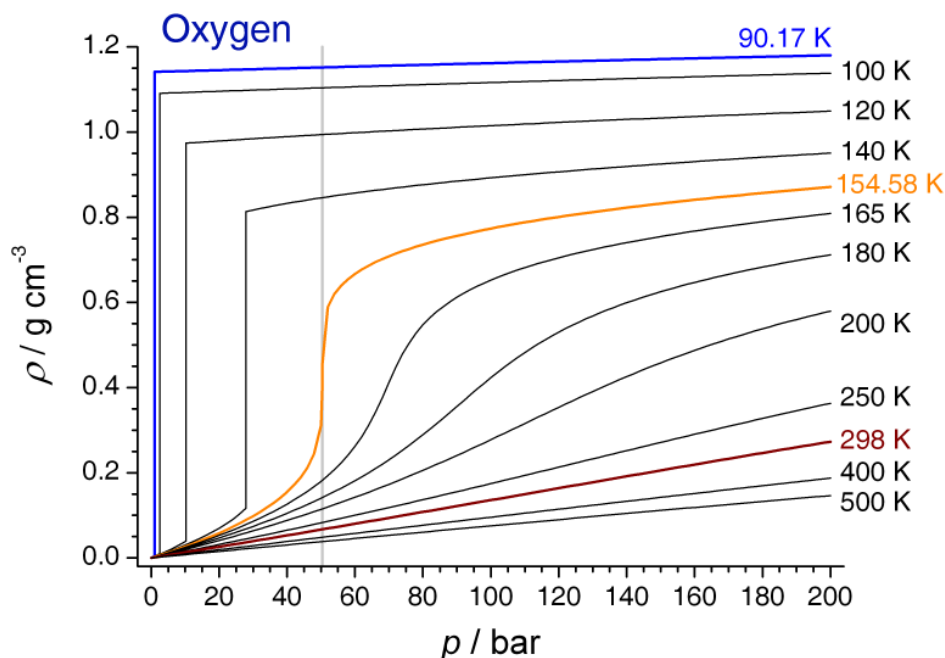
Figure A.34. Isothermal properties of oxygen, taken from (*232*). The blue curve corresponds to the normal boiling temperature, the orange curve designates the critical temperature, and the dark red curve corresponds to the temperature for which the calculations reported in this work were performed. The critical pressure is shown as a thin grey line.
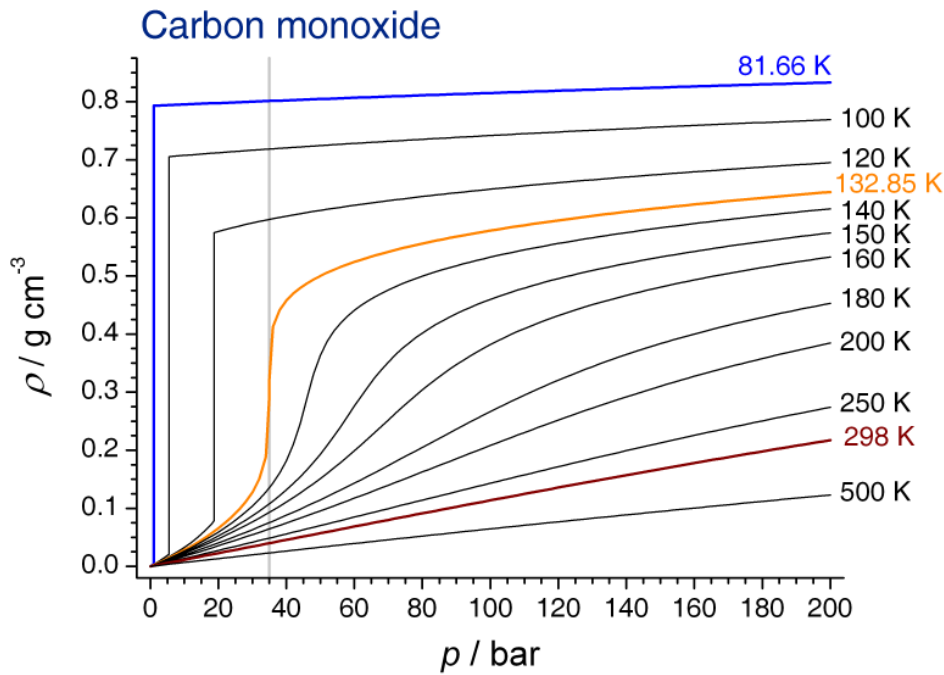
Figure A.35. Isothermal properties of carbon monoxide, taken from (*232*). The blue curve corresponds to the normal boiling temperature, the orange curve designates the critical temperature, and the dark red curve corresponds to the temperature for which the calculations reported in this work were performed. The critical pressure is shown as a thin grey line.
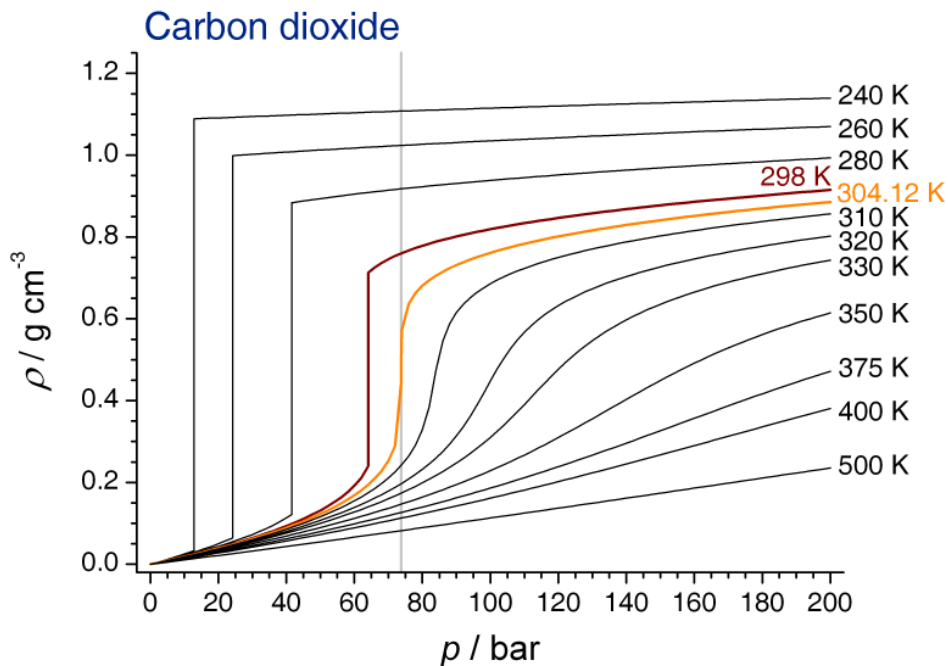
Figure A.36. Isothermal properties of carbon dioxide, taken from (*232*). The orange curve designates the critical temperature, and the dark red curve corresponds to the temperature for which the calculations reported in this work were performed. The critical pressure is shown as a thin grey line. The normal boiling temperature is not defined in this case, because carbon dioxide sublimes at $T = 195\,\text{K}$ and ambient pressure.

287

Gefahrenmerkmale und Sicherheitsratschläge

Im Rahmen der vorliegenden Arbeit wurden keine Gefahrstoffe im Sinne der Gefahrstoffverordnung verwendet. Die Angabe von Gefahrenmerkmalen und Sicherheitsratschlägen entfällt daher.